UNIVERSITÀ DEGLI STUDI DI TRIESTE
e
UNIVERSITÀ CA' FOSCARI DI VENEZIA

XXXIII CICLO DEL DOTTORATO DI RICERCA IN _____CHIMICA_____

PO FRIULI VENEZIA GIULIA - FONDO SOCIALE EUROPEO 2014/2020

THE ENDLESS POSSIBILITIES OF RUTHENIUM-DMSO PRECURSORS IN MODERN COORDINATION CHEMISTRY: FROM NOVEL METALLACYCLES OF PORPHYRINS TO NEW ROUTES TO HETEROLEPTIC POLYPYRIDYL COMPOUNDS

Settore scientifico-disciplinare: **CHIM/03**

DOTTORANDO
ALESSIO VIDAL

COORDINATORE
PROF. ENZO ALESSIO

SUPERVISORE DI TESI
PROF. ENZO ALESSIO

ANNO ACCADEMICO 2019/2020

TABLE OF CONTENTS

Abstract

The research carried out during this Ph.D. project and reported in this Thesis is focused on the design, preparation and characterization of different supramolecular porphyrin systems, both metallacyclic and polymeric.

Chapter 1 contains a general introduction on the key role of porphyrins as functional and structural building units for the assembly of artificial discrete supramolecular structures, together with the main designing concepts of the metal-mediated assembly.

Chapter 2 is focused on the investigation of the reactivity of the two stereoisomers [*cis,cis,cis*-$RuCl_2(CO)_2$(dmso-*O*)(dmso-*S*)] and [*cis,cis,trans*-$RuCl_2(CO)_2$(dmso-*S*)$_2$] towards 4′*cis*DPyP. The complexes were first tested toward the model ligand 4′MPyP and then 4′*cis*DPyP obtaining, besides the already known 2+2 metallacycle of porphyrins [*trans,cis,cis*-$RuCl_2(CO)_2$(4′*cis*DPyP)]$_2$, the chiral stereoisomeric metallacycles [{*trans,cis,cis*-$RuCl_2(CO)_2$}(4′*cis*DPyP)$_2${*cis,cis,cis*-$RuCl_2(CO)_2$}] and [*cis,cis,cis*-$RuCl_2(CO)_2$(4′*cis*DPyP)]$_2$, in which the chiral {*cis,cis,cis*-$RuCl_2(CO)_2$} fragment has either a *C* or *A* handedness.

In Chapter 3 a synthetic strategy for the expansion of porphyrin metallacycles is described. This strategy afforded triporphyrin arrays that, after metalation, might lead to more stable supramolecular assemblies. Furthermore, we also synthesized heteroleptic metallacycles containing different porphyrins (i.e. 3′ and 4′-pyridylporphyrins) that have unprecedented geometries (i.e. vase, ladder, zig-zag).

During my three years of Ph.D. I have also been involved in other projects involving Ru(II)-dmso complexes, in particular:

In Chapter 4 we demonstrate that ruthenation of a porphyrin can be performed under relatively mild conditions using the Ru(II) monocarbonyl complex $[Ru(CO)(dmso)_5][PF_6]_2$ that – besides CO – features exclusively labile dmso ligands. Even though this finding might seem trivial, it is only the second example that uses a Ru(II) carbonyl for porphyrin ruthenation, the first one having been reported almost 50 years ago and then neglected. From a practical point of view, we show the spectacular effect of propionic acid as solvent for performing the ruthenation of neutral and anionic model porphyrins with $Ru_3(CO)_{12}$.

The Ru(CO)-porphyrins were then exploited, in Chapter 5 to prepare Ru/Zn porphyrin polymeric networks. In particular we demonstrate that PTA (1,3,5-triaza-7-phosphaadamantane) behaves as an orthogonal ligand between Ru(II) and Zn(II), since it selectively binds through the P atom to ruthenium and through one or more of the N atoms to zinc. This property of PTA was exploited for preparing the two monomeric porphyrin adducts with axially bound PTA, [Ru(TPP)(PTA-κ*P*)$_2$] and

[Zn(TPP)(PTA-κ*N*)]. Next, we prepared a number of heterobimetallic Ru/Zn porphyrin polymeric networks — and two discrete molecular systems — mediated by *P,N*-bridging PTA in which either both metals reside inside a porphyrin core, or one metal belongs to a porphyrin, either Ru(TPP) or Zn(TPP), and the other to a complex or salt of the complementary metal.

Chapter 6 reports a new two-step strategy for the synthesis of bis-heteroleptic Ru(II) polypyridyl compounds of general formula $[Ru(chel)_2(chel')]^{2+}$, where chel is a chelating dimmine ligand, starting from *cis*-locked Ru(II) precursors. These were synthesized by replacing either the two chlorides, or a chloride and a dmso, from the [*cis*-$RuCl_2(dmso)_4$] complex with an inert chelating anion (O–O) (i.e. malonate, oxalate, acetylacetonate). This allowed us to have more control in the coordination of the first ligand (chel), decreasing the formation of stereoisomeric mixtures. The acid-sensitive nature of the chelating anion allows its acid-assisted substitution with the second ligand chel′ even at room temperature.

Riassunto

La ricerca svolta durante questo dottorato di ricerca. e riportata in questa Tesi è incentrata sulla progettazione, preparazione e caratterizzazione di diversi sistemi porfirinici supramolecolari, sia metallaciclici che polimerici.

Il Capitolo 1 contiene un'introduzione generale sul ruolo chiave delle porfirine come *building block* funzionali e strutturali per l'assemblaggio di strutture supramolecolari discrete, insieme ai principali concetti del *metal-mediated assembly*.

Il Capitolo 2 è incentrato sullo studio della reattività dei due stereoisomeri [*cis,cis,cis*-$RuCl_2(CO)_2$(dmso-*O*)(dmso-*S*)] e [*cis,cis,trans*-$RuCl_2(CO)_2$(dmso-*S*)$_2$] verso la 4′*cis*DPyP. I complessi sono stati prima testati sul legante modello 4′MPyP e successivamente utilizzando la 4′*cis*DPyP ottenendo, oltre al già noto metallaciclo porfirinico 2+2 [*trans,cis,cis*-$RuCl_2(CO)_2$(4′*cis*DPyP)]$_2$, anche i due relativi stereoisomeri chirali [{*trans,cis,cis*-$RuCl_2(CO)_2$}(4′*cis*DPyP)$_2${*cis,cis,cis*-$RuCl_2(CO)_2$}] e [*cis,cis,cis*-$RuCl_2(CO)_2$(4′*cis*DPyP)], in cui il frammento {*cis,cis,cis*-$RuCl_2(CO)_2$} può avere chiralità C o A.

Nel Capitolo 3 viene descritta una strategia sintetica che permette di ottenere metallacicli porfirinici più estesi. Questa strategia ha permesso di ottenere sistemi triporfirinici, che, dopo metallazione, potrebbero portare a formare assemblati supramolecolari più stabili. Inoltre, sono anche stati sintetizzati metallacicli eterolettici contenenti porfirine diverse (i.e. 3 ′ e 4′-piridilporfirine) e aventi diversi tipi di geometrie (vaso, scala, zig-zag).

Durante i miei tre anni di dottorato di ricerca sono stato anche coinvolto in altri progetti che coinvolgono complessi Ru (II)-dmso, in particolare:

Nel Capitolo 4 è stato dimostrato che la rutenazione di una porfirina può essere eseguita in condizioni relativamente blande utilizzando il complesso monocarbonilico di Ru(II) $[Ru(CO)(dmso)_5][PF_6]_2$ che - oltre al CO - presenta esclusivamente leganti labili. Questo è solo il secondo esempio di utilizzo di un complesso carbonilico di Ru(II) per la rutenazione di una porfirina, dopo il primo riportato quasi 50 anni fa e poi dimenticato. Da un punto di vista pratico, si mostra il sorprendente effetto dell'acido propionico come solvente per eseguire la rutenazione di porfirine modello neutre e anioniche utilizzano il cluster $Ru_3(CO)_{12}$.

Le Ru(CO)-porfirine sono state poi sfruttate, nel Capitolo 5, per preparare network polimerici di Ru/Zn porfirine. In particolare, è stato dimostrato che il PTA (1,3,5-triaza-7-fosfadamamantano) si comporta come un legante ortogonale tra Ru (II) e Zn (II), poiché si lega selettivamente attraverso l'atomo di P al rutenio e attraverso uno o più degli atomi di N allo zinco. Questa proprietà del PTA è stata sfruttata per preparare due addotti porfirinici monomerici aventi un PTA legato assialmente,

Ru(TPP)(PTA-κ*P*)$_2$] e [Zn(TPP)(PTA-κ*N*)]. Successivamente, sono stati preparati una serie di network polimerici di Ru /Zn porfirine eterobimetallici - e due sistemi molecolari discreti - mediati da PTA in cui entrambi i metalli risiedono all'interno di uno dei centri porfirinici, o un metallo appartiene a una porfirina, o Ru (TPP) o Zn (TPP), e l'altro a un complesso o sale dell'altro metallo.
Il Capitolo 6 riporta una nuova strategia a stadi, per la sintesi di composti polipiridilici bis-eterolettici di Ru (II) di formula generale [Ru (chel)$_2$(chel′))]$^{2+}$, dove chel è un legante chelante dimminico, a partire da precursori di Ru(II) *cis* bloccati. Questi sono stati sintetizzati sostituendo i due cloruri, o un cloruro e un dmso, dal complesso [*cis*-RuCl$_2$(dmso)$_4$] con un anione chelante inerte (O – O) (malonato, ossalato, acetilacetonato). Questo permette di avere un maggior controllo nella coordinazione del primo legante (chel), diminuendo la formazione di miscele stereoisomeriche. La sensibilità all'ambiente acido dell'anione chelante ne permette la sostituzione con un secondo legante anche a temperatura ambiente.

CHAPTER 1

1. Introduction

1.1 Metal-mediated self-assembly

Self-assembly is an equilibrium between two or more molecular components to create a more complex entity with a structure that depends only on the intrinsic information contained within the starting materials, termed *building blocks*. Among the different approaches that can be exploited to guide the self-assembling process, the metal-mediated directional-bonding has emerged over the years as a general, high yielding synthetic strategy that gives access to a variety of 2D (rhomboids, squares, rectangles, triangles, etc.) and 3D (trigonal pyramids and prisms, cubes, cuboctahedra, double squares, adamantanoids, dodecahedra, and a variety of other cages) supramolecular ensembles. One of the most attractive characteristics of this approach is that the design of supramolecular structures can be guided by geometrical considerations relying on the highly directional and predictable nature of the metal coordination sphere and the geometry of the donor sites of the rigid organic fragments. Transition metals, with their preferred coordination geometries, have served as Lewis-acid acceptor units, both as naked ions or as metal fragments (*i.e.* bearing some inert ancillary ligands in their coordination sphere), with various rigid or flexible Lewis-base donors to self-assemble into larger and predictable architectures, based on the geometrical codifications of the acceptor and donor units (Figure 1.1).

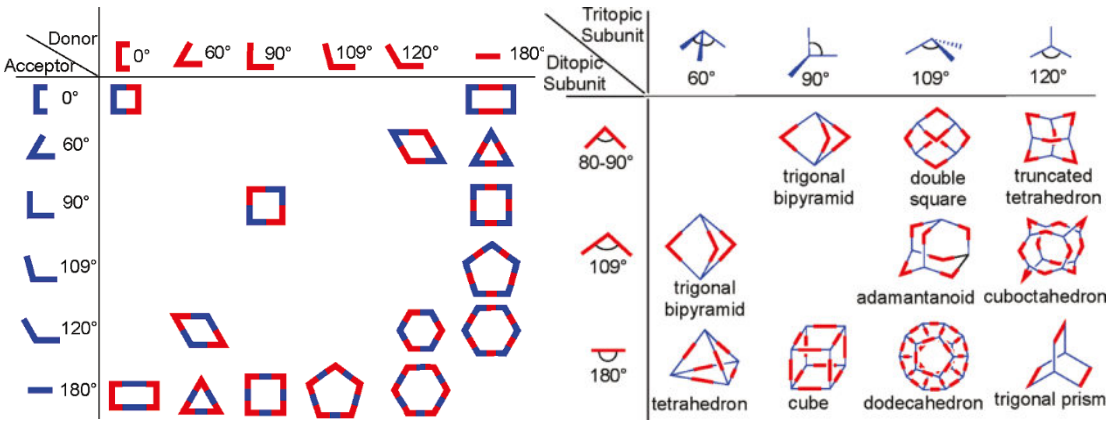

Figure 1.1. Combination of various complementary metal acceptor/ donor building blocks

1.2 Porphyrins as building blocks

Porphyrins are a group of ubiquitous tetrapyrrole compounds; they accomplish different purposes in nature, including light-harvesting, oxygen transport, and catalytic transformations.[1–4]

They have a large planar aromatic surface with a small difference in energy between the HOMO and the LUMO orbitals resulting in an intense absorption band in the visible region between 400-450 nm called Soret band (ε ~10^5 $M^{-1}cm^{-1}$) accompanied by others of lower intensity at higher wavelengths (Q bands), whose number depends on the symmetry of the porphyrin.

Furthermore, they also have rather long fluorescence decay times and interesting redox properties, features that can be fine-tuned by functionalization with appropriate moieties the porphyrin skeleton both on the *β* and *meso* positions.

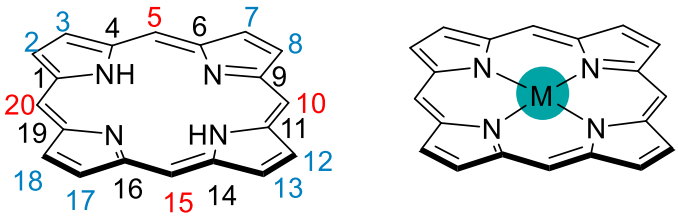

Figure 1.2. Left: general structure of a porphyrin with indicated the α (black), β (blue) and *meso* (red) positions. Right: general structure of a metalloporphyrin, with M that can be a variety of metal cations, e.g. Zn(II)

The functionalization can also vary the solubility; the introduction of alkyl chains increases the solubility in organic solvents (i.e. halogenated solvents), while the introduction of charged or polar groups favors, as expected, the solubility in more polar solvents (i.e. CH_3OH, H_2O) and the introduction of bulky groups can prevent stacking in solution.

Nucleophilic groups (i.e. pyridyl, aminic groups) allow their coordination to metals; on the contrary, the possibility to introduce a metal inside the porphyrin ring allows the porphyrin to act as a Lewis Acceptor.

A plethora of different metals can be introduced, ranging from *soft* metals such as Zn(II) to *hard* metals such as Fe(II) or Sn(IV), affecting both the redox potentials and the catalytic features of the porphyrin.

According to the number of free coordination sites still available on the metal and its *hard*/*soft* nature, a series of different ligands can be coordinated. In particular *soft* metals in low oxidation states such as Zn(II) prefer P or N-ligands leading, usually, to five-coordinate square pyramidal complexes, while *hard* metals such as Co, and Fe prefer oxygen ligands such as carboxylic groups.

For all these reasons, they are unique and versatile building blocks for metal-mediated assemblies since they can perform at the same time a structural (acting as donor, acceptor, or both) and a functional role.

One particular class of porphyrin exploited for self-assembly purposes is that of the *meso-pyridyl/phenyl* porphyrins (**PyPs**); they carry a number (n = 1–4) of pyridyl substituents at the *meso*

positions, with the remaining 4-n positions occupied by aryl groups, the nitrogen atom usually is either in 3′ or in the 4′ position.

In the 4′PyPs, the coordination bonds are established in the porphyrin plane along the *meso* C–C bond axes; on the other hand, the pyridyl rings in the 3′PyPs lay ca. perpendicular to the macrocycle plane and the coordination bonds are directed above or below the plane of the porphyrin.

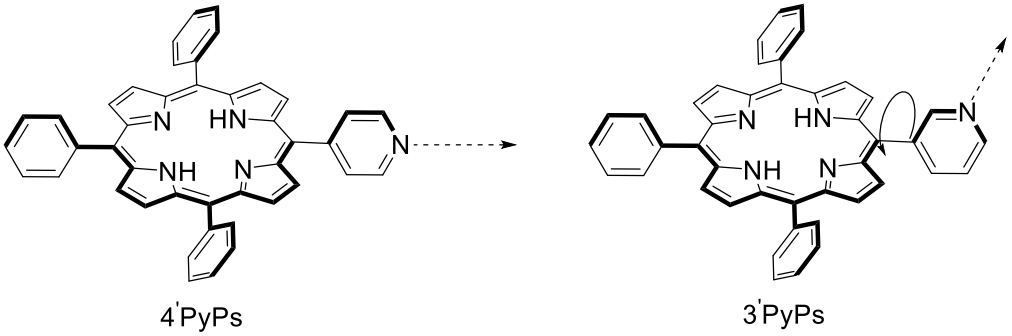

Figure 1.3. Coordination bonds established by 4′PyPs (left) and 3′PyPs (right).

By suitably combining *meso*-pyridylphenylporphyrins and/or their metal derivatives with naked ions or suitable metal fragments, various 2D and 3D discrete or polymeric supramolecular structures have been obtained with even very complex architectures.[5–14] These systems have been the object of study, especially their chemical, electronic, photophysical and photocatalytic properties.

The design of molecular 3D systems including porphyrins as host structural units are indeed very attractive: porphyrin, as a large structural element, will delineate the molecular cavity and usually produce a considerably hydrophobic inner environment; the large π-delocalized surface may establish constructive interactions with other π-conjugated guest molecules or with protons of aliphatic chains of guests. Furthermore, metalloporphyrin structural units may use the inner metals as guest binders and as catalyst for the transformation of bound substrates.

1.3 Modular self-assembling approach for the synthesis of multiporphyrin structures

The construction of assemblies requires that porphyrins featuring peripheral binding sites are treated with appropriate metal precursors with two or more labile ligands. The large majority of examples concern homoleptic systems of the type $M_x(porp)_y$, i.e., composed by a single porphyrin (porp) and a single metal connector (M). Among the 2D structures, several examples of 2+2 and 4+4 metallacycles (i.e., molecular squares) have been reported, in which linear or 90°-angular porphyrins are connected by metal centers, typically either square-planar Pd(II) or Pt(II) fragments with *cis* or *trans* geometry, or octahedral *cis*-protected Ru(II), Re(I) or Rh(II) moieties.[5]

Conversely, two main types of homoleptic 3D porphyrin capsules have been reported: (*i*) trigonal and hexagonal prisms obtained from the self-assembly of either 3′TPyP (5,10,15,20-tetra(3′-pyridyl)porphyrin) or 4′TPyP (5,10,15,20-tetra(4′-pyridyl)porphyrin), respectively, with *cis*-protected square planar Pd(II) or Pt(II) connectors;[15–17] (*ii*) tetrahedral $M_4(porp)_6$, cubic $M_8(porp)_6$, and cuboctahedral $M_{12}(porp)_6$ cages obtained by the self-assembly of porphyrins functionalized with two or four peripheral chelating units with naked octahedral metal ions (e.g., Fe(II), Co(II), Zn(II)).[18–20]

The group in which the current project was developed introduced a modular strategy to obtain multiporphyrin 3D discrete systems.[21–24]

In particular, it has widely used the Ru(II) complex [*trans,cis,cis*-$RuCl_2(CO)_2$(dmso-κ*O*)$_2$] (**1**), which has a good affinity towards N-donor ligands such as pyridines, it has an octahedral geometry and is able to selectively replace the two particularly labile dmso-κ*O* ligands at room temperature without undergoing geometry variations. Therefore **1** can be considered as the precursor of the 90° *cis*-protected neutral metal fragment {*trans,cis,cis*-$RuCl_2(CO)_2$}.

When treated with a stoichiometric amount of 4′-*cis*dipyridylporphyrin (4′*cis*DPyP) it affords in good yield, after column separation, the corresponding neutral 2+2 metallacycle (or molecular square) [*trans,cis,cis*-$RuCl_2(CO)_2$(4′*cis*DPyP)]$_2$ (**2**), in which two adjacent porphyrins are connected through two {*trans,cis,cis*-$RuCl_2(CO)_2$} fragments The metallacycle, is perfectly symmetrical, rigid, kinetically inert, and thermodynamically stable, allowing for subsequent tailoring to construct higher-order porphyrin assemblies.

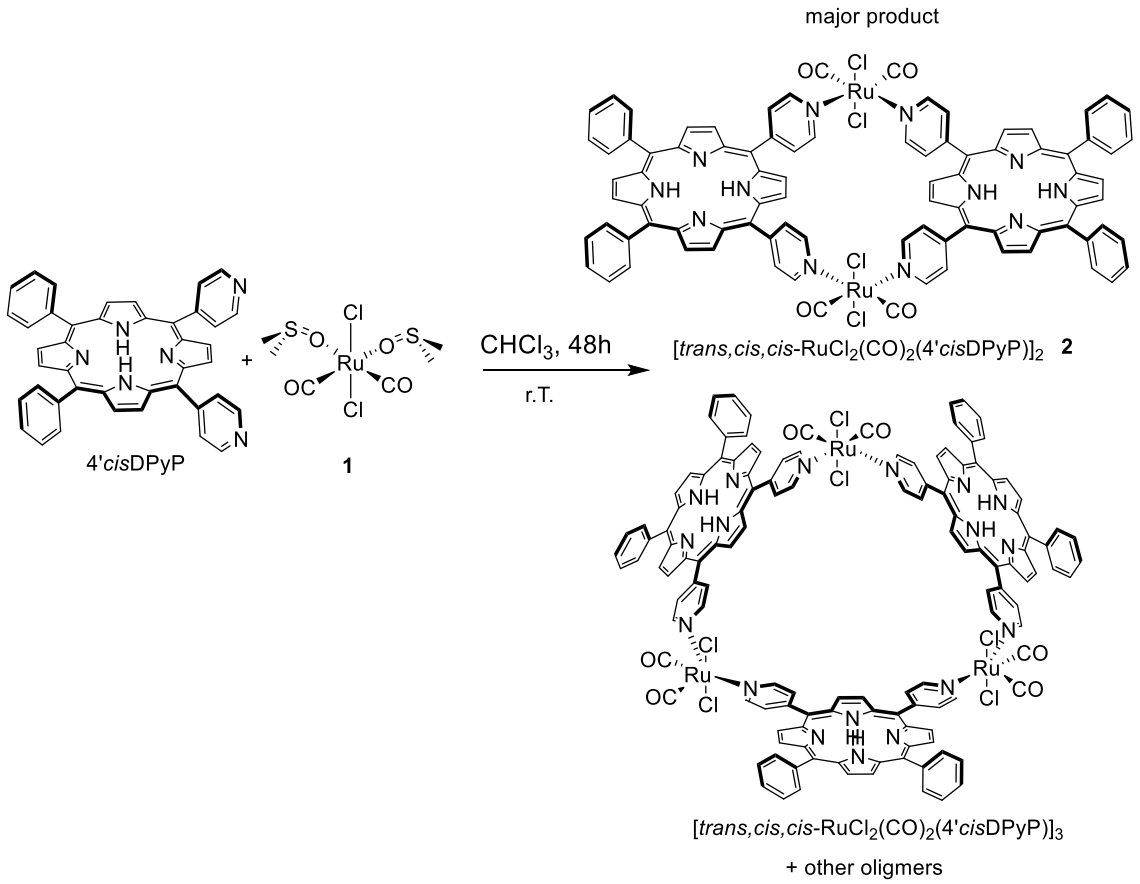

Scheme 1.1. Synthesis of [*trans,cis,cis*-$RuCl_2(CO)_2$(4′*cis*DPyP)]$_2$ (**2**) and [*trans,cis,cis*-$RuCl_2(CO)_2$(4′*cis*DPyP)]$_3$ from 4′*cis*DPyP and **1** in a 1:1 ratio.

Despite the geometrical directional constraints provided by the high convergence of the building blocks acceptor and donor sites, the reaction leads to the concomitant formations of other metalacyclic species. The second most abundant cyclic product is the metallacycle [*trans,cis,cis*-$RuCl_2(CO)_2$(4′*cis*DPyP)]$_3$, in which three 4′*cis*DPyP are held together in a not coplanar mutual and strained disposition by three {*trans,cis,cis*-$RuCl_2(CO)_2$} fragments.

Similarly, the same complex **1** can be treated with one equivalent of 3′*cis*DPyP, obtaining the equivalent 2+2 metallacycle [*trans,cis,cis*-$RuCl_2(CO)_2$(3′*cis*DPyP)]$_2$.

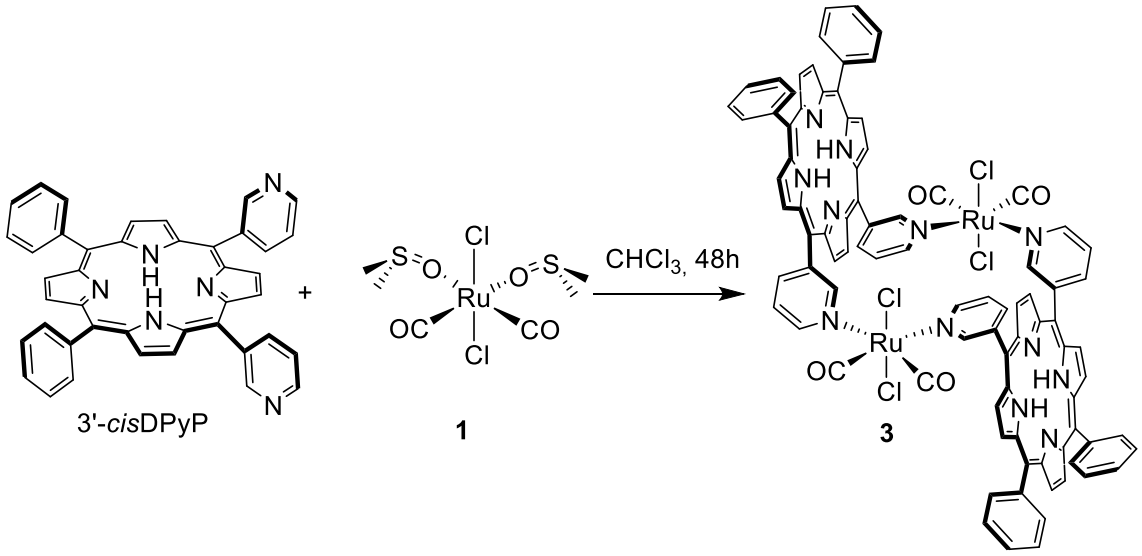

Scheme 1.2. Synthesis of the [*trans,cis,cis*-$RuCl_2(CO)_2$(3′*cis*DPyP)]$_2$ (**3**) from 3'*cis*DPyP and **1** in a 1:1 ratio**.**

Both metallacycles **2** and **3** can be treated with an excess of zinc acetate in $CHCl_3$/MeOH, to isolate in good yield the corresponding zincated species of formula [*trans,cis,cis*-$RuCl_2(CO)_2$(Zn· 4′*cis*DPyP)]$_2$, (**2Zn**) (Scheme 1.3) and [*trans,cis,cis*-$RuCl_2(CO)_2$ (Zn· 3′*cis*DPyP)]$_2$ (**3Zn**) respectively.

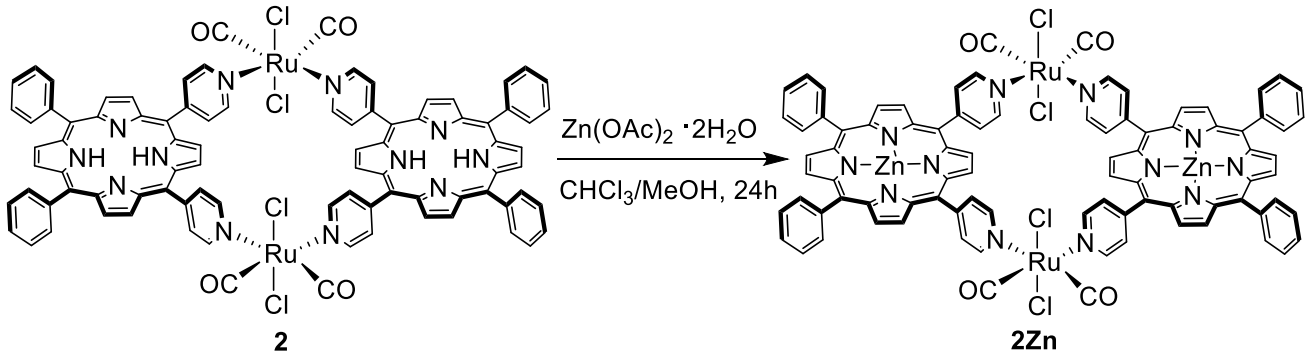

Scheme 1.3. Synthesis of the zincated metallacycle [*trans,cis,cis*-$RuCl_2(CO)_2$(Zn·4′*cis*DPyP)]$_2$ (**2Zn**).

It is known from X-ray structures that the geometry of the **2Zn** metallacycle is perfectly flat and the distances Ru···Ru and Zn···Zn are respectively 14.01 Å and 14.03 Å (Figure 1.4).

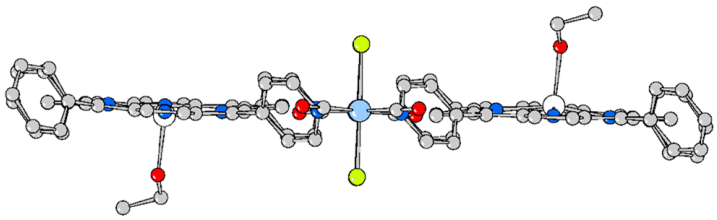

Figure 1.4. X-ray structure of the of **2Zn**, the apical EtOH molecules derive from the crystallization process. Color code: Ru (light blue), Cl (green), O (red), N (blue).

Contrary to **2Zn**, **3Zn** has a staggered geometry with the two chromophores rigidly held in a slipped-cofacial arrangement (interplanar distance 4.18 Å) by the Ru(II) fragment.[11] This geometry derives from the *sin* orientation of both 3′pyridyl rings in each porphyrin and the NMR spectra indicate that this is also maintained in solution.

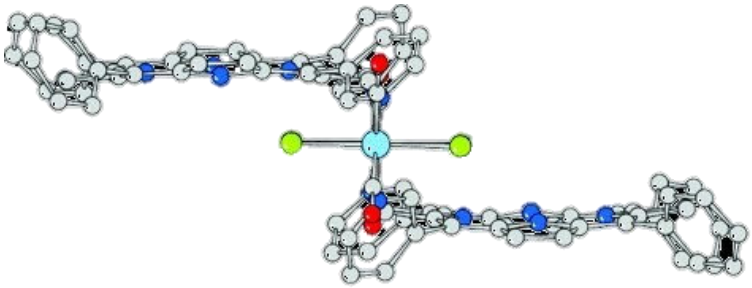

Figure 1.5. X-ray structure of **3Zn** seen along the Ru–CO bond.

Therefore, the metallacycles **2Zn** and **3Zn** can be conveniently described as a flat and a staggered panel, respectively, with two embedded metal connectors (the two zinc atoms). Combining platform **2Zn,** but also **3Zn,** with appropriate different polytopic nitrogen-ligands allows to very efficiently and quantitatively produce a wide variety of multiporphyrin 3D discrete structures, consisting of two up to four porphyrin metallacycles connected face-to-face through the bridging ligands, axially bound to the zinc centers.

As unambiguously evidenced by NMR spectroscopy, treatment of both **2Zn** and **3Zn** in $CDCl_3$ solution with one equivalent of a linear ditopic N-ligand (L) leads rapidly to the quantitative assembling of sandwich-like 2:2 supramolecular adducts of formula [**2Zn/3Zn**·L]$_2$ (L = 4,4′-bipyridine; L = 5,15-(4′-pyridyl)-10,20-phenylporphyrin (4′*trans*DPyP)), formed by two parallel metallacycles connected by two bridging ligands which are axially bound to the zinc-porphyrins.[25] This type of modular assembling is made possible by virtue of Ru–pyridyl bonds' thermodynamic and kinetic stability (as noted above), which allows for the further ligation of other N ligands to the zinc atoms, while the metallacycle **2Zn/3Zn** remains intact.

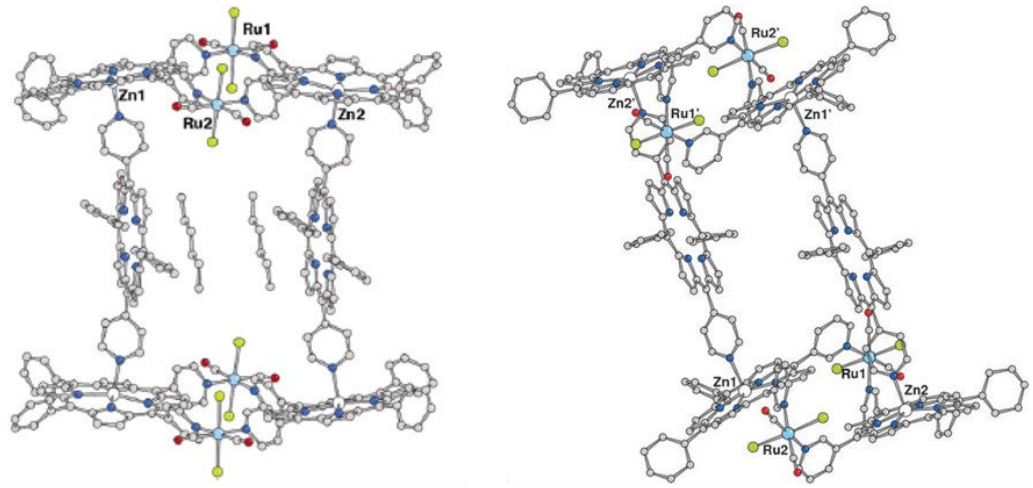

[(**2Zn**)$_2$(4'-*trans*DPyP)$_2$] [(**3Zn**)$_2$(4'-*trans*DPyP)$_2$]

Figure 1.6. Single crystal X-ray structures of [(**2Zn**)$_2$·(4′*trans*DPyP)$_2$] and [(**3Zn**)$_2$·(4′*trans*DPyP)$_2$].

Other types of structures such as cages, prisms and sandwiches compounds have been developed by changing the nature of the bridging ligand; Figure 1.7 shows some examples of 3D structures obtained.

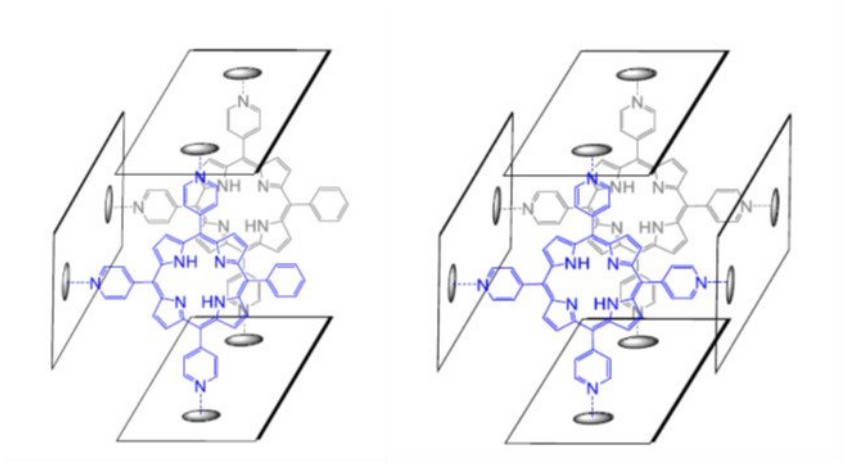

Figure 1.7. Examples of 3D architectures obtained using the **2Zn** panel in combination with other N-donor polytopic ligands (specifically, pyridylporphyrins).

However, the single Zn–N axial bond is neither particularly strong nor inert. For instance, the interaction between the Zn·TPP model porphyrin (TPP = *meso*-tetraphenylporphyrin) and pyridine (py) leads to the formation of the [Zn(TPP)(py)] adduct. This is in equilibrium with its components through a constant of the order of 10^3 M^{-1} and, at room temperature, the equilibrium is fast on the NMR time scale, therefore in the ^{1}H NMR spectrum of a titration of ZnTPP with py only a single set of enlarged signals is visible.[26] However, using the **2Zn** or **3Zn** molecular panels the cooperativity between the axial bonds formed by the Zn atoms allows to obtain more stable and inert 3D

supramolecular structures. For example, in chloroform solution, molecular sandwiches like the one in Figure 1.7 with four axial Zn–N bonds, are stable up to dilutions of the order of 10^{-5} M and the association/dissociation equilibrium of the panels becomes slow on the NMR time scale around 20°C, and for other ligands already at room temperature.

These systems still tend to disassemble at lower concentrations and this aspect is particularly critical for photophysical measurements that typically require concentrations below 10^{-5} M.

One of the possible ways to increase the stability of these supramolecular adducts is to increase the inertness of the bond between the metal and the ligand by changing the nature of the metal (e.g. Ru). But the inertness could prevent the system from being in equilibrium with its components and obtain the most stable assemblies. In addition, replacement of Zn with the heavier atom Ru would deeply affect the photophysical properties of the compound.

Another approach is to increase the cooperative effect by increasing the panel's size, adding other porphyrins in the metallacycle and, therefore, the number of axial connections Zn–L that they can form.

1.4. Heteroleptic metallacycles of porphyrins

As stated before, there are numerous reports of homoleptic 2+2 and 4+4 metallacycles, but the reports of heterometallic or heteroleptic metallacycles are far less.

In the past, the treatment of the "corner" compound [*trans,cis,cis*-$RuCl_2(CO)_2(4'cis$DPyP$)_2$] with the *cis*-protected [Pd(dppp)$(CF_3SO_3)_2$] complex (dppp = diphenylphosphinopropane) allowed to prepare [{*trans,cis,cis*-$RuCl_2(CO)_2$}(4′*cis*DPyP$)_2${Pd(dppp)}]$(CF_3SO_3)_2$, the first (and only) example of an heterobimetallic 2+2 metallacycle of porphyrins, featuring an octahedral Ru(II) and a square planar Pd(II) corner.[10]

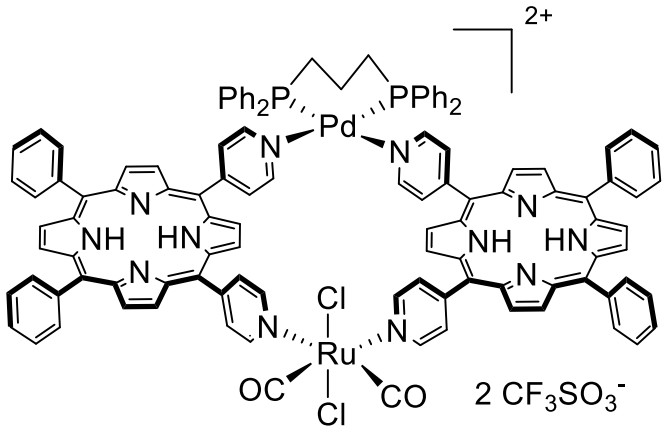

Figure 1.8. Schematic structure of the 2+2 porphyrin metallacycle [{*trans,cis,cis*-$RuCl_2(CO)_2$}(4′*cis*DPyP$)_2${Pd(dppp)}]$(CF_3SO_3)_2$.

We reasoned that instead of changing the metal nature in the metallacycle, we could also change the Ru connectors' geometry connecting the porphyrins or the number and type of porphyrins.
Indeed two other stereoisomers of **1** are known, namely [*cis,cis,trans*-$RuCl_2(CO)_2(dmso\text{-}S)_2$] (**4**) and [*cis,cis,cis*-$RuCl_2(CO)_2(dmso)_2$] (**5**) (Figure 1.9). These can be considered as a 180° connector and a 90° connector respectively, leading – in principle – to new stereoisomeric 2+2 or 4+4 metallacycles.[27–29].

The exploitation of both **4** and **5** for the construction of porphyrin metallacycles is treated in the **second chapter** of this thesis.

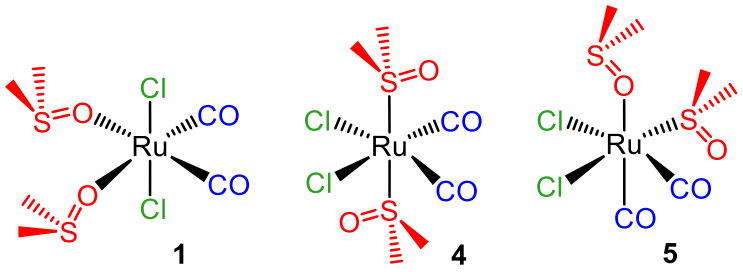

Figure 1.9. The three stereoisomeric Ru(II) precursors (**1**), [*cis,cis,trans*-$RuCl_2(CO)_2(dmso\text{-}S)_2$] (**4**) and [*cis,cis,cis*-$RuCl_2(CO)_2(dmso)_2$] (**5**).

The **third chapter** focuses on increasing the nuclearity of the porphyrin metallacycles, by adding another porphyrin in the metallacycle leading to a three-porphyrin array that after metalation could form more stable supramolecular assembles.
Furthermore, we also synthesized metallacycles containing different porphyrins (i.e. 3′ and 4′-pyridylporphyrins) that have new types of geometries (i.e. Greek-frame, ladder, zig-zag).

1.5 Bibliography

1. Otsuki, J. Supramolecular approach towards light-harvesting materials based on porphyrins and chlorophylls. *J. Mater. Chem. A* **6**, 6710–6753 (2018).
2. Zeng, Y., Chen, J., Yu, T., Yang, G. & Li, Y. Molecular-Supramolecular Light Harvesting for Photochemical Energy Conversion: Making Every Photon Count. *ACS Energy Lett.* **2**, 357–363 (2017).
3. Kundu, S. & Patra, A. Nanoscale strategies for light harvesting. *Chem. Rev.* **117**, 712–757 (2017).
4. Yang, J., Yoon, M. C., Yoo, H., Kim, P. & Kim, D. Excitation energy transfer in multiporphyrin arrays with cyclic architectures: Towards artificial light-harvesting antenna

complexes. *Chem. Soc. Rev.* **41**, 4808–4826 (2012).

5. Iengo, E., Cavigli, P., Milano, D. & Tecilla, P. Metal mediated self-assembled porphyrin metallacycles: Synthesis and multipurpose applications. *Inorganica Chim. Acta* **417**, 59–78 (2014).
6. Wojaczyński, J. & Latos-Grazyński, L. Poly- and oligometalloporphyrins associated through coordination. *Coord. Chem. Rev.* **204**, 113–171 (2000).
7. Imamura, T. ScienceDirect - Coordination Chemistry Reviews : Self-assembly of metallopyridylporphyrin oligomers. *Coord. Chem. Rev.* **198**, 133–156 (2000).
8. Drain, C. M., Nifiatis, F., Vasenko, A. & Batteas, J. D. Porphyrin Tessellation by Design : 2344–2347 (1998).
9. Fan, J. *et al.* Self-assembly of porphyrin arrays via coordination to transition metal bisphosphine complexes and the unique spectral properties of the product metallacyclic ensembles. *J. Am. Chem. Soc.* **121**, 2741–2752 (1999).
10. Iengo, E., Milani, B., Zangrando, E., Geremia, S. & Alessio, E. Novel ruthenium building blocks for the efficient modular construction of heterobimetallic molecular squares of porphyrins. *Angew. Chemie - Int. Ed.* **39**, 1096–1099 (2000).
11. Iengo, E. *et al.* Pyridylporphyrin metallacycles with a slipped cofacial geometry: Spectroscopic, X-ray, and photophysical characterization. *Inorg. Chem.* **44**, 9752–9762 (2005).
12. Prodi, A. *et al.* Wavelength-dependent electron and energy transfer pathways in a side-to-face ruthenium porphyrin/perylene bisimide assembly. *J. Am. Chem. Soc.* **127**, 1454–1462 (2005).
13. Scandola, F., Chiorboli, C., Prodi, A., Iengo, E. & Alessio, E. Photophysical properties of metal-mediated assemblies of porphyrins. *Coord. Chem. Rev.* **250**, 1471–1496 (2006).
14. Milano, D. *et al.* Anion transport across phospholipid membranes mediated by a diphosphine-Pd(ii) complex. *Chem. Commun.* **50**, 9157–9160 (2014).
15. Fujita, N., Biradha, K., Fujita, M., Sakamoto, S. & Yamaguchi, K. A porphyrin prism: Structural switching triggered by guest inclusion. *Angew. Chemie - Int. Ed.* **40**, 1718–1721 (2001).
16. Bar, A. K., Mohapatra, S., Zangrando, E. & Mukherjee, P. S. A series of trifacial Pd 6 molecular barrels with porphyrin walls. *Chem. - A Eur. J.* **18**, 9571–9579 (2012).
17. Bar, A. K., Chakrabarty, R., Mostafa, G. & Mukherjee, P. S. Self-assembly of a nanoscopic Pt12Fe12 heterometallic open molecular box containing six porphyrin walls. *Angew. Chemie - Int. Ed.* **47**, 8455–8459 (2008).

18. Meng, W. *et al.* A self-assembled M8L6 cubic cage that selectively encapsulates large aromatic guests. *Angew. Chemie - Int. Ed.* **50**, 3479–3483 (2011).
19. Wood, D. M. *et al.* Guest-induced transformation of a porphyrin-edged FeII4L6 capsule into a CuIFeII2L4 fullerene receptor. *Angew. Chemie - Int. Ed.* **54**, 3988–3992 (2015).
20. Rizzuto, F. J. & Nitschke, J. R. Stereochemical plasticity modulates cooperative binding in a CoII12L6 cuboctahedron. *Nat. Chem.* **9**, 903–908 (2017).
21. Iengo, E., Zangrando, E., Minatel, R. & Alessio, E. Metallacycles of porphyrins as building blocks in the construction of higher order assemblies through axial coordination of bridging ligands: Solution- and solid-state characterization of molecular sandwiches and molecular wires. *J. Am. Chem. Soc.* **124**, 1003–1013 (2002).
22. Teresa Indelli, M. *et al.* Photoinduced processes in self-assembled porphyrin/perylene bisimide metallosupramolecular boxes. *J. Phys. Chem. B* **114**, 14495–14504 (2010).
23. Alessio, E., Casanova, M., Zangrando, E. & Iengo, E. Modular self-assembled multiporphyrin cages with tunable shape. *Chem. Commun.* **48**, 5112–5114 (2012).
24. Iengo, E., Cavigli, P., Milano, D. & Tecilla, P. Metal mediated self-assembled porphyrin metallacycles: Synthesis and multipurpose applications. *Inorganica Chim. Acta* **417**, 59–78 (2014).
25. Iengo, E., Zangrando, E., Minatel, R. & Alessio, E. Metallacycles of porphyrins as building blocks in the construction of higher order assemblies through axial coordination of bridging ligands: Solution- and solid-state characterization of molecular sandwiches and molecular wires. *J. Am. Chem. Soc.* **124**, 1003–1013 (2002).
26. Anderson, H. L., Anderson, S. & Sanders, J. K. M. Ligand binding by butadiyne-linked porphyrin dimers, trimers and tetramers. (1995).
27. Ronson, T. K., Zarra, S., Black, S. P. & Nitschke, J. R. Metal–organic container molecules through subcomponent self-assembly. *Chem. Commun.* **49**, 2476 (2013).
28. Zhang, D., Ronson, T. K. & Nitschke, J. R. Functional Capsules via Subcomponent Self-Assembly. *Acc. Chem. Res.* **51**, 2423–2436 (2018).
29. Rizzuto, F. J., Ramsay, W. J. & Nitschke, J. R. Otherwise Unstable Structures Self-Assemble in the Cavities of Cuboctahedral Coordination Cages. *J. Am. Chem. Soc.* **140**, 11502–11509 (2018).

.

CHAPTER 2

Vidal, A., Battistin, F., Balducci, G., Demitri, N., Iengo, E., and Alessio, E., Rare Example of Stereoisomeric 2 + 2 Metallacycles of Porphyrins Featuring Chiral-at-Metal Octahedral Ruthenium Corners, *Inorganic Chemistry.* **2019,** 58, 7357–7367

2. Chiral Metallacycles Of Porphyrins

2.1 Introduction

More than twenty years ago, the group where I did my PhD thesis, reported that complex *cis,cis,trans*-$RuCl_2(CO)_2(dmso\text{-}S)_2$ (**4**) reacts with pyridine (py) at room temperature in methanol or chloroform replacing one dmso-*S* and affording a mixture of two mono-substituted isomers: *cis,cis,cis*-$RuCl_2(CO)_2(dmso\text{-}S)(py)$ (**6**, minor) and *cis,cis,trans*-$RuCl_2(CO)_2(dmso\text{-}S)(py)$ (**7**, major). Conversely, when the reaction is performed in refluxing methanol both dmso ligands are replaced by pyridine affording *trans,cis,cis*-$RuCl_2(CO)_2(py)_2$ (**8**), i.e. the same stereoisomer that is obtained from **1** at room temperature (Scheme 2.1). In other words, the substitution process is accompanied by isomerization.[1]

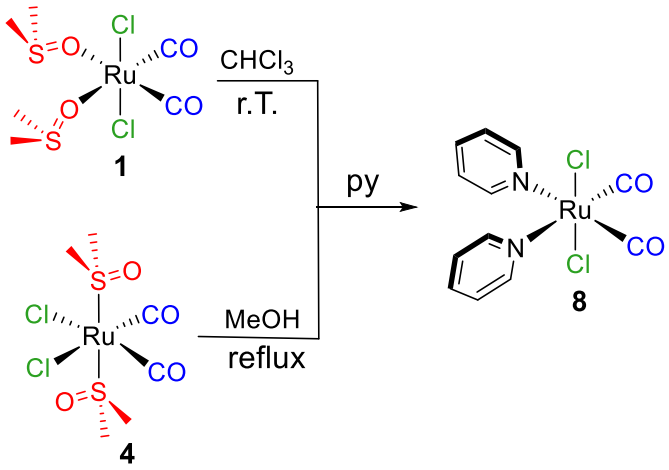

Scheme 2.1. The reactivity of the stereoisomers *trans,cis,cis*-$RuCl_2(CO)_2(dmso\text{-}O)_2$(**1**) and *cis,cis,trans*-$RuCl_2(CO)_2(dmso\text{-}S)_2$ (**4**) towards pyridine.

We now reasoned that – if the reactivity with py is extended to pyridylporphyrins – treatment of **4** with 4′*cis*DPyP is likely to produce also metallacycles of porphyrins, however with a different mechanism compared to **1**, through a process that – as in the reaction with py – might involve the stereochemical rearrangement of the Ru fragment. Therefore, Ru connectors of different geometry might be trapped/obtained, such as {*cis,cis,cis*-$RuCl_2(CO)_2$} and {*cis*,*cis,trans*-$RuCl_2(CO)_2$}, leading to new 2+2 or 4+4 metallacycles. We also reasoned that the same considerations might apply to the all-*cis* isomer **5**, even though its reactivity towards the model ligand pyridine has not been explored yet.

Therefore, we performed a careful investigation of the reactivity of both isomers **4** and **5**, first with the model ligand 4′-monopyridylporphyrin (4′MPyP) and then with 4′*cis*DPyP. We describe here the

isolation and characterization of two new 2+2 metallacycles of porphyrins that are stereoisomers of **2**, namely [{*trans,cis,cis*-$RuCl_2(CO)_2$}(4′*cis*DPyP)$_2${*cis,cis,cis*-$RuCl_2(CO)_2$}] (**13**) and [*cis,cis,cis*-$RuCl_2(CO)_2$(4′*cis*DPyP)]$_2$ (**14**, that exists as a mixture of two stereoisomers defined as *alternate* and *pairwise*), in which the chiral {*cis,cis,cis*-$RuCl_2(CO)_2$} fragment has either a *C* or *A* configuration (Chart 2.1).[2]

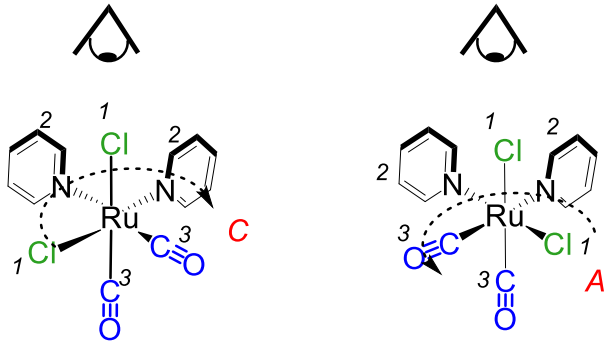

Chart 2.1. Example of how the chirality symbols C (Clockwise) and A (Anti-Clockwise) are assigned to the enantiomers of the model complex *cis,cis,cis*- $RuCl_2(CO)_2(py)_2$, the CIP priority number of each ligand is in italics.[3]

In metallosupramolecular assemblies, chirality can arise from the presence of a stable stereogenic element (either enantiopure or racemic) in the organic bridging ligand or in an auxiliary ligand attached to the metal center.[4] For example, Stang and co-workers described chiral 2+2 and 4+4 metallacycles of porphyrins in which 4′*cis*DPyP or 4′*trans*DPyP units (4′*trans*DPyP = 5,15-bis(4′-pyridyl)-10,20-diphenylporphyrin) are connected by Pd(II) corners bearing R(+)- or S(−)-BINAP as a chiral ancillary ligand.[5] With a similar approach, Shinkai et al. described a chiral $[Pd_4(porp)_2]^{8+}$ square prism in which two porphyrins bearing four pyridyl groups are connected by four *cis*-protected chiral $\{Pd[(R)\text{- }(+)\text{-BINAP}]\}^{2+}$ fragments.[6]

As an alternative, chirality of metallosupramolecular assemblies may derive from the presence of chiral metal connectors. There are many examples, some of which concerning also 3D multiporphyrin assemblies,[7,8] in which chirality is generated by the spatial arrangements of achiral chelating ligands around the connecting octahedral metal centers (Λ or Δ handedness).[9,10] Typically, in the solid state, all the chiral metal centers within each assembly adopt the same Λ or Δ configuration, in particular when the bridging ligands are rigid, since the chirality established at one metal vertex is transmitted to the other centers through strong mechanical coupling.[4] In some cases enantiopure Λ or Δ metallo-ligands were also prepared and then connected through achiral metal centers to afford enantiopure cages.[10] There are also a few examples of 2D or 3D assemblies (not concerning porphyrins) with tetrahedral half-sandwich chiral metal connectors with R or S configuration.[11-13] Nevertheless, both **13** and **14**, are to the best of our knowledge, unprecedented examples of 2D metallosupramolecular assemblies with octahedral chiral-at-metal centers (with C or A handedness),[3] and **13** is the first

example of a 2+2 molecular square with stereoisomeric Ru(II) corners. Indeed, stereogenic octahedral metal connectors with monodentate ligands, which may lead to this type of chirality in metallosupramolecular assemblies, are rare. Aside from the Ru(II) connectors, the other most commonly used octahedral fragment is the achiral {fac-$Re(CO)_3X$} (X = Cl, Br).[14,15]

2.2 Result and Discussion

2.2.1 Reactions with 4′MPyP

First, we briefly investigated the reactivity of the two $RuCl_2(CO)_2(dmso)_2$ isomers – **4** and **5** – towards 4′MPyP. The reactions were monitored through TLC analysis and ^1H NMR spectroscopy. Coordination of 4′MPyP to the Ru(II) fragment induces typical downfield shifts for the resonances of the pyridyl ring protons (H2,6 and H3,5), whereas the other porphyrin resonances are scarcely affected. As a reference we had a sample of *trans,cis,cis*-$RuCl_2(CO)_2(4'MPyP)_2$ (**9**), previously prepared by us from **1**.[16]

Both isomers **4** and **5**, when treated with one equiv of 4′MPyP in $CDCl_3$ at room temperature, slowly replace one dmso yielding a largely prevailing compound that, according to its ^1H NMR spectrum, was identified as *cis,cis,trans*-$RuCl_2(CO)_2$(dmso-S)(4′MPyP) (**10**) (Scheme 2.2), i.e. the analog of the py product **7**. When the reaction between **5** and 4′MPyP was performed in $CDCl_3$ and monitored by NMR spectroscopy we noticed that the formation of **10** – which implies a geometrical rearrangement – is accompanied by a progressive isomerization of the remaining complex into its stereoisomer **4** that was complete after ca. 24h. Thus it is possible that formation of **10** from **5** is subsequent to the isomerization.

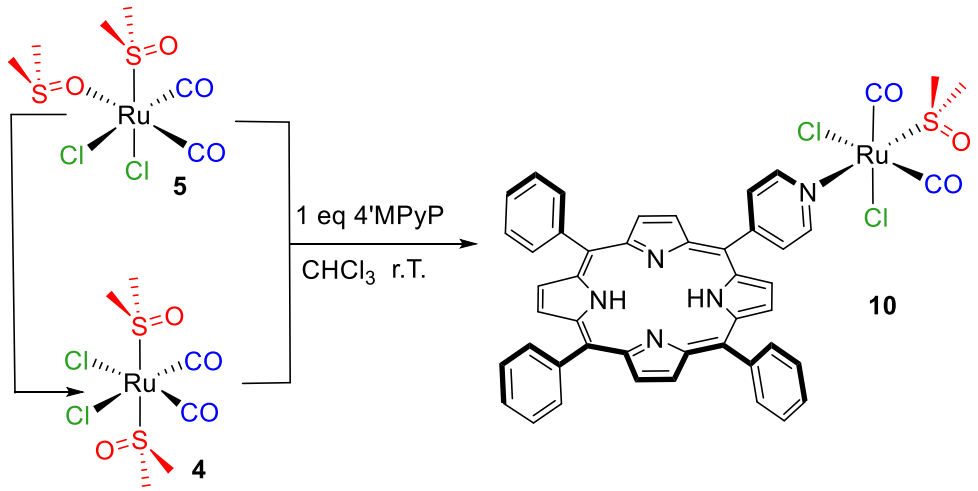

Scheme 2.2. The reactivity of *cis,cis,trans*-$RuCl_2(CO)_2(dmso\text{-}S)_2$ (**4**) and *cis,cis,cis*-$RuCl_2(CO)_2(dmso)_2$ (**5**) towards 4′MPyP in chloroform at room temperature.

Compound **10** was also the main product when either **4** or **5** were treated with a slight excess of 4′MPyP in chloroform at higher temperature (either at reflux for 15h or for 3h at 70°C under MW assisted conditions). The compound could be obtained in almost pure form and its spectroscopic features are fully consistent with the proposed geometry: two CO stretching bands at 2068 and 1980 cm^{-1} – but a single resonance at 188.68 ppm in the $^{13}C\{^{1}H\}$ NMR spectrum – for the adjacent and equivalent carbonyls, a singlet at 3.65 ppm for the equivalent methyl groups of the dmso-S in the ^{1}H NMR spectrum (Appendix).

Substitution of the second dmso ligand from **4** and **5** required, besides higher temperatures and prolonged reaction times, the presence of methanol in the reaction mixture. When different $CHCl_3$:MeOH mixtures were tested, we found that the TLC spots attributable to disubstituted products – that typically have greater TLC mobility compared to 4′MPyP and **10** – increased upon increasing the relative amount of methanol and the temperature. All the reactions described below were eventually performed in a 4:5 $CHCl_3$:MeOH mixture (i.e. the highest content of methanol in which both 4′MPyP and 4′*cis*DPyP are still fully soluble) in a microwave reactor, unless differently specified.

When the MW-assisted reaction between either **4** or **5** and 4′MPyP (2 equiv) was performed at 100°C, the main product was the already known *trans,cis,cis*-$RuCl_2(CO)_2(4'MPyP)_2$ (**9**),[16] suggesting that it is the thermodynamically favored species. Crystals of **9** suitable for X-ray analysis were obtained by slow diffusion of diethyl ether into a $CHCl_3$ solution. The solid state molecular structure (Figure 2.1) fully confirms the nature of **9** as already established spectroscopically in solution.[16]

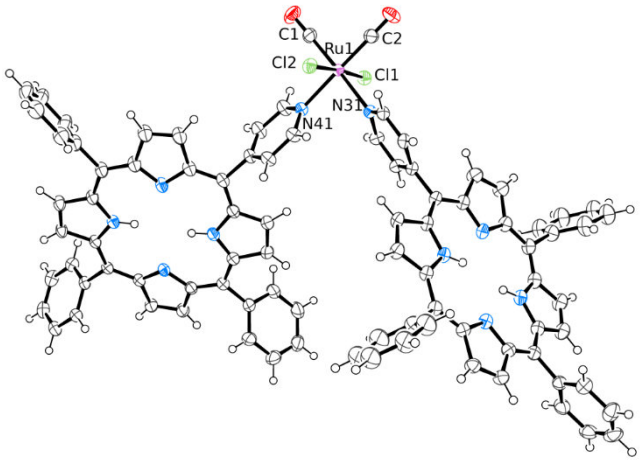

Figure 2.1. ORTEP representation (50% probability ellipsoids) of the solid state molecular structure of *trans,cis,cis*-$RuCl_2(CO)_2(4'MPyP)_2 \cdot 0.5C_6H_{14}$ (**9**). For clarity, an hexane crystallization molecule has been omitted; for the same reason, only major populations (0.88, 0.85) of two disordered phenyl groups of the N31 porphyrin ligand have been included.

More importantly, besides a minor amount of residual **10**, the spots of two new disubstituted products with R_f = 0.24 and 0.18, respectively, were observed in the TLC analysis ($CHCl_3$; under these conditions the R_f of **9** is 0.88). Column chromatography performed on the raw product afforded three main bands. The first band contained pure **9**. The spectral features of the product in the second band, i.e. a single set of resonances for coordinated 4′MPyP and no resonance for dmso in the ^{1}H NMR spectrum (Appendix), and two CO stretching bands in the IR spectrum at 2063 and 1995 cm^{-1}, were consistent with the stereoisomer *cis,cis,trans*-$RuCl_2(CO)_2(4'MPyP)_2$ (**11**). We notice that both carbonyl stretching bands in **11** fall at lower frequencies compared to those in **9** (2073 and 2015 cm^{-1}), as expected for CO being *trans* to the good π-donor Cl rather than to a pyridyl ring.[17] The geometry of **11** was confirmed by single crystal X-ray analysis (Figure 2.4). The pyridyl ring of each 4′MPyP in both **9** and **11** is – as expected – almost orthogonal to the coordination plane and to the porphyrin ring (dihedral angles in the range 56.6 – 79.9°). As a consequence, in the solid state the two porphyrin macrocycles form a dihedral angle of ca. 78° in **9** and ca. 12° in **11**.

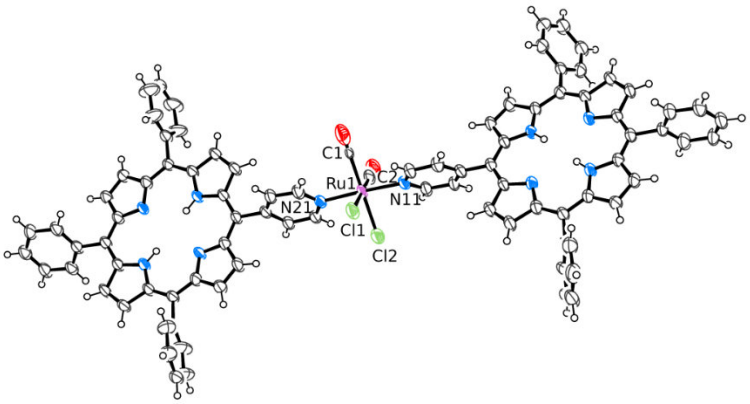

Figure 2.2. ORTEP representation (50% probability ellipsoids) of the solid state molecular structure of *trans*,*cis*,*cis*-$RuCl_2(CO)_2(4'MPyP)_2 \cdot 1.3CHCl_3 \cdot C_4H_{10}O$ (**11**·0.5 C_6H_{14}For clarity, an hexane crystallization molecule has been omitted; for the same reason, only major populations (0.88, 0.85) of two disordered phenyl groups of the N31 porphyrin ligand have been included.

The third band, whose mobility on silica gel is very close to that of unreacted 4′MPyP (R_f=0.15) (note: some unreacted 4′MPyP was found in the mixture even after more prolonged reaction times.), contained a product whose spectral features are fully consistent with the *cis,cis,cis*-$RuCl_2(CO)_2(4'MPyP)_2$ (**12**) stereoisomer. In fact, the ^{1}H NMR spectrum (Figure 2.3) shows two equally intense and well resolved sets of resonances for the H2,6 and H3,5 protons, pairwise connected in the ^{1}H-^{1}H COSY spectrum, for the two inequivalent 4′MPyP ligands, whose other resonances are partially or completely overlapping, including the singlets of the internal NH protons. By comparison with the spectra of **2** and **9** (all pyridyl rings *trans* to CO), we tentatively assign the most upfield pair of H2,6 and H3,5 resonances (red dots in Figure 2.3) to the pyridyl ring *trans* to Cl. To be noted that the phenyl resonances are split into two sets in 2:1 intensity ratio. This feature, that

is observed also in the spectrum of **9** (but is absent in that of **11**), is typical for two mutually *cis* pyridylporphyrins in free rotation about the Ru–$N_{pyridyl}$ bond.[16,18] The IR spectrum shows two CO stretching bands for the adjacent carbonyls at 2072 and 2001 cm^{-1}. No attempts were made to separate the racemic mixture of the *C* and *A* enantiomers.

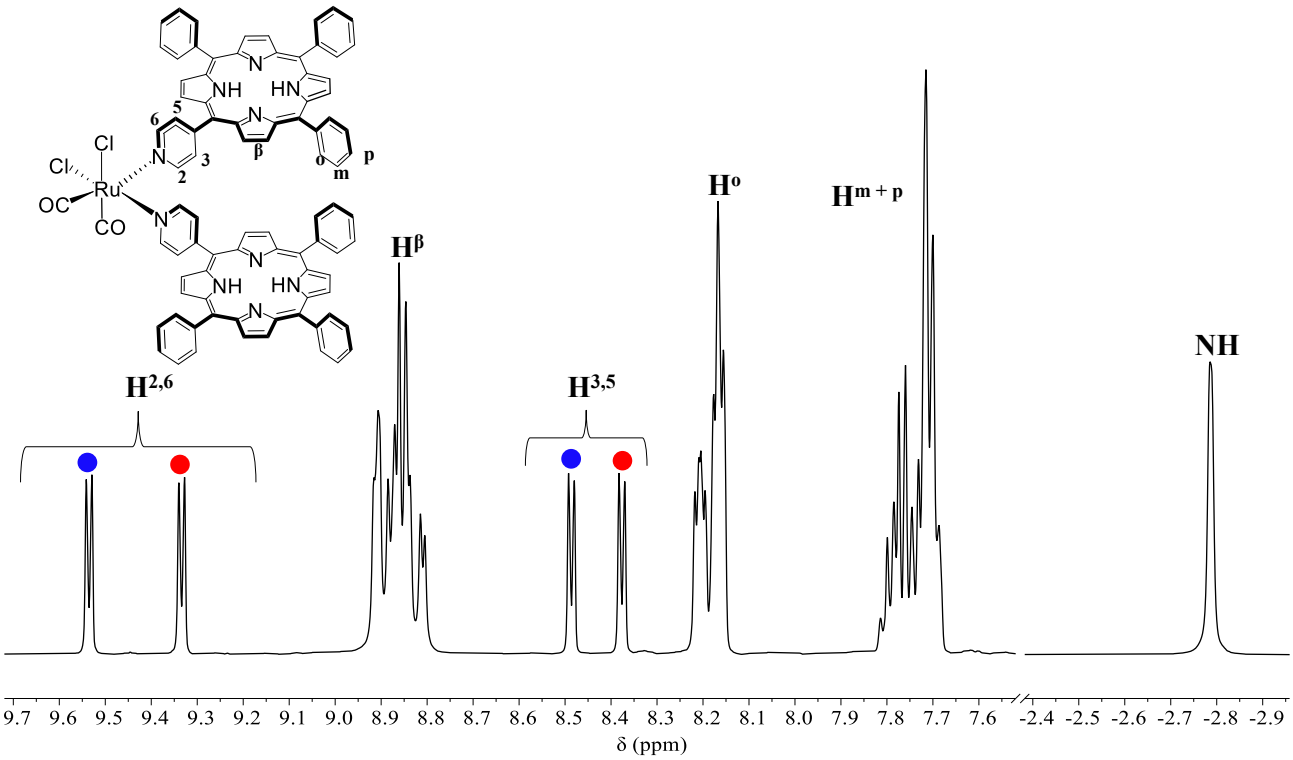

Figure 2.3. ^{1}H NMR spectrum of *cis,cis,cis*-$RuCl_2(CO)_2$(4′MPyP)$_2$ (**12**) in $CDCl_3$. Dots of the same color indicate protons belonging to the same pyridyl ring.

In summary, the main results obtained with the model mono-pyridylporphyrin showed that: *i*) the two stereoisomers **4** and **5** react with 4′MPyP affording the same products, *ii*) in chloroform/methanol mixtures the disubstituted compound **9** is the thermodynamically preferred product, followed by lower amounts of its stereoisomers **11** and **12**.[37] In principle, in analogy to **9**, the geometry of the Ru fragment in **12**, with two adjacent porphyrins, is suitable for the formation of 2+2 metallacycles when using 4′*cis*DPyP. Thus, both **9** and **12** are model corner compounds. Conversely, the geometry of the metal fragment in **11**, with two *trans* porphyrins, might lead to the formation of a statistically less favorable 4+4 metallacycle [*cis*,*cis*,*trans*-$RuCl_2(CO)_2$(4′*cis*DPyP)]$_4$, in which the porphyrins occupy the corners of the square and the Ru fragments define the sides .[1] It is worth noting that the orientation of the two porphyrins in **11** is very close to that expected to be found in such hypothetical 4+4 metallacycle, making it a good model.

2.2.3 Reactions of 4 and 5 with 4′*cis*DPyP

Reactions between either **4** or **5** and an equivalent amount of 4′*cis*DPyP were best performed in a microwave reactor at 100°C in 4:5 $CHCl_3$: MeOH solution, affording a purple precipitate. A preliminary screening showed that the highest conversion was obtained after 2h.

Careful TLC analysis of the precipitate dissolved in chloroform showed that the raw product contained mainly **2** (R_f =0.95). However, the spots of two other compounds of decreasing intensity (**13** and **14**, respectively) were clearly identified.[20] According to their mobility on silica gel (R_f = 0.38 for **13**, and R_f = 0.21 for **14**) both compounds were identified as metallacycles (typically, open oligomeric species are not eluted, and the R_f of the free 4′*cis*DPyP is < 0.1 under these conditions).

Pure samples of **13** and **14** (this latter in a very small amount) were best obtained by preparative TLC. Both species are well soluble in chloroform, again in agreement with being discrete – rather than oligomeric – species. Compound **13** was fully characterized by IR, 1D and 2D NMR spectroscopy. Taken together, the spectroscopic features are fully consistent with the hypothesis that **13** is a stereoisomer of **9**, i.e. the 2+2 metallacycle [{*trans,cis,cis*-$RuCl_2(CO)_2$}(4′*cis*DPyP)$_2${*cis,cis,cis*-$RuCl_2(CO)_2$}] featuring two stereoisomeric Ru(II) corners, one of which is a stereogenic center with *C* or *A* configuration. Consistent with a metallacyclic (closed) structure, the NMR resonances of the pyridyl protons of **13** occur at higher frequency than in the free 4′*cis*DPyP. In the $CDCl_3$ spectrum at room temperature such resonances are rather broad. Upon lowering the temperature to ca. –5°C, they become increasingly sharper, whereas those of the other protons start to broaden (Appendix). For lower temperatures (between –5 and –25°C) all resonances become increasingly broader. This behavior suggests that the rotation about the C_{meso}–C_{ring} for the pyridyl rings (that are also bound to Ru) is already slow on the NMR time scale at ca. 0°C, whereas other motions – most likely the rotation of the phenyl rings – are relatively fast at 25°C and start to slow down at lower temperatures. Even at temperatures as low as –80°C, obtained in CD_2Cl_2 (Appendix), the resonances are still broad. Figure 2.4 shows the spectrum at 5°C in $CDCl_3$, where eight doublets (1H each) are observed both for the H2,6 protons between 9.92 and 9.18 ppm (three partially overlapping at ca. 9.75 ppm) and for the H3,5 protons between 8.75 and 8.48 ppm (two overlapping at 8.63 ppm and four at 8.60 ppm). The assignment was confirmed by the HSQC spectrum (Appendix). The number of pyridyl proton resonances and their spread is consistent with the fact that **13**, in which one of the Ru corners is chiral, has no symmetry elements (and therefore is a racemic mixture). As a consequence, each pyridyl proton resonates at a different frequency (with some accidental overlapping). The low-T ^{1}H ROESY spectrum (Appendix) clearly shows that the two H2,6 resonances that fall at lowest frequencies are pairwise connected with the two at highest frequencies by exchange cross peaks, qualifying them as belonging to two distinct pyridyl rings. Similar cross peaks are found for the H3,5 resonances, even

though their spread is smaller. These findings, together with the COSY connectivity, allowed us to define unambiguously two sets of four resonances (colored dots in Figure 2.4). We tentatively assign them to the two pyridyl rings bound to the asymmetric Ru fragment, since these protons are expected to experience chemical and magnetic environments much more diverse compared to those on the pyridyl rings bound to the symmetrical {*trans,cis,cis*-$RuCl_2(CO)_2$} corner. The resonances of the other types of protons are not resolved. For example, the four NH protons resonate as a relatively broad singlet at –2.8 ppm.

In further agreement with our hypothesis, ^{1}H DOSY spectra of compounds **2** and **14** performed under the same conditions ($CDCl_3$, −5 °C) afforded almost identical diffusion coefficients.

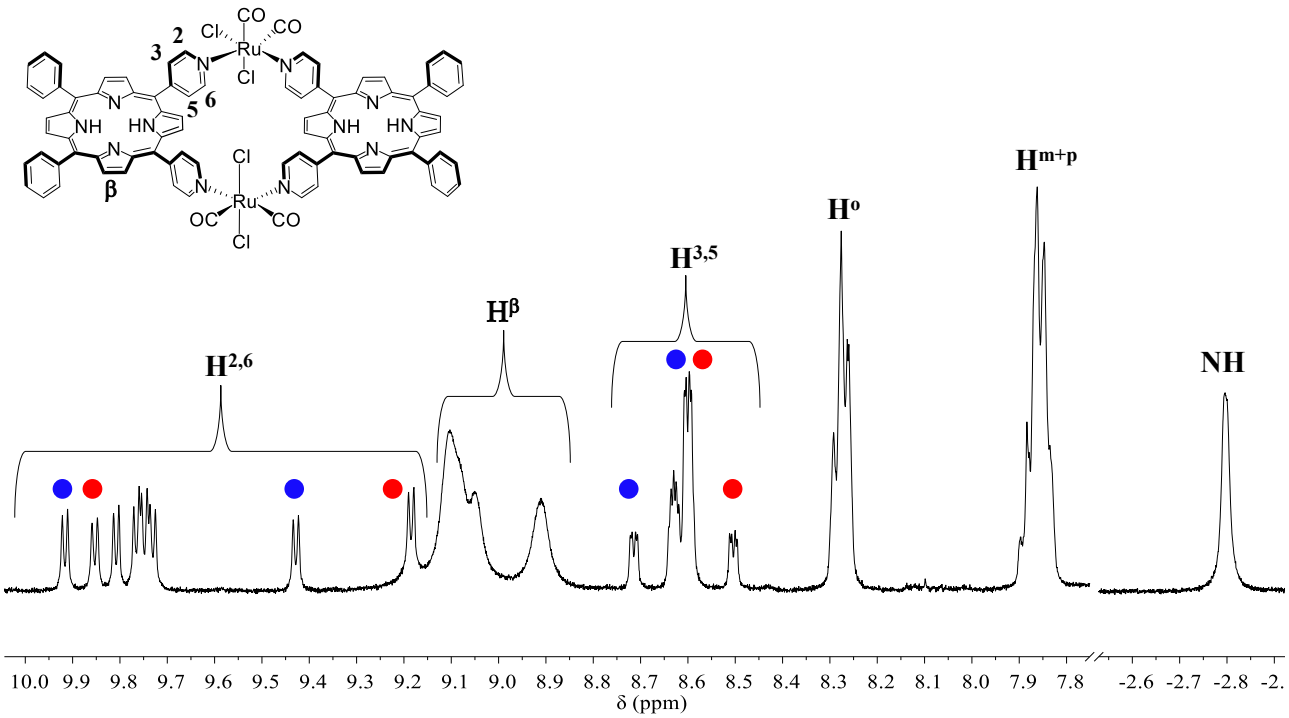

Figure 2.4. ^{1}H NMR spectrum of [{*trans,cis,cis*-$RuCl_2(CO)_2$}(4′*cis*DPyP)$_2${*cis,cis,cis*-$RuCl_2(CO)_2$}] (**13**) in $CDCl_3$ at 5°C. Dots of the same color indicate protons belonging to the same pyridine ring.

The IR spectrum of **13** in chloroform solution shows three bands in ca. 2:1:1 intensity ratio in the CO stretching region (Figure 2.5). The one at highest frequency is almost coincident with the average high-frequency band in the spectra of the model 4′MPyP compounds **9** and **12** (that differ only by ca. 10 cm^{-1}). Similarly, each one the two partially resolved bands in the lower frequency region is almost coincident with the low frequency band of **9** and **12**, respectively (that differ by ca. 20 cm^{-1}). This finding is thus consistent with the presence in **13** of one {*trans,cis,cis*-$RuCl_2(CO)_2$(4′*cis*DPyP)$_2$} corner similar to **9**, and of one {*cis,cis,cis*-$RuCl_2(CO)_2$(4′*cis*DPyP)$_2$} corner similar to **12**. By

comparison, the IR spectrum of **2** shows only two CO stretching bands at 2075 and 2015 cm^{-1}, i.e. very similar to those of the corresponding model complex **9**.

Regretfully, repeated attempts to grow single crystals of **13** suitable for X-ray analysis were unsuccessful.

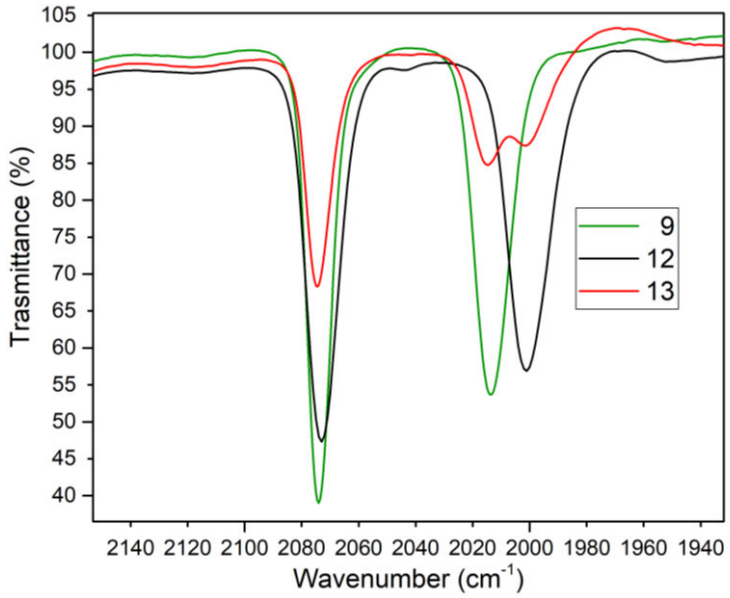

Figure 2.5. CO stretching region in the IR spectra of *trans,cis,cis*-$RuCl_2(CO)_2$(4′MPyP)$_2$ (**9**), *cis,cis,cis*-$RuCl_2(CO)_2$(4′MPyP)$_2$ (**12**) and [{*trans,cis,cis*-$RuCl_2(CO)_2$}(4′*cis*DPyP)$_2${*cis,cis,cis*-$RuCl_2(CO)_2$}] (**13**) in $CHCl_3$ solution.

The NMR spectral features of the least abundant compound **14**, obtained from the third band of the preparative TLC, are similar to those of **13**, but more complicated (Appendix). Even though we could not obtain a sufficient amount of pure compound for performing a detailed spectroscopic analysis, we are confident that it is the third stereoisomeric metallacycle [*cis,cis,cis*-$RuCl_2(CO)_2$(4′*cis*DPyP)]$_2$ (**14**). Consistent with this hypothesis, the IR spectrum of **13** in chloroform (Figure 2.6) shows only two CO stretching bands at 2074 and 2001cm^{-1} , i.e. very similar to those found in the model corner compound **12** (2072 and 2001 cm^{-1}).

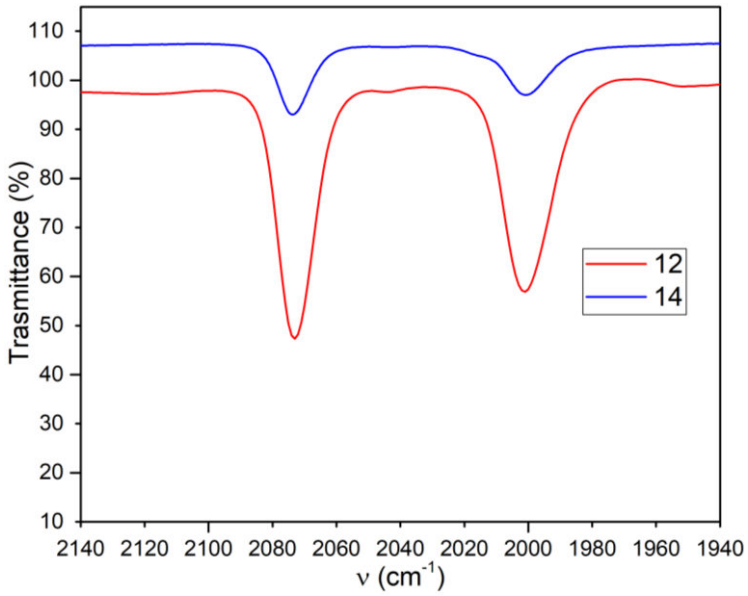

Figure 2.6. CO stretching region in the IR spectra of *cis,cis,cis*-$RuCl_2(CO)_2(4'MPyP)_2$ (**12**) and [*cis,cis,cis*-$RuCl_2(CO)_2(4'cisDPyP)]_2$ (**14**) in $CHCl_3$ solution.

It is not surprising that the proton NMR spectrum of **14** is complicated: this metallacycle actually exists as a mixture (presumably statistical) of two stereoisomers, one in which both porphyrins are *trans* to a Cl and a CO (**14**$_{alt}$, from *alternate*), and the other in which one porphyrin is *trans* to two chlorides and the other to two carbonyls (**14**$_{pw}$, from *pairwise*). In addition, since both {*cis,cis,cis*-$RuCl_2(CO)_2$} corners are chiral (*A* or *C*), each stereoisomer will exist as a statistical mixture of *meso* (*AC*) and *racemic* (*AA* and *CC*) diastereomers. The *meso* and *racemic* forms of **14**$_{alt}$ (**14**$_{alt}$*meso* and **14**$_{alt}$*rac*) are shown in Figure 2.7 (those of **14**$_{pw}$ are shown in the Appendix). Whereas it is reasonable that the four diastereomers have very similar mobility on silica gel and indistinguishable CO stretching bands, they will have potentially different NMR resonances, in particular for the H2,6 protons that are the closest to the Ru centers. Indeed, in the high frequency region of the NMR spectrum of **14** at –5°C (ESI), where the H2,6 resonances are sharper, it is possible to count several partially resolved major resonances for these protons.

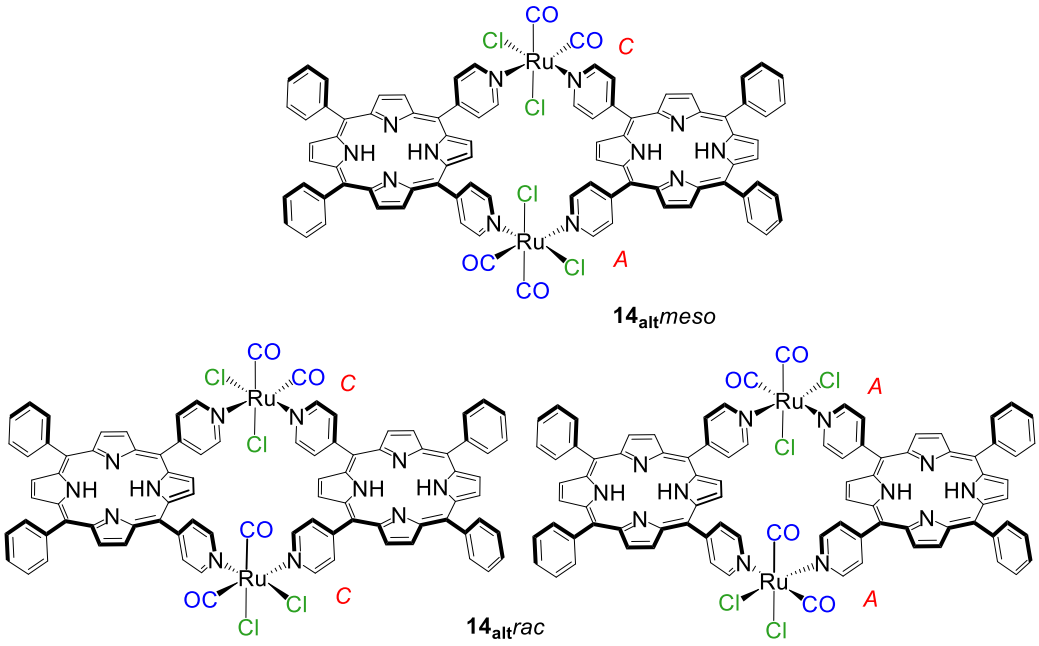

Figure 2.7. The *meso* and *racemic* forms of metallacycle [*cis,cis*-$RuCl_2(CO)_2$}(4′*cis*DPyP)]$_2$ (**14$_{alt}$**) with the *A* and *C* chirality symbols on each corner.[note]

Finally, The UV-vis spectra of the three strereoisomeric metallacycles **9**, **13** and **14** are very similar to one another and to that of free 4′*cis*DPyP (Appendix). As noted already,[21] the insertion of the porphyrin into the metallacycle induces only minor shifts in the absorption maxima of the Soret and Q bands.

Thus, even though a full NMR characterization of **14** was not possible, due to its very low amount and complexity (see above), the TLC mobility, partial NMR characterization and – above all – the IR and UV-vis spectra are fully consistent with the proposed structure.

2.3 Conclusions

We reported three new stereoisomers of the already known 2+2 metallacycle of porphyrins [*trans,cis,cis*-$RuCl_2(CO)_2$(4′*cis*DPyP)]$_2$ (**2**) that have either one or two chiral {*cis,cis,cis*-$RuCl_2(CO)_2$} corners (*C* or *A* handedness). They were obtained, together with 2 (major product), by treatment of *cis,cis,trans*-$RuCl_2(CO)_2$(dmso-S)$_2$ (**4**) or *cis,cis,cis*-$RuCl_2(CO)_2$(dmso)$_2$ (**5**) with an equivalent amount of 4′*cis*DPyP.

The metallacycle [{*trans,cis,cis*-$RuCl_2(CO)_2$}(4′*cis*DPyP)$_2${*cis,cis,cis*-$RuCl_2(CO)_2$}] (**13**) features two stereoisomeric ruthenium centers as connecting units. We notice that **13** escapes prior classifications, since it can be defined as homoleptic in terms of raw formulas but heteroleptic if the stereochemistry of the metal connectors is considered. We suggest that it might be defined as a stereo-homoleptic metallacycle. The least abundant metallacycle [*cis,cis,cis*-$RuCl_2(CO)_2$(4′*cis*DPyP)]$_2$ (**14**)

exists as a mixture of two stereoisomers defined as *alternate* (**14**$_{alt}$, both porphyrins are *trans* to a Cl and a CO) and *pairwise* (**14**$_{pw}$, one porphyrin is *trans* to two chlorides and the other to two carbonyls), each one as a statistical mixture of *meso* (*AC*) and *racemic* (*AA* and *CC*) diastereomers.

Our findings are also consistent with the results obtained with 4′MPyP, showing that the Ru(II) precursors **4** and **5** in solution isomerize to generate mainly the {*trans,cis,cis*-$RuCl_2(CO)_2$} fragment (**a**), whereas the {*cis,cis,cis*-$RuCl_2(CO)_2$} and {*cis,cis,trans*-$RuCl_2(CO)_2$} fragments (**b** and **c**, respectively) are much less abundant. Thus, the combination of two units of 4′*cis*DPyP with two equal (**a**) fragments, leading to **2** as main product, is much more likely compared to the **a**+**b** combination (leading to **13**) and – obviously – to **b**+**b** combination leading to **14**. The combination of **a**+**c** (i.e. a 90°-angular and a linear connector through a 90°-angular porphyrin) is likely to lead to oligomeric species. Finally, we had no evidence of the formation of the 4+4 metallacycle [*cis*,*cis*-$RuCl_2(CO)_2$(4′*cis*DPyP)]$_4$ (**15**, Figure 2.8), that requires the combination of four **c** fragments. It is possible that at the concentrations used in the preparations only open oligomeric species (most likely insoluble) with the **c** fragment are formed and a higher dilution is necessary for obtaining **15** in detectable amounts. It is also possible that the larger **15** might have a negligible mobility of the TLC plate, and thus escaped detection.

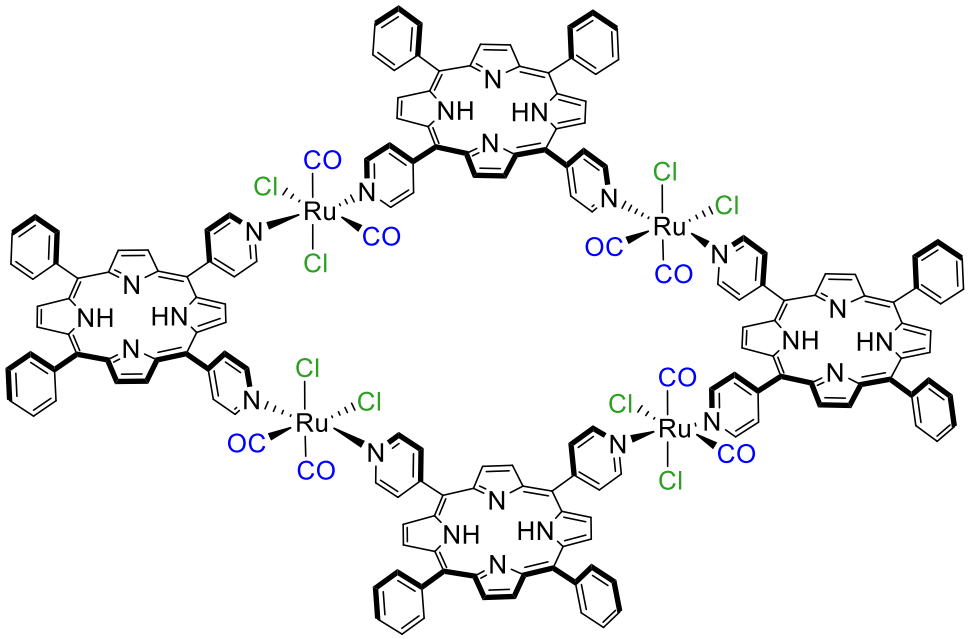

Figure 2.8. The hypothetical 4+4 metallacycle of porphyrins [*cis*,*cis*-$RuCl_2(CO)_2$(4′*cis*DPyP)]$_4$ (**15**).

In conclusion, this work establishes some proofs-of-concept:First, we demonstrate that, by using the appropriate ruthenium precursor (**4** or **5**) in combination with 4′*cis*DPyP, it is possible to obtain new 2 + 2 molecular squares that are not observed when the more stereochemically rigid precursor **1** is used. This feature can be seen as an advantage or as a complication, depending on the objective. Second, and from a more general point of view, it shows that, even for the smallest 2 + 2 metallacycle and using a symmetric organic linker, several stereoisomers can be generated when octahedral metal connectors of the type $\{MA_2B_2\}$ that are not stereochemically rigid are employed.[22] The number of stereoisomers will rapidly increase for larger 2D, or for 3D assemblies. Finally, this work also opens the way to new, even though challenging, opportunities: unprecedented and yet unexplored chiral metallosupramolecular assemblies can be obtained and eventually exploited (e.g., for supramolecular catalysis) by using stereogenic octahedral metal connectors amenable to becoming chiral centers.

2.4 Experimental Section

Materials

All chemicals, including TLC silica gel plates, were purchased from Sigma-Aldrich and used as received. Solvents were of reagent grade. The ruthenium precursors *trans,cis,cis* -$RuCl_2(CO)_2$(dmso-*O*)$_2$ (**1**), *cis,cis,trans*-$RuCl_2(CO)$P(dmso-S)$_2$ (**4**), and *cis,cis*,*cis*-$RuCl_2(CO)_2$(dmso)$_2$ (**5**), the meso-pyridylporphyrins 4′MPyP and 4′*cis*DPyP, and pure samples of *trans,cis,cis*-$RuCl_2(CO)_2$(4′MPyP)$_2$ (**9**) and of the metallacycle [*trans,cis,cis*-$RuCl_2(CO)_2$(4′*cis*DPyP)]$_2$ (**2**) (obtained from **1**) were synthesized and purified as previously reported by us.[10,13,3]

Instrumental Methods

Mono- and bidimensional (1H−1H COSY, 1H−13C HSQC) NMR spectra were recorded at room temperature unless stated otherwise on a Varian 400 or 500 spectrometer (1H, 400 or 500 MHz; 13C{1H}, 100.5 or 125.7 MHz). 1H DOSY experiments were recorded on the Varian 500 spectrometer at −5 °C (CDCl3), using the bipolar pulse pair stimulated echo with convection compensation sequence implemented into the VnmrJ software. 1H and 13C{1H} chemical shifts were referenced to the peak of residual nondeuterated solvent (δ = 7.26 and 77.16 for $CDCl_3$; 5.32 and 54.00 for CD_2Cl_2). Selected carbon resonances, except for carbonyls, were assigned through the HSQC spectra. ESI mass spectra were collected in the positive mode on a PerkinElmer APII spectrometer at 5600 eV. However, as is typical for such neutral systems,1 the ESI-MS spectra of the model complexes and metallacycles of porphyrins only showed peaks deriving from the fragmentation. The UV−vis spectra were obtained on an Agilent Cary 60 spectrophotometer, using

1.0 cm path-length quartz cuvettes (3.0 mL). Infrared spectra of chloroform solutions in the CO stretching region were recorded between CaF_2 windows (0.5 mm spacer) on a PerkinElmer Fourier-transform IR/Raman 2000 instrument in the transmission mode. A CEM Discover microwave reactor was used for the microwave-assisted reactions performed in 10 mL vessels. Elemental analyses were performed on a Thermo Flash 2000 CHNS/O analyzer in the Department of Chemistry of the University of Bologna, Italy. Analysis was not performed on the metallacycles obtained by preparative TLC because of the low amounts. In addition, elemental analysis, unless is performed on the crystal samples (such as those used for X-ray determinations), is poorly significant for these systems due to the typical presence of crystallization molecules whose nature and number vary from batch to batch. X-ray Diffraction. Data collections were performed at the X-ray diffraction beamline (XRD1) of the Elettra Synchrotron of Trieste (Italy) equipped with a Pilatus 2 M image plate detector. Collection temperature was 100 K (nitrogen stream suppliedthrough an Oxford Cryostream 700); the wavelength of the monochromatic X-ray beam was 0.700 Å, and the diffractograms were obtained with the rotating crystal method. The crystals were dipped in N-paratone and mounted on the goniometer head with a nylon loop. The diffraction data were indexed, integrated and scaled using the XDS code.32 The structures were solved by the dual space algorithm implemented in the SHELXT code.33 Fourier analysis and refinement were performed by the full-matrix least-squares methods

Synthesis of the complexes

As written in the Result and Discussion, very similar results were obtained by treatment of either **4** or **5** with the pyridylporphyrins under the same reaction conditions. Thus, only one procedure is reported in each case.

***cis,cis,trans*-$RuCl_2(CO)_2$(dmso-S)(4′MPyP) (10).** A 10.9 mg amount (0.028 mmol) of colorless *cis,cis,trans*-$RuCl_2(CO)_2$(dmso-S)$_2$ (**5**) was dissolved in 7 mL of chloroform. After addition of 25.8 mg of 4′MPyP (0.042 mmol, 1:1.5 ratio) the purple solution was heated in a microwave reactor at 70°C for 2 h. The solvent was then removed by rotary evaporation and the violet powder was partially dissolved in 5 mL of acetone, where the unreacted porphyrin is insoluble. The undissolved 4′MPyP was removed by filtration, the solution was rotary evaporated to dryness and the solid (pure **10** according to the ^{1}H NMR spectrum) was dried *in vacuo*. (Yield 19.3 mg, 75%). Elemental analysis calc for [$C_{47}H_{35}Cl_2N_5O_3SRu$] ($M_w$: 921.1): C 61.24; H 3.83; N 7.60. Found: C 61.33; H 3.94; N 7.68. ^{1}H NMR ($CDCl_3$), δ (ppm): 9.30 (d, 2H: H2,6), 8.87 (m, 8H: Hβ), 8.35 (d, 2H: H3,5), 8.22 (d, 6H: *o*-H), 7.78 (m, 9H: *m*+*p*-H), 3.65 (s, 6H: dmso-S), –2.79 (s, 2H: NH). ^{13}C NMR ($CDCl_3$), δ (ppm): 188.68 (CO), 153.11 (C2,6), 141.76 (Cβ), 134.54 (*o*-C), 131.42 (C3,5), 126.76 (*m*+*p*-C), 46.96

(dmso-S). Selected IR absorption (nujol mull, cm^{-1}): 2068 (ν_{CO}), 1980 (ν_{CO}). UV-vis ($CHCl_3$) λ_{max}, nm (relative intensity, %): 420 (100), 519 (8.7), 554 (4.4), 591 (3.16),646 (2.32).

***trans,cis,cis*-$RuCl_2(CO)_2$(4′MPyP)$_2$ (9), *cis,cis,trans*-$RuCl_2(CO)_2$(4′MPyP)$_2$ (11), and *cis,cis,cis*-$RuCl_2(CO)_2$(4′MPyP)$_2$ (12).**

A 15.0 mg amount (0.039 mmol) of *cis,cis,trans*-$RuCl_2(CO)_2(dmso\text{-}S)_2$ (**5**) was dissolved in 7 mL of a 4:5 $CHCl_3$:MeOH mixture. After addition of 52.9 mg of 4′MPyP (0.086 mmol, 4′MPyP/Ru = 2.2) the purple solution was heated in a microwave reactor at 100°C for 4 h. The solvent was removed under vacuum and the mixture was subjected to column chromatography on silica gel eluted with $CHCl_3$ for the first two fractions, that contained *trans,cis,cis*-$RuCl_2(CO)_2$(4′MPyP)$_2$ (**10**) and *cis,cis,trans*-$RuCl_2(CO)_2$(4′MPyP)$_2$ (**12**), respectively, and then with $CHCl_3$/EtOH 98/2 v/v for the third fraction that contained *cis,cis,cis*-$RuCl_2(CO)_2$(4′MPyP)$_2$ (**12**). Each product was then obtained as a purple solid by rotary evaporation of the eluent. Yields and R_f's (TLC on silica plates using chloroform as eluent): **9** 12%, 0.88; **11** 7%, 0.24; **12** 3%, 0.18. X-ray quality crystals of **9** and **11** were obtained by slow diffusion of *n*-hexane (**9**) or diethyl ether (**11**) into a chloroform solution of each complex.

***trans,cis,cis*-$RuCl_2(CO)_2$(4′MPyP)$_2$** (**9**). Elemental analysis calcd for $[C_{88}H_{58}Cl_2N_{10}O_2Ru]\cdot 0.5(C_6H_{14})$ (M_w: 1502.4): C 72.69; H 4.42; N 9.32. Found: C 72.78; H 4.49; N 9.41. ^{1}H MR ($CDCl_3$), δ (ppm): 9.59 (d, 4H, H2,6), 8.86 (m, 16H, Hβ), 8.45 (d, 4H, H3,5), 8.20 (d, 4H, *o*-H phenyl ring in position 10), 8.15 (d, 8H, *o*-H phenyl rings in positions 5 and 15), 7.77 (m, 6H, *m*+*p*H phenyl ring in position 10), 7.69 (m, 12H, *m*+*p*H phenyl rings in positions 5 and 15), –2.80 (s, 4H, NH). Selected ^{13}C NMR signals (from the HSQC spectrum) in $CDCl_3$, δ (ppm): 154.8 (C2,6), 134.3 (*o*-C), 131.2 (C3,5), 127.8 (*m*+*p*-C). Selected IR absorption (chloroform solution, cm^{-1}): 2073 (ν_{CO}), 2015 (ν_{CO}). UV-vis ($CHCl_3$) λ_{max}, nm (relative intensity, %): 420 (100), 517 (4.8), 552 (2.5), 591 (2.2), 644 (0.6).

***cis,cis,trans*-$RuCl_2(CO)_2$(4′MPyP)$_2$** (**11**). Elemental analysis calcd for $[C_{88}H_{58}Cl_2N_{10}O_2Ru]\cdot CHCl_3\cdot C_4H_{10}O$ (M_w: 1652.3): C 67.58; H 4.21; N 8.47. Found: C 67.65; H 4.24; N 8.52. ^{1}H NMR ($CDCl_3$), δ (ppm): 9.58 (d, 4H, H2,6), 8.98 (d, 4H, Hβ), 8.93 (d, 4H, Hβ), 8.88 (s, 8H, Hβ), 8.34 (d, 4H, H3,5), 8.23 (m, 12H, *o*-H), 7.81 (m, 18H, *m*+*p*H), –2.77 (s, 4H, NH). Selected ^{13}C NMR signals (from the HSQC spectrum) in $CDCl_3$, δ (ppm): 154.4 (C2,6), 134.5 (*o*-C), 131.1 (C3,5), 127.4 (*m*+*p*-C). Selected IR absorption (chloroform solution, cm^{-1}): 2063 (ν_{CO}), 1995 (ν_{CO}). UV-vis ($CHCl_3$) λ_{max}, nm (relative intensity, %): 423 (100), 452 (9.2), 517 (6.0), 550 (3.4), 588 (2.6), 648 (0.9).

***cis,cis,cis*-$RuCl_2(CO)_2$(4′MPyP)$_2$** (**12**). Elemental analysis calcd for $[C_{88}H_{58}Cl_2N_{10}O_2Ru]\cdot CHCl_3$ (M_w: 1578.8): C 67.71; H 3.77; N 8.87. Found: C 67.63; H 3.72; N 8.78. ^{1}H NMR ($CDCl_3$), δ (ppm):

9.54 (d, 2H, H2,6), 9.33 (d, 2H, H2,6), 8.86 (m, 16H, Hβ), 8.49 (d, 2H, H3,5), 8.38 (d, 2H, H3,5), 8.21 (m, 4H, *o*-H phenyl ring in position 10), 8.17 (m, 8H, *o*-H phenyl rings in positions 5 and 15), 7.78 (m, 6H, *m* + *p* H phenyl ring in position 10), 7.71 (m, 12H, *m* +*p* H phenyl rings in positions 5 and 15), –2.79 (s, 4H, NH). Selected ^{13}C NMR signals (from the HSQC spectrum) in $CDCl_3$, δ (ppm): 154.5 (C2,6), 134.6 (*o*-C), 131.1 (C3,5), 127.0 (*m*+*p*-C). Selected IR absorption (chloroform solution, cm^{-1}): 2072 (ν_{CO}), 2001 (ν_{CO}). UV-vis ($CHCl_3$) λ_{max}, nm (relative intensity, %): 422 (100), 452 (30), 517 (5.1), 555 (3.0), 592 (2.3), 650 (3.8).

[*trans,cis,cis*-$RuCl_2(CO)_2$(4′*cis*DPyP)]$_2$ (2),[{*trans,cis,cis*-$RuCl_2(CO)_2$}(4′*cis*DPyP)$_2${*cis,cis,cis*-$RuCl_2(CO)_2$}] (13), [*cis,cis,cis*-$RuCl_2(CO)_2$(4′*cis*DPyP)]$_2$ (14)

A 20.0 mg amount of 4′-*cis*DPyP (0.032 mmol), was dissolved in a CH_3OH:HCl_3 5:4 mixture (2.6 mL of $CHCl_3$ and 3.2 mL of MeOH). After addition of 11.2 mg of **5** (0.029 mmol, 4′*cis*DPyP/Ru = 1.1) the purple solution was heated in a microwave reactor at 100°C for 2 h.

The purple precipitate formed was filtered, washed with methanol and subjected to preparative TLC on silica plates using chloroform as eluent. According to TLC analysis, the mother liquor contained smaller amounts of the three metallacycles plus unreacted 4′*cis*DPyP and other unidentified minor species with R_f <0.2 , i.e. most likely intermediates in the formation of the 2+2 molecular squares.

Three main products were separated, in the order: [*trans,cis,cis*-$RuCl_2(CO)_2$(4′*cis*DPyP)]$_2$ (**2**), [{*trans,cis,cis*-$RuCl_2(CO)_2$}(4′*cis*DPyP)$_2${*cis,cis,cis*-$RuCl_2(CO)_2$}] (**13**), and [*cis,cis,cis*-$RuCl_2(CO)_2$}(4′*cis*DPyP)]$_2$ (**14**).

Yields and R_f's on TLC silica plates eluted with $CHCl_3$:EtOH 99.5:0.5: [*trans,cis,cis*-$RuCl_2(CO)_2$(4′*cis*DPyP)]$_2$ (**2**) 24%, 0.95; [{*trans,cis,cis*-$RuCl_2(CO)_2$(4′*cis*DPyP)$_2${*cis,cis,cis*-$RuCl_2(CO)_2$}] (**13**) 14%, 0.38; [*cis,cis,cis*-$RuCl_2(CO)_2$(4′*cis*DPyP)]$_2$ (**14**) 0.7 %, 0.21.

[{*trans,cis,cis*-$RuCl_2(CO)_2$}(4′*cis*DPyP)$_2${*cis,cis,cis*-$RuCl_2(CO)_2$}] (**13**). ^{1}H NMR ($CDCl_3$, –5 °C), δ (ppm) 9.92 (d, 1H, H2,6), 9.85 (d, 1H, H2,6), 9.81 (d, 1H, H2,6), 9.75(m, 3H, H2,6), 9.43 (d, 1H, H2,6), 9.18 (d, 1H, H2,6),), 9.07 (m, 12H, Hβ), 8.91 (m, 4H, Hβ), 8.71 (dd, 1H, H3,5), 8.61 (m, 6H, H3,5), 8.50 (dd, 1H, H3,5), 8.27 (m, 8H, *o*-H phenyl rings), 7.86 (m, 12H, *m*+*p*-H phenyl rings), –2.72 (s, 4H, NH). Selected ^{13}C NMR signals (from the HSQC spectrum) in $CDCl_3$, δ (ppm): 154.1, 154.0, 152.1, 151.4, 150.8, and 150.7 (C2,6); 132.9, 132.6, 132.5, 132.1, and 131.8 (C3,5); 134.5 (*o*C-phenyl rings); 128.3 and 127,0. (*m*+*p*C-phenyl rings). Selected IR absorption (chloroform solution, cm^{-1}): 2075 (ν_{CO}), 2015 (ν_{CO}), 2002(ν_{CO}). UV-vis ($CHCl_3$) λ_{max}, nm (relative intensity, %): 429.5 (100), 521.0 (7.7), 557 (4.4), 594 (3.3),650 (2.3).

[*cis,cis,cis*-$RuCl_2(CO)_2$(4′cisDPyP)]$_2$ (**14**). Selected IR absorption (chloroform solution, cm^{-1}): 2074 and 2001 cm^{-1}. UV-vis ($CHCl_3$) λ_{max}, nm (relative intensity, %): 430.0 (100), 522.0 (6.9), 559 (4.3), 595 (3.4), 651 (3.0.).

2.5 Bibliography

1. Alessio, E.; Milani, B.; Bolle, M.; Mestroni, G.; Faleschini, P.; Todone, F.; Geremia, S.; Calligaris, M. Carbonyl derivatives of chloride-dimethyl sulfoxide-ruthenium(II) complexes: synthesis, structural characterization and reactivity of $Ru(CO)_X(DMSO)_{4-X}Cl_2$ complexes (X = 1−3). *Inorg. Chem*. **1995**, 34, 4722−4734.
2. Brown, M. F.; Cook, B. R.; Sloan, T. E. Stereochemical Notation in Coordination Chemistry. Mononuclear Complexes. *Inorg. Chem*. **1975**, 14, 1273−1278.
3. Even though this is a textbook issue, a short description of the seldom seen rules for assigning the C and A chirality symbols in octahedral complexes is reported: (i) CIP priority numbers are assigned to the ligands and the principal axis, defined by the ligand of highest CIP priority and the ligand trans to it, identified. In this case Cl = 1, py = 2, CO = 3, and the Cl−Ru−CO axis is the principal axis. It is to be noted that when there is an ambiguity as in this case, where Cl is trans to both pyridine and CO ligands, preference is arbitrarily given to the axis with the largest CIP priority number opposite to 1 (in this case CO). (ii) The chirality symbol C is assigned to that configuration in which the CIP priority numbers of the ligands in the plane perpendicular to the principal axis increase in a clockwise direction when viewed from the most preferred atom of CIP priority number 1 on the principal axis (i.e., Cl). The chirality symbol A is assigned to the opposite configuration.
4. Chen, L.-J.; Yang, H.-B.; Shionoya, M. Chiral metallosupramolecular architectures. *Chem. Soc. Rev*. **2017**, 46, 2555−2576.
5. Fan, J.; Whiteford, J. A.; Olenyuk, B.; Levin, M. D.; Stang, P. J.; Fleischer, E. B. Self-Assembly of Porphyrin Arrays via Coordination to Transition Metal Bisphosphine Complexes and the Unique Spectral Properties of the Product Metallacyclic Ensembles. *J. Am. Chem. Soc*. **1999**, 121, 2741−2752.
6. Ayabe, M.; Yamashita, K.; Sada, K.; Shinkai, S.; Ikeda, A.; (25) Ayabe, M.; Yamashita, K.; Sada, K.; Shinkai, S.; Ikeda, A.; Polymeric Porphyrin Compartments by a Pd(II)-Pyridine Interaction and Their Chiral Twisting by a BINAP Ligand. *J. Org. Chem*. **2003**, 68, 1059−1066.
7. Bar, A. K.; Mohapatra, S.; Zangrando, E.; Mukherjee, P. S. A Series of Trifacial Pd_6 Molecular Barrels with Porphyrin Walls. *Chem -Eur. J*. **2012**, 18, 9571−9579.
8. Meng, W. J.; Breiner, B.; Rissanen, K.; Thoburn, J. D.; Clegg, J. K.; Nitschke, J. R. A Self-Assembled M_8L_6 Cubic Cage that Selectively Encapsulates Large Aromatic Guests. *Angew. Chem., Int. Ed*. **2011**, 50, 3479−3483. (b) Wood,D.M.; Meng, W.; Ronson,T. K.;

Stefankiewicz, A. R.; Sanders, J. K.; Nitschke, J. R. Guest-induced transformation of a porphyrin-edged $Fe^{II}_4L_6$ capsule into a $Cu^{I}Fe^{II}_2L_4$ fullerene receptor. *Angew. Chem., Int. Ed.* **2015**, 54, 3988−3992. (c) Rizzuto, F. J.; Nitschke, J. R. Stereochemical plasticity modulates cooperative binding in a $Co^{II}_{12}L_6$ cuboctahedron. *Nat. Chem*. **2017**, 9, 903−908.

9. Hong, C. M.; Bergman, R. G.; Raymond, K. N.; Toste, F. D. Self-Assembled Tetrahedral Hosts as Supramolecular Catalysts. *Acc. Chem. Res*. 2018, 51, 2447−2455.
10. Rota Martir, D.; Zysman-Colman, E. Photoactive supra- molecular cages incorporating Ru(II) and Ir(III) metal complexes. *Chem. Commun*. **2019**, 55, 139−158.
11. Mimassi, L.; Guyard-Duhayon, C.; Rager, M. N.; Amouri, H. Chiral Recognition and Resolution of the Enantiomers of Supra- molecular Triangular Hosts: Synthesis, Circular Dichroism, NMR, and X-ray Molecular Structure of [Li⊂(R,R,R)-{Cp*Rh(5-chloro-2,3-dioxopyridine)}$_3$][Δ-Trisphat]. *Inorg. Chem*. **2004**, 43, 6644−6649.
12. Granzhan, A.; Schouwey, C.; Riis-Johannessen, T.; Scopelliti, R.; Severin, K. Connection of Metallamacrocycles via Dynamic Covalent Chemistry: A Versatile Method for the Synthesis of Molecular Cages. *J. Am. Chem. Soc*. **2011**, 133, 7106−7115
13. Garci, A.; Dobrov, A. A.; Riedel, T.; Orhan, E.; Dyson, P. J.; Arion, V. B.; Therrien, B. Strategy to Optimize the Biological Activity of Arene Ruthenium Metalla-Assemblies. *Organometallics* **2014**, 33, 3813−3822.
14. Iengo, E.; Cavigli, P.; Milano, D.; Tecilla, P. Metal mediated self-assembled porphyrin metallacycles: Synthesis and multipurpose applications. *Inorg. Chim. Acta* **2014**, 417,59−78.
15. Durot, S.; Taesch, J.; Heitz, V. Multiporphyrinic Cages: Architectures and Functions. *Chem. Rev.* **2014**, 114, 8542−8578.
16. Alessio, E.; Macchi, M.; Heath, S. L.; Marzilli, L. G. Ordered supramolecular porphyrin arrays from a building block approach utilizing pyridylporphyrins and peripheral ruthenium complexes and identification of a new type of mixed-metal building block. *Inorg. Chem*. **1997**, 36, 5614−5623.
17. Battistin, F.; Balducci, G.; Milani, B.; Alessio, E. Water-Soluble Ruthenium(II) Carbonyls with PTA (PTA = 1,3,5-triaza-7- phosphoadamantane). *Inorg. Chem*. **2018**, 57, 6991−7005.
18. Iengo, E.; Milani, B.; Zangrando, E.; Geremia, S.; Alessio, E. Novel Ruthenium Building Blocks for the Efficient Modular Construction of Heterobimetallic Molecular Squares of Porphyrins. *Angew. Chem., Int. Ed*. **2000**, 39, 1096−1099.
19. (37) At ambient temperature, the three stereoisomers **9**, **11**, and **12** are stable in chloroform solution and do not interconvert into each other. According to NMR spectroscopy, partial isomerization of both 11 and 12 into 9, accompanied by decomposition, occurs very slowly

(days) in $CDCl_3$ at 50 °C

20. The TLC spot of the 3 +3 metallacycle [*trans,cis,cis*- $RuCl_2(CO)_2$(4′*cis*DPyP)]**3,** that we prepared as a reference from **1**, was not detected.
21. Iengo, E.; Zangrando, E.; Minatel, R.; Alessio, E. Metallacycles of porphyrins as building blocks in the construction of higher order assemblies through axial coordination of bridging ligands: solution and solid state characterization of molecular sandwiches and molecular wires. *J. Am. Chem. Soc*. **2002**, 124, 1003−1013.

Appendix of Chapter 2

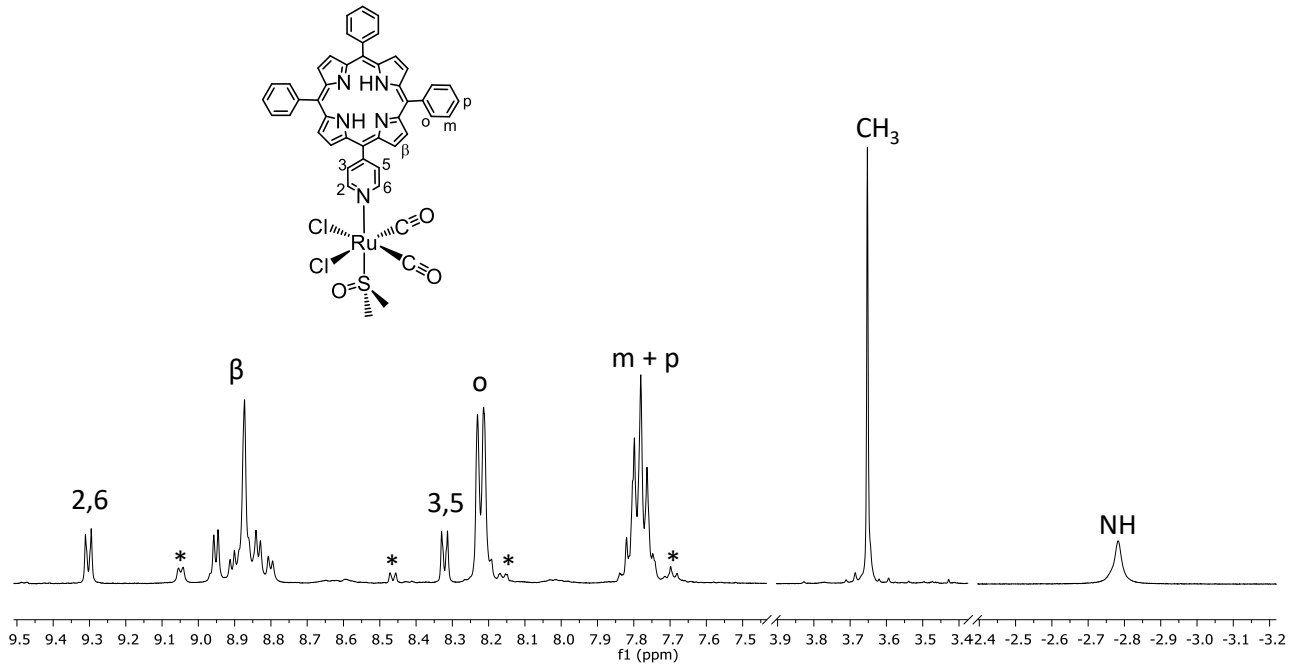

Figure A2.1. ^{1}H NMR spectrum of *cis,cis,trans*-$RuCl_2(CO)_2$(dmso-S)(4′MPyP) (**10**) in $CDCl_3$ with numbering scheme Some peaks of a minor unidentified species are labeled with *.

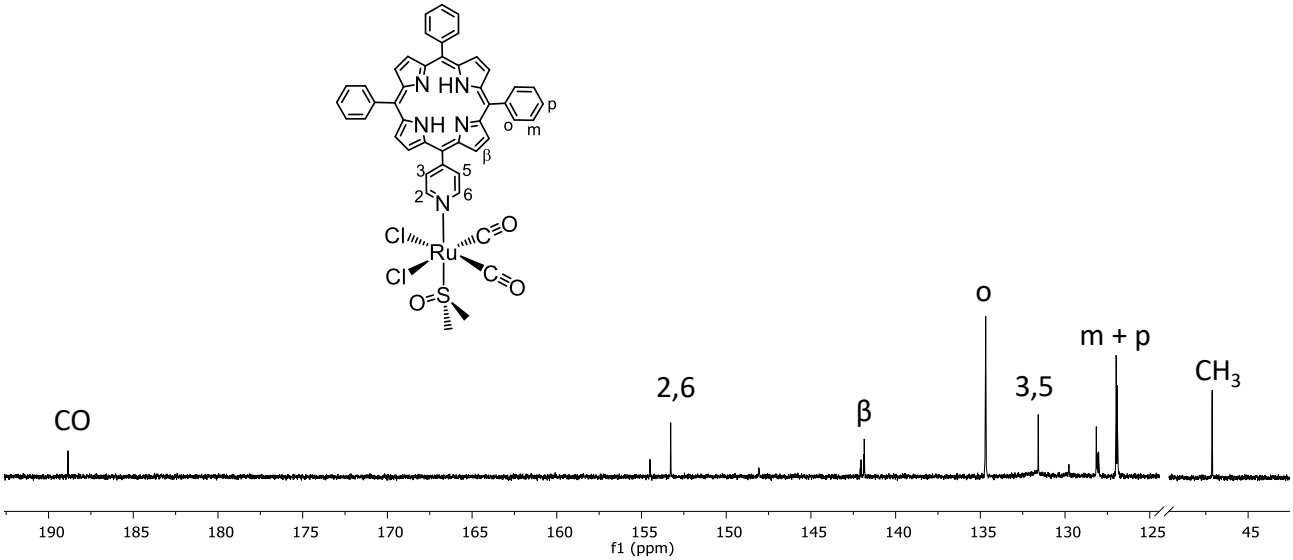

Figure A2.2. ^{13}C NMR spectrum of *cis,cis,trans*-$RuCl_2(CO)_2$(dmso-S)(4′MPyP) (**10**) in $CDCl_3$.

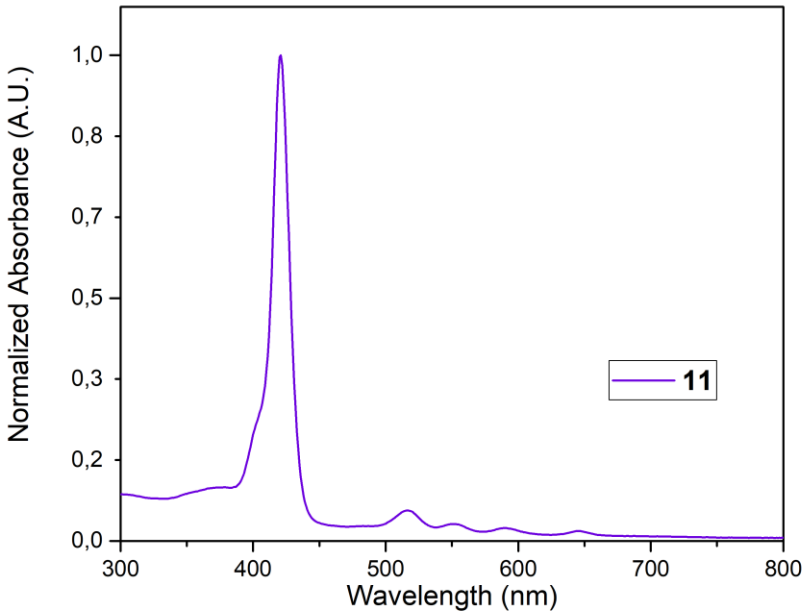

Figure A2.3. UV-vis spectrum of *cis,cis,trans*-$RuCl_2(CO)_2$(dmso-S)(4′MPyP) (**10**) ca. 10^{-6} M in $CHCl_3$.

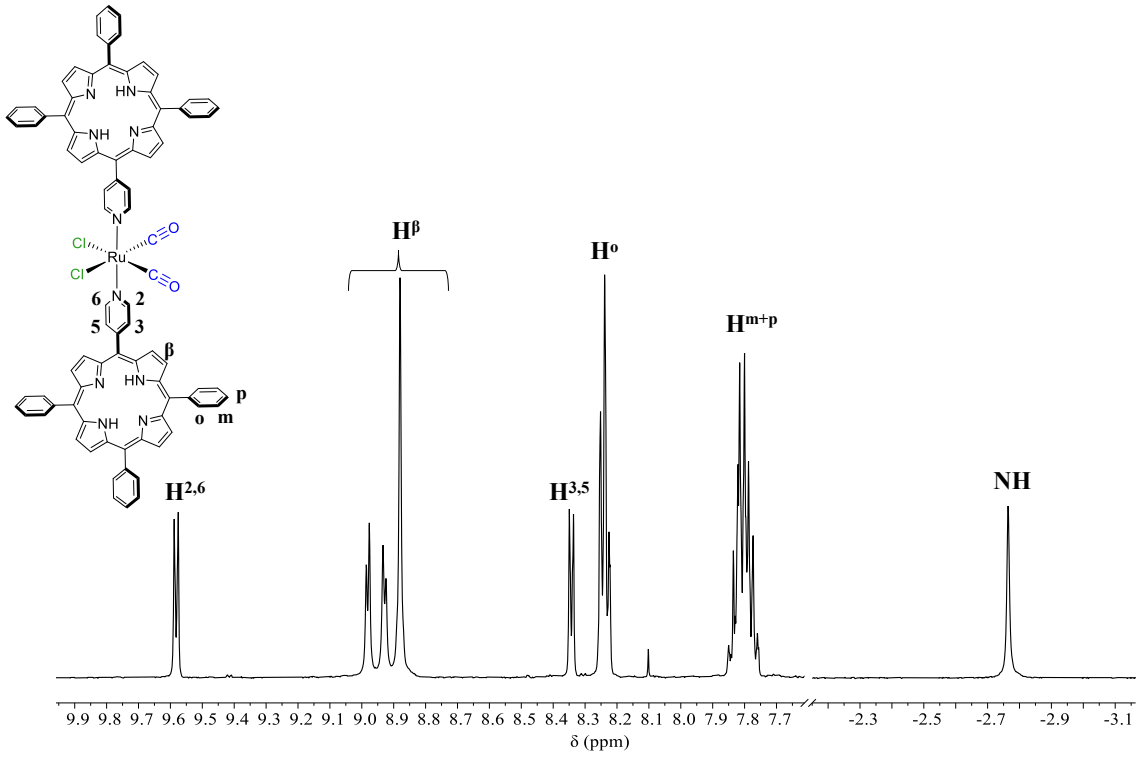

Figure A2.4. ^{1}H NMR spectrum of *cis,cis,trans*-$RuCl_2(CO)_2(4'MPyP)_2$ (**11**) in $CDCl_3$ with numbering scheme.

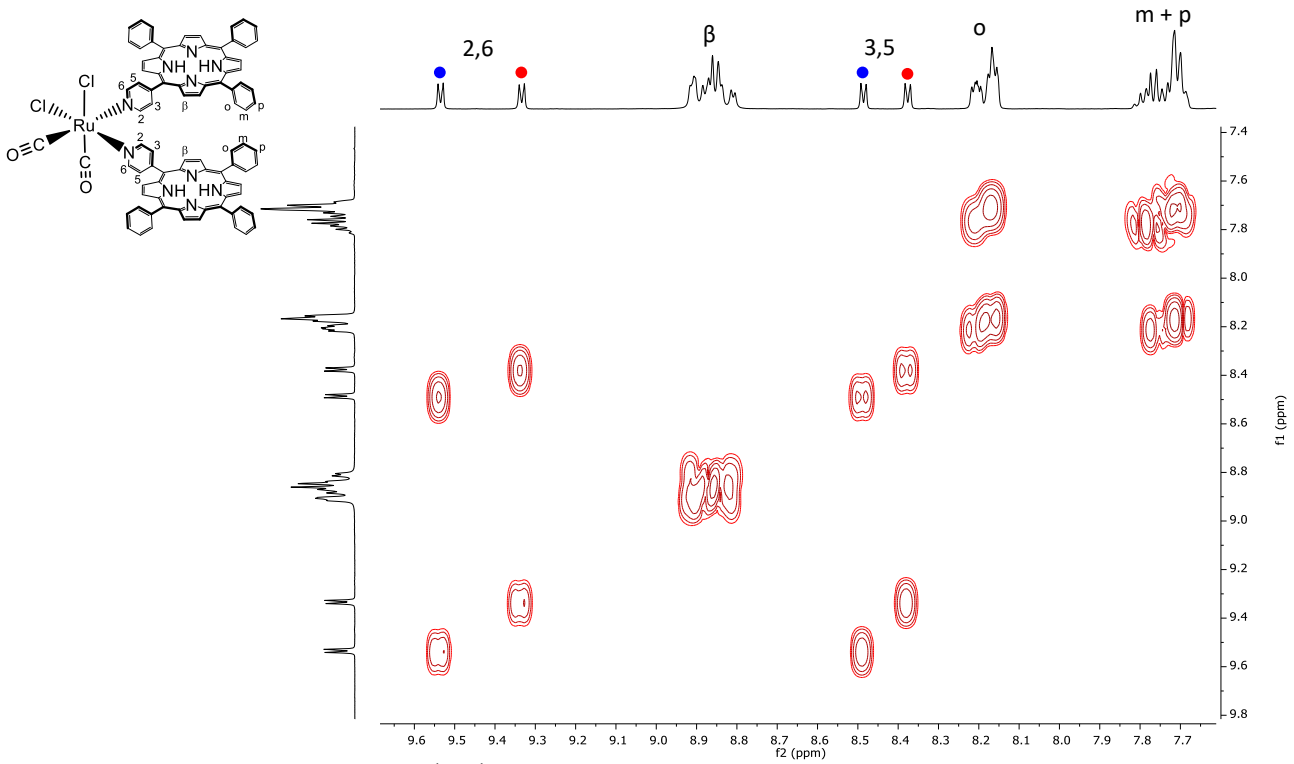

Figure A2.5. Aromatic region of ^{1}H-^{1}H COSY spectrum of *cis,cis,cis*-$RuCl_2(CO)_2(4'MPyP)_2$ (**12**) in $CDCl_3$. Dots of the same color indicate protons belonging to the same pyridyl ring.

Table A2.1. Crystallographic data and refinement details for compounds *trans,cis,cis*-$RuCl_2(CO)_2(4'MPyP)_2 \cdot 0.5C_6H_{14}$ (**9**) and *cis,cis,trans*-$RuCl_2(CO)_2(4'MPyP)_2 \cdot 1.3CHCl_3 \cdot C_4H_{10}O$ (**11**).

	9	**11**
Empirical Formula	$C_{88}H_{58}Cl_2N_{10}O_2Ru \cdot 0.5C_6H_{14}$	$C_{88}H_{58}Cl_2N_{10}O2Ru \cdot 1.3CHCl_3 \cdot C_4H_{10}O$
Formula weight (Da)	1502.50	1688.71
Temperature (K)	100(2)	100(2)
Wavelength (Å)	0.700	0.700
Crystal system	triclinic	monoclinic
Space Group	*P* -1	*P* 21/c
a (Å)	13.781(5)	17.733(4)
b (Å)	16.085(2)	13.271(3)
c (Å)	16.928(2)	34.343(7)
α (°)	89.931(2)	90
β (°)	97.25(1)	93.35(3)
γ (°)	94.45(1)	90
V (Å^3)	3711(2)	8068(3)
Z	2	4

ρ (g·cm^{-3})	1.345	1.390
F(000)	1550	3470
μ (mm^{-1})	0.324	0.425
θ min, max (°)	1.472, 28.227	1.133, 25.266
Resolution (Å)	0.74	0.78
Total refl. collctd	118885	28038
Independent refl.	19134	15146
Obs. Refl. [Fo>4σ(Fo)]	18234	9905
I/σ(I) (all data)	53.72	2.2
I/σ(I) (max res)	36.73	1.4
Completeness (all data)	0.995	0.991
R_{merge} (all data)	2.1%	0.060
R_{merge} (max res)	3.0%	0.540
Multiplicity (all data)	6.2	3.1
Multiplicity (max res)	6.0	2.9
Data/restraint/parameters	19134/2/934	15146/59/1056
GooF	1.050	1.030
R[I>2.0σ(I)],[a] wR2 [I>2.0σ(I)][a]	0.0435, 0.1139	0.0748, 0.2071
R (all data),[a] wR2 (all data)[a]	0.0451, 0.1153	0.1136, 0.2367

[a] $R_1 = \Sigma\, ||Fo|-|Fc|| \,/\, \Sigma|Fo|$, $wR_2 = [\Sigma\, w\,(Fo^2 - Fc^2)^2 \,/\, \Sigma w\,(Fo^2)^2]^{½}$

Table A2.2. Selected coordination distances (Å) and angles (°) for *trans,cis,cis*-$RuCl_2(CO)_2(4'MPyP)_2 \cdot 0.5C_6H_{14}$ (**9**).

Bond distances (Å)			
Ru1–C1	1.880(2)	Ru1–Cl2	2.3818(6)
Ru1–C2	1.873(2)	Ru1–N31	2.154(2)
Ru1–Cl1	2.3921(7)	Ru1–N41	2.157(2)
Bond angles (°)			
C1–Ru1–Cl1	91.86(7)	C2–Ru1–N41	179.34(7)
C1–Ru1–Cl2	90.05(7)	Cl2–Ru1–Cl1	176.20(2)
C1–Ru1–N31	177.84(7)	N31–Ru1–Cl1	89.07(4)
C1–Ru1–N41	91.52(8)	N31–Ru1–Cl2	88.92(4)
C2–Ru1–C1	89.10(9)	N31–Ru1–N41	86.53(6)
C2–Ru1–Cl1	90.21(7)	N41–Ru1–Cl1	89.54(4)

C2–Ru1–Cl2	93.10(7)	N41–Ru1–Cl2	87.13(4)
C2–Ru1–N31	92.85(7)		

Table A2.3. Dihedral angles (°) for *trans,cis,cis*-$RuCl_2(CO)_2(4'MPyP)_2 \cdot 0.5C_6H_{14}$ (**9**).* See Figure S6 for labeling scheme.

Dihedral angles (°)			
[Por3]···[R31]	56.63(5)	[Por4]···[R42]	60.65(6)
[Por3]···[R32]	70.88(8)	[Por4]···[R43]	60.31(5)
[Por3]···[R33]	68.36(5)	[Por4]···[R44]	68.63(6)
[Por3]···[R34]	81.40(7)	[Por3]···[Por4]	77.22(3)
[Por4]···[R41]	79.73(6)		

* For phenyl rings [R32] and [R34] only the major population (0.85 and 0.88, respectively) has been considered

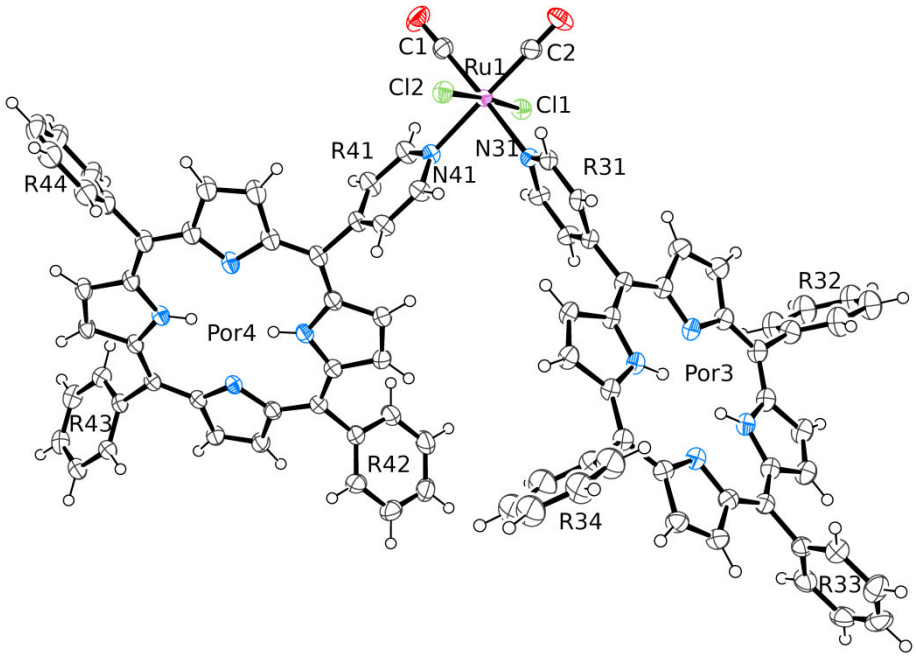

Figure A2.6. ORTEP representation (50% probability ellipsoids) of the solid state molecular structure of *trans,cis,cis*-$RuCl_2(CO)_2(4'MPyP)_2 \cdot 0.5C_6H_{14}$ (**9**) with labeling scheme for the dihedral angles reported in Table A2.3. For clarity, an hexane crystallization molecule has been omitted.

Table A2.4. Selected coordination distances (Å) and angles (°) for *cis*,*cis*,*trans*-$RuCl_2(CO)_2(4'MPyP)_2 \cdot 1.3CHCl_3 \cdot C_4H_{10}O$ (**11**).

Bond distances (Å)			
Ru1–C1	1.922(7)	Ru1–Cl2	2.403(2)
Ru1–C2	1.997(6)	Ru1–N11	2.114(4)
Ru1–Cl1	2.369(2)	Ru1–N21	2.116(4)
Bond angles (°)			
C1–Ru1–Cl1	88.8(2)	C2–Ru1–N21	91.4(2)
C1–Ru1–Cl2	178.1(1)	Cl2–Ru1–Cl1	89.56(6)
C1–Ru1–N11	91.1(2)	N11–Ru1–Cl1	90.0(1)
C1–Ru1–N21	92.1(2)	N11–Ru1–Cl2	87.9(1)
C2–Ru1–C1	91.6(2)	N11–Ru1–N21	176.3(2)
C2–Ru1–Cl1	179.5(1)	N21–Ru1–Cl1	88.3(1)
C2–Ru1–Cl2	90.1(2)	N21–Ru1–Cl2	88.9(1)
C2–Ru1–N11	90.3(2)		

Table A2.5. Dihedral angles (°) for *cis*,*cis*,*trans*-$RuCl_2(CO)_2(4'MPyP)_2 \cdot 1.3CHCl_3 \cdot C_4H_{10}O$ (**11**). See Figure A2.7 for labeling scheme.

Dihedral angles (°)			
[Por1]···[R11]	79.9(1)	[Por2]···[R22]	65.3(1)
[Por1]···[R12]	83.9(2)	[Por2]···[R23]	89.7(2)
[Por1]···[R13]	57.0(2)	[Por2]···[R24]	60.5(2)
[Por1]···[R14]	83.3(2)	[Por1]···[Por2]	11.96(8)
[Por2]···[R21]	78.6(1)		

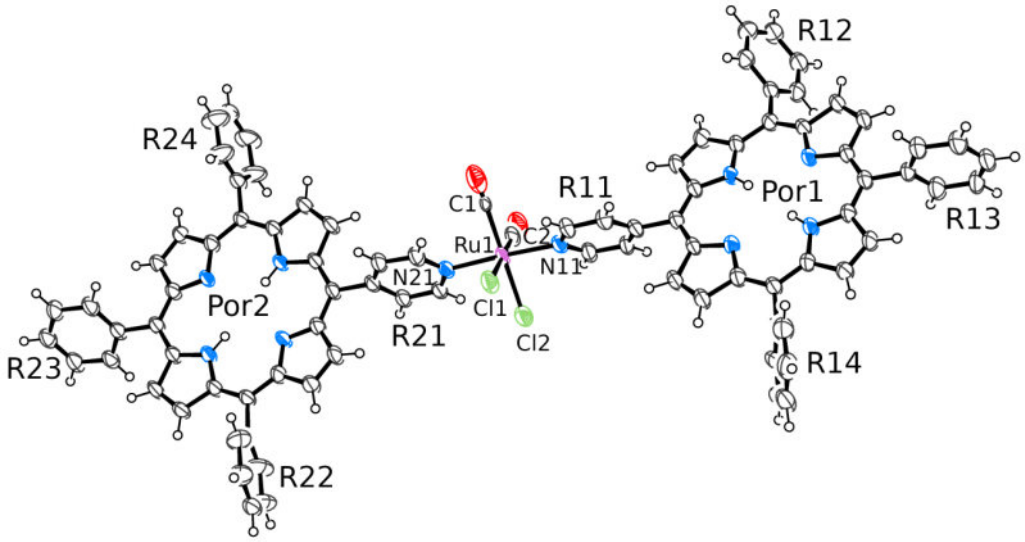

Figure A2.7. ORTEP representation (50% probability ellipsoids) of the solid state molecular structure of *cis*,*cis*,*trans*-$RuCl_2(CO)_2(4'MPyP)_2 \cdot 1.3CHCl_3 \cdot C_4H_{10}O$ (**11**) with labeling scheme for the dihedral angles reported in Table S5. For clarity, the chloroform and hexane crystallization molecules have been omitted.

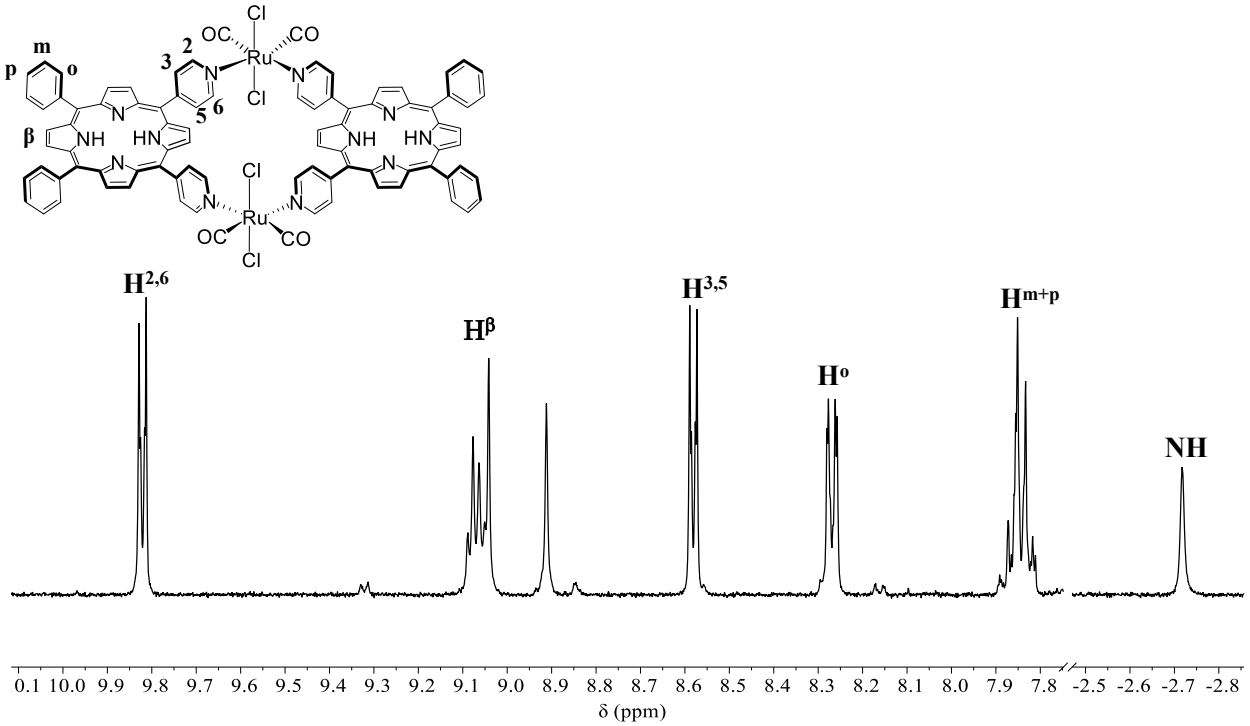

Figure A2.8. ^{1}H NMR spectrum at room temperature of [*trans*,*cis*,*cis*-$RuCl_2(CO)_2(4'cisDPyP)]_2$ (**2**) in $CDCl_3$ with numbering scheme.

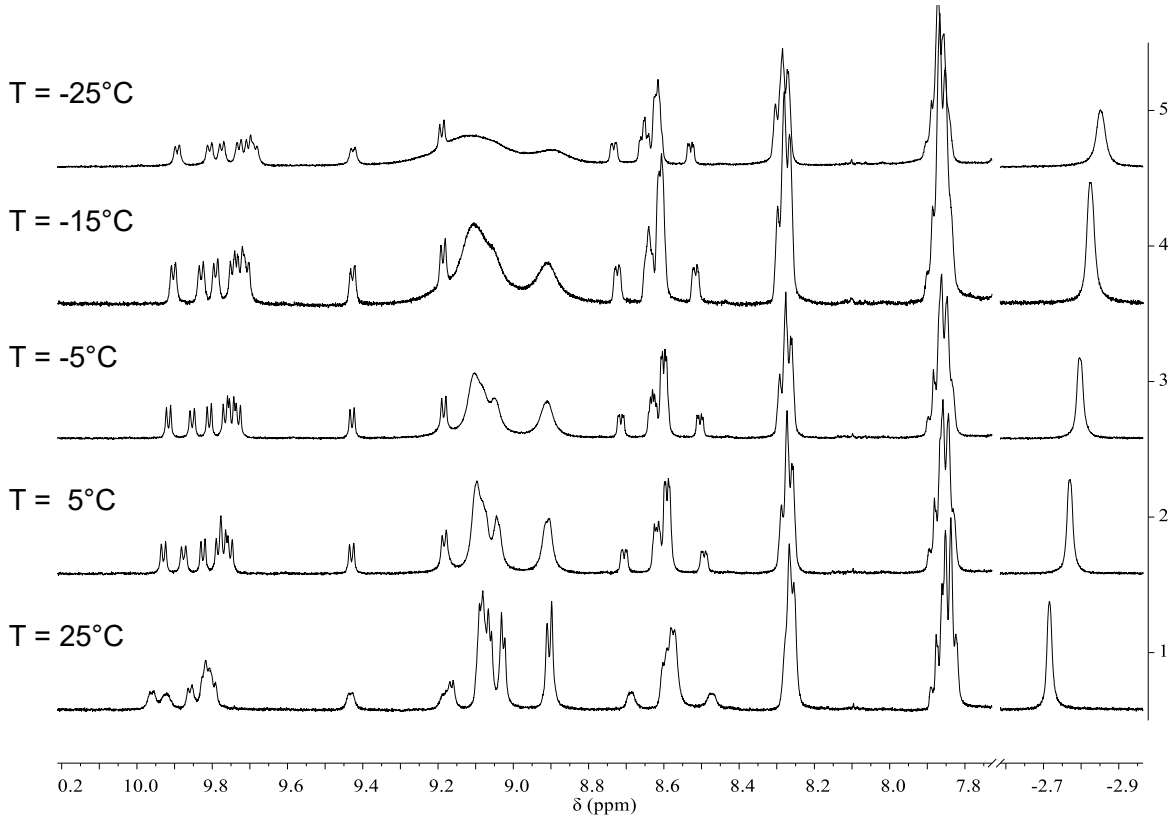

Figure A2.9. ^{1}H NMR spectrum of [{*trans,cis,cis*-$RuCl_2(CO)_2$}(4′*cis*DPyP)$_2${*cis,cis,cis*-$RuCl_2(CO)_2$}] (**13**) in $CDCl_3$ at different temperatures from -25 to 25°C.

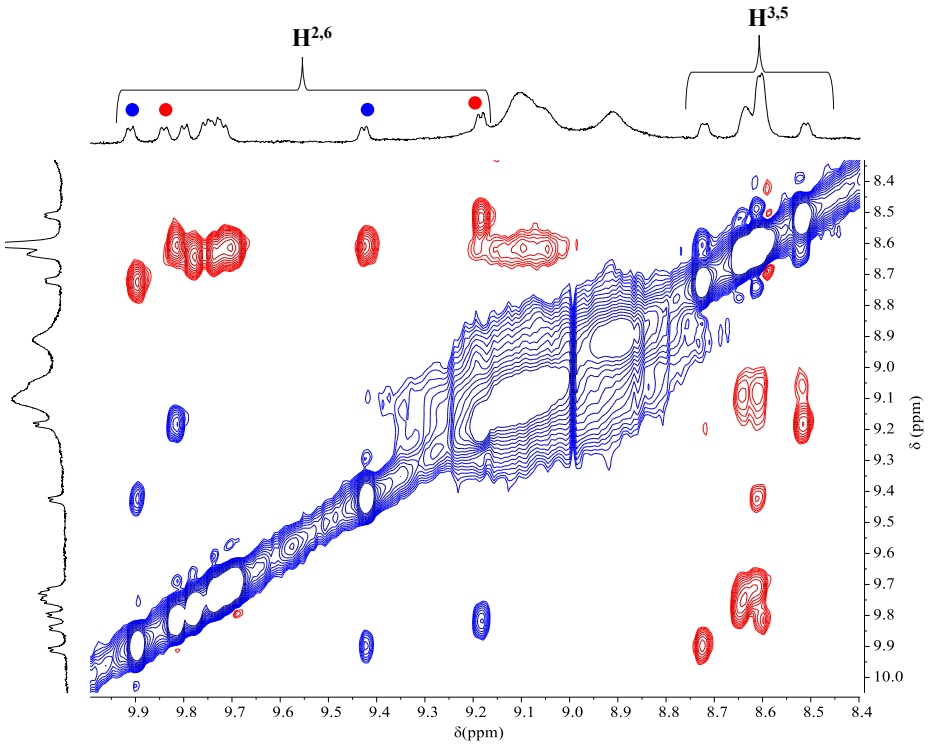

Figure A2.10. ROESY spectrum of [{*trans,cis,cis*-$RuCl_2(CO)_2$}(4′*cis*DPyP)$_2${*cis,cis,cis*-$RuCl_2(CO)_2$}] (**13**) in $CDCl_3$ at –10°C. Exchange cross-peaks are in blue, whereas COSY cross-peaks are in red.

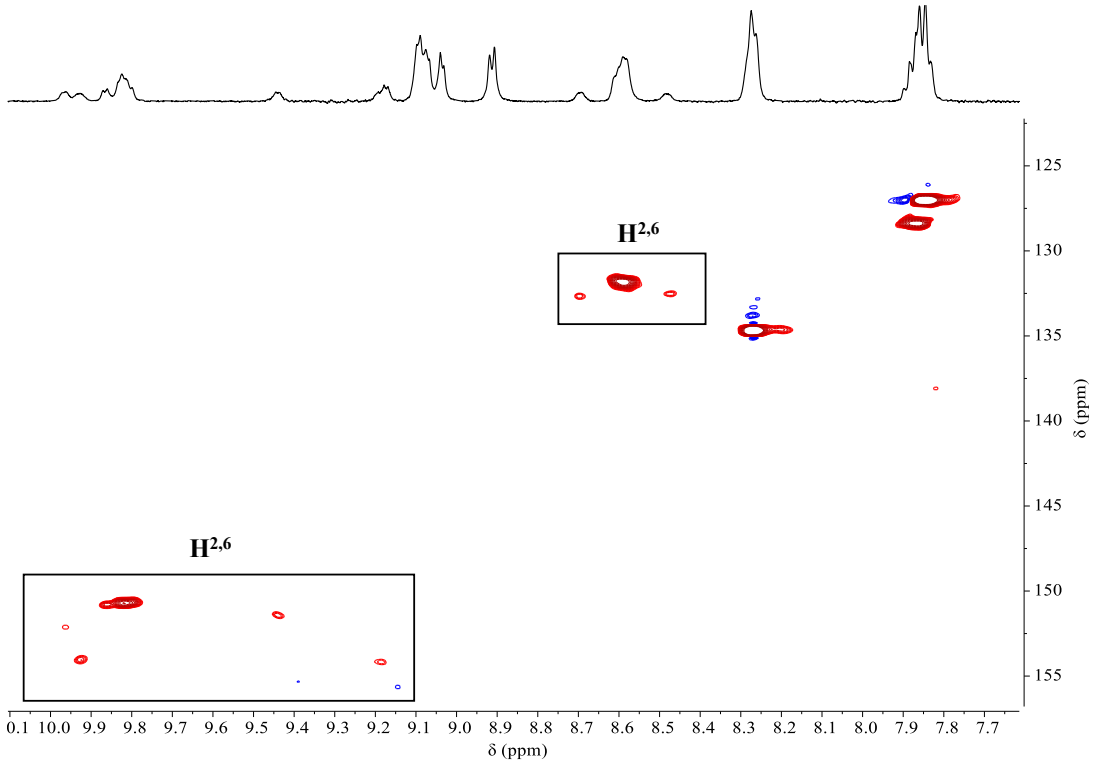

Figure A2.11. ^{1}H-^{13}C HSQC spectrum of [{*trans,cis,cis*-$RuCl_2(CO)_2$}(4′*cis*DPyP)$_2${*cis,cis,cis*-$RuCl_2(CO)_2$}] (**13**) in $CDCl_3$ at –10°C.

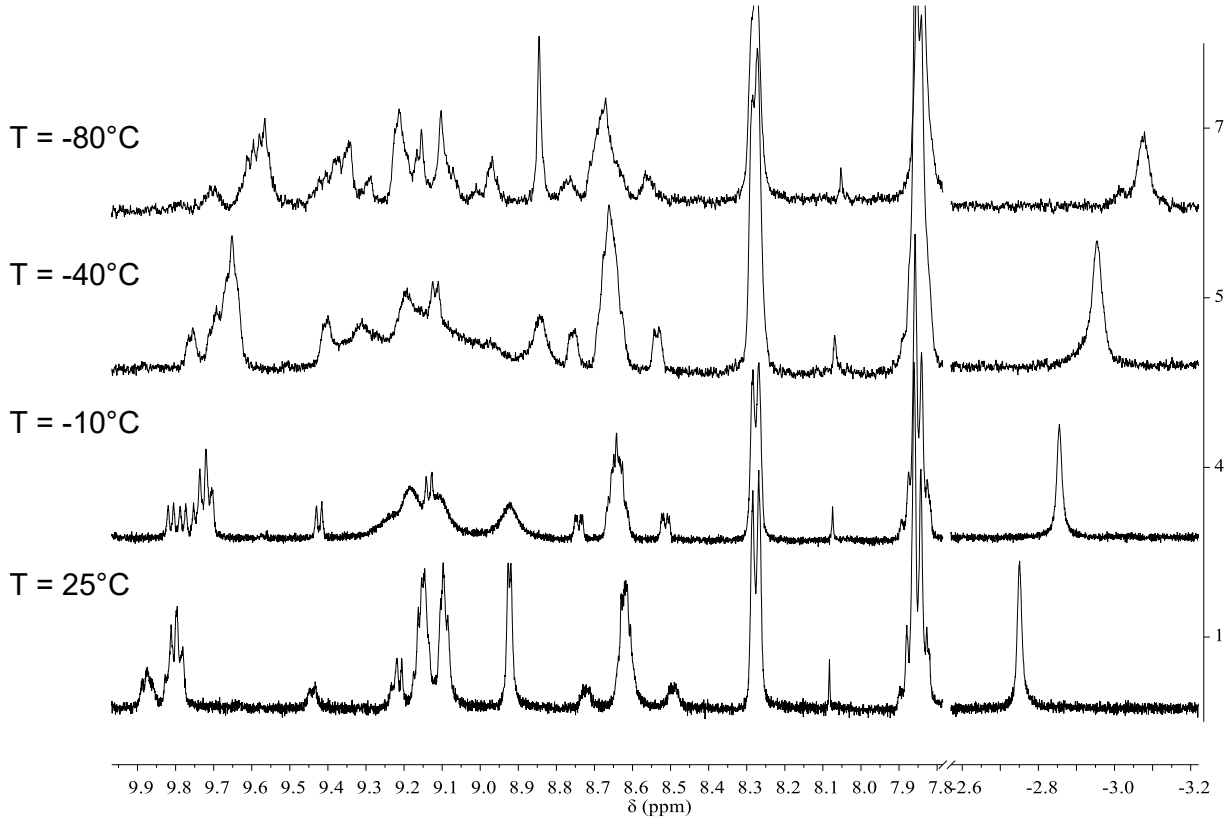

Figure A2.12. ^{1}H NMR spectrum of [{*trans,cis,cis*-$RuCl_2(CO)_2$}(4′*cis*DPyP)$_2${*cis,cis,cis*-$RuCl_2(CO)_2$}] (**13**) in CD_2Cl_2 at different temperatures from 25 to –80°C.

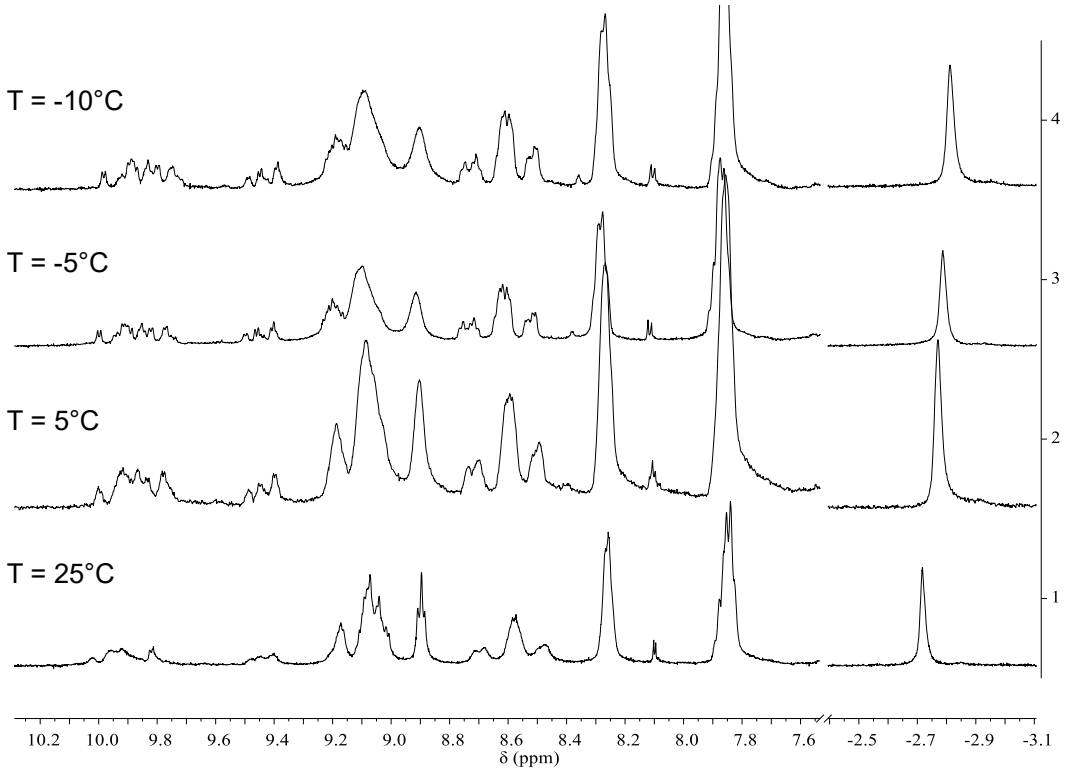

Figure A2.13. ^{1}H NMR spectrum of [*cis,cis,cis*-$RuCl_2(CO)_2$(4′*cis*DPyP)]$_2$ (**14**) in CD_2Cl_2 at different temperatures from 25 to –10°C.

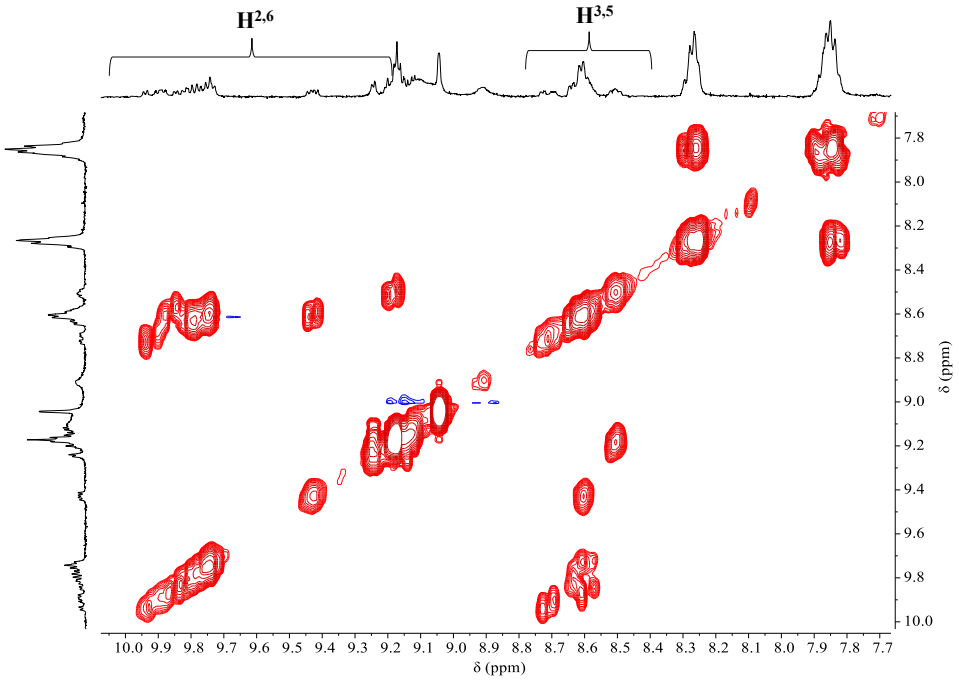

Figure A2.14. ^{1}H-^{1}H COSY spectrum of [*cis,cis,cis*-$RuCl_2(CO)_2$(4′*cis*DPyP)]2 (**14**) in $CDCl_3$ at –5°C.

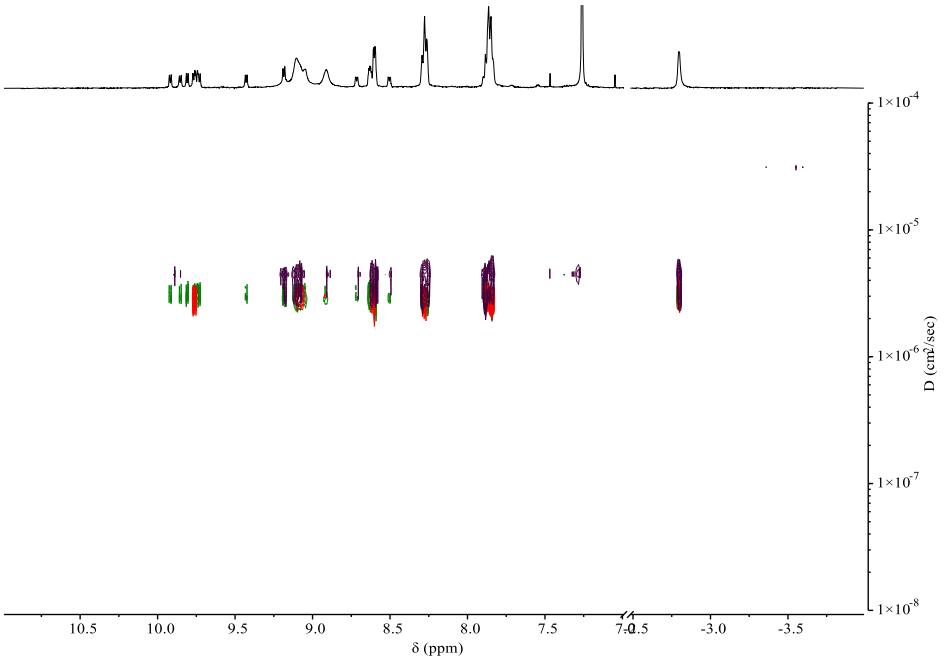

Figure A2.15. Overlapped ^{1}H DOSY spectra of [*trans,cis,cis*-$RuCl_2(CO)_2$(4′-*cis*DPyP)]$_2$(**2**) (red dots), [{*trans,cis,cis*-$RuCl_2(CO)_2$}(4′-*cis*DPyP)$_2${*cis,cis,cis*-$RuCl_2(CO)_2$}] (**13**) (green dots), and [*cis,cis,cis*-$RuCl_2(CO)_2$(4′-*cis*DPyP)]$_2$ (**14**) (blue dots) in CDCl3 at –5°C. In the case of 15, only the decay of the most intense resonances in the spectrum were fitted. Only the ^{1}H NMR spectrum of **13** is reported on the abscissa for simplicity

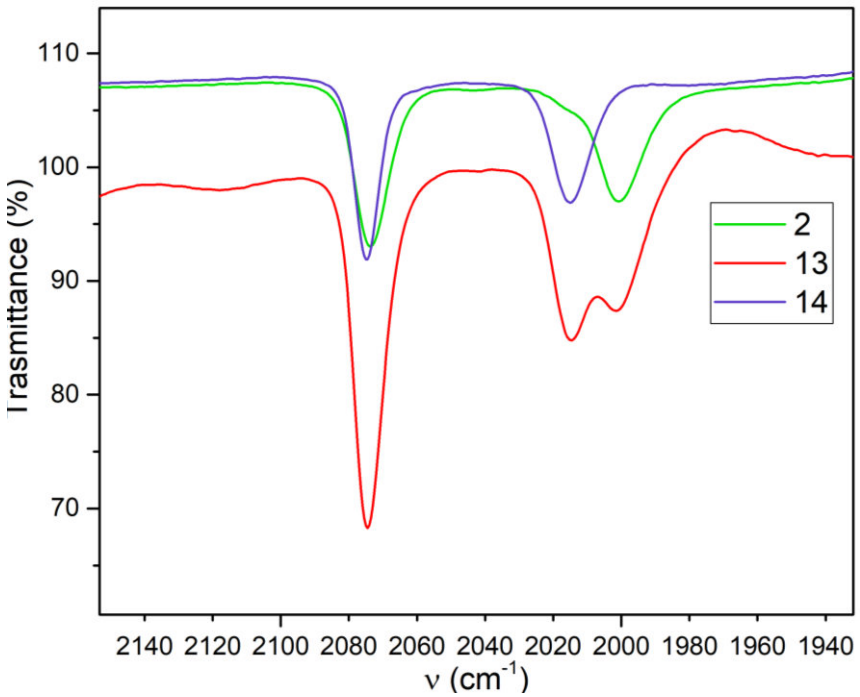

Figure A2.16. CO stretching region in the IR spectra of the three diastrereoisomeric 2+2 metallacycles [*trans,cis,cis*-$RuCl_2(CO)_2$(4′*cis*DPyP)]$_2$ (**2**), [{*trans,cis,cis*-$RuCl_2(CO)_2$}(4′*cis*DPyP)$_2${*cis,cis,cis*-$RuCl_2(CO)_2$}] (**13**), and [*cis,cis,cis*-$RuCl_2(CO)_2$}(4′*cis*DPyP)]$_2$ (**14**) in $CHCl_3$ solution.

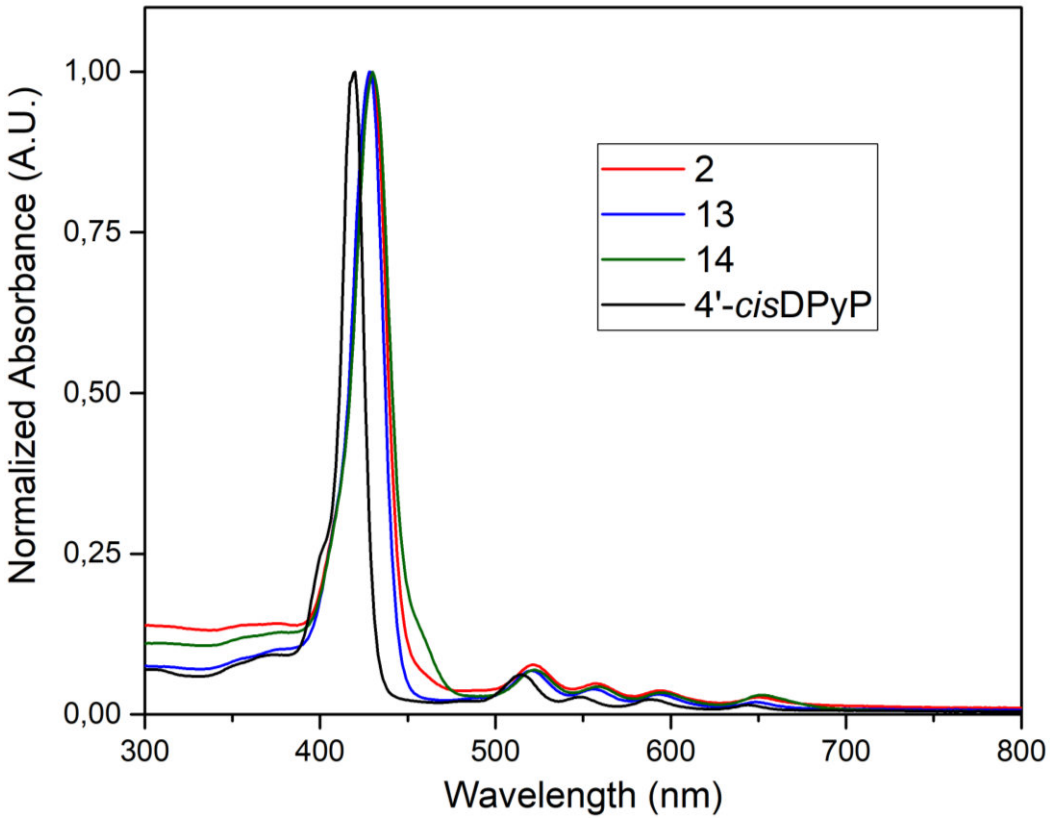

Figure A2.17. UV-vis spectra of the three strereoisomeric 2+2 metallacycles [*trans,cis,cis*-$RuCl_2(CO)_2$(4′*cis*DPyP)]$_2$ (**2**), [{*trans,cis,cis*-$RuCl_2(CO)_2$}(4′*cis*DPyP)$_2${*cis,cis,cis*-$RuCl_2(CO)_2$}] (**13**), and [*cis,cis,cis*-$RuCl_2(CO)_2$}(4′*cis*DPyP)]$_2$ (**14$_{alt}$**+**14$_{pw}$**), and, for comparison, of 4′*cis*DPyP ca. 10^{-6} M in $CHCl_3$.

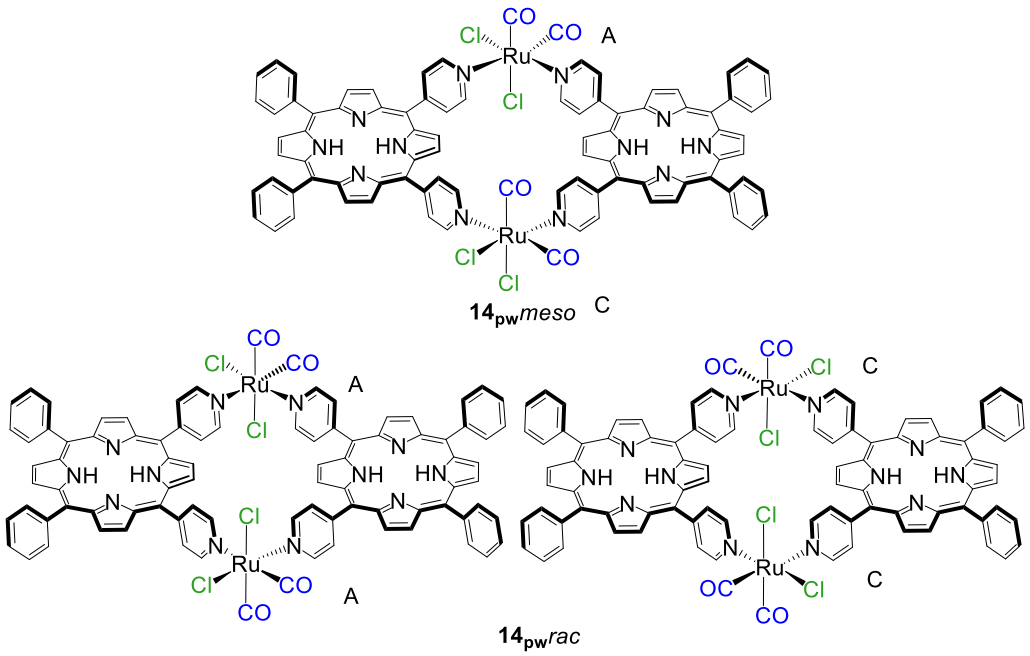

Figure A2.18. The meso and racemic forms of metallacycle [*cis,cis,cis*-$RuCl_2(CO)_2$}(4′*cis*DPyP)]$_2$ (**14$_{pw}$)** with the A and C chirality symbols on each corner.

CHAPTER 3

3 Expanded Porphyrin Metallacycles

3.1 Introduction

One way to increase the stability of the supramolecular adducts is to increase the cooperative effect by increasing the size of the molecular panels and therefore the number of axial Zn–N connections they can form.

Using the metal-mediated self-assembly approach, it is possible – in principle – to extend the porphyrin metallacycles exploiting the same metal connector used for the molecular squares **2** and **3**. An example is the molecular panel of formula [{*trans,cis,cis*-$RuCl_2(CO)_2$}$_4$(4′*cis*DPyP)$_2$(4′TPyP)] (**19**) that contains three 4′pyridylporphyrins – two of one type and one of another – connected via four identical Ru(II) fragments. Reasonably, this metallacycle, which can be thought of as deriving from **2** by insertion of a 4′TPyP in the center, should have a substantially planar geometry and, after zincation, three axial coordination sites available.

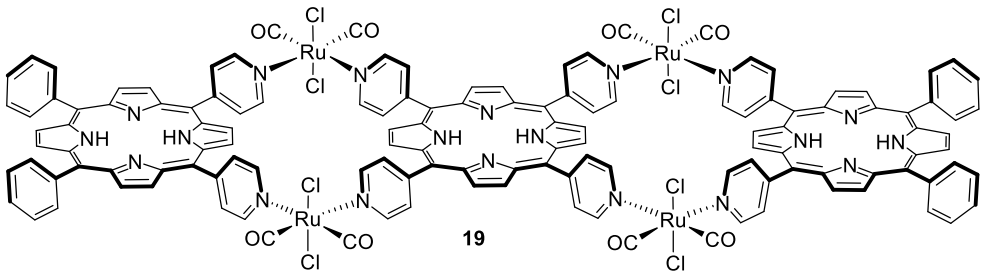

Figure 3.1. Predicted structure for the triporphyrin metallacycle [{*trans,cis,cis*-$RuCl_2(CO)_2$}$_4$(4′*cis*DPyP)$_2$(4′TPyP)] (**19**).

In principle, two synthetic approaches are possible for metallacycles of this type: one is statistical (one-pot), in which the three components are mixed in a stoichiometric ratio; the second is a two-step synthesis, in which the two different porphyrins are coordinated to the ruthenium fragments in two stages (Scheme 3.1).

Previously, Drain et al. used a one-pot approach to obtain a discrete nona-porphyrin system mediated by Pd(II).[1] In that case, four equivalents of 4′*cis*DPyP, four equivalents of 4′*tris*PyP and one equivalent of 4′TPyP were added to twelve equivalents of [*trans*-$PdCl_2(NCPh)_2$]. The reaction occurs under thermodynamic control; therefore, the formation of the Pd–N(py) bond is reversible and thus the most stable product is obtained. Thirty minutes after adding the Pd(II) complex to the mixture of

4′PyPs in $CHCl_3$ at room temperature, the desired product was obtained with a 90% yield (Figure 3.2).

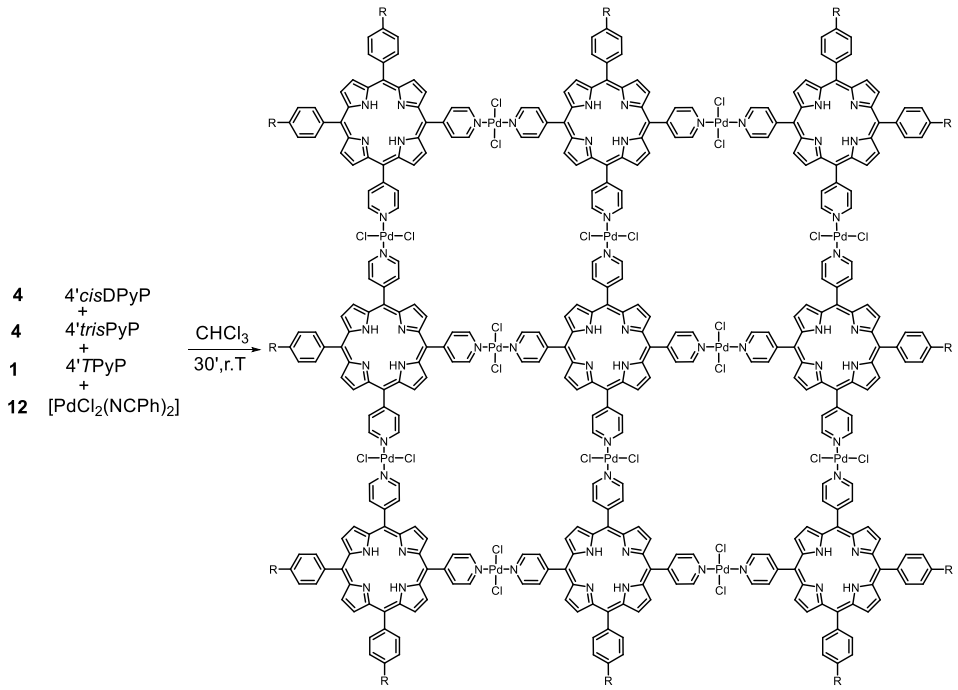

Figure 3.2. Reaction scheme for the synthesis of the nona-porphyrin system described by Drain et al.

In general, considering that the reactions involving Ru(II) and N-donor ligands occur substantially under kinetic control, it can be expected that a one-pot approach would lead to mixtures of species, both cyclic and oligomers, which have to be separated by column chromatography.

On the other hand, the stepwise strategy requires that the two labile ligands in the metal connectors, specifically the two dmso-*O*, are replaced in different stages. The treatment of one of the two porphyrins with an excess of **1** should afford the replacement of only one of the labile dmso-*O* ligands, generating an intermediate in which all the pyridyl rings of the porphyrin are coordinated to a ruthenium complex that still has reactive site, i.e. a dmso-*O*, in the *cis* position.

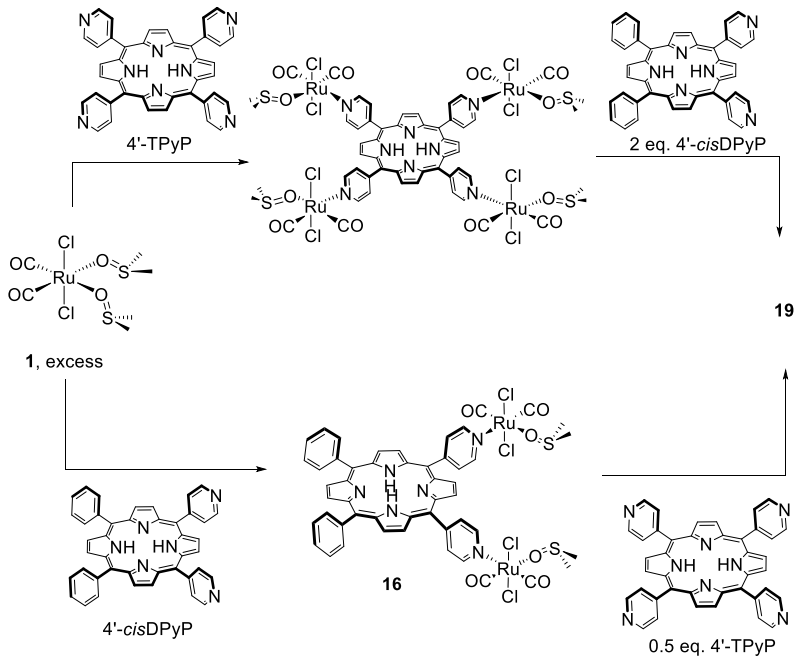

Scheme 3.1. Reaction scheme of the possible stepwise synthetic strategies for the synthesis of the metallacycle **19**.

Using similar synthetic strategies, it is also possible to link together two porphyrins that differ in the position of the nitrogen atom. The simplest adduct is a heteroleptic 2+2 metallacycle of formula [{*trans,cis,cis*-$RuCl_2(CO)_2$}$_2$(4′*cis*DPyP)(3′*cis*DPyP)] (**18**), resulting from the union of two different *cis*-dipyridylporphyrins, 4′*cis*DPyP and 3′*cis*DPyP, via the same metallic Ru(II) connector used before.

In the hypothesis that the two porphyrins maintain a coordination geometry similar to the one they have in the homoleptic squares **2** and **3**, we would expect to obtain a folded molecular square, in which the planes of the two porphyrins should form an angle of ca. 90° (Figure 3.3).

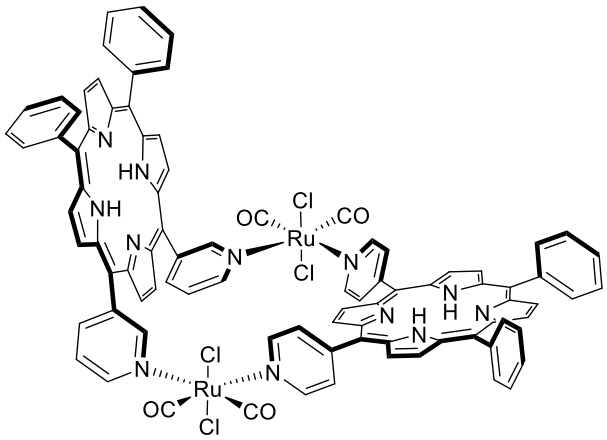

Figure 3.3. Predicted structure for the heteroleptic 2+2 molecular square [{*trans*,*cis*,*cis*-$RuCl_2(CO)_2$}$_2$(4′*cis*DPyP)(3′*cis*DPyP)] **(18).**

Similarly, it should be possible to synthesize even more complicated systems, such as heteroleptic triporphyrinic metallacycles whose predicted geometries are appealing in the context of supramolecular chemistry (Figure 3.4).

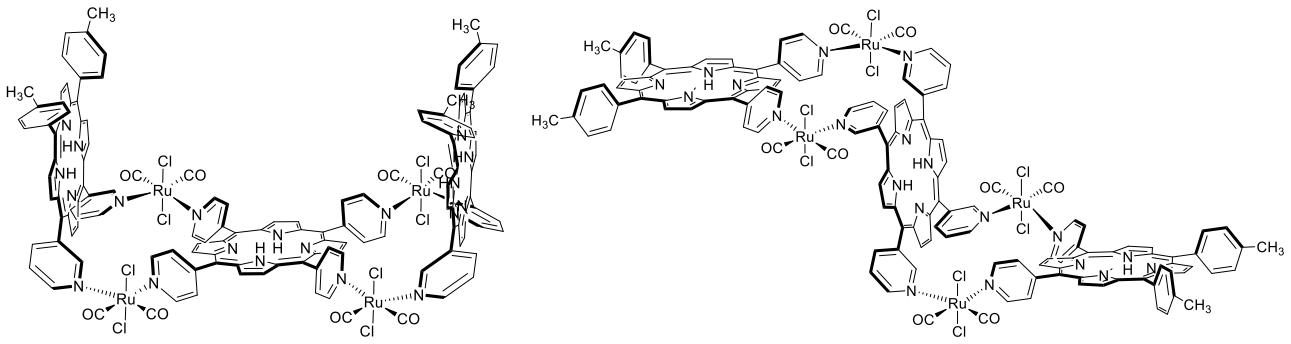

Figure 3.4: Examples of heteroleptic triporphyrinic metallacycles obtainable combing 3′ and 4′pyridylporphyrins, [{*trans,cis,cis*-$RuCl_2(CO)_2$}$_4$(3′*cis*DPyMP)$_2$(4′TPyP)] (left) and [{*trans,cis,cis*-$RuCl_2(CO)_2$}$_4$(4′*cis*DPyMP)$_2$(3′TPyP)] (right).

3.2 Results and discussion

3.2.1 Synthesis of [{*trans,cis,cis*-$RuCl_2(CO)_2$}$_2$(4′*cis*DPyP)(3′*cis*DPyP)] (18)

The first part of this chapter is focused on the synthesis and characterization of the heteroleptic 2+2 metallacycle **18**.

The synthetic two-step strategy adopted for obtaining **18** is described first. The first step consists in the preparation of a reactive precursor, already containing one of the two porphyrins, of formula [{*trans*,*cis*,*cis*-$RuCl_2(CO)_2$(dmso-*O*)}$_2$(4′*cis*DPyP)] (**16**) or [{*trans,cis,cis*-$RuCl_2(CO)_2$(dmso-*O*)}$_2$(3′*cis*DPyP)] (**17**). Each one of these intermediates, that can be thought of as a ditopic acceptor fragment, allows – upon replacement of the dmso-O ligands – the coordination of the two Ru(II) complexes to the complementary porphyrin, respectively 3′*cis*DPyP or 4′*cis*DPyP, leading to **18**. One of the two possible synthetic pathways is reported in the following reaction scheme (Scheme 3.2):

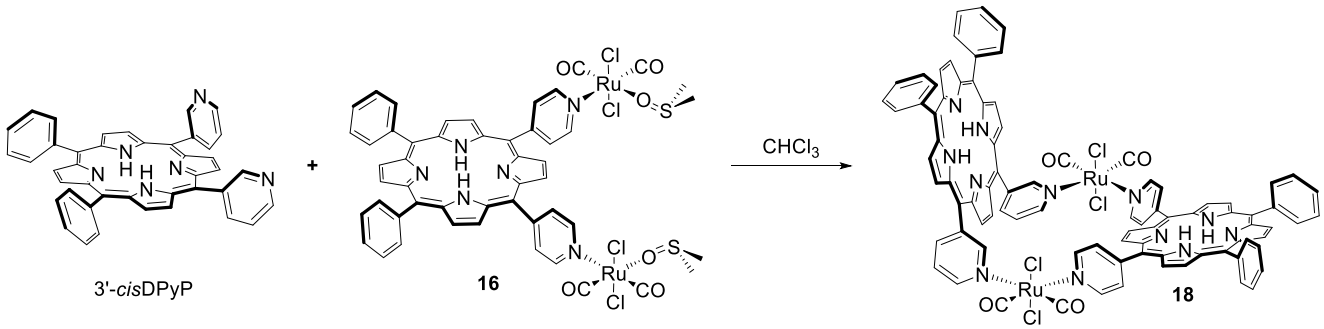

Scheme 3.2. Preparation of the heteroleptic porphyrin metallacycle [{*trans*,*cis*,*cis*-$RuCl_2(CO)_2$}$_2$(4′*cis*DPyP) (3′*cis*DPyP)] (**18**) starting from the reactive precursor **16**.

The intermediate **16** was obtained by treating 4′*cis*DPyP with an excess (at least 4 equivalents) of **1** in chloroform at room temperature. Under these conditions, only one of the labile ligands (dmso-*O*) of the complex was replaced (Scheme 3.3).

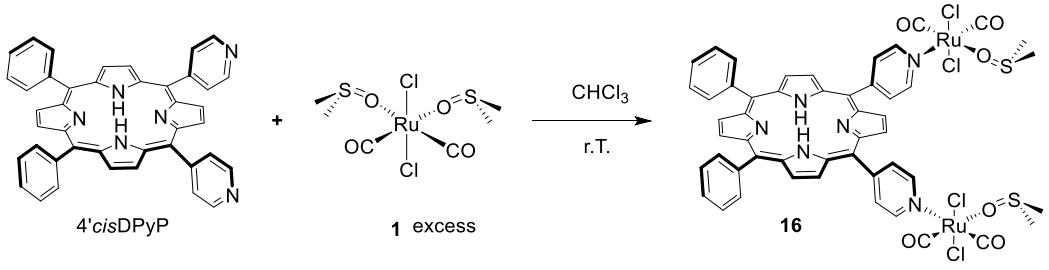

Scheme 3.3. Reaction scheme for the synthesis of the reactive precursor [{*trans*,*cis*,*cis*-$RuCl_2(CO)_2$(dmso-*O*)}$_2$(4′*cis*DPyP)] **(16).**

The reaction was monitored by TLC ($CHCl_3$:EtOH 98:2); after 50 minutes there was no trace of unreacted 4′*cis*DPyP (R_f = 0.35), sign of the complete conversion. The solvent was removed under reduced pressure and the solid was washed with H_2O to remove the unreacted ruthenium complex and the released DMSO (the product is soluble in all the other solvents tested), then it was redissolved in $CHCl_3$ and anhydrified on Na_2SO_4.

The washings with H_2O gave rise – in part – to an aqua species of the product of formula [{*trans,cis,cis*-$RuCl_2(CO)_2(H_2O)$}$_2$(4′*cis*DPyP)] (**16H$_2$O**), in which the dmso-*O*s were replaced by water molecules.[a]

The ^{1}H NMR spectrum of **16H$_2$O** in DMSO-d_6 (Figure 3.5), after the washing with H_2O, presents only one main set of resonances in agreement with a species in which 4′*cis*DPyP is symmetrically coordinated to two equal complexes of Ru(II); conversely, the spectrum recorded in $CDCl_3$ (Figure 3.6) shows the presence of two sets of partially resolved signals, one attributed to the aqua species **16H$_2$O** and the other to **16.**

[a] In theory two aqua species are possible, depending if one or both residual dmso-*O* ligands are replaced by water molecules

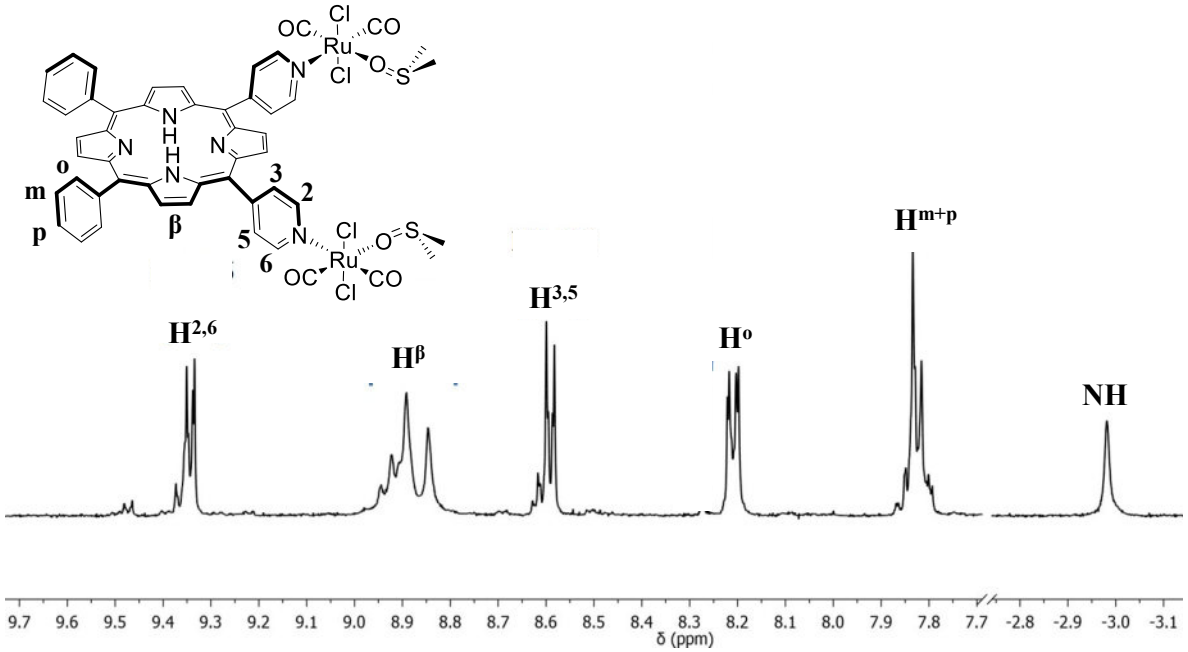

Figure 3.5. ^{1}H NMR spectrum of [{*trans*,*cis*,*cis*-$RuCl_2(CO)_2$(dmso-*O*)}$_2$(4′*cis*DPyP)] (**16**) in DMSO-d_6.

The addition of DMSO-d_6 causes a progressive decrease of the minor set of signals, attributed to the aqua species (**16H$_2$O**), untill its complete disappearance. Simultaneously, the resonances become sharper, particularly that of NH, confirming that in case of an excess of DMSO, the equilibrium between **16** and **16H$_2$O** is shifted towards **16**. The small shifts of all signals after every addition of DMSO-d_6 derive from the co-presence of the two solvents.

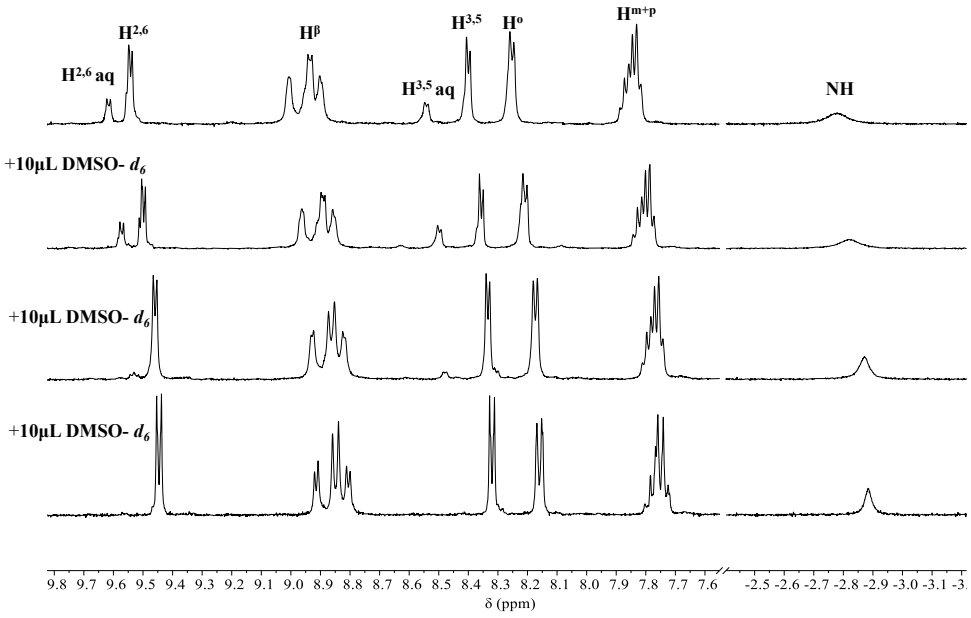

Figure 3.6. The ^{1}H NMR spectrum of **16+16H$_2$O** in $CDCl_3$ (top); the spectra below are recorded after subsequent additions of 10 μL aliquots of DMSO-d_6.

The synthesis of **18** was carried out treating 3′*cis*DPyP with a slight excess of **16**+**16H₂O** (**16**/3′-*cis*DPyP 1.5:1) at 40°C in dried CH_2Cl_2 in the presence of DMSO (to restore species **16** and minimize the possible formation of OH bridged by-products). The reaction was monitored by TLC (silica gel, $CHCl_3$), following the vanishing of the spot of the 3′*cis*DPyP. The crude was purified by flash chromatography and a single fraction was collected (R_f = 0.31). The ^{1}H NMR spectrum of **18** is reported in Figure 3.7 (yield 26%). Assignments were made according to 2D spectra and by comparison with the symmetrical metallacycles **2** and **3**.

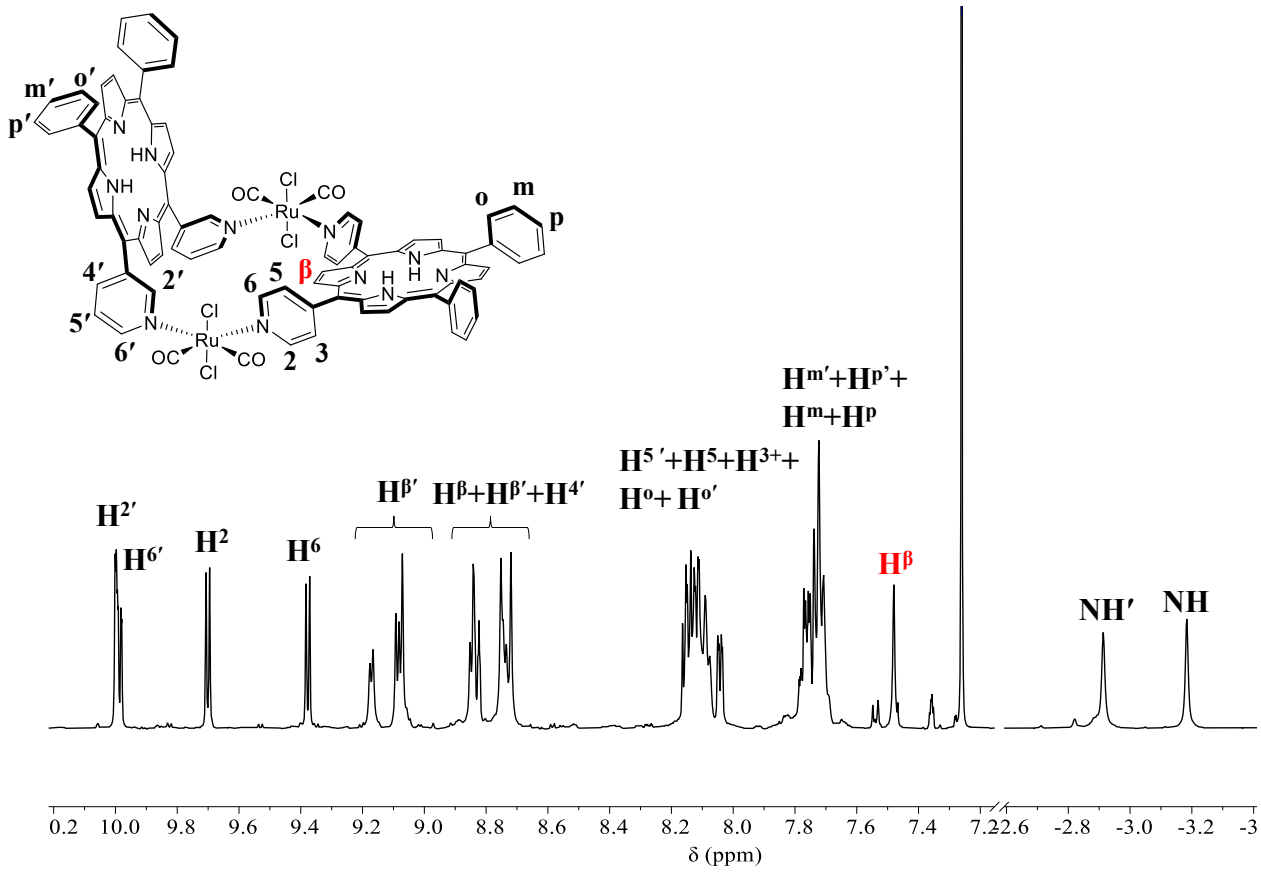

Figure 3.7. ^{1}H-NMR spectrum ($CDCl_3$) of [{*trans,cis,cis*-$RuCl_2(CO)_2$}$_2$(4′*cis*DPyP)(3′*cis*DPyP)] (18) after column chromatography.

In the high frequency region, the ^{1}H NMR spectrum displays the usual signals of 4′*cis*DPyP and 3′*cis*DPyP coordinated in a symmetrical fashion to two {*trans,cis,cis*-$RuCl_2(CO)_2$} fragments.

There is no evidence of coordinated dmso, in agreement with the complete substitution of the two labile dmso-*O*'s of **16**. The two doublets at 9.70 and 9.38 ppm were assigned to H2 and H6 of the 4′*cis*DPyP; in all these systems, the two pyridyl rings coordinated to the ruthenium are ca. perpendicular to the porphyrin ring and in slow rotation on the Ru–N bond and, since the plane of each macrocycle is not a plane of symmetry of the metallacycle, they appear as two distinct signals. This hypothesis was also confirmed by the ^{1}H-^{1}H ROESY spectrum (Figure 3.8) where an exchange cross peak between H2 and H6 is visible.

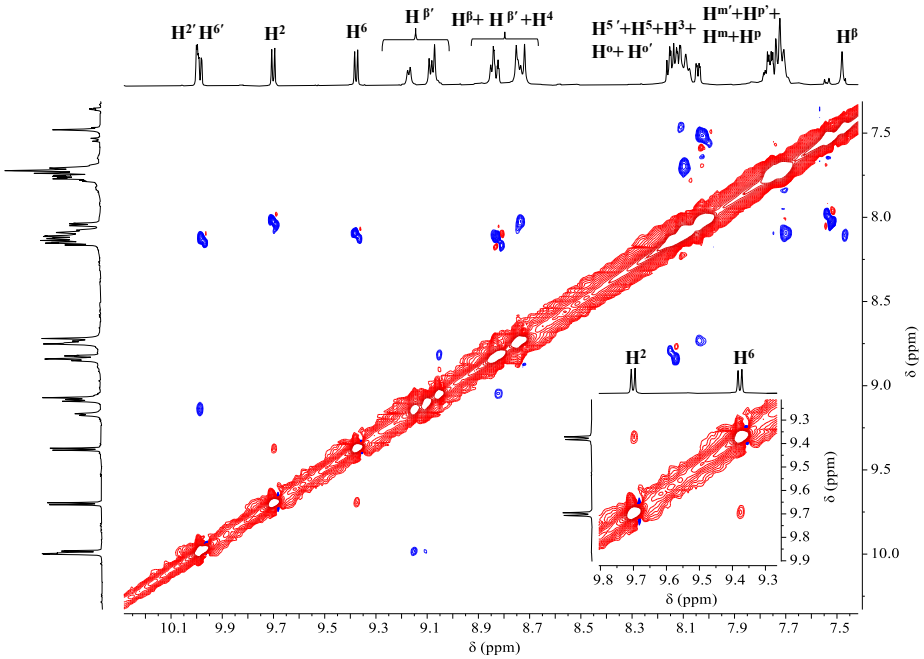

Figure 3.8. ^{1}H-^{1}H ROESY spectrum ($CDCl_3$) of **18** and enlargement showing the exchange cross peaks (red) between H2 and H6.

The doublet at lower frequencies was attributed to the proton above the average plane of 4′*cis*DPyP, that partially falls in the shielding cone of the adjacent 3′*cis*DPyP porphyrins. H3 and H5 are more distant from the other porphyrin and so their signals fall closer to each other, together with other signals, in a multiplet at 8.13 ppm and are distinguishable in the ^{1}H-^{1}H COSY spectrum. The resonances of H2′ and H6′ of 3′*cis*DPyP, a singlet and a doublet respectively, are partially overlapped at ca. 10 ppm and account for 4H. In analogy with what was observed for the homoleptic step-like metallacycle **3**, the singlet at 7.47 ppm of intensity 2H was assigned to the two Hβ protons of the 4′*cis*DPyP in positions 7 and 8 (red label). These are the two equivalent protons between the pyridyl rings pointing towards 3′*cis*DPyP, which partially fall in its shielding cone. Finally, at lower frequencies, we find the signals of the pyrrole protons of both porphyrins. They appear as two very well resolved singlets, respectively at –2.91 and –3.18 ppm, which correspond to 2H each. The NH at lower frequencies (–3.18 ppm) was assigned to 4′*cis*DPyP, because in the COSY spectrum (Figure 3.9) it has a cross peak with the Hβ singlet at 7.47 ppm; accordingly, the singlet at lower frequencies (–2.91 ppm) was assigned to 3′*cis*DPyP.

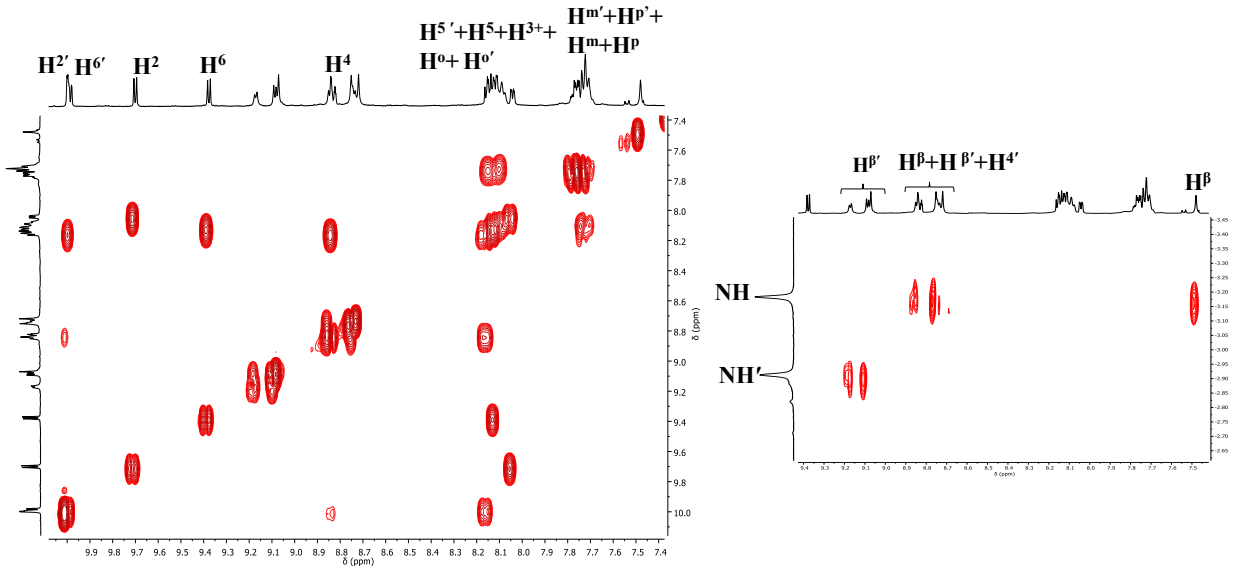

Figure 3.9. ^{1}H-^{1}H COSY spectrum of **18**, aromatic region and enlargement showing the cross peaks between βH and NH signals.

A test was done switching the order of coordination of the porphyrins, using as reactive precursor [{*trans,cis,cis*-$RuCl_2(CO)_2$(dmso-*O*)}$_2$(3′*cis*DPyP)] **(17)** and reacting it with an excess 4′*cis*DPyP. Complex **17** was synthesized using the same strategy used for precursor **16** and in Figure 3.10 is reported its ^{1}H NMR spectrum in $CDCl_3$+DMSO-d_6.

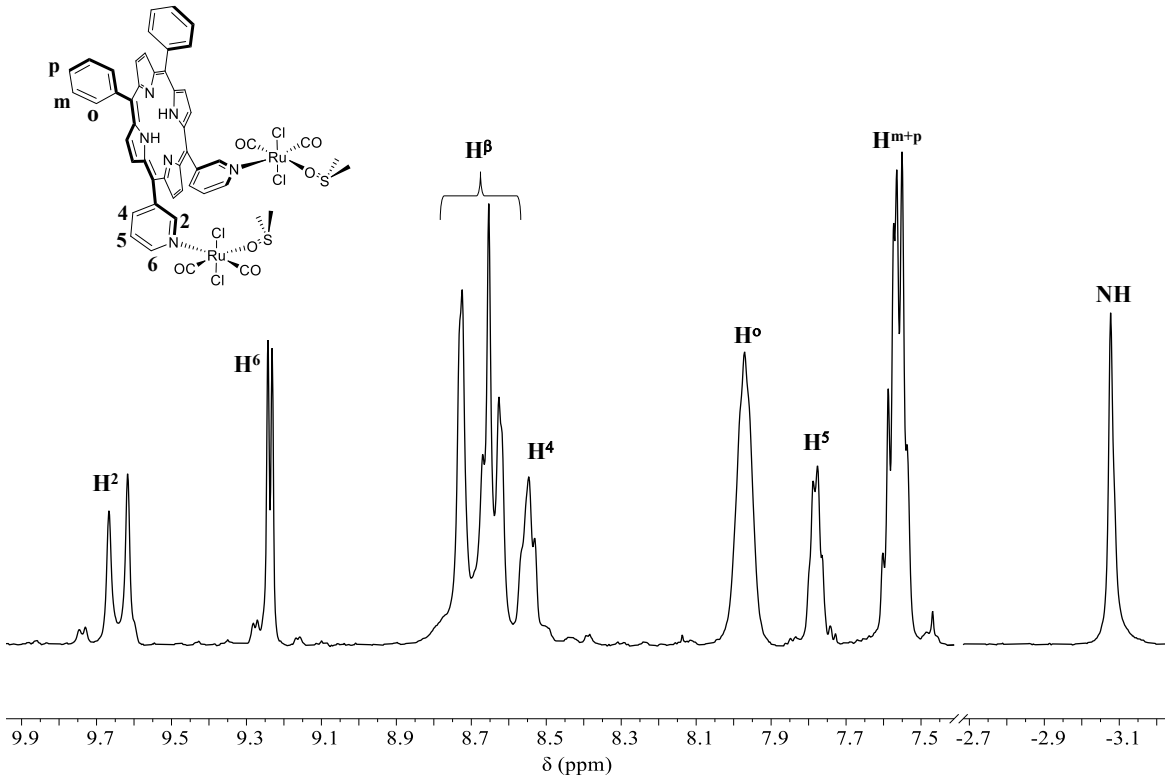

Figure 3.10. ^{1}H-NMR spectrum of [{*trans,cis,cis*-$RuCl_2(CO)_2$(dmso-*κO*)}$_2$(3′*cis*DPyP)] **(17)** in $CHCl_3$+DMSO-d_6.

In the ^{1}H-NMR spectrum it is visible the typical pattern of the 3′*cis*DPyP coordinated symmetrically to two fragments of {*trans,cis,cis*-$RuCl_2(CO)_2$(dmso-*O*)}. At higher frequencies are visible two broadened singlets and a sharp doublet assigned respectively to H2 and H6, and integrating for 2H each. The reason why only the resonance of H2 is split into two distinct singlets is unclear; the splitting may be caused by the presence of two different conformers *anti* and *syn*, in slow equilibrium on the NMR time scale and of similar concentrations, or by the presence of a ca. 50:50 mixture of **17** and **17H$_2$O**. In the ^{1}H-^{13}C HSQC (Figure A.3.5) spectrum the two singlets correlate with the same carbon atom.

17 was then treated with a slight defect of 4′*cis*DPyP, on a small scale in an NMR tube, in a $CDCl_3$+DMSO-d_6 mixture at 40°C.

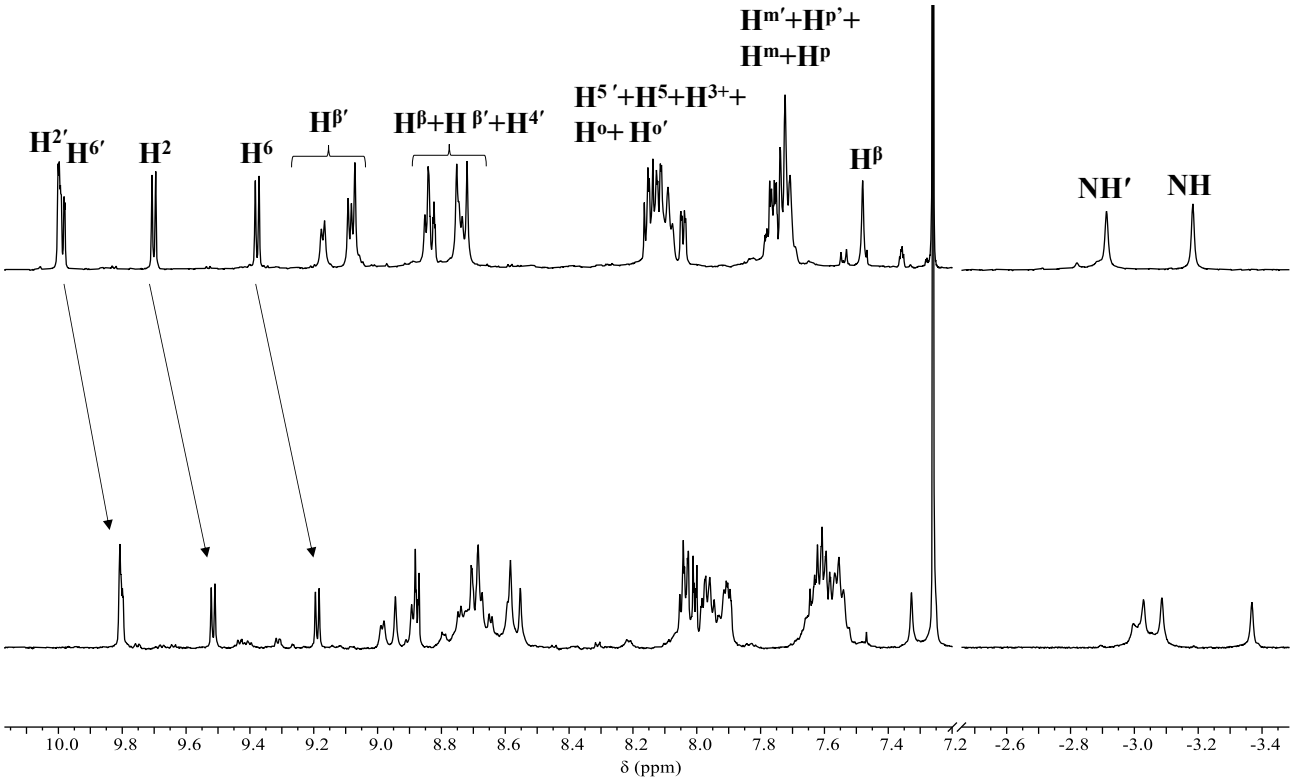

Figure 3.11. Comparison of the ^{1}H NMR spectra of **18** (top) and the reaction crude between **17** and 4′*cis*DPyP after 72h (bottom).

The ^{1}H NMR spectrum recorded after 72 h shows a pattern attributable to **18** (Figure 3.11), the shift of all resonances to slightly higher fields is due to the aforementioned effect of the DMSO-d_6. The presence of some additional signals, evident in the area of NH′ and NH resonances, could be caused by unreacted precursor **17** or to by the formation of other oligomeric byproducts. This experiment confirms that the metallacycle **18** can be obtained from both synthetic pathways.

Using the same strategy, we also synthesized the equivalent metallacycle containing 4′*cis*DPyMP, i.e. the analog of 4′*cis*DPyP methylated in *para* position of the phenyl rings. This choice has two

reasons: 1) it facilitates the interpretation of the ^{1}H NMR spectrum; in fact, it reduces the number and multiplicity of signals in the already very crowded aromatic region and adds the methyl singlet in a free zone of the spectrum, and 2) increases the solubility of all derivatives in chlorinated solvents.

First the intermediate [{*trans,cis,cis*-$RuCl_2(CO)_2$(dmso-κ*O*)}$_2$(4′*cis*DPyMP)] (**16Me**) was prepared, under the same reaction conditions used for **16**. Next, in a procedure similar to that leading to **18**, 3′*cis*DPyP was treated with a slight excess of **16Me** and the reaction was monitored by TLC (silica gel, $CHCl_3$). After 48h the crude was purified by flash chromatography obtaining two fractions, the first containing the 2+2 homoleptic metallacycle **2Me**, and the second containing the desired product **18Me** (Figure 3.12).

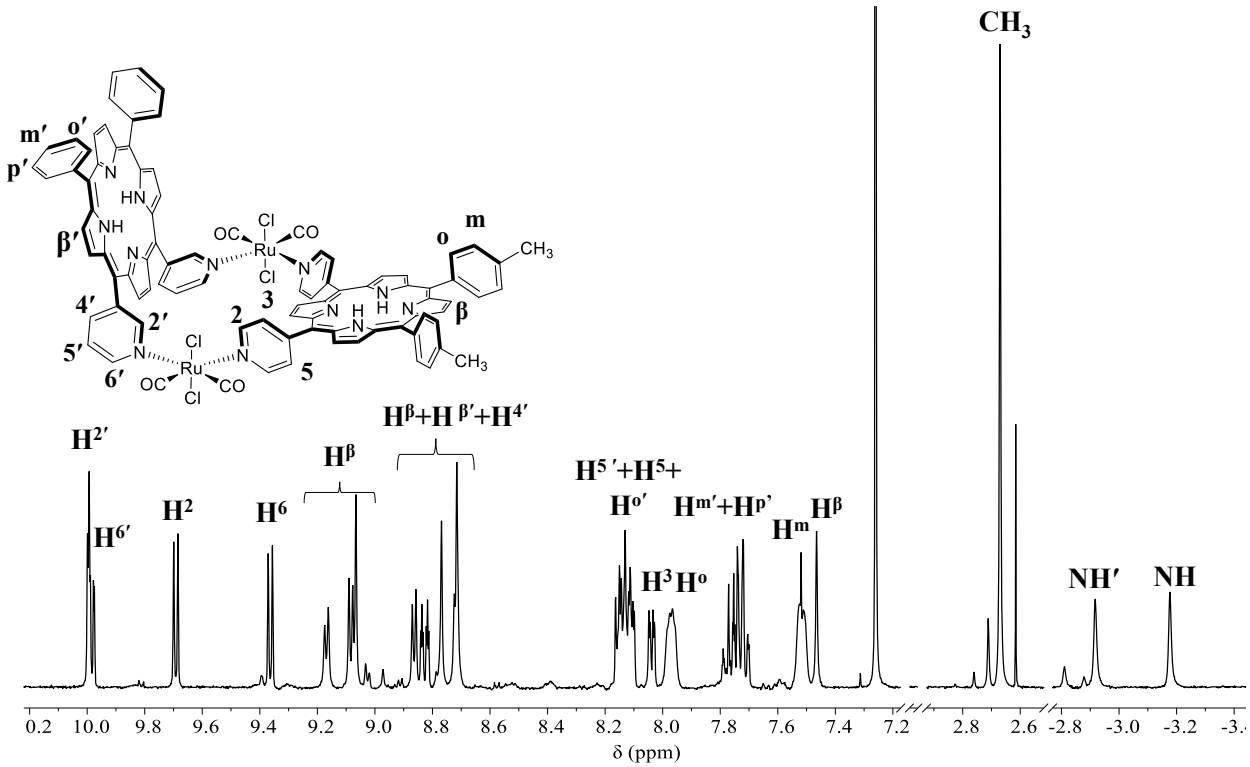

Figure 3.12. ^{1}H-NMR spectrum ($CDCl_3$) of the heteroleptic 2+2 metallacycle [{*trans*,*cis*,*cis*-$RuCl_2(CO)_2$}$_2$(4′*cis*DPyMP) (3′*cis*DPyP)] **(18Me)**

The ^{1}H NMR of **18Me** is similar to that of **18**, with the addition of the singlet for the methyl groups at 2.65 ppm and a better resolution of the signals in the crowded aromatic region.

18Me was then treated with 5 equivalents of $Zn(OAc)_2{\cdot}2H_2O$ in a $CHCl_3$:MeOH mixture obtaining the zincated metallacycle **18MeZn** (Scheme 3.4).

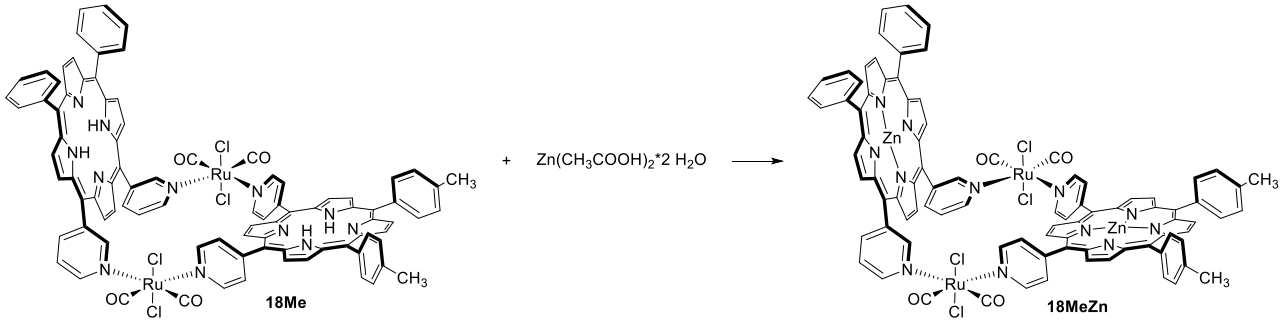

Scheme 3.4: Reaction scheme for the synthesis of the zincated metallacycle **18MeZn**.

The reaction was monitored by TLC and UV-vis spectroscopy, following the decrease of the number of Q bands from four to two, caused by the enhanced symmetry of the molecule, and the slight shift of the Soret band from 432nm to 427nm (Figure 3.13).

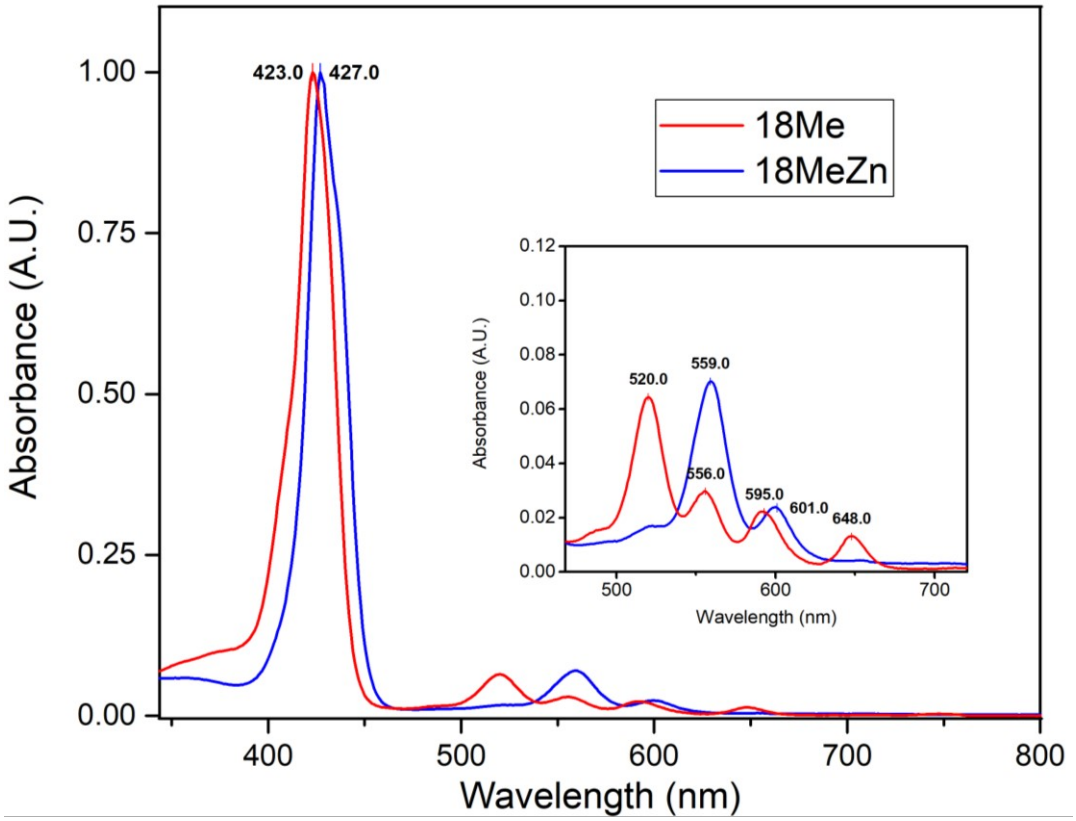

Figure 3.13. Comparison between the normalized UV-Vis absorption spectra in $CHCl_3$ of **18Me** (red) and of the corresponding zincated metallacycle **18MeZn** (blue), with enlargement of the Q bands region.

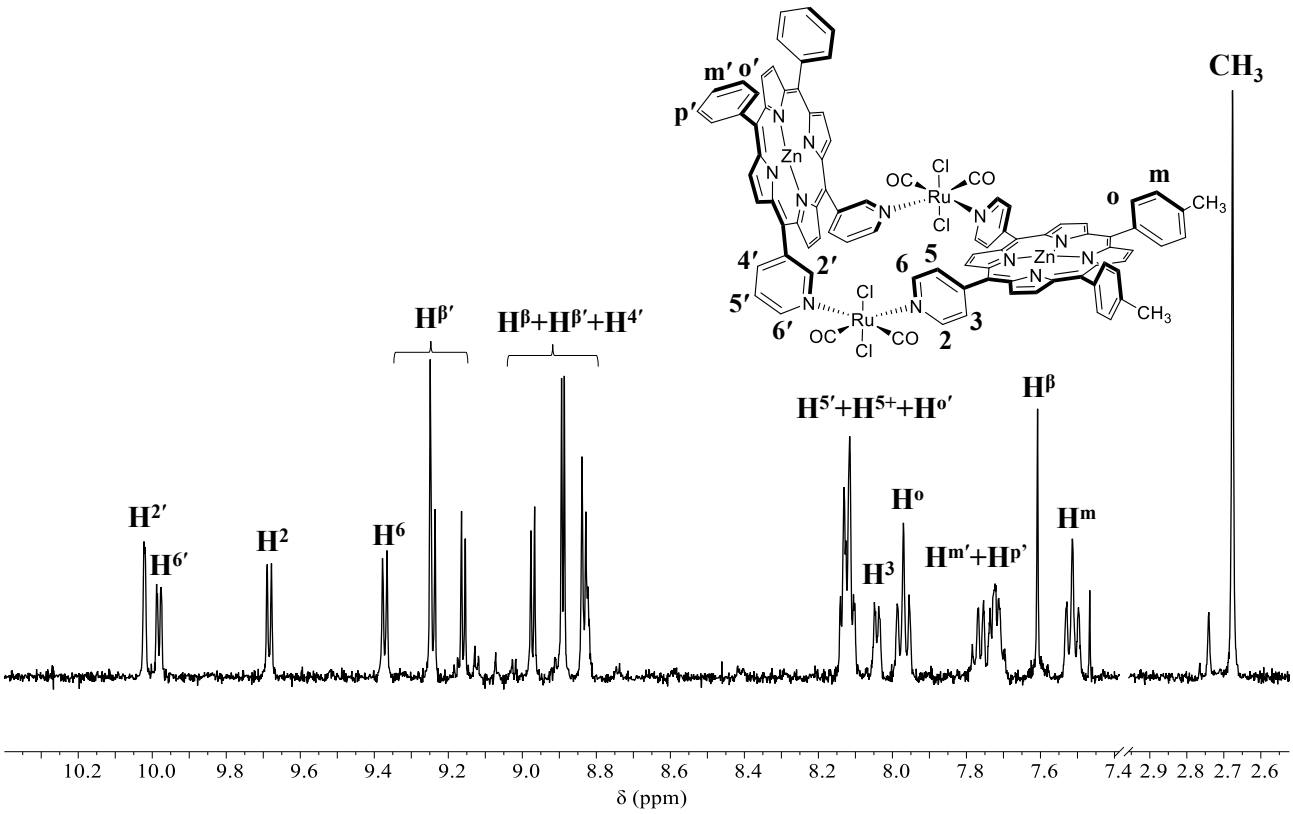

Figure 3.14. ^{1}H-NMR spectrum ($CDCl_3$) of metallacycle [{*trans*,*cis*,*cis*-$RuCl_2(CO)_2$}$_2$(Zn·4′*cis*DPyMP) (Zn·3′*cis*DPyP)] (**18MeZn**).

The ^{1}H NMR spectrum of **18MeZn** shows the same pattern of the free base metallacycle **18Me**, some signals are better resolved and low-field shifted, and the absence of the NH signals confirms the complete zincation of both porphyrins.

A DOSY spectrum was recorded to obtain more information on the size of **18MeZn**, in particular, the measure of the diffusion coefficient (D_t) allowed us to determine the hydrodynamic radius (r_H) of the molecule.

The correlation between the diffusion coefficient and the hydrodynamic radius follows the Stokes-Einstein equation for linear diffusion and spherical approximation:

$$D_t = \frac{k_B T}{6\pi\eta r_H}$$

where k_B is the Boltzmann constant, T is the temperature in Kelvin, and η is the fluid viscosity, which also depends on the solvent and the temperature.

The measured D_t for **18MeZn** is $6.06 \pm 0.10\times10^{-6}$ cm^2 s^{-1}, which corresponds to an r_H of 6.7 Å. This data compare well with the D_t and the r_H of the homoleptic metallacycle 2+2 (**2Zn**), measured under the same conditions, that are equal to $5.55 \pm 0.01\times10^{-6}$ cm^2 s^{-1} and 7.3 Å, respectively.

Considering the uncertainties inherent in these measurements, the diffusion coefficients of the two metallacycles are quite comparable.

In Figure 3.15 the two-dimensional representation of the DOSY spectrum of **18MeZn** is reported, where the ^{1}H NMR spectrum appears in the horizontal dimension and the diffusion coefficient in the other. The signals are all aligned along the same horizontal line, indicating that they belong to a single species.

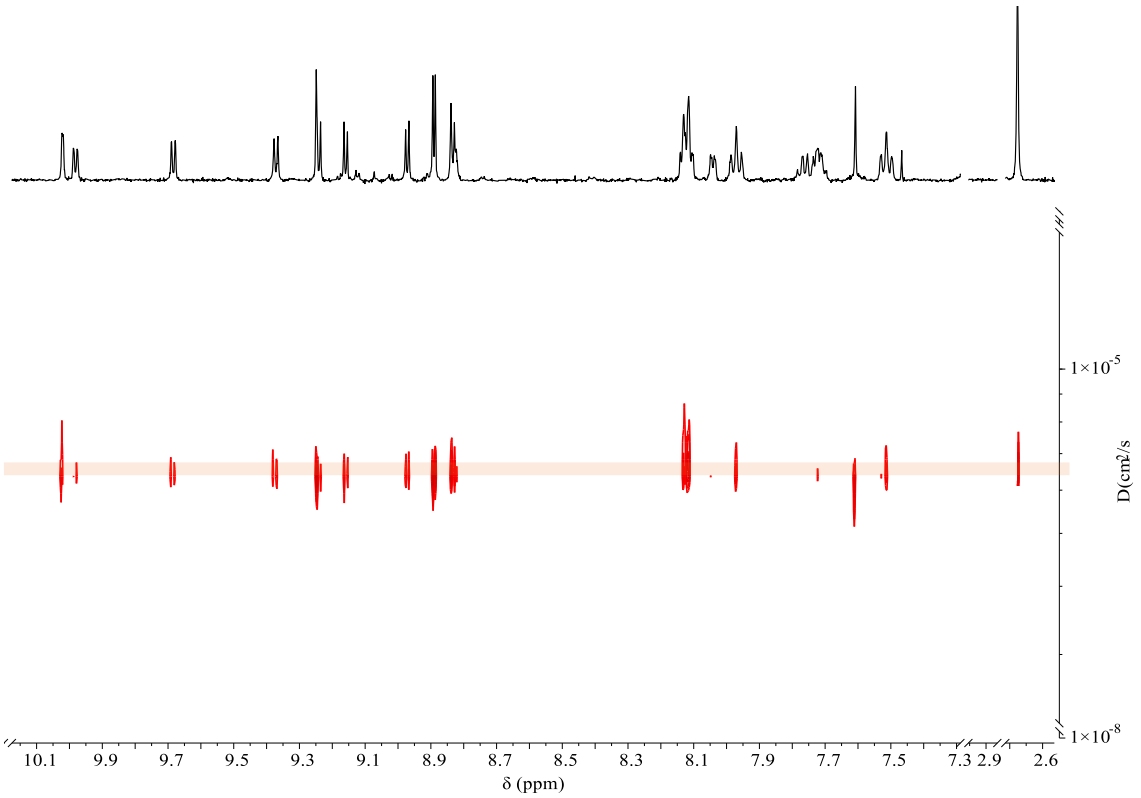

Figure 3.15. Bidimensional ^{1}H NMR DOSY spectrum of **18MeZn**.

We then compared the stepwise synthetic strategy, effective but rather laborious, with the one-pot approach which, as already mentioned, consists in treating the Ru(II) precursor **1** with stoichiometric amounts of the two porphyrins 4′*cis*DPyMP and 3′*cis*DPyP in a ca. 2:1:1 ratio. In this case, it can be expected that the reaction will produce the three possible 2+2 metallacycles (in addition to oligomeric species) **18Me**, **2Me** and **3** in almost equal quantities.

The one-pot reaction was performed on a small scale in an NMR tube and monitored by ^{1}H NMR spectroscopy. In Figure 3.16 are reported the ^{1}H NMR spectra, in the diagnostic NH region, of the reaction crude compared with the two homoleptic metallacycles **2Me** and **3**.

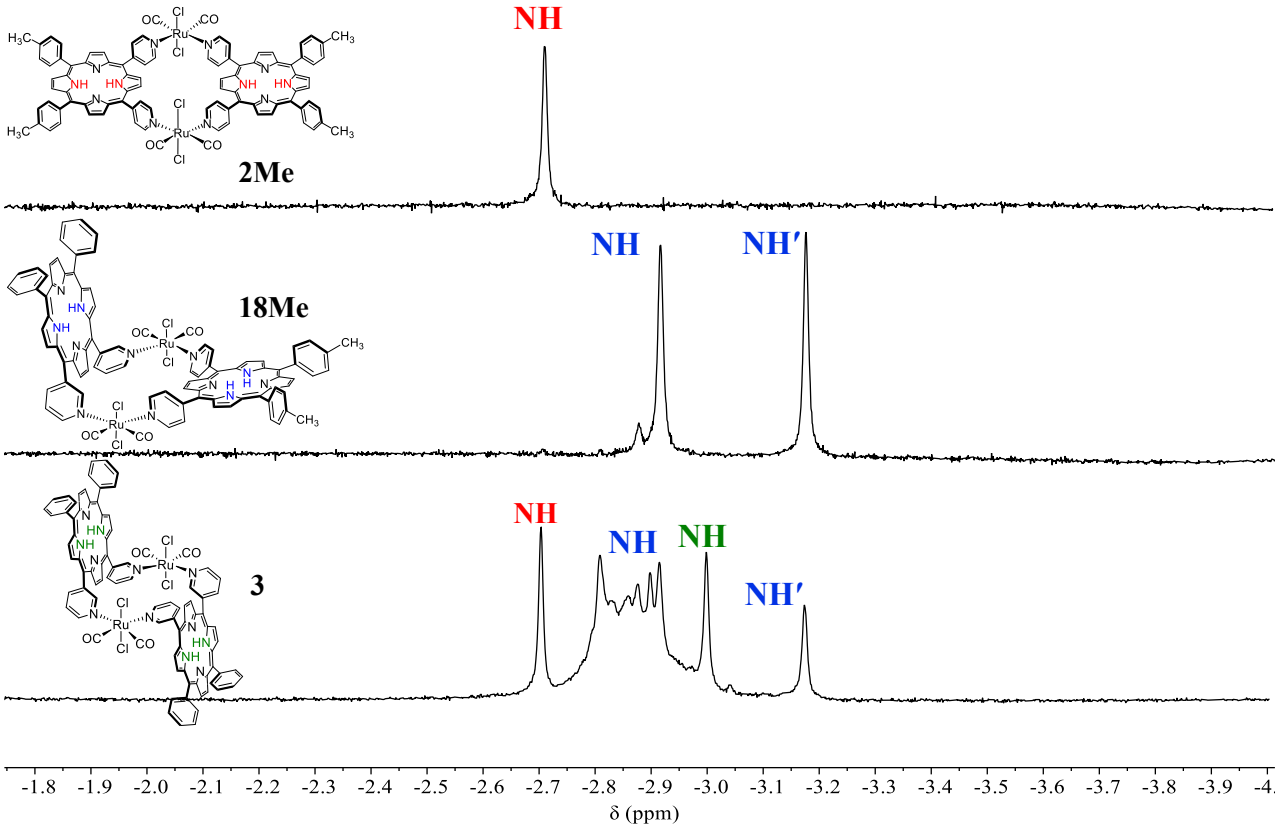

Figure 3.16. NH region of the ^{1}H NMR spectra of **2Me** (top), **18Me** (middle) and of the reaction crude (bottom); the NH signal of **3** is labeled in green.

From the comparison, and the spectral data already known in literature for **3**, the three metallacycles are indeed present ca. in a 1:1:1 ratio. It is also visible a set of unresolved resonances around 2.80 ppm, presumably attributable to uncharacterized oligomeric species.

When the reaction was repeated on a larger scale, we found that this statistical mixture of products is not easily separable by column chromatography, which afforded lower yields of pure **18Me** compared with the stepwise strategy. In conclusion, even for this relatively simple metallacycle the one-pot turned out to be less suitable than the stepwise approach..

We performed an NMR titration of **18MeZn** with 4′*cis*DPyMP, since the 90° geometry of the donor groups of this latter might allow its axial coordination to the two zinc atoms, forming a tris-porphyrin metallacycle where plane of 4′*cis*DPyMP is perpendicular to those of the other two porphyrins (Figure 3.17).

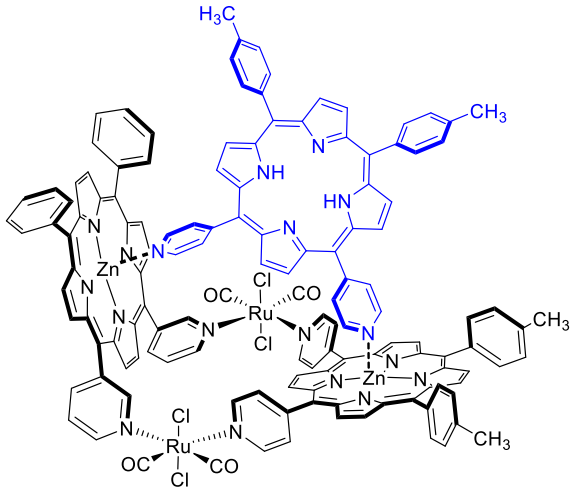

Figure 3.17. Hypothetical structure for the [**18MeZn**·4′*cis*DPyMP] assembly.

This system might resemble the metallacycle [**ZnP2**·4′*cis*DPyP] described some years ago by Iengo et al. (Figure 3.18), obtained by treating **ZnP2**, a system formed by two zinc-porphyrins connected via a 2,9-diphenylphenatroline (which acts as a linker) with 4′*cis*DPyP, which coordinates axially to the two zinc atoms.[2]

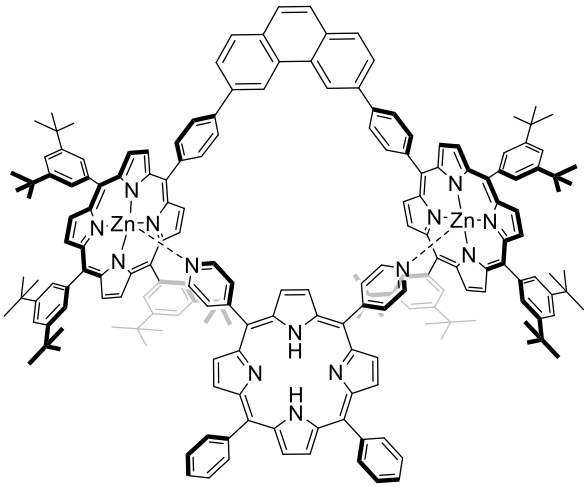

Figure 3.18. Schematic structure of the [**ZnP2**·4′*cis*DPyP] ·assembly.

The metallacycle **18MeZn** was dissolved in $CDCl_3$ (ca. 2 mM) and subsequent additions of small aliquots of 4′*cis*DPyMP were made. The ^{1}H NMR spectra recorded after every addition of 4′*cis*DPyMP are reported below until a **18MeZn**:4′*cis*DPyMP ratio ca. 1:1 was reached (Figure 3.19). The integration of the signals of the methyl groups, that fall in an uncrowded area of the spectrum, allows to determine the exact ratio between the two species.

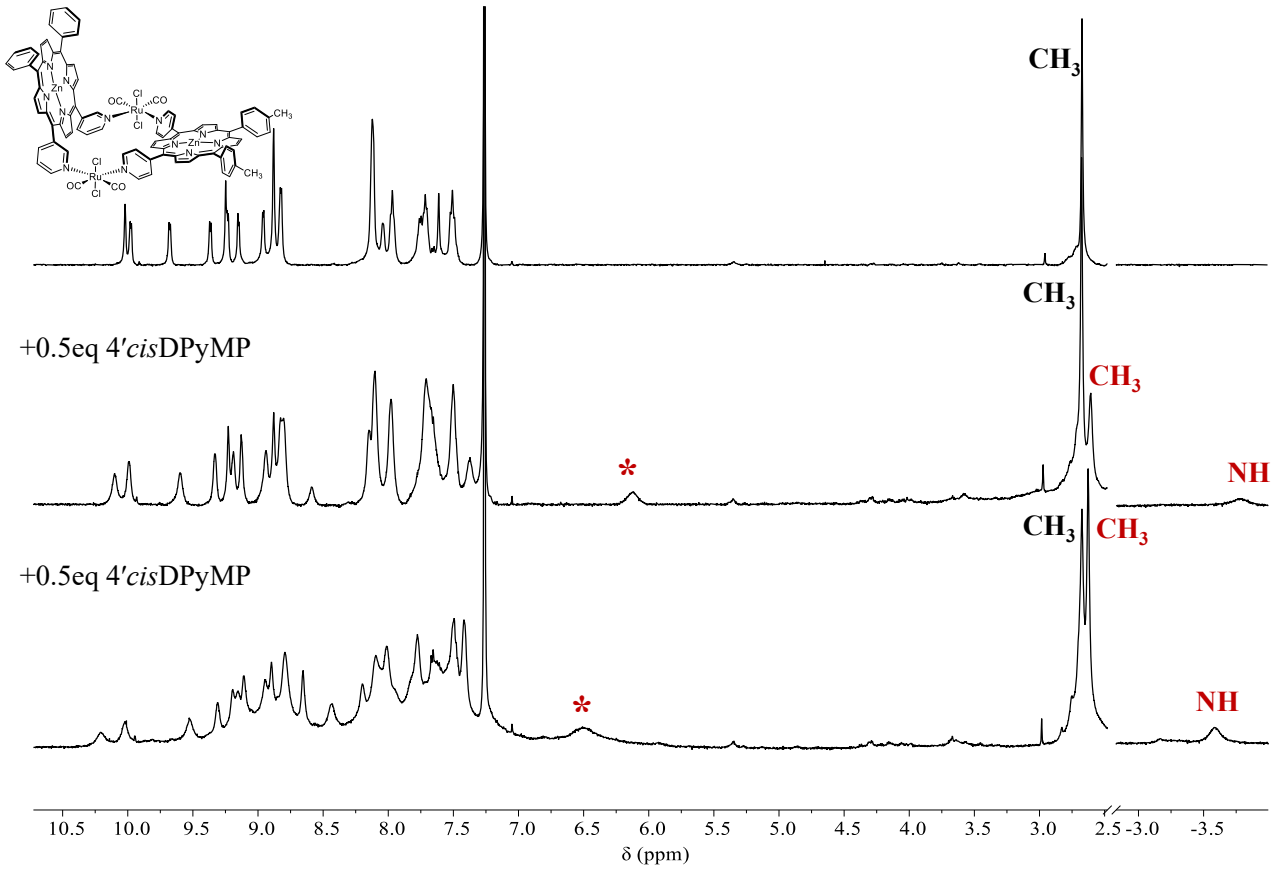

Figure 3.19. ^{1}H NMR spectra ($CDCl_3$) of the titration of **18MeZn** (top) with increasing amounts of 4′*cis*DPyMP (middle and bottom).

Overall, the ^{1}H NMR spectra in $CDCl_3$ at room temperature of the **18MeZn** titration does not suggest the formation of a discrete supramolecular structure. The ligand additions caused a generalized broadening of the signals of **18MeZn** and the appearance of two very broad signals, one at ca. 6.0 ppm and the second at –3.7 ppm (this latter assigned to the NH of the 4′*cis*DPyMP). On the other hand, the growing signal of the methyl groups of 4′*cis*DPyMP appears as a sharp singlet. This suggests that the 4′*cis*DPyMP resonances are very broadened and upfield shifted due to fast coordination equilibria with Zn, incompatible with the formation of a metallacycle like the one predicted in Figure 3.18. The NH singlet resonates at lower frequencies than free 4′*cis*DPyMP (–2.83 ppm), in agreement with an axial interaction with zinc. In the metallacycle [**ZnP2**·4′*cis*DPyP], the coordination of the 4′*cis*DPyP to the two zinc-porphyrins led to a stable metallacycle (association constant 6×10^{8} M^{-1}) and sufficiently inert, characterized by an NMR spectrum very diagnostic. For instance, the protons H2,6 and H3,5 of the pyridyl rings coordinated to the zinc atoms gave broad but well distinguishable resonances already at room temperature, respectively at 2.98 and 6.26 ppm.

It is possible that the formation of the predicted triporphyrin metallacycle, although possible from the geometric point of view, is prevented by steric interactions, for instance, by the chlorides pointing towards the 4′*cis*DPyP.

3.2.2 Synthesis of the triporphyrin metallacycle [{*trans,cis,cis*-$RuCl_2(CO)_2$}$_4$(4′*cis*DPyP)$_2$(4′TPyP)] (19)

The second part of this chapter concerns the synthesis and characterization of the triporphyrin metallacycle [{*trans,cis,cis*-$RuCl_2(CO)_2$}$_4$(4′*cis*DPyP)$_2$(4′TPyP)] (**19**) and its peripherally methylated analog, [{*trans,cis,cis*-$RuCl_2CO)_2$}$_4$(4′*cis*DPyMP)$_2$(4′TPyP)] (**19Me**). Similarly to **18**, we tried to synthesize the metallacycle **19** using the stepwise synthetic strategy described in the following reaction scheme (Scheme 3.5). The 4′TPyP was reacted in CH_2Cl_2:DMSO 24:1 mixture at room temperature for 48 h with a slight excess of the reactive precursor [{*trans,cis,cis*-$RuCl_2(CO)_2$(dmso-*O*)}$_2$(4′*cis*DPyP)] (**16**).

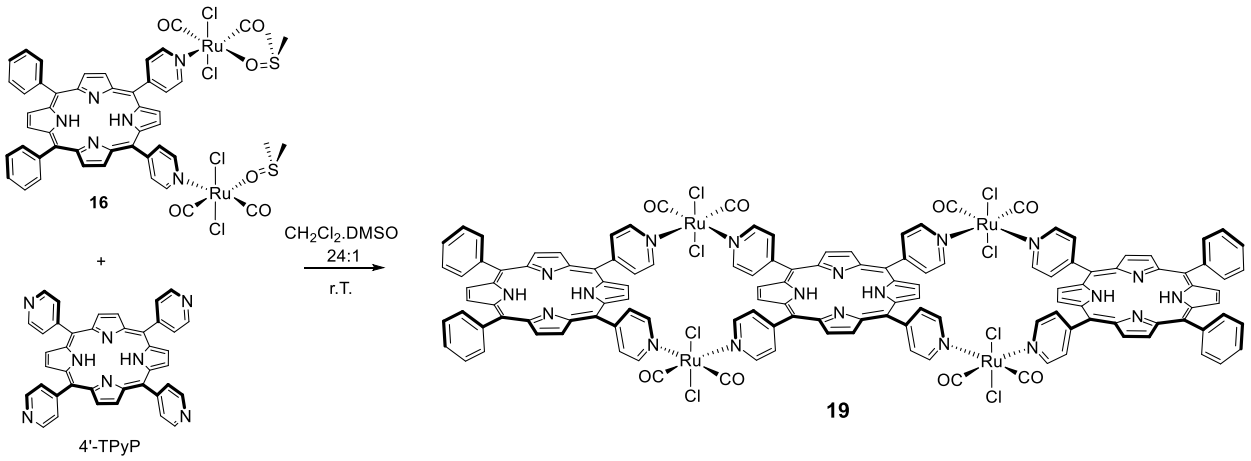

Scheme 3.5. Preparation of the triporphyrin metallacycle [{*trans,cis,cis*-$RuCl_2(CO)_2$}$_4$(4′*cis*DPyP)$_2$(4′TPyP)] (**19**).

At the end of the reaction, the solvent was removed and the crude was washed with acetone to remove the DMSO. After column chromatography (silica gel, $CHCl_3$), it was possible to recover a fraction containing **19** sufficiently pure, although with very a low yield (9%). The ^{1}H NMR spectrum of the product is shown in Figure 3.20.

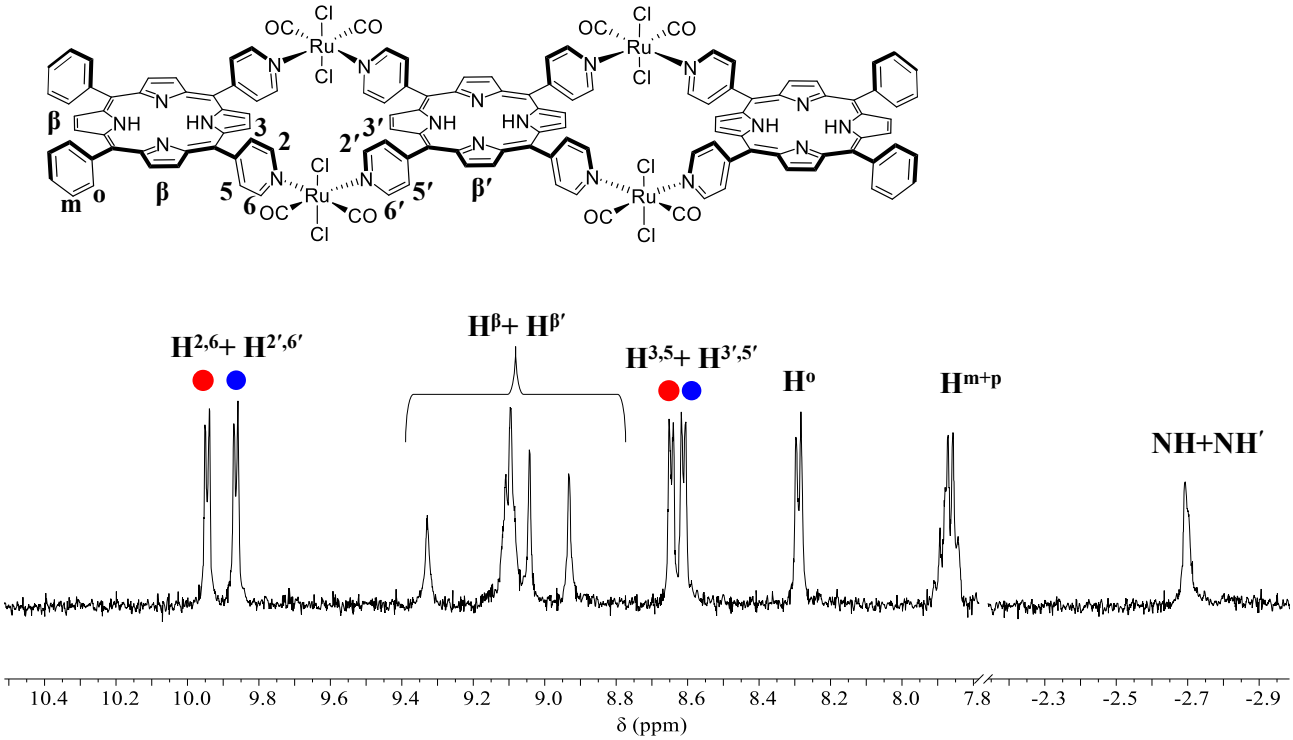

Figure 3.20. ^{1}H-NMR spectrum ($CDCl_3$) of **19**; the dots of the same color indicate the protons belonging to the same pyridyl ring according to the ^{1}H-^{1}H COSY spectrum

In the ^{1}H NMR spectrum is visible only one pattern of signals, attributable to the highly symmetrical species **19**. In the low field region, at 9.93 and 9.85 ppm, there are two doublets with equal intensity (8H) attributable to H2,6 and H2′,6′ of the pyridyl rings present in the molecule, four belonging to the central 4′TPyP (H2′,6′) and four to the two peripheral 4′*cis*DPyP units (H2,6), all coordinated to {*trans,cis,cis*-$RuCl_2(CO)_2$} fragments. They are pairwise correlated in the ^{1}H-^{1}H COSY spectrum to the two doublets belonging to the H3,5 and H3′,5′, which fall at 8.63 and 8.59 ppm, respectively, and integrate for 8H each. The resonances labeled with the same color in Figure 3.20 belong to the same type of pyridyl ring, but it was not possible to distinguish which signals belong to the 4′TPyP and which to the two equivalent 4′*cis*DPyPs.

At higher fields (–2.70 ppm), there is a single enlarged singlet integrating for 6H, attributed to the overlapping of the NH singlets of the three porphyrins.

The UV-spectrum is very similar to the spectra of the free porphyrins (Figure A.3.10).

When we tried to switch the order of insertion of the porphyrins, reacting the 4′TPyP with an excess of **1**, the reaction was very slow due to the low solubility of the 4′TPyP in halogenated solvents. Furthermore, the isomerization of **1** occurred to a large extent leading to a mixture of the two stereoisomers [*cis,cis,trans*-$RuCl_2(CO)_2$(dmso-*S*)$_2$] (**4**) and [*cis,cis,cis*-$RuCl_2(CO)_2(dmso)_2$] (**5**). Accordingly, this synthetic pathway was discarded.

The work already carried out, while indicating that with the synthetic strategy followed it is possible to obtain the triporphyrin metallacycle **19**, it also highlighted a series of difficulties (in addition to the

low yield): 1) 4′TPyP is poorly soluble in halogenated solvents. This can lead to incomplete or very slow reactivity, which can favor parallel reactions of the species in solution. 2) In the reaction mixture there is always a very thin suspension, which can derive from not completely dissolved 4′TPyP or from the formation of poorly soluble species, possibly polymeric in nature. 3) Even after chromatographic purification, the recovered product, despite being all in solution once leaving the column, is no longer entirely soluble in $CDCl_3$. Furthermore, even if the dark and very thin solid that remains undissolved is removed by filtration, a very thin suspension soon re-forms, presumably due to phenomena of aggregation and/or degradation/hydrolysis of the product.

We also synthesized the analog metallacycle containing 4′*cis*DPyMP, [{*trans,cis,cis*-$RuCl_2(CO)_2$}$_4$(4′*cis*DPyMP)$_2$(4′TPyP)] (**19Me**), with the aim to increase the solubility of the product. The 4′TPyP was treated with 2.5eq of **16Me** in a 24:1 CH_2Cl_2:DMSO mixture and the crude was purified by column chromatography collecting two fractions, the first containing the desired product **19Me.**

The solvent was removed and partially dissolved in $CDCl_3$, the thin suspension was removed through an HPLC filter, and the ^{1}H NMR of the clear solution is reported in Figure 3.21.

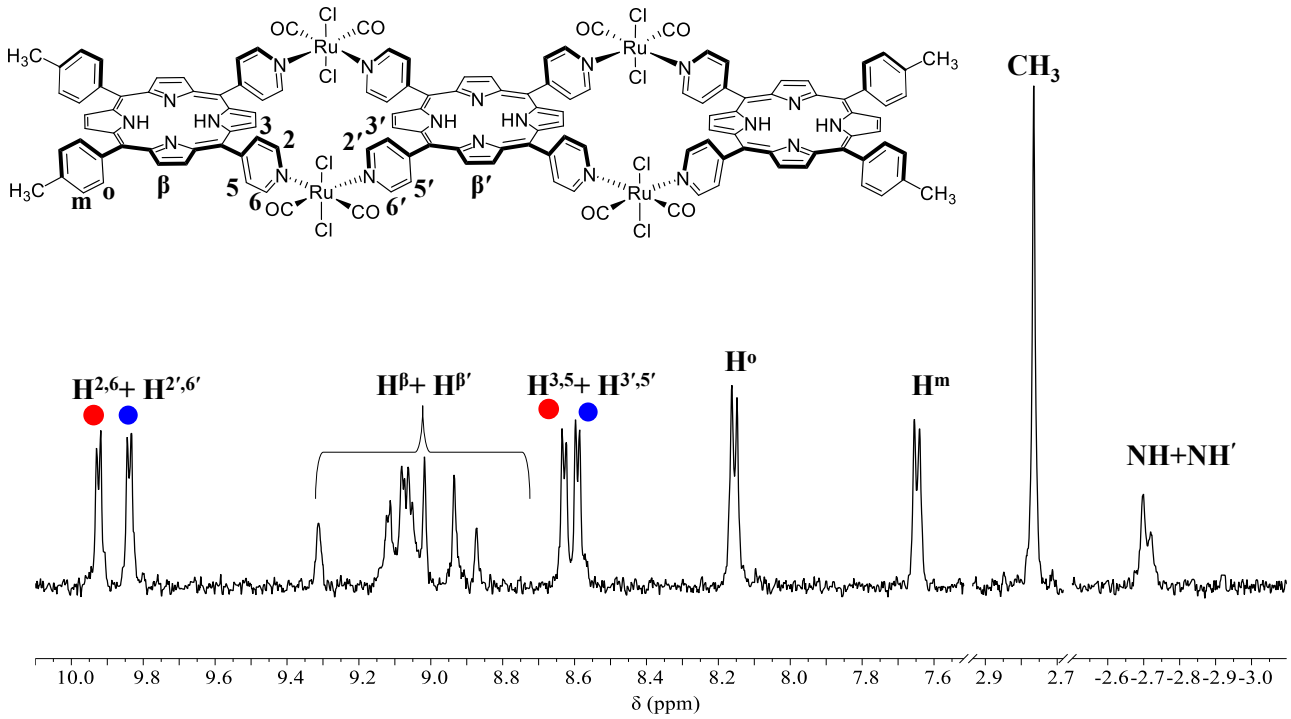

Figure 3.21. ^{1}H NMR spectrum ($CDCl_3$) of [{*trans,cis,cis*-$RuCl_2CO)_2$}$_4$(4′*cis*DPyMP)$_2$(4′TPyP)] **19Me**; the dots of the same color indicate the protons belonging to the same type of pyridyl ring according to the ^{1}H-^{1}H COSY spectrum.

Even in this case, a thin suspension reforms a few hours after the preparation of the NMR sample (originally a clear solution).

We also tried to enhance the solubility of the 4′TPyP; consistent with literature reports, it was found to be well soluble in $CHCl_3$:TFE mixtures, even when contain very small percentages of the fluorinated solvent (i.e. 200:1 $CHCl_3$:TFE).[3]

The reaction was performed in 6.1 mL of a 66:1 $CHCl_3$:TFE mixture, in which a 4.5 mg amount of 4′TPyP was completely dissolved; a slight excess of **16**, dissolved in 50μL of DMSO, was then added to the solution, and heated at 40°C. After 24h and the crude was purified by flash chromatography (silica gel, $CHCl_3$:*n*-hexane 98:2).

Regretfully, as evidenced by the NMR spectrum, the fraction containing the metallacycle **19Me** contained other species, with very similar retention factors, that were not separable by column chromatography (Figure 3.22).

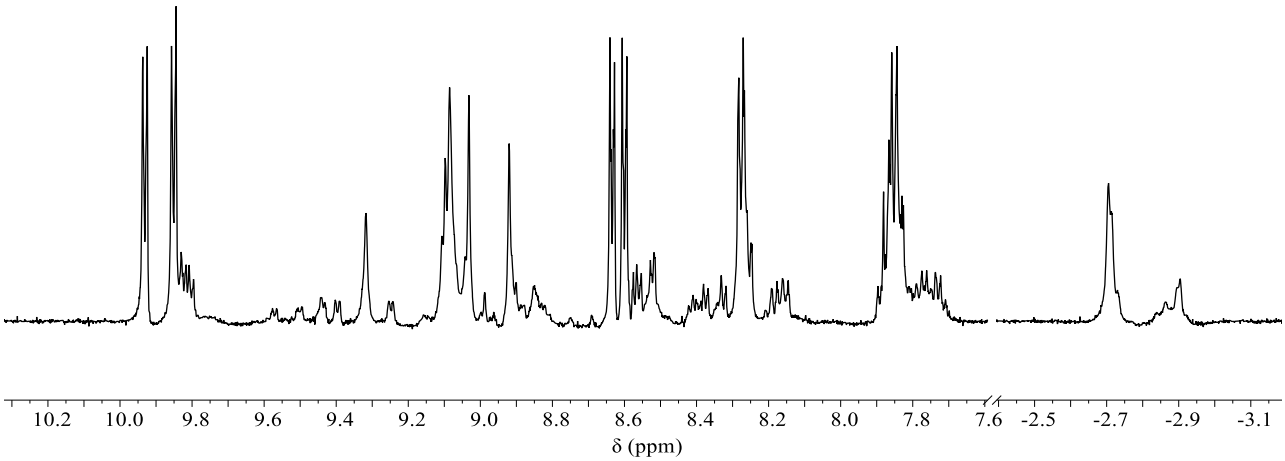

Figure 3.22. ^{1}H NMR spectrum of the fraction containing **19Me**.

These minor signals are not attributable to known species but are very similar to those of the stereoisomeric 2+2 metallacycles [{*trans,cis,cis*-$RuCl_2(CO)_2$}(4′*cis*DPyP)$_2${*cis,cis,cis*-$RuCl_2(CO)_2$}] (**13**) and [{*cis,cis,cis*-$RuCl_2(CO)_2$}(4′*cis*DPyP)$_2$] (**14**). In particular, the signals around 9.8, 9.4 and 9.2 ppm could be attributable to homo- or heteroleptic stereoisomeric metallacycles, in which one or more ruthenium connectors are isomerized, assuming {*cis,cis,cis*-$RuCl_2(CO)_2$} rather than {*trans,cis,cis*-$RuCl_2(CO)_2$} geometry. In fact, as observed for the molecular square **13**, and discussed in the Chapter 1, the loss of the symmetry plane of the metallacycle, following the isomerization of a metal connector, leads to the presence of resonances of protons H2 and H6 (no longer equivalent) in those regions of the spectrum.

The presence of this species only when TFE was used, made us suspect that that the solvent was somehow involved. Indeed, we found that when the [*trans,cis,cis*-$RuCl_2(CO)_2$(dmso-*O*)$_2$] (**1**) complex was dissolved in a $CHCl_3$:TFE 200:1 mixtures, it isomerized faster to its stereoisomers (and

linkage isomer) [*cis,cis,cis*-$RuCl_2(CO)_2$(dmso-*O*)(dmso-*S*)] (**4**) and [*cis,cis,trans*-$RuCl_2(CO)_2$(dmso-*S*)$_2$] (**5**) compared to pure chloroform (Figure 3.23).

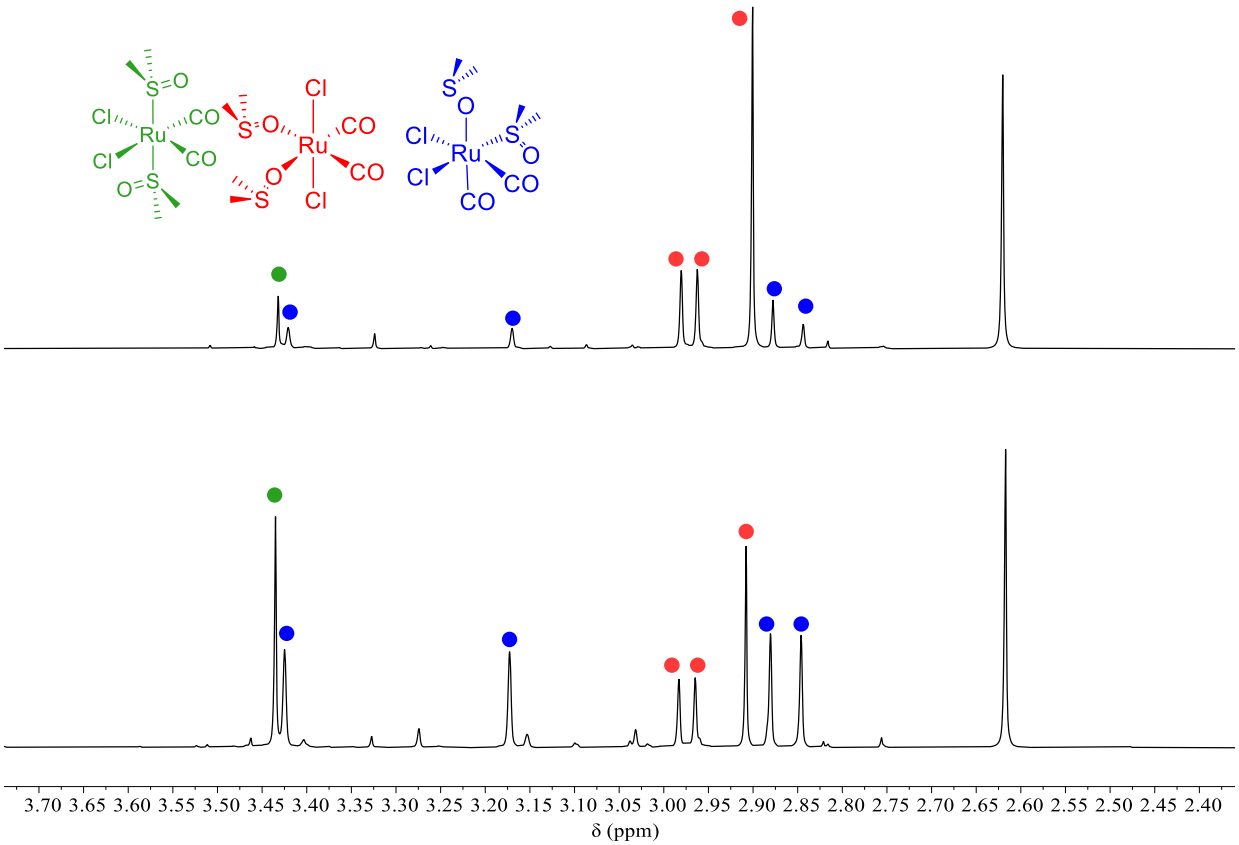

Figure 3.23. ^{1}H NMR spectra of complex **1** after 24h in $CHCl_3$ (top) and in $CHCl_3$:TFE 200:1 mixture (bottom), the signals of **1**, **4** and **5** are labeled respectively in red, green, and blue.

This reaction was also tested in the one-pot conditions, reacting the two porphyrins and the complex **1** in a 1:2:4 stoichiometric ratio in $CHCl_3$:TFE 65:1. Regretfully, the major products in this case were the 2+2 homoleptic metallacycle **2Me** and the 3+3 [*trans,cis,cis*-$RuCl_2(CO)_2$(4′*cis*DPyMP)]$_3$, whereas only a minor amount of the desired product **19Me** was present, not even enough for being isolated by column chromatography. Thus, the one pot approach turned out to be unfeasible for the preparation of the extended metallacycles.

3.2.3 Synthesis and characterization of the homoleptic metallacycle [{*trans,cis,cis*-$RuCl_2(CO)_2$}$_4$(3′*cis*DPyMP)$_2$(3′TPyP)] (20Me)

Contrary to 4′TPyP, 3′TPyP has the advantage of being more soluble in chlorinated solvents and thus more reactive, minimizing potential side reactions (e.g. isomerization of the reactive precursor).

On the other hand, the pyridyl rings in the 3′PyPs can be directed above or below the plane of the porphyrin (*syn* or *anti*), leading to different possible conformers.

Initially, we tested its reactivity in combination with the reactive precursor [{*trans*,*cis*,*cis*-$RuCl_2(CO)_2$(dmso-*O*)}$_2$(3′*cis*DPyMP)}] (**17Me**), obtained as **17** from the 3′*cis*DPyMP.

In principle, the reaction between two equivalents of **17Me** and one equivalent of 3′TPyP could lead to two different conformers of the homoleptic triporphyrin metallacycle [{*trans,cis,cis*-$RuCl_2(CO)_2$}$_4$(3′*cis*DPyP)$_2$(3′TPyP)] (**20Me**)[b]. One conformer where all the four pyridyl rings of the 3′TPyP have a *syn* orientation and one where they are in pairs in *anti* conformation. The conformer **20Me$_l$** should have a *ladder* geometry (i.e. an extended version of **3**), where the two 3′*cis*DPyMP are on opposite sides of the 3′TPyP plane, while conformer **20Me$_g$** should have a *Greek frame* geometry where the two 3′*cis*DPyMP are on the same side.

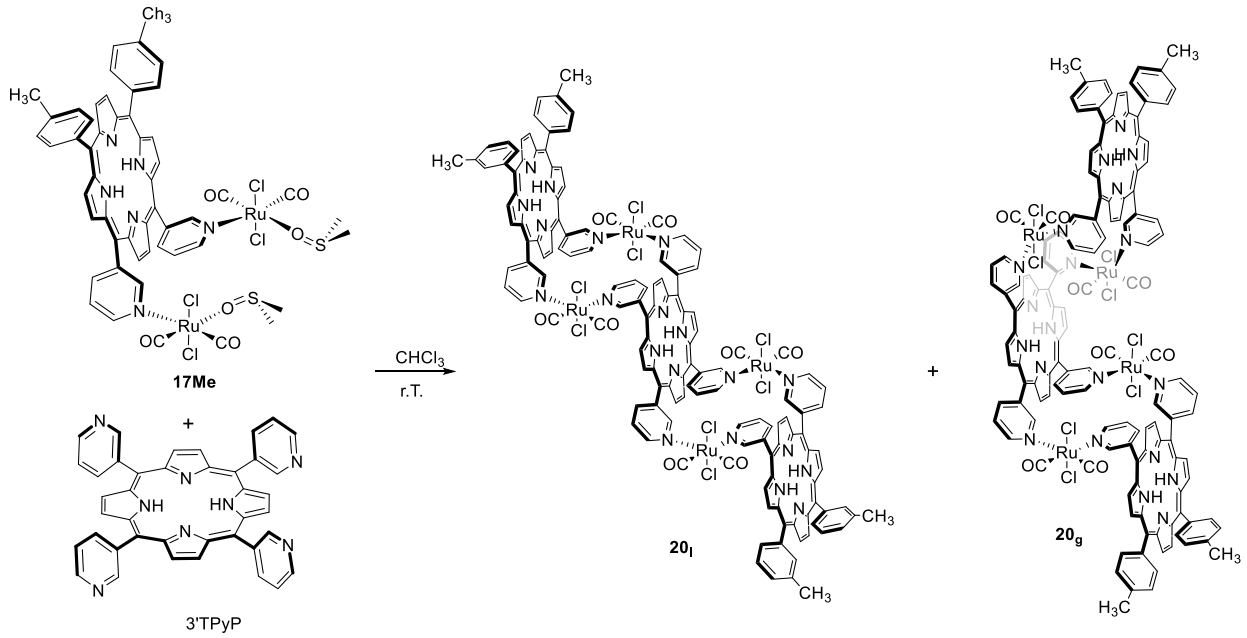

Scheme 3.6. Reaction scheme for the synthesis of the homoleptic metallacycle **20Me**.

The reaction was conducted in $CHCl_3$, a 20.0 mg (2.2 eq) amount of **17Me** was added to a solution of 4.9 mg of 3′TPyP at room temperature. The reaction was monitored by TLC (silica gel, $CHCl_3$:EtOH 98:2) and by ^{1}H NMR, following the disappearance of the 3′TPyP. After 6h the solvent

[b] **Note** The number without subscripts indicates the mixture of conformers

was removed, and the purple solid was purified by flash chromatography (silica gel $CHCl_3$:*n*-hexane 97:3), affording a single band.

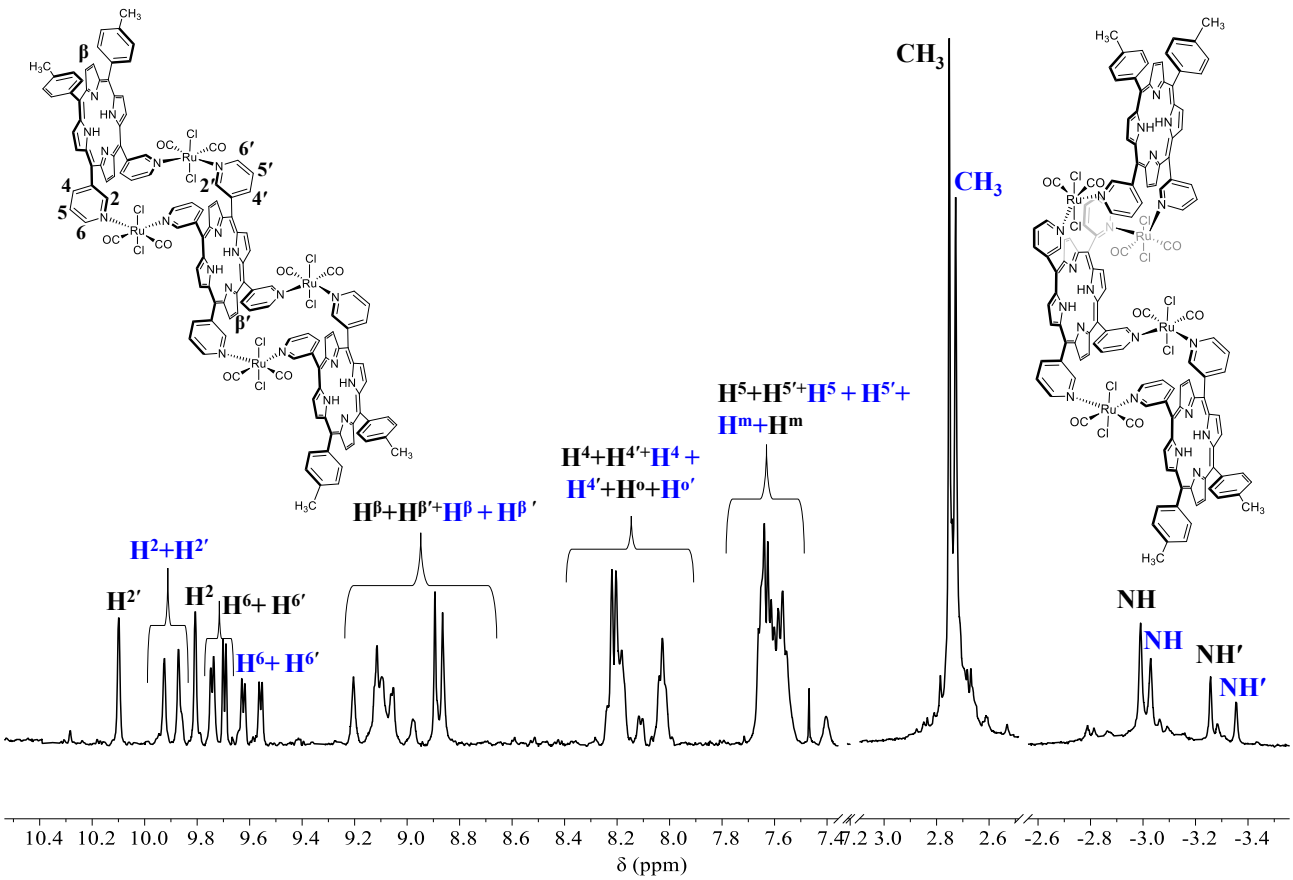

Figure 3.24. ^{1}H NMR spectrum of [{*trans,cis,cis*-$RuCl_2(CO)_2$}$_4$(3′*cis*DPyMP)$_2$(3′TPyP)] (**20Me**) in $CDCl_3$, the two sets of signals – corresponding to the two conformers – are labeled in black and blue.

Even if the product was pure according to TLC analysis, in the ^{1}H-NMR spectrum in $CDCl_3$ (Figure 3.24) are visible two sets of signals (black and blue labels), indicating the presence of two different species in solution in a ratio of ca. 1:0.66. The two sets of signals were distinguished based upon the intensities (where resolved) and through 2D NMR spectra. The integrations of the NH resonances allowed us to say that in each species the 3′*cis*DPyMP:3′TPyP ratio is 2:1.

When the same sample was redissolved in CD_2Cl_2, the two sets of signals were almost in a 1:1 ratio, consistent with the hypothesis that the two species are two conformers in slow exchange on the NMR time scale and the equilibrium between them shifts according to the solvent. Furthermore, in the ROESY spectrum, is visible a cross peak between the H2′ of the major species and the H2′ of the minor species at lower frequencies, confirming that they are in exchange (Figure 3.25)

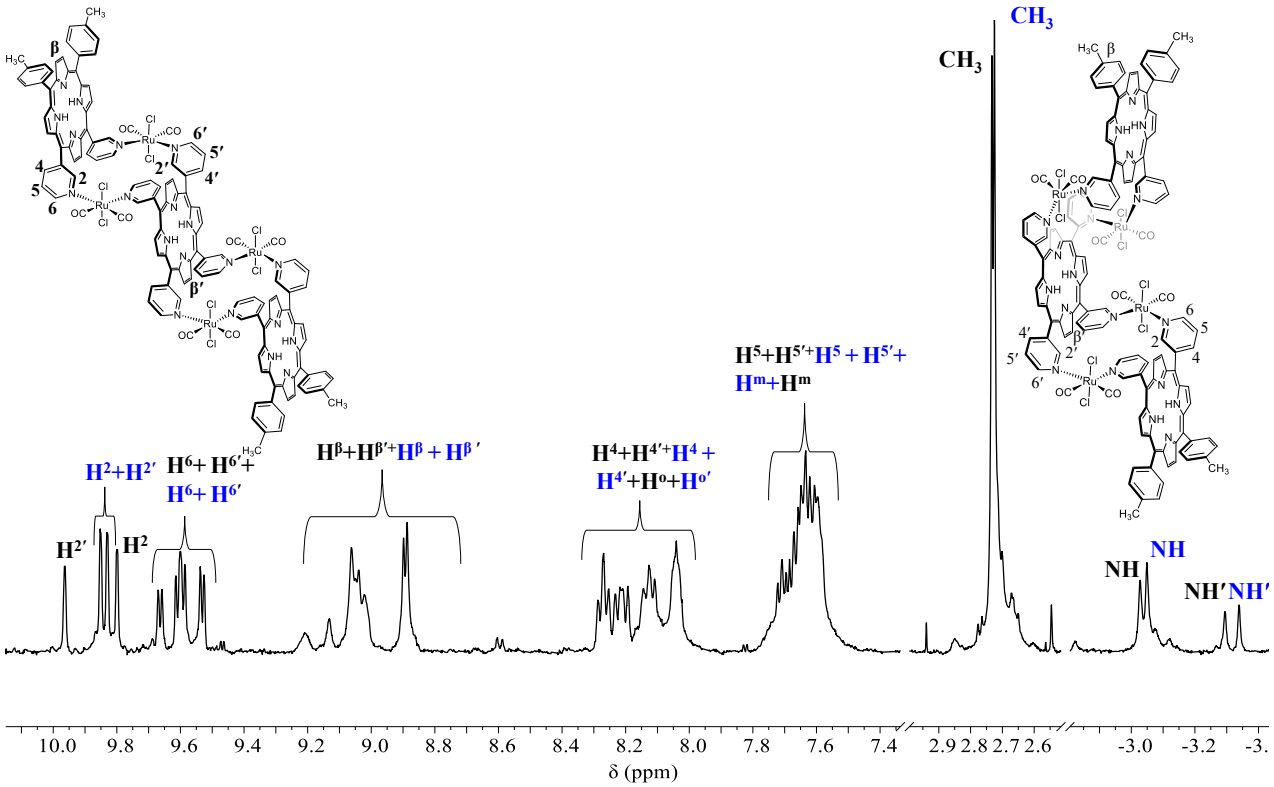

Figure 3.25. ^{1}H NMR spectrum of [{*trans,cis,cis*-RuCl$_2$(CO)$_2$}$_4$(3′*cis*DPyMP)$_2$(3′TPyP)] (**20Me**) in CD_2Cl_2.

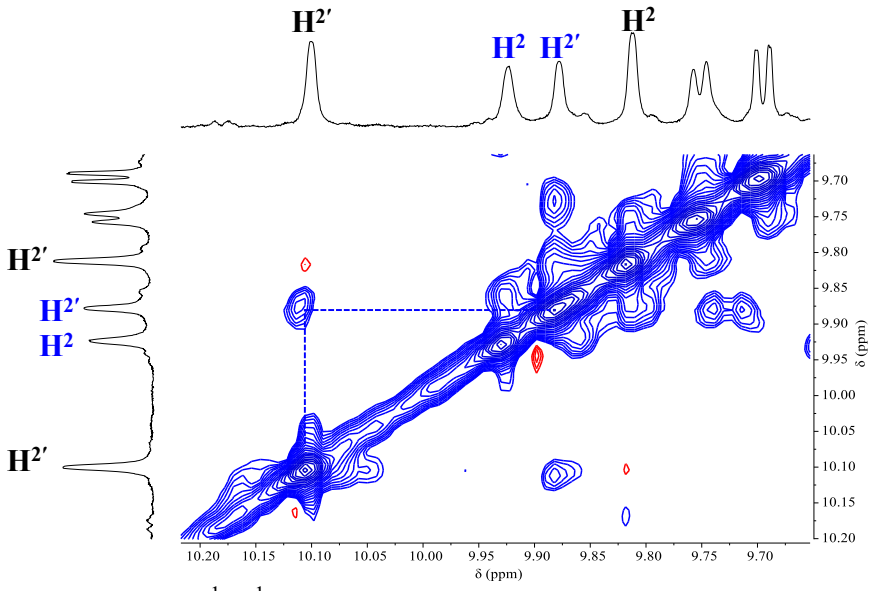

Figure 3.26. Enlargement of the ^{1}H-^{1}H ROESY ($CDCl_3$) spectrum showing the exchange cross peak between the H2′ of the two conformers

We were also able to distinguish, at least for the major species, the signals of 3′*cis*DPyMP from those of the 3′TPyP. Apart from the signals of H2 and H6 of both species, the other signals are mostly overlapped and were assigned using the information from the ^{1}H-^{1}H COSY, ^{1}H-^{13}C HSQC, ^{1}H-^{1}H ROESY spectra. The DOSY spectrum clearly shows that the two species have the same diffusion coefficient 3.74±0.02 cm^{2}s^{-1}, with a hydrodynamic radius of ca. 10.9 Å, which is in good agreement

with the expected radius for a triporphyrin metallacycle. In Figure 3.27 is reported the bidimensional DOSY spectrum of **20Me** compared with **18MZne**.

All these findings allowed us to say the two species are indeed the two conformers **20Me$_g$** and **20Me$_l$** but regretfully it was not possible to distinguish which is which; repetitive attempts to grow single crystals were – thus far – not successful.

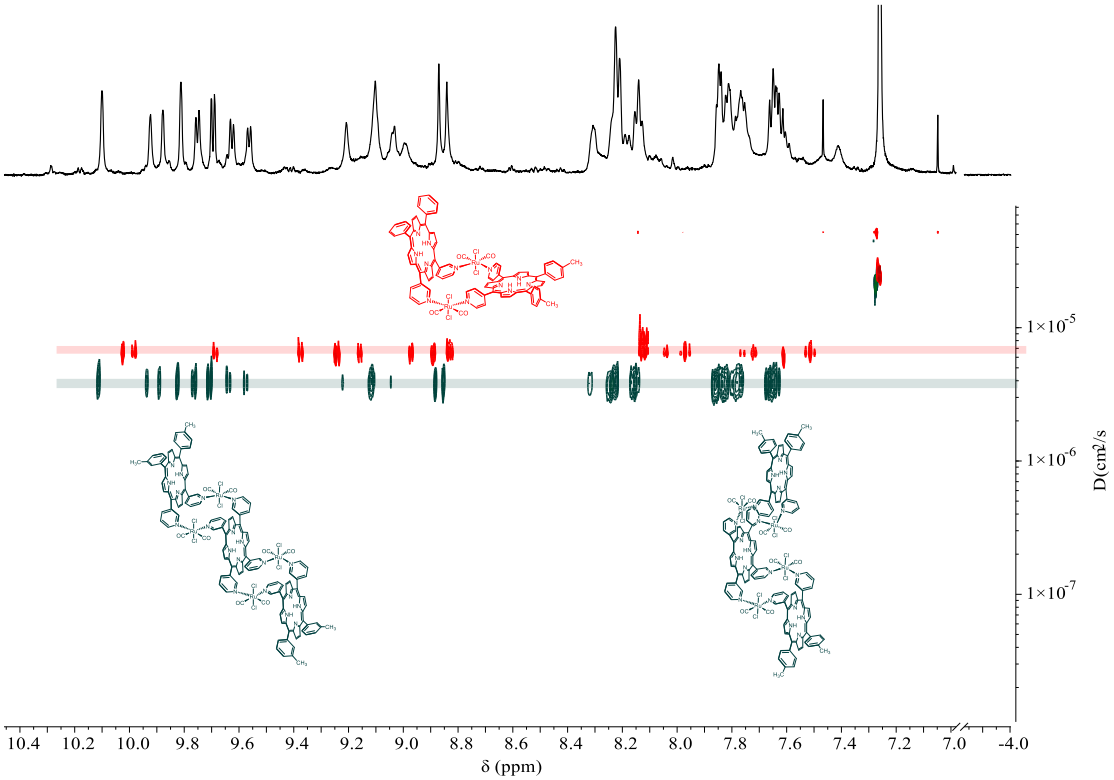

Figure 3.27. Bidimensional DOSY spectrum of **20Me** (green) in $CDCl_3$ compared with the spectrum of **18MeZn** (red)**.**

In the UV-vis spectrum of **20Me**, as found for metallacycle **3**, is visible an exciton splitting in the Soret band. This splitting is even larger compared to that found in **3**, 659 cm^{-1} vs 500 cm^{-1}. This splitting was not visible in the metallacyle **18** (Figure 3.13), probably because of the perpendicular disposition of the chromophores which allows only minor interactions between the porphyrins resulting in a smaller splitting, probably covered by the natural bandwidth of the Soret band.[4–6]

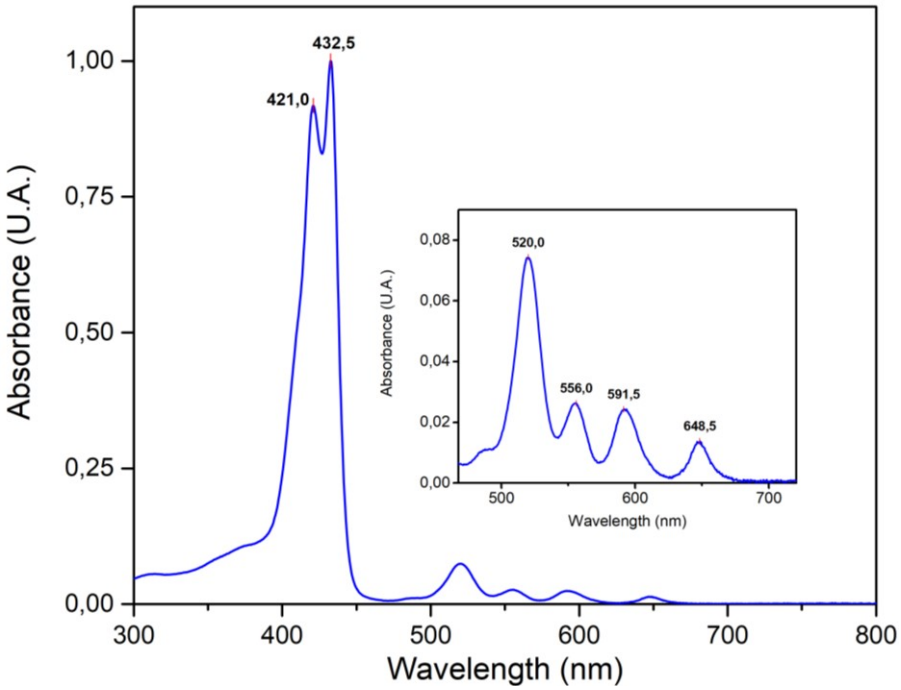

Figure 3.28. Normalized UV-vis spectrum ($CHCl_3$) of **20Me**.

20Me was then treated with 5 equivalents of $Zn(OAc)_2{\cdot}2H_2O$ in a $CHCl_3$:MeOH mixture obtaining the zincated metallacycle [{*trans,cis,cis*-$RuCl_2(CO)_2$}$_4$(Zn·3′*cis*DPyMP)$_2$(Zn·3′TPyP)] (**20ZnMe**), whose NMR spectrum is reported in Figure 3.29.

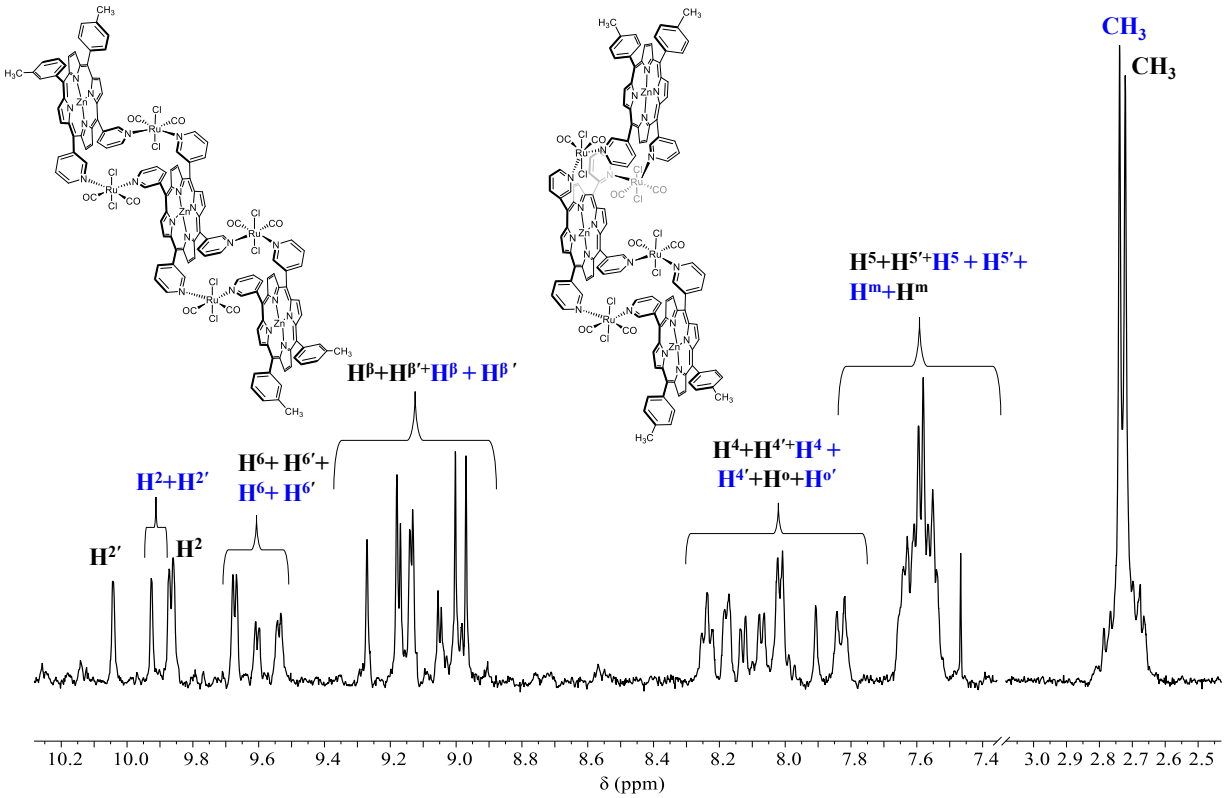

Figure 3.29. ^{1}H NMR spectrum (CDCl3) of the zincated metallacycle **20MeZn**.

In the ^{1}H NMR spectrum of the zincated metallacycle **20MeZn** the two conformers are present in a 1:1 ratio also in $CDCl_3$ complicating also the assignments of the signals.
We also performed an NMR titration of **20MeZn** with 4,4'-bpy, but even in this case it didn't afford a discrete assembly. After every addition of 4,4'-bpy the signal of **20MeZn** became very broad and also were not visible signals of coordinated bipyridine probably broadened beyond detection.

3.2.4 Synthesis and characterization of the heteroleptic triporphyrin metallacycles [{*trans,cis,cis*-$RuCl_2(CO)_2$}$_4$(4′*cis*DPyMP)$_2$(3′TPyP)] (21Me) and [{*trans,cis,cis*-$RuCl_2(CO)_2$}$_4$(3′*cis*DPyMP)$_2$(4′TPyP)] (22Me)

The above described synthetic strategy was also exploited for the synthesis of the heteroleptic triporphyrin systems [{*trans,cis,cis*-$RuCl_2(CO)_2$}$_4$(4′*cis*DPyMP)$_2$(3′TPyP)](**21Me)** and [{*trans,cis,cis*-$RuCl_2(CO)_2$}$_4$(3′*cis*DPyMP)$_2$(4′TPyP)](**22Me)**. These metallacycles are similar to **19** and **20**, but they both contain one porphyrin of one type and two of the other. In **21Me** the 3′-pyridylporphyrin is in the middle and the two 4′-pyridylporphyrins occupy the sides, whereas the opposite distribution occurs in **22Me**. In both cases two conformers are possible.
In **21Me** the two possible conformers have a *zig-zag* **21Me$_z$** or a *taco* shape **21Me$_t$**.

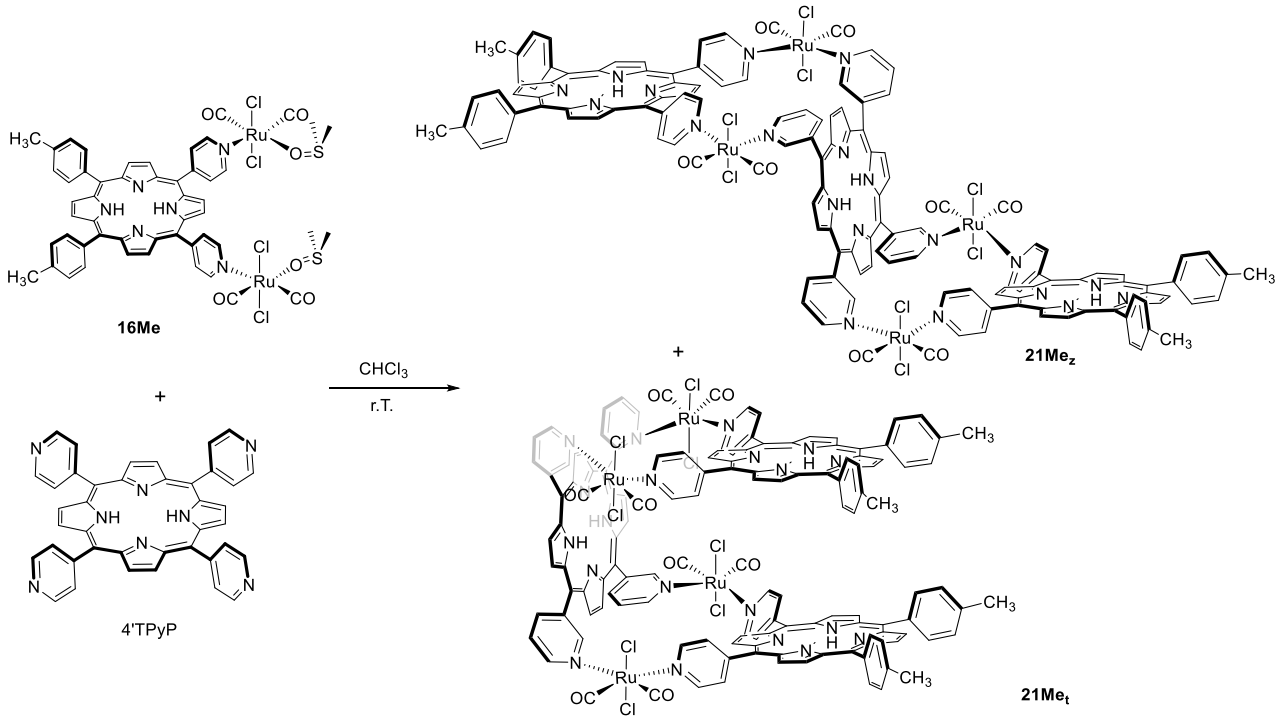

Scheme 3.7. Reaction scheme for the synthesis of the heteroleptic triporphyrin metallacycle [{*trans,cis,cis*-$RuCl_2(CO)_2$}$_4$(4′*cis*DPyMP)$_2$(3′TPyP)] (**21Me**).The *zig-zag* and the *taco* conformers are shown.

21Me$_t$ is very appealing for supramolecular purposes because it defines a cavity (it could be thought of as three faces of a cube). The reaction was performed in the same reaction condition that led to **20Me**. A 64 mg amount of **16Me** was dissolved in 12 mL of $CHCl_3$ and 16 mg (0.5 eq) of 3′TPyP

were added to the solution. The reaction was monitored by TLC following the progressive decrease of the 3′TPyP spot. After 24h the reaction was stopped and the crude purified by flash chromatography (silica gel, $CHCl_3$:*n*-hexane 97:3). Two fractions were collected, the second containing the desired product **21Me** (Yield 20%), whose NMR spectrum is reported in Figure 3.30.

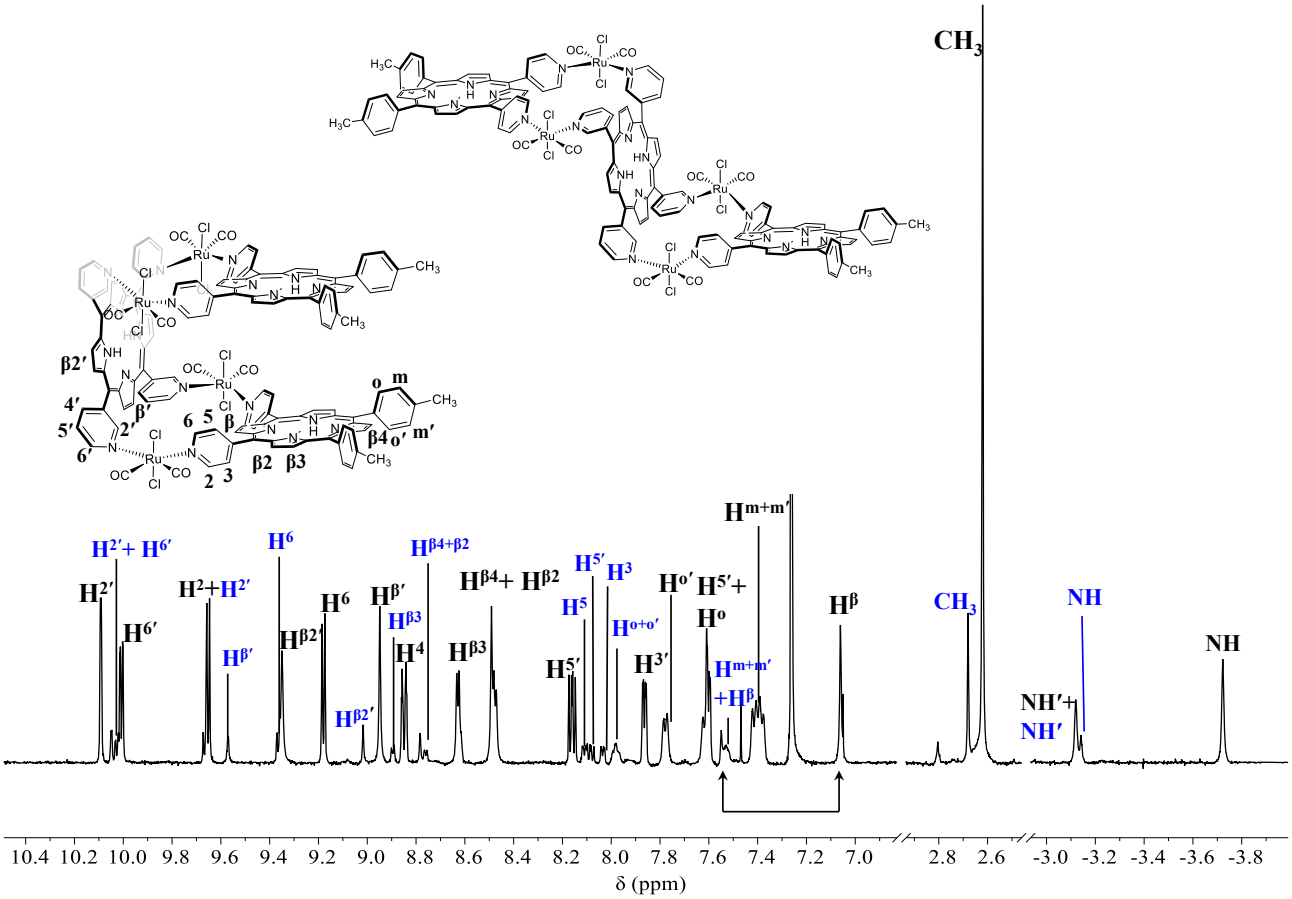

Figure 3.30. ^{1}H NMR spectrum ($CDCl_3$) of the metallacycle [{*trans,cis,cis*-$RuCl_2(CO)_2$}$_4$(4′*cis*DPyMP)$_2$(3′TPyP)] (**21Me**). Black and blue labels distinguish the two conformers.

Similarly of what was observed for the **20Me**, also in this case, despite observing a single spot in the TLC, in the ^{1}H NMR spectrum are visible two sets of sharp signals in a ca. 1:0.23 ratio (black and blue labels).

The two species have very similar patterns of signals, with some overlapping. When the spectrum was recorded in CD_2Cl_2 the ratio between the two sets changed suggesting that, also in this case, they belong to two conformers that are in slow exchange on the NMR time scale.

The two sets of signals show features similar to those of the corresponding 2+2 heteroleptic metallacycle **18Me**: in the high frequencies region are visible the resonances of H2′ and H6′ of the 3′TPyP of both species while those of the H2 and H6 of the two equivalents 4′*cis*DPyMPs fall at lower frequencies. In the ROESY spectrum are visible the intramolecular exchange cross peaks between the H2 and H6 caused by the rotation of the pyridyl ring but no intermolecular exchange

cross peaks between the two conformers are visible. This may be explained by assuming, that contrary to the rotation of the pyridyl ring, the exchange between the two species is too slow compared to the time scale of the NMR experiment.

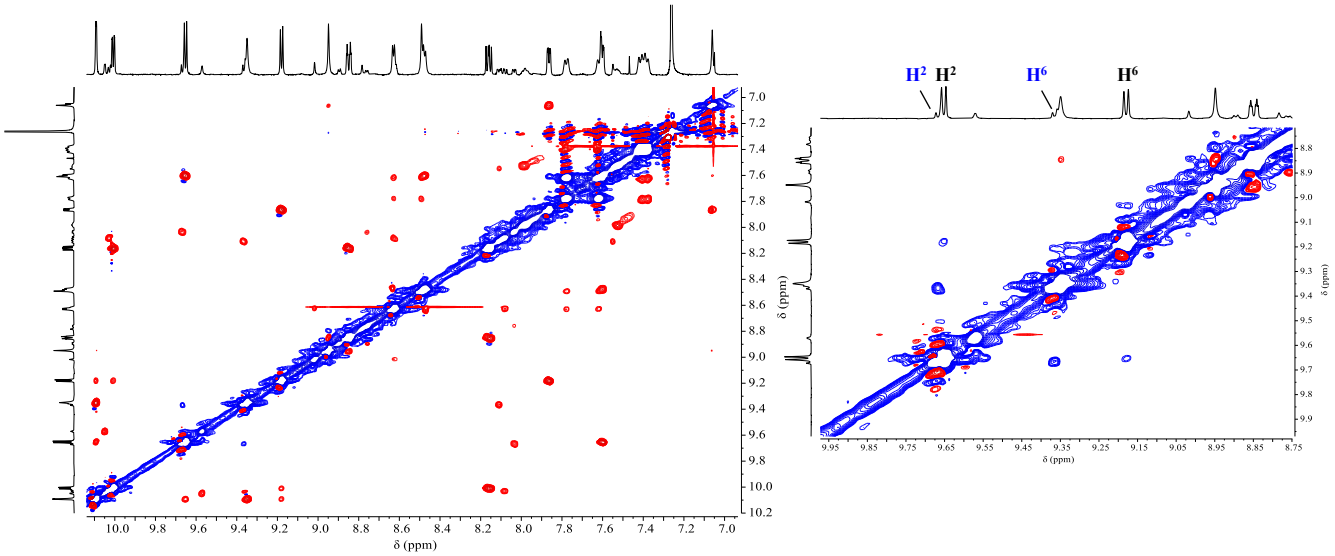

Figure 3.31. On the left ROESY spectrum of **21Me**, on the right enlargement showing the exchange cross peaks between H2 and H6 of both species.

It is also visible a rather large shift of the diagnostic singlet of the 7,8 Hβ protons of the 4′*cis*DPyMP between the two species (indicated with two arrows in Figure 3.30). While the resonance in the minor conformer falls at ca. 7.4 ppm, similarly to **18Me** and **3**, in the major species the signal falls at lower frequencies (7.2 ppm) and the same effect is visible for the NH singlet of the 4′*cis*DPyMP that are more upfield shifted in the major species.

This upfield shift can be tentatively explained by considering the reciprocal shielding effects of the two peripheral porphyrins in the two conformers. In this hypothesis the major species should be the *taco* conformer where the two 4′*cis*DPyMP are on the same side of the 3′TPyP's plane, facing each other and thus reinforcing their mutual shielding.

The diffusion coefficient calculated from the DOSY spectrum is 3.84±0.03 $cm^2 \cdot s^{-1}$ very similar to that found for the metallacycle **20Me.**

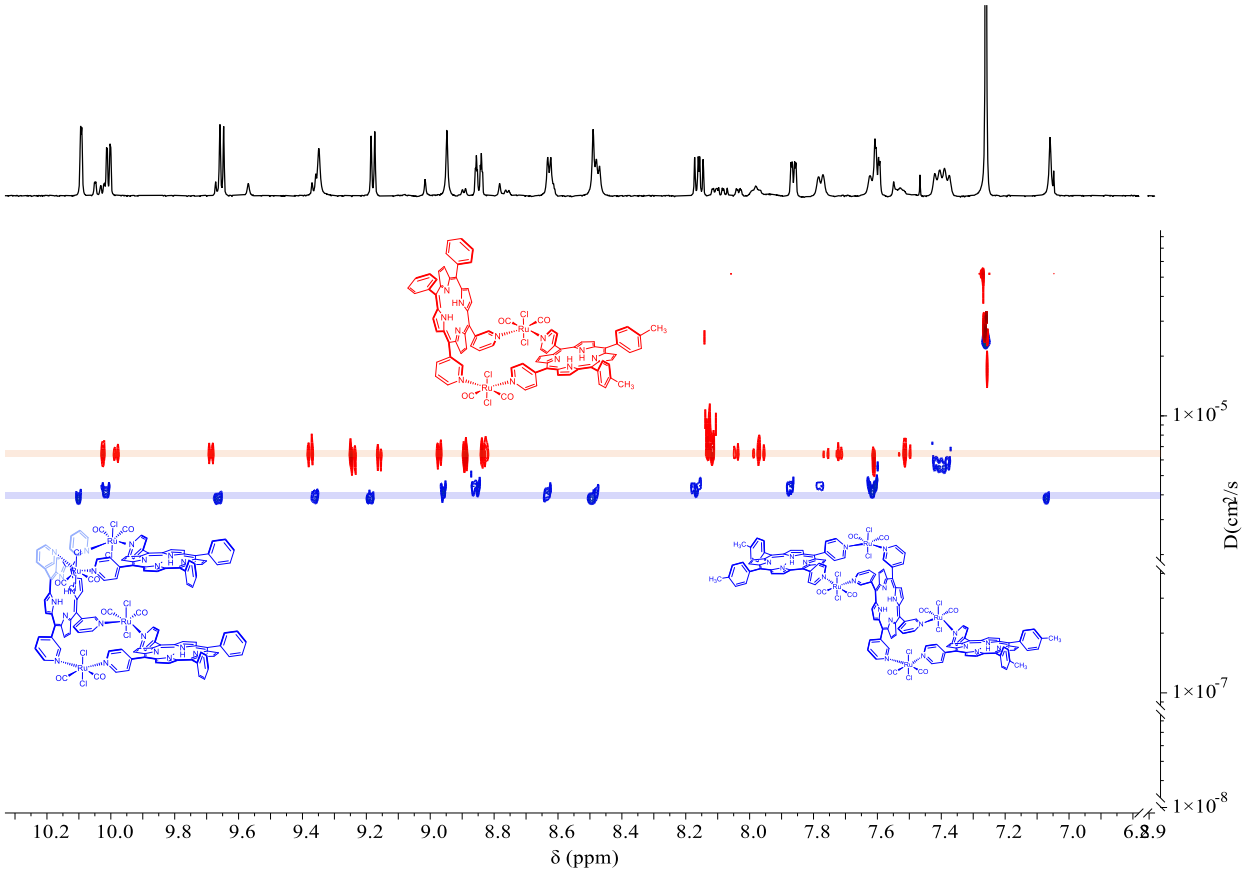

Figure 3.32. Bidimensional DOSY spectrum ($CDCl_3$) of **21Me** (blue) in $CDCl_3$ compared with the spectrum of **18MeZn** (red).

Slow diffusion of *n*-hexane in a solution of **21Me** in CH_2Cl_2 afforded crystals of X-ray quality allowing to determine the X-ray structure that was found to belong to the *zig-zag* conformer (Figure 3.33). To our knowledge this is the first X-ray structure of a triporphyrin metallacycle.

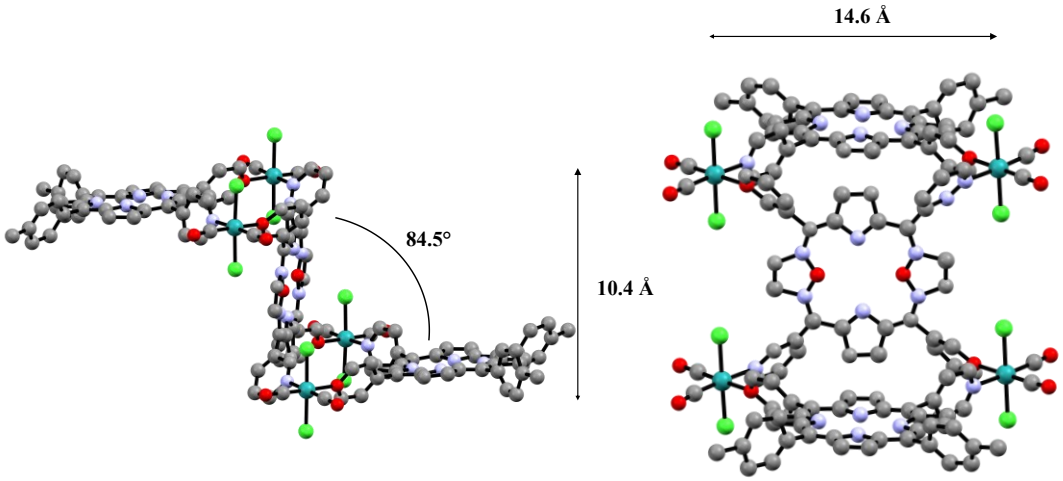

Figure 3.33. X-Ray structure of the metallacycle **21Me$_Z$**, on the left side view, on the right frontal view.

The two 4′*cis*DPyMPs are positioned in a slipped cofacial disposition with an interplanar distance of 10.1 Å and almost perpendicular (84°) to the plane of the central 3′TPyP. This affects the UV-vis spectrum (Figure A3.17) where is not visible an exciton splitting, indeed, despite the parallel disposition of the 4′*cis*DPyMPs their distance is too large to allow a strong interaction. Furthermore, this structure is in excellent agreement with the predicted structure of **18Me** which can be described as **21Me** less one of the peripherical 4′*cis*DPyMP.

We also synthesized the other heteroleptic triporphyrin metallacycle, [{*trans,cis,cis*-$RuCl_2(CO)_2$}$_4$(3′*cis*DPyMP)$_2$(4′TPyP)] (**22Me**), where 4′TPyP is in the middle of the array and two 3′*cis*DPyMPs are on the sides. The predicted geometries of the two possible conformers, **22Me$_t$** and **22Me$_z$**, are similar to those of **21Me$_t$** and **21Me$_z$.**

The synthesis was performed in the same reaction conditions used for the metallacycle **21Me**, and its NMR spectrum after column chromatography is reported in Figure 3.34

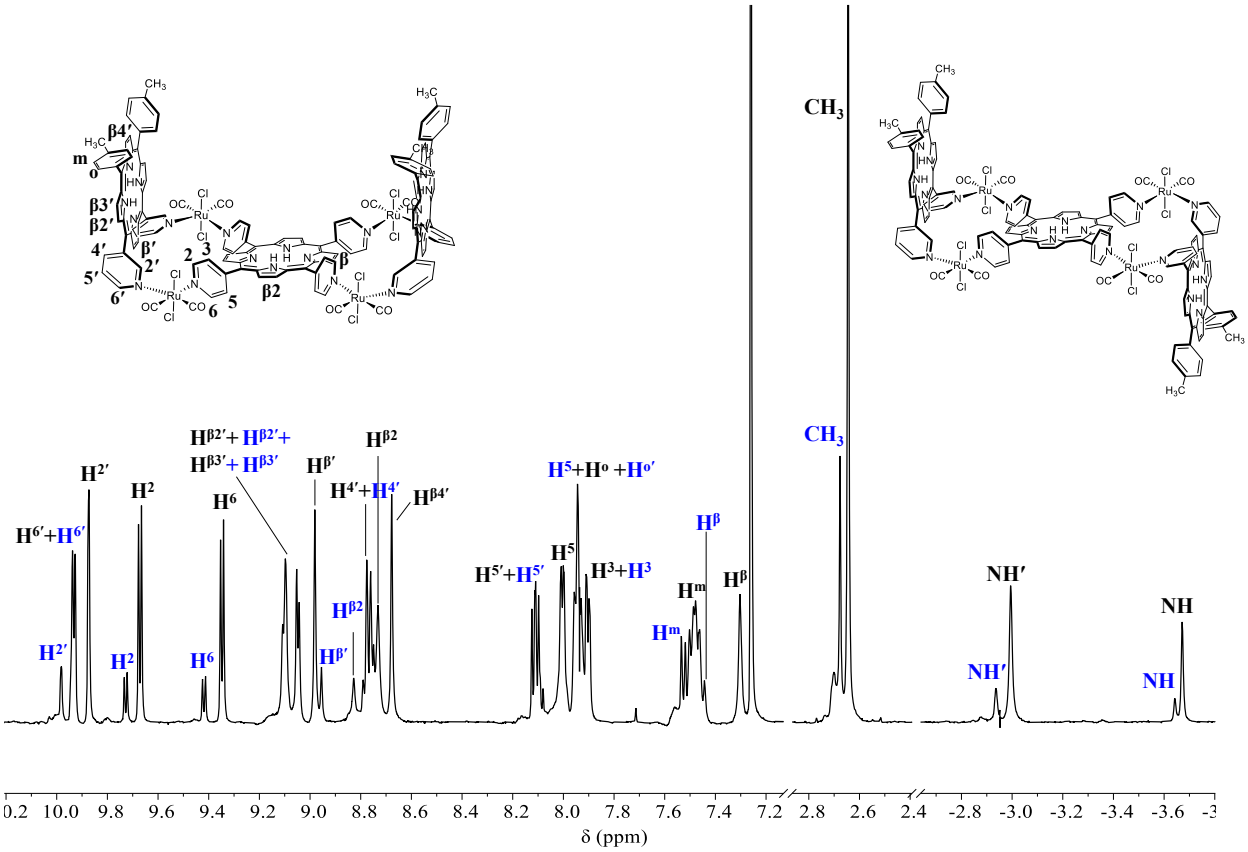

Figure 3.34. ^{1}H NMR spectrum ($CDCl_3$) of **22Me** in $CDCl_3$, the black and blue labels indicate the major and the minor species respectively.

Also, in this case we observe two sets of signals in a ca.1:0.23 ratio, in agreement with the presence of two conformers in solution in slow exchange on the NMR time scale. Also in this case are visible, in the ^{1}H-^{1}H ROESY spectrum, the intramolecular exchange cross peaks between H2 and H6 of both species but not the intermolecular ones.

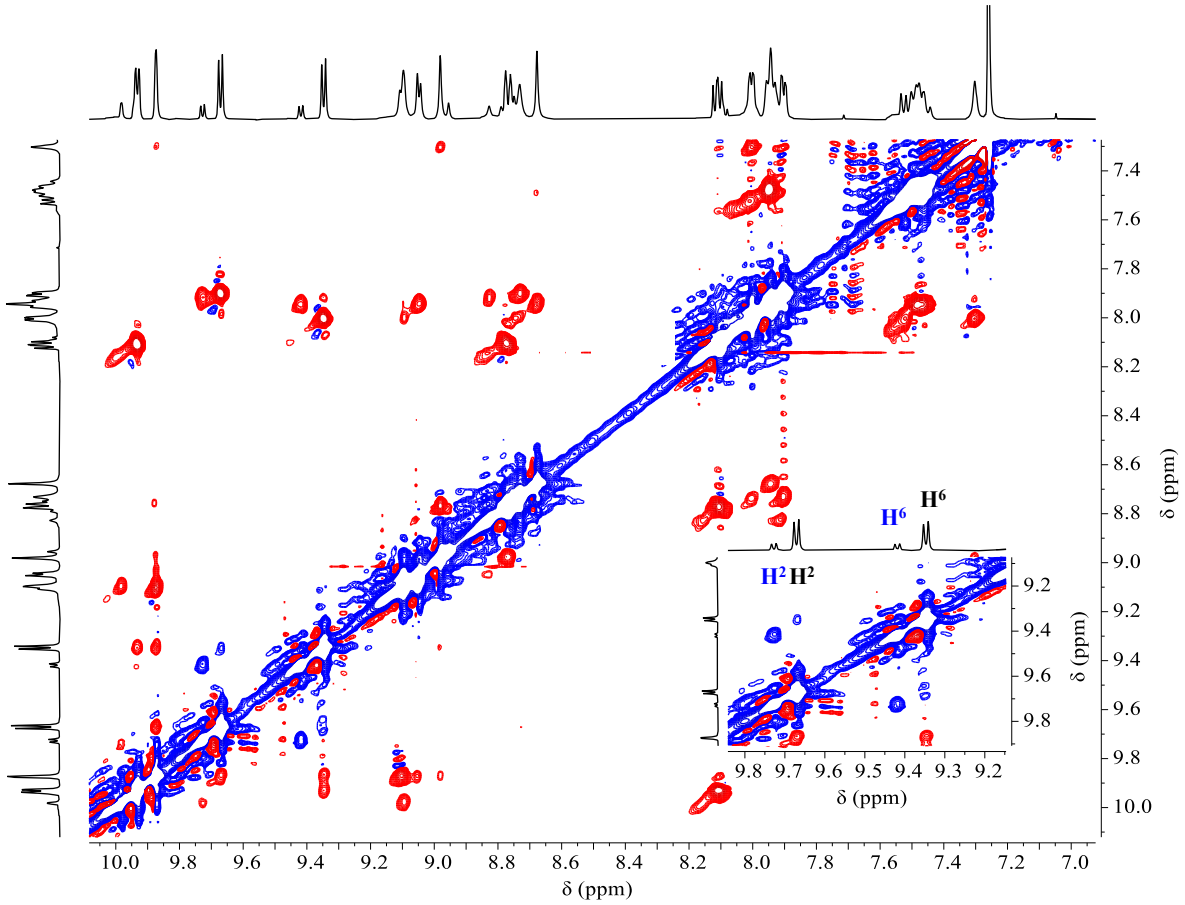

Figure 3.35. ^{1}H-^{1}H ROESY spectrum ($CDCl_3$) of [{*trans,cis,cis*-$RuCl_2(CO)_2$}$_4$(3′*cis*DPyMP)$_2$(4′TPyP)] **(22Me)**.

The calculated Diffusion coefficient of 3.75±0.06 cm^2s^{-1}, as expected, is almost identical to those found for **21Me** and **20Me.**

3.3 Conclusions

In this work we reported a new strategy for the synthesis of 2+2 heteroleptic metallacycles of porphyrins and for homoleptic and heteroleptic triporphyrin metallacycles.

The stepwise strategy was found to be more effective compared to the one-pot reaction, in which the complicate mixture of products is difficult to separate and also leads to lower yields.

In particular the heteroleptic 2+2 metallacycle **18** [{*trans,cis,cis*-$RuCl_2(CO)_2$}$_2$(4′*cis*DPyP)(3′*cis*DPyP)] and the corresponding species containing 4′*cis*DPyMP, **18Me**, were synthesized and characterized. This strategy also allowed us to obtain the homoleptic triporphyrin metallacycle [{*trans,cis,cis*-$RuCl_2(CO)_2$}$_4$(4′*cis*DPyP)$_2$(4′TPyP)] **(19)** and its analog **19Me**, but the low solubility, probably caused by aggregation processes, strongly limit their study.

On the other hand, the analog homoleptic triporphyrin metallacycle containing 3′-pyiridylporphyrins [{*trans,cis,cis*-$RuCl_2(CO)_2$}$_4$(3′*cis*DPyP)$_2$(3′TPyP)] (**20Me)** was fully characterized and exist as a mixture of two conformers **20Me$_g$** and **20Me$_l$** having a *Greek-frame* and *ladder* geometry respectively. The two conformers, at room temperature, are in slow exchange on the NMR time scale. The heteroleptic triporphyrin metallacycles **21Me** and **22Me** were also synthesized and also these exist as a mixture of the two conformers, the *Greek-frame* and the *ladder* conformer. The X-ray structure of one of the conformers of **21Me** allowed us to confirm the zig-zag shape of the metallacycle**.**

The unprecedented geometries of these metallacycles, in particular the *taco* conformers, are very appealing in supramolecular chemistry. In particular, the methyl groups in this conformer point outside the metallacycle, and if they are substituted with other reactive groups (e.g. –OH, COOH, terminal olefins) these can act as anchor points for a linker, allowing the connections of two triporphyrin metallacycles, affording a capsule.

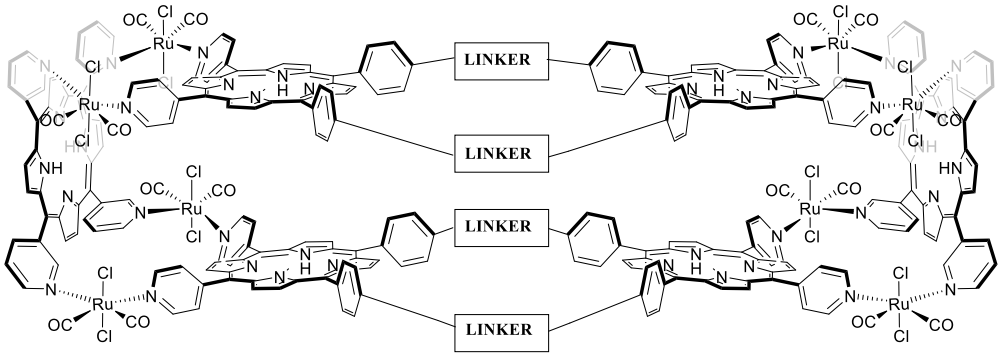

Figure 3.36. Possible structure deriving from the linking of two **21Me$_v$** units.

In addition, two *taco* conformers might self-assemble (e.g. upon treatment of the zincated derivatives with a suitable templating agent) to afford a cubic-like capsule.

3.4 Experimental Section

Materials

All chemicals, including TLC silica gel plates, were purchased from Sigma-Aldrich and used as received. Solvents were of reagent grade. The ruthenium precursors *trans,cis,cis* -$RuCl_2(CO)_2$(dmso-*O*)$_2$ (**1**), and the *meso*-pyridylporphyrins were synthesized and purified as previously reported by us.[7,8]

Instrumental Methods

Mono- and bidimensional ($^1H-^1H$ COSY, $^1H-^{13}C$ HSQC) NMR spectra were recorded at room temperature unless stated otherwise on a Varian 400 or 500 spectrometer (^1H, 400 or 500 MHz; $^{13}C\{1H\}$, 100.5 or 125.7 MHz). ^1H DOSY experiments were recorded on the Varian 500 spectrometer at 25°C ($CDCl_3$), using the bipolar pulse pair stimulated echo with convection compensation sequence implemented into the VnmrJ software. ^1H and $^{13}C\{1H\}$ chemical shifts were referenced to the peak of residual nondeuterated solvent (δ = 7.26 and 77.16 for $CDCl_3$ and 2.50 and 39.52 for DMSO-d_6).Selected carbon resonances, except for carbonyls, were assigned through the HSQC spectra. The UV−vis spectra were obtained on an Agilent Cary 60 spectrophotometer, using 1.0 cm path-length quartz cuvettes (3.0 mL). Infrared spectra of chloroform solutions in the CO stretching region were recorded between CaF_2 windows (0.5 mm spacer) on a PerkinElmer Fourier-transform IR/Raman 2000 instrument in the transmission mode. A CEM Discover microwave reactor was used for the microwave-assisted reactions performed in 10 mL vessels. Elemental analysis, unless is performed on the crystal samples (such as those used for X-ray determinations), is poorly significant for these systems due to the typical presence of crystallization molecules whose nature and number vary from batch to batch. X-ray Diffraction. Data collections were performed at the X-ray diffraction beamline (XRD1) of the Elettra Synchrotron of Trieste (Italy) equipped with a Pilatus 2 M image plate detector. Collection temperature was 100 K (nitrogen stream supplied through an Oxford Cryostream 700); the wavelength of the monochromatic X-ray beam was 0.700 Å, and the diffractograms were obtained with the rotating crystal method. The crystals were dipped in N-paratone and mounted on the goniometer head with a nylon loop. The diffraction data were indexed, integrated and scaled using the XDS code.32 The structures were solved by the dual space algorithm implemented in the SHELXT code.33 Fourier analysis and refinement were performed by the full-matrix least-squares methods

Synthesis of the complexes

[{*trans,cis,cis*-$RuCl_2(CO)_2$(dmso-*O*)}$_2$(4′*cis*DPyP)] (16). A 87.0 mg (0.486 mmol) amount of *trans,cis,cis*-$RuCl_2(CO)_2$(dmso-*O*)$_2$ (**1**) was dissolved in 20 mL of $CHCl_3$. 50.0 mg (0.081 mmol) of 4'*cis*DPyP (ratio **1**/4'*cis*DPyP 6:1) were added to the yellow solution. The violet solution was stirred

at room temperature for 50 minutes and afterwards the solvent was removed under reduced pressure. The recovered violet solid was washed with H_2O to remove the unreacted complex and the free DMSO and dried under vacuum. The solid was redissolved in chloroform and anhydrified on Na_2SO_4. The solution was recovered, the solvent was removed by evaporation at reduced pressure and dried under vacuum. Yield: 89.6 mg, 98%. ^{1}H NMR ($CDCl_3$ with addition of DMSO-*d*$_6$) δ: ppm 9.41 (d, 4H, H2,6), 8.88 (d, 2H, Hβ), 8.82 (s, 2H, Hβ), 8.80 (s, 2H, Hβ), 8.77 (d, 2H, Hβ), 8.28 (d, 4H, H3,5), 8.12 (d, 4H, Ho), 7.72 (m, 6H, Hm+p), −2.92 (s, 2H, NH). UV-vis λ_{max}, nm, $CHCl_3$ (relative intensity%): 424 (100), 526 (5.97), 560 (2.96), 600 (2.39), 650 (1.94). IR (bands selected in $CHCl_3$, cm^{-1}): 2072 (νCO), 2002 (νCO).

[{*trans,cis,cis*-RuCl$_2$(CO)$_2$(dmso-*O*)}$_2$(4′*cis*DPyMP)](16Me) The procedure is similar to **16**. A 178.8 mg (0.465 mmol) amount of **1** was dissolved in 20 mL of $CHCl_3$. 50.0 mg (0.078 mmol) of 4'*cis*DPyMP (ratio **1** / 4'*cis*DPyMP 6: 1) were added to the yellow solution and stirred for 50 minutes at room temperature. The solvent was removed under reduced pressure and the solid washed with water and dried under vacuum. The solid was redissolved in chloroform, and anhydrified of Na_2SO_4. Yield: 71.2 mg, 81%. ^{1}H NMR in DMSO-*d*$_6$, δ (ppm): 9.37 (d, 4H, H2,6), 8.92 (m, 8H, Hβ), 8.62 (d, 4H, H3, H5), 8.12 (d, 4H, Ho), 7.66 (d, 4H, Hm), 2.68 (s, 6H, Me), – 2.95 (s, 2H, NH). UV-vis λ_{max}, nm, $CHCl_3$ (relative intensity%): 424 (100), 526 (5.97), 560 (2.96), 600 (2.39), 650 (1.94). IR (bands selected in $CHCl_3$, cm^{-1}): 2072 (νCO), 2002 (νCO).

[{*trans,cis,cis*-RuCl$_2$(CO)$_2$(dmso-*O*)}$_2$(3′*cis*DPyP)](17). A186.9 mg (0.486 mmol) amount of *trans,cis,cis*-$RuCl_2$ $(CO)_2$(dmso-κ*O*)$_2$ (**1**) was dissolved in 50 mL of $CHCl_3$. 50.0 mg (0.081 mmol) of 3'*cis*DPyP (ratio **1**:3'*cis*DPyP 6:1) were added to the yellow solution The violet solution was stirred at room temperature for 50 minutes and afterwards the solvent was removed under reduced pressure. The recovered violet solid was washed with H_2O to remove the unreacted complex and the free DMSO and was dried under vacuum. The solid was redissolved in chloroform and anhydrified on Na_2SO_4. The solution was recovered, the solvent was removed by evaporation at reduced pressure and dried under vacuum. Yield: 84.7 mg, 94%. ^{1}H NMR ($CDCl_3$+DMSO-*d*$_6$), δ (ppm): 9.67, 9.62 (2s, 2H, H2), 9.24 (d, 2H, H6), 8.68 (m, 8H, Hβ), 8.55 (m, 2H, H4), 7.97 (m, 4H, Ho), 7.78 (t, 2H, H5), 7.56 (m, 6H, Hm+p), −3.08 (s, 2H, NH). IR (bands selected in $CHCl_3$, cm^{-1}): 2073 (νCO), 2003 (νCO).

[{*trans,cis,cis*-RuCl$_2$(CO)$_2$}$_2$(4'*cis*DPyP)(3'*cis*DPyP)](18). A 15.0 mg (0.014 mmol) amount of **16** was dissolved in 4 mL of anhydrous CH_2Cl_2. 5.6 mg ($9.0x10^{-3}$ mmol) of 3'*cis*DPyP were added to the purple solution (ratio **16**/3'*cis*DPyP 1.5: 1) and 50μL of DMSO. The solution was stirred at 40°C for 50 minutes. The solvent was removed under reduced pressure and the violet solid was washed first with H_2O then with MeOH and finally with diethyl ether. The solid was dried under vacuum and

purified by pipette column chromatography (SiO_2, $CHCl_3$). A single fraction, containing the desired product was collected. Yield: 4 mg, 26%. ^{1}H NMR ($CDCl_3$), δ (ppm): 9.99 (m, 2H, H2'+H6'), 9.70 (d, 2H, H2), 9.38 (d, 2H, H6), 9.17 (d, 2H, Hβ), 9.08 (s+d, 4H, Hβ), 8.83 (m, 4H, Hβ'+H4'), 8.74 (m, 6H, Hβ')8.13 (m,8H, H5+Ho+Ho'), 8.04 (m, 2H, H3), 7.74 (m, 12H, Hm+Hp+ Hm'+Hp'), 7.48 (s, 2H, Hβ '), –2.91 (s, 2H, NH')), –3.18 (s, 2H, NH). UV-vis λ_{max}, nm, $CHCl_3$ (relative intensity%): 422 (100),520 (6.83), 555 (3.37), 592 (2.61), 648 (1.76). IR (bands selected in $CHCl_3$, cm^{-1}): 2074 (νCO), 2014 (νCO). R_f ($CHCl_3$) = 0.31

[{*trans,cis,cis*-RuCl$_2$(CO)$_2$}$_2$(4'*cis*DPyMP)(3'*cis*DPyP)](18Me). A 50.0 mg amount of **16Me** (0.044 mmol) was dissolved in 13 mL of $CHCl_3$. 21.0 mg (0.034 mmol) of 3'*cis*DPyP (ratio **16Me:**3'*cis*DPyP 1.3:1) and 0.17 mL of DMSO were added to the solution and stirred at 40°C for 50 minutes. Afterwards the solvent was removed under reduced pressure, and the crude obtained and washed first with distilled H_2O, then with MeOH and finally with diethyl ether. The crude was purified by column chromatography (silica gel $CHCl_3$:*n*-hexane 94:6), collecting a fraction containing three species with Rf equal to 0.23, 0.15, 0.09, the first two assigned to **2Me** and **18Me** , the last belonging to an unknown species. This fraction was purified through another column (silica gel, CHCl:*n*-hexane 80:20) collecting two fractions, the first containing **2Me** and the second **18Me**. Yield: 12 mg, 20%. ^{1}H NMR ($CDCl_3$), δ (ppm): 9.99 (s, 2H, H2'+ H6'), 9.69 (d, 2H, H2), 9.36 (d, 2H, H6), 9.17 (d , 2H, Hβ′), 9.08 (d, 2H, Hβ′), 9.07 (s, 2H, Hβ′), 8.86 (d, 2H, Hβ), 8.83 (dt, 2H, H4'), 8.77 (s, 2H, Hβ), 8.72 (m, 4H, Hβ'+Hβ), 8.13 (m, 8H, H5'+H5+Ho'), 8.04 (dd, 2H, H3), 7.97(m ,4H, Ho), 7.74 (m, 6H, Hm'+Hp'), 7.51 (m, 4H, Hm), 7.47 (s, 2H, Hβ), 2.67 (s, 6H, Me), −2.92 (s, 2H, NH′), −3.19 (s, 2H, NH). UV-vis λ_{max}, nm, $CHCl_3$ (relative intensity%): 423 (100), 520 (6.45), 555 (2.97), 591 (2.22), 647 (1.32).

[{*trans,cis,cis*-RuCl$_2$(CO)$_2$}$_2$(Zn·4′*cis*DPyMP)(Zn·3′*cis*DPyP)](18ZnMe). A 12.0 mg (0.0096 mmol) amount of **18Me** was dissolved in 20 mL of $CHCl_3$. 6.5 mg (0.030 mmol) of Zn $(AcO)_2{\cdot}2H_2O$ were dissolved in 1 mL of MeOH (ratio $CHCl_3$:MeOH 20:1, ratio **16Me**:Zn$(AcO)_2{\cdot}2H_2O$ 1:4) and added to the solution. The solution was stirred at room temperature in the dark for 48 h. The solvent was removed under reduced pressure, washed with H_2O and. dried under vacuum. Yield: 6.4 mg, 50%. ^{1}H NMR ($CDCl_3$), δ (ppm): 10.2 (s, 2H, H2'), 9.98 (m, 2H, H6'), 9.69 (d, 2H, H6), 9.37 (d, 2H , H2), 9.24 (s, 2H, Hβ), 9.24 (d, 2H, Hβ), 6.19 (d, 2H, Hβ), 8.97 (d, 2H, Hβ'), 8.89 (s, 2H, Hβ), 8.89 (s, 2H, Hβ'), 8.83 (d, 2H, Hβ'), 8.83 (m, 2H, H4'), 8.12 (m, 8H, H5+H5'+Ho'), 8.04 (m, 2H ,H3), 7.97 (m, 4H,Ho), 7.74 (m, 6H, Hm'+Hp'), 7.61 (s, 2H, Hβ), 7.52 (m, 4H, Hm), 2.68 (s, 6H , Me). UV-vis λ_{max}, nm, $CHCl_3$ (relative intensity%): 427 (100) (Soret), 559 (6.97), 600 (2.39)

[{*trans,cis,cis*-RuCl$_2$(CO)$_2$}$_4$(4′*cis*DPyP)$_2$(4′TPyP)] (19). A 11.1 mg of (0.018 mmol) of 4′TPyP was partially solubilized in a microwave test tube in CH_2Cl_2 at 90° for 20 minutes to promote its

solubilization. 250 µL of DMSO and 50 mg (0.045 mmol) of **16** (**16** :4′TPyP 2.5:1) were added to the the violet solution and stirred at room temperature. The reaction was followed by TLC (SiO_2, $CHCl_3$:EtOH ratio 97.5:2.5) After 48 hours, the solvent was removed under reduced pressure and the solid was suspended in acetone, centrifuged (5 min, 5500 rpm × 5) and the supernatant was removed. The solid was purified by chromatography, using a Pasteur pipette as a column (silica gel, $CHCl_3$). Two fractions were collected, the first containing the desired product. The product, despite being all in solution once leaving the column, when the solvent is removed is no longer entirely soluble in $CDCl_3$. [{*trans,cis,cis*-$RuCl_2(CO)_2$}$_4$(4′*cis*DPyP)$_2$(4′TPyP)] (**19**). Yield 4.5 mg (9%). ^{1}H NMR ($CDCl_3$), δ (ppm): 9.93 (d, 8H, H2,6 + H2',6'), 9.85 (d, 8H, H2,6 + H2',6'), 9.09 (m, 24H, Hβ), 8.63 (d, 8H, H3,5 + H3',5'), 8.59 (d, 8H, H3,5 + H3',5'), 8.27 (d, 8H, H*o*), 7.86 (m, 12H, Hm+p), –2.70 (s, 6H, NH). IR (selected bands in $CHCl_3$, cm^{-1}): 2075 (ν_{CO}), 2016 (ν_{CO}). UV–vis ($CHCl_3$) λ_{max}, nm (relative intensity, %): 426 (100), 517 (7.7), 553 (4.23), 590 (3.01), 645 (1.92).

R_f ($CHCl_3$) = 0.24

[{*trans,cis,cis*-$RuCl_2(CO)_2$}$_4$(3′*cis*DPyMP)$_2$(3′TPyP)] (20Me). A 199.0 mg amount of [{*trans,cis,cis*-$RuCl_2(CO)_2$(dmso-*O*)}$_2$(3′*cis*DPyMP)] (**17Me**) (0.796 mmol) was dissolved in 40 mL of $CHCl_3$. After addition of 2.2 eq of 3′TPyP (49.5 mg) the purple solution was stirred at room temperature for 17h and monitored by TLC (SiO_2, $CHCl_3$:EtOH 98:2). The solvent was removed under reduced pressure and the crude purified by column chromatography (silica gel, $CHCl_3$:*n*-hexane 97:3). One main fraction was collected. Yields 50.6mg (23%) ^{1}H NMR ($CDCl_3$), δ (ppm) δ10.10 (s, 4H, H2′), 9.92, 9.87 (s+s, 8H, H2+H2′), 9.81 (s, 4H, H2), 9.74, 9.69 (d+d, 8H, H6+H6′), 9.62, 9.56 d+d, 8H, H6+H6′) , 9.27 – 8.83 (m, 7H), 8.25 – 8.16 (m, 24H+24H, Hβ′+ Hβ+ Hβ+ Hβ′), 8.28-7.96 (m, 16H+16H, H^4+$H^{4'}$+H^4+ $H^{4'}$+H^o+H^o), 8.03 (d, 2H), 7.74 – 7.50 (m, 16+H, H^5+$H^{5'}$+H^5 + $H^{5'}$+H^m+H^m), 2.75 (s, 12H, CH_3), 2.73 (s, 12H, CH_3), -2.99 (s, 4H, NH), -3.03 (s, 4H, NH), -3.26 (s, 2H, NH′), -3.36 (s, 2H, NH′).IR (bands selected in $CHCl_3$, cm^{-1}): 2074 (νCO), 2014 (νCO). UV-vis λ_{max}, nm, $CHCl_3$ (relative intensity%): $CHCl_3$ (ε x 10^4 (cm^{-1} M^{-1})): 420.5(50.4), 433 (54.8), 520.5 (4.93), 555 (1.79), 591.5 (1.58), 647 (0.93). R_f ($CHCl_3$) = 0.12

[{*trans,cis,cis*-$RuCl_2(CO)_2$}$_4$(Zn·3′*cis*DPyMP)$_2$(Zn·3′TPyP)] (20MeZn). A 40.0 mg (0.0145 mmol) amount of [{*trans,cis,cis*-$RuCl_2(CO)_2$(dmso-*O*)}$_2$(4′*cis*DPyMP)] **20Me** was dissolved in 45 mL of $CHCl_3$. 12.8 mg (4 eq) of Zn $(AcO)_2$·$2H_2O$ were dissolved in 1 mL of MeOH (ratio $CHCl_3$:MeOH 20: 1, ratio **20Me**:Zn$(AcO)_2$·$2H_2O$ 1:4) and added to the solution. The solution was stirred at room temperature in the dark for 22 h. The solution was washed with water, the organic phase was anhydrified on Na_2SO_4 Yield 29.3 (30%). ^{1}H NMR ($CDCl_3$), δ (ppm) 10.10-9.82 (m, 8H+8H, H2′+H2′+H2+H2′), 9.72-9.48 (m, 8H+8H, H6′+H6′+H6+H6′), 9.34-8.81(m, 8.25 – 8.16 (m, m, 24H+24H, Hβ′+ Hβ+ Hβ+ Hβ′), 8.34-7.77 (m, 16H+16H, H^4+$H^{4'}$+H^4+ $H^{4'}$+H^o+H^o), 8.03 7.57 (m,

16H+16H, H^5+$H^{5'}$+H^5 + $H^{5'}$+H^m+H^m), 2.74 (s, 12H, CH_3), 2.74 (s, 12H, CH_3). IR (bands selected in $CHCl_3$, cm^{-1}): 2074 (νCO), 2014 (νCO) UV-vis λ_{max},nm, $CHCl_3$ (ε x 10^4 (cm^{-1} M^{-1})): 426(58.4), 438.5 (42.6), 560.5 (4.53), 600(1.55)

[{*trans,cis,cis*-$RuCl_2(CO)_2$}$_4$(4′*cis*DPyMP)$_2$(3′TPyP)] (21Me) A 64.3 mg amount of [{*trans,cis,cis*-$RuCl_2(CO)_2$(dmso-κ*O*)}$_2$(4′*cis*DPyMP)] (**16Me**) (0.796 mmol) was dissolved in 40 mL of $CHCl_3$. After addition of 2.2 eq of 3′TPyP (15.9 mg) the purple solution was stirred at room temperature for 23h monitored by TLC (SiO_2, $CHCl_3$:EtOH 98:2). The solvent was removed under reduced pressure and the crude purified by column chromatography (silica gel, $CHCl_3$:*n*-hexane 97:3). Yield 10.7mg (15%)

^{1}H NMR ($CDCl_3$), blue and black label indicate minor and major conformer respectively, δ (ppm): 10.09 (s, 4H, H2′), 10.05 (s, 4H, H2′),10.03 (d, 4H, H6′), 10.01(d, 4H, H6′**),** 9.66 (d, 4H, H2**)** 9.65 (d, 4H, H2), 9.57 (s, 2H, Hβ′), 9.36 (d, H6), 9.35 (s, 2H, Hβ2′) 9.18 (d, 4H, H6), 9.02 (s, 2H, Hβ2′), 8.95 (s, 2H, Hβ′), 8.89 (d, 4H, Hβ3), 8.85 (d, 4H, H4), 8.78 (s, 4H, Hβ2), 8.76 (d,4H, Hβ2), 8.63 (d, 4H, Hβ3), 8.52 – 8.43 (m, 8H Hβ4+Hβ2), 8.16 (dd, 4H, H5′),8.11 (d, 4H, H5), 8.08 (d, 4H, H5′) 8.04 (br t, 4H, H3), 7.98 (s, 8H, Ho+o′), 7.86 (d, 4H, H3′), 7.78 (d, 4H, Ho′), 7.65 – 7.57 (m, 8H, H5′+Ho), 7.54 (m, 12H, Hβ+ Hm+m′) 7.40 (m, 8H, Hm+m′), 7.06 (s, 4H, Hβ) 2.68 (s, 12H, CH_3), 2.62 (s, 12H, CH_3), -3.12 (s, 2H+2H, NH′+NH′), -3.14 (s, 4H, NH), -3.72 (s, 4H, NH). IR (bands selected in $CHCl_3$, cm^{-1}): 2069 (νCO), 2005 (νCO). UV-vis λ_{max}, nm, $CHCl_3$ (ε x 10^4 (cm^{-1} M^{-1}): 423 (57.9) ,519 (4.2), 555 (1.96), 592 (1.95), 648 (0.83). R_f ($CHCl_3$):0.10

[{*trans,cis,cis*-$RuCl_2(CO)_2$}$_4$(3′*cis*DPyMP)$_2$(4′TPyP)] (22Me) A 47.6 mg amount of 4′TPyP (0.0763 mmol) was partially dissolved in 40 mL of $CHCl_3$. The purple suspension was heated to reflux to promote the solubilization of the 4′TPy. 2.2 eq of [{*trans,cis,cis*-$RuCl_2(CO)_2$(dmso-κ*O*)}$_2$(3′*cis*DPyMP)] (**17Me**) (190.5 mg) were added at room temperature to the purple suspension. The reaction was monitored by TLC (SiO_2, $CHCl_3$:EtOH 98:2) and stopped after 17h. The solvent was removed under reduced pressure and the crude purified by column chromatography (silica gel, $CHCl_3$:*n*-hexane 95:5). One main fraction was collected containing the desired product. Yield 7.8 mg (3%)^{1}H NMR ($CDCl_3$) blue and black label indicate minor and major conformer respectively, δ (ppm): δ 9.98 (s, 4H, H2′), 9.92 (m, 4H+4H, H6′+H6′), 9.87 (d, 4H, H2′), 9.73 (d, 4H, H2′), 9.67 (d, 4H, H2), 9.42 (d, 4H, H6), 9.35 (d, 4H, H6), 9.13-9,02 (m,, 8H+4H,), 8.98 (s, 4H, Hβ′), 8.96 (s, 4H, Hβ′), 8.83 (s, 2H, Hβ2), 8.80 (m, 4H+4H, H6′+H6′), 8.73 (s, 4H, Hβ2), 8.68 (s, 4H, Hβ4′), 8.11 (m, 4H+4H, H5′+H5′), 8.00 (d, 4H, H5), 7.98 – 7.86 (m, 16H +12H, H5+Ho +H3 +Ho+H3), 7.57 – 7.43 (m, 4H+4H, Hm+Hm) 7.44 (d, 4H, Hβ), 2.68 (s, 12H, NH), 2.64 (s, 12H, CH_3), -2.93 (s, 4H, NH′), -2.99 (s, 4H, NH′), -3.64 (s, 2H, NH), -3.67 (s, 2H, NH). IR (bands selected in $CHCl_3$, cm^{-1}): 2067

(νCO), 20052 (νCO). UV-vis λ_{max}, nm, $CHCl_3$ (ε x 10^4 (cm^{-1} M^{-1}): 424 (71.6) ,521 (4.93), 557 (2.57, 593.5 (1.83), 649.5 (1.29)

3.5 Bibliography

1 Drain, C. M., Nifiatis, F., Vasenko, A. & Batteas, J. D. Porphyrin Tessellation by Design. *Angew. Chem., Int. Ed*. **1998,** 2344–2347.

2 Iengo, E., Zangrando, E., Alessio, E., Chambron, J.C., Heitz, V., Flamigni, L., and Sauvage, J.P.. A Functionalized Noncovalent Macrocyclic Multiporphyrin Assembly from a Dizinc(II) Bis-Porphyrin Receptor and a Free-Base Dipyridylporphyrin. Chemistry. *Chem. - A Eur. J.* **2003**, 9, 5879–5887.

3 Araki, K., Dovidauskas, S., Winnischofer, H., Alexiou, A. D. P. & Toma, H. E. A new highly efficient tetra-electronic catalyst based on a cobalt porphyrin bound to four m 3 -oxo-ruthenium acetate clusters. *Journal of Electroanalytical Chemistry.* **2001**, 498, 152–160.

4 Yoshida, N., Ishizuka, T., Osuka, A., Jeong, D.H., Cho, H.S., Kim, D., Matsuzaki, Y., Nogami, A., and Tanaka, K. Fine tuning of photophysical properties of meso-meso-linked ZnII-diporphyrins by dihedral angle control. *Chem. - A Eur. J.* **2003**, 9, 58–75.

5 Zanetti-Polzi, L., Amadei, A., Djemili, R., Durot, S., Schoepff, L., Heitz, V., Ventura, B., and Daidone, I. Interpretation of Experimental Soret Bands of Porphyrins in Flexible Covalent Cages and in Their Related Ag(I) Fixed Complexes. *J. Phys. Chem. C*. **2019**, 123, 13094–13103.

6 Telfer, S. G., McLean, T. M. & Waterland, M. R. Exciton coupling in coordination compounds. *Dalt. Trans.* **2011**, 40, 3097–3108.

7 Alessio, E.; Milani, B.; Bolle, M.; Mestroni, G.; Faleschini, P.; Todone, F.; Geremia, S.; Calligaris, M. Carbonyl derivatives of chloride-dimethyl sulfoxide-ruthenium(II) complexes: synthesis, structural characterization and reactivity of $Ru(CO)_X(DMSO)_{4-X}Cl_2$ complexes (X = 1−3). *Inorg. Chem*. **1995**, 34, 4722−4734

8 Iengo, E.; Milani, B.; Zangrando, E.; Geremia, S.; Alessio, E. Novel Ruthenium Building Blocks for the Efficient Modular Construction of Heterobimetallic Molecular Squares of Porphyrins. *Angew. Chem., Int. Ed*. **2000**, 39, 1096−1099

Appendix of Chapter 3

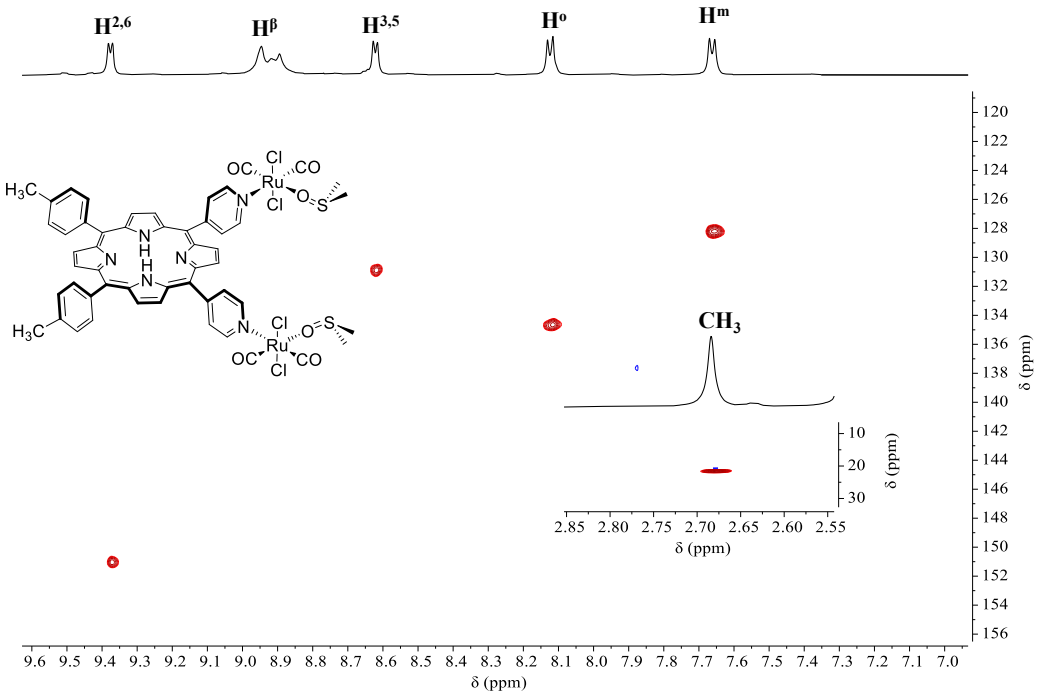

Figure A3.1. ^{1}H-^{13}C HSQC spectrum (DMSO-d_6) of [{*trans*,*cis*,*cis*-$RuCl_2(CO)_2$}$_2$(3′*cis*DPyP) (dmso-*O*)] (**16**)

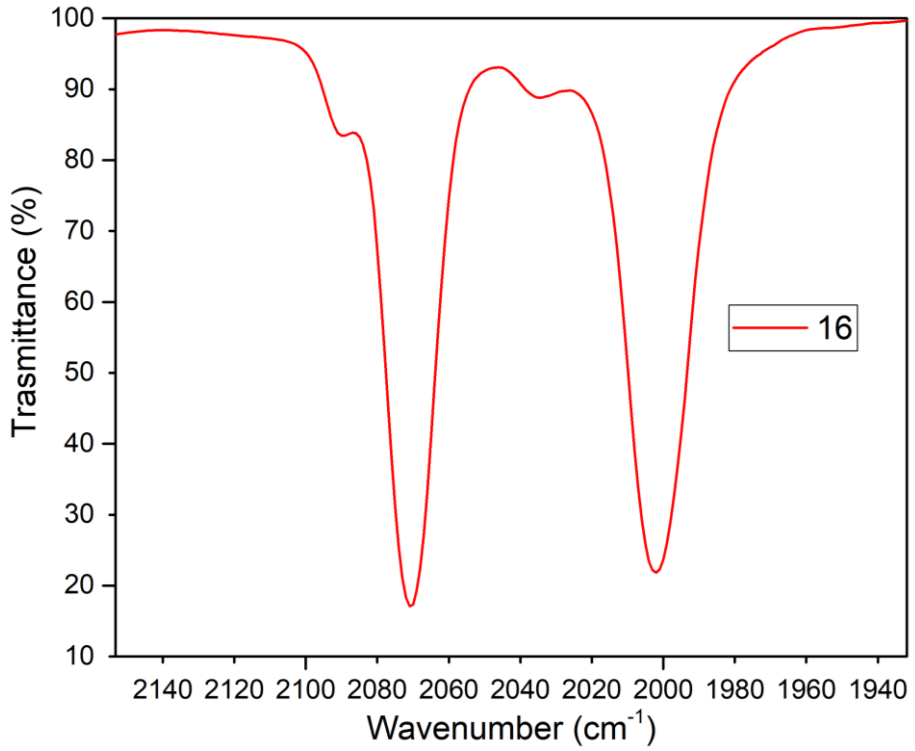

Figure A3.2. IR spectrum of [{*trans*,*cis*,*cis*-$RuCl_2(CO)_2$}$_2$(4′*cis*DPyP) (dmso-*O*)] (**16**) in the CO stretching region

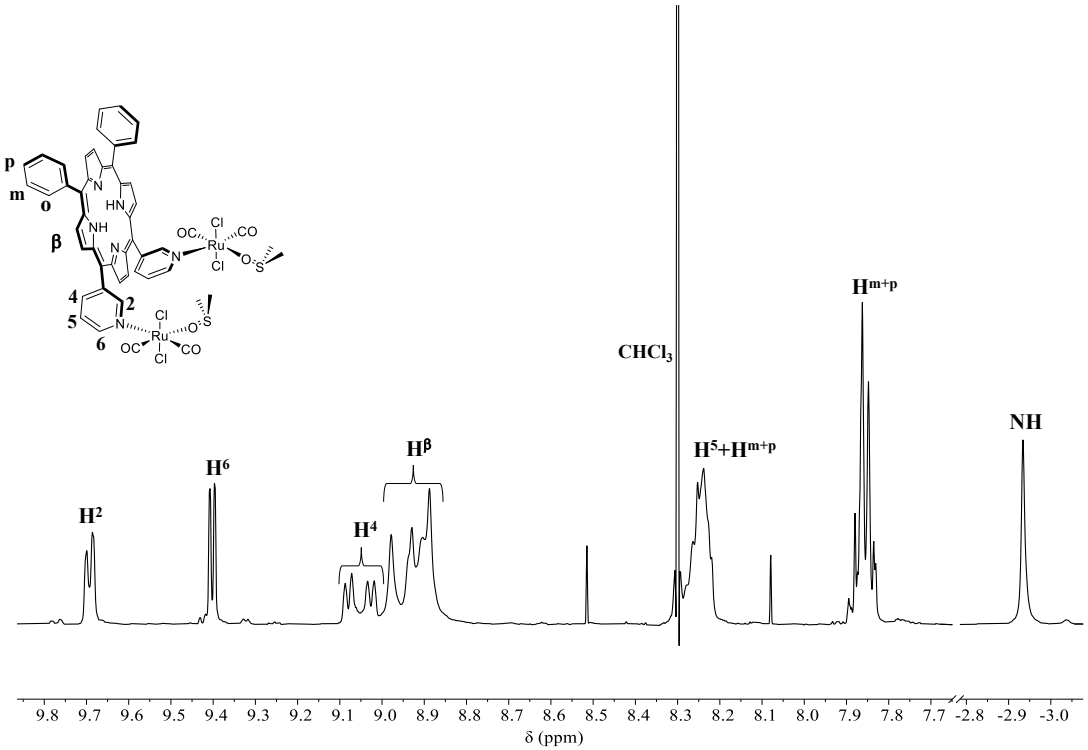

Figure A3.3.: ^{1}H NMR spectrum (DMSO-*d*$_6$) of [{*trans*,*cis*,*cis*-RuCl$_2$(CO)$_2$}$_2$(3′*cis*DPyP)(dmso-*O*)] (**17**)

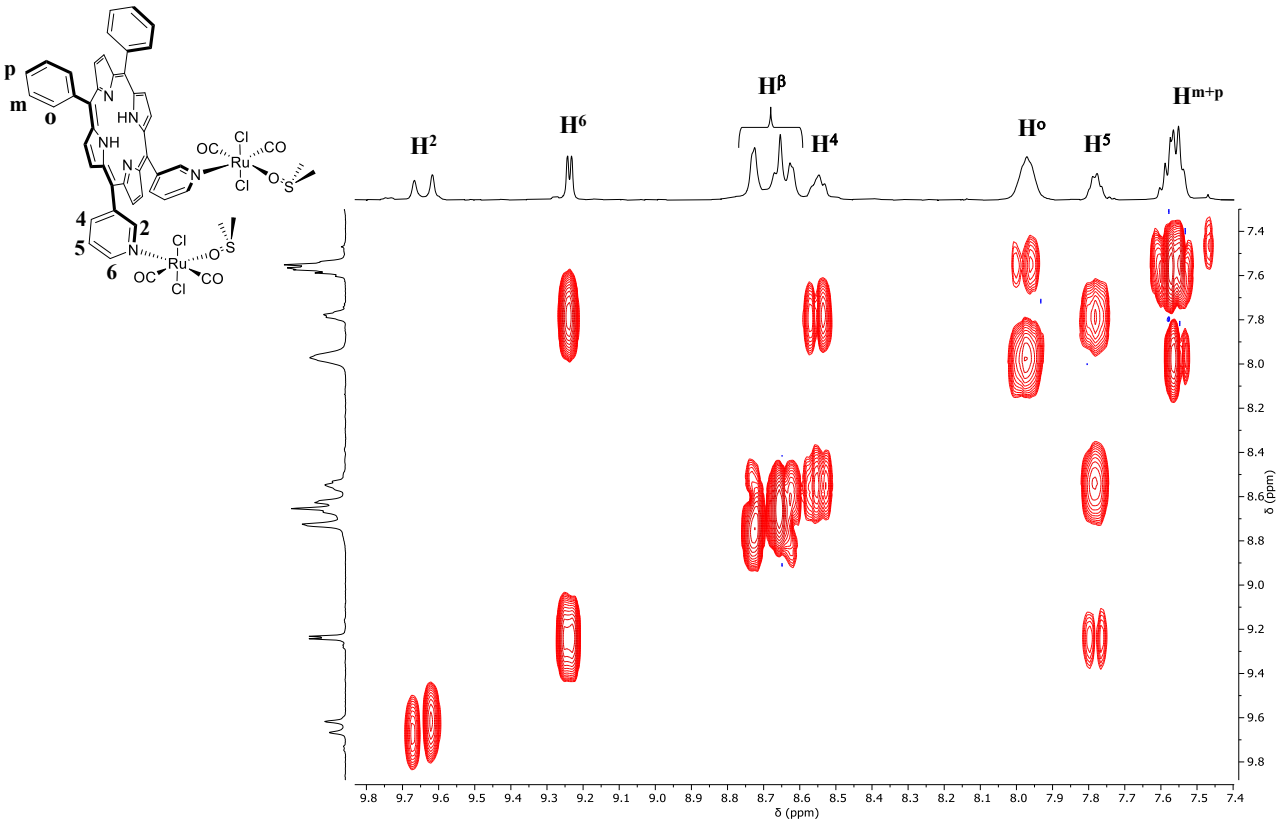

Figure A3.4.:^{1}H-^{1}H COSY spectrum ($CDCl_3$) of [{*trans*,*cis*,*cis*-RuCl$_2$(CO)$_2$}$_2$(3′*cis*DPyP) (dmso-*O*)] (**16**)

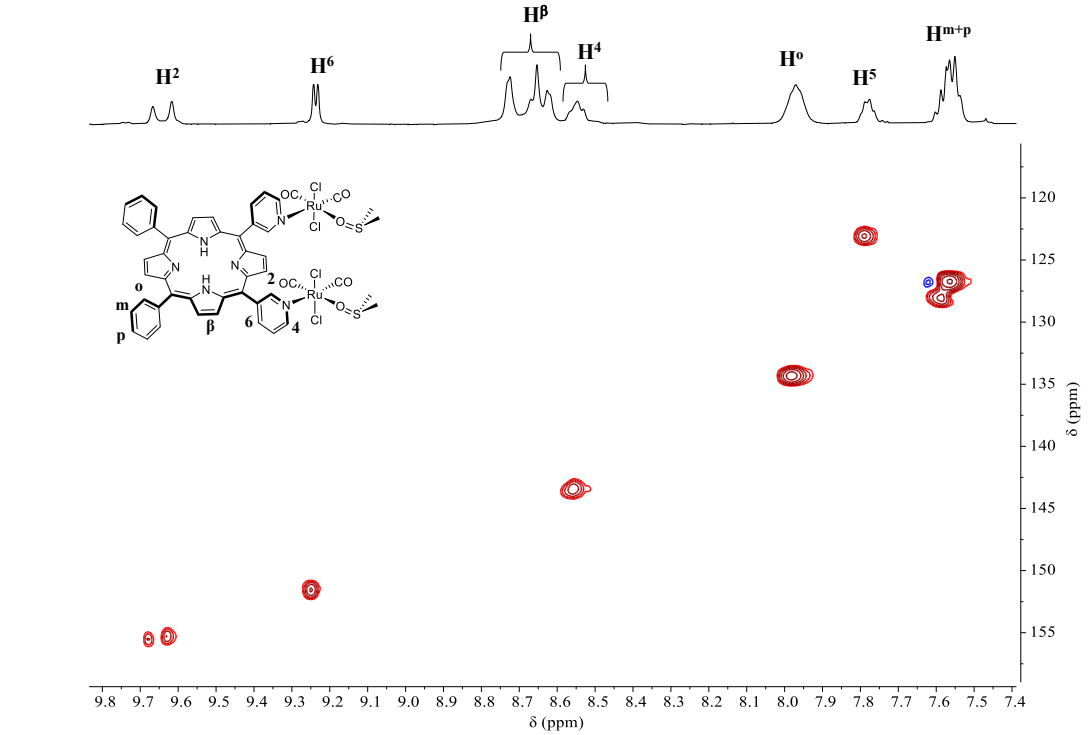

Figure A3.5.: ^{1}H-^{13}C HSQC spectrum ($CDCl_3$) of [{*trans*,*cis*,*cis*-$RuCl_2(CO)_2$}$_2$(3′*cis*DPyP) (dmso-*O*)] (**17**)

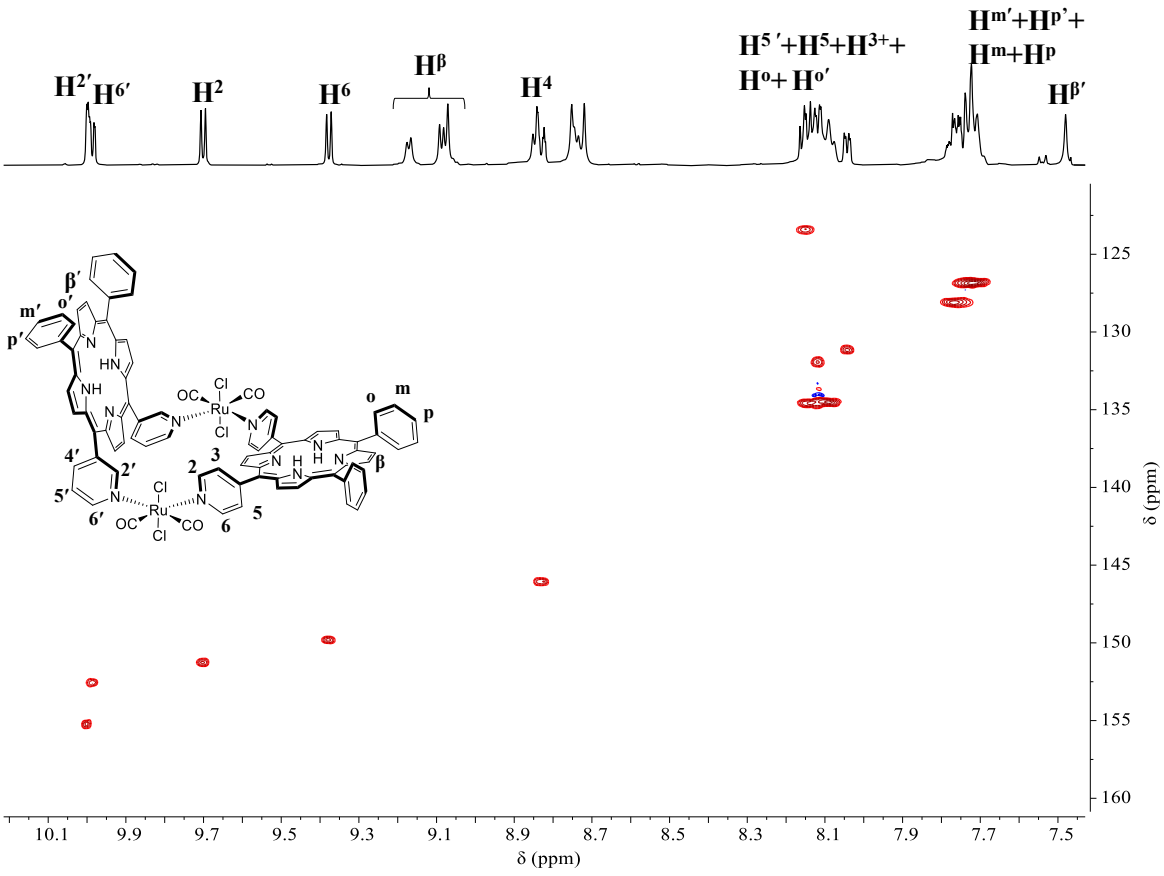

Figure A3.5. ^{1}H-^{13}C HSQC ($CDCl_3$) of [{*trans*,*cis*,*cis*-$RuCl_2(CO)_2$}$_2$(4′*cis*DPyP) (3′*cis*DPyP)] (**18**)

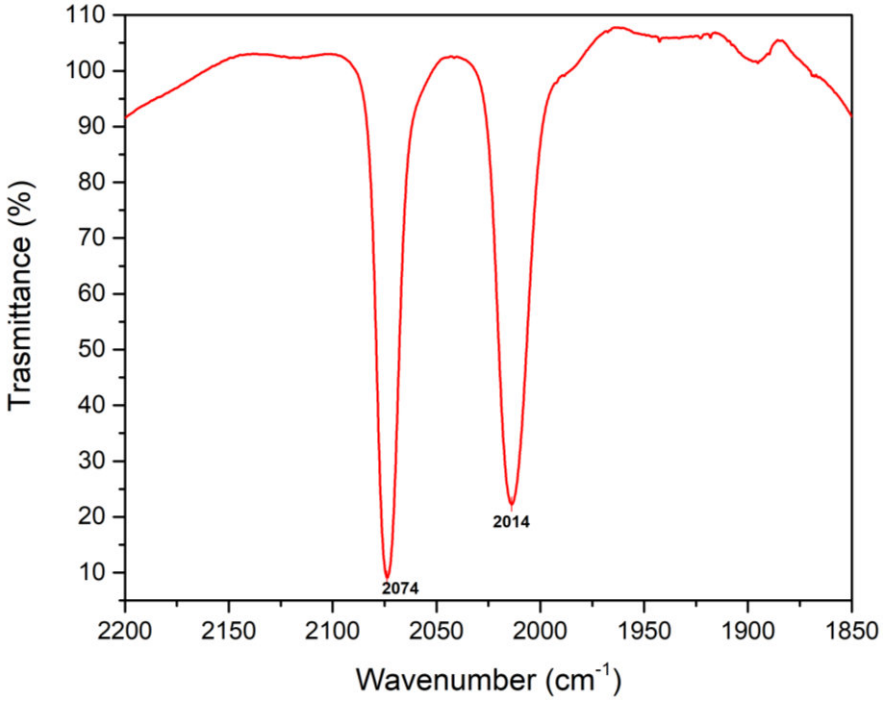

Figure A3.7. IR spectrum of [{*trans*,*cis*,*cis*-$RuCl_2(CO)_2$}$_2$(4′*cis*DPyP) (3′*cis*DPyP)] (**18**) in the CO stretching region

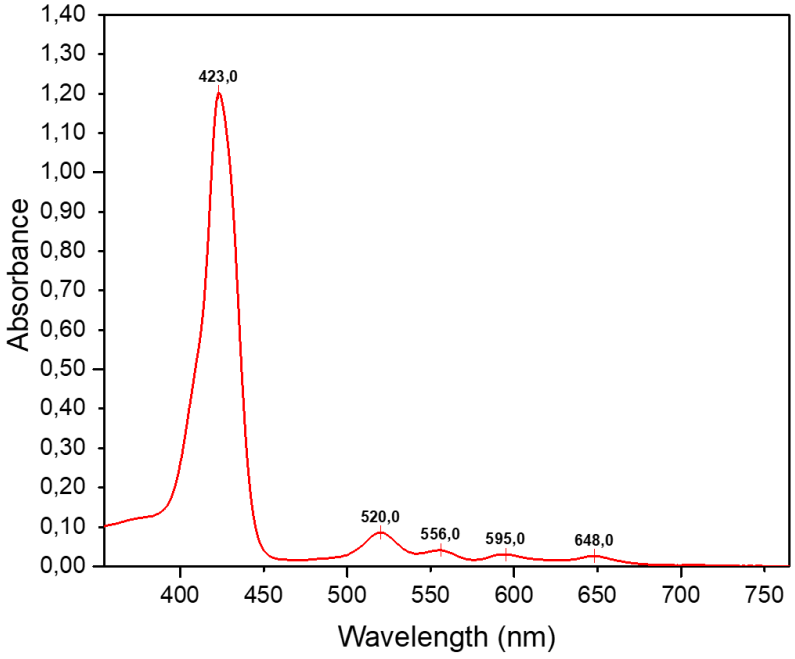

Figure A3.8. UV-vis absorption spectrum in $CHCl_3$ of [{*trans*,*cis*,*cis*-$RuCl_2(CO)_2$}$_2$(4′*cis*DPyP) (3′*cis*DPyP)] (**18**)

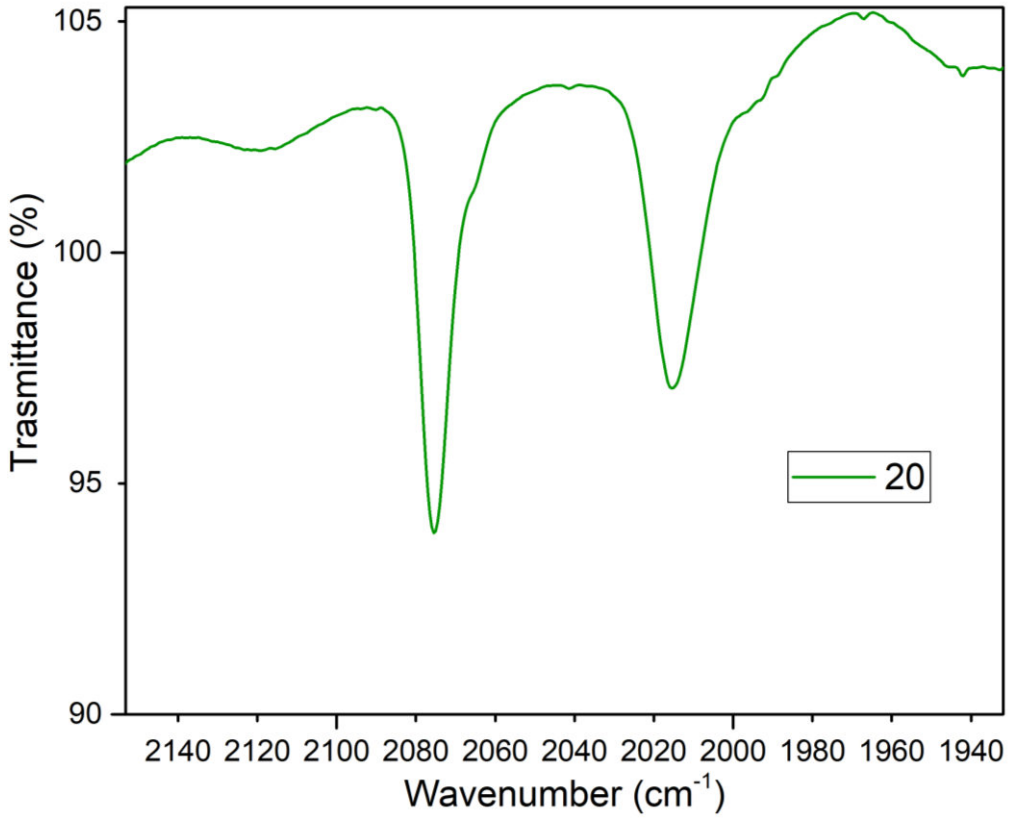

Figure A3.9. IR spectrum of [{*trans,cis,cis*-$RuCl_2(CO)_2$}$_4$(4′*cis*DPyP)$_2$(4′TPyP)] (**19**) in the CO stretching region

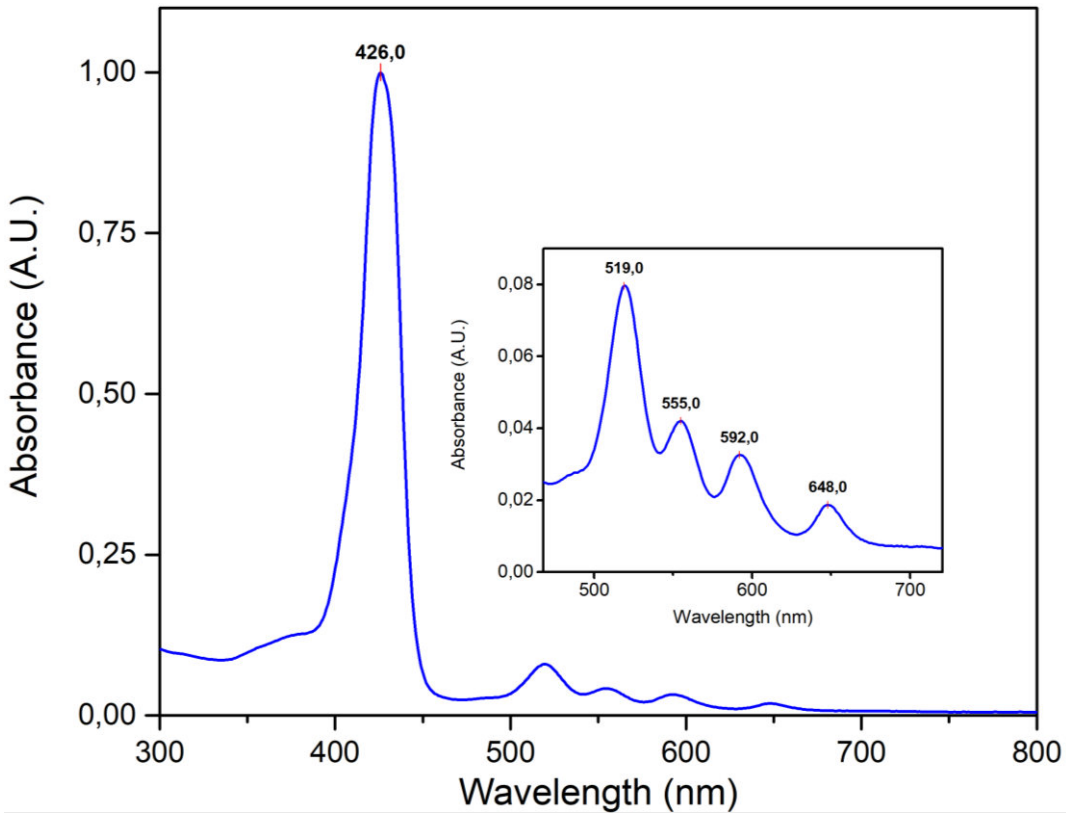

Figure A.3.10. Normalized UV-vis spectrum in $CHCl_3$ of **19**

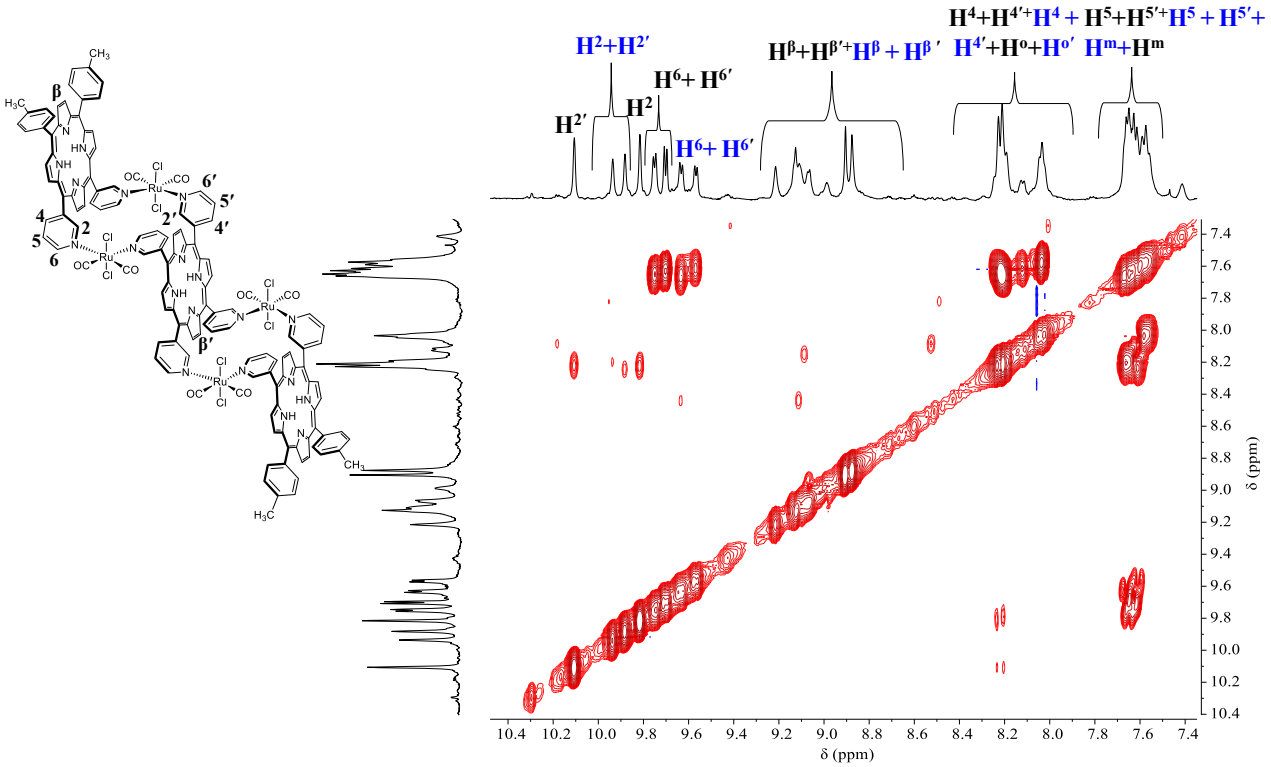

Figure A3.11. ^{1}H-^{1}H COSY spectrum ($CDCl_3$) of [{*trans,cis,cis*-$RuCl_2(CO)_2$}$_4$(3′*cis*DPyMP)$_2$(3′TPyP)] **(20)**

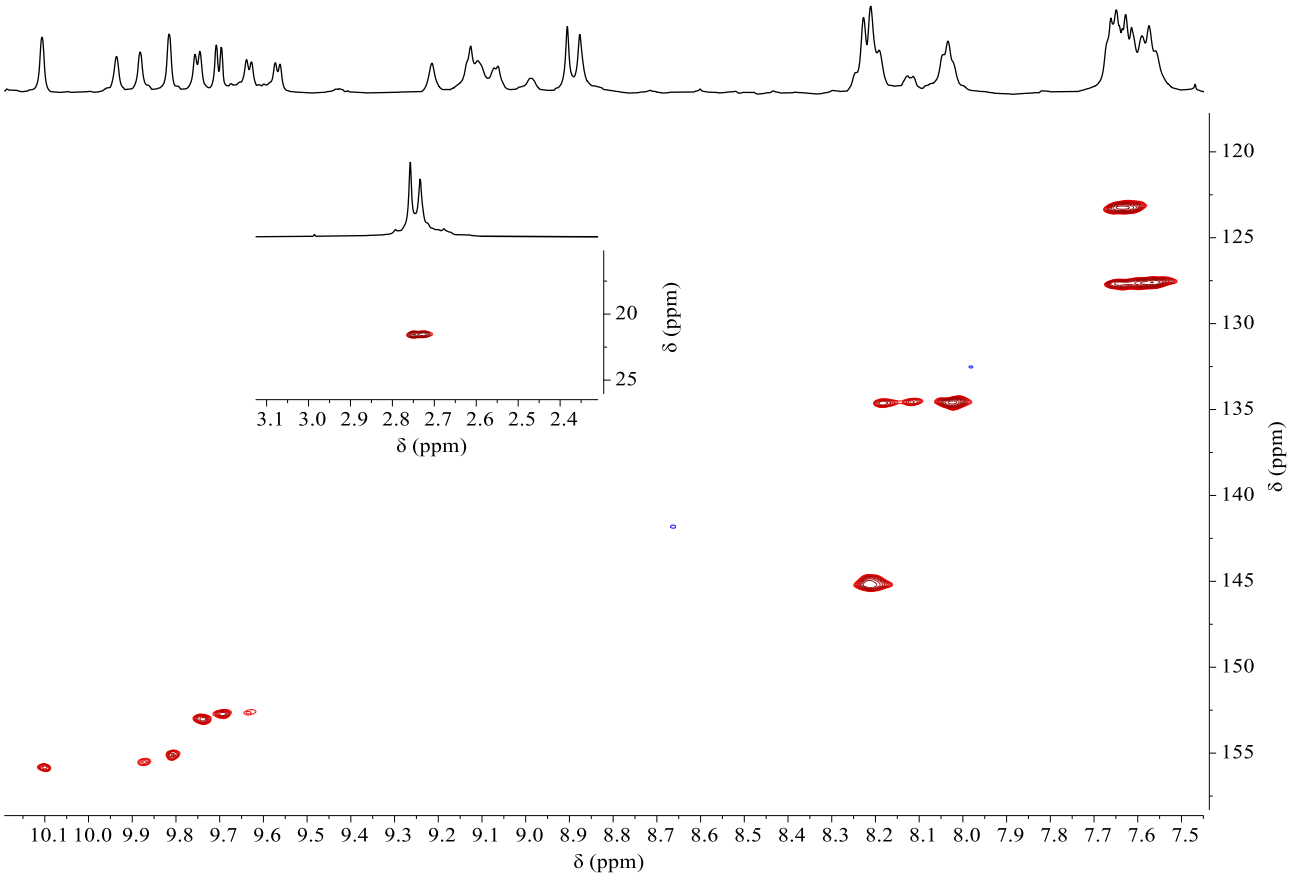

Figure A3.12. ^{1}H-^{13}C HSQC ($CDCl_3$) of [{*trans,cis,cis*-$RuCl_2(CO)_2$}$_4$(3′*cis*DPyMP)$_2$(3′TPyP)] **(20)**

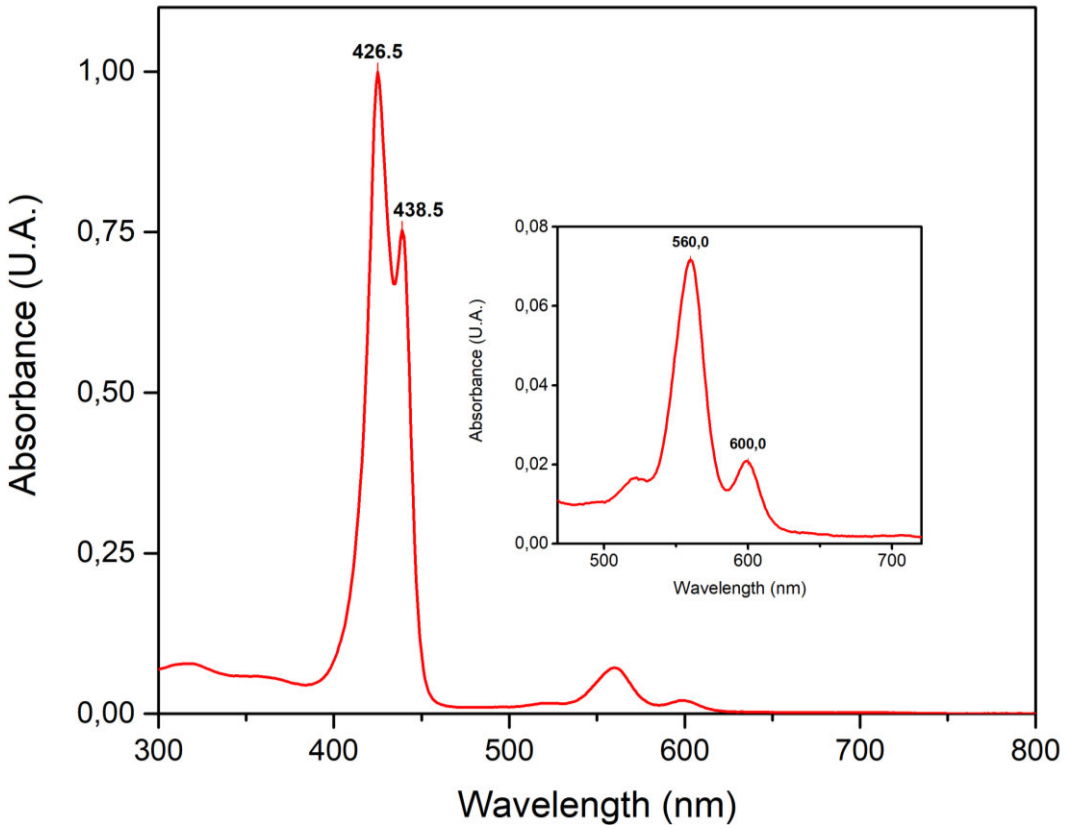

Figure A.3.13. Normalized UV-vis spectrum in $CHCl_3$ of **20MeZn**

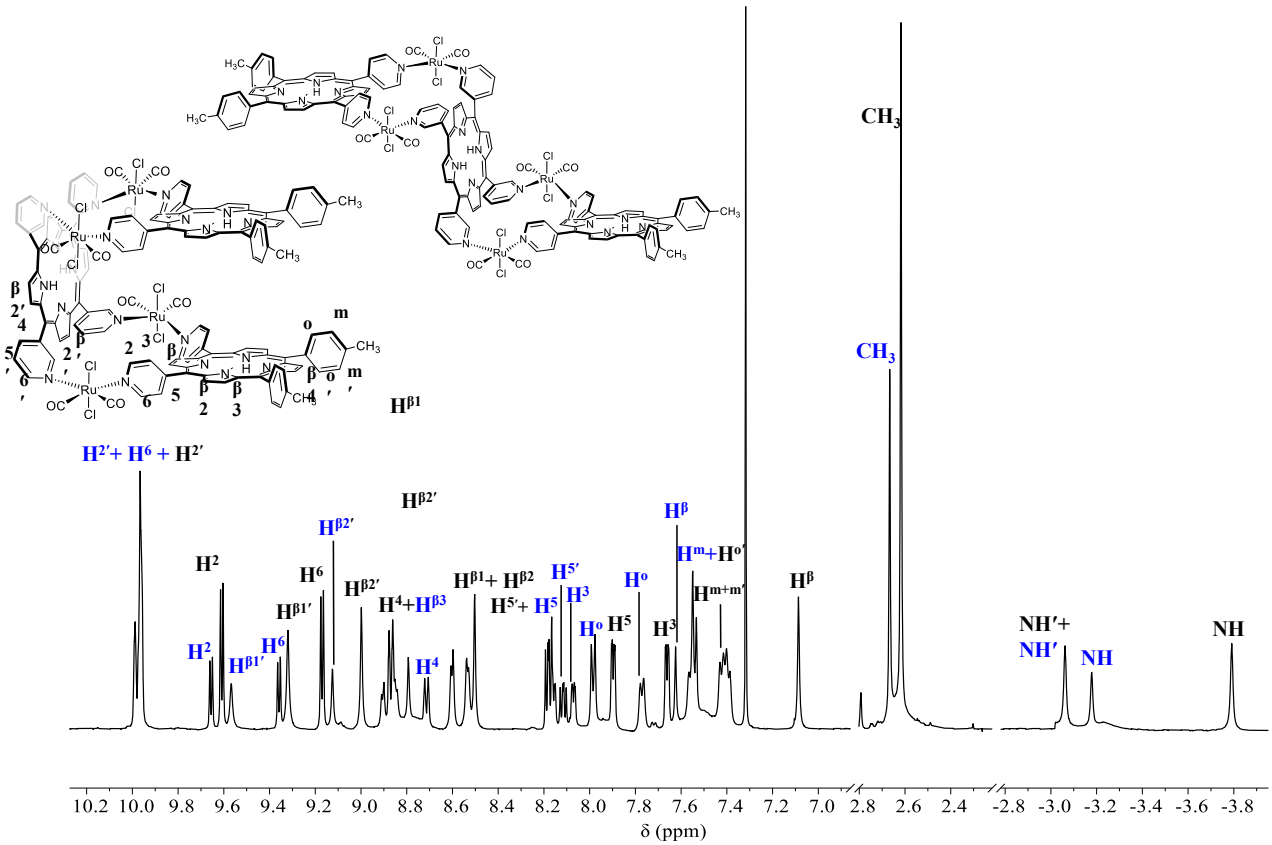

Figure A.3.14. ^{1}H NMR spectrum (CD_2Cl_2) of [{*trans,cis,cis*-$RuCl_2(CO)_2$}$_4$(4′*cis*DPyMP)$_2$(3′TPyP)] (**21Me**)

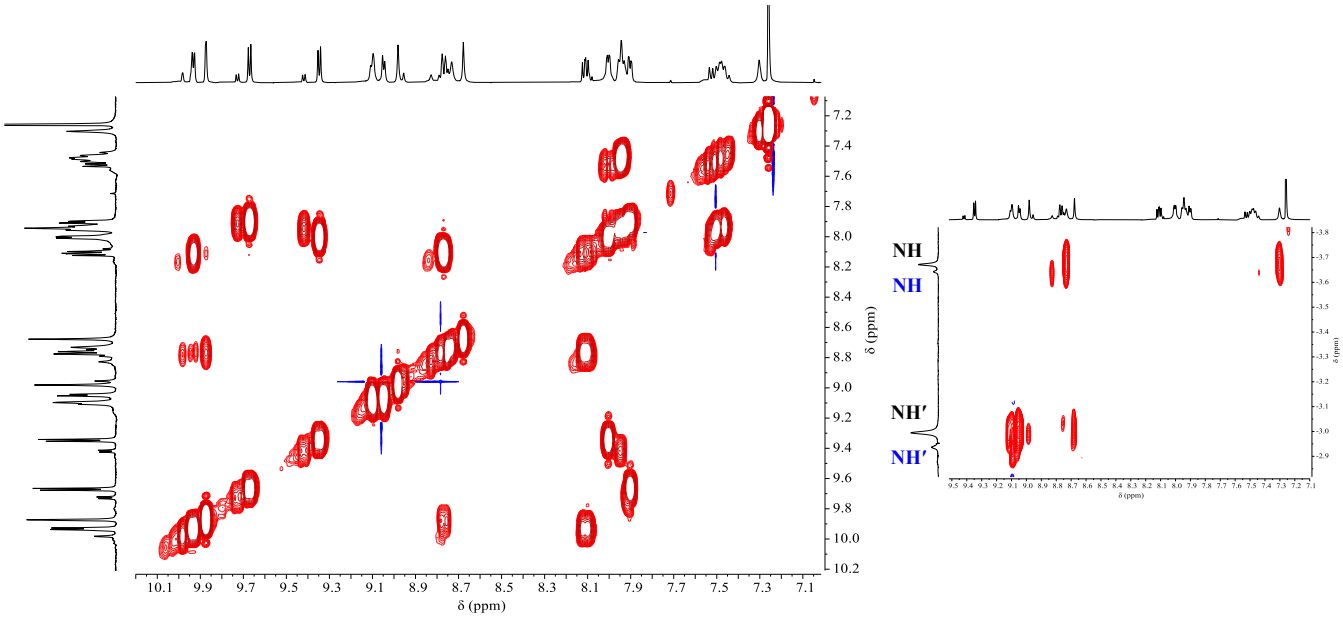

Figure A3.15. ^{1}H-^{1}H COSY NMR spectrum of [{*trans,cis,cis*-$RuCl_2(CO)_2$}$_4$(4′*cis*DPyP)$_2$(3′TPyP)] (**21**) on the left aromatic region, on the right NH region

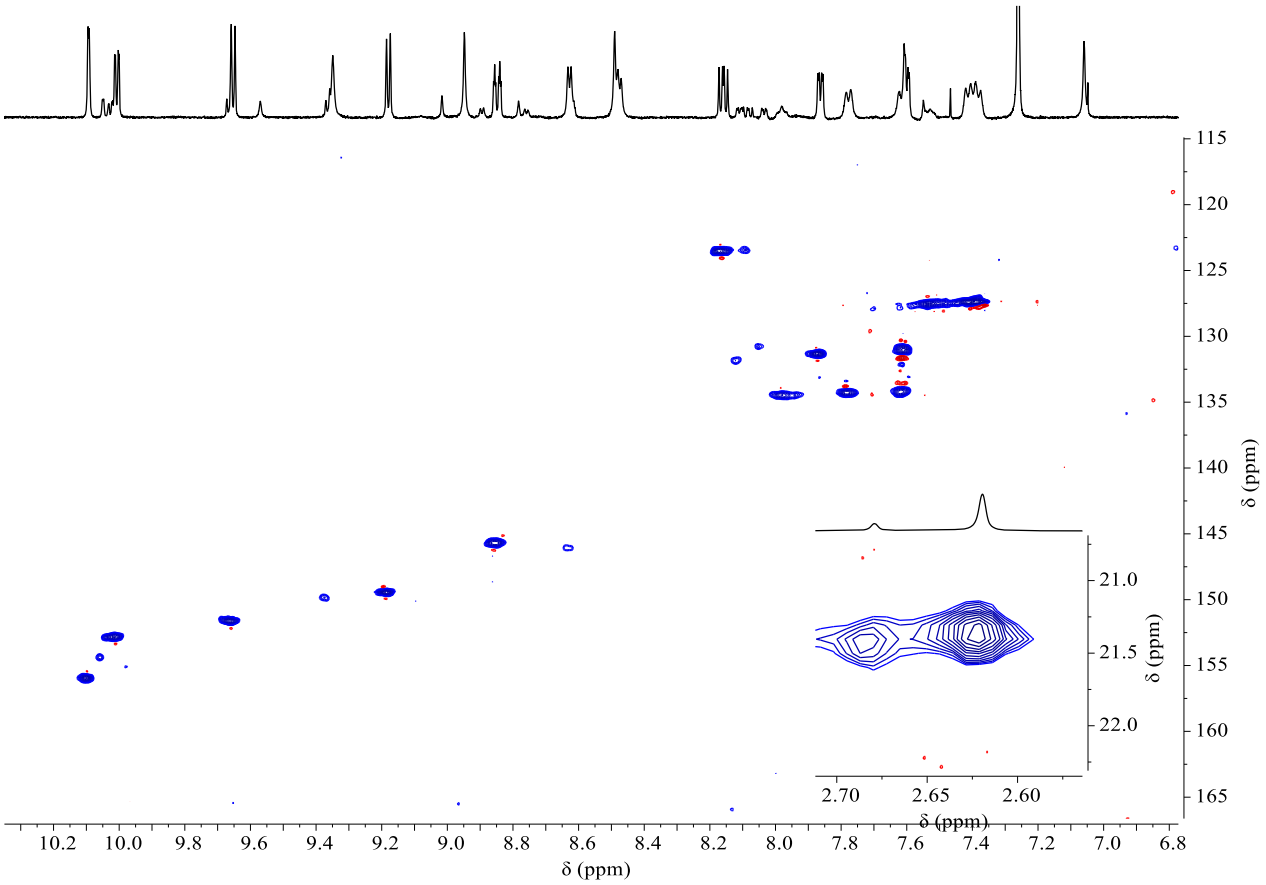

Figure A3.16. ^{1}H-^{13}C HSQC NMR spectrum of [{*trans,cis,cis*-$RuCl_2(CO)_2$}$_4$(4′*cis*DPyP)$_2$(3′TPyP)] (**21Me**)

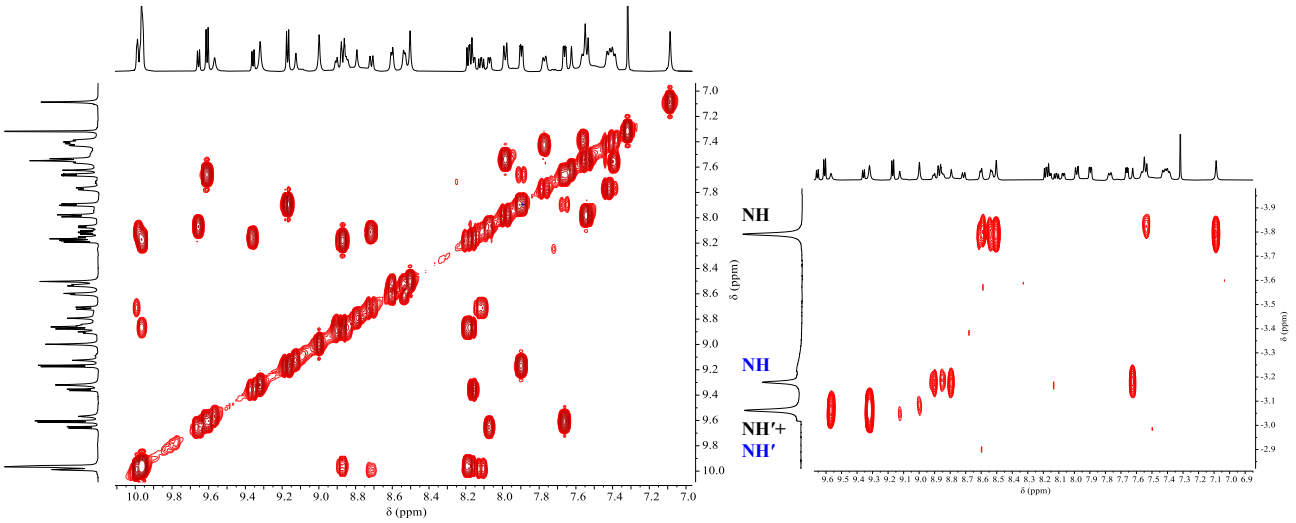

Figure A3.17 ^{1}H-^{1}H COSY NMR spectrum of [{*trans,cis,cis*-$RuCl_2(CO)_2$}$_4$(4′*cis*DPyP)$_2$(3′TPyP)] (**21**) on the left aromatic region, on the right NH region

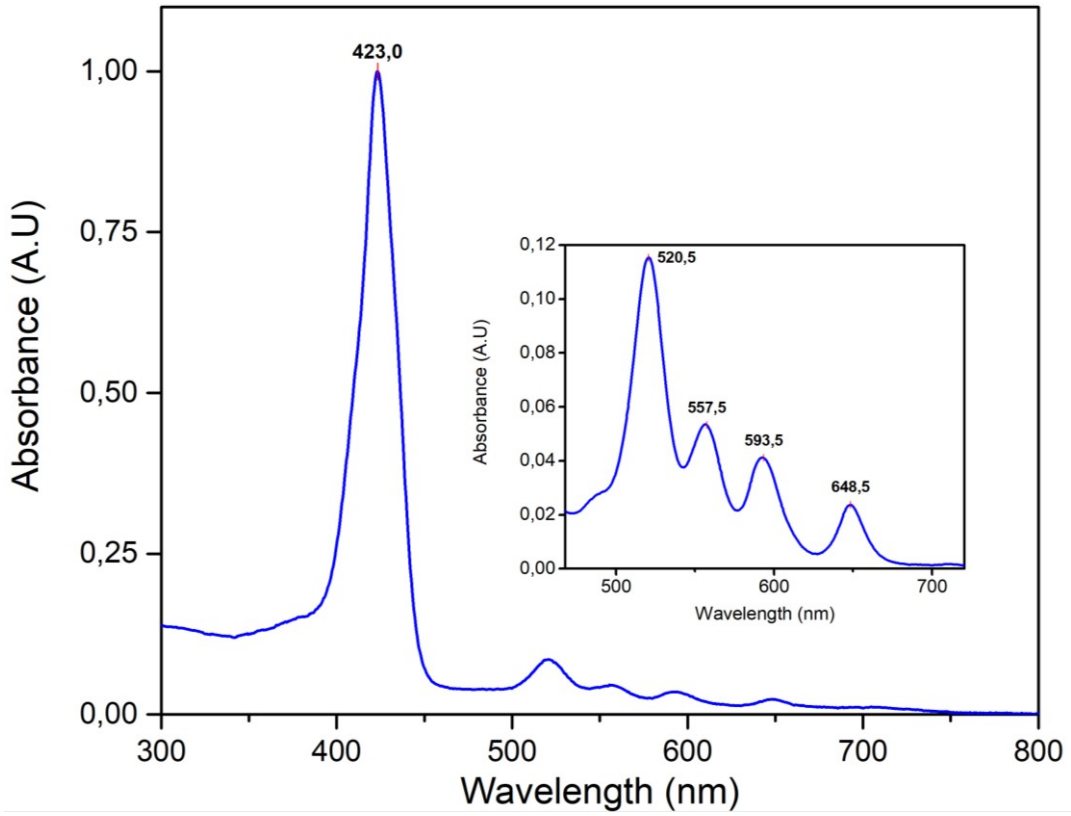

Figure A3.17 Normalized UV-vis spectrum in $CHCl_3$ of **21Me**

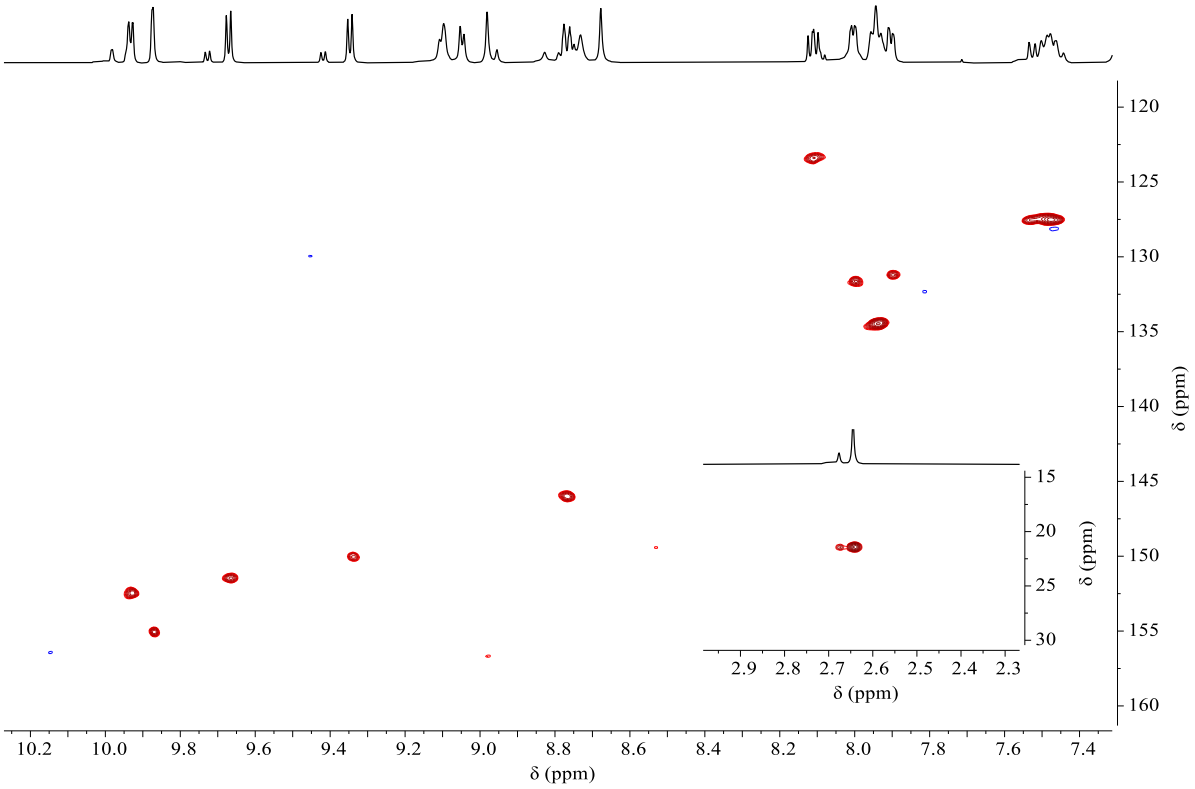

Figure A3.18. ^{1}H-^{13}C HSQC NMR spectrum of [{*trans,cis,cis*-$RuCl_2(CO)_2$}$_4$(3′*cis*DPyP)$_2$(4′TPyP)] (**22Me**)

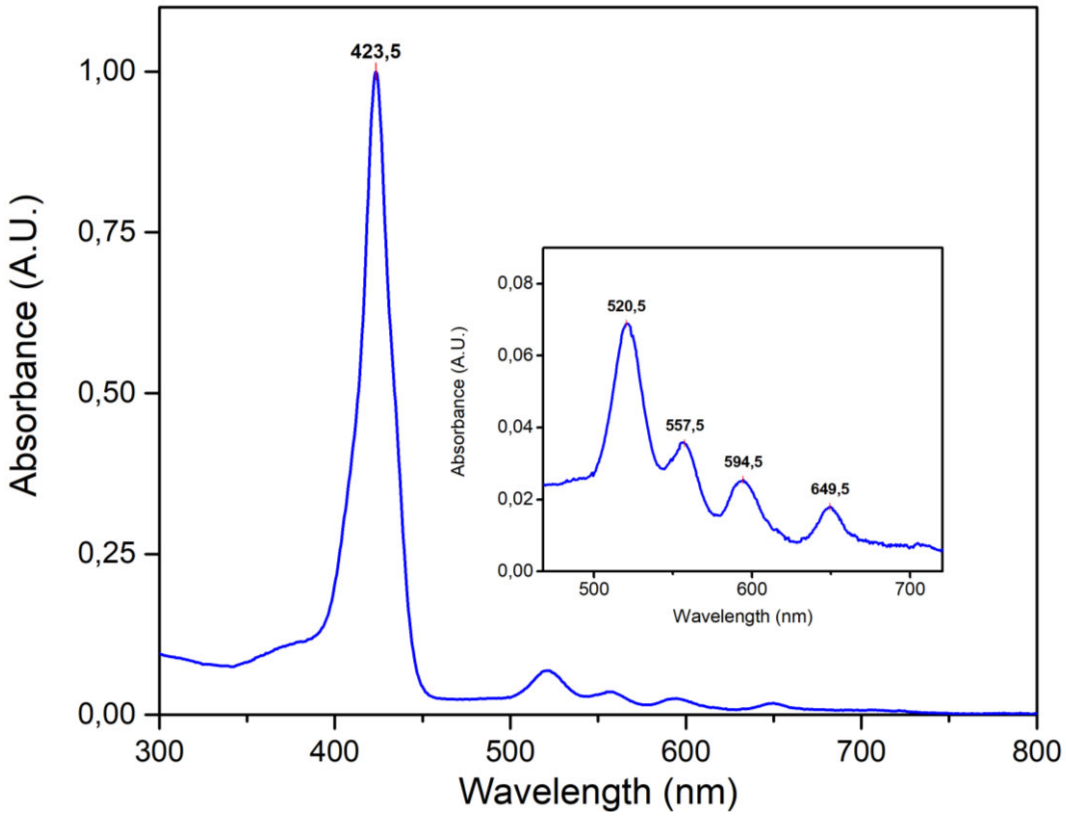

Figure A3.19 Normalized UV-vis spectrum in $CHCl_3$ of **22Me**

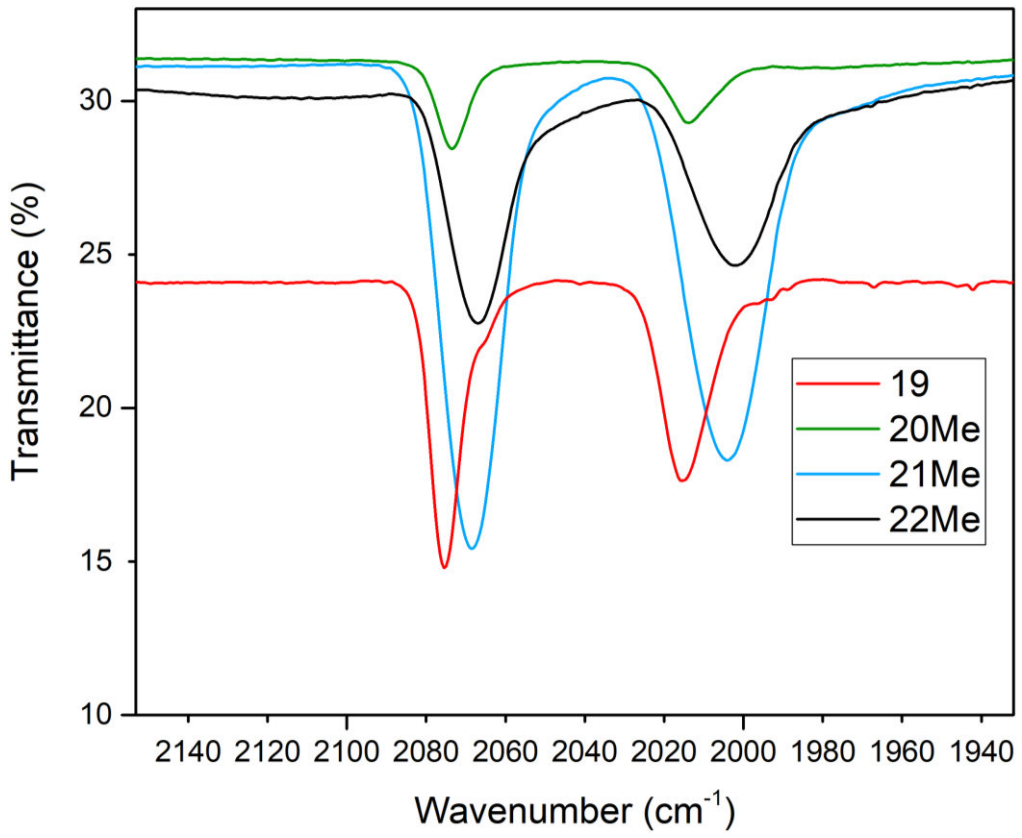

Figure A3.20. IR spectrum of the triporphyrin metallacycles **19**, **20Me**, **21Me** and **22Me**

CHAPTER 4

Vidal, A., Battistin, F., Iengo, E., Milani, B., and Alessio, E., The Insertion of Ruthenium into Porphyrins Revisited and Improved: Proof of Concept Results with a Ruthenium(II) Monocarbonyl Compound, and the Spectacular Effect of Propionic Acid. *Eur. J. Inorg. Chem*..**2019**, 2883–2890

4. Ruthenation Of Porphyrins Revisited

4.1 Introduction

Metalation of porphyrins (Por) is typically accomplished by the reaction of the free-base analogue with a metal salt (or complex) in an organic solvent, such as chloroform, toluene, or DMF. The metalation is in general a slow process, with a high activation barrier attributed mainly to the distortion that the relatively rigid porphyrin ring must undergo to allow the formation of the first bond of an internal pyrrolenine nitrogen to the metal, which seems to be rate-limiting.[1] The insertion of ruthenium is no exception. Initially ruthenium porphyrins were prepared as low-spin air-stable biomimetic models of Fe(II) porphyrins: adducts and intermediates (e.g. with oxygen) are expected to be more stable and more inert for the ruthenium than for the iron compounds.[2-4] Later on they were also investigated as catalysts,[5] in particular for oxidation reactions,[6] and sensors.[7]

For simple free-base neutral porphyrins (e.g. *meso*-tertaphenylporphyrin (TPP), octaethylporphyrin (OEP), and similar) the conditions for ruthenium insertion are much more demanding compared to iron, typically requiring high temperatures and long reaction times.[8] In addition, contrary to iron but similarly to osmium,[9] ruthenium is inserted into porphyrins *exclusively* as the Ru(II)–CO fragment, yielding neutral products of the type Ru(CO)(Por). No examples of the direct insertion either of "naked" Ru(II)/Ru(III) ions or other RuL or RuL_2 fragments are known. It might be argued that the presence of a strong π-acceptor ligand such as CO is necessary for removing from the relatively soft metal ion (Ru^{II} or Os^{II}) part of the charge density provided by the Por^{2-} macrocycle. Indeed, consistent with a strong π-back donation contribution, the CO stretching mode in Ru(CO)(TPP) occurs at rather low frequencies, e.g. ca. 1930-1945 cm^{-1}, depending on the report.[10-12]

The axial coordination position *trans* to CO is typically occupied by a weak and labile solvent molecule deriving from the workup (e.g. ethanol),[11] which can be easily replaced by a stronger σ and/or π-donor ligand (e.g. pyridine, imidazole).[13-15] The Ru–N(pyridyl) bond is relatively strong and inert.[16] For this reason, ruthenium porphyrins and pyridyl ligands have been largely exploited as building blocks in the construction of supramolecular assemblies by us and by others.[17-19] The coordinated CO can be removed by prolonged photolysis in weakly coordinating solvents (S), affording $Ru(Por)(S)_2$ adducts.[20] Similarly, Ru(OEP)(CO)(py) in degassed pyridine solution is photochemically converted to $Ru(OEP)(py)_2$.[21] Conversely, strong σ-donor and π-acceptor ligands such as phosphines (P) readily displace the CO ligand from the parent Ru(CO)(Por) under mild conditions affording $Ru(Por)(P)_2$ derivatives.[22,23]

As users of ruthenium porphyrins, we have been surprised by the lack of a reliable, high yielding and widely adopted synthetic procedure for ruthenium insertion in the literature. More specifically, the ruthenation of free-base porphyrins uses one of the following precursors (Scheme 4.1): *i*) The Ru(0) carbonyl cluster $Ru_3(CO)_{12}$ (**23**). This is the most widely adopted procedure, even though no two equal preparations can be found in the literature. The reaction is typically performed by refluxing the porphyrin and an excess of cluster (Ru/Por in the range 3-10) under an inert atmosphere for several hours (often days or even weeks). Hydrocarbon solvents (i.e. benzene (b.p. 80.1 °C),[10] toluene (b.p. 110.6 °C),[11,24-26] 1,2,4-trichlorobenzene (b.p. ca. 214°C),[27] or decalin (b.p. 190°C)[28,29]) are used for neutral porphyrins,[30] whereas DMF is preferred for water-soluble charged porphyrins.[31,32] In a single report acetic or propionic acid were used as solvent (see below).[33] To be noted that – regardless of the solvent – the reaction requires that ruthenium, besides breaking several Ru–Ru and Ru–CO bonds, is oxidized to Ru(II). *ii*) A Ru(III) species. The most common procedures involve the universal Ru(III) precursor $RuCl_3 \cdot 3H_2O$ and are typically performed in two steps. In the first step hydrated $RuCl_3$ is treated at high temperature (e.g. in refluxing ethylene glycol or 2-(2- methoxyethoxy)ethanol) with a source of CO, either a stream of CO or formaldehyde, that decomposes thermally and yields CO.[23,26,34] This procedure generates a yellow-orange solution containing an undefined "ruthenium carbonyl", later found to be an equilibrium mixture of the Ru(II) dimer [*fac*-$RuCl(CO)_3(\mu\text{-}Cl)]_2$ (**24**) and of the poorly characterized Ru(II) polymer $[RuCl_2(CO)_2]_n$ in which each unit is believed to feature two adjacent carbonyls and four bridging chlorides.[35] It is instead unlikely that this solution contains the Ru(0) cluster **23**, whose preparation under these conditions requires the addition of a base.[35] In the second step, the free-base porphyrin is added and the reaction mixture further heated at high temperature for hours. In some cases a one-pot procedure was also reported.[36] More recently James and co-workers have described a one-pot reaction in which the Ru(III) precursor $[Ru(DMF)_6](SO_3CF_3)_3$ is treated with the free-base porphyrin in refluxing DMF (that partially decomposes generating CO).[8] However, the generally good yields need to accomodate the preparation of the Ru(III) precursor from hydrated $RuCl_3$ that also requires the use of three equivalents of silver triflate.[37] In all these procedures, carbon monoxide has the double role of reductant and ligand. *iii*) A Ru(II) precursor (not prepared *in situ*). To the best of our knowledge, the one and only example of this type dates back to 1971, when Chow and Cohen reported the ruthenation of TPP with [*fac*-$RuCl(CO)_3(\mu\text{-}Cl)]_2$ (**24**) in refluxing propionic or acetic acid (24h).[33]

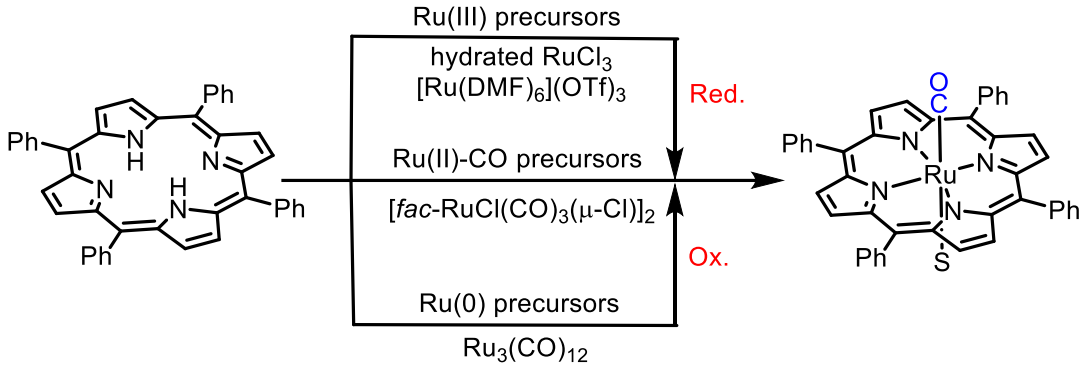

Scheme 4.1. Ruthenation procedures exemplified for the free-base *meso*-tetraphenylporphyrin (TPP); S is a molecule of solvent, typically EtOH or MeOH, from the workup procedure.

In all cases, the ruthenation reaction is followed by one or more purification steps, typically column chromatography and/or recrystallization. Yields (when reported) range from low (30-40%) to excellent (96%), depending on the porphyrin and the procedure, but it is often unclear if they concern the whole procedure or the purification step only.

The detailed literature survey leads to a quite obvious general conclusion: Regardless of the adopted procedure, the ruthenation of porphyrins is a very complex reaction. Mechanistic studies are missing and in no case the exact stoichiometry is known. Except when **23** is used as precursor, it is typically assumed that the two inner H atoms are removed as protons. In addition, the reactions require that all the supporting ligands (except one CO in **23** and **24**) are replaced and – with a single exception – that ruthenium also changes its original oxidation state.

In this general picture that spans the last 50 years (the first Ru-porphyrin was reported in 1969, even though its formulation was incorrect),[38] we found particularly surprising that only in one case – quite old and apparently never repeated – the ruthenation of a porphyrin had been performed with a Ru(II) precursor, i.e. in the same oxidation state as in the final compound (Scheme 4.1).[33]

In the past we have described a number of neutral Ru(II)-dmso carbonyls of the general formula $RuCl_2(CO)_n(dmso)_{4-n}$ (n = 1-3).[39,40] More recently, cationic mono- and di-carbonyl Ru(II)-dmso compounds were obtained from the neutral ones by silver-assisted replacement of chlorides with dmso.[41,42] We reasoned that these carbonyls, that feature relatively labile Cl^- and/or dmso supporting ligands, might be good precursors for the ruthenation of porphyrins. Two neutral compounds, the monocarbonyl *cis*,*fac*-$RuCl_2(dmso)_3(CO)$ (**25**) and the triscarbonyl *fac*-$RuCl_2(CO)_3$(dmso-O) (**26**) (that can be considered as the activated form of the dinuclear species **24**),[43] and the chloride-free $[Ru(CO)(dmso)_5][PF_6]_2$ (**27**) (Figure 4.1) were selected for testing.

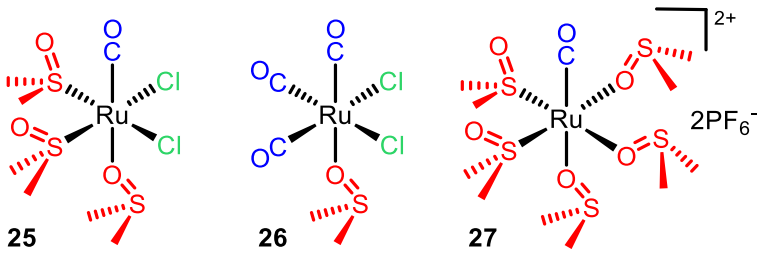

Figure 4.1. The three Ru(II) carbonyls selected for being tested in the ruthenation of porphyrins.

For comparison, we also reinvestigated the ruthenation procedures described in the literature for $Ru_3(CO)_{12}$, using TPP as model porphyrin. Given the unexpected findings when propionic acid was used as solvent, this investigation was extended to other neutral and charged porphyrins. Trans-metalation reactions, with Zn·TPP and Ag·TPP as starting materials, were also investigated. The results of this systematic investigation are reported in this manuscript.

4.2. Results and Discussion

4.2.1. Ru(II)-dmso carbonyls as precursors

After an extensive – and unsuccessful – investigation, in which treatment of TPP with the Ru(II) carbonyls **25** and **26** was systematically tested under different conditions, we eventually observed the formation of Ru(CO)(TPP) when the reaction was performed in a microwave reactor at 100°C in a 2:1 chloroform/methanol mixture (in which TPP is fully soluble), in the presence of a slight amount of KOH (presumably to either deprotonate the TPP or remove any H^+ that might be formed in the ruthenation process). However, the insertion of Ru(CO) into TPP occurred only when an excess of a soluble silver salt (e.g. $AgPF_6$) was added to remove the chlorides from the Ru precursor. However, the addition of Ag^+ also led to the contemporary formation of Ag·TPP (evidenced by TLC analysis by comparison with a sample of pure Ag·TPP). Thus, we focused on the chloride-free precursor $[Ru(CO)(dmso)_5][PF_6]_2$ (**27**) and systematically investigated several parameters (Ru/TPP, KOH/TPP, temperature and reaction time) for optimizing the yield. It is noteworthy that, contrary to TPP, **27** is not fully soluble in the reaction medium, thus the initial system is an heterogeneous mixture. We found that best results were obtained at Ru/TPP = 4 and KOH/TPP = 2. Under these conditions, a moderate 21% yield of Ru(CO)(TPP) (established by ^1H NMR spectroscopy, see Experimental) was obtained after 1h reaction at 100°C in a MW reactor (Scheme 2). However, the final reaction mixture had a brown-green color, indicating that – despite the addition of the base – at least partial protonation of residual TPP, with formation of the deep-green $TPPH_2^{2+}$, had occurred.[44,45] The presence of $TPPH_2^{2+}$ was confirmed by the UV-vis and ^1H NMR spectra. We believe that during the reaction KOH, besides contributing to the removal of the inner TPP protons, is mainly consumed by reacting

with the Ru(II) precursor, leading to its (partial) decomposition (e.g. through the formation of polymeric hydroxo- or oxo-bridged species).[46] In other words, the added base is insufficient for neutralizing the two equiv of protons that may be liberated per each equiv of inserted Ru.[47] The initial addition of larger amounts of KOH prevented the protonation of residual TPP (i.e. afforded purple final solutions), but lowered the conversion, presumably due to increased decomposition of **27**. We found that, if the "green" mixture obtained after 1h reaction (i.e. a mixture of Ru(CO)TPP, TPP, and $TPPH_2^{2+}$) was further heated in the MW reactor at 100°C, no increase – or even a moderate decrease – in the relative amount of Ru(CO)(TPP) vs TPP was observed. Consistent with this result, we investigated shorter reaction times and found that after 30 min the ruthenation of TPP is only slightly lower than after 1h. Eventually, improved conversion was obtained by performing the reaction in a stepwise manner. After each 30 min step, the purple color of the mixture was restored – if necessary – with the addition of small amounts of a methanol solution of KOH. For example, we obtained 33% of Ru(CO)(TPP) when the ruthenation of TPP was performed in two subsequent steps of 30 min, compared to ca. 21% in a single step of 1h. A ca. 50% conversion was achieved in two additional steps.

No formation of Ru(CO)(TPP) was observed when, under these reaction conditions, either Zn·TPP or Ag·TPP where used as substrate.

Since we are well aware that this ruthenation procedure – even though quite well reproducible – is impractical (in particular in view of the results reported below), the achievement of higher conversions was not further pursued.

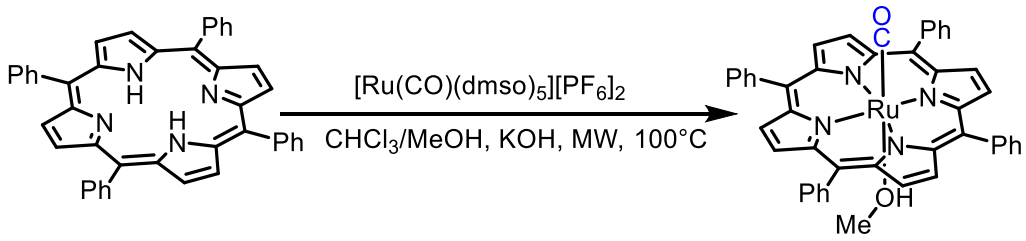

Scheme 4.2. Ruthenation of TPP with the chloride-free Ru(II) carbonyl precursor $[Ru(CO)(dmso)_5][PF_6]_2$ (**27**). See text for reaction time and yields.

4.2.2. $Ru_3(CO)_{12}$ as precursor

When the ruthenation of TPP with **23** (Ru/TPP = 6) was performed in refluxing toluene or decalin, according to literature procedures, the best results were obtained – not surprisingly – in the solvent with the highest boiling point. Nevertheless, even after 36h of reflux in decalin (under an argon atmosphere), less than 50% conversion was estimated by TLC and UV-vis analysis, and the final isolated yield of Ru(CO)(TPP) after purification by column chromatography was even lower. Trans-metallation reactions using Zn·TPP and Ag·TPP were also investigated. We reasoned that the replacement of Zn(II) by Ru(II) should be thermodynamically favored (the X-ray structures show that

both ions have an excellent size match with the of the inner cavity of TPP, and Ru is expected to form stronger bonds with the macrocycle). The redox-induced *trans*-metalation of Ag(II) porphyrins is an established strategy:[48] Reduction of Ag(II) to Ag(I) involves a significant increase of the ionic radius that facilitates demetalation and subsequent replacement.[49] However, in neither case formation of Ru(CO)(TPP) was observed.

Ruthenation of TPP was not observed when the reaction in refluxing decalin was performed using the Ru(II) carbonyls **25**-**27**. In these cases, however, the initially purple mixture turned gradually brown-green, suggesting the partial formation of $TPPH_2^{2+}$, and a dark precipitate formed most likely due to the decomposition of the Ru complex. It should be noted that neither the porphyrins nor the Ru precursors are particularly soluble in decalin and each system remains heterogeneous throughout the procedure. No reactivity was observed also when the reaction between TPP and **27** was performed in refluxing DMF and DMSO, where the complex (but not TPP) is soluble.

Finally, the reaction between **23** and TPP was carried out in refluxing propionic acid, as in the work by Chow and Cohen.[33] We were rather skeptical about this procedure. In general, in metalation procedures, either the solvent is a good proton-acceptor or – when a metal salt is used – the anion is a mild base. For example, insertion of zinc is best performed at room temperature with zinc acetate.[4] Conversely, demetalation of metal-porphyrins is typically performed in acidic medium.[50] Thus, the choice of propionic acid for the ruthenation of TPP is counter-intuitive. In the original procedure described in 1971, TPP and either $Ru_3(CO)_{12}$ (**23**) or [*fac*-$RuCl(CO)_3(\mu\text{-}Cl)]_2$ (**24**) (Ru/TPP = 1.1) were refluxed under nitrogen in propionic acid (141°C) for 24h .[33] Thus, we were quite surprised to see that after refluxing **23** and TPP (Ru/TPP = 6) under Ar for barely 30min a clear red-orange solution was obtained from the original purple/brown mixture (the initial color suggests that partial protonation of TPP occurs) and no residual TPP (that is partially soluble in propionic acid at room temperature) remained according to TLC and UV-vis analysis.

Given these results, we analyzed in detail the ruthenation reaction in propionic acid and investigated how the yield of Ru(CO)(TPP) is affected by the nature of the precursors, the Ru/porphyrin ratio, time and temperature. The use of a microwave reactor was also investigated. Overall, the best performance in the ruthenation of TPP in propionic acid was obtained with **23**, that afforded 100% conversion after 30 min of reflux (or in MW reactor at 140 °C) at a Ru/TPP ratio = 1.5 (Figure 4.2).

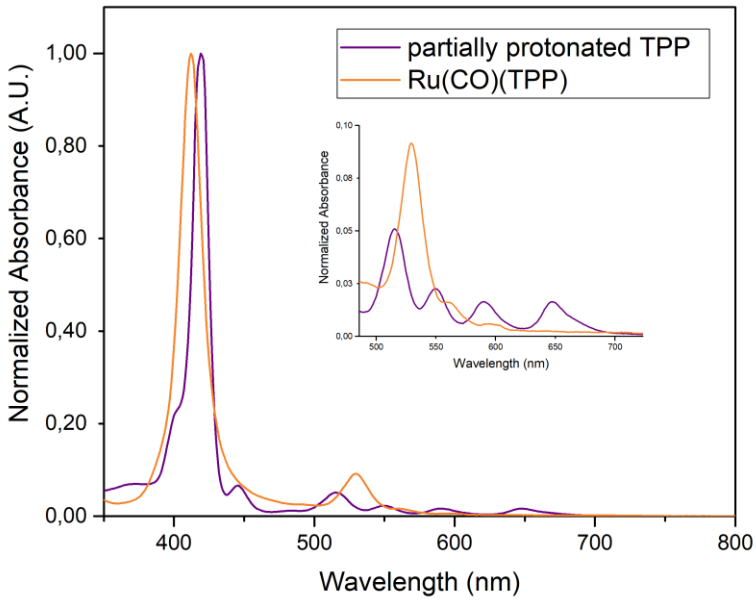

Figure 4.2. UV-vis spectra (propionic acid solutions diluted ca. 50× in $CHCl_3$) of TPP (purple) and after 30 min of reflux with **23** (Ru/TPP = 1.5). The initial spectrum corresponds to a mixture of TPP (major species) and $TPPH_2^{2+}$; the final spectrum (orange) corresponds to Ru(CO)(TPP).

When this reaction was performed on a larger scale, followed by chromatographic purification, a 92% isolated yield of Ru(CO)(TPP) was obtained (see Experimental). Systematic studies were carried out on the Ru/TPP ratio, and the properties of the acids used (both in terms of their pKa and boiling points). We found that, at constant Ru/TPP ratio, the concentration of TPP plays a relevant role: when the TPP concentration was lower than 0.6 mg/mL, the initial solution is deep-green, suggesting consistent formation of $TPPH_2^{2+}$, and no ruthenation occurred even after hours at refluxing conditions with **23**. Conversely, when the concentration of TPP was higher than 2.6 mg/mL, 100% conversion was obtained (see above) and within a few hours after the end of the reaction some Ru(CO)(TPP) precipitated spontaneously from the mother liquor kept at room temperature. A lower reactivity was found when **23** and TPP were refluxed in acetic acid (b.p. = 117.9 °C), whereas no reaction occurred, even after several hours, in refluxing trifluoroacetic acid (TFA, b.p. = 72.4 °C). The ruthenation of TPP with **23** in propionic acid was found to occur also at lower temperatures, obviously with lower rates (for example, at 100°C ca. 50% conversion according to TLC analysis was obtained after 1h, at Ru/TPP = 5.5). Performing a MW-assisted reaction at the same temperature brought no significant improvement in the yield of the product.

The Ru(II) triscarbonyl complex *fac*-$RuCl_2(CO)_3$(dmso-O) (**26**) was slightly less active than **23** in propionic acid at reflux (90% conversion after 30min, and 100% after 1h), whereas the monocarbonyl *cis*,*fac*-$RuCl_2(dmso)_3(CO)$ (**25**) was considerably less active (e.g. ca. 50% conversion in 1h at Ru/TPP = 6). This result is counterintuitive since, in principle, compound **25** has more labile ligands than **26** (two dmso's vs two CO's).[51] Conversely, the chloride-free carbonyl **27** in this case turned out

inactive: When refluxed with TPP in propionic acid, the initially insoluble complex afforded a deep-green solution from which a dark precipitate gradually formed, most likely a Ru decomposition product.[52] Under the best conditions, ruthenation (*trans*-metalation) of Zn·TPP and Ag·TPP also occurred with both **23** and **26**, with the following order of activity: TPP > Ag·TPP » Zn·TPP.

Very similar results were obtained also with octaethylporphyrin (OEP, Figure 4.3), another commonly used neutral porphyrin: similarly to TPP, when OEP was treated with **23** in refluxing propionic acid (Ru/OEP = 1.5) 100% conversion to Ru(CO)(OEP) was obtained in 30 min according to UV-vis analysis (Figure 4.4).

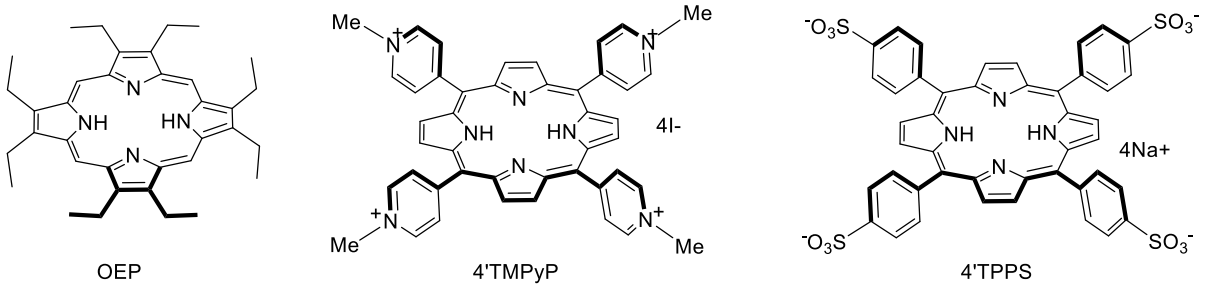

Figure 4.3. Additional neutral and charged model porphyrins investigated in this work besides TPP.

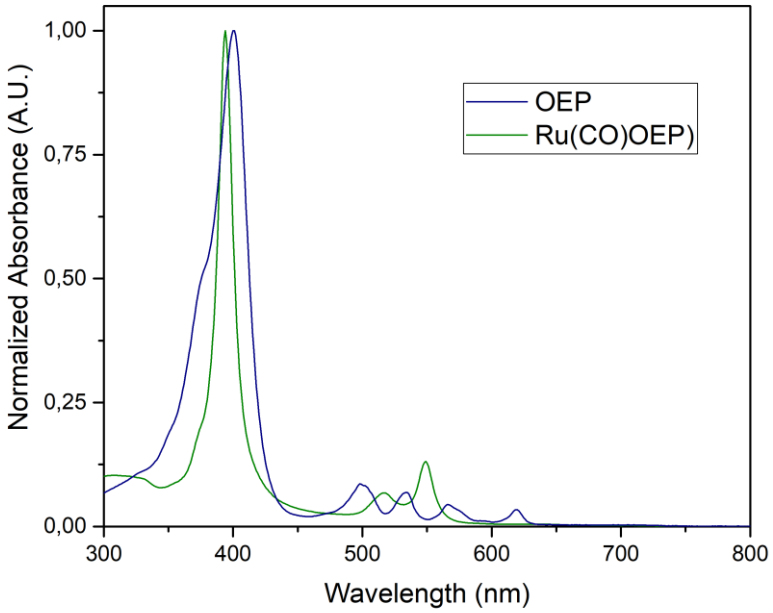

Figure 4.4. UV-vis spectra (propionic acid solutions diluted ca. 50× in $CHCl_3$) of OEP (green) and after 30 min of reflux with **23** (Ru/OEP = 1.5). The initial spectrum corresponds to a mixture of OEP (major species) and $OEPH_2^{2+}$; the final spectrum (purple) corresponds to Ru(CO)(OEP).

4.2.3. Charged model porphyrins

Given the above reported results, the investigation was extended to model cationic and anionic porphyrins: *meso*-tetrakis(4′-*N*-methylpyridiniumyl)porphyrin (4′TMPyP, iodide salt) and *meso*-tetrakis(4′-sulfonatophenyl)porphyrin (4′TPPS, sodium salt), respectively (Figure 4.3). In the literature, ruthenation of the charged porphyrins 4′TMPyP and 4′TPPS was performed with **23** in refluxing DMF (Ru/por = 15), in the presence of 2,4,6-trimethylpyridine (presumably as a non-coordinating proton acceptor).[31] Interestingly, ruthenium insertion into the tetra-cationic 4′TMPyP was reported to occur in a much shorter time and with higher yield than into the tetra-anionic 4′TPPS (2h at 110°C vs 24h at 140°C; yield 57 vs 36%). Apparently, in the absence of 2,4,6-trimethylpyridine, the ruthenation of 4′TPPS (unknown Ru/porphyrin ratio) in refluxing DMF required much longer times, from 1 to 3 weeks.[32] When the Ru(III) complex $[Ru(DMF)_6](SO_3CF_3)_3$ was used as precursor, ruthenation of 4′TMPyP in refluxing DMF was found to depend strongly on the nature of the counter-ion: metalation of the tosilate salt occurred in 17h, whereas the chloride salt was totally unreactive.[8]

In our hands, MW-assisted ruthenation of 4′TPPS with **23** was best performed in 1:3 water/propionic acid mixtures, where a good compromise of the solubility of the two reactants was found.[53] Working at Ru/4′TPPS = 6, 100% conversion to Ru(CO)(4′TPPS) was obtained in 1.5h at 140°C, as assessed by UV-vis spectroscopy (Figure 4.5). A very similar result was obtained using the tricarbonyl complex **26** as ruthenium source, however at lower temperatures **26** proved again to be less reactive than **23** (for example at 100°C **26** – unlike **23** – was basically unreactive). No reaction was found with **27**. Remarkably, no ruthenation was observed under the same conditions when the reaction between 4′TPPS and **23** was performed in DMF (where both reactants are soluble), thus stressing the role of propionic acid.

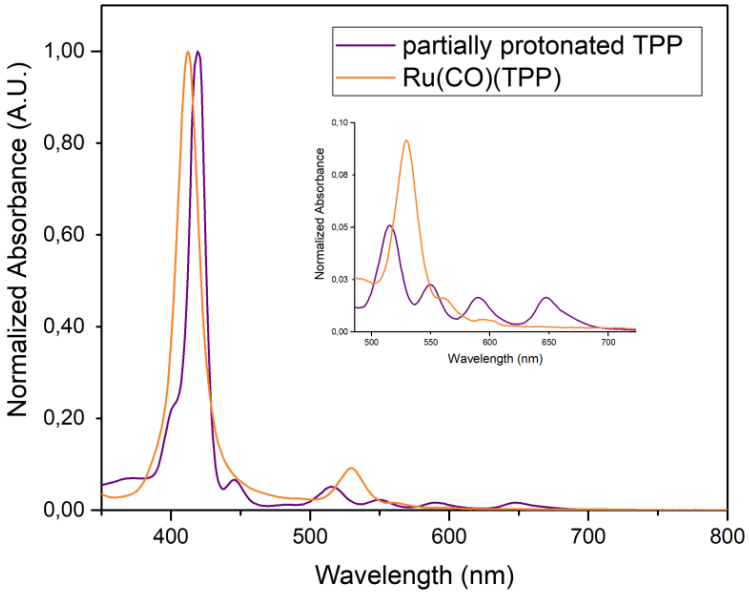

Figure 4.5. UV-vis spectra (1:3 water/propionic acid mixture diluted ca. 50× in water) of 4′TPPS (green), fully protonated to 4′TPPSH_2^{2+} in the reaction conditions, and after treatment with **23** (Ru/4′TPPS = 6, 2h at 140°C in a MW reactor of reflux). The final spectrum (blue) corresponds to Ru(CO)(4′TPPS).

Conversely, ruthenation of 4′TMPyP with **23** under similar conditions used for 4′TPPS proved unsuccessful. It is noteworthy that the tetra-cationic porphyrin , even though fully soluble in the 1:3 water/propionic acid mixture, according to the UV-vis spectrum, undergoes no protonation . Consistent with previous reports,[31.32] full conversion to Ru(CO)(4′TMPyP) was obtained in 1h when 4′TMPyP was treated with **23** in DMF at 140°C in a MW reactor (Ru/4′TMPyP = 6, Figure 4.6).

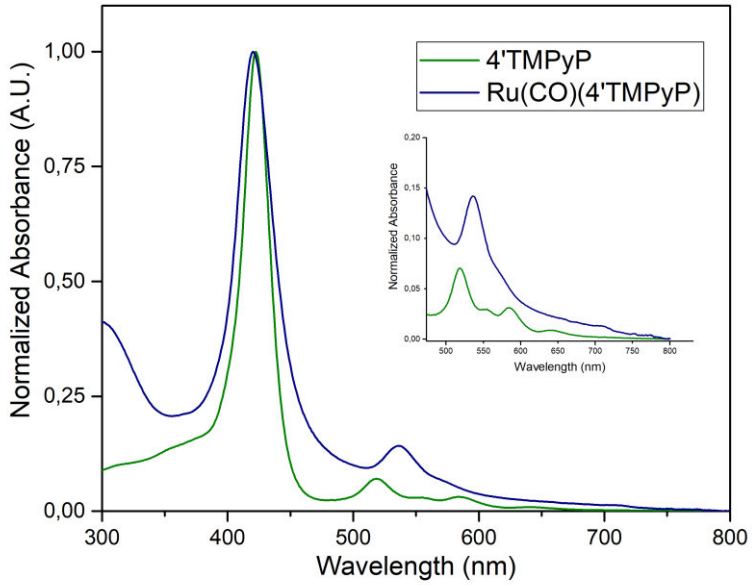

Figure 4.6. UV-vis spectra (DMF diluted ca. 50× in water) of 4′TMPyP (green), and after treatment with **23** (DMF, Ru/4′TMPyP = 6, 1h at 140°C in a MW reactor). The final spectrum (blue) corresponds to Ru(CO)(4′TMPyP).

4.3. Conclusions

The results obtained for the ruthenation of TPP with the Ru(II) carbonyl complex $[Ru(CO)(dmso)_5][PF_6]_2$ (**27**) are of moderate practical impact. Nevertheless, we believe that they establish a proof of concept: for the first time, almost 50 years after the single experimental report by Chow and Cohen,[33] we demonstrated that the Ru(II)–CO fragment can be inserted into a porphyrin under relatively moderate conditions using a well-defined Ru(II) monocarbonyl precursor that – besides CO – features exclusively labile dmso ligands (Scheme 4.2). We believe that this or similar complexes might turn out useful for performing a mechanistic investigation, both from the experimental and computational point of view.

On the other hand, from a practical point of view, the use of propionic acid as solvent for the ruthenation of neutral and anionic model porphyrins with $Ru_3(CO)_{12}$ (**23**) – suprisingly – turned out be extremely efficient and advantageous in terms of both reaction rates and yields compared to the procedures described in the literature. The Ru(0) cluster is commercially available or easily prepared from hydrated $RuCl_3$,[35, 54] the ruthenation reaction is fast at 140°C but can be performed also at lower temperatures and does not require an inert atmosphere, its workup is very simple and the yield of isolated pure product is excellent.

Table 1 summarizes the best results for the insertion of Ru(CO) into the model neutral (TPP, OEP), tetra-anionic (4′TPPS), and tetra-cationic (4′TMPyP) porphyrins with different Ru precursors.

Table 4.1. Best reaction conditions for the 100% ruthenation (based on spectroscopic analysis) of model porphyrins.

Porphyrin (porp)	Ru precursor	Ru/porp	T (°C)	Time (h)
TPP[a]	**23**	1.5	141[d]	0.5
TPP[a]	**26**	1.5	141[d]	1
OEP[a]	**23**	1.5	141[d]	0.5
4′TPPS[b]	**23**	6	140[e]	1.5
4′TPPS[b]	**26**	6	140[e]	1.5
4′TMPyP[c]	**23**	6	140[e]	1

[a] in propionic acid; [b] in 1:3 water/propionic acid mixture; [c] in DMF; [d] either at reflux or in MW reactor at 140°C; [e] in MW reactor.

From a mechanistic point of view, since both the Ru(0) cluster **23** and the (less practical) Ru(II) tricarbonyl precursor *fac*-$RuCl_2(CO)_3$(dmso-O) (**26**) gave similar ruthenation performances, the needed change in oxidation state from Ru(0) to Ru(II) in the case of **23** does not seem to play a very relevant role. Nevertheless, the combination of high yield and fast rate of metalation in an acidic medium is rather surprising. Indeed in the first part of this work we observed that the ruthenation of TPP with **27** required the addition of a base and did not occur at all in acidic conditions.

Relatively recent papers – through both experimental and computational approaches – postulated (with simpler metal ions such as Zn^{2+}, Mg^{2+} and Fe^{2+}), that the processes of protonation and metalation of a porphyrin share common mechanistic intermediates.[1,55] In the presence of an acid, protonation of the pyrrolenine nitrogen atoms induces a distortion in the macrocycle (tilting of the diagonally opposing core N-rings) that, with the assistance of the acid-conjugate anion, favors metal coordination. The process is completed by the expulsion of the core protons with concomitant return to planarity of the metalated porphyrin and release of the strain. Our experimental results indicate that, in the moderately acidic environment provided by propionic acid, the large enthalpic driving force for the ruthenation of TPP is not particularly affected by the competition with the double protonation leading to $TPPH_2^{2+}$. It is likely that for neutral and anionic porphyrins propionic acid provides a good combination of solubilizing properties, moderate acidity (pK_a 4.87), boiling point and that – at least in the case of **23** and **26** – the kinetic effect (acid-induced acceleration) largely prevails over equilibrium considerations (i.e. ruthenation vs double protonation). It is arguable that acetic acid, with a comparable pK_a value, is less effective because of its lower boiling point (i.e. slower kinetics at reflux temperature), whereas TFA is much more acidic (pK_a = –0.25, i.e. stronger competition for protonation) and also has a lower boiling point. As noticed above, in propionic acid also the concentration of TPP is relevant for the performance of the reaction, since protonation occurs to a larger extent. With other Ru precursors such as **25** and **27** other factors must prevail and the ruthenation process is either much slower (**25**) or does not occur at all (**27**). Among such factors, solubility of the Ru compound and its stability in that environment are likely to be particularly relevant. Finally, propionic acid is unable to protonate the tetra-cationic porphyrin 4′TMPyP and its ruthenation with **23** is best performed in DMF.

4.4. Experimental Section

Materials

All chemicals were purchased from Sigma-Aldrich and used as received. Solvents were of reagent grade. The Ru precursors *cis*-$RuCl_2(dmso)_4$,[56] $Ru_3(CO)_{12}$ (**23**),[35] *cis*,*fac*-$RuCl_2(dmso)_3(CO)$ (**25**),[39] *fac*-$RuCl_2(CO)_3$(dmso-O) (**26**),[41] Zn·TPP,[4] Ag·TPP,[57] and $[Na]_4$[4′TPPS][58] were synthesized as

described in the literature. [4′TMPyP][I]$_4$ was a gift from Dr. Rita De Zorzi, Department of Chemical and Pharmaceutical Sciences, University of Trieste.

Instrumental methods.

^{1}H NMR spectra were recorded at room temperature on a Varian 400 or 500 spectrometer (^{1}H: 400 or 500 MHz). ^{1}H chemical shifts were referenced to the peak of residual non-deuterated solvent (δ = 7.26 for $CDCl_3$). The UV-vis spectra were obtained on an Agilent Cary 60 spectrophotometer, using 1.0 cm path-length quartz cuvettes (3.0 mL). ESI mass spectra were collected in the positive mode on a Perkin-Elmer APII spectrometer at 5600 eV. A thermostatted Berghof stainless steel vessel (autoclave), equipped with a 100 mL Teflon liner, was used for the reactions with CO under pressure. A CEM Discover microwave reactor was used for the microwave-assisted reactions performed in 10 mL vessels. Elemental analyses were performed on a Thermo Flash 2000 CHNS/O analyzer in the Department of Chemistry of the University of Bologna (Italy).

Synthesis

$Ru_3(CO)_{12}$ (23).

In the course of this work, we developed two alternative synthetic procedures for **23**. In both cases the spectroscopic and analytical features of the isolated compound were coincident with those previously reported.[35,54]

1) as a proof of concept, we demonstrated that *fac*-$RuCl_2(CO)_3$(dmso-O) (**25**) affords **23** in moderate yield when treated with a stream of CO in refluxing ethanol in the presence of a base. This procedure confirms what reported by Lavigne and coworkers,[35] i.e. that the dinuclear species [*fac*-$RuCl(CO)_3(\mu\text{-}Cl)]_2$ (of which **25** is the activated form)[43] is an intermediate in the two-step preparation of **23** from hydrated $RuCl_3$. Even though **25** is certainly a less practical precursor compared to $RuCl_3 \cdot 3H_2O$,[35] the following procedure occurs in a single step and uses the easily available ethanol instead of 2-ethoxyethanol. A 401.0 mg amount of **25** (1.20 mmol) was partially dissolved in 20 mL of ethanol in a two-necked flask connected to a condenser. The system was deaerated (first connected to a vacuum line and then to a reservoir of CO for 3 times), and then warmed to 80°C under a stream of CO. Addition of 2 equiv of KOH (conc. aqueous solution) induced the deep-yellow solution to turn progressively darker and an orange-brown precipitate of **23** formed. After 45 min at 80°C, the mixture was allowed to cool under the CO stream. The precipitate was removed by filtration, washed with water and cold methanol and vacuum dried at room temperature (Yield: 100 mg, 39%). The raw solid was recrystallized from *n*-hexane (22 mL).

2) Reductive carbonylation of the chloride-free Ru(II)-dmso precursor $[Ru(dmso)_6][CF_3SO_3]_2$. The Ru(0) cluster **23** was obtained as the result of an unsuccessful attempt to perform the ruthenation of TPP by treating the porphyrin with $[Ru(dmso)_6][CF_3SO_3]_2$ under a CO pressure. Thus we developed

the following procedure: A 100.0 mg amount of $[Ru(dmso)_6][CF_3SO_3]_2$ (0.115 mmol) was partially dissolved in 20 mL of methanol and treated with CO (30 atm, 60°C) in an autoclave for 24h. The resulting yellow solution was rotary evaporated to an oil. Addition of water (5 mL) induced the formation of an orange solid that was removed by filtration and redissolved in dichloromethane. The DCM solution was treated with anhydrous Na_2SO_4 and then evaporated to dryness, affording pure **23** (according to the IR spectrum) as an orange solid that was vacuum dried (Yield: 15.0 mg, 61%).

$[Ru(CO)(dmso)_5][PF_6]_2$ (27).

The synthetic protocol previously reported by us for the preparation of **27**,[41] turned out to be scarcely reproducible. Thus, a modified procedure was developed for the efficient preparation of **27**, that used pure DMSO instead of the original acetone/DMSO solvent mixture. A 191.3 mg amount of *cis,fac*-$RuCl_2(dmso)_3(CO)$ (**25**) (0.44 mmol) was dissolved in 1 mL of DMSO. To the colorless solution a slight excess of $AgPF_6$ (257.1 mg, 1.0 mmol) was added and the solution warmed to 80°C for 1h, during which time a greyish precipitate of AgCl formed. After cooling, the precipitate was removed by filtration on a celite pad that was then thoroughly washed with acetone. The solvent mixture (DMSO + acetone) was completely evaporated under vacuum, yielding a yellow solid, that was dissolved in 3 mL of acetone. Additional undissolved AgCl was removed by filtration as above. The yellow acetone solution was concentrated to ca. 2 mL. Dropwise addition of diethyl ether until cloudiness induced the slow precipitation of the product as pale-yellow crystals, that were recovered by filtration, washed with diethyl ether and vacuum dried at room temperature. Yield: 227 mg (64%). The spectroscopic features of the complex were coincident with those previously reported.[41] Elemental analysis calcd for $[C_{11}H_{30}F_{12}O_6P_2RuS_5]$ (M_w: 809.64): C 16.32; H 3.73. Found: C 16.5; H 3.89.

Methods for qualitative and quantitative assessment of the ruthenation of the model porphyrins.

The formation of the ruthenated porphyrins was qualitatively monitored by UV-vis spectroscopy. TLC analysis was also used for the neutral porphyrins Ru(CO)(TPP) or Ru(CO)(OEP). The ^{1}H NMR, IR (νCO), ESI-MS, and UV-vis data for Ru(CO)(TPP), Ru(CO)(OEP),[25] Ru(CO)(4′TPPS),[31,32] and Ru(CO)(4′TMPyP)[31] – obtained from solutions where, according to the UV-vis spectra, the full conversion of the free-base porphyrin was achieved – were consistent with those previously reported in the literature for those compounds.

In the case of the most deeply investigated TPP, the UV-vis spectra (a drop of original solution was diluted in ca. 2 mL of chloroform into the cuvette) were useful for quantitatively assessing conversions >90%, but less practical and informative for lower conversion rates, due to the partial

overlap of the Q bands of the product with those of the corresponding free base (Figure 4.2). Thus, in particular for the reactions performed in the MW reactor with **27** as Ru precursor, quantitative analysis was performed by ^{1}H NMR spectroscopy. The following procedure was adopted to treat the sample: 1/3 of the solution was removed from the MW vial and rotary-evaporated to dryness. The purple-greenish solid (depending on the reaction conditions) was washed with a small amount of water, thoroughly dryed under vacuum, and then dissolved in $CDCl_3$. The percentage of ruthenation was obtained through the integration of the well-resolved βH singlets of TPP (8.84 ppm), $TPPH_2^{2+}$ (if present) (8.75 ppm), and Ru(CO)(TPP) (8.69 ppm).[45]

Procedures for the ruthenation of TPP.

The protocols that afforded the best results, both using compound **27** in $CHCl_3$/methanol mixtures and **23** in propionic acid, are reported.

Synthesis of Ru(CO)(TPP) from [Ru(CO)(dmso)$_5$][PF$_6$]$_2$ (27) in the MW reactor.

In a MW vial, a 5.0 mg amount of TPP (0.0074 mmol) was completely dissolved in 3.0 mL of a 2:1 chloroform/methanol mixture. Four equiv of **27** (24.0 mg, 0.030 mmol, only partially soluble) and two equiv of KOH (21 μL of a 0.7 M methanol solution) were added to the purple solution and the mixture was heated at 100°C for the desired time (typically 30 or 60 min) in the MW reactor, yielding a dark green solution with a grayish precipitate (undissolved and/or decomposed complex). At this stage, either the amount of Ru(CO)(TPP) was quantitatively assessed by NMR spectroscopy (and the reaction was terminated), or it was qualitatively assessed by TLC analysis and then, after addition of 2-3 equiv of KOH until the solution turned purple, the mixture was further reacted as above. With this stepwise protocol, a 33% of Ru(CO)(TPP) was obtained in two 30 min steps, whereas a 50% in four 60 min steps.

Preparative synthesis of Ru(CO)(TPP) from Ru$_3$(CO)$_{12}$ (23) in refluxing propionic acid or in MW reactor.

In a 10 mL MW vial, a 20.0 mg amount of TPP (0.0326 mmol) was partially dissolved in 4 mL of propionic acid. Half equivalent of **23** (8.25 mg) was added to the mixture and heated in a microwave reactor at 140°C for 1h. Conversion was quantitative according to the UV-vis spectrum. The solvent was then removed *in vacuo* and the Ru(CO)(TPP) was purified, in order to remove traces of propionic acid and Ru compounds, by passage through a small column of silica gel eluted with $CHCl_3$. A single red-orange band was collected. To this solution 10 mL of EtOH were added and then the solvent was removed and the solid residue of Ru(CO)(TPP) was vacuum dried. (Isolated yield: 23.7 mg, 92%).

4.5 Bibliography

1 Y. Shen, U. Ryde, Reaction Mechanism of Porphyrin Metallation Studied by Theoretical Methods. *Chem. Eur. J.* **2005**, *11*, 1549-1564.

2 N. Farrell, D. H. Dolphin, B. R. Reversible binding of dioxygen to ruthenium(II) porphyrins James, *J. Am. Chem. Soc.* **1978**, *100*, 324-326.

3 H. Masuda, T. Taga, K. Osaki, H. Sugimoto, M. Mori, H. Ogoshi, The crystal and molecular structure of new tetravalent ruthenium porphyrin. μ-Oxo-bis[(octaethylporphinato)ruthenium(IV) hydroxide]. *J. Am. Chem. Soc*. **1981**, *103*, 2199-2203.

4 J. K. M. Sanders, N. Bampos, Z. Clyde-Watson, S. L. Darling, J. C. Hawley, H.-J. Kim, C. C. Mak, S. J. Webb in *The Porphyrin Handbook* (K. M. Kadish, K. M. Smith, R. Guillard Eds.), Academic Press, New York, Vol. 3, **2000**, pp. 1-48 and refs. therein.

5 a) G. Simonneaux, P. Le Maux, Optically active ruthenium porphyrins: chiral recognition and asymmetric catalysis. *Coord. Chem. Rev.* **2002**, *228*, 43-60; b) G. Simonneaux, P. Le Maux, Y. Ferrand, J. Rault-Berthelot, Asymmetric heterogeneous catalysis by metalloporphyrins. *Coord. Chem. Rev.* **2006**, *250*, 2212-2221; c) D. Intrieri, D. M. Carminati, E. Gallo, The ligand influence in stereoselective carbene transfer reactions promoted by chiral metal porphyrin catalysts. *Dalton Trans.* **2016**, *45*, 15746-15761; d) C. Damiano, D. Intrieri, E. Gallo, Aziridination of alkenes promoted by iron or ruthenium complexes. *Inorg. Chim. Acta* **2018**, *470*, 51-67.

6 a) Groves, J. T.; Shalyaev, K.; Lee, J. in *The Porphyrin Handbook*; Kadish, K. M., Smith, K. M., Guilard, R., Eds.; Academic Press: New York, **2000**;Vol. 4,Chapter 27, 17-40; b) D. Chatterjee, Asymmetric epoxidation of unsaturated hydrocarbons catalyzed by ruthenium complexes. *Coord. Chem. Rev.* **2008**, *252*, 176-198; c) C.-M. Che, J.-S. Huang, Metalloporphyrin-based oxidation systems: from biomimetic reactions to application in organic synthesis. *Chem. Commun.* **2009**, 3996-4015; d) S. M. Ujwaldev, K. S. Sindhu, A. P. Thankachan, G. Anilkumar, Recent developments and perspectives in the ruthenium-catalyzed olefin epoxidation. *Tetrahedron* **2016**, *72*, 6175-6190.

7 a) A. A. Umar, M. M. Salleh, M. Yahaya, Influence of surface microstructure on optical response of ruthenium-porphyrins thin films gas sensor. *Eur. Phys. J. Appl. Phys.* **2005**, *29*, 215-221; b) M. H. Lim, S. J. Lippard Metal-Based Turn-On Fluorescent Probes for Sensing Nitric Oxide *Acc. Chem. Res.* **2007**, *40*, 41-51; c) M. B. Winter, E. J. McLaurin, S. Y. Reece, C. Olea Jr., D. G. Nocera, M. A. Marletta, Ru-Porphyrin Protein Scaffolds for Sensing O_2. *J. Am. Chem. Soc.* **2010**, *132*, 16, 5582-5583.

8 For a relatively recent exhaustive overview of porphyrin ruthenation procedures see: J. S. Rebouças, E. L. S. Chew, C. J. Ware, B. R. James, K. A. Skov, Synthetic and Mechanistic Aspects of a New Method for Ruthenium-Metalation of Porphyrins and Schiff-Bases. *Inorg. Chem.* **2008**, *47*, 7894-7907.

9 C.-M. Che, C.-K. Poon, W.-C. Chung, H. B. Gray, Synthesis and Characterization of Osmium Porphyrins. *Inorg. Chem.* **1985**, *24*, 1277-1278.

10 M. Tsutsui, D. Ostfeld, L. M. Hoffman, Unusual Metalloporphyrins. VI. Metal Shuttling between Imidazole Nitrogens in a Ruthenium Porphyrin Imidazole. *J. Am. Chem. Soc*. **1971**, *93*, 1820-1823.

11 J. J. Bonnet, J. A. Ibers, S. S. Eaton, G. R. Eaton, R. H. Holm, Spectroscopic and Structural Characterization of Ruthenium(II) Carbonyl-Porphine Complexes. *J. Am. Chem. Soc.* **1973**, *95*, 2141-2149.

12 G. M. Brown, F. R. Hopf, J. A. Ferguson, T. J. Meyer, D. G. Whitten, Metalloporphyrin Redox Chemistry. The Effect of Extraplanar Ligands on the Site of Oxidation in Ruthenium Porphyrins. *J. Am. Chem. Soc.* **1973**, *95*, 5939–5942.

13 S. S. Eaton, G. R. Eaton, R. H. Holm, Inter-and intramolecular ligand exchange reactions of ruthenium (II) carbonyl porphine complexes with nitrogen bases. *J. Organomet. Chem.* **1972**, *39*, 179-195.

14 R. G. Little, J. A. Ibers, Structure of (tetraphenylporphinato)(carbonyl)(pyridine) ruthenium (II)-1.5-toluene. *J. Am. Chem. Soc.* **1973**, *95*, 8583-8590.

15 C. Slebodnick, W. K. Seok, K. Kim, J. A. Ibers, Syntheses and characterization of the ruthenium carbonyl porphyrin complexes Ru (TPP)(CO)(1-MeIm) and Ru (α-PocPivP)(CO)(1-MeIm). *Inorg. Chim. Acta* **1996**, *243*, 57-65.

16 a) S. S. Eaton and G. R. Eaton, Substituent effects on rates of 4-tert-butylpyridine exchange in ruthenium carbonyl complexes of para-substituted tetraphenylporphyrins. *Inorg. Chem.* **1977**, *16*, 72-75; b) J. W. Faller, C. C. Chen, C. J. Malerich, Amine adducts of porphinato carbonylruthenium (II): studies of conformational effects and dynamics. *J. Inorg. Biochem.* **1979**, *11*, 151-170; c) H. D Samachetty,N. R. Branda, Photomodulation of Lewis basicity in a pyridine-functionalized 1,2-dithienylcyclopentene. *Chem. Commun.* **2005**, 2840-2842.

17 a) E. Alessio, M. Macchi, S. Heath, L. G. Marzilli, A novel open-box shaped pentamer of vertically linked porphyrins that selectively recognizes S-bonded Me2SO complexes. *Chem. Commun.* **1996**, 1411-1412; b) E. Alessio, S. Geremia, S. Mestroni, E. Iengo, I. Srnova, M. Slouf, Solution and solid state structure of a canted, side-to-face, bis (porphyrin) adduct. *Inorg. Chem.* **1999**, *38*, 869-875; c) E. Alessio, S. Geremia, S. Mestroni, I. Srnova, M. Slouf, T.

Gianferrara, A. Prodi, Porphyrin "flying-saucers": Solid state and solution structure of a novel pentameric array of axially-ligated canted porphyrins. *Inorg. Chem.* **1999**, *38*, 2527-2529.

18 K. Chichak, M. C.Walsh, N. R. Branda, Axially coordinated porphyrins as new rotaxane stoppers. *Chem. Commun.* **2000**, 847-848; d) K. Chichak, N. R. Branda, The metal-directed self-assembly of three-dimensional porphyrin arrays. *Chem. Commun.* **2000**, 1211-1212.

19 For comprehensive review papers see: a) E. Iengo, P. Cavigli, D. Milano, P. Tecilla, Metal mediated self-assembled porphyrin metallacycles: Synthesis and multipurpose applications. *Inorg. Chim. Acta* **2014**, *417*, 59-78; b) S. Durot, J. Taesch, V. Heitz, Multiporphyrinic cages: architectures and functions. *Chem. Rev.* **2014**, *114*, 8542-8578.

20 M. J. Camezind, B. R. James, D. Dolphin, Synthesis and reactivity of a monomeric 14-electron 'bare' ruthenium(II) porphyrin complex; reversible binding of dinitrogen to form mono- and bis-dinitrogen complexes. *J. Chem. Soc., Chem. Commun.* **1986**, 1137-1139.

21 F. R. Hopf, T. P. O'Brien, W. R. Scheidt, D. G. Whitten, Structure and reactivity of ruthenium (II) porphyrin complexes. Photochemical ligand ejection and formation of ruthenium porphyrin dimers. *J. Am. Chem. Soc.* **1975**, *97*, 277-281.

22 T. Boschi, G. Bontempelli, G.-A. Mazzocchin, *Inorg. Chim. Acta* **1979**, *37*, 155-160; b) R. G. Ball, G. Domazetis, D. Dolphin, B. R. James, J. Trotter, Studies of Ruthenium (II) Porphyrins Containing Tertiary Diphosphine Ligands, Including the Crystal Structure of (5,10,15,20-Tetraphenylporphinato)bis(bis(diphenylphosphino)methane)ruthenium(II)-Dichloromethane *Inorg. Chem.* **1981**, *20*, 1556-1562; c) A. D. Bond, J. K. M. Sanders, E. Stulz, Ruthenium (II) and rhodium (III) porphyrin phosphine complexes: influence of substitution pattern on structure and electronic properties. *New J. Chem.* **2011**, *35*, 2691-2696.

23 M. Massoudipour, K. K. Pandey, Preparation and characterization of ruthenium (II) porphyrins *Inorg. Chim. Acta* **1989**, *160*, 115-118.

24 D. Cullen, E. Meyer Jr., T. S. Srivastava, M. Tsutsui, Unusual metalloporphyrins. XXIII. Unusual metalloporphyrin complexes of rhenium and technetium. *J. Am. Chem. Soc.*., **1972**, 584-585. (To be noted that the X-ray structure and the formulation of the Ru-porphyrin reported in this work were later found to be wrong).

25 M. Barley, J. Y. Becker, G. Domazetis, D. Dolphin, B. R. James, Synthesis and redox chemistry of octaethylporphyrin complexes of ruthenium (II) and ruthenium (III). *Can. J. Chem.* **1983**, *61*, 2389-2396.

26 J. P. Collman, C. E. Barnes, P. J. Brothers, T. J. Collins, T. Ozawa, J. C. Gallucci, J. A. Ibers, Oxidation of ruthenium (II) and ruthenium (III) porphyrins. Crystal structures of μ-oxo-bis [(p-methylphenoxo)(meso-tetraphenylporphyrinato) ruthenium (IV)] and Ethoxo(meso-

tetraphenylporphyrinato)-(ethanol)ruthenium(III)-Bisethanol *J. Am. Chem. Soc.* **1984**, *106*, 5151-5163.

27 C.-M. Che, J.-L. Zhang, R. Zhang, J.-S. Huang, T.-S. Lai, W.-M. Tsui, X.-G. Zhou, Z.-Y. Zhou, N. Zhu and C. K. Chang, Hydrocarbon Oxidation by β-Halogenated Dioxoruthenium(^{VI}) Porphyrin Complexes: Effect of Reduction Potential ($Ru^{VI/V}$) and C-H Bond-Dissociation Energy on Rate Constants *Chem.–Eur. J.* **2005**, *11*, 7040-7053.

28 D. P. Rillema, J. K. Nagle, L. F. Barringer Jr., T. J. Meyer, Redox Properties of Metalloporphyrin Excited States, Lifetimes, and Related Properties of a Series of Para-Substituted Tetraphenylporphine Carbonyl Complexes of Ruthenium(II) *J. Am. Chem. Soc.* **1981**, *103*,56-62.

29 V. Marvaud, A. Vidal-Ferran, S. J. Webb, J. K. M. Sanders, Stereospecific templated synthesis of a triruthenium butadiyne-linked cyclic porphyrin trimer*, Dalton Trans.* **1997**, 985-990.

30 The reaction mixtures are heterogeneous, since the reactants are not particularly well-soluble in hydrocarbons.

31 M. Hartmann, A. Robert, V. Duarte, B. K. Keppler, B. Meunier, Synthesis of water-soluble ruthenium porphyrins as DNA cleavers and potential cytotoxic agents. *J. Biol. Inorg. Chem.* **1997**, *2*, 427-432.

32 M. Pawlik, M. F. Hoq, R. E. Shepherd, Catalysis of the water gas shift reaction by $Ru(TPPS)CO_4$–[TPPS = meso-tetra(4-sulphonatophenyl)porphyrinato]. *J. Chem. Soc., Chem. Commun.* **1983**, 1467-1468.

33 B. C. Chow, I. A Cohen, Derivatives of tetraphenylporphineruthenium (II). *Bioinorg. Chem.* **1971**, *1*, 57-63.

34 V. Marvaud, J.-P. Launay, Control of intramolecular electron transfer by protonation: oligomers of ruthenium porphyrins bridged by 4, 4'-azopyridine. *Inorg. Chem.* **1993**, *32*, 1376-1382.

35 a) M. Fauré, L. Maurette, B. Donnadieu, G. Lavigne, Reactions of a Transient Carbonyl(chloro)(hydrido)ruthenium(II) Complex with Ethylene, Alkynes, and CO; Chemistry of the New Anion $[Ru_2(CO)_4Cl_5]^{-}$. *Angew. Chem. Int. Ed.***1999**, *38*, 518-522; b) M. Fauré, C. Saccavini, G. Lavigne Dodecacarbonyltriruthenium, $Ru_3(CO)_{12}$. *Inorg. Synth.* **2004**, *34*, 110-115.

36 J. P. Collman, C. E. Barnes, P. N. Swepston, J. A. Ibers, Synthesis, proton NMR, and structural characterization of binuclear ruthenium porphyrin dimers. *J. Am. Chem. Soc.* **1984**, *106*, 3500-3510.

37 R. J. Judd, R. Cao, M. Biner, T. Armbruster, H.-B. Boergi, A. E. Merbach, A. Ludi, Syntheses and Crystal and Molecular Structures of the Hexakis (N, N-dimethylformamide) Complexes of Ruthenium (II) and Ruthenium (III). *Inorg. Chem.* **1995**, *34*, 5080-5083.

38 E. B. Fleisher, R. Thorp, D. Venerable, Ruthenium and rhodium carbonyl tetraphenylporphin chloride. *J. Chem. Soc., Chem. Commun.* **1969**, 475-476.

39 Alessio, E.; Milani, B.; Bolle, M.; Mestroni, G.; Faleschini, P.; Todone, F.; Geremia, S.; Calligaris, M. Carbonyl Derivatives of Chloride-Dimethyl Sulfoxide-Ruthenium(II) Complexes: Synthesis, Structural Characterization, and Reactivity of $Ru(CO)_x(DMSO)_{4-x}Cl_2$ Complexes (x = 1-3). *Inorg. Chem.* **1995**, *34*, 4722-4734.

40 Alessio, E.; Iengo, E.; Geremia, S.; Calligaris, M. Carbonyl Derivatives of Chloride-Dimethyl Sulfoxide-Ruthenium(III) Complexes: Synthesis, Crystal Structure, and Reactivity of $[(DMSO)_2H][$*trans*-$RuCl_4$(dmso-*O*)(CO)] and *mer,cis*-$RuCl_3$(dmso-*O*)$_2$(CO). *Inorg. Chim. Acta* **2003**, *344*, 183-189.

41 Bratsos, I.; Calmo, S.; Zangrando, E.; Balducci, G.; Alessio, E. New cationic and neutral Ru (II)-and Os (II)-dmso carbonyl compounds. *Inorg. Chem.* **2013**, *52*, 12120-12130.

42 In the following formulas of the complexes the coordination mode of the dmso ligands is indicated explicitly (either dmso-*S* or dmso-*O*) only when a single mode is present. The Ru-carbonyl compounds share a common feature: when *trans* to CO, dmso is always bound through the oxygen atom (dmso-O) for avoiding π-back bonding competition.

43 Balducci, G.; Iengo, E.; Demitri, N.; Alessio, E. New Insight into a Deceptively Simple Reaction: The Coordination of bpy to RuII-Carbonyl Precursors - The Central Role of the fac-$[Ru(bpy)Cl(CO)_3]^+$ Intermediate and the Chloride Rebound Mechanism. *Eur. J. Inorg. Chem.* **2015**, *26*, 4296-4311.

44 M. Meot-Ner, A. D. Adler, Substituent effects in noncoplanar π systems. *ms*-Porphins *J. Am. Chem. Soc.* **1975**, *97*, 5107-5111.

45 R. I. Walter, E. C. A. Ojadi, H. Linschitzl, A Proton NMR Study of the Reactions with Acid of meso-Tetraphenylporphyrins with Various Numbers of 4-Dimethylamino Groups. *J. Phys. Chem.* **1993**, *97*, 13308-13312.

46 E. Alessio, Synthesis and reactivity of Ru-, Os-, Rh-, and Ir-halide−sulfoxide complexes. *Chem. Rev.* **2004**, *104*, 4203-4242.

47 The possibility that the excess of protons derives from a catalyzed decomposition of $CHCl_3$, that might generate HCl, was also considered. However, the replacement of $CHCl_3$ with the more stable CH_2Cl_2 led to very similar results, thus ruling out this hypothesis.

48 a) J. P. Collman, C. S. Bencosme, R. R. Durand, Jr., R. P. Kreh, F. C. Anson, Mixed-metal face-to-face porphyrin dimers. *J. Am. Chem. Soc.* **1983**, 105, 2699-2703; b) J. A. Cowan, J. K. M. Sanders, Reductive demetallation of porphyrins: Evidence for peripheral and axial modes of reduction. *Tetr. Lett.* **1986**, *27*, 1201-1204.

49 a) A. Giraudeau, A. Louati, H. J. Callot, M. Gross, Electrochemical reduction and demetalation of silver and thallium porphyrins. *Inorg. Chem.* **1981**, *20*, 769-772; b) A. Kumar, P. Neta, Reduction and demetalation of silver porphyrins in aqueous solutions. *J. Phys. Chem.* **1981**, *85*, 2830-2832; c) H. Kunkely, A. Vogler, Photodemetalation of silver (II) tetraphenylporphyrin *Inorg. Chem. Commun.* **2007**, *10*, 479-481.

50 a) M. Inamo, N. Kamiya, Y. Inada, M. Nomura, S. Funahashi, Structural Characterization and Formation Kinetics of Sitting-Atop (SAT) Complexes of Some Porphyrins with Copper(II) Ion in Aqueous Acetonitrile Relevant to Porphyrin Metalation Mechanism. Structures of Aquacopper(II) and Cu(II)−SAT Complexes As Determined by XAFS Spectroscopy. *Inorg. Chem.* **2001**, *40*, 5636-5644; b) J. L. Gárate-Morales, F. S. Tham, C. A. Reed, Do Sitting-Atop Metalloporphyrin Complexes Exist? Observation of N−H- - -π Bonding in Arene Solvates of a Diprotonated Porphyrin Dication. *Inorg. Chem.* **2007**, *46*, 1514-1516.

51 Under the same conditions, the carbonyl-free precursor *cis*-$RuCl_2(dmso)_4$ led to no product formation.

52 No reactivity was observed when acetone/$CHCl_3$ or $CH_3CN/CHCl_3$ mixtures, where both TPP and **27** are rather soluble, were used as solvent.

53 In this solvent mixture the initial solution is deep green, indicating extensive protonation of the porphyrin to 4′TPPSH_2^{2+}. No reaction occurred in pure propionic acid (where 4′TPPS is insoluble) or in water (where **23** is not soluble).

54 M. I. Bruce, C. M. Jensen, N. L. Jones Photochemical Synthesis and Ligand Exchange Reactions of $Ru(CO)_4(\eta^2$-alkene) Compounds. *Inorg. Synth.* **1989**, *26*, 259-261.

55 M. J. Webb, N. Bampos, Noncovalent interactions in acid–porphyrin complexes. *Chem. Sci.* **2012**, *3*, 2351-2366.

56 I. Bratsos, E. Alessio, Ruthenium (II)-chlorido complexes of dimethylsulfoxide. *Inorg. Synth.* **2010**, *35*, 148-152.

57 G. D. Dorough, J. R. Miller, F. M. Huennekens Spectra of the Metallo-derivatives of α, β, γ, δ-Tetraphenylporphine. *J. Am. Chem. Soc.* **1951**, *73*, 4315-4320.

58 G. G. Meng, B. R. James, K. S. Skov, M. Korbelic, Porphyrin chemistry pertaining to the design of anti-cancer drugs; part 2, the synthesis and in vitro tests of water-soluble porphyrins containing, in the meso positions, the functional groups: 4-methylpyridinium, or 4-

sulfonatophenyl, in combination with phenyl, 4-pyridyl, 4-nitrophenyl, or 4-aminophenyl*Can. J. Chem.* **1994**, *72*, 2447.

CHAPTER 5

Battistin, F., Vidal, A., Cavigli, P., Balducci, G., Iengo, E., and Alessio, E. Orthogonal Coordination Chemistry of PTA toward Ru(II) and Zn(II) (PTA = 1,3,5-Triaza-7-phosphaadamantane) for the Construction of 1D and 2D Metal-Mediated Porphyrin Networks. *Inorg. Chem.* **2020**, *59*, 4068–4079

5. The Orthogonal Coordination Of PTA

5.1 Introduction

The cage-like 1,3,5-triaza-7-phosphaadamantane (PTA, Chart 1), is an amphiphilic, air-stable, neutral ligand of low steric demand (cone angle 103°) characterized by a high solubility in water (ca. 235 g/L). For this reason, PTA and related species – whose coordination chemistry has been thoroughly reviewed by Peruzzini and co-workers – have been largely investigated as supporting ligands for applications in homogeneous aqueous biphasic catalysis and medicinal inorganic chemistry.[1-3]
PTA typically binds strongly to most transition metal ions through the soft P atom in a monodentate fashion (PTA-κ*P*). However, having also three hard N donor atoms, it is actually a hetero-polytopic PN_3 ligand and might also potentially bridge two or more metal ions with different HSAB preferences (Chart 1).[1]

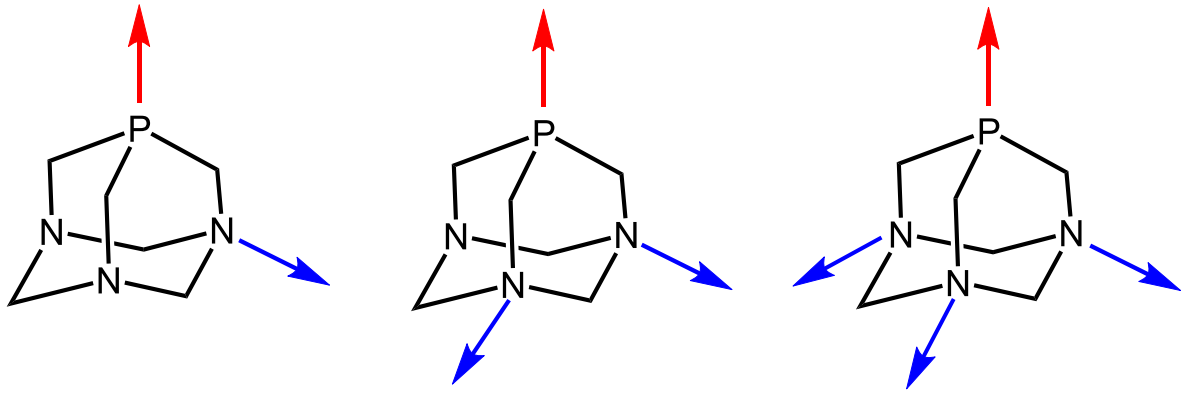

Chart 5.1. The schematic structure of PTA and its possible coordination modes as a bridging ligand through P (red arrow) and through N atoms (blue arrow). Left: (κ^2*P,N*); center: (κ^3*P,2N*); right: (κ^4*P,3N*).

The bridging κ*P,N* coordination mode of PTA was found to be rather common, even though its first example, the hetero-bimetallic coordination polymer [{RuCp(dmso-κ*S*)(PTA-κ^2*P,N*)$_2$}{$AgCl_2$}]$_\infty$, was described by Romerosa, Peruzzini and co-workers only in 2005.[4, 5] Subsequently, Romerosa and co-workers described a series of water-soluble 1D ruthenium-metal coordination polymers featuring a Ru–CN–Ru–M backbone (M = Au, Ni, Cd, Co).[6] They are formed by inert [{RuCp(PTA)$_2$}(μ-CN){RuCp(PTA)$_2$}]$^+$ moieties connected at both ends through bridging PTA-κ^2*P,N* ligands to metal anions (i.e. $[Au(CN)_4]^-$, $[NiCl_3]^-$, $[CdCl_3]^-$, $[CoCl_3]^-$). In addition, besides two discrete molecular entities featuring a {Re(III)(PTA-κ^2*P,N*)M(II)} moiety (M = Cu, Zn),[7] many other examples of PTA-driven polymeric networks with Ag(I),[8,9] and Cu(I)[10] – often with different ancillary ligands – were reported, mainly by Kirillov, Pombeiro and co-workers. In these structures PTA assumes double (κ^2*P,N*), triple (κ^3*P,2N*) and even quadruple (κ^4*P,3N*) bridging coordination modes. An example of

homometallic mixed-valence Cu(I/II) polymeric network, in which PTA binds to Cu(I) with the soft P atom and to Cu(II) with the hard N atom was also described.[11] Taken together, the results with Ag(I) and Cu(I) suggest that these metal ions are rather promiscuous towards PTA, without a marked preference for N- or P-bonding.

There are instead relatively few examples of complexes containing exclusively N-bonded PTA (PTA-κ*N*). They concern hard metal ions such as Mn(II) and Co(II),[12,13] or the d^{10} metal ion Zn(II). After the first Zn-PTA complex – the distorted tetrahedral $[ZnCl_2(PTA\text{-}\kappa N)_2]$ – was described in 2009 by Pombeiro and co-workers,[14] Reek, Kleij et al. investigated the reactivity of PTA with a number of square-planar Zn(salphen) complexes (salphen = N,N′-bis(salicylidene)imine-1,2-phenylenediamine) in the context of supramolecular catalysis. It was found that PTA binds to zinc exclusively through the N atoms and can act as a bridge between two or even three Zn(salphen) units, giving $[\{Zn(salphen)\}_2(PTA\text{-}\kappa^2 N)]$ and $[\{Zn(salphen)\}_3(PTA\text{-}\kappa^3 N)]$ adducts in which the zinc ions have a distorted square planar geometry.[15]

In the past we and others have explored the coordination chemistry of PTA towards Ru-compounds (where it binds through P exclusively).[16,17] We have also largely exploited the axial coordination of Ru and Zn porphyrins towards polydentate pyridyl ligands for the construction of numerous supramolecular assemblies.[18,19] Considering that, according to the literature, PTA binds always through P to ruthenium and through N to zinc, we reasoned that it might be exploited as an orthogonal bridging ligand for the preparation of hetero-bimetallic supramolecular assemblies and/or polymeric networks containing Ru- and Zn-porphyrins. In addition, the presence of PTA might improve their solubility in water or at least in protic solvents.

Phosphine ligands have high association constants with Ru-porphyrins, in the range of 10^6 to 10^8 M^{-1},[20] whereas N ligands, in particular hard tertiary amines, have lower constants. For example, it has been reported that $Ph_2P(CH_2)_2NEt_2$ binds to ruthenium porphyrins exclusively through P and the NEt_2 group remains dangling.[21] Zn-porphyrins make less robust axial bonds with N-ligands (compared to Ru), that depend also on N hybridization. For example, the association constant of pyridine with Zn(TPP) (TPP = *meso*-tetraphenylporphyrin) was found to be 7.7×10^3 M^{-1} (CH_2Cl_2, 25°C), whereas under the same – or very similar – conditions amines (including tertiary amines) have ca. ten-fold larger association constants.[22,23] By comparison, hexamethylenetetramine (HTMA) – the all-nitrogen analogue of PTA – was found to make stronger axial bonds with Zn-porphyrins compared to pyridyl functions (probably also because of its low steric demand),[24] and binding constants in the range 10^5 to 10^6 M^{-1} were measured for the axial N-binding of PTA to square planar Zn(salphen) complexes in toluene.[15]

The interactions of PTA with Ru- and Zn-porphyrins have not been investigated before. Thus, in this work we first established the coordination mode of this ligand towards the neutral model metallo-porphyrins [Ru(TPP)(CO)] and Zn(TPP), obtaining the monomeric adducts [Ru(TPP)(PTA-κ*P*)$_2$] (**28**) and [Zn(TPP)(PTA-κ*N*)] (**30**), in which PTA is axially bound to the metal inside the porphyrin. Then, we prepared and structurally characterized a number of hetero-bimetallic Ru/Zn porphyrin polymeric networks mediated by *P,N*-bridging PTA (PTA-κ^2*P,N*) and, in one case, (PTA-κ^3*P*,*2N*). In such assemblies either both metal centers reside inside a porphyrin core or one of the two belongs to a coordination compound. Our findings demonstrate that indeed PTA behaves as a selective orthogonal ligand, binding to Ru exclusively through the P atom and to Zn exclusively through the N atoms.

5.2 Results and Discussion

5.2.1 Reactivity of [Ru(TPP)(CO)] towards PTA

It is well known from the literature that whereas pyridine or azole ligands (N) replace the labile solvent molecule *trans* to CO in [Ru(por)(CO)(S)] compounds (e.g. por = TPP; S = MeOH or EtOH, typically not indicated in the formula), affording derivatives of the general formula [Ru(por)(CO)(N)],[25-28] most phosphine and phosphite ligands (P) under mild conditions replace easily also the carbonyl ligand yielding di-substituted compounds of formula [Ru(por)(P)$_2$].[20,29-35] Mono-substituted [Ru(por)(CO)(P)] intermediates with tertiary phosphines have been occasionally isolated,[31] whereas in most other cases, due to the weakening of the carbonyl ligand by the phosphine *trans* effect, they could not be isolated but were characterized spectroscopically in solution.[20a] To our knowledge, with the exception of a private communication from Sanders and co-workers,[36] no X-ray structure of such an intermediate has been reported yet.

We found that PTA reacts with [Ru(TPP)(CO)] as most other phosphines. When treated with a slight excess of PTA in chloroform solution at room temperature, [Ru(TPP)(CO)] rapidly affords [Ru(TPP)(PTA-κ*P*)$_2$] (**28**) in high yield. Axial coordination of two *trans* PTA moieties, bound through the P atom, was clearly evident from NMR spectroscopy (Figure 5.1). The ^{31}P resonance, that is not significantly influenced by the porphyrin shielding cone, occurs as a singlet at –50.6 ppm, i.e. in the typical region for mutually *trans* PTAs coordinated to Ru(II).[16c] The ^{1}H resonances of the PTA methylene protons, and that of the PCH$_2$N protons in particular, are shifted to lower frequencies compared to free PTA because the protons fall in the shielding cone of the porphyrin. Thus, the NCH$_2$N protons resonate as two well resolved doublets (6H each) at 3.21 e 2.55 ppm,[37] whereas the PCH$_2$N protons, closer to the macrocycle, give a singlet (12H) at –0.26 ppm. The assignments were

confirmed by the HSQC spectrum (Appendix), since the corresponding carbon atoms have characteristic and well-resolved resonances that are only marginally affected by coordination.[1] The Hβ singlet of TPP is shifted to lower frequencies by ca. 0.35 ppm by the replacement of CO with two PTAs. Even though the chemical shifts of the phenyl signals are not particularly affected, by virtue of the increased symmetry the *o*H resonance – that was split into two well resolved doublets in the spectrum of [Ru(TPP)(CO)] – is a sharp doublet in that of [Ru(TPP)(PTA-κ*P*)$_2$] (Figure 5.1 and Appendix). Consistent with what found with similar [Ru(por)(P)$_2$] adducts ,[20,29-35] the Soret band in the electronic absorption spectrum of **28** is considerably red-shifted compared to [Ru(TPP)(CO)] (431 vs 408 nm).

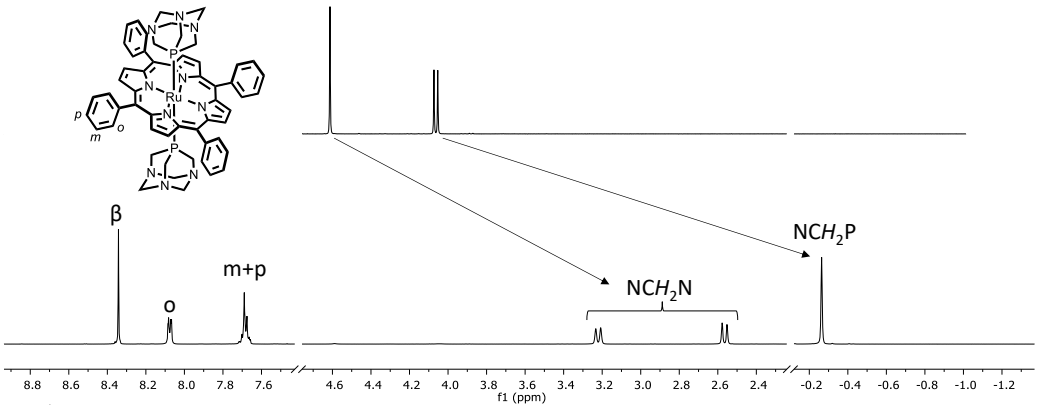

Figure 5.1 ^{1}H NMR spectra ($CDCl_3$) of PTA (top) and [Ru(TPP)(PTA-κ*P*)$_2$] (**28**) (bottom).

The geometry of **28** was confirmed by single crystal X-ray analysis (Figure 5.2). The Ru–P distance in **28** compares well with those in similar [Ru(por)(P)$_2$] compounds as well as with Ru(II) coordination compounds that feature the {*trans*-Ru(PTA-κ*P*)$_2$} fragment (Table 5.1).[16,20,31]

Table 5.1. Ru–(PTA κ*P*) bond lengths in the X-ray structurally characterized compounds.

Compound	Ru–P distance (Å)	Ref.
[Ru(TPP)(PTA-κ*P*)$_2$] (**1**)	2.3253(7)	t.w.
[Ru(TPP)(dpm)$_2$] (dpm = diphenylphosphinomethane)	2.398(3)	31a
[Ru(OEP)(PPh_3)$_2$] (OEP = octaethylporphyrin)	2.428 (average)	31c
[Ru(OEP)(dpap)$_2$] (dpap = diphenyl phenylacetylene phosphine)	2.3777(5)	20c
[Ru(DPP)(dpap)$_2$] (DPP = 5,15-bis(3′,5′-di-*tert*-butyl)phenyl-2,8,12,18-tetraethyl-3,7,13,17-tetramethylporphyrin)	2.340(5) – 2.3623(10)	20a
[Ru(TPP)(dpap)$_2$]	2.3597(10) – 2.3784(10)	20c
Ru(II) compounds with {*trans*-Ru(PTA-κ*P*)$_2$} fragment	2.290 – 2.400	16c

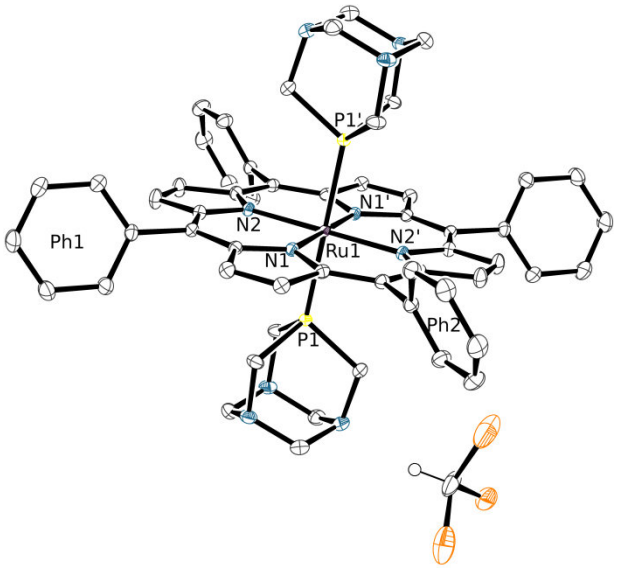

t.w. = this work.

Figure 5.2. ORTEP representation (50% probability ellipsoids) of the solid state molecular structure of [Ru(TPP)(PTA-κ*P*)$_2$]·2CHCl$_3$ (**28**·2CHCl$_3$). Primed atoms are symmetry mates via (1-x,1-y,1-z). Only one of the two symmetry related CHCl$_3$ crystallization molecules is shown. The H atoms of the complex are omitted for clarity. The Ph1 and Ph2 labels allow to visualize on the figure the dihedral angles reported in Table A5.2 (Appendix).

Finally, compound **28** was rapidly obtained at room temperature also upon addition of two equiv of PTA to a CDCl$_3$ solution of [Ru(TPP)(CO)(py)] (py = pyridine), thus demonstrating that, besides ethanol, PTA readily replaces also axially-bound pyridine.

Regretfully, compound **28** was found to be completely insoluble is water, even at acidic pH where protonation of PTA would be expected to improve solubility. For instance, the Ru(0) cluster Ru$_3$(CO)$_9$(PTA)$_3$ can be extracted from a chloroform solution into acidic water (pH < 4).[38]

An NMR titration of PTA into a CDCl$_3$ solution of [Ru(TPP)(CO)] allowed us to detect the resonances of the elusive intermediate species [Ru(TPP)(CO)(PTA-κ*P*)] (**29**). The PTA singlet of **29** in the ^{31}P{^{1}H}NMR spectrum (Appendix, Figure A.5.4) is remarkably shifted compared to **28** and falls at –60.5 ppm (Appendix), i.e. in the typical spectral region of PTA *trans* to CO in Ru(II) compounds.[16] The ^{1}H NMR features of **29** (Appendix, Figure A5.5) are rather similar to those of **28** in terms of chemical shifts, the most noticeable difference being the split resonance of the *o*H and *m*H protons due to the absence of the macrocycle mirror plane (as in the precursor) that makes the α- and β-side of the porphyrin inequivalent. The solution CO stretching frequency in **29** falls at 1989 cm^{-1}.[39]

5.2.2 Interaction of PTA with Zn(TPP)

The interaction of PTA with the model zinc-porphyrin Zn(TPP) was investigated in chloroform solution. The occurrence of the axial binding of PTA to Zn(TPP) was evident from an NMR titration, in which the PTA/Zn(TPP) ratio ranged from 0.5 to 5. For each PTA/Ru ratio the $^{31}P\{^{1}H\}$ resonance of PTA occurred as a singlet at ca. –102.1 ppm (i.e. the same chemical shift of free PTA).Whereas the ^{1}H resonances of Zn(TPP) were only slightly affected, those of PTA were broadened and shifted to lower frequencies compared to the free ligand (Appendix, Figure A5.6). At PTA/Zn(TPP) = 0.5 the PTA protons gave two equally intense broad resonances, a singlet at ca. 0.9 ppm and a doublet centered at ca. 0.1 ppm. Upon increasing the PTA/Zn ratio the upfield shift of the PTA resonances progressively decreased.

The NMR findings are consistent with the occurrence of relatively weak and reversible axial interactions between PTA and Zn(TPP), in an equilibrium that is fast on the NMR time scale: the chemical shifts of the PTA resonances are a weighed average between those of PTA axially bound to Zn(TPP), and thus upfield shifted, and those of the free ligand. Actually, assuming that such interaction involves the N atoms of PTA, multiple equilibria can occur as in the case of Zn(salphen)–(PTA-κ*N*) adducts, where PTA can bind axially up to three Zn(salphen) units.[15] In addition, even though zinc-porphyrins are expected to bind preferentially one axial N ligand making square pyramidal adducts, the formation of octahedral products with two axial ligands is not uncommon and cannot be excluded.[24,40-45] Thus, the NMR spectrum is expected to depend also on the concentration and temperature, in addition to the PTA/Zn ratio. To be noted that, consistent with N-coordination of PTA to Zn(TPP) (and contrary to what observed for **28**), in the ^{1}H NMR spectrum at high Zn(TPP)/PTA ratio the resonance of the NCH_2N protons is shifted more upfield than the NCH_2P resonance (Appendix, Figures A5.6 and A5.7).

Slow diffusion of diethyl ether onto the chloroform solution of the PTA/Zn(TPP) = 0.5 mixture afforded crystals of the discrete [Zn(TPP)(PTA-κ*N*)] adduct (**30**), whose X-ray structure is shown in Figure 5.3. As clear also from the lattice representation (Appendix, Figure A5.13), zinc is five-coordinate (i.e. binds to a single PTA molecule), and each PTA is bound to a single Zn(TPP) unit.

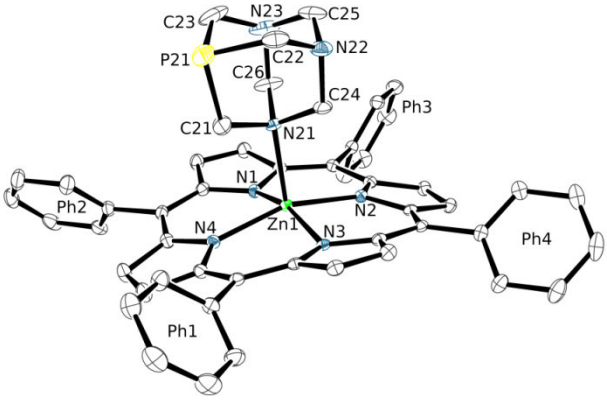

Figure 5.3. ORTEP representation (50% probability ellipsoids) of the crystal structure of complex [Zn(TPP)(PTA-κ*N*)]·H_2O·$CHCl_3$ (**30**·H_2O·$CHCl_3$); for the sake of clarity, H atoms, one disordered water, and one $CHCl_3$ crystallization molecule are omitted. The Ph1 – Ph4 labels allow to visualize on the figure the dihedral angles reported in Table A5.3 (Appendix).

As already observed for N-coordination of PTA, as well as for protonation and alkylation, the N21–C bond distances are slightly elongated – compared to the other N–C distances – upon coordination to Zn. The axial Zn–N(PTA) bond length is longer than in the distorted tetrahedral complex [$ZnCl_2$(PTA-κ*N*)$_2$][14] (and in similar complexes with O=PTA and S=PTA),[46] but compares rather well with those found in the square-pyramidal Zn(salphen)–(PTA-κ*N*) adducts where PTA occupies the axial position (Table 5.2).[15]

Table 5.2. Zn–(PTA-κ*N*) and Zn–(HTMA-κ*N*) bond lengths in the X-ray structurally characterized compounds.

Compound	Axial Zn–N distance (Å)	Ref.
[Zn(TPP)(PTA-κ*N*)] (**30**)	2.186(2)	t.w.
[$ZnCl_2$(PTA-κ*N*)$_2$]	2.055(3) – 2.101(3)	14
[$ZnCl_2$(O=PTA-κ*N*)(OH_2)]	2.0931(10)	46
[{Zn(salphen)}$_2$(PTA-κ^2*N*)]	2.103(6), 2.172(7)	15
[{Zn(salphen)}$_3$(PTA-κ^3*N*)]	2.194(4), 2.201(4), 2.200(3)	15
[Zn(TOHPP)(HTMA)$_2$] (TOHPP = tetra(4-hydroxyphenyl)porphyrin,	2.520(2)	24
[Zn(TCPP)(HTMA)$_2$] (TCPP = tetra(4-carboxyphenyl)porphyrin)	2.510(2)	24
[Zn(TPyP)(HTMA)] (TPyP = tetra(4′-pyridyl)porphyrin)	2.189(3)	24

t.w. = this work

5.2.3 PTA-bridged hetero-bimetallic Ru/Zn compounds

The above results indicate that the axial binding of PTA towards Ru- and Zn-porphyrins is truly orthogonal and might be exploited to create hetero-dinuclear supramolecular porphyrin assemblies connected by bridging PTA moieties.

Thus, we investigated the interaction between [Ru(TPP)(PTA-κ*P*)$_2$] (**28**) and Zn(TPP). An NMR titration of Zn(TPP) into a $CDCl_3$ solution of **28**, in which the Zn(TPP)/**28** ratio ranged from 1 to 4 (Appendix, Figure A5.8) showed that the PTA resonances were broadened and gradually shifted to lower frequencies upon increasing the number of Zn(TPP) equivalents. Conversely, the resonances of the two porphyrins, as well as the $^{31}P\{^1H\}$ resonance of PTA, were only marginally affected. These findings are consistent with the establishment of an axial Zn–(PTA-κ*N*) labile interaction between the stable and inert Ru–(PTA-κ*P*) moieties and Zn(TPP). In further agreement with this hypothesis the final spectrum of this series was substantially coincident with that obtained by adding two equiv of PTA to a 1:4 mixture of [Ru(TPP)(CO)] and Zn(TPP) (Appendix, Figures A5.9 and A5.10), indicating that PTA discriminates between Ru and Zn even when is not preventively bound to Ru and in the presence of a stoichiometric excess of Zn.

X-ray quality single crystals of the 1D polymeric compound [{Ru(TPP)(PTA-κ^2*P,N*)$_2$}{Zn(TPP)}]$_\infty$ (**31**) were obtained by slow diffusion of *n*-hexane onto a chloroform solution of a mixture containing two equiv of Zn(TPP) per mole of **28**. The crystal structure of compound **31** consists of parallel zig-zag polymeric chains, oriented along the crystallographic *c* axis, each formed by a sequence of alternating Ru(TPP) and Zn(TPP) units (Figure 5.4).

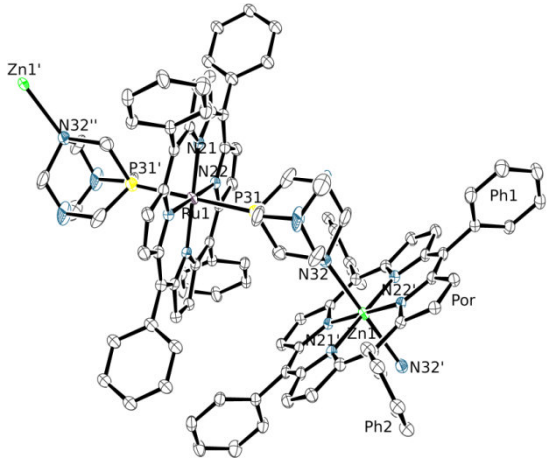

Figure 5.4 ORTEP representation (50% probability ellipsoids) of the "monomeric" unit of the polymeric zig-zag chains which constitute the crystal structure of compound [{Ru(TPP)(PTA-κ^2*P,N*)$_2$}{Zn(TPP)}]$_\infty$ (**31**) (hydrogen atoms and minor population of one disordered phenyl group omitted for clarity).[47] The connections of the monomeric unit with the infinite polymeric 1D chain are also evidenced. The Ph1 and Ph2 labels allow to visualize on the figure the dihedral angles reported in Table A5.4 (Appendix).

Adjacent Ru/Zn units are connected by a PTA bridging ligand which coordinates to Ru through the phosphorus atom and to Zn through one of the nitrogen atoms (Appendix, Figures A5.14-A5.16). Thus, both Ru and Zn are six-coordinate and feature two equal axial ligands. Each {*trans*-Ru(PTA)$_2$} unit binds two zinc atoms with *anti* geometry, thus generating the zig-zag motif. Since the equatorial environment of Ru and Zn is identical and the P/N bonding modes of the PTA ligand are nearly geometrically equivalent, the symmetry of the observed diffraction pattern (space group C2/c) does not distinguish the two metal ions and the corresponding PTA binding modes. This leads to a crystallographically independent fragment in which a single metal site (M) is equally partitioned between Ru and Zn and, correspondingly, two symmetry related binding sites (L) of the PTA are partitioned at 50% between P and N (Appendix). Consistently, the M–L bond distance of 2.3800(7) Å is intermediate between that of the Ru–(PTA-κ*P*) bond in [Ru(TPP)(PTA-κ*P*)$_2$] (**28**, 2.3253(7) Å, see above) and that of the Zn–(PTA-κ*N*) bond in the six-coordinate {Zn(TPP)(PTA-κ^2*P,N*)$_2$} fragment (2.534(2) Å, see below compound **33**). To be noted that the Zn–(PTA-κ*N*) bond length is remarkably shorter for five-coordinate [Zn(TPP)(PTA-κ*N*)] (**30**, Table 5.2). For comparison, the Zn–N bond lengths in similar six-coordinate zinc-porphyrin compounds with HTMA, [Zn(TOHPP)(HTMA)$_2$] and [Zn(TCPP)(HTMA)$_2$] (TOHPP = tetra(4-hydroxyphenyl)porphyrin, TCPP = tetra(4-carboxyphenyl)porphyrin), are remarkably larger than in the five-coordinate [Zn(TPyP)(HTMA)] (TPyP = tetra(4′-pyridyl)porphyrin) (Table 5.2).[24] When dissolved in chloroform, compound **31** disassembles into the components, as indicated by the NMR spectra (e.g. the ^{31}P NMR spectrum in $CDCl_3$ is coincident with that of **28**, see Experimentals).

Next, we addressed the preparation of PTA-bridged Ru/Zn species containing a single metallo-porphyrin, either Ru(TPP) or Zn(TPP), and a complex of the complementary metal, i.e. Zn(II) or Ru(II), respectively. As a first example we choose the symmetrical and coordinatively saturated Ru–PTA complex *cis,cis,trans*-[RuCl$_2$(CO)$_2$(PTA-κ*P*)$_2$] (**32**)[16c] that features the same {*trans*-Ru(PTA-κ*P*)$_2$} fragment as **28**. The results of an NMR titration of Zn(TPP) (from 2 to 4 equiv) into a $CDCl_3$ solution of **32** were similar to those described above with **28**, i.e. upfield shift and broadening of the PTA proton resonances (Appendix, Figure A5.11). Also in this case, the ^{31}P resonance was not particularly affected by the addition of Zn(TPP) and occurred as a singlet at –48.9 ppm (to be compared with –51.0 ppm in the free complex), indicating that the Ru complex remains intact.

X-ray quality single crystals of the 1D polymeric compound *cis,cis,trans*-[{Ru(CO)$_2$Cl$_2$(PTA-κ^2*P,N*)$_2$}{Zn(TPP)}]$_\infty$ (**33**) were obtained upon diffusion of diethyl ether onto a chloroform solution of a 2:1 mixture of Zn(TPP) and **32**. The crystal structure of compound **33** (Figure 5.5) is similar to that of **31** and consists of parallel polymeric chains in which the Zn atom of each Zn(TPP) is six-coordinate and binds axially two PTA ligands belonging to different Ru complexes. However, since

each Ru complex bridges two Zn(TPP) units with *syn* geometry, the resulting chain has "Greek frame" shape (rather than zig-zag as in **31**) (Appendix, Figure A5.17). The two polymeric chains of **31** and **33** are compared in Figure 5.6.

Figure 5.5 ORTEP representation (50% probability ellipsoids) of the "monomeric" unit of the

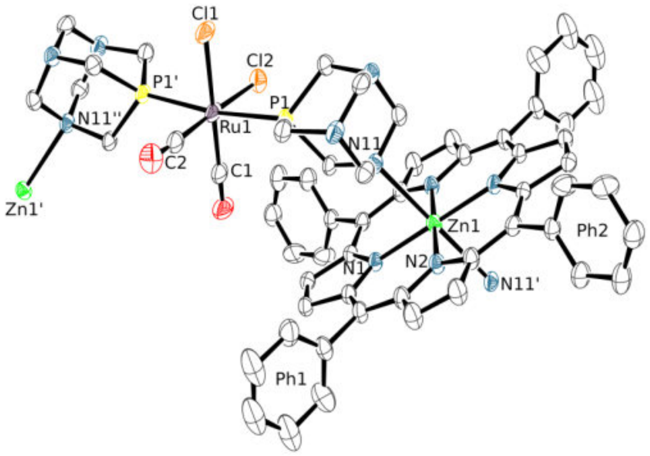

polymeric Ru-Zn chains which constitute the crystal structure of compound *cis,cis,trans*-[{$Ru(CO)_2Cl_2$(PTA-$\kappa^2 P,N)_2$}{Zn(TPP)}·9.2(H_2O)]$_\infty$ (**33**·9.2(H_2O)). The connections of the monomeric unit with the infinite polymeric 1D chain are also evidenced. Disordered cocrystallized water molecules (that do not interact with the chains) and hydrogen atoms are omitted for clarity. Only half of the Ru and Zn units are crystallographically independent. In the Ru complex, the *trans* C2 carbonyl and Cl2 ligands exchange their positions around a 2-fold axis due to disorder: only one of the two identical populations is represented.[48] Labels Ph1 and Ph2 allow to visualize on the figure the dihedral angles reported in Table A5.5 (Appendix).

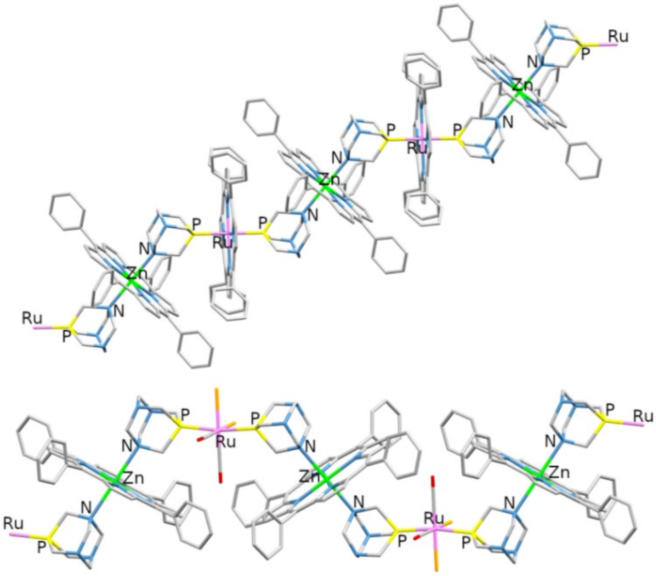

Figure 5.6. The zig-zag and "Greek frame" polymeric chains of [{Ru(TPP)(PTA-$\kappa^2 P,N)_2$}{Zn(TPP)}]$_\infty$ (**31**, top) and *cis,cis,trans*-[{$Ru(CO)_2Cl_2$(PTA-$\kappa^2 P,N)_2$}{Zn(TPP)}·9.2(H_2O)]$_\infty$ (**33**·9.2(H_2O), bottom), respectively, with the {*trans*-Ru$(PTA)_2$} fragments iso-oriented (crystallization molecules omitted). Color code: Ru = light purple, Zn = green, P = yellow, N = blue, O = red, Cl = orange.

Conversely, the crystallization of Zn(TPP) with another symmetrical Ru–PTA complex, *trans*-[$RuCl_2$(PTA-κ*P*)$_4$] (**34**),[16, 17] afforded different results, depending on the Zn/PTA ratio adopted. Using a stoichiometric or a slight excess of Zn(TPP) (i.e. Zn/PTA = 1 or 1.5) the discrete molecular species *trans*-[{$RuCl_2$(PTA-κ^2*P,N*)$_4$}{Zn(TPP)}$_4$] (**35**, Figure 5.7 and Appendix), in which each one of the four coplanar PTA ligands of **34** is axially bound through an N atom to a five-coordinate Zn(TPP), was obtained.

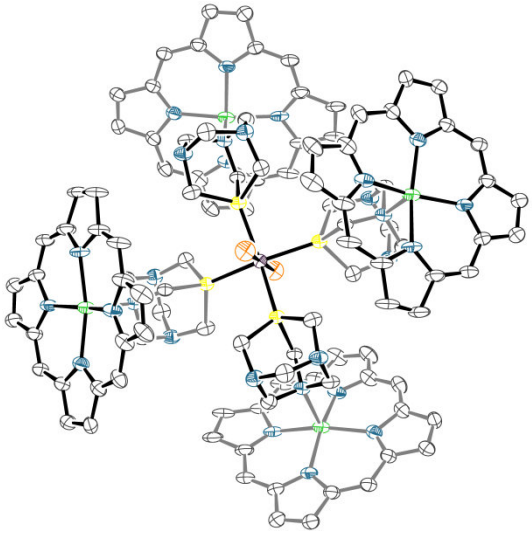

Figure 5.7 ORTEP representation (50% probability ellipsoids) of the molecule of compound *trans*-[{$RuCl_2$(μ-PTA-κ^2*P,N*)$_4$}{Zn(TPP)}$_4$]·8/3$CHCl_3$·2*n*-hexane (**35**·8/3$CHCl_3$·2*n*-hexane) in the crystal structure. The phenyl rings, hydrogen atoms, $CHCl_3$ and *n*-hexane solvent molecules are omitted for clarity. The bonds of the two porphyrins that lay below the equatorial plane of the Ru complex and of the two PTA moieties that are partially overlapped by the two upward porphyrins are in grey.

The four porphyrins in **35** lay alternatively above and below the equatorial plane of the Ru complex, generating a very compact arrangement (Appendix, Figure A5.21) that closely resembles that of the porphyrin pentamer [Zn(3′TPyP){Ru(TPP)(CO)}$_4$] (3′TPyP = 5,10,15,20-tetra(3′-pyridyl)porphyrin) described by us twenty years ago.[49] Similarly to what found for **33**, when redissolved in $CDCl_3$ the crystals of **35** give a singlet in the $^{31}P\{^1H\}$ NMR spectrum at –51.1 ppm (cfr –50.6 ppm in **34**).
Conversely, when a defect of Zn(TPP) was used (Zn/PTA = 0.5) crystals of the polymeric network *trans*-[{$RuCl_2$(PTA-κ^2*P,N*)$_4$}{Zn(TPP)}$_2$]$_\infty$ (**36**) were obtained. In **36**, each Ru center is surrounded by four Zn(TPP) units with a geometry very similar to that found in **35**. However, in this case the Zn atoms are six-coordinate thus originating a 3D polymeric network (Figure 5.8), a texture of orthogonal 1D threads that intersect each other at every Ru center (Figure 5.9). Each 1D thread of the network, originated by a {*trans*-Ru(PTA-κ^2*P,N*)$_2$} fragment, has the "Greek frame" shape found in **33**.

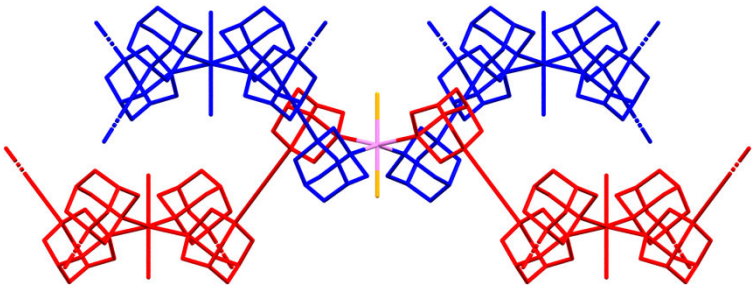

Figure 5.8 Crystal structure of compound *trans*-[{$RuCl_2$(PTA-κ^2*P,N*)$_4$}{Zn(TPP)}$_2$] (**36**): View along the b cell axis of six 1D chains (parallel to b and normal to the page), evidencing the parallel and interconnected planes formed by the Ru atoms. The interchain connections are built by PTA–ZnTPP–PTA bridges. When viewed along this direction, the plane of each porphyrin is normal to the page. The Ru atoms along the 1D chains are alternatively connected also to pairs of Ru atoms in adjacent threads that lay in the plane above and below, respectively. Color code: Ru (light purple), Zn (green), P (yellow), N (blue).

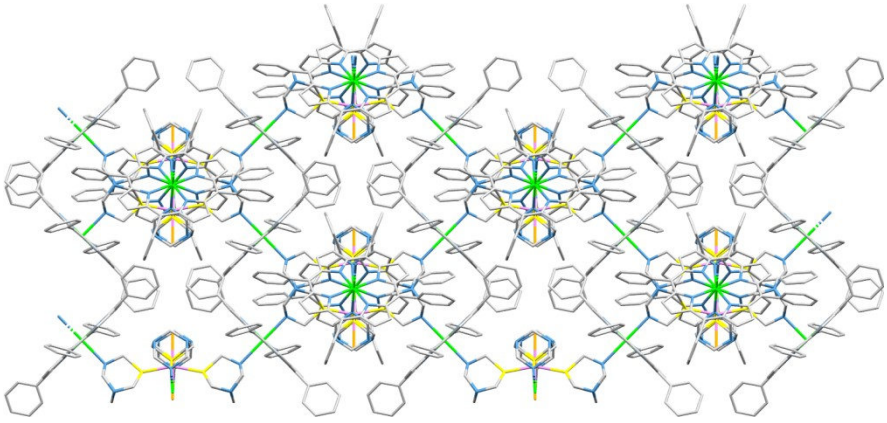

Figure 5.9 Schematic crystal structure of compound *trans*-[{$RuCl_2$(PTA-κ^2*P,N*)$_4$}{Zn(TPP)}$_2$] (**36**): Perspective view (porphyrins omitted) of two orthogonal {Ru(PTA-κ^2*P,N*)Zn}$_\infty$ 1D chains (red and blue) crossing at a Ru center in the crystal structure of complex **36**. The Zn atom is located half-way between the pairs of PTA ligands of any two neighboring Ru moieties.

Consistent with what observed above (Table 5.2), the axial Zn–N bond length in six-coordinate **36** (2.4869(2) Å) is similar to that found in **33** (2.534(2) Å), and remarkably longer than in five-coordinate **35** (2.242(6) Å).

The crystallization of [Ru(TPP)(PTA-κ*P*)$_2$] (**28**) with a ca. 8:1 excess of $Zn(CH_3COO)_2$ afforded crystals of [{Ru(TPP)(PTA-κ^3*P,2N*)$_2$}{$Zn_9(CH_3COO)_{16}(CH_3OH)_2(OH)_2$}·3$CHCl_3$]$_\infty$ (**37**·3$CHCl_3$). The crystal structure of compound **37** (Figure 5.10) can be described as a stack of 2D polymeric layers, almost perfectly parallel to the plane defined by the b axis and the diagonal of the ac face of the unit cell. Each polymeric layer contains the Ru porphyrin and an intricate neutral Zn-acetate cluster in 1:1 ratio (for the description of the Zn_9 cluster see the Appendix). The Ru and the central Zn atom (Zn4) sit on inversion points, so that only half of the Ru porphyrin and Zn cluster are crystallographically independent. Four Zn atoms of each cluster are N-bound to four PTA ligands of different Ru(TPP) units and, correspondingly, each Ru porphyrin connects with four Zn clusters, two

for each axial PTA ligand (Figure 5.11). Thus, in this case PTA has a triple-bridging $\kappa^3P,2N$ binding mode.

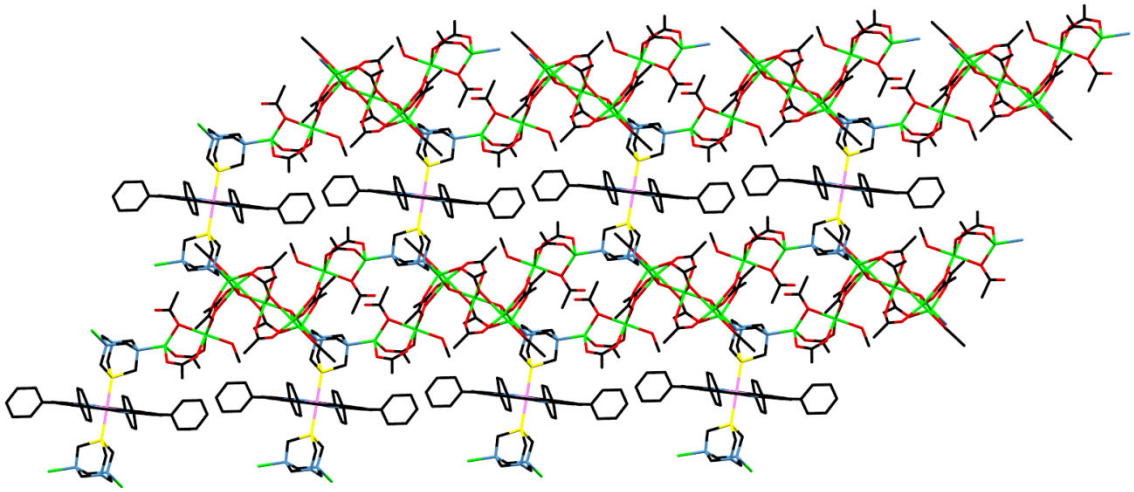

Figure 5.10 Stick representation of a portion of one of the 2D parallel polymeric layers that constitute the crystal structure of compound [{Ru(TPP)(PTA-$\kappa^3P,2N$)$_2$}{Zn$_9$(CH$_3$COO)$_{16}$(CH$_3$OH)$_2$(OH)$_2$}·3CHCl$_3$]$_\infty$ (**37**·3CHCl$_3$). Color code: Ru (light purple), Zn (green), P (yellow), N (blue), O (red).

Due to the layered structure, the unit cell contains a cavity whose volume amounts to 16% of the total (see Experimental).

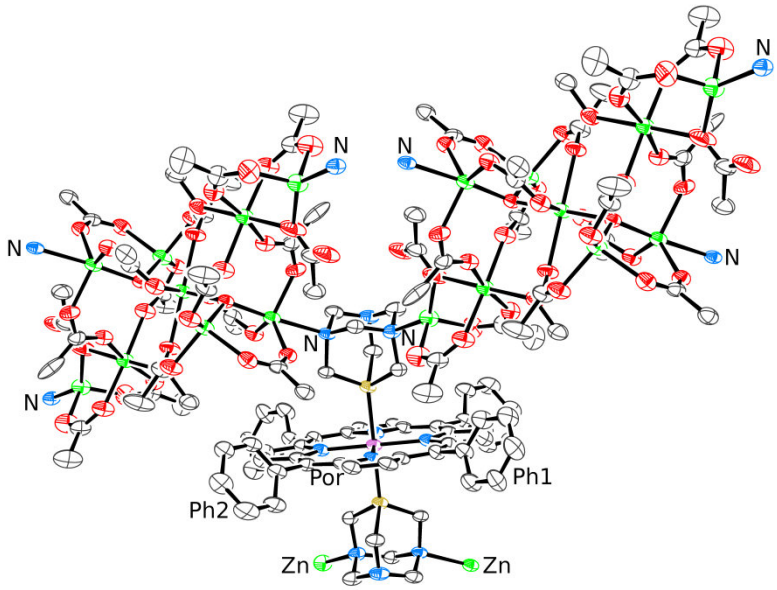

Figure 5.11 ORTEP representation of a fragment of the structure of compound [{Ru(TPP)(PTA-$\kappa^3P,2N$)$_2$}{Zn$_9$(CH$_3$COO)$_{16}$(CH$_3$OH)$_2$(OH)$_2$}·3CHCl$_3$]$_\infty$ (**37**·3CHCl$_3$) showing one {Ru(TPP)(PTA-$\kappa^3P,2N$)$_2$} unit with two polynuclear Zn moieties, each one connected to two N atoms of one of the PTA axial ligands. The two N–Zn bonds connecting the second (lower) PTA ligand to corresponding Zn clusters are also shown, together with the four connections of each Zn cluster with the N atoms of PTA ligands belonging to four distinct [{Ru(TPP)(PTA-$\kappa^3P,2N$)$_2$} units. Labels Ph1 and Ph2 allow to visualize on the figure the dihedral angles reported in Table A5.8. Color code: Ru (light purple), Zn (green), P (yellow), N (blue), O (red).

By changing the nature of the zinc salt a remarkably different compound was obtained. In fact, diffusion of *n*-hexane into a chloroform/ethanol solution of a 1:2 mixture of **28** with $ZnCl_2$ afforded crystals of the dinuclear compound [{Ru(TPP)(PTA-κ*P*)(PTA-κ^2*P,N*)}{$ZnCl_2(OH_2)$}] (**38**) in which one of the two *trans* PTA-κ*P* ligands of **28** binds through an N atom to a {$ZnCl_2(OH_2)$} fragment (Figure 5.12). The distorted tetrahedral coordination environment of the Zn atom is similar to that found in [$ZnCl_2(OH_2)$(PTA=O)].[46] The crystal structure consists of an arrangement of parallel 1D sequences of molecules of complex **38**, oriented along the [101] direction, with a shape that closely resembles the "Greek frame" found in **33** and **36** (Appendix, Figure A5.25). Regretfully, due to the low quality of the X-ray data (see also the Experimentals for details) the expected slight elongation of the PTA C–N11(Zn) bond distances could not be detected.[50]

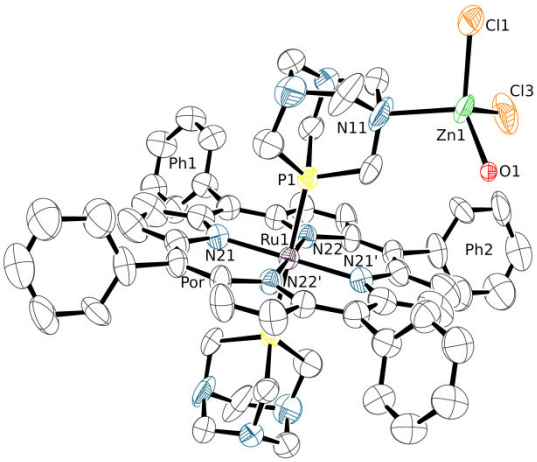

Figure 5.12 ORTEP representation (50% probability ellipsoids) of compound [{Ru(TPP)(PTA-κ*P*)(PTA-κ^2*P,N*)}{$ZnCl_2(OH_2)$}·0.6$CHCl_3$] (**38**·0.6$CHCl_3$). Only the major population (SOF = 0.3) of the disordered {$ZnCl_2(OH_2)$} group has been represented. Primed labels indicate symmetry mates. Hydrogen atoms and a disordered $CHCl_3$ crystallization molecule are omitted for clarity. Labels Ph1 and Ph2 allow to visualize on the figure the dihedral angles reported in Table A5.9. Color code: Ru (light purple), Zn (green), P (yellow), N (blue), Cl (orange).

5.3 Conclusions

We demonstrated that PTA (1,3,5-triaza-7-phosphaadamantane) behaves as an orthogonal ligand between Ru(II) and Zn(II), since it selectively binds through the P atom to ruthenium and through one or more of the N atoms to zinc. This property of PTA was first exploited by us for preparing the two monomeric porphyrin adducts [Ru(TPP)(PTA-κ*P*)$_2$] (**28**) and [Zn(TPP)(PTA-κ*N*)] adduct (**30**), in which PTA is axially bound to the inner metal. Then, we prepared a number of hetero-bimetallic Ru/Zn porphyrin polymeric networks – and two discrete species – mediated by *P,N*-bridging PTA in

which either both metals reside inside a porphyrin core, or one metal belongs to a porphyrin, either Ru(TPP) or Zn(TPP), and the other to a complex or salt of the complementary metal (i.e. *cis,cis,trans*-$[RuCl_2(CO)_2(PTA\text{-}\kappa P)_2]$ (**32**), *trans*-$[RuCl_2(PTA\text{-}\kappa P)_4]$ (**34**), $Zn(CH_3COO)_2$, and $ZnCl_2$). Both the molecular compounds **28**, **30**, *trans*-$[RuCl_2(PTA\text{-}\kappa^2 P,N)_4\}\{Zn(TPP)\}_4]$ (**35**), and $[\{Ru(TPP)(PTA\text{-}\kappa P)(PTA\text{-}\kappa^2 P,N)\}\{ZnCl_2(OH_2)\}]$ (**38**), and the polymeric species $[\{Ru(TPP)(PTA\text{-}\kappa^2 P,N)_2\}\{Zn(TPP)\}]_\infty$ (**31**), *cis,cis,trans*-$[\{Ru(CO)_2Cl_2(PTA\text{-}\kappa^2 P,N)_2\{Zn(TPP)\}]_\infty$ (**33**), *trans*-$[\{RuCl_2(PTA\text{-}\kappa^2 P,N)_4\}\{Zn(TPP)\}_2]_\infty$ (**36**), and $[\{Ru(TPP)(PTA\text{-}\kappa^3 P,2N)_2\}\{Zn_9(CH_3COO)_{16}(CH_3OH)_2(OH)_2\}]_\infty$ (**37**) have been structurally characterized by single crystal X-ray diffraction. The number of compounds with the relatively rare six-coordinate Zn(TPP) (three, the polymeric networks of **31**, **33** and **36**, out of five) is largely above-average (see ref. 45), strongly suggesting that the stereo-electronic features of PTA are particularly well-suited for this type of coordination. In **31**, **33**, **35**, **36**, and **38** the bridging PTA has the $\kappa^2 P,N$ binding mode, whereas in the 2D polymeric layers of **37** it has the triple-bridging mode $\kappa^3 P,2N$. In one case we demonstrated that, by tuning the PTA/Zn(TPP) ratio, it is possible to control the number of axial Zn–N coordination bonds and thus to switch from a molecular species (**35**, five-coordinate Zn) to a 2D polymeric network (**36**, six-coordinate Zn). Similarly, we are confident that also in the case of **38** by operating at higher Ru/$ZnCl_2$ ratios a second PTA ligand (from a different **28**) is likely to replace the residual water molecule on the Zn fragment, thus affording a polymeric network upon crystallization. Interestingly, we also found that when Zn(TPP) is sandwiched between two {*trans*-$Ru(PTA\text{-}\kappa^2 P,N)_2$} fragments, similar 1D polymeric chains with two different shapes – zig-zag in **31** vs "Greek frame" in **33** and **36** – are obtained depending on whether the connecting bonds of each Ru fragment have an *anti* (**31**) or *syn* geometry (**33** and **36**).

Due to the rather weak and labile nature of the Zn–N(PTA) bond, and consistent with literature data about Zn-PTA adducts,[14,15,46] the compounds are not stable in solution and disassemble into the mononuclear fragments in concentration-dependent equilibria. Thus, their main interest resides in solid-state features. Porphyrin MOFs[51] – of which compounds **31**, **33**, **36**, and **37** are the first examples mediated by PTA – are extensively investigated in several fields, such as light-harvesting, guest inclusion, photodynamic therapy, and (photo)catalysis.[52]

We believe that the examples reported here represent robust proofs-of-concept that firmly establish the binding preferences of PTA towards Ru(II) and Zn(II), and are confident that a variety of discrete species and networks can be produced by changing the nature of the Ru and Zn partners and their ratio. In particular, there are several inert Ru(II) compounds (in addition to **32** and **34**) that feature two or more P-bonded PTA ligands that might be exploited as linkers of well-defined geometry for the rational design of solid state networks with Zn-porphyrins (or other Zn compounds). The

remaining ancillary ligands on the Ru center would allow to fine-tune the properties of the network, e.g. by providing interactions for the selective binding of host molecules. Finally, the uncoordinated N atoms of PTA in the networks might undergo protonation, thus introducing positive charges and the possibility of making additional electrostatic and H-bonding interactions.

5.4 Experimental section

Materials

All chemicals, including TLC silica gel plates, were purchased from Sigma-Aldrich and used as received. Solvents were of reagent grade. The ruthenium precursor *cis,cis,trans*-[$RuCl_2(CO)_2$(PTA-κ*P*)$_2$] (**32**),[16c] *trans*-[$RuCl_2$(PTA-κ*P*)$_4$] (**34**),[16a,17] and the porphyrins TPP,[53] [Ru(TPP)(CO)],[54] and Zn(TPP) were synthesized and purified as previously reported by us or by others.[55]

Instrumental methods

Mono- and bi-dimensional (^{1}H-^{1}H COSY, ^{1}H-^{13}C HSQC) NMR spectra were recorded at room temperature on a Varian 400 or 500 spectrometer (^{1}H: 400 or 500 MHz, ^{31}P{^{1}H}: 161 or 202 MHz). ^{1}H chemical shifts in $CDCl_3$ were referenced to the peak of residual non-deuterated solvent (δ = 7.26). ^{31}P{^{1}H} chemical shifts were measured relative to external 85% H_3PO_4 at 0.00 ppm. ESI mass spectra were collected in the positive mode on a Perkin-Elmer APII spectrometer at 5600 eV. The UV-vis spectra were obtained on an Agilent Cary 60 spectrophotometer, using 1.0 cm path-length quartz cuvettes (3.0 mL). Chloroform spectra in the CO stretching region were recorded between CaF_2 windows (0.5 mm spacer) on a Perkin-Elmer Fourier-transform IR/Raman 2000 instrument in the transmission mode. Elemental analyses were performed on a Thermo Flash 2000 CHNS/O analyzer in the Department of Chemistry of the University of Bologna (Italy).

X-ray diffraction

Data collections were performed at the X-ray diffraction beamline (XRD1) of the Elettra Synchrotron of Trieste (Italy) equipped with a Pilatus 2M image plate detector.

Collection temperature was 100K (nitrogen stream supplied through an Oxford Cryostream 700); the wavelength of the monochromatic X-ray beam was 0.700 Å and the diffractograms were obtained with the rotating crystal method. The crystals were dipped in N-paratone and mounted on the goniometer head with a nylon loop. The diffraction data were indexed, integrated and scaled using the XDS code.[56] The structures were solved by the dual space algorithm implemented in the SHELXT code.[57] Fourier analysis and refinement were performed by the full-matrix least-squares methods based on F^2 implemented in SHELXL.[58] The Coot program was used for modeling.[59] Anisotropic

thermal motion was allowed for all non-hydrogen atoms. Hydrogen atoms were placed at calculated positions with isotropic factors U = 1.2×U_{eq}, where U_{eq} is the equivalent isotropic thermal factor of the bonded non hydrogen atom. Crystal data and details of refinements are in the Appendix.

In the case of compound **33** an initial refinement of the structure afforded an R value of 12.78% and two Fourier peaks at unreasonable positions; a first intense peak was found at about 0.90 Å from the Ru atom, while a second less intense peak was located between the N atoms of two PTA ligands of adjacent chains, making completely unreasonable bonding angles. This made us suspect the presence of a lattice translocation defect (LTD).[60] This suspicion was reinforced by the inspection of the diffractograms, where alternating rows of well-defined and streaky spots were apparent. A translocation vector *(0,1/2,1/2)* could be found by assuming that the intense peak near the Ru site was due to another Ru atom of the translocated lattice and by matching the distance of the LTD peak from the Ru site (at *(1/2,0.79,1/2)*). The measured reflection intensities were then corrected according to eq. 3 in reference 60. An optimal value of 0.094 for the translocated cell fraction could be found by trial and error until the intensities of the two peaks due to the LTD were reduced to negligible values.

For compound **36** no Fourier peaks of appreciable intensity could be located inside the mentioned cavity, which was then assumed to contain heavily disordered methanol solvent molecules and modeled with the Squeeze procedure of the PLATON code.[61] The "squeezed" electronic charge was 148 (in electron charge units), corresponding to about eight methanol solvent molecules.

In the asymmetric unit of the crystal structure of complex **38**, the {$ZnCl_2(OH_2)$} group is very close to a 2-fold axis, thus ruling out the possibility that it is present on both PTA ligands of the *same* Ru complex: in this case, two {$ZnCl_2(OH_2)$} groups of adjacent Ru complexes would overlap (Appendix, Figure 5.25). For this reason we refined a model in which the {$ZnCl_2(OH_2)$} has a total occupation factor of 0.5, which ensures a Ru:Zn ratio of 1:1 (also the Ru atom sits on a special position with occupation factor 0.5). An additional complication is that the {$ZnCl_2(OH_2)$} group is disordered over two positions, which led to a further partition of the 0.5 occupation factor into two populations with occupations of 0.3 and 0.2, respectively (Appendix, Figure 5.26).

Synthesis of the complexes

[Ru(TPP)(PTA-κ*P*)$_2$] (28). A 20 mg amount of [Ru(TPP)(CO)] (0.027 mmol) was dissolved in 8 mL of chloroform, obtaining a clear red-purple solution. Upon addition of 2.4 equiv of PTA (10 mg) the solution became immediately darker. The solution was concentrated to ca. 2 mL. Slow evaporation of the solvent afforded within a few hours X-ray quality purple crystals of [Ru(TPP)(PTA-κ*P*)$_2$]· 2$CHCl_3$ that were filtered after 24h, washed with diethyl ether and dried *in vacuo.* (Yield 25.0 mg, 90%). Elemental analysis calcd for [$C_{56}H_{52}N_{10}P_2Ru$]·2($CHCl_3$) (M_w: 1266.9): C 54.99; H 4.30; N 11.06. Found: C 54.90; H 4.36; N 11.12. ^{1}H NMR ($CDCl_3$), δ (ppm): 8.34 (s, 8H,

β), 8.06 (m, 8H, *o*), 7.67 (m, 12H, *m*+*p*), 3.20 (d, *J* = 12.9 Hz, 6H NC*H*$_2$N), 2.55 (d, *J* = 12.9 Hz, 6H NC*H*$_2$N), –0.26 (br s, 12H NC*H*$_2$P). Selected ^{13}C NMR signals (from the HSQC spectrum) in $CDCl_3$, δ (ppm): 133.8 (*o*), 131.9 (β), 126.8 (*m*+*p*), 71.3 (N*C*H$_2$N), 45.0 (N*C*H$_2$P). ^{31}P{^{1}H} NMR ($CDCl_3$), δ (ppm): –50.6 (s, 2P, mutually *trans* PTAs). ESI mass spectrum (m/z): 1020.1 ([M+H]$^+$), 874.1 ([M–PTA+H]$^+$), 718.1 ([M–2PTA+H]$^+$). UV-vis ($CHCl_3$): λ_{max} (ε, L mol^{-1} cm^{-1}) = 431 (125400), 523 (8300), 554 (5400) nm.

[Ru(TPP)(CO)(PTA-κ*P*)] (28). As said in the text, this elusive intermediate was observed during the titration of [Ru(TPP)(CO)] with PTA but could not be isolated. ^{1}H NMR ($CDCl_3$), δ (ppm): 8.62 (s, 8H, β), 8.24, 8.02 (m, 8H, *o*+*o'*), 7.68 (m, 12H, *m*+*m'*+*p*), 3.11 (d, *J* = 13.0 Hz, 3H NC*H*$_2$N), 2.39 (d, *J* = 13.0 Hz, 3H NC*H*$_2$N), –0.71 (br s, 6H NC*H*$_2$P). ^{31}P{^{1}H} NMR ($CDCl_3$), δ (ppm): –60.5 (s, 1P, PTA *trans* CO). Selected IR absorption (chloroform solution, cm^{-1}): 1989 (ν_{CO}).

The following preparations were performed on a small scale (max 5-6 mg of the limiting reagent) with the specific aim of obtaining X-ray quality single crystals by slow diffusion of a precipitating solvent into ca. millimolar solutions of the reagents in the indicated molar ratios. Yields were not measured. The ^{1}H NMR spectra of the adducts are not reported, since – due to the labile nature of the Zn–N bonds – they depend on the concentration. In the NMR titrations the metallo-porphyrin concentration was ca. 5 mM.

[Zn(TPP)(PTA-κ*N*)]·H$_2$O·CHCl$_3$ (30·H$_2$O·CHCl$_3$**).** Crystals of **30**·H$_2$O·CHCl$_3$ were obtained by slow diffusion of diethyl ether into a ca. 5 mM chloroform solution of a 2:1 Zn(TPP)/PTA mixture. ^{31}P{^{1}H} NMR ($CDCl_3$) δ (ppm): –102.1 (s).

[{Ru(TPP)(PTA-κ^2*P,N*)$_2$}{Zn(TPP)}]$_\infty$ (31). X-ray quality crystals of **31** were obtained upon diffusion of *n*-hexane into a chloroform solution of a ca. 3 mM 2:1 mixture of Zn(TPP) and **28**. ^{31}P{^{1}H} NMR ($CDCl_3$) δ (ppm): –50.1 (s).

***cis,cis,trans*-[{Ru(CO)$_2$Cl$_2$(PTA-κ^2*P,N*)$_2$}{Zn(TPP)}·9.2(H$_2$O)]$_\infty$ (33**·9.2(H$_2$O)**).** X-ray quality crystals of **33**·9.2(H$_2$O) were obtained upon diffusion of diethyl ether into a chloroform solution of a 1:2 mixture of *cis,cis,trans*-[RuCl$_2$(CO)$_2$(PTA-κ*P*)$_2$] (**32**, 6.1 mg, 0.011 mmol) and Zn(TPP) (2.5 mg, 2 equiv). ^{31}P{^{1}H} NMR ($CDCl_3$) δ (ppm): –49.0 (s).

***trans*-[{RuCl$_2$(PTA-κ^2*P,N*)$_4$}{Zn(TPP)}$_4$]**·8/3CHCl$_3$·2*n*-hexane **(35**·8/3CHCl$_3$·2*n*-hexane**).** X-ray quality crystals of **35**·8/3CHCl$_3$·2C$_6$H$_{14}$ were obtained upon diffusion of *n*-hexane into 5 mL of a 1:4 chloroform solution of *trans*-[RuCl$_2$(PTA-κ*P*)$_4$] (**34**, 5.3 mg, 0.0062 mmol) and Zn(TPP) (17.9 mg, 4 equiv). ^{31}P{^{1}H} NMR ($CDCl_3$) δ (ppm): –51.1 (s).

***trans*-[{RuCl$_2$(PTA-κ^2*P,N*)$_4$}{Zn(TPP)}$_2$·4CHCl$_3$]$_\infty$ (36**·4CHCl$_3$**).** X-ray quality crystals of **36**·4CHCl$_3$·were obtained upon diffusion of hexane into 4 mL of a 1:2 chloroform solution of *trans*-

[$RuCl_2$(PTA-κ*P*)$_4$] (**34**, 5.0 mg, 0.0062 mmol) and Zn(TPP) (8.4 mg, 2 equiv). $^{31}P\{^1H\}$ NMR ($CDCl_3$) δ (ppm): –50.7 (s).

[{Ru(TPP)(PTA-κ^3*P,2N*)$_2$}{Zn$_9$(CH$_3$COO)$_{16}$(CH$_3$OH)$_2$(OH)$_2$}·3CHCl$_3$]$_\infty$ (37·3$CHCl_3$**).** X-ray quality crystals of **37**·3($CHCl_3$) were obtained by slow diffusion of *n*-hexane into 3 mL of a 5:1 chloroform/methanol solution of a ca. 8:1 mixture of $Zn(CH_3COO)_2$ and [Ru(TPP)(PTA-κ*P*)$_2$] (**28**, 3 mg, 0.0023 mmol).

[{Ru(TPP)(PTA-κ*P*) (PTA-κ^2*P,N*) }{ZnCl$_2$(OH$_2$)}·0.6CHCl$_3$] (38·0.6$CHCl_3$**).** X-ray quality crystals of **38**·0.6$CHCl_3$ were obtained by slow diffusion of *n*-hexane onto 2.4 mL of a 5:1 chloroform/ethanol solution of a 1:2 mixture of [Ru(TPP)(PTA-κ*P*)$_2$] (**28**, 3 mg, 0.0023 mmol) and $ZnCl_2$.

5.5 Bibliography

1 a) Phillips, A. D.; Gonsalvi, L.; Romerosa, A.; Vizza, F.; Peruzzini, M. Coordination Chemistry of 1,3,5-triaza-7-phosphaadamantane (PTA). Transition Metal Complexes and Related Catalytic, Medicinal and Photoluminescent Applications *Coord. Chem. Rev.,* **2004**, *248*, 955-993; b) Bravo, J.; Bolaño, S.; Gonsalvi, L.; Peruzzini, M. Coordination Chemistry of 1,3,5-triaza-7-phosphaadamantane (PTA) and Derivatives. Part II. The Quest for Tailored Ligands, Complexes and Related Applications *Coord. Chem. Rev.,* **2010**, *254*, 555-607; c) Guerriero, A.; Peruzzini, M.; Gonsalvi, L. Coordination Chemistry of 1,3,5-triaza-7-phosphatricyclo[3.3.1.1]decane (PTA) and Derivatives. Part III. Variations on a Theme: Novel Architectures, Materials and Applications *Coord. Chem. Rev.,* **2018**, *355*, 328-361.

2 Crochet, P.; Cadierno, V. Arene-ruthenium(II) complexes with hydrophilic P-donor ligands: versatile catalysts in aqueous media *Dalton Trans.* **2014**, *43*, 12447‑12462.

3 Murray, B. S.; Babak, M. V.; Hartinger, C. G.; Dyson, P. J. The development of RAPTA compounds for the treatment of tumors *Coord. Chem. Rev.* **2016**, *306*, 86‑114.

4 Lidrissi, C.; Romerosa, A.; Saoud, M.; Serrano-Ruiz, M.; Gonsalvi, L.; Peruzzini, M. Stable, Water-Soluble PTA-Based Ru–Ag Organometallic Polymers *Angew. Chem. Int. Ed*. **2005**, *44*, 2568-2572.

5 Interestingly, Romerosa and co-workers very recently described a similar 1D Ru-Ag polymer with Cl in the place of DMSO, Na[{RuCpCl(PTA-κ^2*P,N*)$_2$}{$AgCl_2$}]$_\infty$: Sierra-Martin, B.; Serrano-Ruiz, M.; Scalambra, F.; Fernandez-Barbero, A.; Romerosa, A. Novel Ruthenium-Silver PTA-Based Polymers and Their Behavior in Water *Polymers* **2019**, *11*, 1249.

6 a) Serrano-Ruiz, M.; Romerosa, A.; Sierra-Martin, B.; Fernandez-Barbero, A. A Water Soluble Diruthenium-Gold Organometallic Microgel *Angew. Chem. Int. Ed.* **2008**, *47*, 8665-8669; b) Scalambra, F.; Serrano-Ruiz, M.; Romerosa, A. First Water-Soluble Backbone Ru–Ru–Ni Heterometallic Organometallic Polymer *Macromol. Rapid Commun.* **2015**, *36*, 689-693; c) Scalambra, F.; Serrano-Ruiz, M.; Gudat, D.; Romerosa, A. Amorphization of a Ru–Ru–Cd Coordination Polymer at Low Pressure *ChemistrySelect* **2016**, *5*, 901‑905; d) Scalambra, F.; Serrano-Ruiz, M.; Romerosa, A. Water driven formation of channels: unusual solid-state structural transformation of a heterometallic polymer *Dalton Trans.*, **2018**, *47*, 3588-3595; e) Sierra-Martin, B.; Serrano-Ruiz, M.; García-Sakai, V.; Scalambra, F.; Romerosa, A.; Fernandez-Barbero, A. Self-Organization and Swelling of Ruthenium-Metal Coordination Polymers with PTA (Metal = Ag, Au, Co) *Polymers* **2018**, *10*, 528; f) Scalambra, F.; Rudić, S.; Romerosa, A. Molecular Insights into Bulk and Porous κ^2*P,N*-PTA Metal-Organic Polymers by Simultaneous Raman Spectroscopy and Inelastic Neutron Scattering *Eur. J. Inorg. Chem.* **2019**, 1155-1161.

7 Tu, X.; Nichol, G. S.; Zheng, Z. Zn(II) and Cu(II) Complexes with the Cluster-based Ligand $[Re_6(\mu_3\text{-}Se)_8(PEt_3)_5(PTA)](SbF_6)_2$ (PTA = 1,3,5-Triaza-7-phosphaadamantane) *J. Cluster Sci.* **2009**, *20*, 93-103.

8 Mohr, F.; Falvello, L. R.; Laguna, M. A Silver(I) Coordination Polymer Containing Tridentate N- and P-Coordinating 1,3,5-Triaza-7-phosphaadamantane (PTA) Ligands *Eur. J. Inorg. Chem.* **2006**, 3152-3154.

9 a) Lis, A.; Guedes da Silva, M. F. C.; Kirillov, A. M.; Smoleński, P.; Pombeiro, A. J. L. Design of Silver(I)−PTA Coordination Polymers through Controlled N,P-Coordination of 1,3,5-Triaza-7-phosphaadamantane (PTA) with Arylcarboxylates *Cryst. Growth Des.* **2010**, *10*, 5244-5253; b) Kirillov, A. M.; Wieczorek, S. W.; Guedes da Silva, M. F. C.; Sokolnicki, J.; Smoleński, P.; Pombeiro, A. J. L. Crystal engineering with 1,3,5-triaza-7-phosphaadamantane (PTA): first PTA-driven 3D metal–organic frameworks *CrystEngComm* **2011**, *13*, 6329-6333; c) Jaros, S. W.; Guedes da Silva, M. F. C.; Florek, M.; Oliveira, M. C.; Smoleński, P.; Pombeiro, A. J. L.; Kirillov, A. M. Aliphatic Dicarboxylate Directed Assembly of Silver(I) 1,3,5-Triaza-7-phosphaadamantane Coordination Networks: Topological Versatility and Antimicrobial Activity *Cryst. Growth Des*. **2014**, *14*, 5408-5417; d) Jaros, S. W.; Guedes da Silva, M. F. C.; Florek, M.; Smoleński, P.; Pombeiro, A. J. L.; Kirillov, A. M. Silver(I) 1,3,5-Triaza-7-phosphaadamantane Coordination Polymers Driven by Substituted Glutarate and Malonate Building Blocks: Self-Assembly Synthesis, Structural Features, and Antimicrobial Properties *Inorg. Chem.* **2016**, *55*, 5886-5894; e) Jaros, S. W.; Guedes da Silva, M. F. C.; Król, J.; Oliveira,

M. C.; Smoleński, P.; Pombeiro, A. J. L.; Kirillov, A. M. Bioactive Silver−Organic Networks Assembled from 1,3,5-Triaza-7-phosphaadamantane and Flexible Cyclohexanecarboxylate Blocks *Inorg. Chem.* **2016**, *55*, 1486-1496.

10 Jaremko, Ł.; Kirillov, A. M.; Smoleński, P.; Pombeiro, A. J. L. Engineering Coordination and Supramolecular Copper-Organic Networks by Aqueous Medium Self-Assembly with 1,3,5-Triaza-7-phosphaadamantane (PTA) *Cryst. Growth Des.* **2009**, *9*, 3006-3010.

11 Smoleński, P.; Kłak, J.; Nesterov, D. S.; Kirillov, A. M. Unique Mixed-Valence Cu(I)/Cu(II) Coordination Polymer with New Topology of Bitubular 1D Chains Driven by 1,3,5-Triaza-7-phosphaadamantane (PTA) *Cryst. Growth Des.* **2012**, *12*, 5852-5857.

12 Frost, B. J.; Bautista, C. M.; Huang, R.; Shearer, J. Manganese Complexes of 1,3,5-Triaza-7-phosphaadamantane (PTA): The First Nitrogen-Bound Transition-Metal Complex of PTA *Inorg. Chem.* **2006**, *45*, 3481-3483.

13 Smoleński, P.; Kochel, A. Synthesis of the first monodentate S- and O-coordinating 1,3,5-triaza-7-phosphaadamantane-7-chalcogenides $[CoCl(bpy)_2(Z\text{-PTA=Z})]X$ (Z = S, O; bpy = 2,2′-bipyridine; X = BF_4, PF_6) and $[CoCl(bpy)_2(N\text{-PTA})]BF_4$ (PTA = 1,3,5-triaza-7-phosphaadamantane) *Polyhedron* **2010**, *29*, 1561-1566.

14 Smoleński, P.; Benisvy, L.; Guedes da Silva, M. F. C.; Pombeiro, A. J. L. Syntheses and Crystal Structures of the First Zinc Complex with 1,3,5-Triaza-7-phosphaadamantane (PTA), $[ZnCl_2(PTA)_2]$, and of the Hybrid Organic–Inorganic Salts of *N*-Methyl-1,3,5-triaza-7-phosphaadamantane with Tetrahalozinc $[PTA–Me]_2[ZnI_2X_2]$ (X = I, Cl) *Eur. J. Inorg. Chem.* **2009**, 1181-1186.

15 Anselmo, D.; Gramage-Doria, R.; Besset, T.; Escárcega-Bobadilla, M. V.; Salassa, G.; Escudero-Adán, E. C.; Martínez Belmonte, M.; Martin, E.; Reek, J. N. H.; Kleij, A. W. Supramolecular bulky phosphines comprising 1,3,5-triaza-7-phosphaadamantane and Zn(salphen)s: structural features and application in hydrosilylation catalysis *Dalton Trans.* **2013**, *42*, 7595–7603.

16 a) Battistin, F.; Balducci, G.; Iengo, E.; Demitri, N.; Alessio, E. Neutral Ru(II)-PTA and Ru(II)-PTA-dmso Complexes (PTA = 1,3,5-triaza-7-phosphaadamantane) as Precursors for the Preparation of Highly Water-soluble Derivatives *Eur. J. Inorg. Chem.* **2016**, 2850-2860; b) Battistin, F.; Scaletti, F.; Balducci, G.; Pillozzi, S.; Arcangeli, A.; Messori, L.; Alessio, E. Water-soluble Ru(II)- and Ru(III)-halide-PTA Complexes (PTA = 1,3,5-triaza-7-phosphaadamantane): Chemical and Biological Properties *J. Inorg. Biochem.* **2016**, *160*, 180-188; c) Battistin, F.; Balducci, G.; Milani, B.; Alessio, E. Water-Soluble Ruthenium(II) Carbonyls with 1,3,5-Triaza-7-Phosphoadamantane *Inorg. Chem.* **2018**, *57*, 6991-7005.

17 a) Darensbourg, D. J.; Joó, F.; Kannisto, M.; Kathó, A.; Reibenspies, J. H.; Daigle, D. J. Water-Soluble Organometallic Compounds. 4. Catalytic Hydrogenation of Aldehydes in an Aqueous Two-Phase Solvent System Using a 1,3,5-Triaza-7-phosphaadamantane Complex of Ruthenium *Inorg. Chem.* **1994**, *13*, 200-208; b) Mebi, C. A.; Frost, B. J. Isomerization of *trans*-[$Ru(PTA)_4Cl_2$] to *cis*-[$Ru(PTA)_4Cl_2$] in Water and Organic Solvent: Revisiting the Chemistry of [$Ru(PTA)_4Cl_2$] *Inorg. Chem.* **2007**, *46*, 7115-7120; c) Girotti, R.; Romerosa, A.; Mañas, S.; Serrano-Rui, M.; Perutz, R. N. Visible-Light Photoisomerization and Photoaquation of *trans*-[Ru(1,3,5-triaza-7-phosphaadamantane)$_4Cl_2$] in Organic Solvent and Water *Inorg. Chem.* **2009**, *48*, 3692-3698; d) Udvardy, A.; Benyei, A. C.; Katho, A. The dual role of *cis*-[$RuCl_2(dmso)_4$] in the synthesis of new water-soluble Ru(II)-phosphane complexes and in the catalysis of redox isomerization of allylic alcohols in aqueous organic biphasic systems *J. Organomet. Chem.* **2012**, *717*, 116‑122.

18 a) Alessio, E.; Macchi, M.; Heath, S.; Marzilli, L. G. A novel open-box shaped pentamer of vertically linked porphyrins that selectively recognizes S-bonded Me_2SO complexes *Chem. Commun.* **1996**, 1411-1412; b) Alessio, E.; Geremia, S.; Mestroni, S.; Iengo, E.; Srnova, I.; Slouf, M. Solution and solid state structure of a canted, side-to-face, bis-porphyrin adduct *Inorg. Chem.* **1999**, *38*, 869‑875.

19 a) Iengo, E.; Zangrando, E.; Minatel, R.; Alessio, E. Metallacycles of porphyrins as building blocks in the construction of higher order assemblies through axial coordination of bridging ligands: solution and solid state characterization of molecular sandwiches and molecular wires. *J. Am. Chem. Soc.* **2002**, *124*, 1003-1013; b) Iengo, E.; Gatti, T.; Zangrando, E.; Indelli, M. T.; Scandola, F.; Alessio, E. Concerted motions in supramolecular systems: metal-mediated assemblies of porphyrins that behave like nanometric step-machines *Chem. Commun.* **2011**, *47*, 1616-1618; c) Alessio, E.; Casanova, M.; Zangrando, E.; Iengo, E. Modular self-assembled multiporphyrin cages with tunable shape *Chem. Commun.* **2012**, *48*, 5012-5015; d) Iengo, E.; Cavigli, P.; Milano, D.; Tecilla, P. Metal mediated self-assembled porphyrin metallacycles: Synthesis and multipurpose applications *Inorg. Chim. Acta* **2014**, *417*, 59-78.

20 a) Stulz, E.; Maue, M.; Feeder, N.; Teat, S. J.; Ng, Y. F.; Bond, A. D.; Darling, S.; Sanders, J. K. M. Phosphine and Phosphonite Complexes of a Ruthenium(II) Porphyrin. 1. Synthesis, Structure, and Solution State Studies *Inorg. Chem.* **2002**, *41*, 5255-5268; b) Stulz, E.; Scott, S. M.; Bond, A. D.; Otto, S.; Sanders, J. K. M. Complexation of Diphenyl(phenylacetenyl)phosphine to Rhodium(III) Tetraphenyl Porphyrins: Synthesis and Structural, Spectroscopic, and Thermodynamic Studies *Inorg. Chem.* **2003**, *42*, 3086-3096; c) Bond, A. D.; Sanders, J. K. M.; Stulz, E. Ruthenium(II) and rhodium(III) porphyrin phosphine

complexes: influence of substitution pattern on structure and electronic properties *New J. Chem.* **2011**, *35*, 2691-2696.

21 Domazetis, G.; James, B. R.; Dolphin, D. Ruthenium(II) Porphyrin Complexes: NMR Spectral Evidence for Out-of-Plane Ruthenium, and for Seven-Coordinate Species *Inorg. Chim. Acta* **1981**, *54*, L47-L49.

22 Mizutani, T.; Wada, K.; Kitagawa, S. Molecular Recognition of Amines and Amino Esters by Zinc Porphyrin Receptors: Binding Mechanisms and Solvent Effects *J. Org. Chem.* **2000**, *65*, 6097-6106.

23 Rukin, P. S.; Kashchenko, P. A.; Malyavskaya, A. Yu.; Bagaturyants, A. A.; Alfimov M. V., Experimental and Theoretical Study of the Interaction of Volatile Amines with Zinc Porphyrins *Nanotechnol. Russ.* **2014**, *9*, 136–144.

24 Vinodu, M.; Goldberg, I. Complexes of hexamethylenetetramine with zinc-tetraarylporphyrins, and their assembly modes in crystals as clathrates and hydrogen-bonding network polymers *New J. Chem.* **2004**, *28*, 1250-1254.

25 Eaton, S. S.; Eaton, G. R.; Holm, R. H. Inter- and Intramolecular Ligand Exchange Reactions of Ruthenium(II) Carbonyl Porphine Complexes with Nitrogen Bases *J. Organomet. Chem.* **1972**, *39*, 179-195.

26 Little, R. G.; Ibers, J. A. Structure of (Tetraphenylporphinato)-(carbonyl)(pyridine)ruthenium(II)-l.5-Toluene *J. Am. Chem. Soc.* **1973**, *95*, 8583-8590.

27 Antipas, A.; Buchler, J. W.; Gouterman, M.; Smith, P. D. Porphyrins. 36. Synthesis and optical and electronic properties of some ruthenium and osmium octaethylporphyrins *J. Am. Chem. Soc.* **1978**, *100*, 3015-3024.

28 Slebodnick, C.; Seok, W. K.; Kim, K.; Ibers, J. A. Syntheses and characterization of the ruthenium carbonyl porphyrin complexes Ru(TPP)(CO)(1-Melm) and Ru(a-PocPivP)(CO)(1-Melm) *Inorg. Chim. Acta* **1996**, *243*, 57-65.

29 Chow, B. C.; Cohen, I. A. Derivatives of Tetraphenylporphineruthenium(II) *Bioinorg. Chem.* **1971**, *1*, 57-63.

30 Boschi, T.; Bontempelli, G.; Mazzocchin, G.-A. Synthesis and Electrochemical Behaviour of Novel Ruthenium(II) Tetraphenylporphynate Derivatives *Inorg. Chim. Acta* **1979**, *37*, 155-160.

31 a) Ball, R. G.; Domazetis, G.; Dolphin, D.; James, B. R.; Trotter, J. Studies of Ruthenium(II) Porphyrins Containing Tertiary Diphosphine Ligands, Including the Crystal Structure of (5,10,15,20-Tetraphenylporphinato)bis(bis(diphenylphosphino)methane)ruthenium(II)-Dichloromethane *Inorg. Chem.* **1981**, *20*, 1556-1562; b) Barley, M.; Becker, J. Y.; Domazetis, G.; Dolphin, D.; James, B. R. Synthesis and redox chemistry of octaethylporphyrin complexes

of ruthenium(II) and ruthenium(III) *Can. J. Chem.* **1983**, *61*, 2389-2396; c) Ariel, S.; Dolphin, D.; Domazetis, G.; James, B. R.; Leung, T. W.; Rettig, S. J.; Trotter, J.; Williams, G. M. Preparation and characterization of some ruthenium(II) porphyrins containing tertiary phosphine axial ligands, including the crystal structure of (octaethylporphinato)bis(triphenylphosphine)ruthenium(II) *Can. J. Chem*. **1984**, *62*, 755-762.

32 Massoudipour, M.; Pandey, K. K. Preparation and Characterization of Ruthenium(II) Porphyrins *Inorg. Chim. Acta* **1989**, *160*, 115-118.

33 a) Stulz, E.; Scott, S. M.; Ng, Y.-F.; Bond, A. D.; Teat, S. J.; Darling, S. L.; Feeder, N.; Sanders, J. K. M. Construction of Multiporphyrin Arrays Using Ruthenium and Rhodium Coordination to Phosphines *Inorg. Chem.* **2003**, *42*, 6564-6574; b) Stulz, E.; Maue, M.; Scott, S. M.; Mann, B. E.; Sanders, J. K. M. Ru(II) and Rh(III) porphyrin complexes of primary phosphine-substituted porphyrins *New J. Chem.* **2004**, *28*, 1066-1072.

34 a) Xie, J.; Huang, J.-S.; Zhu, N.; Zhou, Z.-Y.; Che, C.-M. Primary and Secondary Phosphane Complexes of Metalloporphyrins: Isolation, Spectroscopy, and X-ray Crystal Structures of Ruthenium and Osmium Porphyrins Binding Phenyl- or Diphenylphosphane *Chem. Eur. J.* **2005**, *11*, 2405-2416; b) Huang, J.-S.; Yu, G.-A.; Xie, J.; Zhu, N.; Che, C.-M. One-Pot Synthesis of Metal Primary Phosphine Complexes from $O{=}PCl_2R$ or PCl_2R. Isolation and Characterization of Primary Alkylphosphine Complexes of a Metalloporphyrin *Inorg. Chem.* **2006**, *45*, 5724-5726.

35 According to some authors (e.g. refs 20a, 29, 31c, PPh_3 is an exception and the preparations of $[Ru(TPP)(PPh_3)_2]$ or $[Ru(OEP)(PPh_3)_2]$ (OEP = octaethylporphyrin) require extensive boiling of the reactants in chloroform or toluene, whereas according to others (ref. 30) $[Ru(TPP)(PPh_3)_2]$ is obtained within 1h at room temperature.

36 Darling, S.; Sanders, J. K. M.; Davies, J. E. **1999**, CSD Communication (Private Communication).

37 The original AB spin system of the NCH_2N protons becomes an AX system in **28** by virtue of the increased spread of chemical shifts.

38 Darensbourg, D. J.; Beckford, F. A.; Reibenspies, J. H. Water-Soluble Organometallic Compounds. 8. Synthesis, Spectral Properties, and Crystal Structures of 1,3,5-Triaza-7-phosphaadamantane (PTA) Derivatives of Metal Carbonyl Clusters: $Ru_3(CO)_9(PTA)_3$ and $Ir_4(CO)_7(PTA)_5$ *J. Clust. Sci.* **2000**, *11*, 95-107.

39 Consistent with the expected weakening of the Ru–CO bond, the CO stretching frequency in the intermediate **2** falls at remarkably higher wavelengths compared to [Ru(TPP)(CO)] (1989 vs 1949 cm^{-1}, with a $\Delta\nu$ of 40 cm^{-1}). For comparison, in a series of [Ru(DPP)(CO)(P)]

compounds Δν of 18 – 39 cm^{-1} – compared to [Ru(DPP)(CO)] – were observed,[20a] and CO stretching frequencies (solid state) of 1952 and 1956 cm^{-1} were reported for [Ru(OEP)(CO)(PPh_3)] and [Ru(TPP)(CO)(PPh_3)], respectively.[31b, 31c]

40 Byrn, M. P.; Curtis, C. J.; Hsiou, Y.; Khan, S. I.; Sawin, P. A.; Tendick, S. K.; Terzis, A.; Strouse, C. E. Porphyrin Sponges: Conservation of Host Structure in over 200 Porphyrin-Based Lattice Clathrates *J. Am. Chem. Soc.* **1993**, *115*, 9480-9497.

41 Shukla, A. D.; Dave, P. C.; Suresh, E.; Das, A.; Dastidar, P. Multicomponent Zn-tetraphenylporphyrins: syntheses, characterization and their self assembly in the solid state *J. Chem. Soc., Dalton Trans.* **2000**,4459-4463.

42 Ozarowski, A.; Lee, H. M.; Balch, A. L. Crystal Environments Probed by EPR Spectroscopy. Variations in the EPR Spectra of Co^{II}(octaethylporphyrin) Doped in Crystalline Diamagnetic Hosts and a Reassessment of the Electronic Structure of Four-Coordinate Cobalt(II) *J. Am. Chem. Soc.* **2003**, *125*, 12606-12614.

43 Kleij, A. W.; Kuil, M.; Tooke, D. M.; Spek, A. L.; Reek, J. N. H. Template-Assisted Ligand Encapsulation; the Impact of an Unusual Coordination Geometry on a Supramolecular Pyridylphosphine-Zn(II)porphyrin Assembly *Inorg. Chem.* **2005**, *44*, 7696-7698.

44 Nasri, S.; Zahou, I.; Turowska-Tyrk, I.; Roisnel, T.; Loiseau, F.; Saint-Amant, E.; Nasri, H. Synthesis, Electronic Spectroscopy, Cyclic Voltammetry, Photophysics, Electrical Properties and X-ray Molecular Structures of meso-{Tetrakis[4-(benzoyloxy)phenyl]porphyrinato} zinc(II) Complexes with Aza Ligands *Eur. J. Inorg. Chem.* **2016**,5004-5019.

45 A search on the Cambridge Structural Database, March 2019, afforded 382 hits for X-ray structures of [Zn(por)(N)] vs 18 hits for [Zn(por)$(N)_2$], See in Cambridge Structural Database: Allen, F. H. *Acta Crystallogr., Sect. B*, **2002**, *58*, 380-388.

46 Frost, B. J.; Lee, W.-C.; Pal, K.; Kim, T. H.; Van Derveer, D.; Rabinovich, D. Synthesis, structure, and coordination chemistry of O=PTA and S=PTA with group 12 metals (PTA = 1,3,5-triaza-7-phosphaadamantane) *Polyhedron* **2010**, *29*, 2373-2380.

47 Ru1 corresponds to the M site in Figure A5.16 (Appendix), Zn1 and Zn1' are its symmetry images via *(1–x, y, 3/2–z)* and *(x, 1–y, –1/2+z)*, respectively. Similarly, P31 corresponds to the L site in Figure A5.16 (Appendix), whereas P31', N32, N32' and N32'' are symmetry images of that site via *(1–x, 1–y, 1–z)*, *(1–x, y, 3/2–z)*, *(x, 1–y, 1/2+z)*, *(x, 1–y, –1/2+z)*, respectively. N21' and N22' are symmetry images of N21 and N22 via *(1–x, y, 3/2–z)* and *(x, 1–y, 1/2+z)*, respectively.

48 Primed atoms indicate symmetry images of corresponding non primed atoms (N1':*(1–x, 1–y, 1–z)*, N2':*(1–x, 1–y, 1–z)*, N11':*(1–x, 1–y, 1–z)*, P1':*(1–x, y, 1/2–z)*, N11"*(1–x, y, 1/2–z)*, Zn1':*(1–x, y, 1/2–z)*).

49 Alessio, E.; Geremia, S.; Mestroni, S.; Srnova, I.; Slouf, M.; Gianferrara, T.; Prodi, A. Porphyrin "flying saucers": solid state and solution structure of a novel pentameric array of axially-ligated canted porphyrins *Inorg. Chem.* **1999**, *38*, 2527-2529.

50 Due to the low quality of the X-ray data, the observed electron density map of the disordered $\{ZnCl_2(OH_2)\}$ fragment could be modeled also by a $ZnCl_3^-$ fragment. Protonation of the opposite PTA ligand ($PTAH^+$) would balance the negative charge, yielding the zwitterionic molecule $[\{Ru(TPP)(PTAH\text{-}\kappa P)(PTA\text{-}\kappa^2 P,N)\}^+\{ZnCl_3\}^-]$ (see Appendix for further details).

51 The pioneering work of Israel Goldberg in studying microporous structures based on porphyrin building units cannot be easily cited, due to its vastness. It can perhaps be best appreciated by reading this commemorative article, and the references cited therein: Titi, H. M.; Konar, S. The Voyage of Goldberg: Supramolecular Chemistry and Memories *Cryst. Growth Des.* **2019**, *19*, 3603-3606.

52 a) Lee, C. Y.; Farha, O. K.; Hong, B. J.; Sarjeant, A. A.; Nguyen, S.T.; Hupp, J. T. Light-harvesting metal-organic frameworks (MOFs): Efficient strut-to-strut energy transfer in bodipy and porphyrin-based MOFs J. Am. Chem. Soc. 2011, 133, 15858-15861; b) Gao, W.-Y.; Chrzanowski, M.; Ma, S. Metal-metalloporphyrin frameworks: a resurging class of functional materials *Chem. Soc. Rev.* **2014**, *43*, 5841-5866; c) So, M. C.; Guo, Z.; Chen, B. Recent developments in metal-metalloporphyrin frameworks *Dalton Trans.* **2015**, *44*, 14574-14583; d) Wiederrecht, G. P.; Mondloch, J. E.; Hupp, J. T.; Farha, O. K. Metal-organic framework materials for light-harvesting and energy transfer *Chem. Commun.* **2015**, *51*, 3501-3510; e) Chughtai, A. H.; Ahmad, N.; Younus, H. A.; Laypkovc, A.; Verpoort, F. Metal-organic frameworks: versatile heterogeneous catalysts for efficient catalytic organic transformations *Chem. Soc. Rev.* **2015**, *44*, 6804-6849; f) Lismont, M.; Dreesen, L.; Wuttke, S. Metal-Organic Framework Nanoparticles in Photodynamic Therapy: Current Status and Perspectives *Adv. Funct. Mater.* **2017**, *27*, 1606314; g) Zhang, J.; Wang, J.; Long, S.; Peh, S. B.; Dong, J.; Wang, Y.; Karmakar, A.; Yuan, Y. D.; Cheng, Y.; Zhao, D. Luminescent Metal-Organic Frameworks for the Detection and Discrimination of o‑Xylene from Xylene Isomers *Inorg. Chem.* **2018**, *57*, 13631-13639; h) Chen, K.; Wu, C.-D. Designed fabrication of biomimetic metal-organic frameworks for catalytic applications *Coord. Chem. Rev.* **2019**, *378*, 445-465; i) Alkhatiba, I. I; Garlisia, C.; Pagliaro, M.; Al-Alia, K.; Palmisano, G. Metal-organic frameworks for

photocatalytic CO_2 reduction under visible radiation: A review of strategies and applications *Catalysis Today* **2020**, *340*, 209-224;

53 Alessio, E.; Macchi, M.; Heath, S. L.; Marzilli, L. G. Ordered supramolecular porphyrin arrays from a building block approach utilizing pyridylporphyrins and peripheral ruthenium complexes and identification of a new type of mixed-metal building block *Inorg. Chem.* **1997**, *36*, 5614-5623.

54 Vidal, A.; Battistin, F.; Iengo, E.; Milani, B.; Alessio, E. The insertion of ruthenium into porphyrins revisited and improved: proof of concept results with a Ru(II) mono-carbonyl compound, and the spectacular effect of propionic acid *Eur. J. Inorg. Chem.* **2019**, 2883-2890.

55 Sanders, J. K. M.; Bampos, N.; Clyde-Watson, Z.; Darling, S. L.; Hawley, J. C.; Kim, H.-J.; Mak, C. C.; Webb, S. J. Axial Coordination Chemistry of Metalloporphyrins in *The Porphyrin Handbook* (Kadish, K. M.; Smith, K. M.; Guillard, R. Eds.), Academic Press, New York, Vol. 3, **2000**, pp. 1-48.

56 Kabsch, W. XSD *Acta Cryst. D* **2010**, *66*, 125-132.

57 Sheldrick, G. M. SHELXT - Integrated Space-Group and Crystal-Structure Determination *Acta Cryst. A* **2015**, *72*, 3-8.

58 Sheldrick, G. M. A Short History of SHELX *Acta Cryst.* **2008**, *64*, 112-122.

59 Emsley, P.; Cowtan, K. Coot: Model-Building Tools for Molecular Graphics *Acta Cryst. D* **2004**, *60*, 2126-2132.

60 Wang, J.; Kamtekar, S.; Berman, A. J.; Steitz, T. A. Correction of X-ray intensities from single crystals containing lattice-translocation defects *Acta Cryst. D* **2005**, *61*, 67-74.

61 Spek, A. L. Structure validation in chemical crystallography *Acta Cryst.* **2009**, *D65*, 148-155.

Appendix of Chapter 5

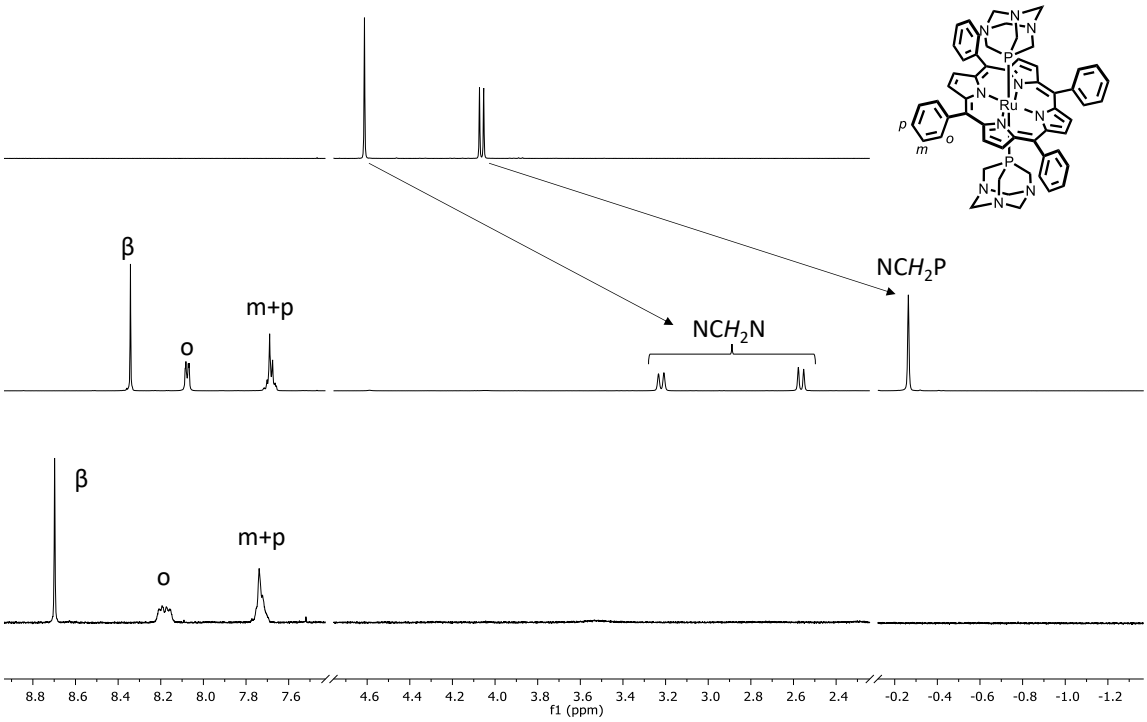

Figure A5.1: ^{1}H NMR spectra of free PTA (top), [Ru(TPP)(PTA-κ*P*)$_2$] (**28**) (middle) and [Ru(TPP)(CO)] (bottom) in $CDCl_3$.

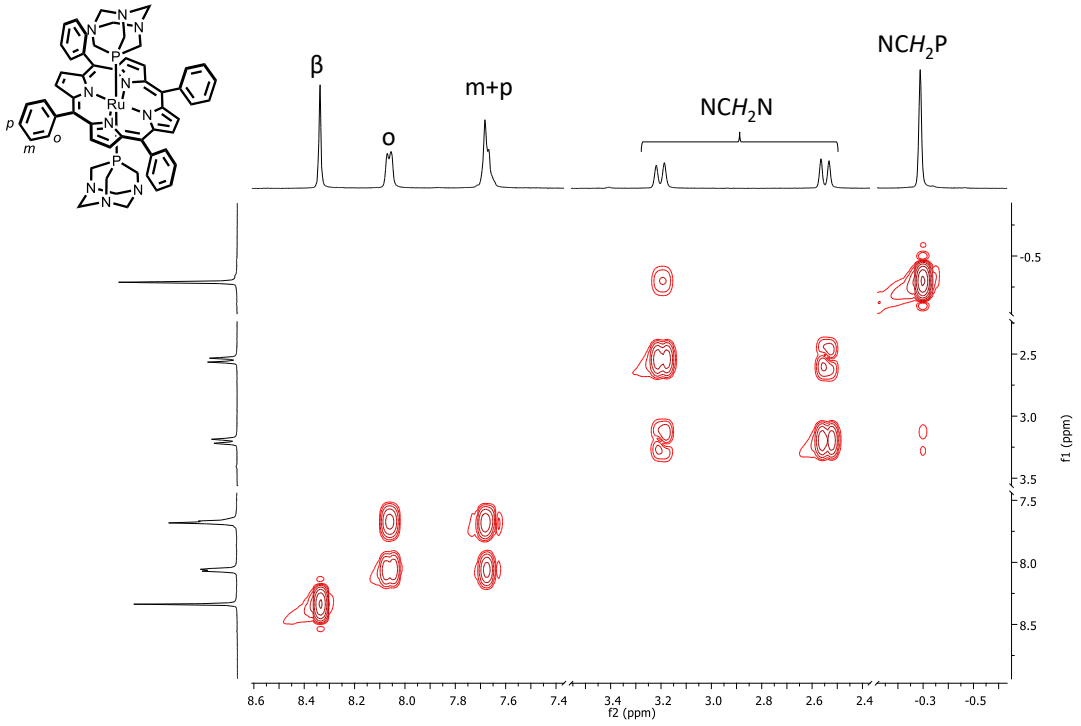

Figure A5.2.: ^{1}H-^{1}H COSY NMR spectrum of [Ru(TPP)(PTA-κ*P*)$_2$] (**28**) in $CDCl_3$.

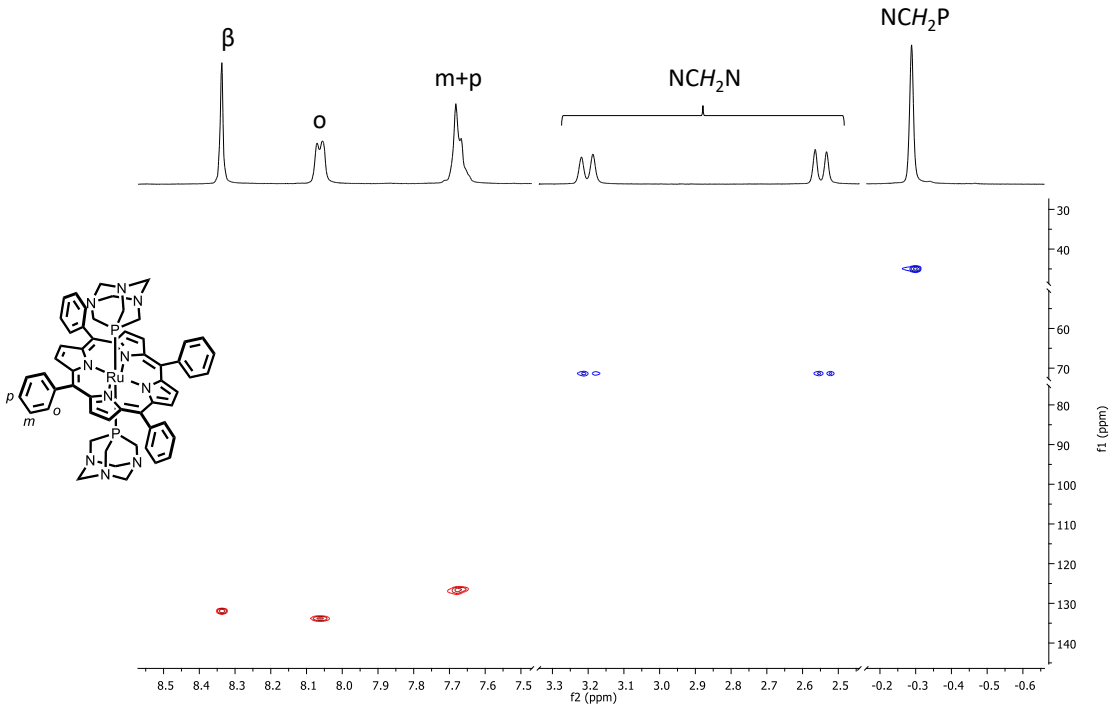

Figure A5.3: ^{1}H-^{13}C HSQC NMR spectrum of [Ru(TPP)(PTA-κ*P*)$_2$] (**28**) in $CDCl_3$.

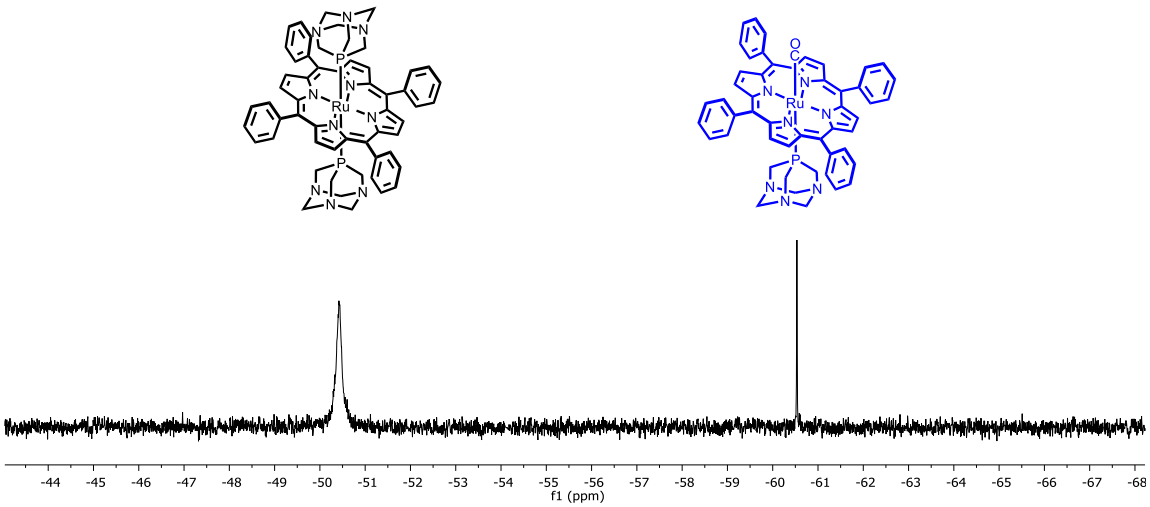

Figure A5.4. $^{31}P\{^{1}H\}$ NMR spectrum of a mixture of [Ru(TPP)(PTA-κ*P*)$_2$] (**28**) and [Ru(TPP)(CO)(PTA-κ*P*)] (**29**) $CDCl_3$ obtained after the addition of ca. 1 equiv of PTA into a $CDCl_3$ solution of [Ru(TPP)(CO)].

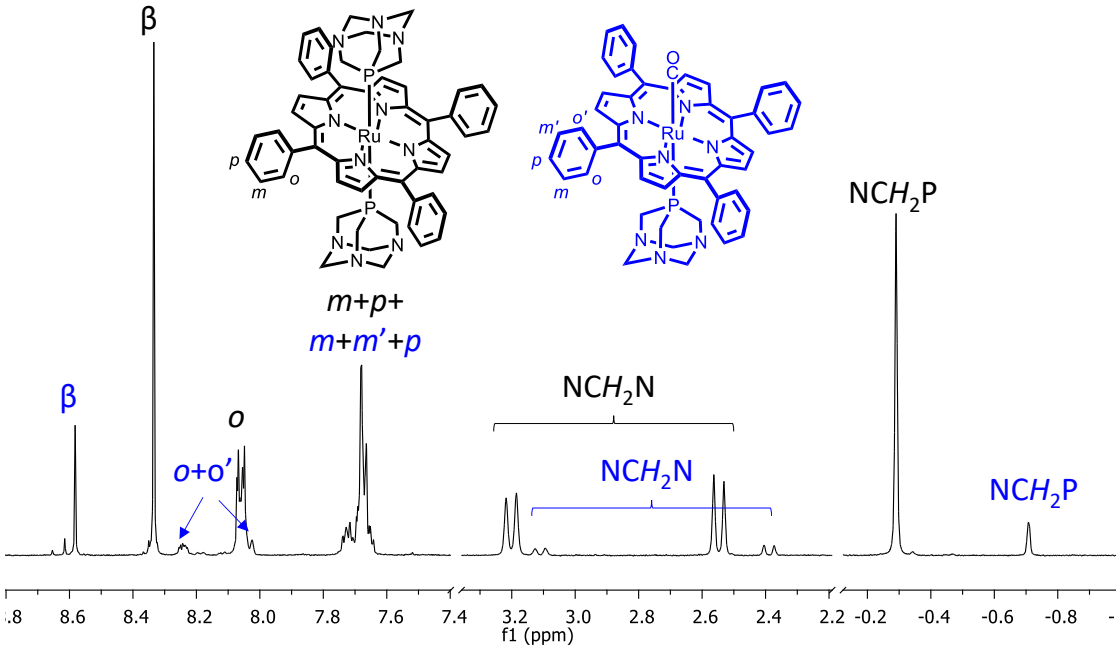

Figure A5.5: ^{1}H NMR spectrum ($CDCl_3$) of a ca. 3:1 mixture of [Ru(TPP)(PTA-κ*P*)$_2$] (**28**, black labels) and [Ru(TPP)(CO)(PTA-κ*P*)] (**29**, blue labels) obtained during a titration of a [Ru(TPP)(CO)] solution with PTA.

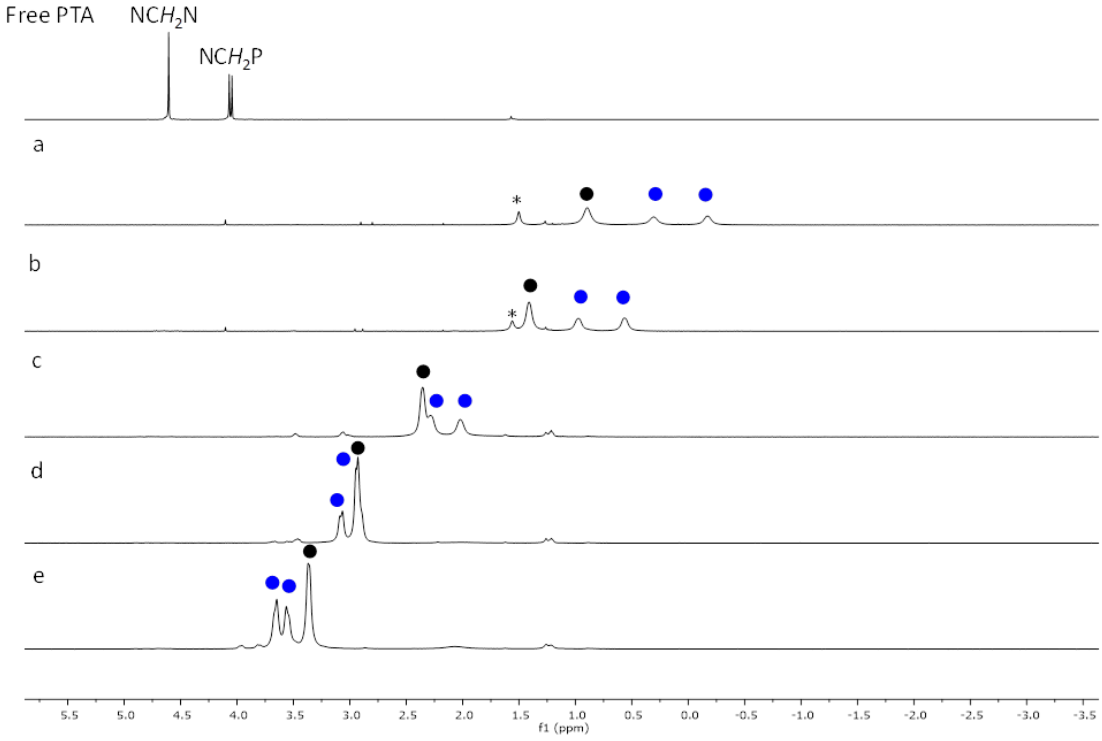

Figure A5.6. ^{1}H NMR titration of Zn(TPP) with 0.5 (a), 1 (b), 2 (c), 3 (d) and 5 (e) equiv of PTA in $CDCl_3$. The resonance of the NCH_2N protons is labeled with blue dots, and that of the NCH_2P protons with black dots. In the more magnified spectra (a) and (b) the peak of residual water is labeled with *. The porphyrin resonances are not shown.

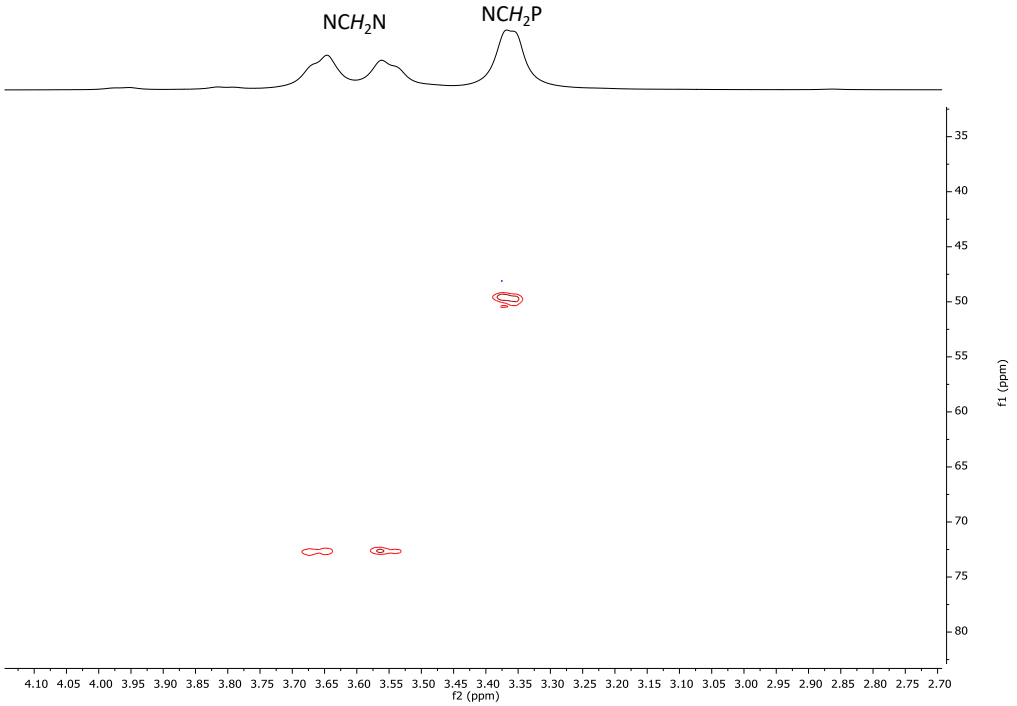

Figure A5.7. PTA region of the ^{1}H-^{13}C HSQC NMR spectrum of the 1:5 mixture of Zn(TPP) and PTA in $CDCl_3$ (i.e. of spectrum (e) in Figure A5.6).

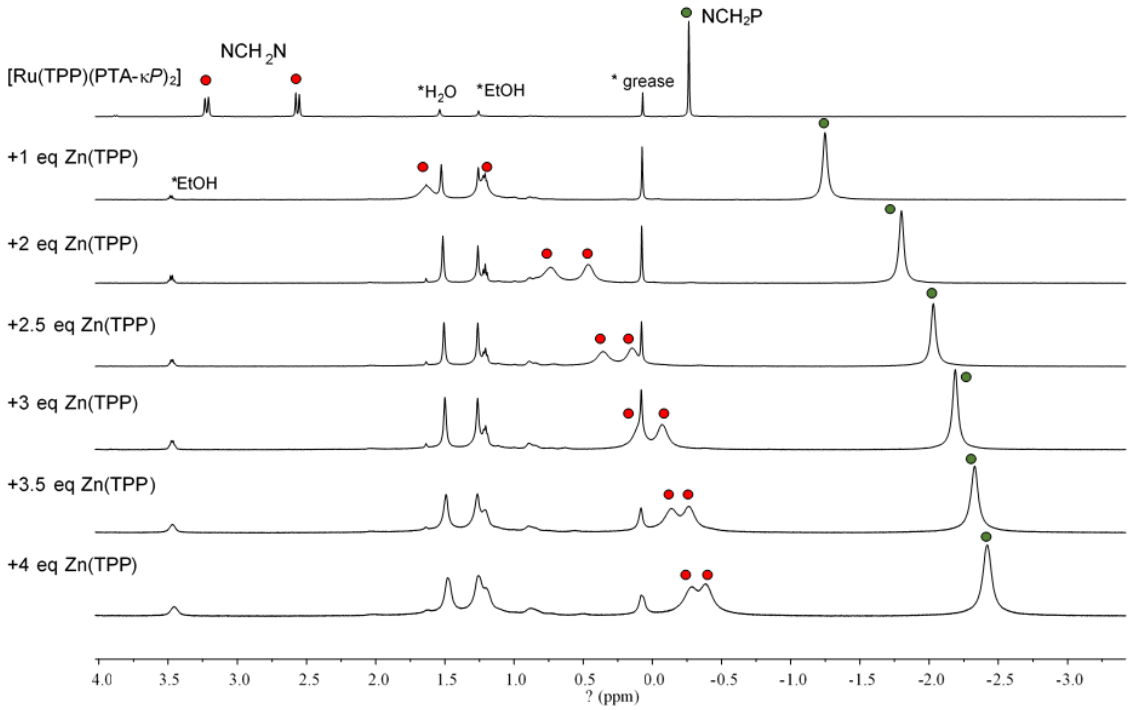

Figure A5.8.. Region of the PTA resonances (red and green dots) in ^{1}H NMR titration of [Ru(TPP)(PTA-κ*P*)$_2$] (**28**) with Zn(TPP) (from 1 to 4 equiv) in $CDCl_3$. The additional resonances in the upfield region, that do not shift in the titration but become broader, belong to grease, H_2O and EtOH. This latter increases since it derives also from Zn(TPP), that should be formulated as [Zn(TPP)(EtOH)].

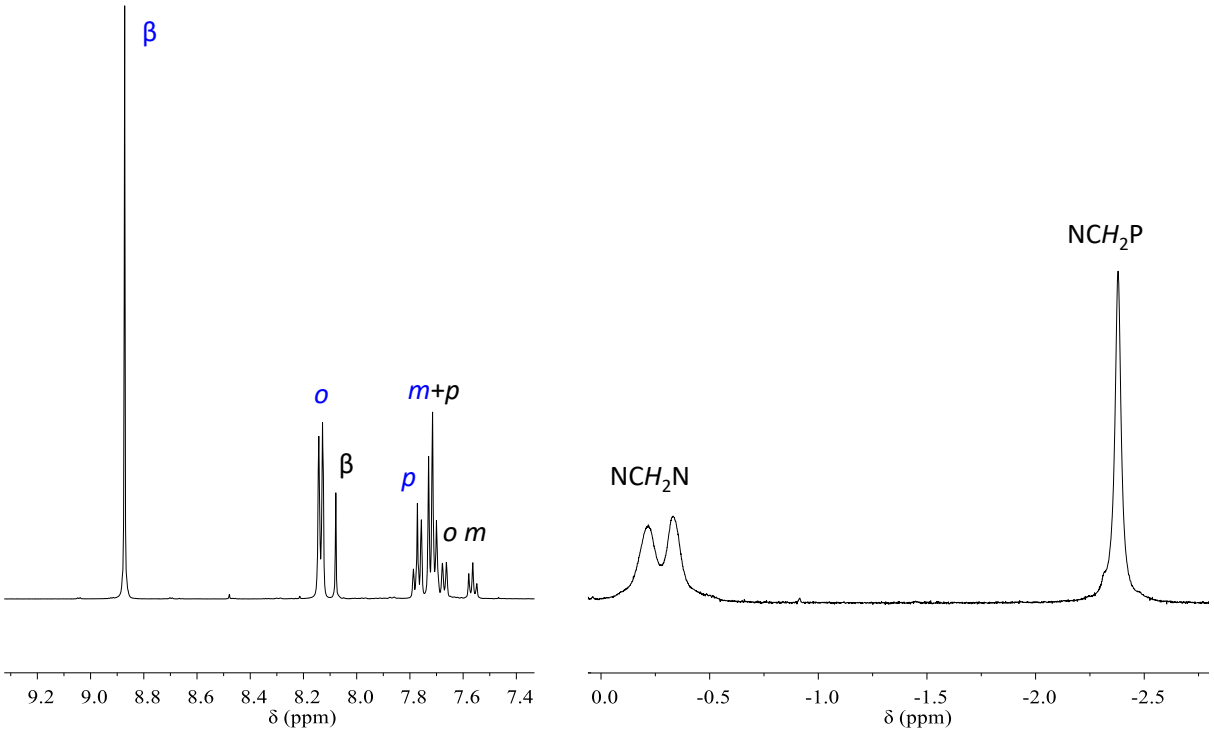

Figure A.5.9. ^{1}H NMR spectrum (aromatic and PTA regions) of a 1:4:2 mixture of [Ru(TPP)(CO)] (black labels), Zn(TPP) (blue labels), and PTA. The downfield and upfield regions are not in scale: The PTA region has been amplified in order to better show the broad PTA resonances.

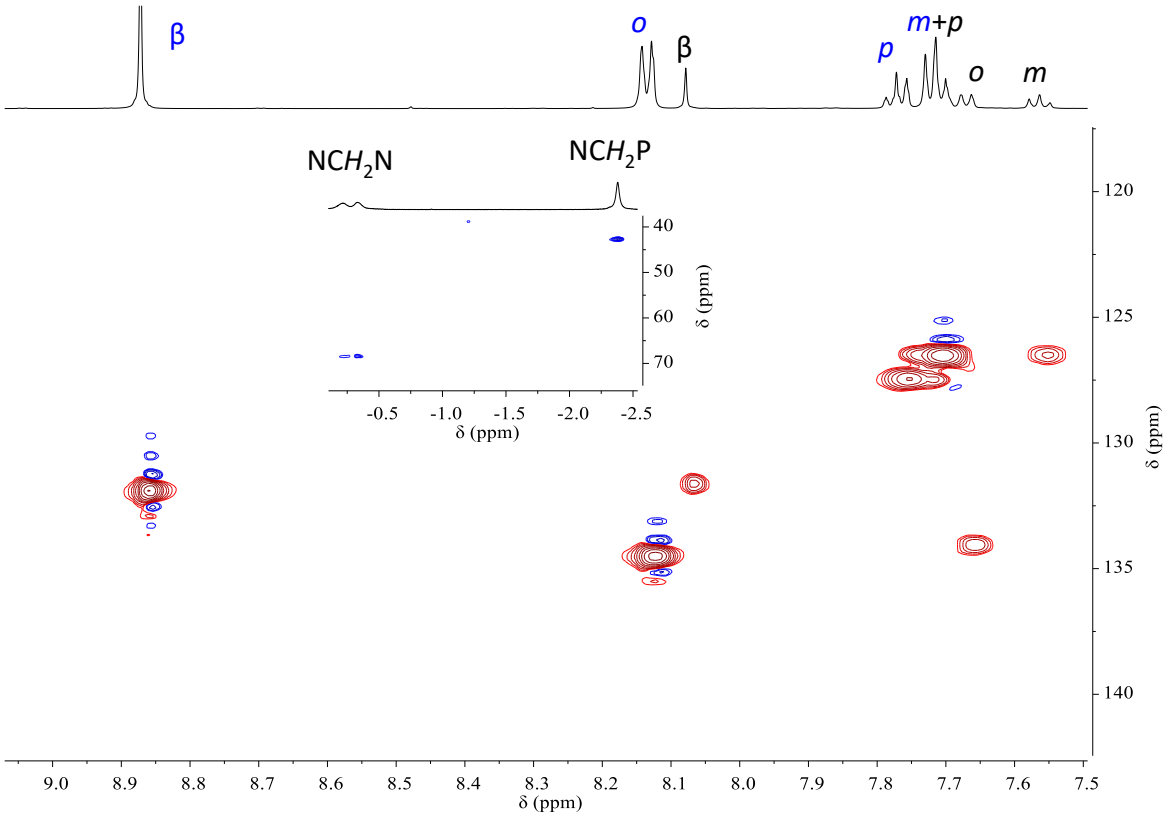

Figure A.5.10: ^{1}H-^{13}C HSQC NMR spectrum of the 1:4:2 mixture of [Ru(TPP)(CO)] (black labels), Zn(TPP) (blue labels), and PTA. The PTA region is in the insert.

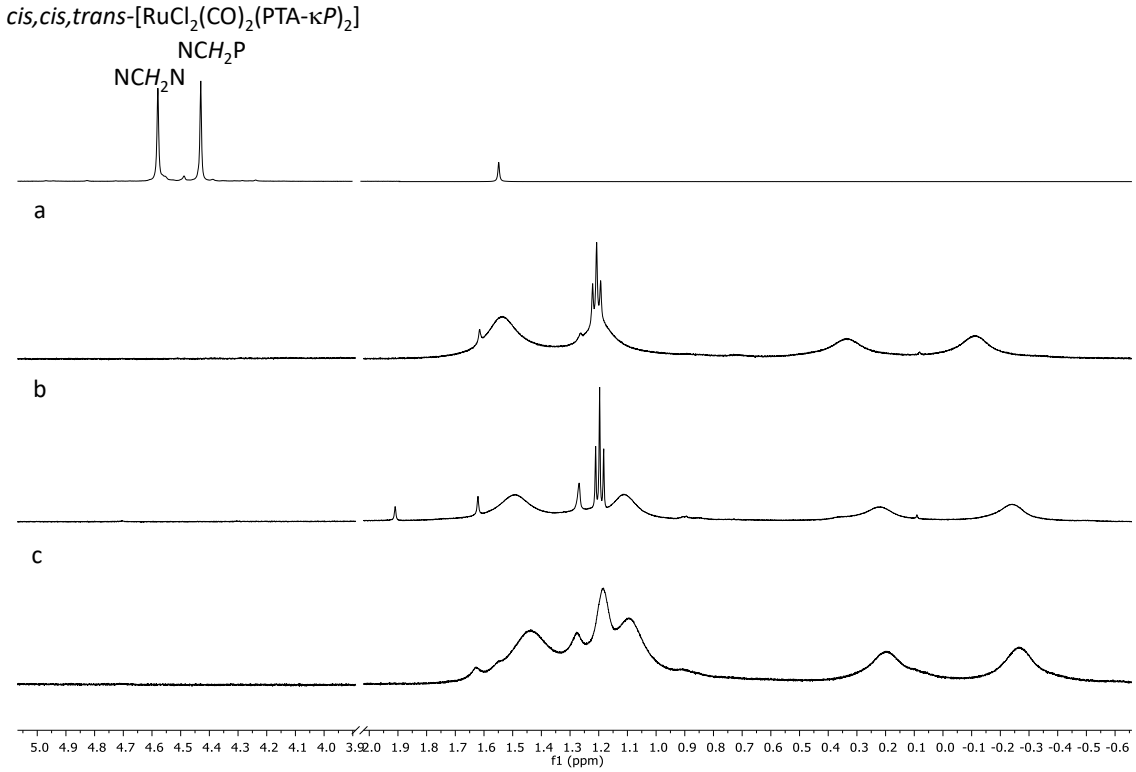

Figure A5.11. ^{1}H NMR titration of *cis,cis,trans*-[$RuCl_2(CO)_2$(PTA-κ*P*)$_2$] (**32**) (top) with 2 (a), 3 (b) and 4 (c) equiv of Zn(TPP) in $CDCl_3$. The porphyrin resonances are not shown. The triplet at ca. 1.2 ppm belongs to the EtOH originally bound to Zn(TPP).

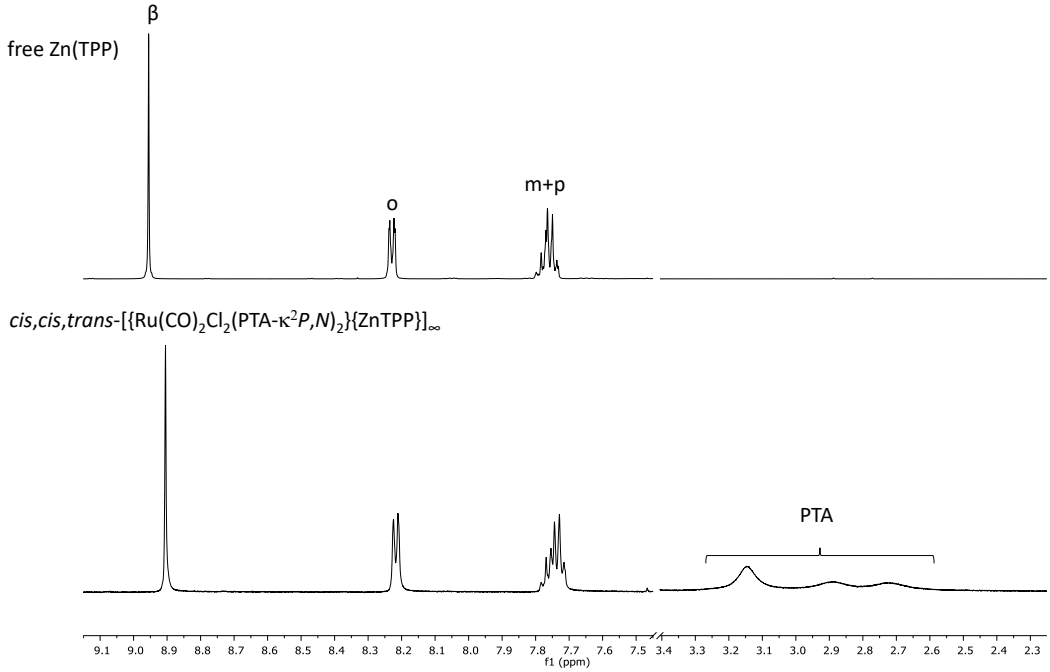

Figure A5.12. ^{1}H NMR spectrum of the crystals of *cis,cis,trans*-[{$Ru(CO)_2Cl_2$(PTA-κ^2*P,N*)$_2$}{ZnTPP}]$_\infty$ (**33**) dissolved in $CDCl_3$.

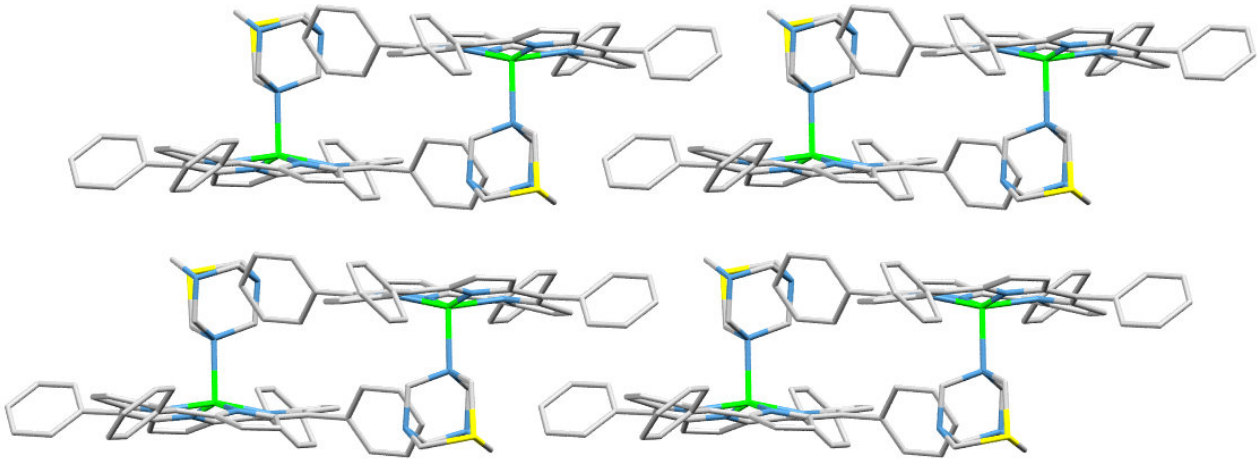

Figure A5.13. View along the b axis of a portion of the crystal structure of complex [Zn(TPP)(PTA-κ*N*)]·H_2O·$CHCl_3$ (**30**·H_2O·$CHCl_3$) evidencing the packing of the molecules and the κ*N* coordination of the PTA ligand to the Zn metal. Color code: C = grey, N = purple, P = orange. Crystallization molecules omitted.

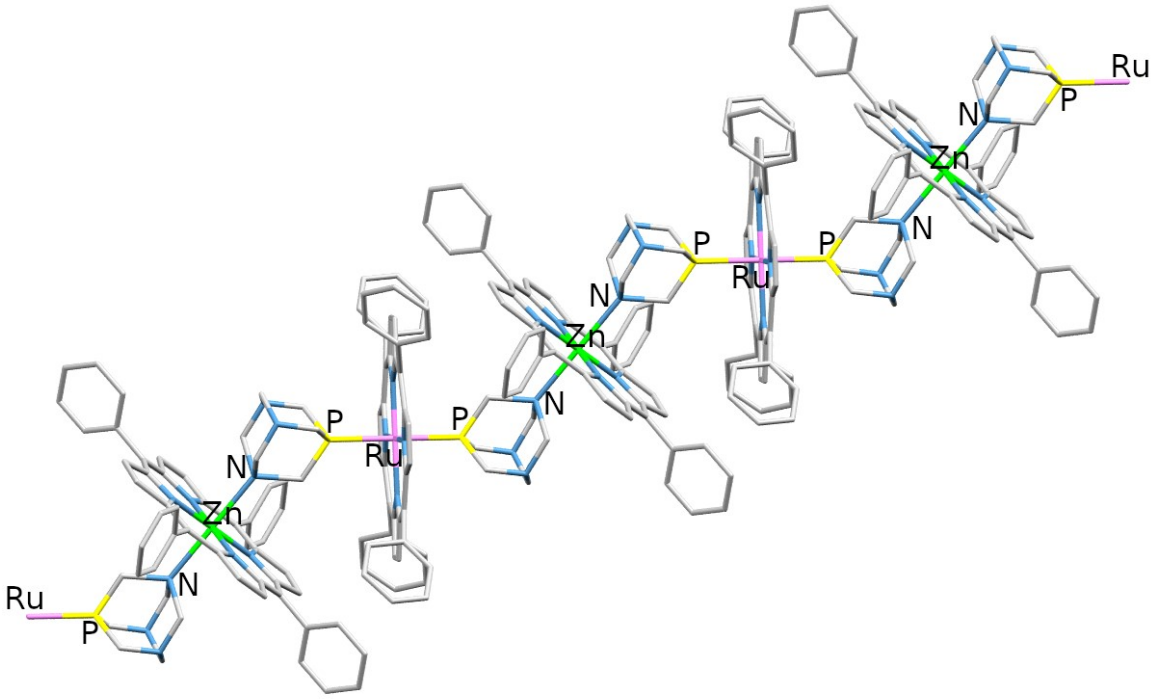

Figure A5.14. Stick representation of a portion of the zig-zag Ru(TPP)/Zn(TPP) chain present in the crystal structure of compound [{Ru(TPP)(PTA-κ^2*P,N*)$_2$}{Zn(TPP)}]$_\infty$ (**31**). Color code: Ru = light purple, Zn = green, P = yellow, N = blue.

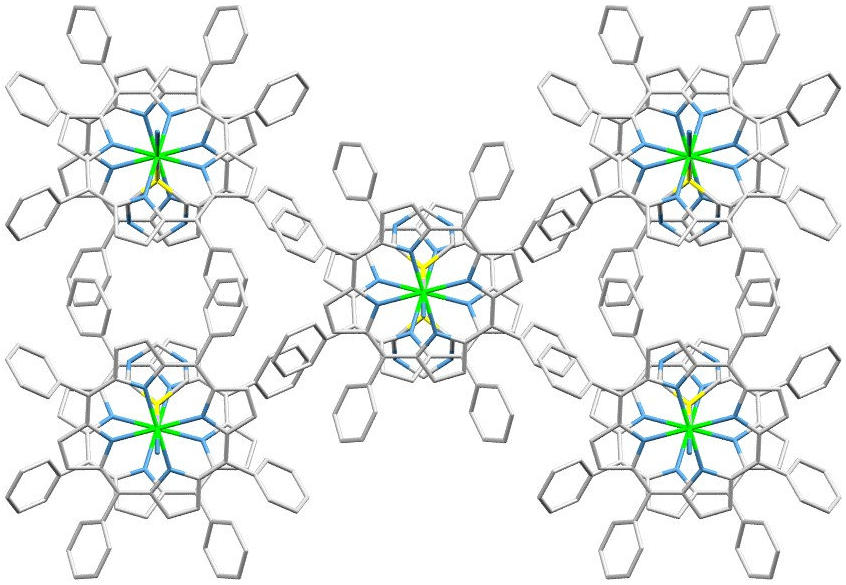

Figure A5.15. View along the c cell axis of five Ru(TPP)/Zn(TPP) chains in the crystal structure of compound [{Ru(TPP)(PTA-κ^2*P,N*)$_2$}{Zn(TPP)}]$_\infty$ (**31**).

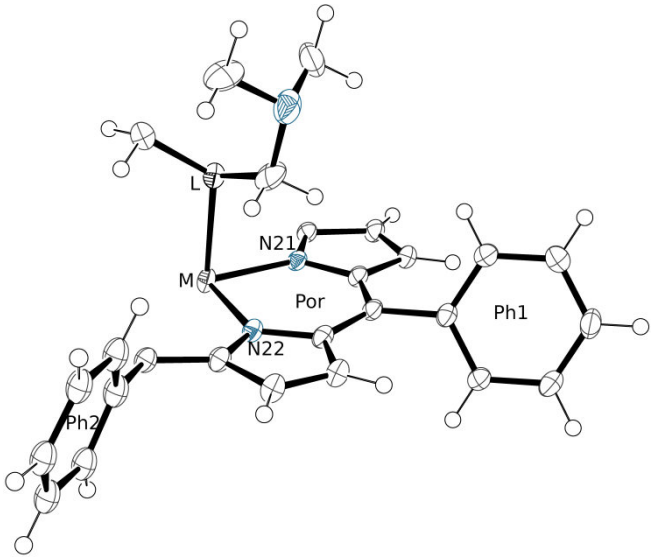

Figure A5.16. ORTEP representation (at 50% probability) of the asymmetric unit of the crystal structure of compound [{Ru(TPP)(PTA-κ^2*P,N*)$_2$}{Zn(TPP)}]$_\infty$ (**31**) (hydrogen atoms and minor population of a disordered phenyl group omitted for clarity). M and L indicate the crystallographic sites shared at 50% by Ru and Zn cations and P and N atoms, respectively; Por, Ph1 and Ph2 allow to visualize on the figure the dihedral angles reported in Table A5.4.

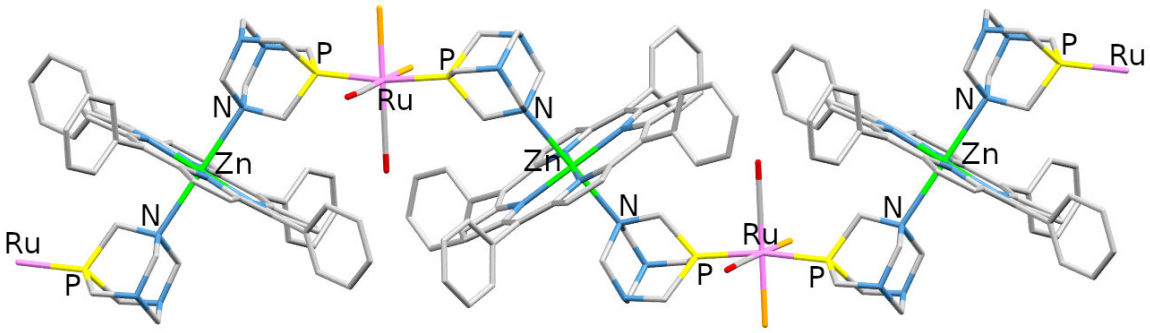

Figure A5.17: Stick representation of a portion of the linear "Greek frame" shaped Ru-Zn chain present in the crystal structure of compound *cis,cis,trans*-[{$Ru(CO)_2Cl_2$(PTA-κ^2*P,N*)$_2$}{Zn(TPP)}·9.2(H_2O)]$_\infty$ (**33**·9.2(H_2O)). Color code: Ru = light purple, Zn = green, P = yellow, N = blue, O = red, Cl = orange.

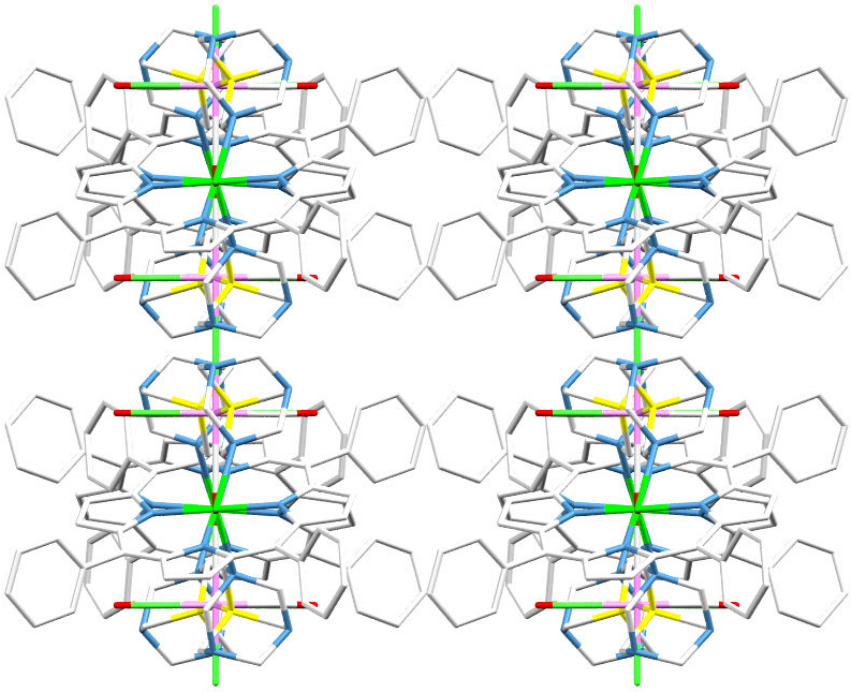

Figure A5.18. View along the c cell axis of four Ru-Zn chains in the crystal structure of compound *cis,cis,trans*-[{$Ru(CO)_2Cl_2$(PTA-κ^2*P,N*)$_2$}{Zn(TPP)}·9.2(H_2O)]$_\infty$ (**33**·9.2(H_2O)). The disordered water molecules – not shown – are located along the c axis, between the polymeric chains, and make hydrogen bonds among themselves but not with the chains. Color code: Ru = light purple, Zn = green, P = yellow, N = blue, O = red, Cl = orange.

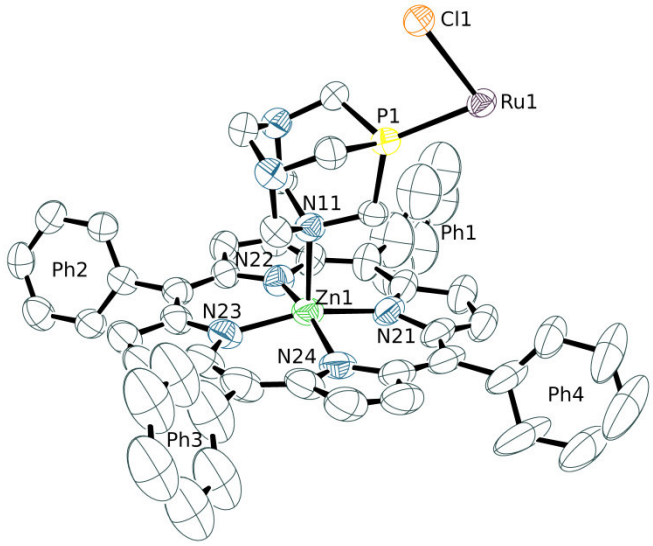

Figure A5.19: ORTEP representation (50% probability ellipsoids) of the asymmetric unit of the crystal structure of compound *trans*-[{$RuCl_2$(PTA-κ^2*P,N*)$_4$}{Zn(TPP)}$_4$]·8/3$CHCl_3$·2*n*-hexane (**36**·8/3$CHCl_3$·2*n*-hexane). Hydrogen atoms, two $CHCl_3$ and one *n*-hexane solvent molecules have been omitted for clarity. Labels PhX (X = 1 - 4) allow to visualize on the figure the dihedral angles quoted in Table A5.6. Color code: Ru = light purple, Zn = green, P = yellow, N = blue, O = red, Cl = orange.

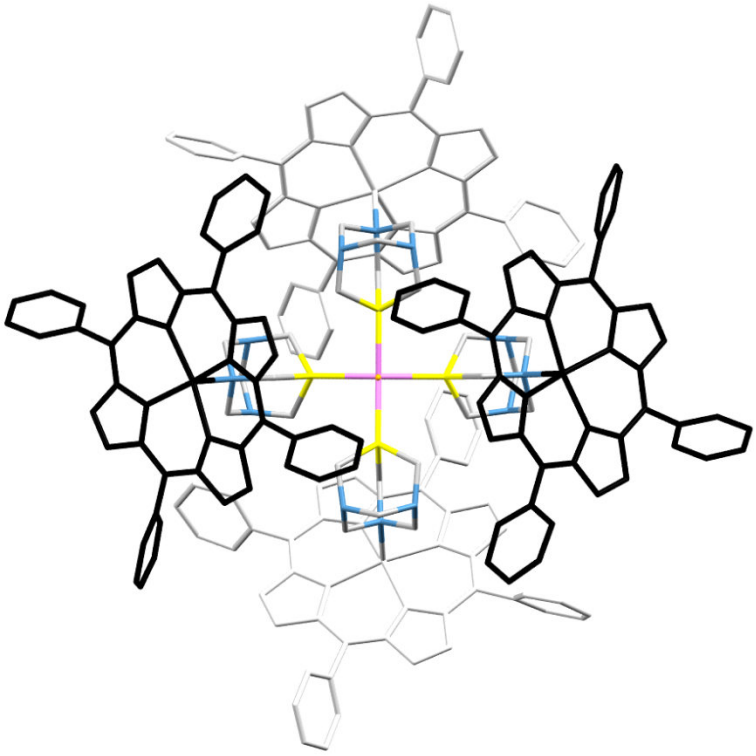

Figure A5.20: Stick representation of the molecule of complex *trans*-[{$RuCl_2$(PTA-κ^2*P,N*)$_4$}{Zn(TPP)}$_4$] (**36**) in the crystal structure viewed along the Cl–Ru–Cl axis. The ZnTPP units above and below the Ru equatorial plane have been evidenced with black and light gray colors, respectively.

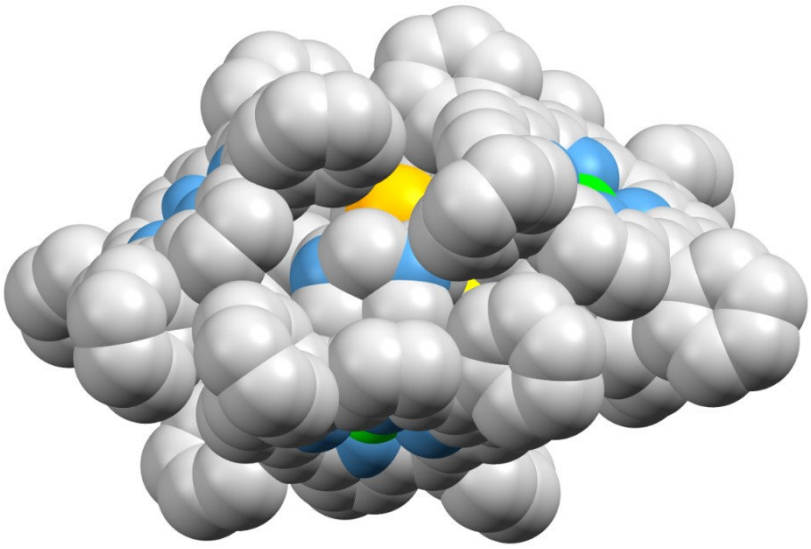

Figure A5.21: The space-fill representation of the molecule of complex *trans*-[{$RuCl_2$(PTA-κ^2*P,N*)$_4$}{Zn(TPP)}$_4$] (**36**) in the crystal structure evidences its very compact nature.

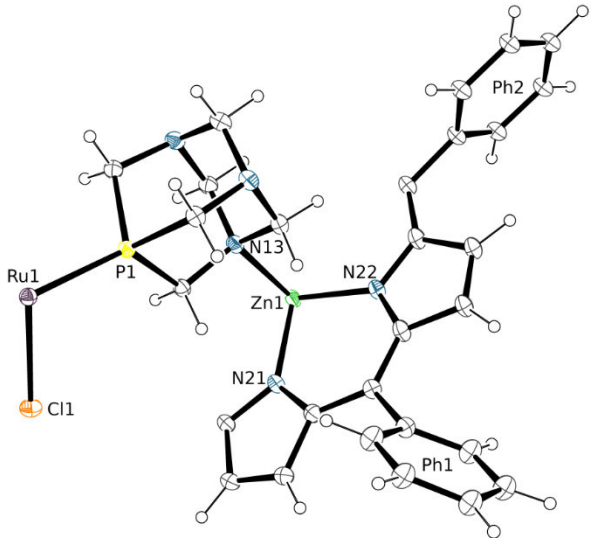

Figure A5.22: ORTEP representation (50% probability ellipsoids) of the asymmetric unit of the crystal structure of complex *trans*-[{$RuCl_2$(PTA-κ^2*P,N*)$_4$}{Zn(TPP)}$_2$·4$CHCl_3$]$_\infty$ (**36**·4$CHCl_3$). A disordered $CHCl_3$ solvent molecule has been omitted for clarity. For the same reason, only major populations of disordered phenyls and pyrrolic moieties of the TPP ligand have been included. Ph1 and Ph2 allow to visualize on the figure the dihedral angles reported in Table A5.7.

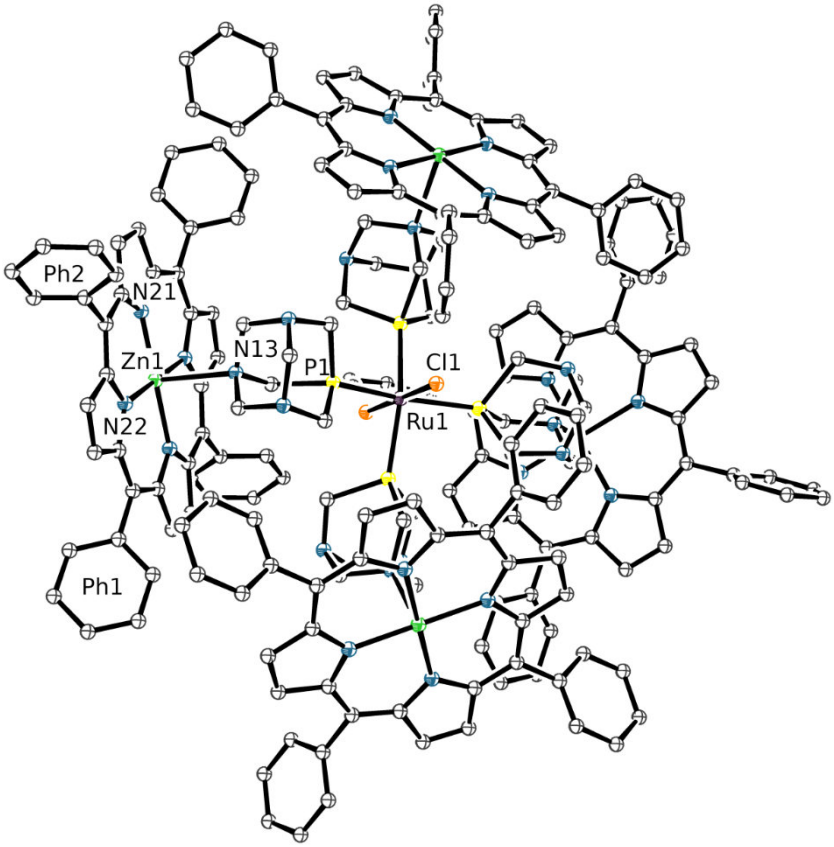

Figure A5.23: ORTEP representation (50% probability ellipsoids) of a "$RuZn_4$" fragment of the polymeric 3D net present in the crystal structure of complex *trans*-[{$RuCl_2$(PTA-$\kappa^2P,N)_4$}{Zn(TPP)}$_2$·4$CHCl_3$]$_\infty$ (**36**·4$CHCl_3$). Hydrogen atoms and a disordered $CHCl_3$ solvent molecule have been omitted for clarity. For the same reason, only major populations of disordered phenyls and pyrrolic moieties of the porphyrins have been included.

The zinc-acetate cluster of compound [{Ru(TPP)(PTA-$\kappa^3P,2N)_2$}{$Zn_9(CH_3COO)_{16}(CH_3OH)_2(OH)_2$}·9.2($H_2O$)]$_\infty$ (37·3$CHCl_3$).

The atomic arrangement of a single Zn_9 cluster of compound **37** is represented in Figure A5.24. There are nine Zn(II) cations, one of which, Zn4, occupies an inversion center. The remaining eight Zn cations are partitioned in two groups, related by the inversion center and therefore the description of the bonding environment is restrict to a single group of four Zn cations (Zn1, Zn2, Zn3, Zn5) plus Zn4 sitting on the inversion center. Overall, the Zn cations are connected to each other by bridging acetate anions, with some notable exceptions, as detailed below.

Zn4 has an octahedral environment in which an equatorial plane is formed by four O atoms (O311, O313, O311', O313') belonging to four distinct acetate anions, which provide bridging connections via their second O atom to Zn3, Zn5, Zn3' and Zn5', respectively. The axial positions of Zn4 are occupied by two (symmetry related) OH^- ions (O316 and O316'), that also cap in a μ_3 fashion Zn3 and Zn5 (O316), and Zn3' and Zn5' (O316').

Zn3 has a trigonal bipyramidal coordination with three O atoms (O35, O310, O314) from distinct bridging acetate anions in the equatorial plane, and axial positions occupied by the μ_3-hydroxo ligand mentioned above (O316) and an N atom (N22) of a PTA ligand *P*-bound to a Ru(TPP).

The coordination around Zn5 is less well defined. Zn5 is substantially five-coordinate by O atoms (equatorial: O37, O312, O316; apical: O39, O313), however the apical O313 is at a rather long distance of 2.473(4) Å (O313 also binds Zn4 at 2.126(4) Å). Moreover, a fourth weak interaction (bond length 2.570(4) Å) with an acetate O atom (O38) is also present in the equatorial plane.

Zn2 is connected via acetate bridges to both Zn3 and Zn5. Its octahedral coordination environment is provided by five O atoms of distinct bridging acetate ions (O31, O33, O36, O38, and O318) and a methanol ligand (O315). As mentioned above, O38 is also involved in an additional weak interaction with Zn5. Zn1 has a tetrahedral coordination, which is provided by the O atoms (O32, O33, and O317) of three distinct bridging acetate ions that connect Zn1 to Zn2, and by an N atom (N21) of a PTA ligand P-bound to a Ru(TPP).

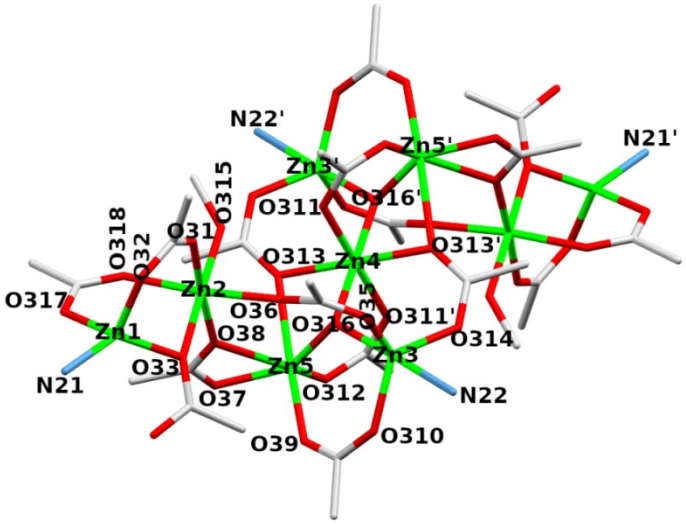

Figure A5.24. Stick representation of the Zn_9 cluster in the crystal structure of compound $[\{Ru(TPP)(PTA\text{-}\kappa^3P,2N)_2\}\{Zn_9(CH_3COO)_{16}(CH_3OH)_2(OH)_2\}\cdot 3CHCl_3]_\infty$ (**37**·3$CHCl_3$) (hydrogen atoms omitted for clarity). The nitrogen atoms of the four PTA ligands to which the Zn cluster binds are also shown. Primed atoms are symmetry images of corresponding non primed atoms via the inversion center at Zn4. Color code: Zn = green, N = blue, O = red.

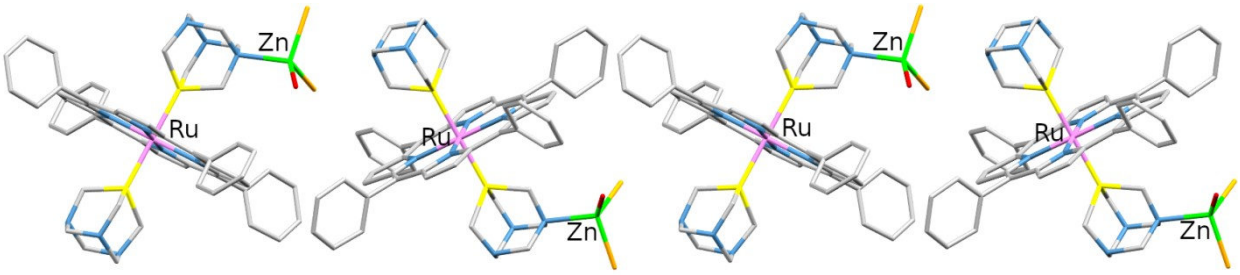

Figure A5.25. Stick representation of a portion of the 1D sequence present in the crystal structure of compound [{Ru(TPP)(PTA-κ*P*)(PTA-κ^2*P,N*)}{ZnCl$_2$(OH$_2$)}] (**38**). Color code: Ru = purple, Zn = green, P = yellow, N = blue, Cl = orange, O = red.

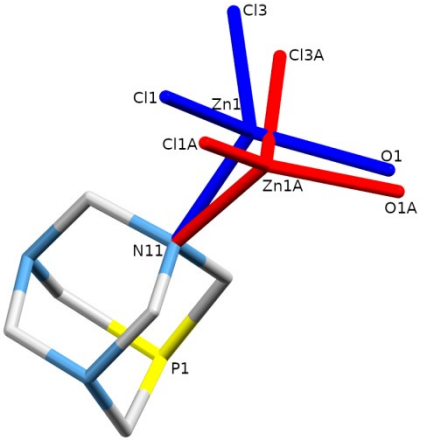

Figure A5.26: Stick representation of the disordered ZnCl$_2$(H$_2$O) group in the crystal structure of compound [{Ru(TPP)(PTA-κ*P*)(PTA-κ^2*P,N*)}{ZnCl$_2$(OH$_2$)}] (**38**). The two populations are evidenced in blue (SOF=0.3) and red (SOF=0.2). The symmetry mates generated by a 2-fold axis close to the Zn atoms (see text) have been omitted for clarity.

Additional comments on the X-ray structure of [{Ru(TPP)(PTA-κ*P*)(PTA-κ^2*P,N*)}{ZnCl$_2$(OH$_2$)}] (38)

As said in the main text, due to the low quality of the X-ray data and to the large disorder found around the Zn atom (Figure A5.26), the observed Fourier map for compound **38** could be refined also with a model consisting of the zwitterionic molecule [{Ru(TPP)(PTAH-κ*P*)(PTA-κ^2*P,N*)}$^+${ZnCl$_3$}$^-$]. We believe that chloroform, which is known to generate small amounts of HCl in the presence of oxygen and light,[A1] could be a plausible source of the adventitious protons for the generation of PTAH$^+$. In this hypothesis, adjacent zwitterions would be connected by the electrostatic interaction of the ZnCl$_3^-$ group of one with the PTAH$^+$ ligand of the other, forming a 1D ionic polymer. No similar structures can be found in the literature. However, crystallization of hexamethylenetetramine (HTMA) with ZnCl$_2$ in aqueous ammonia afforded (NH$_4$) [ZnCl$_3$(HTMA)]·1.5H$_2$O,[A2] whereas crystals of [Zn(OH$_2$)$_6$][ZnCl$_3$(HTMA)]$_2$·0.5H$_2$O were obtained from an aqueous solution containing equimolar amounts of Zn^{2+}, Cl$^-$ and HTMA.[A3]

Even though the X-ray data are not conclusive about the nature of compound **38**, we prefer the "neutral" formulation [{Ru(TPP)(PTA-κ*P*)(PTA-κ^2*P,N*)}{$ZnCl_2(OH_2)$}] over the zwitterionic one for the following reasons: 1) it is more chemically reasonable, since it does not require protonation of PTA in the absence of added acid; 2) the *R* factor of the X-ray structure is lightly better (8.4 vs 9.4); 3) the Zn–ligand bond lengths are more consistent with literature data. In fact, in the $ZnCl_3^-$ hypothesis, one of the three Zn–Cl bond lengths is particularly short (2.199(7) Å vs 2.239(4) and 2.25(1) Å for the other two)

Finally, we note that as far as the binding behavior of PTA is concerned, the two structural solutions are very similar.

References

[A1] a) Hill, B. G. Photochemical decomposition of chloroform *J. Am. Chem. Soc.* **1932**, *54*, 32-40; b) Kawai, S. Discussion on decomposition of chloroform *J-Stage* **1966**, *86*, 1125-1132.

[A2] Cheng, Y.-Q.; Lv, L.-P.; Xie, J.-W.; Wang, H.-B.; Jin, Z.-M. Ammonium trichloro(hexamethylenetetramine) zincate(II) sesquihydrate *Acta Crystallogr., Sect. E: Struct. Rep. Online* **2006***, 62*, m3591-m3593.

[A3] Basdouri, Z.; Trojette, B.; Falvello, L. R.; Graia, M.; Tomas, M. Synthesis, crystal structure, infrared spectroscopy, thermal analysis and Hirshfeld surface analysis of a new hemihydrate of $[Zn(H_2O)_6][\{(CH_2)_6N_4\}ZnCl_3]_2\cdot 0.5H_2O$ *J. Mol. Struct.* **2019**, *1176*, 165-180.

Table A5.1. Crystallographic data and refinement details for compounds [Ru(TPP)(PTA-κ*P*)$_2$]·2CHCl$_3$ (**28**·2CHCl$_3$) and [Zn(TPP)(PTA-κ*N*)]·H$_2$O·CHCl$_3$ (**30**·H$_2$O·CHCl$_3$).

	28·2CHCl$_3$	**30**·H$_2$O·CHCl$_3$
Empirical Formula	$C_{56}H_{52}N_{10}P_2Ru \cdot 2CHCl_3$	$C_{50}H_{40}N_7PZn \cdot H_2O \cdot CHCl_3$
Formula weight (Da)	1266.82	1945.31
Temperature (K)	173(2)	100(2)
Wavelength (Å)	0.700	0.700
Crystal system	monoclinic	triclinic
Space Group	*P* 21/c	*P* –1
a (Å)	13.770(5)	8.752(2)
b (Å)	18.932(4)	14.364(3)
c (Å)	10.952(2)	19.295(4)
α (°)	90	109.39(3)
β (°)	98.71(2)	100.96(3)
γ (°)	90	97.50(3)
V (Å^3)	2822(1)	2196.6(9)
Z	2	2
ρ (g·cm^{-3})	1.491	1.470
F(000)	1296	1004
μ (mm^{-1})	0.632	0.790
θ min, max (°)	1.815, 29.084	1.514, 28.227
Resolution (Å)	0.72	0.74
Total refl. collctd	49719	20757
Independent refl.	7811	10915
Obs. Refl. [Fo>4σ(Fo)]	7522	10630
I/σ(I) (all data)	18.75	52.26
I/σ(I) (max res)	15.92	36.70
Completeness (all data)	0.981	0.962
R_{merge} (all data)	7.3%	3.1%
R_{merge} (max res)	7.8%	3.3%
Multiplicity (all data)	6.3	19.2
Multiplicity (max res)	6.0	6.2
Data/restraint/parameters	7811/0/350	10915/98/678
GooF	1.050	1.063
R[I>2.0σ(I)],[a] wR2 [I>2.0σ(I)][a]	0.0453, 0.1255	0.0511, 0.1309
R (all data),[a] wR2 (all data)[a]	0.0460, 0.1263	0.0522, 0.1319

[a] $R_1 = \Sigma\, ||Fo|-|Fc|| \,/\, \Sigma|Fo|$, $wR_2 = [\Sigma\, w\,(Fo^2 - Fc^2)^2 \,/\, \Sigma w\,(Fo^2)^2]^{1/2}$

Table A5.1cont. Crystallographic data and refinement details for compounds [{Ru(TPP)(PTA-κ^2*P,N*)$_2$}{Zn(TPP)}]$_\infty$ (**31** and *cis,cis,trans*-[{Ru(CO)$_2$Cl$_2$(PTA-κ*P,N*)$_2$}{Zn(TPP)}·9.2(H$_2$O)]$_\infty$ (**33**·9.2(H$_2$O)).

	31	**33**·9.2(H$_2$O)
Empirical Formula	$C_{100}H_{80}N_{14}P_2RuZn$	$C_{58}H_{52}N_{10}Cl_2O_2P_2RuZn$· 9.2($H_2O$)
Formula weight (Da)	1706.16	2606.49
Temperature (K)	100(2)	100(2)
Wavelength (Å)	0.700	0.700
Crystal system	monoclinic	monoclinic
Space Group	C 2/c	*P* 2/c
a (Å)	23.524(3)	13.067(1)
b (Å)	11.925(4)	10.149(3)
c (Å)	14.409(3)	24.8580(9)
α (°)	90	90
β (°)	98.200(4)	91.568(5)
γ (°)	90	90
V (Å^3)	4001(2)	3295(1)
Z	4	1
ρ (g·cm^{-3})	1.416	1.313
F(000)	1764	1340
μ (mm^{-1})	0.563	0.740
θ min, max (°)	2.281, 28.225	2.552, 29.084
Resolution (Å)	0.74	0.72
Total refl. collctd	62648	57176
Independent refl.	5127	9173
Obs. Refl. [Fo>4σ(Fo)]	4650	8477
I/σ(I) (all data)	31.39	16.62
I/σ(I) (max res)	20.55	11.92
Completeness (all data)	0.986	0.991
R_{merge} (all data)	6.3%	7.4%
R_{merge} (max res)	17.2%	10.7%
Multiplicity (all data)	12.0	6.1
Multiplicity (max res)	11.4	5.8
Data/restraint/parameters	5127/0/256	9173/23/343
GooF	1.062	1.046
R[I>2.0σ(I)],[a] wR2 [I>2.0σ(I)][a]	0.0341,0.0895	0.0684, 0.1910
R (all data),[a] wR2 (all data)[a]	0.0374,0.0914	0.0715,0.1950

[a] $R_1 = \Sigma\,||Fo|-|Fc|| / \Sigma|Fo|$, $wR_2 = [\Sigma\, w\,(Fo^2 - Fc^2)^2 / \Sigma w\,(Fo^2)^2]^{½}$

Table A5.1cont. Crystallographic data and refinement details for compounds *trans*-[$RuCl_2$(PTA-$\kappa^2P,N)_4${Zn(TPP)}$_4$]·8/3$CHCl_3$·2*n*-hexane (**35**·8/3$CHCl_3$·2*n*-hexane) and *trans*-[{$RuCl_2$(PTA-$\kappa^2P,N)_4$}{Zn(TPP)}$_2$·4$CHCl_3$]$_\infty$ (**36**·4$CHCl_3$).

	35·8/3$CHCl_3$·2*n*-hexane	**36**·4$CHCl_3$
Empirical Formula	$C_{200}H_{160}N_{28}Cl_2P_4RuZn_4$·8/3$CHCl_3$·2$C_6H_{14}$	$RuZn_2Cl_2P_4C_{112}H_{104}N_{20}$·4$CHCl_3$
Formula weight (Da)	4003.54	2634.21
Temperature (K)	100(2)	100(2)
Wavelength (Å)	0.700	0.700
Crystal system	cubic	tetragonal
Space Group	I –4 3 d	I 41/a
a (Å)	38.537(7)	27.014(5)
b (Å)	38.537(7)	27.014(5)
c (Å)	38.537(7)	15.507(2)
α (°)	90	90
β (°)	90	90
γ (°)	90	90
V (Å^3)	57231(29)	11316(4)
Z	12	4
ρ (g·cm^{-3})	1.394	1.546
F(000)	24824	5384
μ (mm^{-1})	0.773	0.951
θ min, max (°)	1.275, 26.656	1.485, 29.080
Resolution (Å)	0.78	0.72
Total refl. collctd	389280	101816
Independent refl.	10529	7932
Obs. Refl. [Fo>4σ(Fo)]	10195	7695
I/σ(I) (all data)	77.13	67.79
I/σ(I) (max res)	23.75	45.42
Completeness (all data)	1.000	1.000
R_{merge} (all data)	4.7%	2.7%
R_{merge} (max res)	27.2%	3.7%
Multiplicity (all data)	68.7	12.8
Multiplicity (max res)	69.4	12.3
Data/restraint/parameters	10529/49/498	7932/19/348
GooF	1.031	1.033
R[I>2.0σ(I)],[a] wR2 [I>2.0σ(I)][a]	0.0785, 0.2284	0.0478, 0.1390
R (all data),[a] wR2 (all data)[a]	0.0798, 0.2317	0.0485,0.1397

[a] $R_1 = \Sigma\,||Fo|-|Fc|| / \Sigma|Fo|$, $wR_2 = [\Sigma\, w\,(Fo^2 - Fc^2)^2 / \Sigma w\,(Fo^2)^2]^{½}$

Table A5.1cont. Crystallographic data and refinement details for compounds [{Ru(TPP)(PTA-κ^3*P,2N*)$_2$}{Zn$_9$(CH$_3$COO)$_{16}$(CH$_3$OH)$_2$(OH)$_2$}·3CHCl$_3$]$_\infty$ (**37**·3CHCl$_3$) and [{Ru(TPP)(PTA-κ*P*)(PTA-κ^2*P,N*)}{ZnCl$_2$(OH$_2$)}·0.6CHCl$_3$] (38·0.6CHCl$_3$).

	37·3CHCl$_3$	**38**·0.6CHCl$_3$
Empirical Formula	$C_{56}H_{52}N_{10}P_2Ru$ + $C_{34}H_{58}O_{36}Zn_9$·3CHCl$_3$	$C_{56}H_{54}N_{10}Cl_2OP_2RuZn$·0.6CHCl$_3$
Formula weight (Da)	1508.66	1253.99
Temperature (K)	100(2)	100(2)
Wavelength (Å)	0.700	0.700
Crystal system	triclinic	monoclinic
Space Group	*P* –1	C 2/c
a (Å)	14.04(1)	17.404(4)
b (Å)	15.457(5)	19.878(5)
c (Å)	17.954(6)	17.524(2)
α (°)	110.15(1)	90
β (°)	109.19(2)	91.143(8)
γ (°)	94.31(2)	90
V (Å^3)	3375(4)	6061(2)
Z	1	4
ρ (g·cm^{-3})	1.484	1.347
F(000)	1526	2563
μ (mm^{-1})	1.866	0.868
θ min, max (°)	1.414, 28.227	1.899, 28.227
Resolution (Å)	0.74	0.74
Total refl. collctd	111508	89921
Independent refl.	17166	7375
Obs. Refl. [Fo>4σ(Fo)]	10951	6547
I/σ(I) (all data)	8.96	19.02
I/σ(I) (max res)	1.79	8.40
Completeness (all data)	0.982	0.922
R_{merge} (all data)	13.5%	8.5%
R_{merge} (max res)	136.0%	24.7%
Multiplicity (all data)	6.5	11.9
Multiplicity (max res)	6.2	11.8
Data/restraint/parameters	17166/0/746	7375/96/469
GooF	1.028	1.002
R[I>2.0σ(I)],[a] wR2 [I>2.0σ(I)][a]	0.0658, 0.1697	0.0840, 0.2396
R (all data),[a] wR2 (all data)[a]	0.1075, 0.1952	0.0893, 0.2481

[a] $R_1 = \Sigma\,||Fo|-|Fc|| / \Sigma|Fo|$, $wR_2 = [\Sigma\, w\,(Fo^2 - Fc^2)^2 / \Sigma w\,(Fo^2)^2]^{½}$

Table A5.2. Selected coordination distances (Å) and angles (°) for [Ru(TPP)(PTA-κ*P*)$_2$]·2CHCl$_3$ (**28**·2CHCl$_3$).

Bond distances (Å)			
Ru1–N1	2.064(1)	Ru1–P1	2.3253(7)
Ru1–N2	2.056(2)		
Bond angles (°)			
N1–Ru1–P1	88.04(4)	N2–Ru1–P1	88.82(5)
N1–Ru1–N2	90.09(6)		
Dihedral angles (°)			
Ru(TPP)⋯ Ph1	68.60(4)	Ru(TPP)⋯ Ph2	63.45(5)

The Ru atom sits on an inversion center, therefore some distances/angles are fixed (e.g. angle N1–Ru–N1' = 180°) and are not reported in the Table.

Table A.5.3. Selected coordination distances (Å) and angles (°) for [Zn(TPP)(PTA-κ*N*)]·H_2O·$CHCl_3$ (**30**·H_2O·$CHCl_3$).

Bond distances (Å)			
Zn1–N1	2.079(2)	Zn1–N3	2.068(2)
Zn1–N2	2.070(2)	Zn1–N4	2.067(2)
Zn1–N21	2.186(2)		
Bond angles (°)			
N1–Zn1–N21	97.74(7)	N3–Zn1–N21	100.14(7)
N2–Zn1–N1	88.13(6)	N4–Zn1–N1	88.16(6)
N2–Zn1–N21	99.11(7)	N4–Zn1–N2	159.47(6)
N3–Zn1–N1	162.10(6)	N4–Zn1–N3	89.10(6)
N3–Zn1–N2	88.25(6)	N4–Zn1–N21	101.40(7)
Dihedral angles (°)			
Zn(TPP)··· Ph1	46.41(4)	Zn(TPP)··· Ph2	50.95(4)
Zn(TPP)··· Ph3	62.28(5)	Zn(TPP)··· Ph4	43.19(4)

Table A.5.3bis. Selected bond distances (Å) for the PTA ligand in [Zn(TPP)(PTA-κ*N*)]·H_2O·$CHCl_3$ (**30**·H_2O·$CHCl_3$).

Bond distances (Å)			
N21–C21	1.487(3)	N23–C23	1.463(4)
N21 C24	1.496(3)	N23–C25	1.447(4)
N21 C26	1.493(3)	N23–C26	1.451(3)
N22–C22	1.468(3)	P21–C21	1.860(2)
N22–C24	1.458(3)	P21–C22	1.854(3)
N22–C25	1.471(3)	P21–C23	1.855(3)

Table A5.4. Selected coordination distances (Å) and angles (°) for [{Ru(TPP)(PTA-$\kappa^2P,N)_2$}{Zn(TPP)}]$_\infty$ (**4**).

Bond distances (Å)			
M–N21	2.049(1)	M–L	2.3800(7)
M–N22	2.062(1)		
Bond angles (°)			
N21–M–N22	89.92(5)	N22–M–L	89.00(4)
N21–M–L	88.46(4)		
Dihedral angles (°)			
M(TPP)··· Ph1	62.97(5)	M(TPP)··· Ph2	76.80(8)

Since in **4** the equatorial environment of Ru and Zn is identical and the P/N bonding modes of the PTA ligand are nearly geometrically equivalent, the symmetry of the observed diffraction pattern (space group C2/c) does not distinguish the two metal ions and the corresponding PTA binding modes leading to a crystallographically independent fragment in which a single metal site (M) is equally partitioned between Ru and Zn and, correspondingly, two symmetry related binding sites (L) of the PTA are partitioned at 50% between P and N. See also Figure A5.14 and A5.16.

Table A5.5. Selected coordination distances (Å) and angles (°) for *cis,cis,trans*-[{$Ru(CO)_2Cl_2$(PTA-κ^2*P,N*)$_2$}{Zn(TPP)}·9.2(H_2O)]$_\infty$ (**6**·9.2(H_2O)).

Bond distances (Å)			
Ru1–C1	1.907(5)	Ru1–P1	2.3480(7)
Ru1–C2	1.960(1)	Zn1–N1	2.059(2)
Ru1–Cl1	2.414(1)	Zn1–N2	2.058(2)
Ru1–Cl2	2.285(2)	Zn1–N11	2.532(2)
Bond angles (°)			
C1–Ru1–C2	89.6(3)	Cl2–Ru1–P1	87.74(7)
C1–Ru1–Cl2	90.29(7)	P1–Ru1–Cl1	85.41(2)
C1–Ru1–P1	94.59(2)	N1–Zn–N2	90.70(9)
C2–Ru1–Cl1	90.4(3)	N1–Zn–N2′	89.30(9)
C2–Ru1–P1	89.9(4)	N1–Zn–N11	87.77(8)
Cl2–Ru1–Cl1	89.71(7)	N2–Zn–N11	89.53(9)
Dihedral angles (°)			
Zn(TPP)⋯ Ph1	77.5(1)	Zn(TPP)⋯ Ph2	65.1(1)

Table A5.6. Selected coordination distances (Å) and angles (°) for *trans*-[$RuCl_2$(PTA-$\kappa^2P,N)_4${Zn(TPP)}$_4$]·8/3$CHCl_3$·2*n*-hexane (**8**·8/3$CHCl_3$·2*n*-hexane).

Bond distances (Å)			
Ru1–P1	2.324(2)	Zn1–N22	2.066(6)
Ru1–Cl1	2.412(2)	Zn1–N21	2.069(8)
Zn1–N11	2.242(6)	Zn1–N24	2.078(7)
Zn1–N23	2.044(8)		
Bond angles (°)			
P1–Ru1–Cl1	80.10(4)		
Dihedral angles (°)			
Zn(TPP)··· Ph1	78.1(2)	Zn(TPP)··· Ph3	63.2(3)
Zn(TPP)··· Ph2	68.2(2)	Zn(TPP)··· Ph4	55.5(4)

Table A5.7. Selected coordination distances (Å) and angles (°) for *trans*-[{$RuCl_2$(PTA-$\kappa^2P,N)_4$}{Zn(TPP)}$_2$·4$CHCl_3$]$_\infty$ (**9**·4$CHCl_3$).

Bond distances (Å)			
Ru1–P1	2.3359(7)	Zn1–N21	2.063(2)
Ru1–Cl1	2.4246(8)	Zn1–N22	2.055(2)
Zn1–N13	2.4869(2)		
Bond angles (°)			
P1–Ru1–Cl1	100.60(1)	N22–Zn1–N13	89.78(7)
N21–Zn1–N13	87.83(7)	N21–Zn1–N22	89.74(7)
Dihedral angles (°)			
Zn(TPP)··· Ph1	60.20(8)	Zn(TPP)··· Ph2	73.90(8)

Table A5.8. Selected coordination distances (Å) and angles (°) for the {Ru(TPP)} part of [{Ru(TPP)(PTA-κ^3*P,2N*)$_2$}{Zn$_9$(CH$_3$COO)$_{16}$(CH$_3$OH)$_2$(OH)$_2$}·3CHCl$_3$]$_\infty$ (**37**·3CHCl$_3$).

Bond distances (Å)			
Ru1–N11	2.058(4)	Zn1–N21	2.063(4)
Ru1–N12	2.060(4)	Zn3–N22	2.363(4)
Ru1–P21	2.322(2)		
Bond angles (°)			
N11–Ru1–N12	90.2(2)	O33–Zn1–N21	133.4(2)
N11–Ru1–P21	92.6(1)	O310–Zn3–N22	80.6(2)
N12–Ru1–P21	89.9(1)	O35–Zn3–N22	81.6(1)
O317–Zn1–N21	98.3(2)	O314–Zn3–N22	82.19(2)
O32–Zn1–N21	99.6(2)	O316–Zn3–N22	175.1(1)
Dihedral angles (°)			
Ru(TPP)··· Ph1	63.3(2)	Ru(TPP)··· Ph2	65.6(2)

Table A5.8bis. Selected coordination distances (Å) and angles (°) for the zinc-acetate cluster part of [{Ru(TPP)(PTA-κ^3*P,2N*)$_2$}{Zn$_9$(CH$_3$COO)$_{16}$(CH$_3$OH)$_2$(OH)$_2$}·3CHCl$_3$]$_\infty$ (**37**·3CHCl$_3$).

Bond distances (Å)			
Zn1–O317	1.962(4)	Zn3–O316	2.039(3)
Zn1–O32	1.936(6)	Zn3–O35	2.009(4)
Zn1–O33	1.960(4)	Zn4–O311	2.170(4)
Zn2–O31	2.073(4)	Zn4–O313	2.126(4)
Zn2–O315	2.077(4)	Zn4–O316	2.015(3)
Zn2–O318	2.074(4)	Zn5–O312	1.983(4)

Zn2–O33	2.121(5)	Zn5–O313	2.473(4)
Zn2–O36	2.087(4)	Zn5–O316	1.958(4)
Zn2–O38	2.081(4)	Zn5–O37	1.990(4)
Zn3–O310	1.984(4)	Zn5–O38	2.570(4)
Zn3–O314	1.971(3)	Zn5–O39	2.040(4)
Bond angles (°)			
O32–Zn1–O33	100.9(2)	O314–Zn3–O35	116.8(2)
O32–Zn1–O317	113.0(2)	O310–Zn3–O35	117.5(2)
O33–Zn1–O317	111.1(2)	O314–Zn3–O310	119.1(2)
O38–Zn2–O36	83.0(2)	O313–Zn4–O311	90.7(2)
O315–Zn2–O36	84.8(2)	O316–Zn4–O311	90.2(1)
O318–Zn2–O315	85.4(2)	O316–Zn4–O313	97.5(1)
O315–Zn2–O38	89.4(2)	O312–Zn5–O313	84.5(2)
O31–Zn2–O33	89.4(2)	O312–Zn5–O37	104.7(2)
O38–Zn2–O33	90.0(2)	O312–Zn5–O39	97.4(2)
O31–Zn2–O318	90.3(2)	O316–Zn5–O312	111.3(2)
O31–Zn2–O315	91.1(2)	O316–Zn5–O313	75.1(1)
O318–Zn2–O38	93.1(2)	O316–Zn5–O37	140.1(2)
O31–Zn2–O36	93.7(2)	O316–Zn5–O39	101.1(1)
O36–Zn2–O33	94.1(2)	O37–Zn5–O313	92.2(1)
O318–Zn2–O33	95.7(2)	O37–Zn5–O39	90.5(2)
O318–Zn2–O36	169.5(1)	O38–Zn5–O312	156.2(2)

O31–Zn2–O38	176.7(2)	O38–Zn5–O313	83.5(1)
O315–Zn2–O33	178.8(2)	O38–Zn5–O316	85.3(1)
O35–Zn3–O316	94.5(1)	O38–Zn5–O37	55.4(2)
O310–Zn3–O316	98.8(2)	O38–Zn5–O39	95.9(2)
O314–Zn3–O316	102.3(2)	O39–Zn5–O313	176.2(1)

Table A5.9. Selected coordination distances (Å) and angles (°) for [{Ru(TPP)(PTA-κ*P*)(PTA-κ^2*P,N*)}{$ZnCl_2(OH_2)$}·0.6$CHCl_3$] (**38**·0.6$CHCl_3$).

Bond distances (Å)			
Ru1–N21	2.049(3)	Zn1–O1[a]	2.10(1)
Ru1–N22	2.052(3)	Zn1–Cl1[a]	2.23(1)
Ru1–P1	2.310(1)	Zn1–Cl3[a]	2.367(2)
Zn1–N11[a]	2.192(7)		
Bond angles (°)			
N21–Ru1–P1	88.96(9)	O1–Zn1–Cl1[a]	120.6(7)
N22–Ru1–P1	90.2(1)	O1–Zn1–Cl3[a]	101.2(7)
N21–Ru1–N22	90.3(1)	O1–Zn1–N11[a]	113.7(4)
Cl1–Zn1–Cl3[a]	115.0(7)	Cl3–Zn1–N11[a]	99.7(5)
Cl1–Zn1–N11[a]	104.5(5)		
Dihedral angles (°)			
Ru(TPP)··· Ph1	73.5(2)	Ru(TPP)··· Ph2	72.1(1)

[a] values averaged over the two populations of the {$ZnCl_2(OH_2)$} group

CHAPTER 6

6 New Route To Ru(II)-Polypyridyl Compounds

6.1 Introduction

Ruthenium(II) polypyridyl-type complexes are well known to the inorganic chemistry community, mainly because of their appealing photophysical and photochemical properties (strong absorption and emission bands in the visibleto-NIR region, long-lived triplet excites states).[1] Most importantly, by varying the nature and the numbers of the polypyridyl ligands around Ru(II) such properties can be accurately fine-tuned.[2] The numerous applications of Ru(II) polypyridyl-type complexes span widely different fields, from light-into electrical energy conversion (e.g. in dye-sensitized solar cells)[3] and photo-redox catalysis.[4,5] to biomedicine.[2,6,7] In this latter field, by virtue of their multiple excited state relaxation pathways, Ru(II) polypyridyl complexes can be exploited either for sensing and imaging applications or as photosensitizers in photodynamic therapy (PDT) and photochemotherapy (PCT).[2,6-16] Remarkably, the first metal-based sensitizer for photodynamic therapy to be investigated in the clinic is a Ru(II)-polypyridyl complex (named TDL143).[17] In addition, Ru(II) polypyridyl complexes are being actively investigated for their light-independent anticancer properties.[18-20]

Notwithstanding the widespread interest in this class of compounds, we found that the synthetic aspects leading to their preparation are still amenable to be improved.

The synthetic procedures leading to polypyridyl Ru(II) complexes bearing three equal or different diimine chelating ligands (chel) have been thoroughly reviewed by Spiccia and co-workers in 2004.[21] Quite obviously, upon going from homoleptic $[Ru(chel)_3]^{2+}$ to tris-heterlopetic $[Ru(chel)(chel')(chel'')]^{2+}$ compounds the synthetic procedures become more challenging. Optical resolution of the chiral-at-metal Δ and Λ enantiomers adds an additional level of complexity.[22] The reader interested to this specific topic is referred to the relatively recent review by Meggers and co-workers.[23]

Bis-heteroleptic $[Ru(chel)_2(chel')]^{2+}$ compounds are typically obtained from the neutral intermediate *cis*-$[RuCl_2(chel)_2]$,[24] which is synthesized predominantly by the procedure described by Meyer and co-workers in 1978.[25] It requires treatment of hydrated $RuCl_3$ with chel in hot DMF in the presence of an excess of LiCl and, in some preparations, of a reducing agent.[26] In some cases the dichloride intermediate was not isolated but further reacted in situ with chel′.[22] Even though apparently straightforward, this procedure – that works well for simple diimines such as bpy and for large-scale preparations – has a number of drawbacks (unknown mechanism, poor control of the stoichiometry due to the uncertain nature of the ruthenium precursor, formation of carbonyl byproducts due the non-innocent and thermally unstable solvent,[27] very high concentration unpractical for small-scale

preparations, removal of excess LiCl, that led to the investigation of alternative procedures. Stepwise synthetic methods, that might allow also the preparation of the more demanding tris-heteroleptic compounds, are particularly interesting. Synthetic procedures starting from a Ru(II) precursor would seem particularly logical. There are essentially three such routes, two that utilize an organometallic precursor,[28] either the oligomeric carbonyl $[RuCl_2(CO)_2]_n$ (that involves either a photo-assisted or a chemically-assisted decarbonylation route)[29-33] or the dinuclear half-sandwich compound $[Ru(\eta^6\text{-}C_6H_6)Cl_2]_2$ (that requires the photo-assisted release of the aromatic ring)[34,35] or the coordination complex [*cis*-$RuCl_2(dmso)_4$] (**39**). Compound **39** has a number of advantages over the others, beside its low cost and commercial availability: *i*) unlike $[RuCl_2(CO)_2]_n$ and $RuCl_3\cdot 3H_2O$ it is a well-defined species and allows precise control of the stoichiometry of the reactants; *ii*) it is obtained in a single step preparation from the universal ruthenium precursor $RuCl_3\cdot 3H_2O$ in high-yield and excellent purity;[36] *iii*) it is non-toxic, perfectly stable and soluble in a wide range of solvents, from water to chloroform;[37] *iv*) it does not require the use of a photoreactor. The route from complex **39** is treated in more detail below.

6.1.1 [*cis*-$RuCl_2(dmso)_4$] as precursor for the preparation of Ru(II) polypyridyl complexes

When [*cis*-$RuCl_2(dmso)_4$] is treated with neutral ligands, the dmso ligands are expected to be replaced preferentially, and in a stepwise manner, to yield neutral products.[37,38] In particular, consistent with the reactivity observed by us with neutral monodentate pyridyl and azole ligands,[38,39] a neutral diimine ligand (chel) should replace quite easily the dmso-O (i.e. the weakest ligand) and an adjacent dmso-S, whereas the two remaining dmso-S's are expected to require relatively harsher conditions to be substituted, thus allowing – in principle – for the stepwise introduction of different diimines.[40] However, contrasting reports are present in the literature and the results seem to depend not only on the nature of the solvent (and therefore on the temperature) and chel/Ru ratio but also on the nature of chel.[23,37] For example, Keyes and Burke reported that treatment of **39** with one equiv of chel (chel = dipyrido[3,2-a:2′,3′-c]phenazine, dppz) in refluxing EtOH affords [*cis,cis*-$RuCl_2$(chel)(dmso-S)$_2$] selectively and with high yield,[41] whereas for Grätzel and co-workers this reaction (chel = 4,4′-dimethyl-bpy) must be run at lower temperatures (refluxing $CHCl_3$) for being selective[40] In fact, according to these authors, protic solvents (e.g. EtOH) or high boiling aprotic solvents afforded mixtures of mono- and bis-substituted complexes. On the other hand, Bowman and co-workers reported that reaction of **39** with one equiv. of phen in refluxing $CHCl_3$ gave only a low conversion, whereas in refluxing toluene [*cis,cis*-$RuCl_2$(dmso-S)$_2$(phen)] precipitated with excellent yield.[42] Similarly, according to Toyama, Nagao and co-workers [*cis,cis*-$RuCl_2$(dmso-S)$_2$(bpy)] is selectively obtained by refluxing **39** with one equiv. of bpy in a 9:1 EtOH:DMSO mixture.[43] Finally, we and

others found that the substitution of two dmso ligands in **39** with chelating diimines can be accompanied by isomerization of the remaining ligands, affording stereoisomers.[43,44]

According to literature reports, treatment of **39** with two equiv. of chel (or one equiv. of chel and one of chel′) in refluxing organic solvents (ranging from chloroform to ethylene glycol) leads usually to the replacement of all four dmso ligands affording $[RuCl_2(chel)_2]$ species. The reaction can be accompanied by isomerization of the two chlorides from *cis* to *trans* geometry.[45,46] However, there are examples in which the neutral diimines replace three dmso ligands and a chloride, yielding cationic complexes of the type [*cis*-$RuCl(chel)_2$(dmso-S)]Cl.[47,48]

Stimulated by these often contradicting literature reports, we investigated the reactions of **39** with selected diimine chelating ligands (e.g. chel = bpy, phen, and dppz) in different conditions, and found that it typically yields mixtures of substitutional isomers, often as stereoisomers (see below). To be noted that the formation of stereoisomers with *trans* geometry of the remaining monodentate ligands (e.g. [*trans,cis*-$RuCl_2$(chel)$(dmso\text{-}S)_2$], [*cis,trans*-$RuCl_2$(chel)$(dmso\text{-}S)_2$], and [*trans*-$RuCl_2(chel)_2$]) and/or substitutional isomers (e.g. $[RuCl(chel)_2(dmso\text{-}S)]Cl$) creates practical problems (isolation and characterization of mixtures of intermediates), but it is not necessarily detrimental for the obtainment of the final $[Ru(chel)_2(chel')]^{2+}$ product (even though it cannot be excluded that the required *trans*-to-*cis* stereochemical rearrangement might induce significant kinetic barriers in the process).

Both Meggers and co-workers and, more recently, Burke and Keyes proposed synthetic strategies for the preparation of bis- and tris-heteroleptic polypyridyl Ru complexes from **39** that avoid the formation of stereoisomers:[41,49] either in the first or second step of the synthetic procedure an auxiliary bidentate ligand of switchable binding strength (aux) is introduced in the coordination sphere of Ru(II), obtaining intermediates of the type $[Ru(chel)_2(aux)]^{n+}$ or $[Ru(chel)(chel')(aux)]^{n+}$ (aux = oxalate, n = 0; or a chiral salicyloxazoline, n = 1). The coordination of the last diimine ligand is preceded by the acid-assisted removal of the aux ligand.

Building on this approach and on our own experience on Ru-dmso compounds,[37,38] we thought of developing new *cis*-locked Ru(II)-dmso precursors by replacing either the two chlorides, or a chloride and a dmso, in **39** with an inert chelating anion (O–O, Figure 6.1), and to investigate them for the two-step preparation of bis-heteroleptic products $[Ru(chel)_2(chel')]^{2+}$, as detailed in Scheme 6.1.

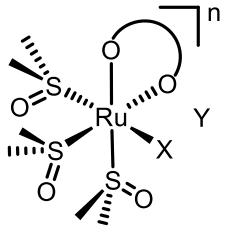

Figure 6.1. Schematic representation of a *cis*-locked Ru(II)-dmso precursor with a chelating oxygenated anion (O–O) developed in this work. X = dmso or Cl. The charge (n = –1/0/+1) depends on the nature and charge of X and O–O. When present, Y = K^+ or PF_6^-.

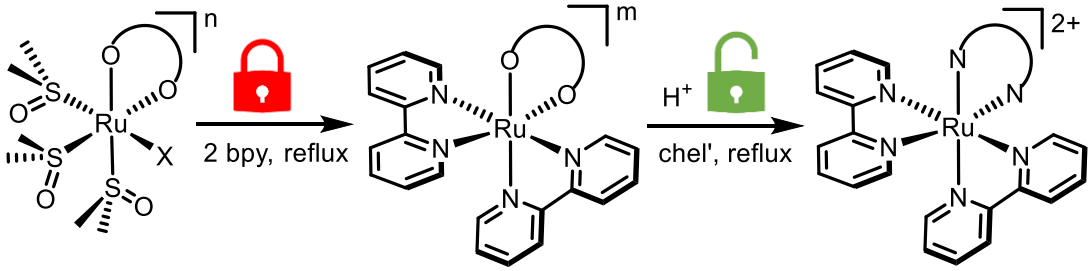

Scheme 6.1. Schematic representation of the two-step preparation of bis-heteroleptic products $[Ru(chel)_2(chel')]^{2+}$ (exemplified for chel = bpy) from a *cis*-locked Ru(II)-dmso precursor. The charge of the starting compound (n) and of the intermediate (m) depend on the nature and charge of X and O–O. Counter-ion omitted.

Such precursors are expected to have, in principle, a number of advantages over compound **39**: *i*) the presence of a chelate that locks the geometry should avoid the formation of stereoisomers. Replacement of the four relatively labile dmso/Cl ligands by chelating diimines (chel) will thus be stereo-controlled; *ii*) since the chelating O–O ligand is supposed to be more strongly bound to ruthenium compared to the chlorides in **39**, the possibility of obtaining substitutional by-products (e.g. $[Ru(chel)_3]^{2+}$) should be lower compared to **39**; *iii*) in the second step, the proton-sensitive nature of O–O is expected to allow its replacement under relatively mild acidic conditions. Thus, contrary to what often found in the literature, this step might be performed at relatively low temperature. This feature might become particularly relevant if the auxiliary ligand has a chiral center and is enantiomerically pure: in this case an excess of one diastereoisomer of the bischelate adduct is obtained, and low temperature should limit potential racemization in the last step; *iv*) in principle, provided that the monodentate ligands can be pairwise replaced in two steps with sufficient selectivity, this approach might be suitable also for the preparation of tris-heteroleptic polypyridyl products.

In order to avoid formation of stereoisomers the symmetrical chelating anions (O–O) oxalate (ox), malonate (mal), and acetylacetonate (acac) were selected. Even though ox might form stronger chelate rings compared to mal and acac, it has some drawbacks: it is proton-NMR silent and has additional binding modes available (besides the η^2-ox) in which it bridges two metal ions using all

four oxygen atoms (η^4,μ-ox) or, occasionally, only three of them (η^3,μ-ox). The dimethyl-malonate ligand (dmmal), that would be excellent for the purpose of NMR detection, was discarded because it preferentially forms the dinuclear species [*fac*-Ru(dmso-S)$_3$(OH$_2$)(η-dmmal)$_2$] when reacted with **39**.[50]

6.2 Results and Discussion

Building on our experience in the chemistry of [*cis*-RuCl$_2$(dmso)$_4$] (**39**), we reinvestigated some of its reactions with the model diimine ligand phen. As detailed in the Appendix, we found that: *i*) contrary to what reported in the literature, the reaction of **39** with one equiv of phen in refluxing chloroform for 1 h (i.e. the conditions of refs. 21 and 40), besides being largely incomplete, affords a ca. 1:1 mixture of the two stereoisomers [*cis*,*cis*-RuCl$_2$(dmso-S)$_2$(phen)] (**a**) and [*trans,cis*-RuCl$_2$(dmso-S)$_2$(phen)] (**b**); *ii*) the same reaction performed in refluxing ethanol for 2 h (i.e. the conditions used in ref. 41 for the selective preparation of [*cis*,*cis*-RuCl$_2$(dmso-S)$_2$(dppz)]) was complete and afforded a ca. 5:1 mixture of **a** and [*cis,trans*-RuCl$_2$(dmso-S)$_2$(phen)] (**c**) and a minor amount of the di-substituted cationic product [*cis*-RuCl(dmso-S)(phen)$_2$]Cl (**d**);[51] *iii*) Similar results, but with a larger amount of compound **d** were obtained also when **39** was treated with two (rather than one) equiv. of phen in refluxing ethanol (up to 8 h). In contrast with literature reports the expected di-substituted neutral species [*cis*-RuCl$_2$(phen)$_2$] was not detected among the products. On the positive side, the dead-end tri-substituted species [Ru(phen)$_3$]$^{2+}$ was not found among the products either. This finding was somehow surprising because, even though some preparations of [Ru(chel)$_3$]$^{2+}$ compounds from **39** are typically performed at higher temperature, it was nevertheless reported that – for example – treatment of **39** with three equiv. of dppz in refluxing ethanol produced [Ru(dppz)$_3$]$^{2+}$ exclusively.[52] The results of this investigation suggested that – in general – compound **39** is not particularly reactive and well-behaved for this type of reactions and that what reported in the literature for a particular diimine ligand is not automatically extensible even to similar ligands.

6.2.1 Preparation of *cis*-locked precursors

In the past we have already developed, for different reasons, the *cis*-locked dicarboxylate complexes K[*fac*-RuCl(dmso-S)$_3$(η^2-mal)] (**40**), [*fac*-Ru(dmso-O)(dmso-S)$_3$(η^2-mal)] (**41**), K[*fac*-RuCl(dmso-S)$_3$(η^2-ox)] (**42**), and [*fac*-Ru(dmso-O)(dmso-S)$_3$ (η^2-ox)] (**43**) (Figure 6.2).[50] We report here, besides improved preparations for **42** and **43**, also the synthesis and characterization of two additional complexes of this series with the monoanionic acetylacetonate (acac) ligand: the neutral [*fac*-

RuCl(dmso-S)$_3$(η^2-acac)] (**44**), and the cationic [*fac*-Ru(dmso-O)(dmso-S)$_3$(η^2-acac)][PF_6] (**45**) (Figure 6.2).

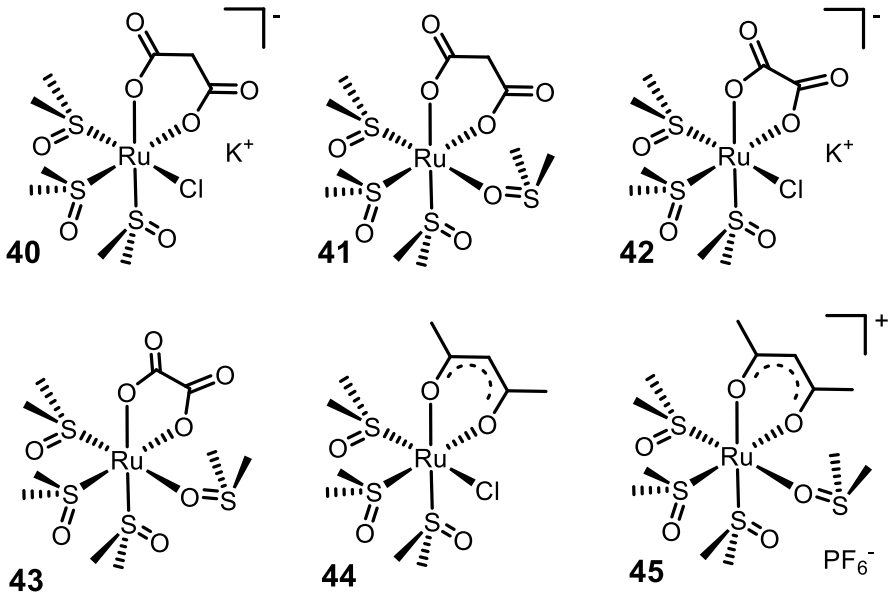

Figure 6.2. The *cis*-locked Ru(II)-dmso precursors K[*fac*-RuCl(dmso-S)$_3$(η^2-mal)] (**40**), [*fac*-Ru(dmso-O)(dmso-S)$_3$(η^2-mal)] (**41**), K[*fac*-RuCl(dmso-S)$_3$(η^2-ox)] (**42**), [*fac*-Ru(dmso-O)(dmso-S)$_3$(η^2-ox)] (**43**), [*fac*-RuCl(dmso-S)$_3$(η^2-acac)] (**44**), and [*fac*-Ru(dmso-O)(dmso-S)$_3$(η^2-acac)][PF_6] (**45**).

In summary, both mono- and di-anionic O–O chelates react with **39** replacing the dmso-O and an adjacent chloride, yielding **40**, **42**, and **44**. We had no evidence of products derived from the spontaneous substitution of both chlorides of **39**, even when the reaction was performed in aqueous DMSO. Chloride-free complexes **41**, **43**, and **45** were prepared by silver-assisted chloride abstraction either in a stepwise manner from the corresponding mono-chloride intermediates or from the chloride-free precursor [*fac*-Ru(dmso-O)$_3$(dmso-S)$_3$](X)$_2$ (which is obtained in one step from **39**, X = CF_3SO_3, NO_3, PF_6)[37,38] or, more conveniently, directly from **39** in a one-pot reaction (Scheme 6.2). The first route requires only one equiv. of silver, but the isolation of an intermediate (and thus lower final yields).

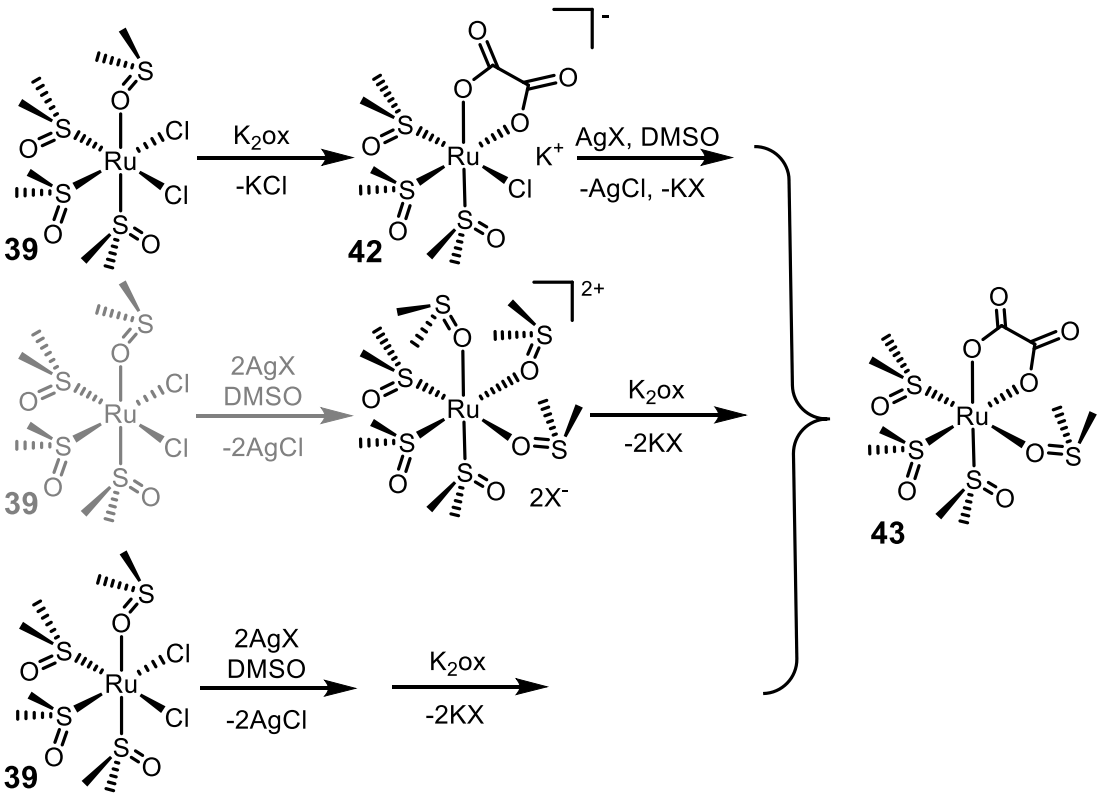

Scheme 6.2 General procedures for the preparations of complexes **41**, **43**, and **45** (X = CF_3SO_3, NO_3, PF_6) exemplified in the case of **43** (O–O = oxalate). The grey part shows the preparation of the chloride-free precursor [*fac*-Ru(dmso-O)$_3$(dmso-S)$_3$](X)$_2$.

All compounds **40**–**45** were fully characterized by IR and NMR spectroscopy and ESI MS spectrometry (including isotope distribution). The ^{1}H NMR spectra are consistent with the C_S symmetry of the complexes (i.e. the O–O ligand is symmetrically bound *trans* to two dmso-S ligands). They show a pattern of three singlets (6H each) in the region for S-bonded dmso, which is typical for the {*fac*-Ru(dmsoS)$_3$} fragment. The dmso-O in **41**, **43**, and **45** resonates as a singlet at about 2.8 ppm. The diastereotopic protons of the mal ligand in **40** and **41** give two doublets (1H each), whereas the acac ligand in **44** and **45** gives two singlets (1H and 6H, respectively). The X-ray structures of the new compounds **44** and **45** are shown in Figure 6.3. At room temperature all complexes are soluble in water (with the exception of **45**), methanol, and DMSO. The neutral complexes **41** and **44** (but not the ox compound **43**) are soluble also in chloroform and the cationic PF_6 complex **45** is soluble in acetone.

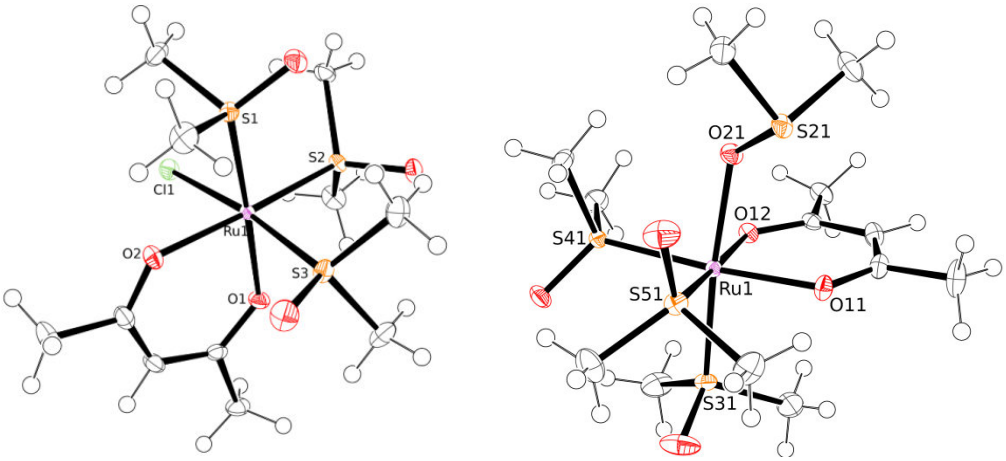

Figure 6.3. X-ray molecular structure (50% probability ellipsoids) of complex [*fac*-RuCl(dmso-S)$_3$(η^2-acac)] (**44**, left) and of the cation of [*fac*-Ru(dmso-O)(dmso-S)$_3$(η^2-acac)][PF$_6$] (**45**, right).

Having in hand this homogeneous set of six *cis*-protected complexes, we investigated their reactivity towards the diimine chelating ligand bpy and, in some cases, phen and 4,7-diphenyphenanthroline (dpphen).

We have previously evidenced how, in water, the release of the chloride from the anionic complexes [*fac*-RuCl(dmso-S)$_3$(O–O)]$^-$ (O–O = ox, mal) is much slower compared to the release of dmso-O from the corresponding [*fac*-Ru(dmso-O)(dmso-S)$_3$(O–O)] species, despite the charge difference. Overall, these findings suggest that the dmso-O complexes **41**, **43**, and **45** are expected to be more reactive than the corresponding chloride compounds **40**, **42**, and **44**. In addition, when treated with chel the formers do not generate inorganic salts (e.g. KCl) as co-products; however, the synthetic effort for their preparation from **39** is higher.

6.2.2 Reactivity of 40 – 45 with bpy

The model reaction with bpy was carried out with all six precursors, and a number of parameters, such as solvent, temperature, concentration, reaction time, and bpy/Ru ratio were systematically investigated. Reactions were carried out in absolute ethanol, that turned out to be the most appropriate solvent among those screened (that include acetone, chloroform, DMSO, toluene, and acetonitrile). The rather slow reaction rates observed under reflux conditions improved substantially by performing the reactions in a MW reactor. NMR and TLC analyses indicated that, at the end of the reaction,[53] the solution typically contains a mixture of two products identified as [Ru(bpy)$_2$(O–O)]$^{n+}$ (n = 0, 1 depending on O–O) and the unwanted (and unexpected) [Ru(bpy)$_3$]$^{2+}$. We choose ^{1}H NMR spectroscopy in DMSO-d_6 as the most appropriate analytical method for a rapid, reliable and quantitative assessment of the reaction outcome. In fact, since the charge of the products can range from 0 to 2+, we found that only DMSO is capable of dissolving the mixture completely, regardless

of the nature of chel and O–O. Other solvents, such as $CDCl_3$ or D_2O, led to underestimate (or overestimate) one of the components. The reaction schemes are reported in Scheme 6.3 for compounds **40** – **43**, and in Scheme 4 for **44** and **45**.

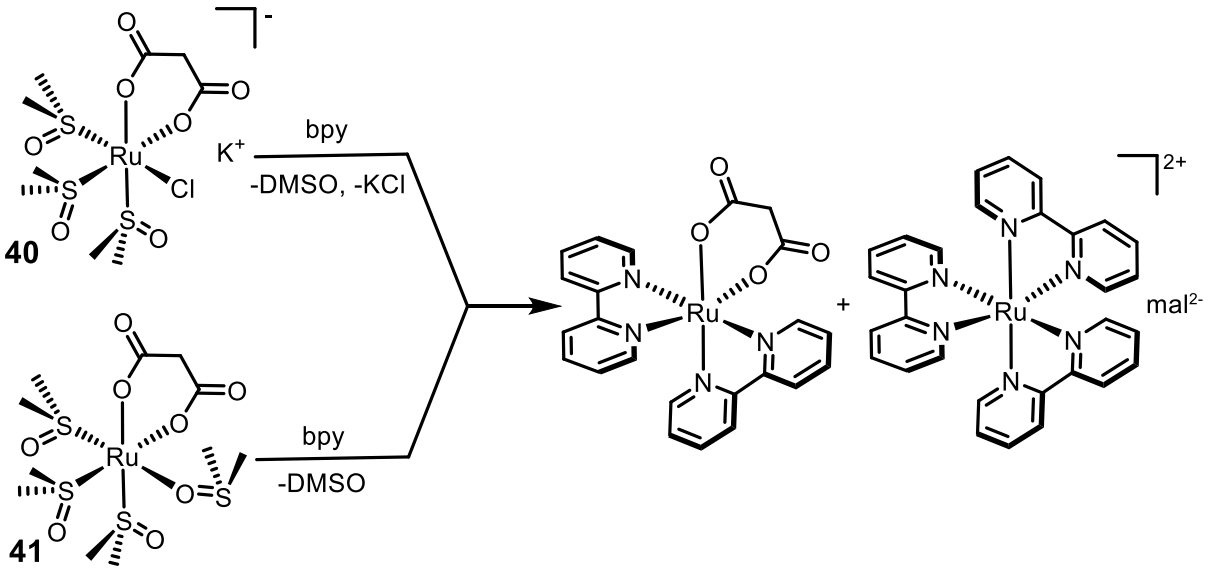

Scheme 6.3. General reactivity of the *cis*-locked dicarboxylate precursors **40**–**43** towards bpy. The case of malonate is exemplified.

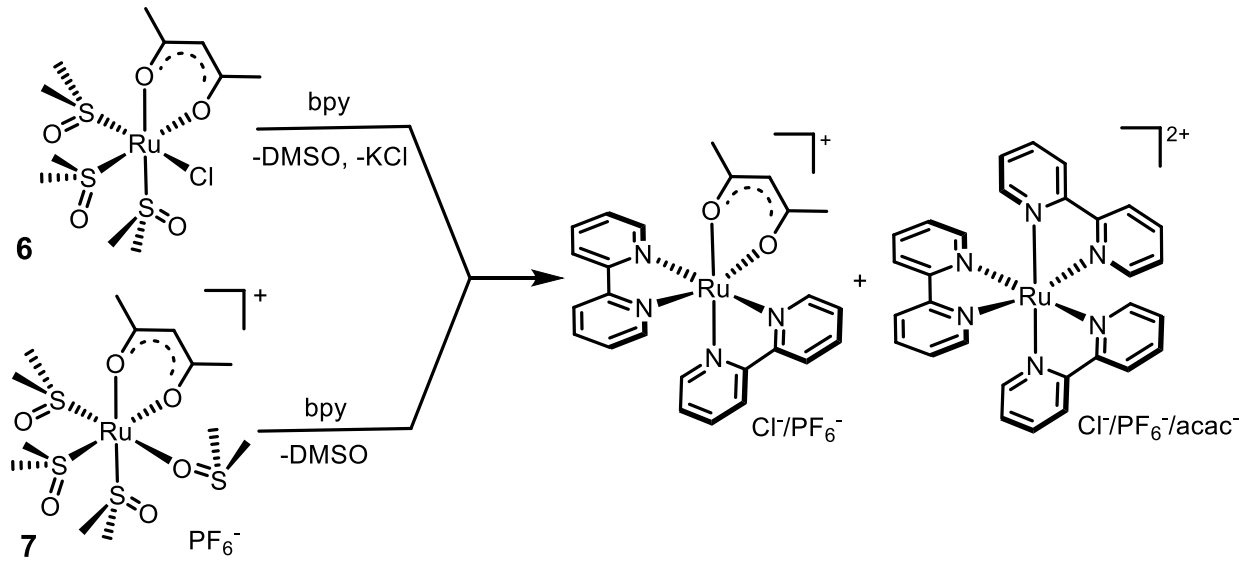

Scheme 6.4. General reactivity of the *cis*-locked acac precursors **44** and **45** towards bpy.

The following reactivity order, based on the amount of residual bpy (after 1h at 120°C) was found: **42** < **43** < **40** < **41**, thus confirming that chloride-free precursors are more reactive. However, the ox compound **43** yielded mainly $[Ru(bpy)_3]^{2+}$. The acac complex **44** was less selective, affording also – besides $[Ru(bpy)_2(\eta^2\text{-acac})]^+$, $[Ru(bpy)_3]^{3+}$ and unreacted bpy – at least two other minor Ru-bpy species. In the case of **45** a dark precipitate was obtained at the end of the reaction that was identified, according to the NMR spectrum, as a mixture of $[Ru(bpy)_2(\eta^2\text{-acac})][PF_6]$ (**46**) and

$[Ru(bpy)_3][PF_6]_2$.[54] Compound **46** was isolated in pure form by extracting the mixture with chloroform.[55]

The selectivity towards the desired bis-bpy product was found to increase upon increasing the temperature and decreasing the concentration (Appendix), even though low concentrations are unpractical for preparative purposes and afford lower conversions. In the case of **40**, an increase of the bpy/Ru ratio from two to four led to no appreciable improvement in selectivity and conversion. A good compromise between conversion and selectivity was obtained with the malonate precursors **40** and **41** that in 10 min at 150°C afforded almost full bpy conversion with % selectivity in $[Ru(bpy)_2(\eta^2\text{-mal})]$ (according to NMR integration). Under similar conditions, the "unlocked" precursor **39** was much less selective, affording a mixture of at least five species, bearing from one to three bpy ligands, identified as [*cis*,*cis*-$RuCl_2$(bpy)(dmso-S)$_2$], [*cis*,*trans*-$RuCl_2$(bpy)(dmso-S)$_2$], [*cis*-$RuCl_2(bpy)_2$], [*cis*-$RuCl(bpy)_2$(dmso-S)]$^+$, and $[Ru(bpy)_3]^{2+}$, whose relative amount was found to depend on temperature, concentration, and reaction time (Appendix).

No systematic attempts were made to obtain the neutral complexes $[Ru(bpy)_2(O–O)]$ in pure form, however, since the main detected by-product has a +2 charge, separation by chromatography or by extraction/washing with an appropriate solvent is easily feasible. As an example, $[Ru(bpy)_2(\eta^2\text{-mal})]$ (**47**) was obtained in pure form from the reaction mixture by column chromatography on silica gel (see also below). The pure compounds **46** and **47** were fully characterized by ^{1}H NMR spectroscopy (Figure 6.4 and Appendix). For both complexes the two equivalent bpy ligands give eight equally intense resonances, that were assigned through COSY and HSQC spectra and considering the mutual-shielding effects.[34,56] The UV-vis spectra of **46** and **47** are very similar (and similar to that of $[RuCl_2(bpy)_2]$) and characterized by two absorption bands in the visible region (at ca. 370 and 530 nm, Appendix).

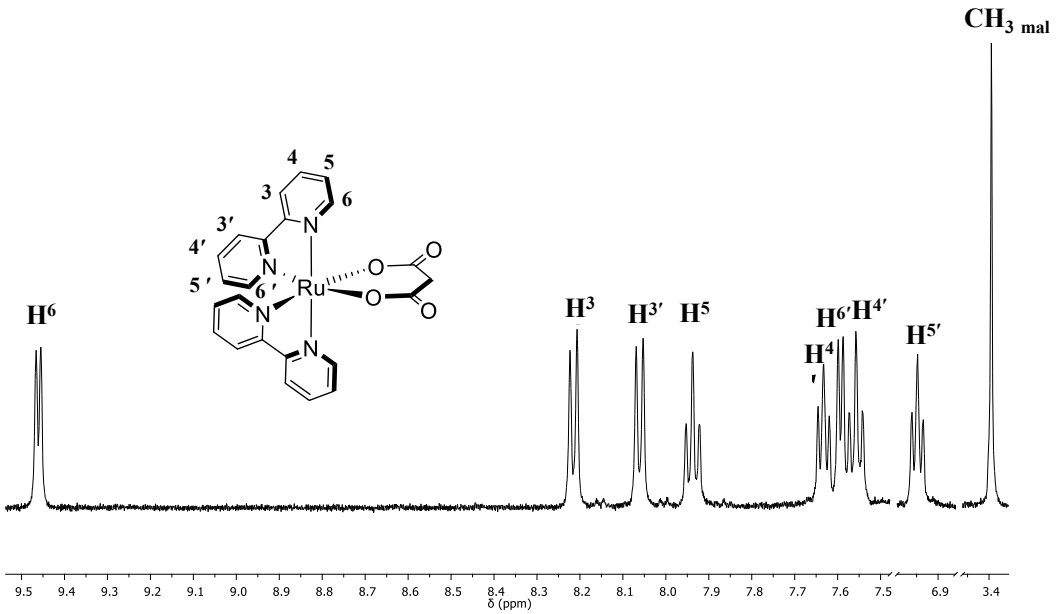

Figure 6.4. ^{1}H NMR spectrum ($CDCl_3$) of [Ru(bpy)$_2$(η^2-mal)] (**47**). See the insert for labeling scheme.

6.2.3 Reactions of selected *cis*-locked Ru(II) precursors with phen and dpphen on a larger scale

We tested our synthetic approach on a slightly larger preparative scale, with the aim of obtaining 100 – 200 mg each of the complexes [Ru(chel)$_2$(O–O)] and [Ru(chel)$_2$(η^2-acac)]Cl (chel = phen and dpphen, O–O = mal and ox), using the chloride compounds **40**, **42**, and **44** as precursors. The reactions were performed at 150°C in 10 or 30 mL MW vials. The concentration of each Ru precursor was in the range 120 – 200 mM. We found that, using an appropriately high concentration of the precursor, the neutral products [Ru(chel)$_2$(O–O)] precipitated spontaneously from the mother liquor at the end of the reaction; conversely, no precipitation was observed with bpy. Thus, the complexes [Ru(phen)$_2$(η^2-mal)] (**48**), [Ru(dpphen)$_2$(η^2-mal)] (**49**), [Ru(phen)$_2$(η^2-ox)] (**50**), and [Ru(dpphen)$_2$(η^2-ox)] (**51**) were easily recovered by filtration. According to ^{1}H NMR spectroscopy they were obtained in pure form; co-precipitated KCl was easily removed by recrystallization from chloroform (except for **50**, see experimental section). The less soluble oxalato complexes were obtained in 70 – 80% yields, whereas those with malonate in quite lower yields. In the case of **48**, however, we found that an increase of the phen/**40** ratio from two to three improved the yield significantly (from 36 to 51%). According to TLC and NMR analysis the mother liquor contained a mixture of [Ru(chel)$_2$(O–O)] and $[Ru(chel)_3]^{2+}$. Column chromatography performed on the mother liquor of the reaction between **40** and phen afforded, as first fraction, a small amount of [*cis*-$RuCl_2(phen)_2$], indicating that at least part of the Cl^- released from **40** upon formation of **48** is capable to replace the malonate. This chloride-rebound mechanism, already encountered by us on similar

complexes,[57] confirms the high affinity of Cl^- for Ru(II) and – consistent with the ubiquitous formation of $[Ru(chel)_3]^{2+}$ species – the insufficient strength of the O–O chelate (see below).
In contrast, the acac complexes $[Ru(phen)_2(\eta^2\text{-acac})]Cl$ (**52**) and $[Ru(dpphen)_2(\eta^2\text{-acac})]Cl$ (**53**) did not precipitate spontaneously and were obtained in pure form by column chromatography in moderate yields.[58]
The X-ray structure of the $[Ru(phen)_2(\eta^2\text{-mal})]$ (**48**) is shown in Figure 6.5.

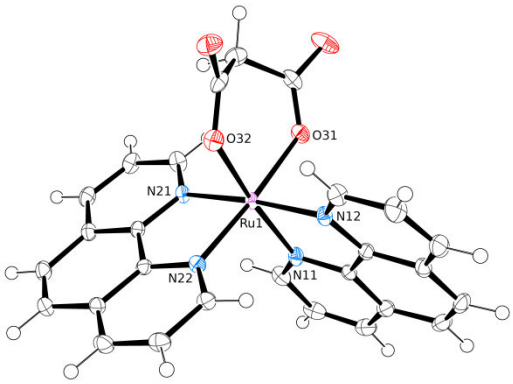

Figure 6.5. X-ray molecular structures (50% probability ellipsoids) of complexes $[Ru(phen)_2(\eta^2\text{-mal})]$ (**48**).

Compounds **48** – **53** are all well soluble in DMSO, and have similar UV-vis spectra, characterized by a broad and intense MLCT absorption band in the range 510 – 560 nm, with shoulders both at lower (453-492 nm) and higher (566-660 nm) wavelengths (Figure 6.6 and Appendix). The absorption maxima of the neutral complexes **48** – **51** are red-shifted by ca. 35 nm compared to the corresponding cationic species **52** and **53**, and those of the dpphen compounds **49**, **51**, and **53** are red-shifted of ca. 15 nm compared to the corresponding phen compounds **48**, **50**, and **52** (Table 6.1).

Table 6.1. Absorption maxima in the UV-vis spectra ($CHCl_3$) of complexes **48** – **53**.

Compound	**λ_{max} (nm)**
$[Ru(phen)_2(\eta^2\text{-mal})]$ (**48**)	544
$[Ru(dpphen)_2(\eta^2\text{-mal})]$ (**49**)	561
$[Ru(phen)_2(\eta^2\text{-ox})]$ (**50**)	544
$[Ru(dpphen)_2(\eta^2\text{-ox})]$ (**51**)	560
$[Ru(phen)_2(\eta^2\text{-acac})]Cl$ (**52**)	509
$[Ru(dpphen)_2(\eta^2\text{-acac})]Cl$ (**53**)	524

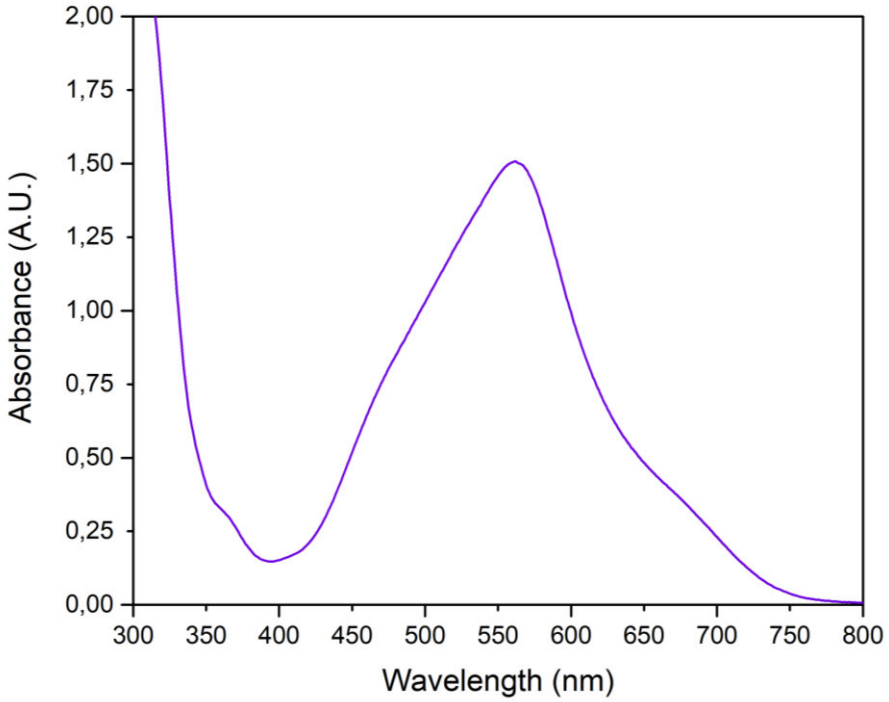

Figure 6.6. UV-vis spectrum in chloroform of $[Ru(dpphen)_2(\eta^2\text{-mal})]$ (**49**).

The ^1H NMR spectra of compounds **48** – **53** are reported in the Appendix with peak assignments. It is to be noted that in the HSQC spectrum the resonances of C2 and C9, i.e. the carbons adjacent to the N atoms, are well distinguished from the others, thus affording unambiguous assignments of all resonances.

6.2.4 Acid-assisted preparation of bis-heteroleptic complexes

The acid-assisted replacement of the O–O chelate with chel′ was investigated on selected $[Ru(chel)_2(O–O)]^{n+}$ compounds (n = 0, 1 depending on O–O). First, we established that the substitution does not occur readily in the absence of added acid. For example treatment of $[Ru(phen)_2(\eta^2\text{-mal})]$ (**48**) with one equiv. of bpy in refluxing ethanol for 6h showed no significant color change (from deep purple to bright orange-red) typical of the formation of $[Ru(phen)_2(bpy)]^{2+}$. No reaction either was observed when the mixture was heated for 1h at 120 °C in the microwave reactor (Scheme 6.5). Conversely, upon addition of ten equiv. of trifluoroacetic acid (TFA) 100% substitution was accomplished within 1h at reflux conditions according to UV-vis spectroscopy (Appendix) (Scheme 6.5). Addition of an excess of NH_4PF_6 to the final solution afforded $[Ru(phen)_2(bpy)][PF_6]_2$ (**54**) as an orange precipitate that was recovered in 93% yield. The reaction occurs also at room temperature in ca. 3 days. Similarly, using $[Ru(bpy)_2(\eta^2\text{-mal})]$ (**47**) as precursor, the complex $[Ru(bpy)_2(phen)][PF_6]_2$ (**55**) was obtained under the same reaction conditions.

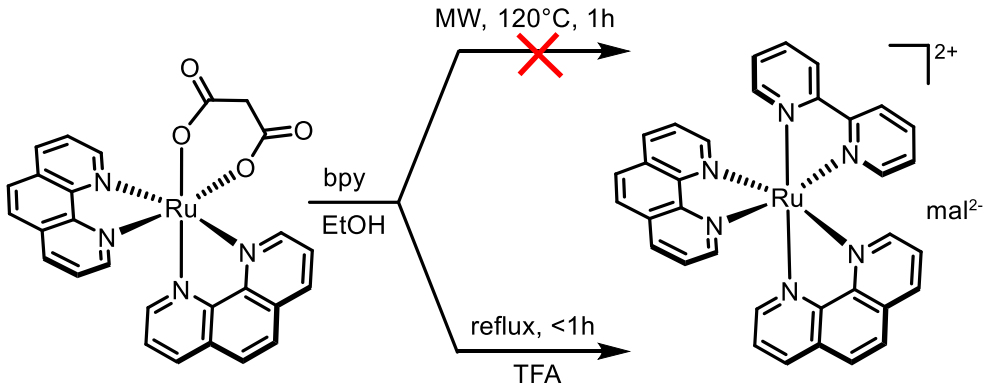

Scheme 6.5. Acid-assisted facile and selective replacement of malonate by bpy. TFA = trifluoracetic acid.

With the precursor $[Ru(bpy)_2(\eta^2\text{-acac})][PF_6]$ (**46**) we found that the replacement of acac by phen was best accomplished in the presence of HPF_6 rather than TFA. The addition of 4 equiv. of HPF_6 afforded quantitative formation of $[Ru(bpy)_2(phen)][PF_6]_2$ (**55**) from **46** in 2.5 h in refluxing ethanol. The bis-heteroleptic compounds **54** and **55** were characterized by UV-vis and ^{1}H NMR spectroscopy (Appendix).

6.3 Conclusions

The efficient preparation from [*cis*-$RuCl_2(dmso)_4$] (**39**) of a series of six neutral, anionic and cationic *cis*-locked Ru(II) precursors (**40** – **45**) of the general formula (Y)[*fac*-$RuX(dmso\text{-}S)_3(O–O)]^n$ (where O–O = mal, ox, acac; X = dmso-O or Cl; n = –1/0/+1 depending on the nature and charge of X and

O–O; when present, Y = K^+ or PF_6^-) was established. When treated with diimine chelating ligands (chel = bpy, phen, dpphen), the dicarboxylate compounds **40** – **43** afforded mixtures of $[Ru(chel)_2(O–O)]$ and $[Ru(chel)_3]^{2+}$ species, whereas the acac precursors **44** and **45** were less selective and yielded also other minor species besides $[Ru(chel)_2(acac)]^+$ and $[Ru(chel)_3]^{2+}$. The formation of $[Ru(chel)_3]^{2+}$can be minimized by carefully adjusting the reaction conditions: in particular, high selectivity towards $[Ru(chel)_2(O–O)]^{n+}$ and almost complete conversion of the precursor was obtained within minutes when the reactions were performed at 150 °C in a microwave reactor. We found that, depending on the nature of chel, O–O, and concentration, the neutral products $[Ru(chel)_2(O–O)]$ precipitate spontaneously form the final mixture, in pure form and acceptable-to-good yields. When spontaneous precipitation of the disubstituted product does not occur, purification from $[Ru(chel)_3]^{2+}$ can be rather easily accomplished by column chromatography or solvent extraction. By comparison, under the same conditions compound **1** is much less selective, thus demonstrating that the choice of locking the geometry of the precursor through the introduction of O–O in the coordination sphere of Ru is a valid strategic approach. Regretfully, the formation ubiquitous of $[Ru(chel)_3]^{2+}$ (as well as that of [*cis*-$RuCl_2(chel)_2$] when the mono-chloride precursors **40**, **42** and **44** are treated with chel) indicates the O–O chelates are not sufficiently strong.

The counterintuitive finding that the $[Ru(chel)_3]^{2+}/[Ru(chel)_2(O–O)]^{n+}$ ratio increases upon lowering the temperature (i.e. the reaction is less selective),[59] suggests that the formation of $[Ru(chel)_3]^{2+}$ from the *cis*-locked precursors occurs in a parallel reaction, rather than in a consecutive step from $[Ru(chel)_2(O–O)]^{n+}$, Consistent with this hypothesis, we found that bpy is unable to replace malonate readily from $[Ru(phen)_2(\eta^2\text{-mal})]$ (**48**) even at 120 °C in a MW. In addition, the finding that the selectivity increases upon lowering the concentration, suggests that the formation of $[Ru(chel)_3]^{2+}$ does not depend (dramatically) on the presence of adventitious water in the EtOH solvent (that might favor the dissociation of O–O): in this hypothesis, since at lower concentrations the H_2O/Ru ratio becomes larger, the opposite trend would have been expected. Consistently, we found that running the reaction in absolute EtOH treated with activated molecular sieves led to no significant improvement in the selectivity.

In conclusion, we hypothesize that the formation of $[Ru(chel)_3]^{2+}$ involves as a first, relatively slow step, the replacement of O–O in [*fac*-$RuX(dmso\text{-}S)_3(O–O)]^n$ by chel, with formation of an unlocked intermediate such as [*fac*-$RuCl(dmso\text{-}S)_3(chel)]^+$ (Scheme 6.6). The subsequent replacement of the remaining monodentate ligands by two additional chel molecules must be rather fast. The experimental findings show that at relatively low temperature (i.e. 80°C) this parasite reaction (branch a) is faster than the parallel reaction leading to $[Ru(chel)_2(O–O)]^n$ (branch b); however, the rate of this latter, and thus the selectivity of the reaction, increases more rapidly with the temperature.

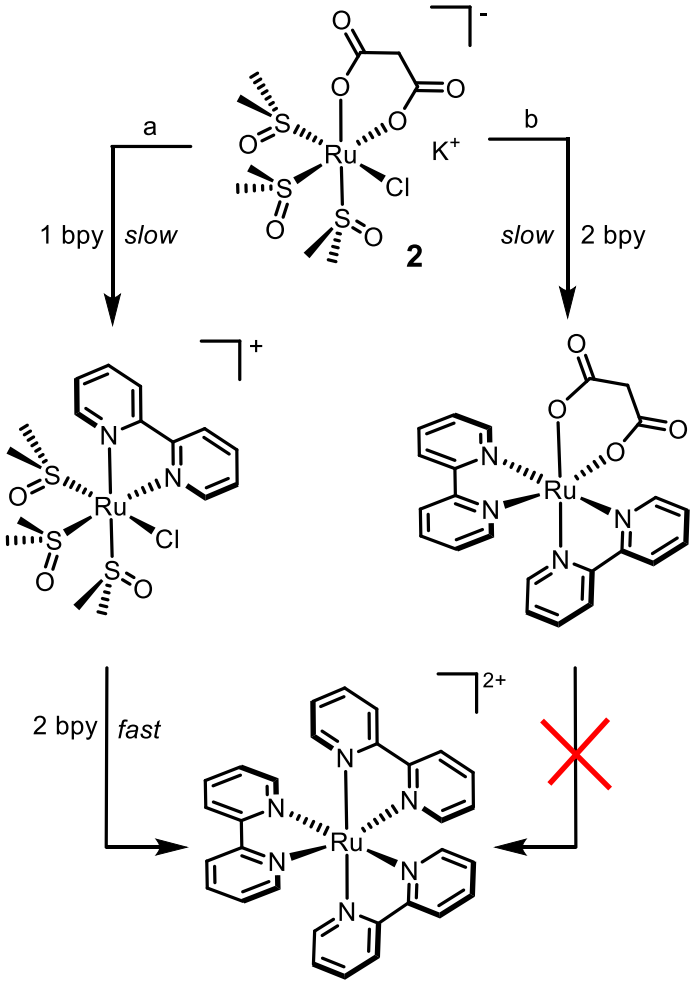

Scheme 6.6. Hypothesis of the two parallel routes leading to the mixture of $[Ru(chel)_2(O–O)]^{n+}$ and $[Ru(chel)_3]^{2+}$ exemplified for case chel = bpy and O–O = mal.

6.4 Experimental Section

Materials

All chemicals were purchased from Sigma-Aldrich and used as received. Solvents were of reagent grade. The Ru(II) precursor [*cis*-$RuCl_2(dmso)_4$] (**39**) was prepared as described in ref. 36.

Instrumental methods

Mono- and bi-dimensional (^{1}H-^{1}H COSY, ^{1}H-^{13}C HSQC) NMR spectra were recorded at room temperature on a Varian 400 or 500 spectrometer (^{1}H: 400 or 500 MHz, ^{31}P{^{1}H}: 202 MHz, ^{19}F: 376 MHz). ^{1}H chemical shifts were referenced to the peak of residual non-deuterated solvent (δ = 7.26 for $CDCl_3$, and 2.50 for DMSO-d_6) or were measured relative to the internal standard DSS (δ = 0.00) for D_2O. Carbon resonances were assigned through the HSQC spectra. ESI mass spectra were collected in the positive and negative mode on a Perkin-Elmer APII spectrometer at 5600 eV. The UV-vis spectra were obtained on an Agilent Cary 60 spectrophotometer, using 1.0 cm path-length quartz cuvettes (3.0 mL). A Anton Paar 400 microwave reactor (with video-camera) was used for the

microwave-assisted reactions performed in 10 or 30 mL vessels. Elemental analyses were performed in the Department of Chemistry of the University of Bologna (Italy).

X-ray diffraction

Data collections were performed at the X-ray diffraction beamline (XRD1) of the Elettra Synchrotron of Trieste (Italy) equipped with a Pilatus 2M image plate detector. Collection temperature was 100K (nitrogen stream supplied through an Oxford Cryostream 700); the wavelength of the monochromatic X-ray beam was 0.700 Å and the diffractograms were obtained with the rotating crystal method. The crystals were dipped in N-paratone and mounted on the goniometer head with a nylon loop. The diffraction data were indexed, integrated and scaled using the XDS code. The structures were solved by the dual space algorithm implemented in the SHELXT code.Fourier analysis and refinement were performed by the full-matrix least-squares methods based on F^2 implemented in SHELXL. The Coot and SHELXLE programs were used for modeling. Anisotropic thermal motion was allowed for all non-hydrogen atoms. Hydrogen atoms were placed at calculated positions with isotropic factors U = 1.2×Ueq, Ueq being the equivalent isotropic thermal factor of the bonded non hydrogen atom. Crystal data and details of refinements are in the ESI.

Preparation of the complexes.

K[*fac*-RuCl(dmso-S)$_3$(η^2-mal)] (40). A procedure similar to that described in ref. 50 was followed: a 1.0 g amount of [*cis*-$RuCl_2(dmso)_4$] (**39**) (2.06 mmol) was partially dissolved in 100 mL of methanol. After addition of one equiv. of K_2mal (373.1 mg), the mixture was heated to reflux affording a pale yellow solution. After 90 min it was evaporated to an oil and washed with acetone to remove DMSO, affording a pale-yellow solid. The product (a mixture of compound **40** and KCl) was recrystallized from warm ethanol (100 mL); the poorly soluble KCl was removed by filtration of the warm solution over fine paper. The yellow filtrate was evaporated to dryness and the solid washed with acetone, diethyl ether and dried under vacuum. Yield 857.3 mg (82%). Anal. Calcd. For $C_9H_{20}ClO_7RuS_3K$, MW = 512.06: C, 21.11; H, 3.94. Found C, 20.92; H, 3.85. ^{1}H NMR (D_2O) δ, ppm: 4.01 (d, 1H, mal), 3.42 (s, 6H, dmso-S), 3.39 (s, 6H, dmso-S), 3.21 (s, 6H, dmso-S), 3.15 (d, 1H, mal). The resonances are coincident with those previously reported by us for this complex.[50] Selected IR absorptions (nujol, cm^{-1}): 1589 $\nu_{symm(COO)}$, 1410 $\nu_{symm(COO)}$, 1111 $\nu_{S=O(dmso-S)}$. ESI mass spectrum (m/z): 472.8 $[M–K]^-$ (calcd. for $C_9H_{20}ClO_7RuS_3$ 472.91).

[*fac*-Ru(dmso-O)(dmso-S)$_3$(η^2-mal)] (41). A 500.7 mg amount of [*cis*-$RuCl_2(dmso)_4$] (**39**) (1.03 mmol) was dissolved in 4.0 mL of DMSO at ca. 100 °C. Addition of 1.1 equiv. of Ag_2mal (360.2 mg) afforded immediately a greyish precipitate of AgCl. After 30 min the mixture was cooled and the precipitate removed by filtration over a Celite pad and extensively washed with MeOH (where **41** is soluble). The product precipitated spontaneously as a pale-yellow solid from DMSO upon

evaporation of the methanol, and its amount was increased by addition of acetone (10 mL). The product was recrystallized from methanol (50 mL): residual AgCl was removed by filtration and washed with additional MeOH. The filtrate was evaporated to dryness and the solid washed with acetone, diethyl ether and dried under vacuum. Yield 375.1 mg (70.6%). Anal. Calcd. for $C_{11}H_{26}O_8RuS_4$, MW = 515.63: C, 25.62; H, 5.08. Found C, 25.91; H, 4.87. ^{1}H NMR (D_2O) δ, ppm: 3.85 (d, 1H, mal), 3.42 (d, 1H, mal), 3.35 (s, 12H, dmso-S), 3.34 (s, 6H, dmso-S), 2.84 (s, 6H, dmso-O). Consistent with the literature, in aqueous solution the complex is in equilibrium with the aquated species [*fac*-Ru(dmso-S)$_3$(OH_2)(η^2-mal)] (**41aq**): ^{1}H NMR (D_2O) δ, ppm: 3.59 (d, 1H, mal), 3.42 (s, 6H, dmso-S), 3.37 (s, 6H, dmso-S), 3.23 (s, 6H, dmso-S), 3.29 (d, 1H, mal). The resonances of **41** and **41aq** are coincident with those previously reported by us for these species.[50] Selected IR absorptions (nujol, cm^{-1}): 1604 $\nu_{asymm(COO)}$, 1376 $\nu_{symm(COO)}$, 1117 $\nu_{S=O(dmso-S)}$, 933 $\nu_{S=O(dmso-O)}$. ESI mass spectrum (m/z): 516.9 $[M+H]^+$ (calcd. for $C_{12}H_{26}O_8RuS_4$ 516.96).

K[*fac*-RuCl(dmso-S)$_3$(η^2-ox)] (42). The procedure was improved compared to that reported in ref. A 502.6 mg amount of [*cis*-$RuCl_2$(dmso)$_4$] (**39**) (1.03 mmol) was partially dissolved in 3.0 mL of DMSO in a 10 mL MW vial. After addition of 2 equiv. of K_2(ox) (344.2 mg, 2.03 mmol), the sealed system was heated at 125 °C for 1h in a MW reactor.[60] The final suspension is filtered warm to remove an abundant white precipitate (KCl + residual K_2(ox)), which is washed with MeOH (where **42** is soluble). Removal of methanol from the filtrate by rotary evaporation, followed by addition of EtOH (ca.10 mL) induced the precipitation of the product as a pale-yellow solid, that was removed by filtration and washed with EtOH and diethyl ether and dried under vacuum. The product was pure **42** according to the ^{1}H NMR spectrum. Yield 352 mg (70%). Anal. Calcd. for $C_8H_{18}ClKO_7RuS_3$, MW = 498.02: C, 19.29; H, 3.64. Found C, 19.48; H, 3.77. ^{1}H NMR (D_2O) δ, ppm: 3.45 (s, 6H, dmso-S), 3.43 (s, 6H, dmso-S), 3.22 (s, 6H, dmso-S). The resonances of **42** are coincident with those previously reported by us for this species.[50] Selected IR absorptions (nujol, cm^{-1}): 1667 $\nu_{asymm(COO)}$, 1388 $\nu_{symm(COO)}$, 1109 $\nu_{S=O(dmso-S)}$. ESI mass spectrum (m/z): 458.8 $[M-K]^-$ (calcd. for $C_8H_{18}ClO_7RuS_3$ 458.89).

[*fac*-Ru(dmso-O)(dmso-S)$_3$(η^2-ox)] (43). The procedure was improved compared to that reported in ref. 50. A 500.1 mg amount of [*cis*-$RuCl_2$(dmso)$_4$] (**39**) (1.03 mmol) was partially dissolved in 3.0 mL of DMSO. After addition of 2.1 equiv. of $AgNO_3$ (372.1 mg, 2.19 mmol), the system was heated to 60°C for 30 min. The whitish precipitate of AgCl was removed by filtration and thoroughly washed with MeOH. A 417.3 mg amount of Na_2(ox) (3 equiv. 3.11 mmol) was added to the filtrate after removal of the MeOH by rotary evaporation and the mixture was heated to 60 °C for 24h. The progressive formation of a white precipitate was observed. After cooling the mixture, the precipitate was removed by filtration, washed with acetone, diethyl ether and dried under vacuum. It was

recrystallized from ethanol (50 mL) at room temperature: residual AgCl was removed by filtration and washed with additional ethanol. The filtrate was evaporated to dryness and the solid washed with acetone, diethyl ether and dried under vacuum. Yield 358.2 mg (69.3%). Anal. Calcd. for $C_{10}H_{24}O_8RuS_4$, MW = 501.60: C, 23.95; H, 4.82. Found C, 23.61; H, 4.67. ^{1}H NMR (D_2O) δ, ppm: 3.41 (s, 6H, dmso-S), 3.37 (s, 6H, dmso-S), 3.21 (s, 6H, dmso-S), 2.80 (s, 6H, dmso-O). The resonances of **43** are coincident with those previously reported by us for this species.[50] Selected IR absorptions (nujol, cm^{-1}): 1661 $\nu_{asymm(COO)}$, 1377 $\nu_{symm(COO)}$, 1106 $\nu_{S=O(dmso-S)}$, 933 $\nu_{S=O(dmso-O)}$. ESI mass spectrum (m/z): 306.8 $[M+K-3dmso]^+$ (calcd for $C_4H_6O_5RuSK$ 306.86).

[*fac*-RuCl(dmso-S)$_3$(η^2-acac)] (44). A 500.0 mg amount of [*cis*-$RuCl_2(dmso)_4$] (**39**) (1.03 mmol) was partially dissolved in 25 mL of methanol. After addition of 1 equiv. of Na(acac) (122.5 mg), the mixture was heated to reflux affording a pale yellow solution. After 2 h the obtained yellow solution was filtered over fine paper for removing a white suspension of NaCl formed during the reaction. The yellow solution was evaporated to dryness and the initially sticking solid was repeatedly crushed in a sonicator with portions of diethyl ether until a yellow powder was obtained. It was removed by filtration, washed with diethyl ether and dried under vacuum. The product was recrystallized from chloroform: residual NaCl was removed by filtration, the filtrate was evaporated to dryness and the solid washed with diethyl ether and dried under vacuum. Yield 358.2 mg (69.3%). Yield 400.7 mg (82%). Crystals of **44** suitable for X-ray analysis were obtained upon layering diethyl ether on top of a chloroform solution of the complex. Anal. Calcd. for $C_{11}H_{25}ClO_5RuS_3$, MW= 470.02: C, 28.11; H, 5.36. Found: C, 27.86; H, 5.21. ^{1}H NMR ($CDCl_3$) δ, ppm: 5.53 (s, 1H, acac), 3.40 (s, 6H, dmso-S), 3.36, (s, 6H, dmso-S), 3.18 (s, 6H, dmso-S), 2.09 (s, 6H, CH_3 acac). Selected IR absorptions (nujol, cm^{-1}): 1578 $\nu_{asymm(CO)}$, 1521 $\nu_{symm(CO)}$, 1122, 1099 $\nu_{S=O(dmso-S)}$. ESI-MS (m/z) 491.9 $[M+Na]^+$ (calcd. for $C_{11}H_{25}ClO_5RuS_3Na$ 492.0).

[*fac*-Ru(dmso-O)(dmso-S)$_3$(η^2-acac)][PF$_6$] (45). A 700.4 mg amount of [*fac*-RuCl(dmso-S)$_3$(η^2-acac)] (**44**) (1.43 mmol) was partially dissolved in a mixture of DMSO (0.3 mL) and acetone (20 mL). After addition of 1.1 equiv. of $AgPF_6$ (381 .0 mg, 1.57 mmol) the system was stirred at 30 °C for 2.5h. The whitish precipitate of AgCl was removed by filtration over a Celite pad and thoroughly washed with acetone. Removal of acetone from the filtrate at reduced pressure afforded a dark-yellow oil; dropwise addition of chloroform induced the formation of a white precipitate that was filtered and abundantly washed with chloroform. The product was recrystallized from ethanol (50 mL) at room temperature: residual AgCl was removed by filtration and washed with additional ethanol. The filtrate was evaporated to dryness and the solid washed with chloroform, diethyl ether and dried under vacuum. Yield 598.8 mg (63.6%). Crystals of **45** suitable for X-ray analysis were obtained upon layering *n*-hexane on top of an acetone solution of the complex. Anal. Calcd. for $C_{13}H_{31}O_6RuPS_4F_6$,

MW= 657.66: C, 23.74; H, 4.75. Found: C, 23.89; H, 4.51. ^{1}H NMR (acetone-d_6) δ, ppm: 5δ 5.92 (s,1H, acac), 3.37 (s, 6H, dmso-S), 3.33 (s, 6H, dmso-S), 3.06 (s, 6H,dmso-S), 2.73 (s, 6H, dmso-O), 2.23 (s, 6H, CH_3 acac).^{31}P NMR(acetone-d_6) δ, ppm:-144.5 (septet) Selected IR absorptions (nujol, cm^{-1}): 1566 $\nu_{asym(COO)}$; 1522$\nu_{sym(COO)}$; 1123, 1093 $\nu_{S=O\ (dmso-S)}$; 933 $\nu_{S=O\ (dmso-O)}$. ESI-MS (m/z) 356.9 $[M–2dmso]^+$ (calcd. for $C_9H_{19}O_4RuPS_2F_6$ 356.97).

Synthesis of $[Ru(chel)_2(O–O)]^{n+}$ compounds

Some representative examples of the many MW-assisted reactions performed between precursors **40** – **45** and a chel ligand (chel = bpy, phen, dpphen) are described below. The reactions with bpy were performed on a relatively small scale for optimizing the conversion and selectivity. The reaction products were analyzed as follows: when no precipitate was found at the end of the run, after TLC analysis ($CHCl_3$: MeOH 7:3) the solvent was removed by rotary evaporation, and the residual oil dissolved in DMSO-d_6 for NMR investigation. For the more concentrated solutions ([Ru] > 6.1 mM), the final ink-dark solution was first diluted with 50 mL of EtOH to make sure that no fine precipitate was present,[53] and the above described analysis was performed on a sample taken from the diluted solution. In the case of precursor **45**, the NMR analysis was performed on the mother liquor after removal of the precipitate of $[Ru(bpy)_2(\eta^2\text{-acac})][PF_6]$ (**46**) and $[Ru(bpy)_3][PF_6]_2$ (see text) and thus the conversion % was not established.

The larger scale MW-assisted reactions with phen and dpphen were performed on precursors **40**, **42**, and **44** at 150°C for 1h; the concentration of Ru precursor was in the range 12 – 20 mM. The workup depended on the presence (or absence) of a precipitate at the end of the run. Precursors **40** and **42** afforded a dark purple precipitate, that was removed by filtration, washed with ethanol and diethyl ether and dried under vacuum. For increasing the amount of precipitate in some cases (e.g. with the more soluble dpphen) the mother liquor was concentrated to ca. half-volume and stored at 4°C for 24h prior to filtration. According to ^{1}H NMR analysis the raw precipitate was, in each case, the pure $[Ru(chel)_2(O–O)]$ compound (**48** – **52**, chel = phen or dpphen, O–O = ox or mal). Recrystallization from chloroform at room temperature was sufficient to remove the co-precipitated KCl (except in the case of **50**, see below). The presence of the $[Ru(chel)_3]^{2+}$ species in the filtrate was ascertained by TLC analysis. Using **44** as precursor, no product precipitated spontaneously from the solution, and both TLC and NMR spectroscopy indicated that it contained a mixture of di and tri-substituted Ru compounds. In this case the $[Ru(chel)_2(\eta^2\text{-acac})][Cl]$ species, (**52**, chel = phen; **53** chel = dpphen) were obtained in pure form by column chromatography on silica gel. Essential details of each preparation are given below (see Appendix for proton labeling schemes).

$[Ru(bpy)_2(\eta^2\text{-acac})][PF_6]$ (46). Starting materials: 60.0 mg of [*fac*-$RuCl(dmso\text{-}S)_3(\eta^2\text{-acac})$] (**44**) (0.128 mmol) and 41.9 mg (2.1 equiv.) of bpy in 5.0 mL of EtOH. At the end of the run the solventwas

removed by evaporation affording an ink-dark purple mixture, that was dissolved in ca. 4 mL of water. Addition of an excess of NH_4PF_6 (400.0 mg, ca. 20 equiv.) afforded the immediate precipitation of a dark-brown precipitate. The mixture was centrifuged and the precipitate, after removal of the supernatant, was washed with water (×3). The solid mixture was extracted with 50 mL of chloroform, and the residual dark-red solid removed by filtration: it is pure $[Ru(bpy)_3][PF_6]_2$ according to the ^{1}H NMR spectrum in DMSO-*d*$_6$ show (Appendix). Removal of the solvent from the deep-purple filtrate afforded **46** as a dark solid that was suspended in diethyl ether and recovered by filtration and dried under vacuum. Yield 55.3 mg (65.0%). ^{1}H NMR (DMSO-*d*$_6$) δ, ppm: 8.75 (d, 2H,H6′), 8.63 (m, 4H, H3+ H3'), 8.17 (m, 2H, H5′), 7.85 (t, 2H, H4), 7.74 (t, 2H, H4') 7.69 (d, 2H, H6), 7.22 (t, 2H, H5), 5.35 (s, 1H, acac), 1.78 (s, 6H, acac). UV−vis (EtOH): 370 nm, 514 nm. ESI-MS (m/z): 513.1 [M–PF_6] (calcd. for $C_{25}H_{23}N_4O_2Ru$ 513.6).

[Ru(bpy)$_2$(η^2-mal)] (47). Starting materials: 50.0 mg of [K]*fac*-[RuCl(dmso-S)$_3$(η^2-mal)] (**40**) (0.098 mmol) and 30.6 mg (2 equiv.) of bpy in 5.0 mL of EtOH. At the end of the run the solvent was removed by evaporation affording a dark purple mixture. Column chromatography on silica gel (eluent $CHCl_3$:MeOH 7:3) afforded pure **47** in the first band. ^{1}H NMR ($CDCl_3$) δ, ppm: 3.39 (s, 2H, mal), 6.95 (t, 2H, H5′), 7.56 (t, 2H, H4′), 7.59 (d, 2H, H6′), 7.63 (t, 2H, H4), 7.94 (t, 2H, H5), 8.06 (d, 2H, H3′), 8.22 (d, 2H, H3), 9.46 (d, 2H, H6).

[Ru(phen)$_2$(η^2-mal)] (48). Starting materials: 50.0 mg of [K]*fac*-[RuCl(dmso-S)$_3$(η^2-mal)] (**40**) (0.098 mmol) and 35.1 mg (2 equiv.) in 5.0 mL of EtOH. Yield: 18.6 mg (34%). ^{1}H NMR (DMSO-*d*$_6$) δ, ppm: 2.94 (s, 2H, mal), 7.44 (dd, 2H, H3), 7.89 (d, 2H, H2), 8.21 (d, 2H, H5), 8.27 (dd, 2H, H8), 8.32-8.37 (m, 4H, H6+H4), 8.78 (d, 2H, H7), 9.57 (d, 2H, H9). UV−vis ($CHCl_3$): λ_{max} (ε, L mol^{-1} cm^{-1}) = 544 (3.4×10^3) nm. ESI-MS (m/z): 565.0 [M+H]$^+$ (calcd. for $C_{27}H_{19}N_4O_4Ru$ 564.54).

[Ru(dpphen)$_2$(η^2-mal)] (49). Starting materials: 200.0 mg of [K]*fac*-[RuCl(dmso-S)$_3$(η^2-mal)] (**40**) (0.390 mmol) and 260.0 mg (2 equiv.) of dpphen in 22.0 mL of EtOH. Yield of **49**: 122.7 mg (36%). ^{1}H NMR (DMSO-*d*$_6$) δ, ppm: 3.02 (s, 2H, CH_2-mal), 7.50 (d, 2H, H3), 7.52-7.62 (m, 10H, H*o,m,p*), 7.66 (t, 2H, H*p*′), 7.73 (t, 4H, H*m*′), 7.87 (d, 4H, H*o*′), 8.11 (d, 2H, H5), 8.17 (d, 2H, H2), 8.25 (d, 2H, H6), 8.30 (d, 2H, H8), 9.70 (d, 2H, H9). UV−vis ($CHCl_3$): λ_{max} (ε, L mol^{-1} cm^{-1}) = 561 (1.9×10^4) nm. ESI-MS (m/z): 869.1 [M+H]$^+$ (calcd. for $C_{51}H_{35}N_4O_4Ru$ 868.9), 891.1 [M+Na]$^+$ (calcd for $C_{51}H_{34}N_4O_4RuNa$ 890.9).

[Ru(phen)$_2$(η^2-ox)] (50). Starting materials: 62.24 mg (0.13 mmol) of K[*fac*-RuCl(dmso-S)$_3$(η^2-ox)] (**42**) and 45.05 mg (2 equiv) of phen in 8.0 mL of EtOH. Since 12 is sparingly soluble in chloroform, the raw product was washed with water to remove KCl and then thoroughly dried under vacuum. Yield: 47.6 mg (69%).^{1}H NMR (DMSO-*d*$_6$) δ, ppm: 7.44 (dd, 2H, H3), 7.91 (d, 2H, H2), 8.21-8.28 (m, 4H, H8+H5), 8.32-8.40 (m, 4H, H6+H4), 8.79 (d, 2H, H7), 9.32 (d, 2H, H9). UV−vis ($CHCl_3$):

λ_{max} (ε, L mol^{-1} cm^{-1}) = 544 (2.4×10^3) nm. ESI-MS (m/z): 551.0 $[M+H]^+$ (calcd for $C_{26}H_{17}N_4O_4Ru$ 550.51), 589.0 $[M+K]^+$ (calcd. for $C_{26}H_{17}N_4O_4RuK$ 588.61).

[Ru(dpphen)$_2$(η^2-ox)] (51). Starting materials: 200.0 mg (0.40 mmol) of K[*fac*-RuCl(dmso-S)$_3$(η^2-ox)] (**42**) and 267.0 mg (2 equiv) of dpphen in 22.0 mL of EtOH. Yield: 274.4 mg (80%).^{1}H NMR (DMSO-d_6) δ, ppm: 7.49 (d, 2H, H3), 7.52-7.62 (m, 10H, H*o,m,p*), 7.65 (t, 2H, H*p′*), 7.73 (t, 4H, H*m′*), 7.82 (d, 4H, H*o′*), 8.14 (d, 2H, H5), 8.20 (d, 2H, H2), 8.26 (d, 2H, H6), 8.29 (d, 2H, H8), 9.44 (d, 2H, H9). UV−vis ($CHCl_3$): λ_{max} (ε, L mol^{-1} cm^{-1}) = 560 (2.0×10^4) nm. ESI-MS (m/z): 855.1 $[M+H]^+$ (calcd for $C_{50}H_{33}N_4O_4Ru$ 854.9), 877.1 $[M+Na]^+$ (calcd. for $C_{50}H_{32}N_4O_4RuNa$ 876.9).

[Ru(phen)$_2$(η^2-acac)][Cl] (52). Starting materials: 188.8 mg (0.40 mmol) of [*fac*-RuCl(dmso-S)$_3$(η^2-acac)] (**44**) and 144.2 mg (2 equiv.) of phen in 22 mL of EtOH. At the end of the run the solvent was removed by evaporation affording a dark purple mixture. Column chromatography on silica gel (eluent $CHCl_3$:MeOH 9:1) afforded pure **52** in the first band. Yield: 110.5 mg (46%). For comparative purposes, the $[Ru(phen)_3][Cl]_2$ compound was then eluted by increasing the eluent polarity to 8.5:1.5. ^{1}H NMR (DMSO-d6) δ, ppm: 9.13 (d, 2H, H9), 8.83 (d, 2H, H7), 8.42 (d, 2H, H4), 8.36 (d, 2H, H6), 8.24 (d, 2H, H5), 8.18 (dd, 2H, H8), 7.96 (d, 2H, H2), 7.47 (dd, 2H, H3), 5.42 (s, 1H, acac), 1.78 (s, 6H, acac). UV−vis ($CHCl_3$): λ_{max} (ε, L mol^{-1} cm^{-1}) = 509 (1.1×10^4) nm. ESI-MS (m/z): 561.1 $[M–Cl]^+$ (calcd for $C_{29}H_{23}N_4O_2Ru$ 560.6), 381.0 $[M–Cl–phen]^+$ (calcd. for $C_{17}H_{15}N_2O_2Ru$ 380.39).

[Ru(dpphen)$_2$(η^2-acac)][Cl] (53). Starting materials: 200.0 mg (0.42 mmol) of [*fac*-RuCl(dmso-S)$_3$(η^2-acac)] (**44**) and 281.7 mg (2 equiv.) of dpphen il 22.0 mL of EtOH. At the end of the run the solvent was removed by evaporation affording a dark purple mixture. Column chromatography on silica gel (eluent acetone:EtOH 91:9) afforded pure **53** in the first band. Yield: 160.7 mg (42%). ^{1}H NMR (DMSO-d_6) δ, ppm: 9.25 (d, 2H, H9), 8.26 (d, 2H, H6), 8.20 (2d, 4H, H2, H8), 8.14 (d, 2H, H5), 7.85 (d, 4H, H*o′*), 7.74 (t, 4H, H*m′*), 7.67 (t, 2H, H*p′*), 7.54-7.63 (m, 10H, H*o,m,p*), 7.51 (d, 2H, H3), 5.51 (s, 1H, acac), 1.88 (s, 6H, acac). UV−vis ($CHCl_3$): λ_{max} (ε, L mol^{-1} cm^{-1}) = 524 (1.8×10^4) nm. ESI-MS (m/z): 865.2 $[M–Cl]^+$(calcd. for $C_{53}H_{39}N_4O_2Ru$ 864.99).

Synthesis of [Ru(chel)$_2$(chel′)][PF$_6$]$_2$ compounds

[Ru(phen)$_2$(bpy)][PF$_6$]$_2$ (54). A 10 mg amount of [Ru(phen)$_2$(η^2-mal)] (**48**) (0.018 mmol) and 2.8 mg of bpy (1 equiv.) were dissolved in 5 mL of EtOH at reflux and 10 equiv. of TFA (15μL) were added. The solution gradually turned from purple to bright red-orange. After 1h the solvent is removed by evaporation and ca. 10 equiv. of NH_4PF_6 dissolved in 2 mL of water were added, affording an orange-red precipitate that was filtered, washed with water, diethyl ether and dried under vacuum. Yield 10.2 mg (93%). ^{1}H NMR (CD_3CN) δ, ppm: (p = phen, b = bpy): 8.65 (d, 2H, H4$_p$), 8.55 (d, 2H, H7$_p$), 8.52 (d, 2H, H3,3′$_b$), 8.24 (m, 4H, H5+H6$_p$), 8.20 (dd, 2H, H2$_p$), 8.03 (t, 2H, H4,4′$_b$), 7.88 (dd, 2H, H9$_p$), 7.79 (dd, 2H, H3$_p$), 7.67 (d, 2H, H6,6′$_b$), 7.56 (dd, 2H, H8$_p$), 7.27 (t, 2H, H5,5′$_b$).

UV−vis (CH_3CN): λ_{max} (ε, L mol^{-1} cm^{-1}) = 265 (4.5×10^4) nm, 287 (4.3×10^4) nm, 450 (1.0×10^4) nm. ESI-MS (m/z) = 763.2 $[M\text{-}PF_6]^+$ (calcd for $C_{34}H_{24}F_6N_6PRu$ 763.1).

$[Ru(bpy)_2(phen)][PF_6]_2$ (55). The same reaction condition as reported above for complex **54** were used. Starting materials: A 10 mg amount of $[Ru(bpy)_2(\eta^2\text{-mal})]$ (**47**) (0.02 mmol) and 3.5 mg of phen (1 equiv.) Yield 15.6 (94%). ^1H NMR (CD_3CN) δ, ppm: (p = phen, b = bpy): 8.61 (dd, 2H, $H2,9_p$), 8.52 (dd, 2H, $H3'_b$), 8.48 (dd, 2H, $H3_b$), 8.24 (s, 2H, $H5,6_p$), 8.09 (m, 4H, $H4'_b$+$H4,7_p$), 7.98 (t, 2H, $H4_b$), 7.84 (dd, 2H, $H6'_b$), 7.73 (dd, 2H, $H3,8_p$), 7.52 (dd, 2H, $H6_b$), 7.45 (t, 2H, $H5'_b$), 7.21 (t, 2H, $H5_b$). $^{31}P\{^1H\}$ NMR (CD_3CN) δ, ppm: –144.63 (septet). ^{19}F NMR (CD_3CN) δ, ppm: –72.91 (d). UV−vis ($CHCl_3$)): λ_{max} = 449 nm. ESI-MS (m/z): 739.0 $[M–PF_6]^+$ (calcd for $C_{32}H_{24}F_6N_6PRu$ 739.6). Alternatively, compound **55** was also prepared on a smaller scale $[Ru(bpy)_2(\eta^2\text{-acac})][PF_6]$ (**46**): a 20.0 mg amount of **46** (0.030 mmol) and 1.1 equiv. of phen (5.4 mg) were refluxed in 5 mL of EtOH after the addition of 22 μL of a 55% aqueous solution of HPF_6 (4 equiv.). The color change from purple to red-orange occurred within 2.5h. Dropwise addition of diethyl ether to the final solution (concentrated to ca. 2 mL) to near cloudiness afforded the slow precipitation of a red.orange microcrystals that, according to NMR and UV-vis spectroscopy, were pure $[Ru(bpy)_2(phen)][PF_6]_2$ (**55**). In this case the yield was not measured.

6.5 Bibliography

1. Balzani, V.; Bergamini, G.; Campagna, S.; Puntoriero, F. (2007) Photochemistry and Photophysics of Coordination Compounds: Overview and General Concepts. In: Balzani, V.; Campagna S. (eds) Photochemistry and Photophysics of Coordination Compounds I. *Top. Curr. Chem*. **2007**, vol 280. Springer, Berlin, Heidelberg pp. 1-36.
2. Mede, T.; Jäger, M.; Schubert, U. S. ‘‘Chemistry-on-the-complex’’: functional Ru^{II} polypyridyl-type sensitizers as divergent building blocks *Chem. Soc. Rev*., **2018**, 47, 7577-7627.
3. Pashaei, B.; Shahroosvand, H.; Graetzel, M.; Nazeeruddin, M. K. Influence of Ancillary Ligands in Dye-Sensitized Solar Cells *Chem. Rev*. **2016**, 116, 9485‑9564.
4. Narayanam, J. M. R.; Stephenson, C. R. J. Visible light photoredox catalysis: applications in organic synthesis *Chem. Soc. Rev*. **2011**, 40, 102–113.
5. Prier, C. K.; Rankic, D. A.; MacMillan D. W. C. Visible Light Photoredox Catalysis with Transition Metal Complexes: Applications in Organic Synthesis *Chem. Rev*. **2013**, 113, 5322−5363.
6. Poynton, F. E.; Bright, S. A.; Blasco, S.; Williams, D. C.; Kelly, J. M.; Gunnlaugsson, T. The development of ruthenium(II) polypyridyl complexes and conjugates for in vitro cellular and in vivo applications *Chem. Soc. Rev*.**, 2017**, 46, 7706-7756.
7. Mital, M.; Ziora, Z. Biological applications of Ru(II) polypyridyl complexes *Coord. Chem. Rev*. **2018**, 375, 434-458.
8. Zayat, L.; Filevich, O.; Baraldo, L. M.; Etchenique, R. Ruthenium polypyridyl phototriggers: from beginnings to perspectives *Phil. Trans. R. Soc. A.* **2013**, 371, 20120330.
9. Knoll, J. D.; Albani, B. A.; Turro, C. New Ru(II) Complexes for Dual Photoreactivity: Ligand Exchange and $^1O_2$ Generation *Acc. Chem. Res*. **2015**, 48, 2280−2287.
10. Kohler, L.; Nease, L.; Vo, P.; Garofolo, J.; Heidary, D. K.; Thummel, R. P.; Glazer, E. C. Photochemical and Photobiological Activity of Ru(II) Homoleptic and Heteroleptic Complexes Containing Methylated Bipyridyl-type Ligands *Inorg. Chem*. **2017**, 56, 12214−12223.
11. Heinemann, F.; Johannes Karges, J.; Gasser, J. Critical Overview of the Use of Ru(II) Polypyridyl Complexes as Photosensitizers in One-Photon and Two-Photon Photodynamic Therapy *Acc. Chem. Res.* **2017**, 50, 11, 2727–2736.
12. Cuello-Garibo,J.-A.; Meijer, M. S.; Bonnet, S. To cage or to be caged? The cytotoxic species in ruthenium-based photoactivated chemotherapy is not always the metal *Chem. Commun.* **2017**, 53, 6768-6771.

13. Liu, J; Zhang, C.; Rees, T. W.; Ke, L.; Ji, L.; Chao, H. Harnessing ruthenium(II) as photodynamic agents: Encouraging advances in cancer therapy *Coord. Chem. Rev.* **2018**, 363, 17–28.
14. Le Gall, T.; Lemercier,G.; Chevreux, S.; Tücking, K.-S.; Ravel, J.; Thétiot, F.; Jonas, U.; Schönherr, H.; Montier, T. Ruthenium(II) Polypyridyl Complexes as Photosensitizers for Antibacterial Photodynamic Therapy: A Structure–Activity Study on Clinical Bacterial Strains *ChemMedChem* **2018**, 13, 2229-2239.
15. Meijer, M. S.; Bonnet, S. Diastereoselective Synthesis and Two-Step Photocleavage of Ruthenium Polypyridyl Complexes Bearing a Bis(thioether) Ligand *Inorg. Chem*. **2019**, 58, 17, 11689–11698.
16. Conti, L.; Bencini, A.; Ferrante, C.; Gellini, C.; Paoli, P.; Parri, M.; Pietraperzia, G.; Valtancoli, B.; Giorgi, C. Highly Charged Ruthenium(II) Polypyridyl Complexes as Effective Photosensitizer in Photodynamic Therapy *Chem. Eur. J.* **2019**, 25, 10606-10615.
17. Monro, S.; Colón, K. L.; Yin, H.; Roque III, J.; Konda, P.; Gujar, S.; Thummel, R. P.; Lilge, L.; Cameron, C. G.; McFarland, S. A. Transition Metal Complexes and Photodynamic Therapy from a Tumor-Centered Approach: Challenges, Opportunities, and Highlights from the Development of TLD1433 *Chem. Rev.* **2019**, 119, 797-828.
18. Pierroz, V.; Joshi, T.; Leonidova, A.; Mari, C.; Schur, J.; Ott, I.; Spiccia, L.; Ferrari, S.; Gasser, G. Molecular and Cellular Characterization of the Biological Effects of Ruthenium(II) Complexes Incorporating 2-Pyridyl-2-pyrimidine-4-carboxylic Acid *J. Am. Chem. Soc*. **2012**, 134, 20376-20387.
19. Joshi, T.; Pierroz, V.; Mari, C.; Gemperle, L.; Ferrari, S.; Gasser, G. A Bis(dipyridophenazine)(2-(2-pyridyl)pyrimidine-4-carboxylic acid) ruthenium(II) Complex with Anticancer Action upon PhotodeprotectionAngew. *Chem. Int. Ed*. **2014**, 53, 2960–2963.
20. Peña, B.; Saha, S.; Barhoumi, R.; Burghardt, R. C.; Dunbar, K. R. Ruthenium(II)-Polypyridyl Compounds with π-Extended Nitrogen Donor Ligands Induce Apoptosis in Human Lung Adenocarcinoma (A549) Cells by Triggering Caspase-3/7 Pathway *Inorg. Chem.* **2018**, 57, 12777−12786.
21. Spiccia, L.; Deacon, G. B.; Kepert, C. M. Synthetic routes to homoleptic and heteroleptic ruthenium(II) complexes incorporating bidentate imine ligands Coord. Chem. Rev. 2004, 248, 1329-1341.
22. Hesek, D.; Inoue, Y.; Everitt, S. R. L.; Ishida, H.; Kunieda, M.; Drew, M. G. B. Novel Synthetic Routes to Several New, Differentially Substituted Ruthenium Tris(4,4′-disubstituted-2,2′-bipyridine) Complexes *Inorg. Chem.* **2000**, 39, 308-316.

23. Gong, L.; Wenzel, M.; Meggers, E. Chiral-Auxiliary-Mediated Asymmetric Synthesis of Ruthenium Polypyridyl Complexes *Acc. Chem. Res*. **2013**, 46, 2635–2644.
24. See, for example Al-Rawashdeh, N. A. F.; Chatterjee, S.; Krause, J. A.; Connick, W. B. Ruthenium Bis-diimine Complexes with a Chelating Thioether Ligand: Delineating 1,10-Phenanthrolinyl and 2,2-Bipyridyl Ligand Substituent Effects *Inorg. Chem.* **2013**, 53, 294-307.
25. Sullivan, B. P.; Salmon, D. J.; Meyer, T. J. Mixed phosphine 2,2'-bipyridine complexes of ruthenium *Inorg. Chem.* **1978**, 17, 3334-3341.
26. Viala, C.; Coudret, C. An expeditious route to *cis*-Ru(bpy)$_2$C1$_2$ (bpy = 2,2′-bipyridine) using carbohydrates as reducers *Inorg. Chim. Acta* **2006**, 359, 984–989.
27. Zabarska, N.; Vos, J. G.; Rau, S. A new method for the utilization of compounds of the type [Ru(bpy)$_2$(CO)Cl]$^+$ as a starting material for the synthesis of [Ru(N$_6$)]$^{2+}$ type compounds *Polyhedron* **2015**, 102, 173-175.
28. Spiccia, L.; Vos, J. G.; Kelly, J. M. Ruthenium polypyridyl chemistry; from basic research to applications and back again *Dalton Trans.* **2006**, 41, 4869-4883.
29. Rutherford, T. J.; Pellegrini, P. A.; Aldrich-Wright, J.; Junk, P. C.; Keene, R. F., Isolation of Enantiomers of a Range of Tris(bidentate)ruthenium(II) Species Using Chromatographic Resolution and Stereoretentive Synthetic Methods. *Eur. J. Inorg. Chem*. **1998**, 1677-1688.
30. Treadway, J. A.; Meyer, T. J., Preparation of Coordinatively Asymmetrical Ruthenium(II) Polypyridine Complexes. *Inorg. Chem.* **1999**, 38, 2267-2278.
31. Kepert, C. M.; Deacon, G. B.; Sahely, N.; Spiccia, L.; Fallon, G. D.; Skelton, B. W.; White, A. H., Synthesis of Heteroleptic Bis(diimine)carbonylchlororuthenium(II) Complexes from Photodecarbonylated Precursors. *Inorg. Chem*. **2004**, 43, 2818-2827.
32. Kepert, C. M.; Bond, A. M.; Deacon, G. B.; Spiccia, L.; Skelton, B. W.; White, A. H., The Synthesis and Structure of Heteroleptic Tris(Diimine)Ruthenium(II) Complexes. *Dalton Trans*. **2004**, 1766-1774.
33. Mulhern, D.; Brooker, S.; Gorls, H.; Rau, S.; Vos, J. G., Synthesis of Mononuclear and Dinuclear Ruthenium(II) Tris(Heteroleptic) Complexes via Photosubstitution in Bis(Carbonyl) Precursors. *Dalton Trans.* 2006, 51-57.
34. Freedman, D. A.; Evju, J. K.; Pomije, M. K.; Mann, K. R. Convenient Synthesis of Tris-Heteroleptic Ruthenium(II) Polypyridyl Complexes Inorg. Chem., 2001, 40, 5711-5715.
35. Myahkostupo, M.; Castellano, F. N. Synthesis and Characterization of Tris(Heteroleptic) Ru(II) Complexes Bearing Styryl Subunits *Inorg. Chem*. 2011, 50, 9714–9727.
36. Bratsos, I.; Alessio, E. Ruthenium(II)-chlorido complexes of dimethylsulfoxide *Inorg. Synth*. **2010**, 35, 148-152.

37. Alessio, E. Synthesis and Reactivity of Ru-, Os-, Rh-, and Ir-halide-sulfoxide Complexes *Chem. Rev*. **2004**, 104, 4203- 4242.
38. Bratsos, I.; Alessio, E. The pivotal role of Ru-dmso compounds in the discovery of well-behaved precursors. *Eur. J. Inorg. Chem*. **2018**, 2996-3013.
39. Alessio, E.; Iengo, E.; Zangrando, E.; Geremia, S.; Marzilli, P. A.; Calligaris, M. Orientation and Restricted Rotation of Lopsided N-donor Heterocyclic Bioligands in Octahedral Ruthenium Complexes *Eur. J. Inorg. Chem*. **2000**, 2207-2219.
40. Zakeeruddin, S. M.; Nazeeruddin, Md. K.; Humphry-Baker, R.; Grätzel, M. Stepwise Assembly of Tris-Heteroleptic Polypyridyl Complexes of Ruthenium(II) *Inorg. Chem*., **1998**, 37, 5251-5259.
41. Burke, C.; Keyes, T. E. An efficient route to asymmetrically diconjugated tris(heteroleptic) complexes of Ru(II) *RSC Adv*. **2016**, 6, 40869-40877.
42. van der Drift, R. C.; Sprengers, J. W.; Bowman, E.; Mul, W. P.; Kooijman, H.; Spek, A. L.; Drent, E. Ruthenium-Catalyzed Isomerization of Allylic Alcohols: Oxidation State Determines Resistance Against Diene Inhibition *Eur. J. Inorg. Chem*. **2002**, 2147-2155.
43. Toyama, M.; Inoue, K.; Iwamatsu, S.; Nagao, N. Syntheses and Crystal Structures of Mono(2,2′-bipyridine)dichlorobis-(dimethyl sulfoxide-*S*)ruthenium(II) Complexes, [$RuCl_2$(bpy)(dmso-*S*)$_2$] *Bull. Chem. Soc. Jpn*. **2006**, 79, 1525-1234.
44. Battistin, F.; Balducci, G.; Demitri, N.; Iengo, E.; Milani, B.; Alessio, E. ^{15}N NMR spectroscopy unambiguously establishes the coordination mode of the diimine linker 2-(2'-pyridyl)pyrimidine-4-carboxylic acid (cppH) in Ru(II) complexes. *Dalton Trans*. **2015**, 44, 15671-15682.
45. Constable, E. C.; Henney, R. P. G.; Leese, T. A.; Tocher, D. A. Cyclometallation Reactions of 6-Phenyl-2,2'-bipyridine; a Potential C,N,N-Donor Analogue of 2,2': 6',2''-Terpyridine. Crystal and Molecular Structure of Dichlorobis(6-phenyl-2,2'-bipyridine)ruthenium(II) *J. Chem. Soc., Dalton Trans*. **1990**, 443-449.
46. Maxwell, K. A.; Sykora, M.; De Simone, J. M.; Meyer, T .J. One-Pot Synthesis and Characterization of a Chromophore-Donor-Acceptor Assembly *Inorg. Chem.* **2000**, *39*, 71-75.
47. Toyama, M.; Mishima, D.; Suganoya, R.; Nagao, N. C_1-symmetrical *cis*-bis(di-2-pyridylamine)chloro(dimethyl sulfoxide-*S*) ruthenium(II) complex: Synthesis, crystal structure, and anion recognition using the NH groups in the chelating ligands *Inorg. Chim. Acta*, **2018**, 478, 104-111.
48. To be noted that complexes of the type [*cis*-RuCl(chel)$_2$(dmso-S)]Cl were prepared by Inoue and co-workers also upon treatment of [$RuCl_2$(chel)$_2$] in DMSO and used as precursors for the preparation of bis-heteroleptic complexes [Ru(chel)$_2$(chel′)]$^{2+}$: a) Hesek, D.; Inoue, Y.; Everitt,

S. R. L.; Ishida, H.; Kuneida, M.; Drew, M. G. B. Preparation and structural elucidation of novel cis ruthenium(II) bis(bipyridine) sulfoxide complexes *J. Chem. Soc., Dalton Trans*. **1999**, 3701-3709; b) Hesek, D.; Inoue, Y.; Everitt, S. R. L.; Ishida, H.; Kuneida, M.; Drew, M. G. B. Conversion of a new chiral reagent Δ-[Ru(bpy)$_2$(dmso)Cl]PF$_6$ to Δ-[Ru(bpy)$_2$(dmbpy)]PF$_6$Cl with 96.8% retention of chirality (dmbpy = 4,4′-dimethyl-2,2′-bipyridine) *Chem. Commun*. **1999**, 403-404.

49. Chen, L.-A.; Ma, J.; Celik, M. A.; Yu, H. L.; Cao, Z.; Frenking, G.; Gong, L.; Meggers, E. Active versus Passive Substituent Participation in the Auxiliary-Mediated Asymmetric Synthesis of an Octahedral Metal Complex. *Chem. Asian J.* **2012**, 7, 2523–2526.
50. Bratsos, I.; Serli, B.; Zangrando, E.; Katsaros, N.; Alessio, E. Replacement of chlorides with dicarboxylate ligands in anticancer active Ru(II)-dmso compounds: a new strategy that might lead to improved activity *Inorg. Chem.* **2007**, 46, 975-992.
51. Similarly, but in contrast with what reported by Burke and Keyes in ref. 41, a mixture of the stereoisomers [*cis*,*cis*-RuCl$_2$(dmso-S)$_2$(dppz)] and [*cis,trans*-RuCl$_2$(dmso-S)$_2$(dppz)] were obtained in the same reaction conditions using dppz instead of phen.
52. Fees, J.; Ketterle, M.; Klein, A.; Fiedler, J.; Kaim, W. Electrochemical, spectroscopic and EPR study of transition metal complexes of dipyrido[3,2-*a*:2′,3′-*c*]phenazine *J. Chem. Soc., Dalton Trans*. **1999**, 2595-2600.
53. Due to the strong absorption bands of the [Ru(chel)$_2$(O–O)]$^{n+}$ and [Ru(chel)$_3$]$^{2+}$ complexes – purple and orange-red, respectively – the solutions are ink-dark even at NMR concentrations (ca. 5 mM), to such an extent that it is hard to detect the presence of a fine precipitate.
54. Besides these two complexes, the mother liquor contains also unreacted bpy.
55. When **44** was used as precursor, the corresponding chloride salts of the two Ru-bpy products remain in solution. Addition of an excess of NH$_4$PF$_6$ induced a Cl$^-$/PF$_6^-$ metathesis and precipitated the [Ru(bpy)$_2$(η^2-acac)][PF$_6$] and [Ru(bpy)$_3$][PF$_6$]$_2$ mixture.
56. Orellana, G.; Carlos Alvarez Ibarra, C. A.; Santoro, J. ^{1}H and ^{13}C NMR Coordination-Induced Shifts in a Series of Tris(α-diimine)ruthenium(II) Complexes Containing Pyridine, Pyrazine, and Thiazole Moieties *Inorg. Chem.* **1988**, 27, 1025-1030.
57. Balducci, G.; Iengo, E.; Demitri, N.; Alessio, E. New Insight into a Deceptively Simple Reaction: The Coordination of bpy to Ru^{II}–Carbonyl Precursors – The Central Role of the *fac*-[Ru(bpy)Cl(CO)$_3$]$^+$ Intermediate and the *Chloride Rebound* Mechanism *Eur. J. Inorg. Chem.* **2015**, 4296-4311.
58. The separation of [Ru(phen)$_2$(η^2-mal)] (**48**) from [Ru(phen)$_3$](Cl)$_2$ can be performed also by washing the raw product with water, where [Ru(phen)$_3$](Cl)$_2$ is soluble and **48** is not.

59. Quite surprisingly, when the reaction between **2** and phen was performed at 80°C (1h), the only detectable product was $[Ru(phen)_3]^{2+}$.
60. If an excess of oxalate is not used, the known dinuclear species $[\{fac\text{-}RuCl(dmso\text{-}S)_3\}_2(\eta^4,\mu\text{-}ox)]$ (see ref. 50) is obtained as by product together with **42**.

Appendix of Chapter 6

The reactions of [*cis*-$RuCl_2(dmso)_4$] (1) with the model diimine chelating ligands phen and dppz

a) Reactions performed in refluxing chloroform.

Complex **1** was treated with one equiv. of phen in refluxing chloroform for 1h, i.e. in the conditions that, according to Grätzel and co-workers,[1S] and Spiccia and co-workers,[2S] are expected to afford selectively the mono-substituted complex [*cis*,*cis*-$RuCl_2$(dmso-S)$_2$(phen)] in good yield. Conversely, according to ^{1}H NMR analysis (Figure 1S), we obtained a ca. 1:1 mixture of the stereoisomers [*cis,cis*-$RuCl_2$(dmso-S)$_2$(phen)] (**a**) and [*trans,cis*-$RuCl_2$(dmso-S)$_2$(phen)] (**b**), together with a good amount of unreacted precursor **1** (Scheme A6.1).

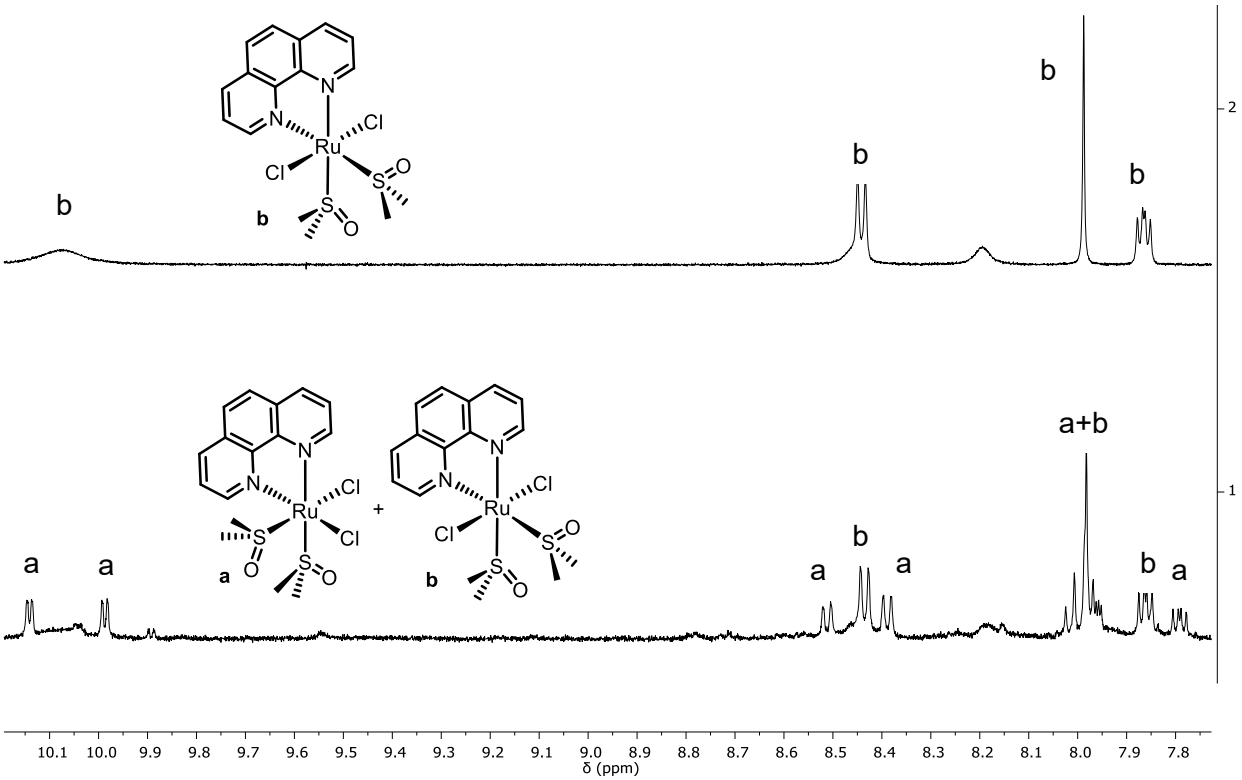

Figure A6.1. Aromatic region of the ^{1}H NMR spectrum ($CDCl_3$) of: (top) complex [*trans,cis*-$RuCl_2$(dmso-S)$_2$(phen)] (**b**); (bottom) the reaction mixture obtained by treatment of **1** with one equiv. of phen in refluxing $CHCl_3$ for 1h.

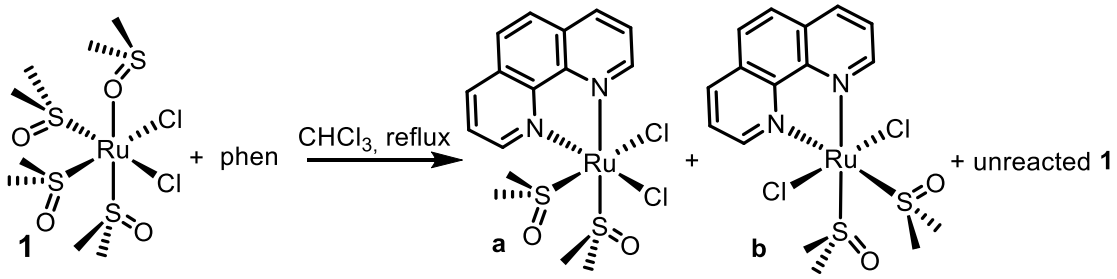

Scheme A6.1. The reactivity of [*cis*-$RuCl_2(dmso)_4$] (**1**) with 1 equiv. of phen in refluxing $CHCl_3$

The NMR spectrum of the more symmetrical isomer **b** (four aromatic resonances, 2H each, and a singlet for two dmso-S ligands) is compatible also with the third stereoisomer [*cis,trans*-$RuCl_2$(dmso-S)$_2$(phen)] (**c**) (Figure A6.2).

For comparative purposes, the stereoisomer **b** was selectively prepared by treatment of [*trans*-$RuCl_2$(dmso-S)$_4$] (**1t**), the stereo and linkage isomer of **1**, with phen at room temperature (its NMR spectrum is shown in Figure 1S). Complex **1t**, in fact, is known to replace selectively two adjacent dmso-S ligands leaving unchanged the geometry of the Ru(II) fragment (Scheme 2S). We also found that, consistent with what previously observed for the corresponding bpy complex,[3S] compound **b** is not stable in chloroform solution at room temperature and within 24 hours isomerizes to a mixture of **a** and of the other symmetrical isomer **c**. From this solution we managed to get crystals of **c** suitable for X-ray analysis that afforded the molecular structure of the complex (Figure A6.3).

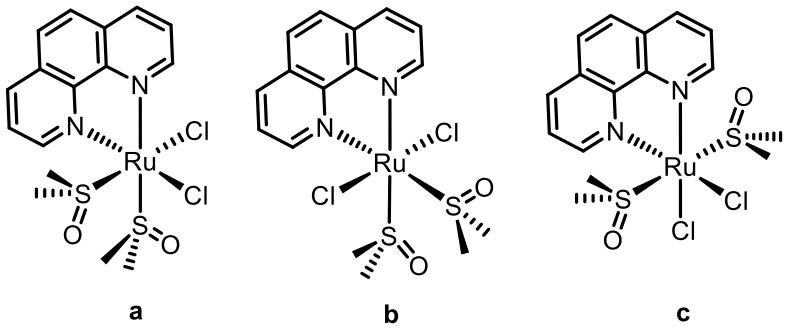

Figure A6.2. The three stereoisomers [*cis,cis*-$RuCl_2$(dmso-S)$_2$(phen)] (**a**), [*trans,cis*-$RuCl_2$(dmso-S)$_2$(phen)] (**b**), and [*cis,trans*-$RuCl_2$(dmso-S)$_2$(phen)] (**c**).

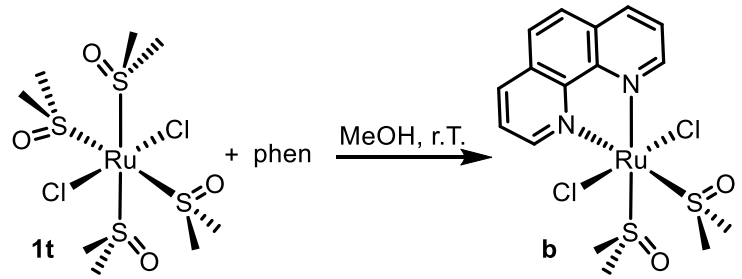

Scheme A6.2. Preparation of [*trans,cis*-$RuCl_2$(dmso-S)$_2$(phen)] (**b**) from [*trans*-$RuCl_2$(dmso-S)$_4$] (**1t**) in MeOH at room temperature.

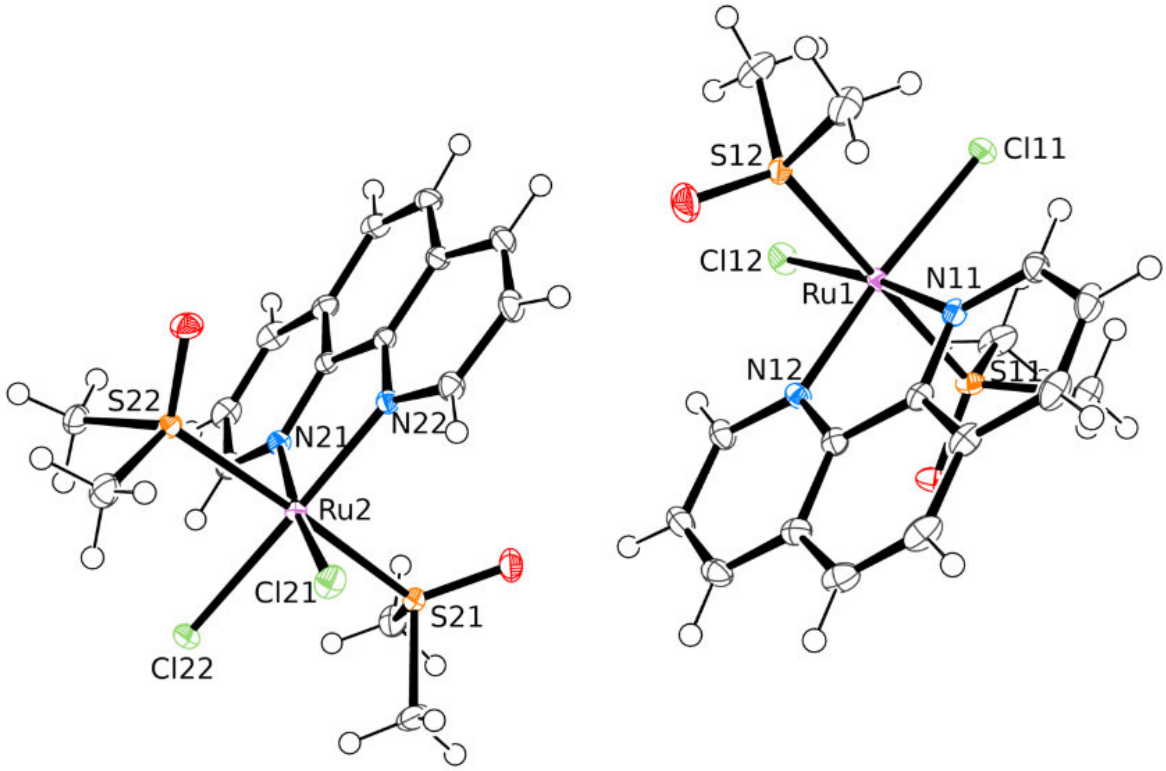

Figure A6.3. The X-ray molecular structure of stereoisomer *cis,trans*-[$RuCl_2$(dmso-S)$_2$(phen)] (**c**).

b) Reactions performed in refluxing ethanol.

Complex **1** was treated with one equiv. of phen in refluxing ethanol for 2h, i.e. in the conditions that – with the similar ligand dppz – according to Burke and Keyes afforded selectively the mono-substituted complex [*cis*,*cis*-$RuCl_2$(dmso-S)$_2$(dppz)] in good yield. The orange product that precipitated spontaneously from the cooled solution turned out to be, according to NMR analysis, a ca. 5:1 mixture of [*cis,cis*-$RuCl_2$(dmso-S)$_2$(phen)] (**a**) and [*cis,trans*-$RuCl_2$(dmso-S)$_2$(phen)] (**c**) (see below Figure 4S). The mother liquor, beside **a** and **c**, contained the disubstituted charged complex [*cis*-RuCl(dmso-S)(phen)$_2$]Cl (**d**). The proton NMR spectrum of this species is characterized by two singlets (3H each) for the residual dmso-S and sixteen resolved aromatic resonances for the two inequivalent phen ligands (see below Figure 4S). No resonances attributable to unreacted **1** were detected.

Thus, the reactivity of 1 with phen in refluxing ethanol can be summarized as reported in Scheme A6.3.

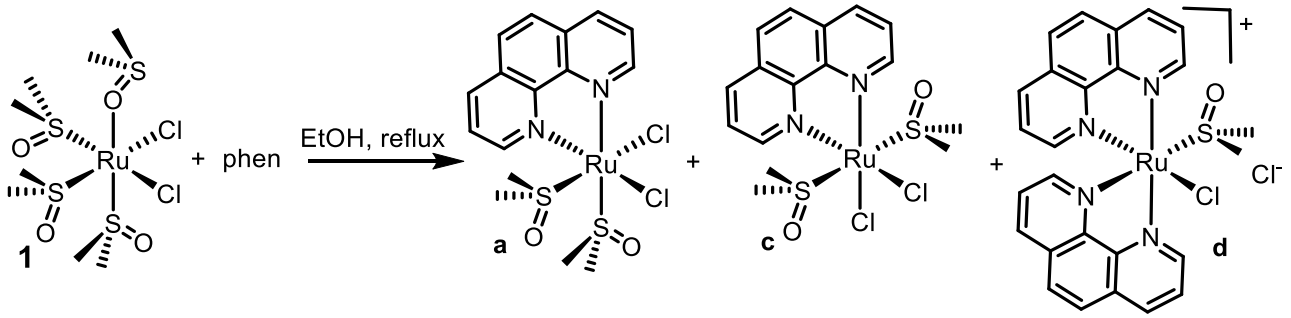

Scheme A6.3. The reactivity of [*cis*-$RuCl_2(dmso)_4$] (**39**) with 1 equiv. of phen in refluxing ethanol.

Very similar results were obtained, under the same conditions, using one equiv. of dppz in the place of phen.

The reaction of **39** with two equiv. of phen in refluxing ethanol (8h) afforded the same three main products **a**, **c**, and **d** as above, even though in different relative ratios. The first fraction was formed by a mixture of **a** and **c** (Figure 4S) , whereas the second fraction, obtained from the concentrated mother liquor, was almost pure **d** (Figure 4S). To be noted that one methyl resonance of the dmso-S in **d** is shifted at very low frequencies. This singlet is attributed to the methyl that falls in the shielding cone of the adjacent phenanthrolines.

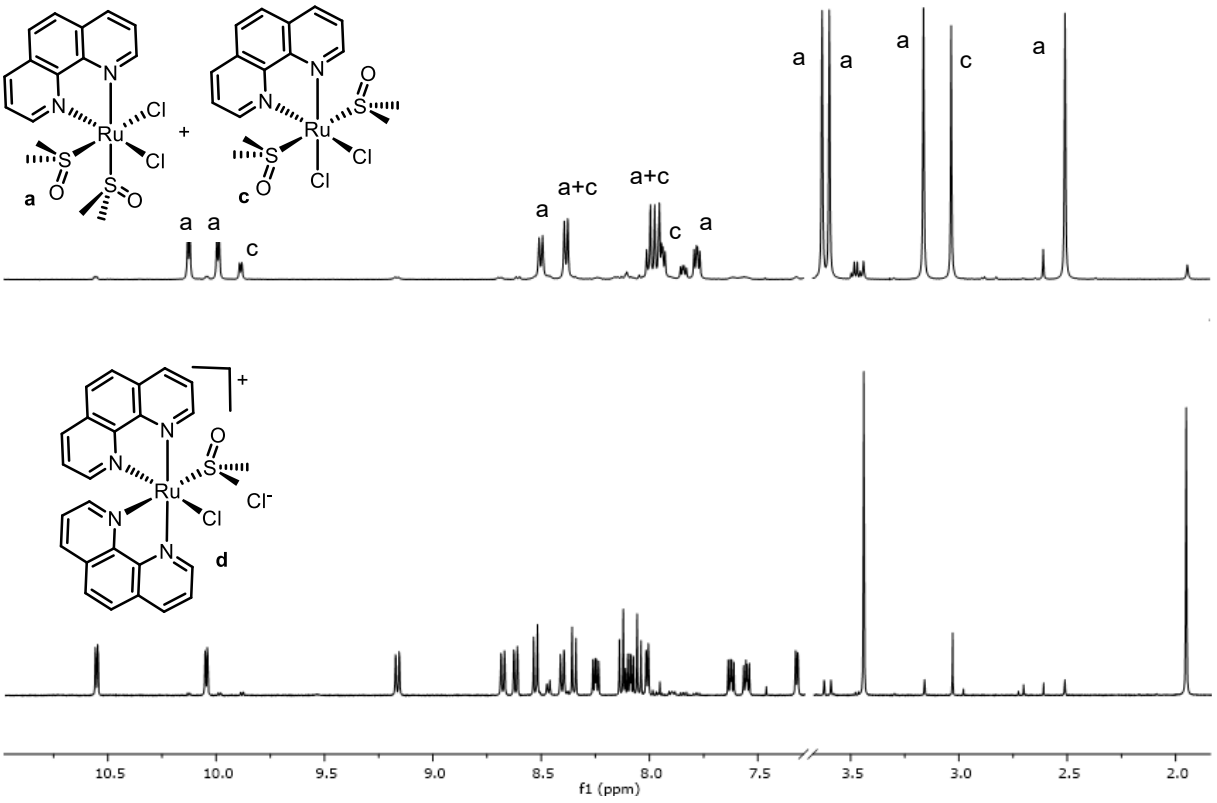

Figure A6.4. ^1H NMR spectra ($CDCl_3$) of the two fractions obtained from the reaction of **1** with two equiv. of phen in refluxing ethanol for 8h. Top: 1st fraction, which is a mixture of **a** and **c**; bottom: 2nd fraction, that consists of almost pure [*cis*-RuCl(dmso-S)$(phen)_2$]Cl (**d**).

References

1A Zakeeruddin, S. M.; Nazeeruddin, Md. K.; Humphry-Baker, R.; Grätzel, M. Stepwise Assembly of Tris-Heteroleptic Polypyridyl Complexes of Ruthenium(II) *Inorg. Chem*., **1998**, 37, 5251-5259.

2A Spiccia, L.; Deacon, G. B.; Kepert, C. M. Synthetic routes to homoleptic and heteroleptic ruthenium(II) complexes incorporating bidentate imine ligands Coord. Chem. Rev. 2004, 248, 1329-1341.

3A Toyama, M.; Inoue, K.; Iwamatsu, S.; Nagao, N. Syntheses and Crystal Structures of Mono(2,2′-bipyridine)dichlorobis-(dimethyl sulfoxide-*S*)ruthenium(II) Complexes, [$RuCl_2$(bpy)(dmso-*S*)$_2$] Bull. Chem. Soc. Jpn. 2006, 79, 1525-1234.

Experimental section

***cis*-$RuCl_2(dmso)_4$ (1) + 1 equiv of phen in refluxing chloroform.**

A 50.0 mg amount of *cis*-$RuCl_2(dmso)_4$ (**39**) (0.10 mmol) was dissolved in 10 mL of chloroform together with one equiv. of phen (18.7 mg). The pale yellow solution was heated to reflux for 1h. The final deep-orange solution was evaporated to an oil that, upon addition of acetone (5 mL), afforded a yellow solid that was removed by filtration, washed with acetone and diethyl ether, and dried under vacuum. According to its ^{1}H NMR spectrum this precipitate is a ca. 1:1 mixture of the stereoisomers **a** and **b** plus unreacted **1**. Upon dropwise addition of diethyl ether to the concentrated mother liquor (ca. 2 mL) a pale yellow – creamy precipitate was obtained that, according to the ^{1}H NMR spectrum in $CDCl_3$, was mainly composed by unreacted **1**. The estimated yield in the **a** + **b** mixture was lower than 50%.

***trans*-$RuCl_2(dmso)_4$ (1t) + phen in methanol.**

A 50.0 mg amount of *trans*-$RuCl_2(dmso)_4$ (**39t**) (0.10 mmol) was dissolved in 5 mL of methanol together with one equiv. of phen (18.7 mg). The orange solution became progressively red and afforded a deep-orange precipitate formed. This was removed by filtration, washed with diethyl ether and dried under vacuum. According to its ^{1}H NMR spectrum this precipitate was pure *cis,trans*-$RuCl_2$(dmso-S)$_2$(phen) (**b**). Upon dropwise addition of diethyl ether to the concentrated mother liquor (ca. 2 mL) a second fraction of the same product was obtained. Total yield of **b**: 41.9 mg (80%).

cis,cis-$RuCl_2$(dmso-S)$_2$(phen) (**a**) ($C_{16}H_{20}Cl_2N_2O_2RuS_2$, MW = 507.94). ^{1}H NMR ($CDCl_3$) δ, ppm: 2.52, 3.17, 3.60, 3.63 (s, 3H, dmso-S), 7.79 (dd, 1H, H8), 7.98 (m, 3H, H3+H5+H6), 8.39 (dd, 1H, H4), 8.51 (dd, 1H, H7), 9.99 (dd, 1H, H2), 10.14 (dd, 1H, H9).

trans,cis-$RuCl_2$(dmso-S)$_2$(phen) (**b**) ($C_{16}H_{20}Cl_2N_2O_2RuS_2$, MW = 507.94). ^{1}H NMR ($CDCl_3$) δ, ppm: 3.66 (s, 12H, dmso-S), 7.86 (m, 2H, H3,8), 7.99 (s, 2H, H5,6), 8.44 (dd, 2H, H4,7), 10.07 (dd, 2H, H2,9).

cis,trans-[$RuCl_2$(dmso-S)$_2$(phen)] (**c**) ($C_{16}H_{20}Cl_2N_2O_2RuS_2$, MW = 507.94). ^{1}H NMR ($CDCl_3$) δ, ppm: 3.04 (s, 12H, dmso-S), 7.84 (dd, 2H, H3,8), 8.01(s, 2H, H5,6), 8.37 (dd, 2H, H4,7), 9.89 (dd, 2H, H2,9).

***cis*-$RuCl_2$(dmso)$_4$ (1) + 1 equiv of phen in refluxing ethanol.**

A 50.0 mg amount of *cis*-$RuCl_2$(dmso)$_4$ (**39**) (0.10 mmol) was dissolved in 10 mL of ethanol together with one equiv. of phen (18.7 mg) and heated to reflux for 2h. The final red-orange solution slowly afforded (72 h) at room temperature an orange precipitate, that was removed by filtration, washed with cold ethanol and diethyl ether, and dried under vacuum. According to its ^{1}H NMR spectrum this precipitate is a ca. 6:1 mixture of the stereoisomers **a** and **c**. Yield 25.3 mg (48%). Upon dropwise addition of diethyl ether to the concentrated mother liquor (ca. 4 mL) a second orange precipitate was obtained that, according to the ^{1}H NMR spectrum in $CDCl_3$, contained comparable amounts of **a**, **c**, and *cis*-[RuCl(dmso-S)(phen)$_2$]Cl (**d**).

***cis*-$RuCl_2$(dmso)$_4$ (1) + 2 equiv of phen in refluxing ethanol.**

A 101.6 mg amount of *cis*-$RuCl_2$(dmso)$_4$ (**39**) (0.21 mmol) was dissolved in 15 mL of ethanol together with two equiv. of phen (74.8 mg) and heated to reflux for 8h. The final deep-red solution was concentrated to ca. half volume. Dropwise addition of diethyl ether until cloudiness afforded an orange precipitate, that was removed by filtration, washed with cold ethanol and diethyl ether, and dried under vacuum. According to its ^{1}H NMR spectrum this precipitate was a ca. 5:1 mixture of the stereoisomers **a** and **c**. Yield 62.45 mg (59%). A small amount of a second fraction precipitated spontaneously from the mother liquor (containing also the diethyl ether from the washing). According to its ^{1}H NMR spectrum it was almost pure *cis*-[RuCl(dmso-S)(phen)$_2$]Cl (**d**).

cis-[RuCl(dmso-S)(phen)$_2$][Cl] (**d**) ($C_{26}H_{22}Cl_2N_4ORuS$, MW = 610.47). ^{1}H NMR ($CDCl_3$) δ, ppm: 1.96 (s, 3H), 3.45 (s, 3H), 7.33 (dd, 1H), 7.56 (dd, 1H), 7.63 (dd, 1H), 8.02 (dd, 1H), 8.05 (dd, 1H), 8.09 (dd, 1H), 8.14 (dd, 1H), 8.25 (dd, 1H), 8.35 (dd, 1H), 8.41 (dd, 1H), 8.53 (dd, 1H), 8.62 (dd, 1H), 8.68 (dd, 1H), 9.17 (dd, 1H), 10.05 (dd, 1H), 10.56 (dd, 1H).

Spectral characterization of the new *cis*-locked precursors 44 and 45.

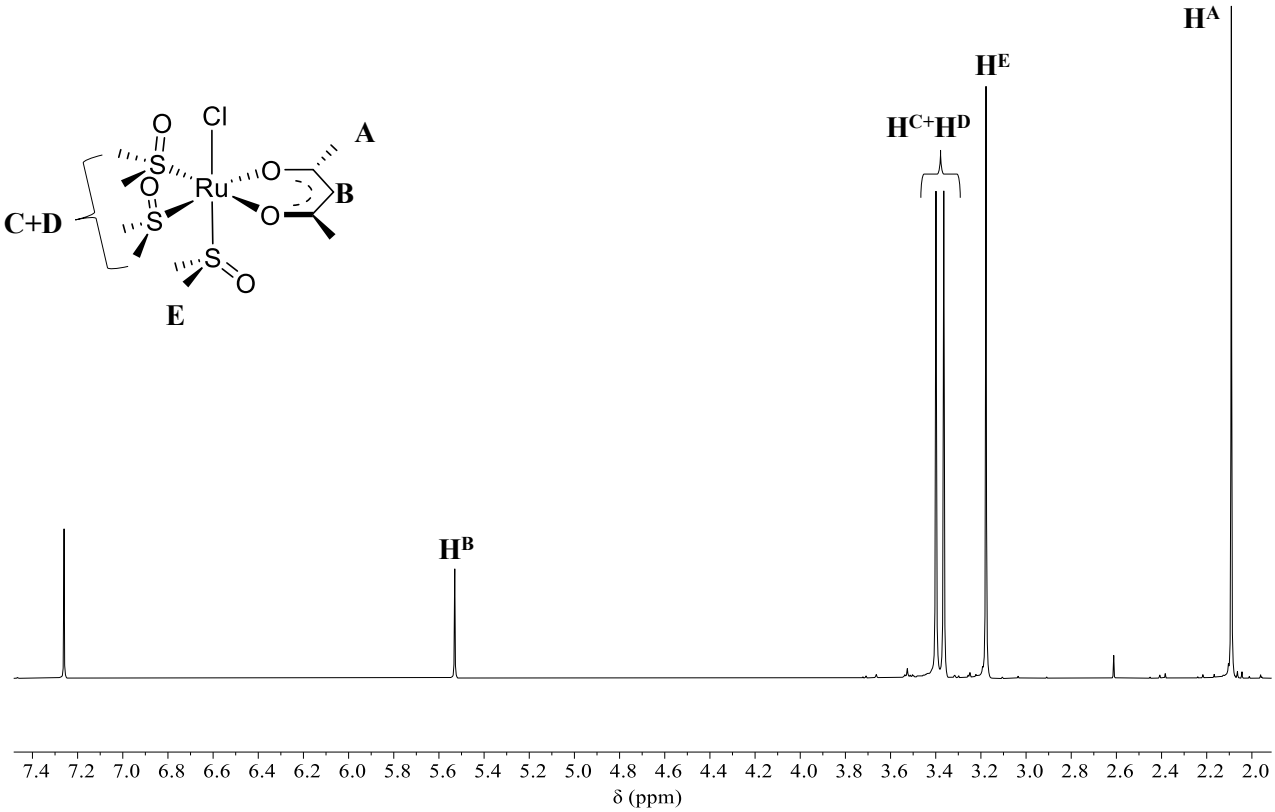

Figure A6.5. ^{1}H NMR spectrum ($CDCl_3$) of [*fac*-RuCl(dmso-S)$_3$(η^2-acac)] (**44**).

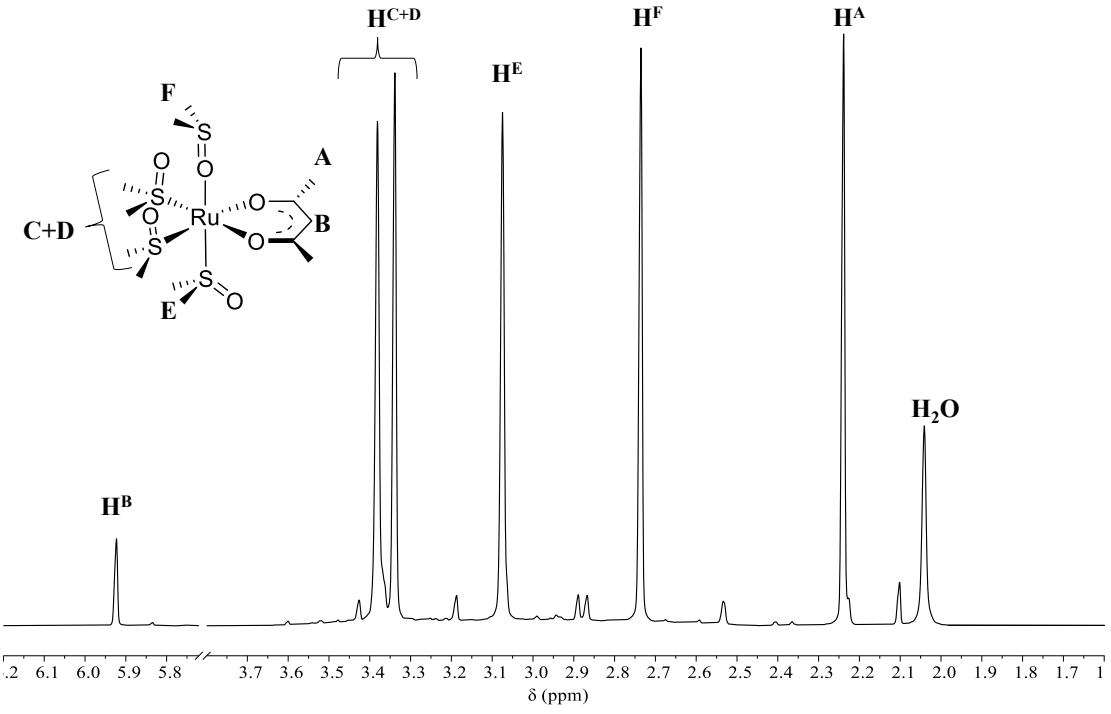

Figure A6.6. ^{1}H NMR spectrum (CD_3NO_2) of [*fac*-Ru(dmso-O)(dmso-S)$_3$(η^2-acac)] (**45**).

Reactions of the *cis*-locked precursors with bpy

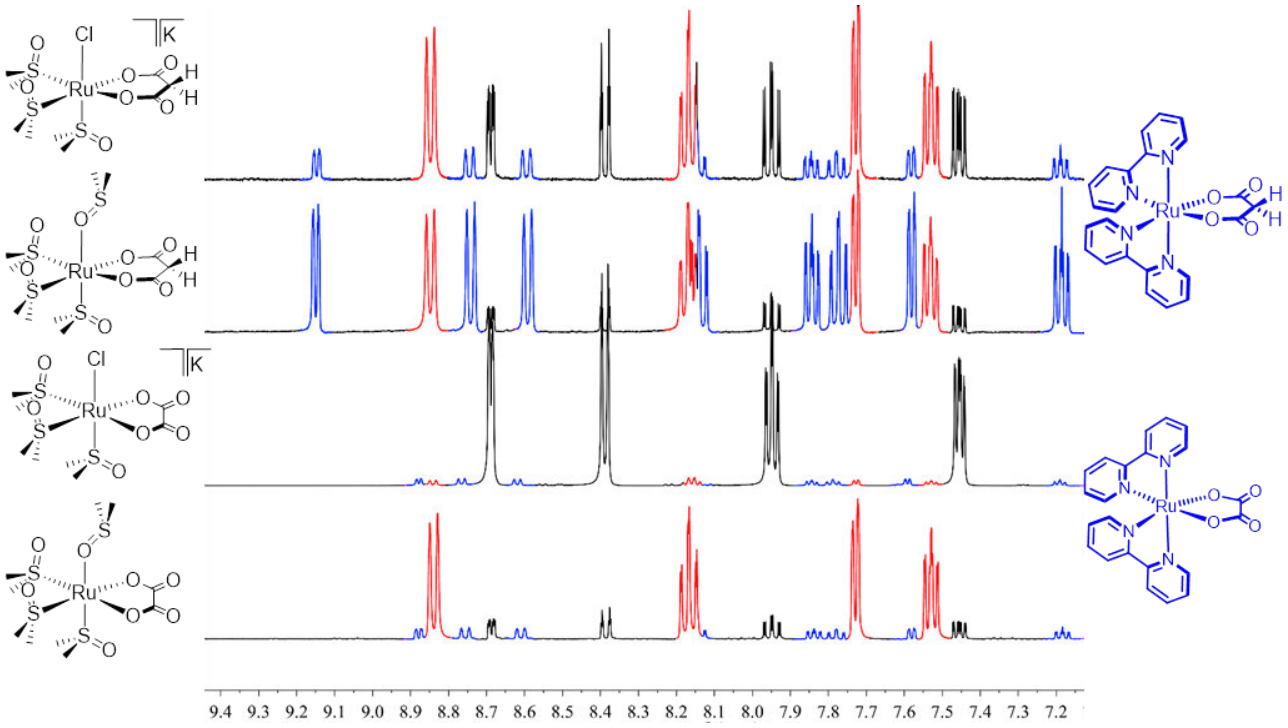

Figure A6.7. ^{1}H NMR spectra (aromatic region) in DMSO-d_6 of the raw product mixtures from the reactions between the *cis*-locked precursors **40** – **43** and bpy performed in a MW reactor. Color code: black = unreacted bpy, blue = the bis-bpy product, red = $[Ru(bpy)_3]^{2+}$. Reaction conditions: [Ru] = 390 mM, absolute ethanol, bpy/Ru = 2, MW, 120°C, 1h.

Table A6.1. Molar percentages determined by NMR integration in the raw product mixtures from the reactions between the *cis*-locked precursors **40** – **45** and bpy performed in a MW reactor. Reaction conditions: [Ru] = 390 mM, absolute ethanol, bpy/Ru = 2, 120°C, 1h.

Complex	**Free bpy**	**$[Ru(bpy)_2(O–O)]^{n+}$**	**$[Ru(bpy)_3]^{2+}$**
K[*fac*-RuCl(dmso-S)$_3$(η^2-mal)] (**40**)	34	18	48
[*fac*-Ru(dmso-O)(dmso-S)$_3$(η^2-mal)] (**41**)	10	64	26
K[*fac*-RuCl(dmso-S)$_3$(η^2-ox)] (**42**)	97	2	1
[*fac*-Ru(dmso-O)(dmso-S)$_3$(η^2-ox)] (**43**)	24	14	62
[*fac*-RuCl(dmso-S)$_3$(η^2-acac)] (**44**)	46	38	15
[*fac*-Ru(dmso-O)(dmso-S)$_3$(η^2-acac)][PF_6] (**45**)	n.d.*	73	27

* In this case a precipitate is found in the vial at the end of the run, a mixture of [Ru(bpy)$_2$(η^2-acac)][PF_6] (**8**) and [Ru(bpy)$_3$][PF_6]$_2$.

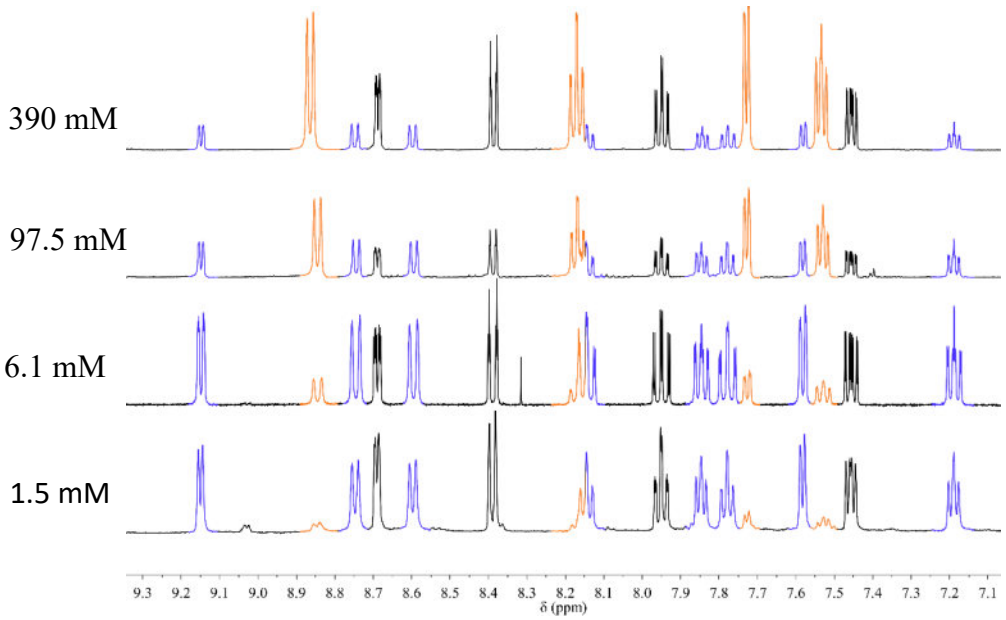

Figure A6.8. The ^{1}H NMR spectra (aromatic region) in DMSO-d_6 show the effect of the concentration on the selectivity towards [Ru(bpy)$_2$(η^2-mal)] in the reaction between K[*fac*-RuCl(dmso-S)$_3$(η^2-mal)] (**40**) and bpy performed in a MW reactor. Color code: black = unreacted bpy, blue = [Ru(bpy)$_2$(η^2-mal)], red-orange = [Ru(bpy)$_3$]$^{2+}$. Reaction conditions: absolute ethanol, bpy/Ru = 2, 120°C, 1h.

Table A6.2. The effect of the concentration on the selectivity towards [Ru(bpy)$_2$(η^2-mal)] in the reaction between K[*fac*-RuCl(dmso-S)$_3$(η^2-mal)] (**40**) and bpy performed in a MW reactor. The % values are obtained by integrating the NMR spectra of Figure S8. Reaction conditions: absolute ethanol, bpy/Ru = 2, 120°C, 1h.

[Ru] mM	Free bpy	[Ru(bpy)$_2$(η^2-mal)]	[Ru(bpy)$_3$]$^{2+}$
390	34	18	48
97.5	32	38	30
6.1	43	51	6
1.5	59	51	3

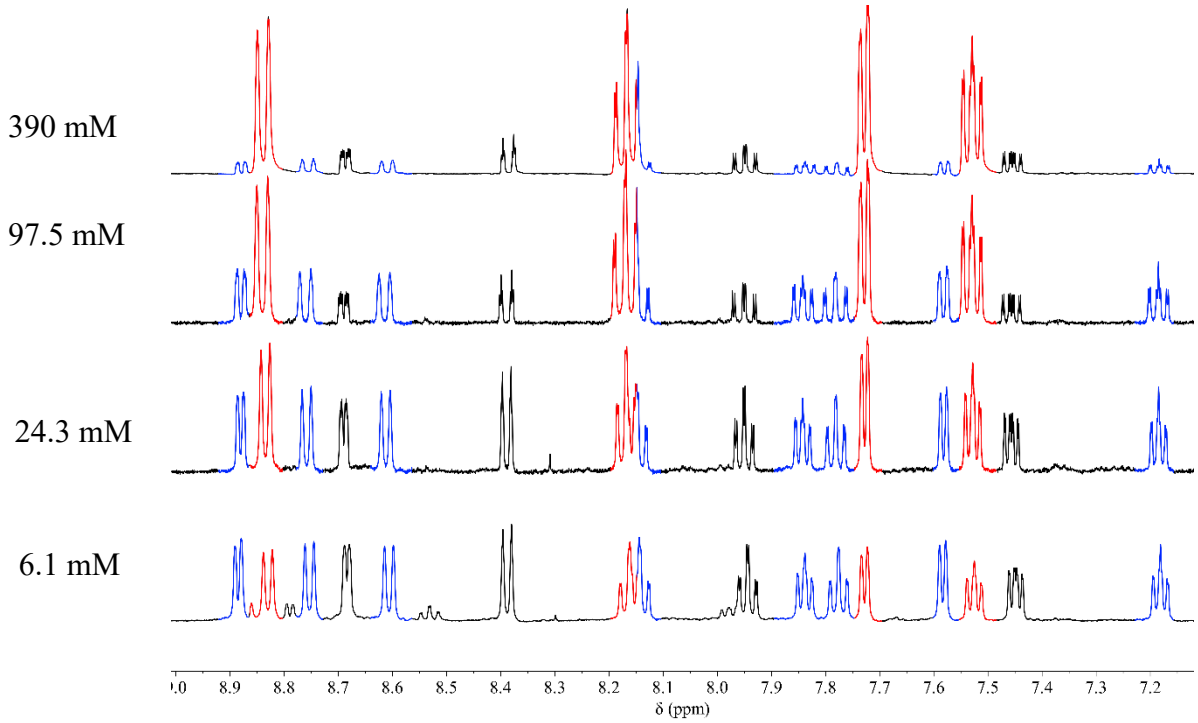

Figure A6.9. The ^{1}H NMR spectra (aromatic region) in DMSO-d_6 show the effect of the concentration on the selectivity towards [Ru(bpy)$_2$(η^2-ox)] in the reaction between [*fac*-Ru(dmso-O)(dmso-S)$_3$(η^2-ox)] (**43**) and bpy performed in a MW reactor. Color code: black = unreacted bpy, blue = [Ru(bpy)$_2$(η^2-ox)], red-orange = [Ru(bpy)$_3$]$^{2+}$. Reaction conditions: absolute ethanol, bpy/Ru = 2, 120°C, 1h.

Table A6.3. The effect of the concentration on the selectivity towards [Ru(bpy)$_2$(η^2-ox)] in the reaction between [*fac*-Ru(dmso-O)(dmso-S)$_3$(η^2-ox)] (**5**) and bpy performed in a MW reactor. The % values are obtained by integrating the NMR spectra of Figure A6.9. Reaction conditions: absolute ethanol, bpy/Ru = 2, 120°C, 1h.

[Ru] mM	Free bpy	[Ru(bpy)$_2$(η^2-ox)]	[Ru(bpy)$_3$]$^{2+}$
390	26	13	62
97.5	22	41	37
24.3	36	42	22
6.1	43	44	13

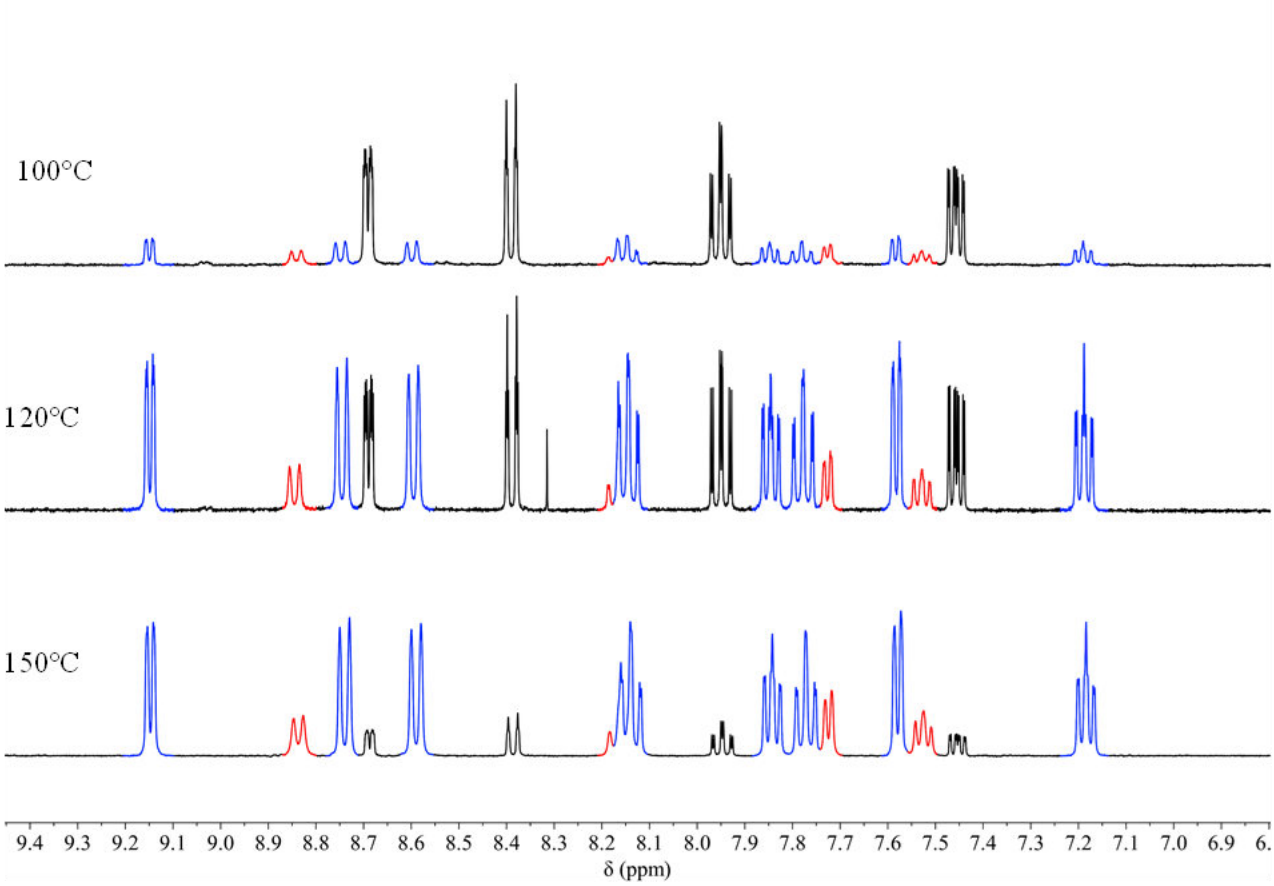

Figure A6.10. The ^{1}H NMR spectra (aromatic region) in DMSO-d_6 show the effect of the temperature on the selectivity towards [Ru(bpy)$_2$(η^2-mal)] in the reaction between K[*fac*-RuCl(dmso-S)$_3$(η^2-mal)] (**2**) and bpy performed in a MW reactor. Color code: black = unreacted bpy, blue = [Ru(bpy)$_2$(η^2-mal)], red-orange = [Ru(bpy)$_3$]$^{2+}$. Reaction conditions: absolute ethanol, [Ru] = 6.1 mM, bpy/Ru = 2, 1h.

Table A6.4. The effect of the temperature on the selectivity towards [Ru(bpy)$_2$(η^2-mal)] in the reaction between K[*fac*-RuCl(dmso-S)$_3$(η^2-mal)] (**40**) and bpy performed in a MW reactor. The % values are obtained by integrating the NMR spectra of Figure A6.10. Reaction conditions: absolute ethanol, [Ru] = 6.1 mM, bpy/Ru = 2, 1h.

T (°C)	Free bpy	[Ru(bpy)$_2$(η^2-mal)]	[Ru(bpy)$_3$]$^{2+}$
100	26	13	62
120	43	51	6
150	16	77	7

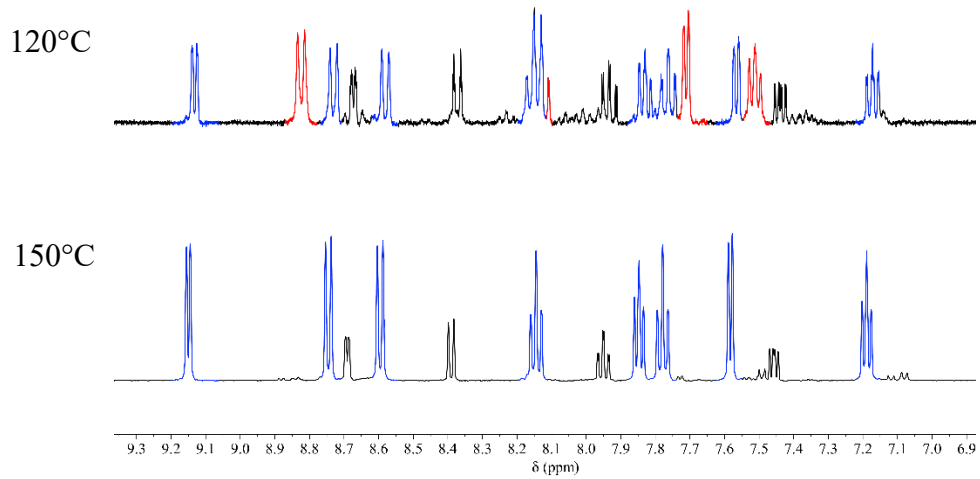

Figure A6.11. The ^{1}H NMR spectra (aromatic region) in DMSO-d_6 show the effect of the temperature on the selectivity towards [Ru(bpy)$_2$(η^2-mal)] in the reaction between [*fac*-Ru(dmso-O)(dmso-S)$_3$(η^2-mal)] (**41**) and bpy performed in a MW reactor. Color code: black = unreacted bpy, blue = [Ru(bpy)$_2$(η^2-mal)], red-orange = [Ru(bpy)$_3$]$^{2+}$. Reaction conditions: absolute ethanol, [Ru] = 6.1 mM, bpy/Ru = 2, 1h.

Table A6.5. The effect of the temperature on the selectivity towards [Ru(bpy)$_2$(η^2-mal)] in the reaction between [*fac*-Ru(dmso-O)(dmso-S)$_3$(η^2-mal)] (**41**) and bpy performed in a MW reactor. The % values are obtained by integrating the NMR spectra of Figure A6.11. Reaction conditions: absolute ethanol, [Ru] = 6.1 mM, bpy/Ru = 2, 1h.

T (°C)	Free bpy	[Ru(bpy)$_2$(η^2-mal)]	[Ru(bpy)$_3$]$^{2+}$
120	27	46	26
150	11	89	<1%

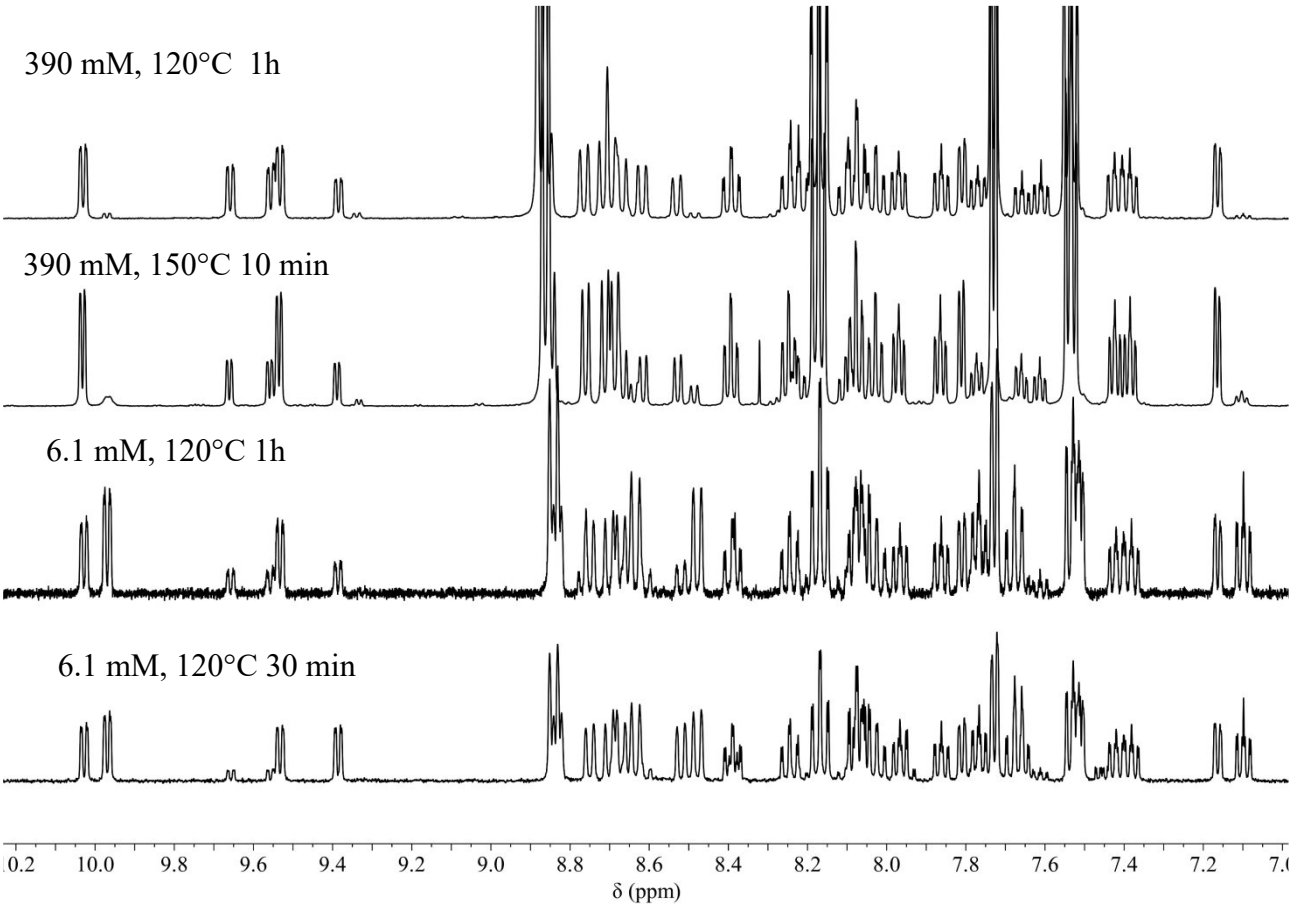

Figure A6.12. The ^{1}H NMR spectra (aromatic region) in DMSO-d_6 show the effect of the concentration, temperature, and reaction time on the outcome of the reaction between [*cis*-$RuCl_2(dmso)_4$] (**39**) and bpy performed in a MW reactor. See Figure S13 for peak assignments. Reaction conditions: absolute ethanol, bpy/Ru = 2, 1h.

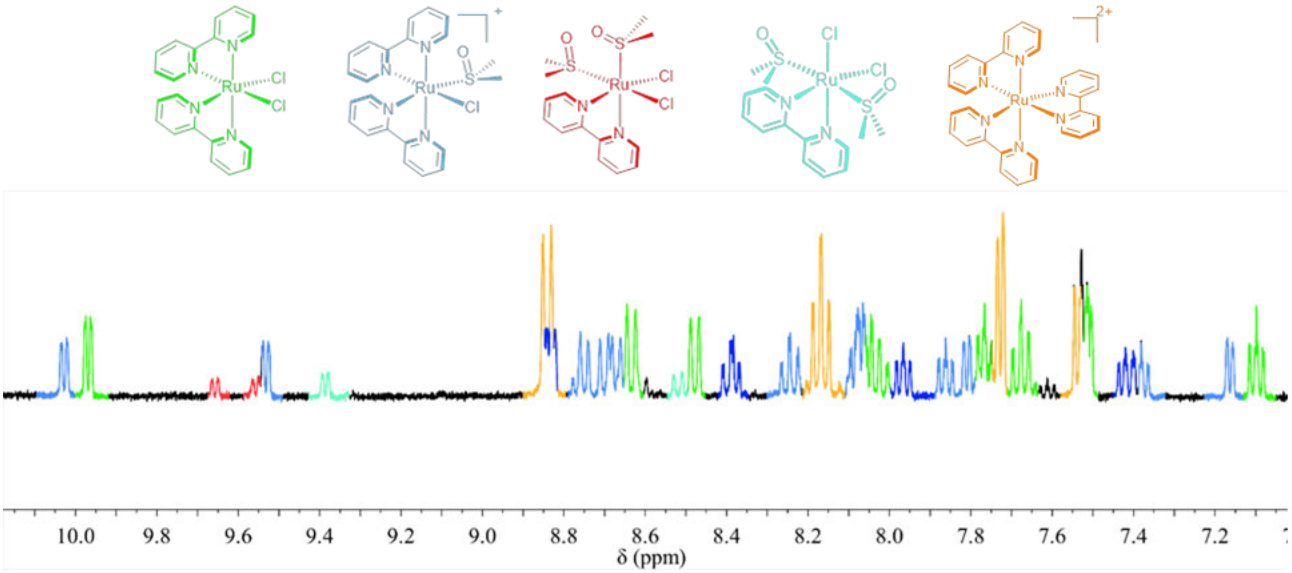

Figure A6.13. Peak assignments in the ^{1}H NMR spectrum (aromatic region) in DMSO-d_6 of the raw reaction mixture from the reaction between [*cis*-$RuCl_2(dmso)_4$] (**39**) and bpy performed in a MW reactor. Reaction conditions: absolute ethanol, [Ru] = 6.1 mM, T = 120°C, bpy/Ru = 2, 1h.

Spectral characterization of compounds 47– 53.

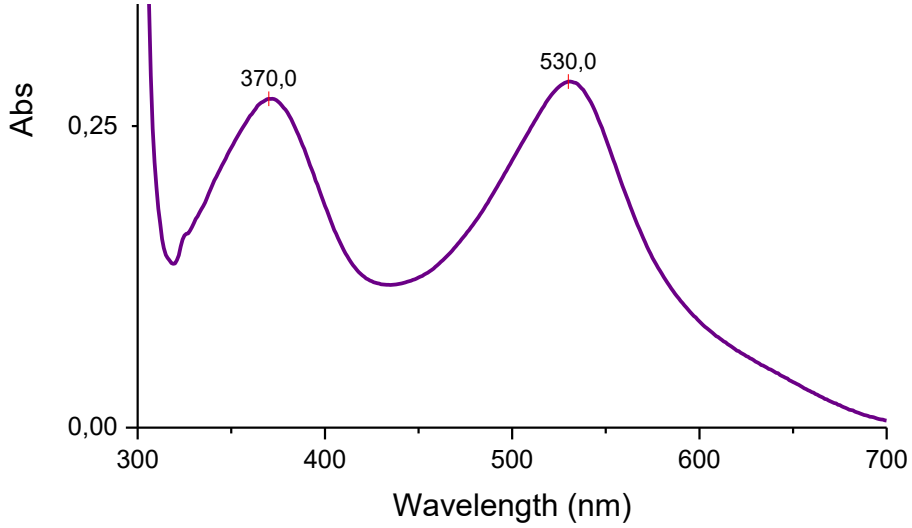

Figure A6.14. UV-vis spectrum in chloroform of [Ru(bpy)$_2$(η^2-mal)] (**47**).

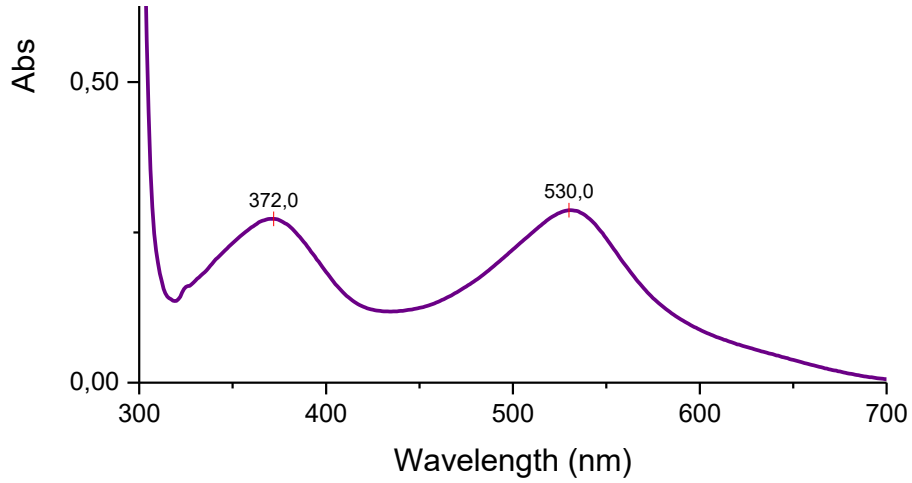

Figure A6.15. UV-vis spectrum in chloroform of [Ru(bpy)$_2$(η^2-acac)][PF_6] (**46**).

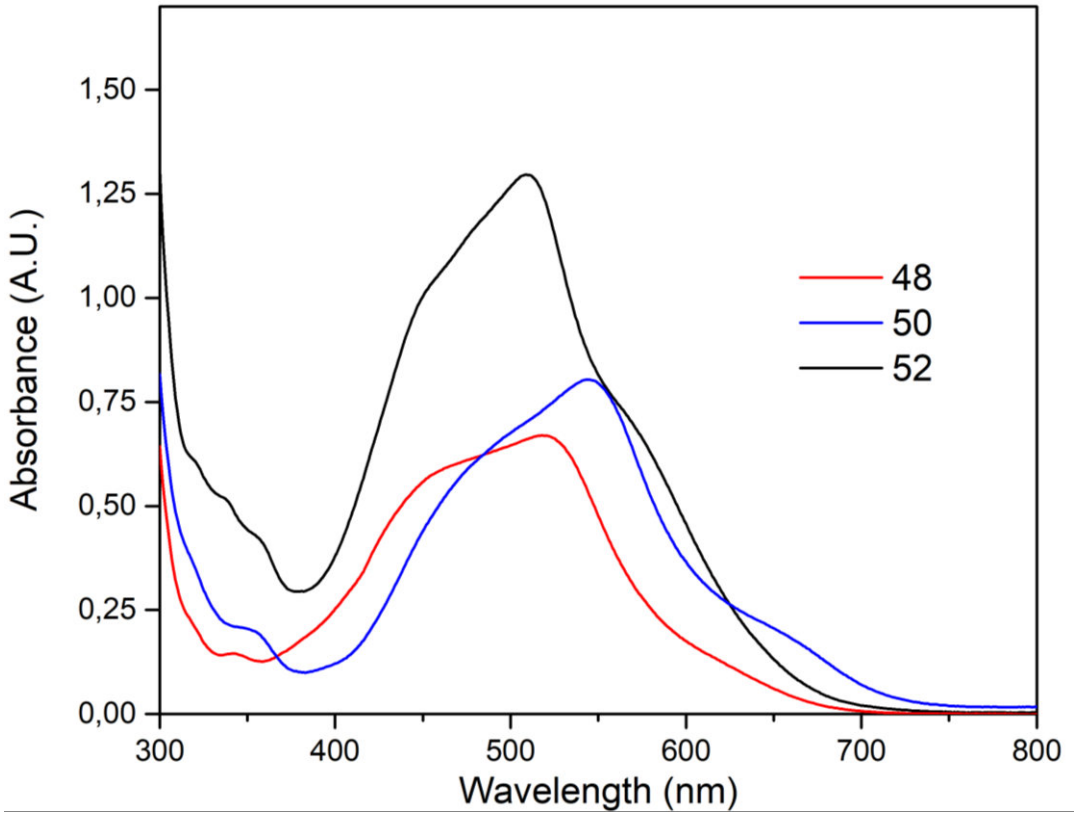

Figure 6.16. UV-vis spectrum in chloroform of [Ru(phen)$_2$(η^2-mal)] (**48**), [Ru(phen)$_2$(η^2-ox)] (**50**). [Ru(phen)$_2$(η^2-acac)][Cl] (**53**).

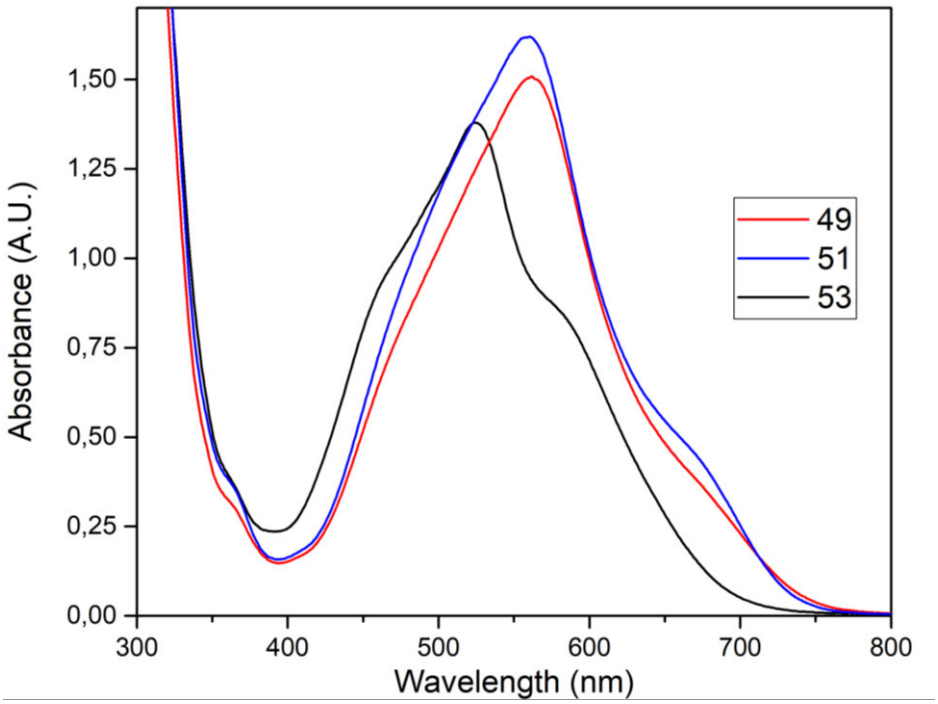

Figure A6.17 UV-vis spectrum in chloroform of [Ru(dpphen)$_2$(η^2-mal)] (**49**), [Ru(dpphen)$_2$(η^2-acac)][Cl] (**53**) and in [Ru(dpphen)$_2$(η^2-ox)] **51.**

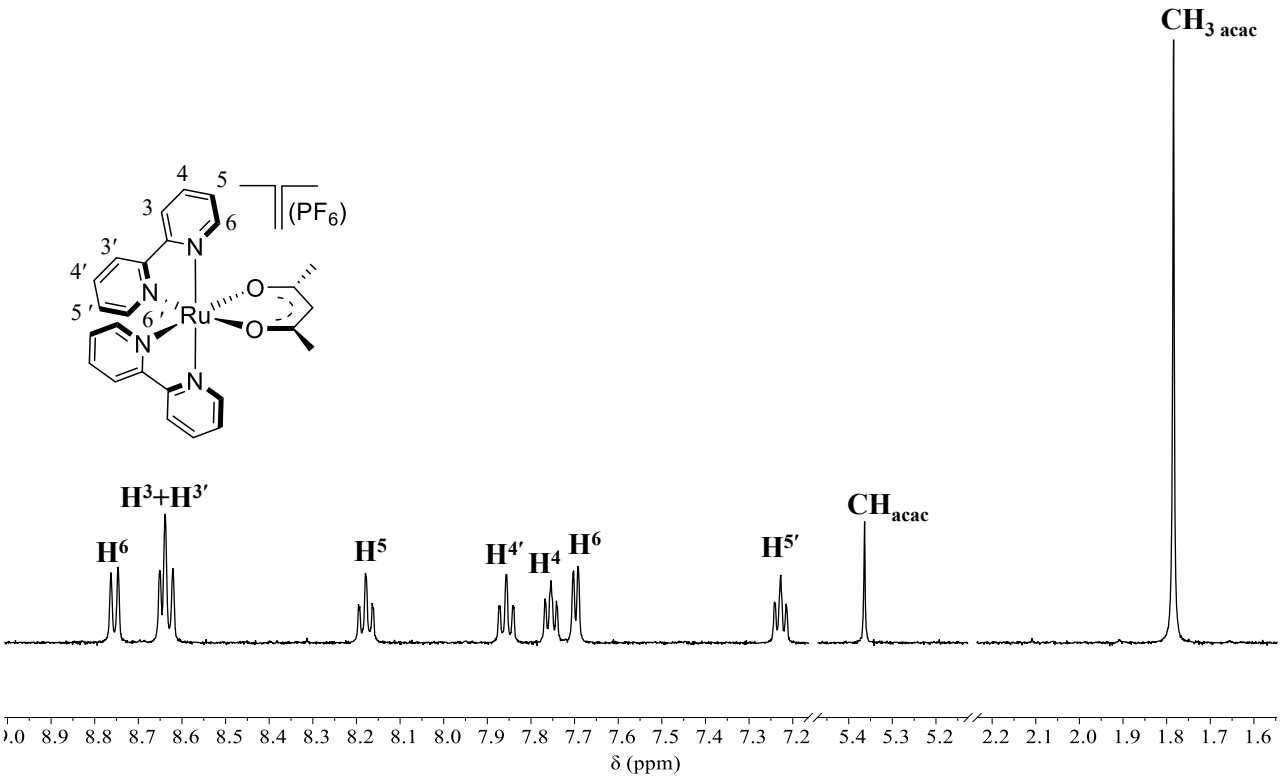

Figure A6.18. ^{1}H NMR spectrum (DMSO-d_6) of [Ru(bpy)$_2$(η^2-acac)][PF$_6$] (**46** with labeling scheme.

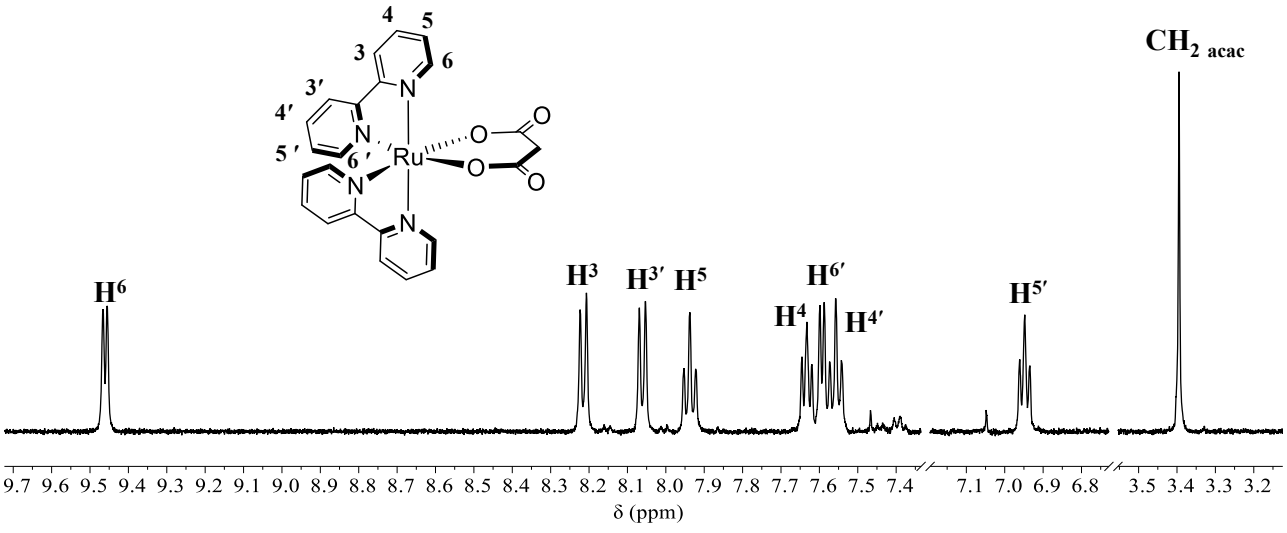

Figure A6.19. ^{1}H NMR spectrum (DMSO-d_6) of [Ru(bpy)$_2$(η^2-mal)] (**47**) with labeling scheme.

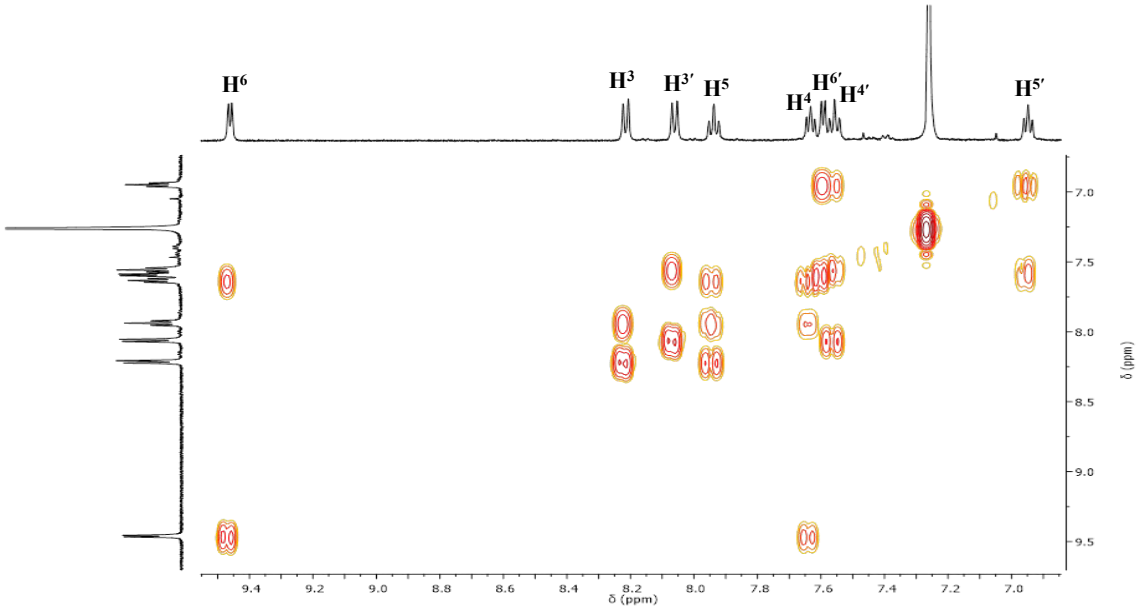

Figure A6.20. Downfield region of the H-H COSY spectrum ($CDCl_3$) of [Ru(bpy)$_2$(η^2-mal)] (**47**). See Figure A6.19 for labeling scheme.

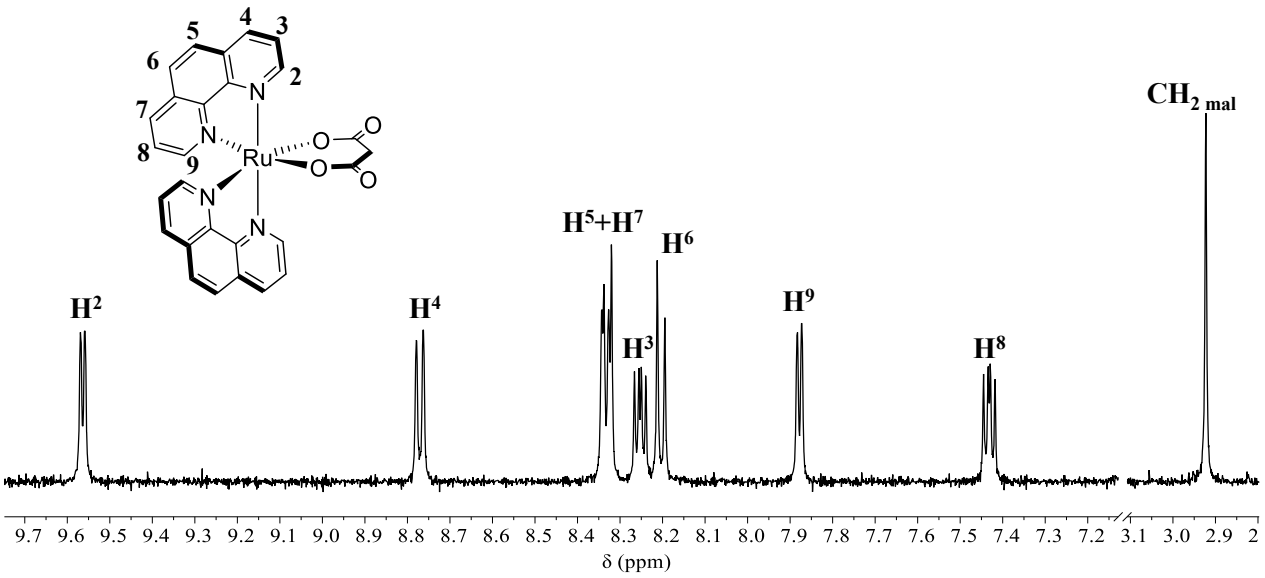

Figure A6.21. ^{1}H NMR spectrum (DMSO-d_6) of [Ru(phen)$_2$(η^2-mal)] (**48**) with labeling scheme. In the insert the resonance of malonate.

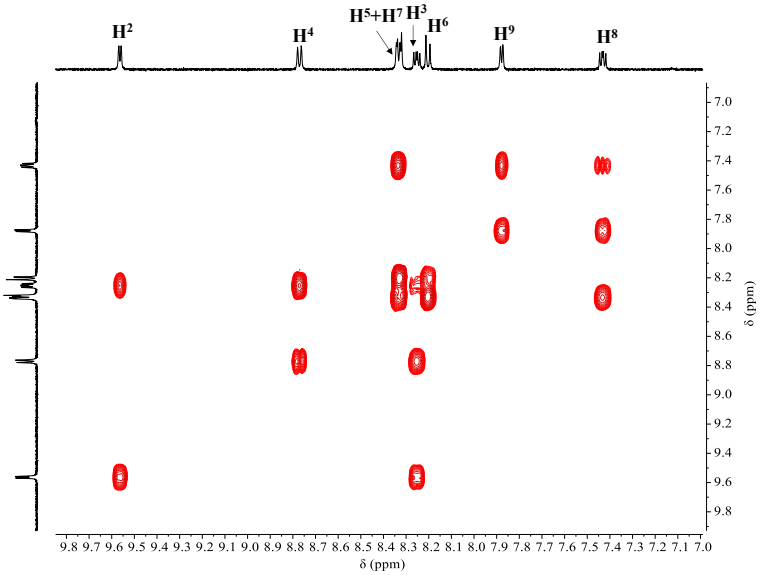

Figure A6.22. Downfield region of the H-H COSY spectrum (DMSO-d_6) of [Ru(phen)$_2$(η^2-mal)] (**48**); see Figure A6.21 for labeling scheme.

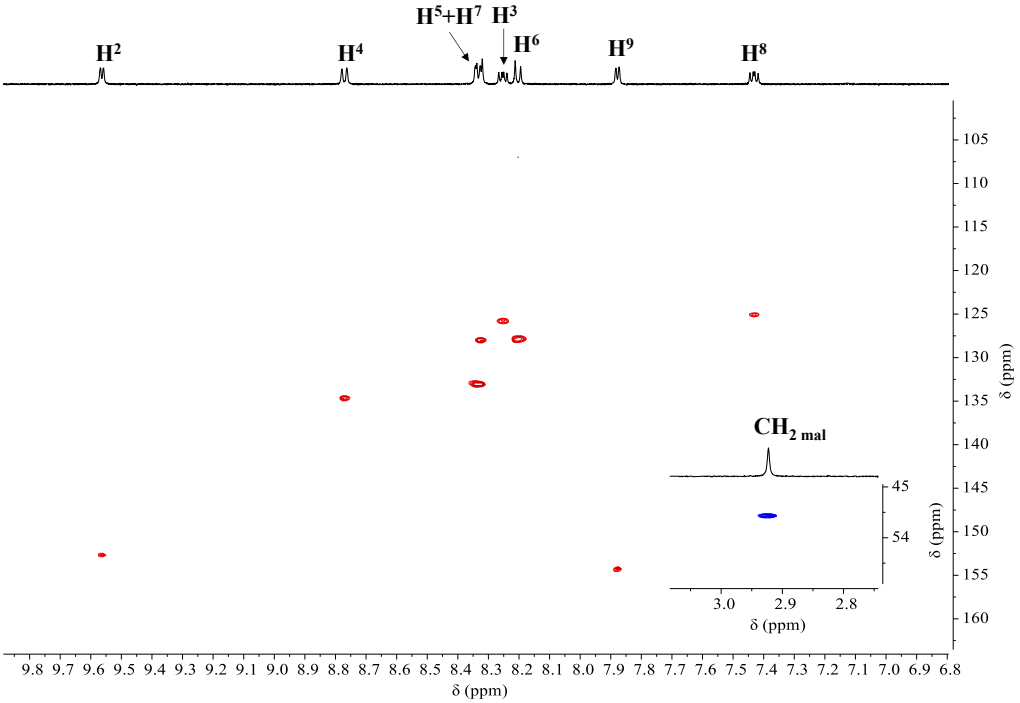

Figure A6.23. Downfield region of the HSQC spectrum (DMSO-d_6) of [Ru(phen)$_2$(η^2-mal)] (**48**); see Figure A6.21 for labeling scheme.

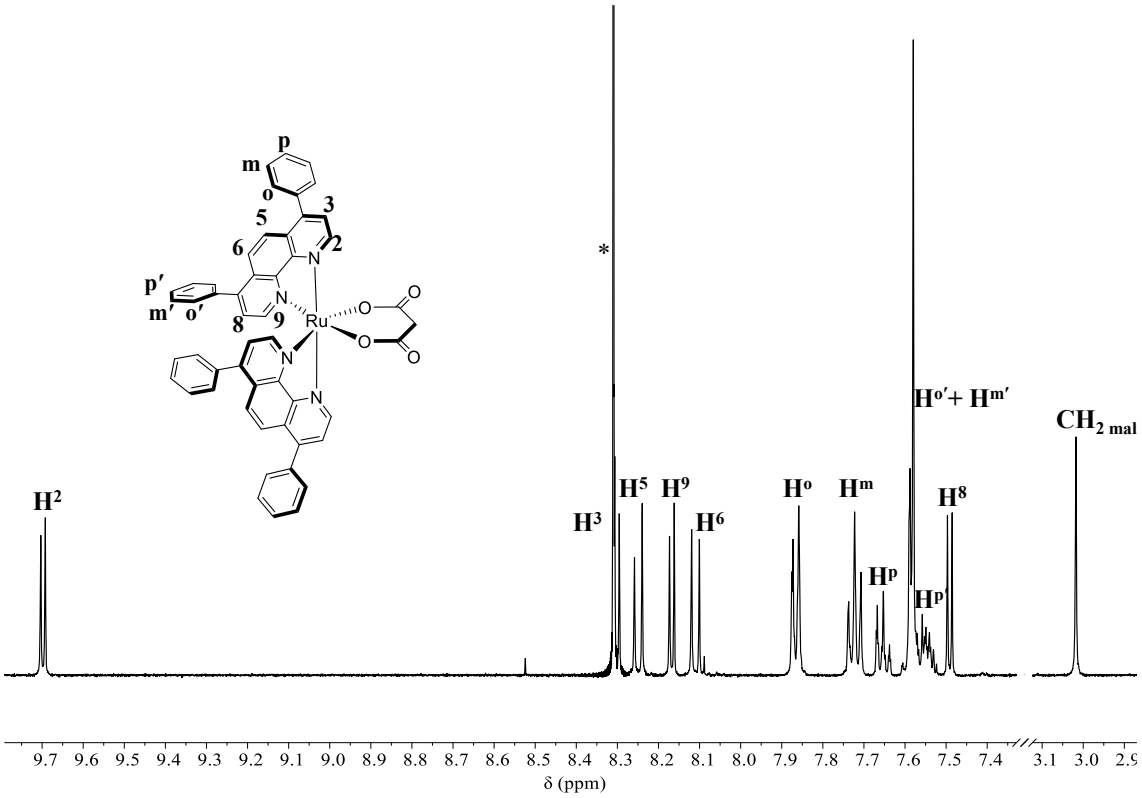

Figure A6.24. ^{1}H NMR spectrum (DMSO-d_6) of [Ru(dpphen)$_2$(η^2-mal)] (**49**) with labeling scheme. In the insert the resonance of malonate. The peak of residual chloroform is marked with an *.

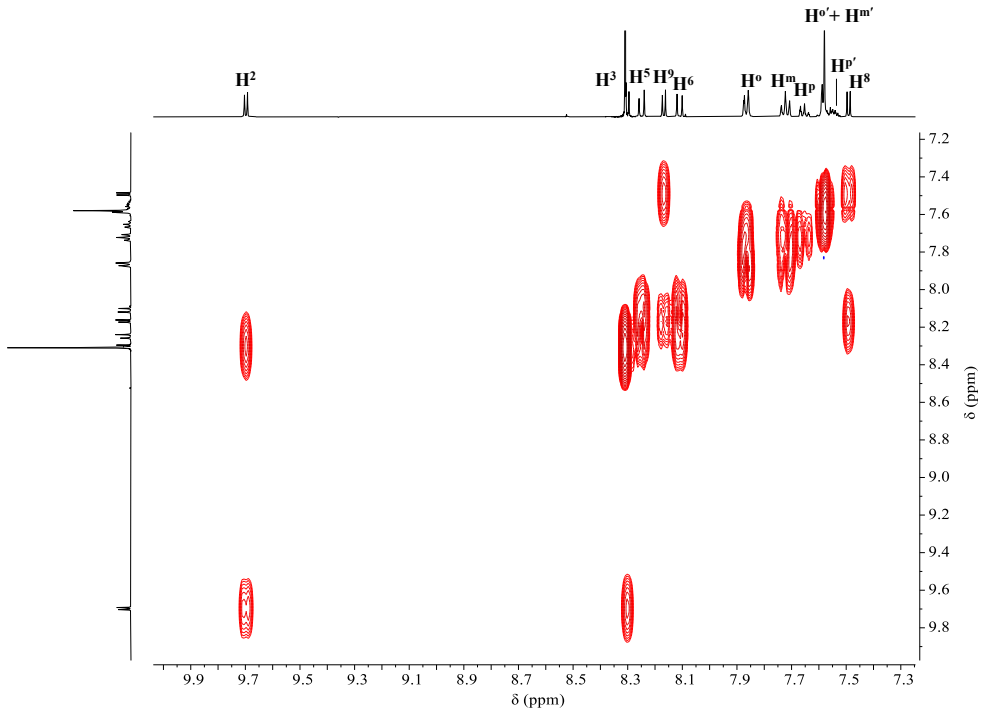

Figure A6.25. Downfield region of the H-H COSY spectrum (DMSO-d_6) of [Ru(dpphen)$_2$(η^2-mal)] (**49**) see Figure A6.24 for labeling scheme.

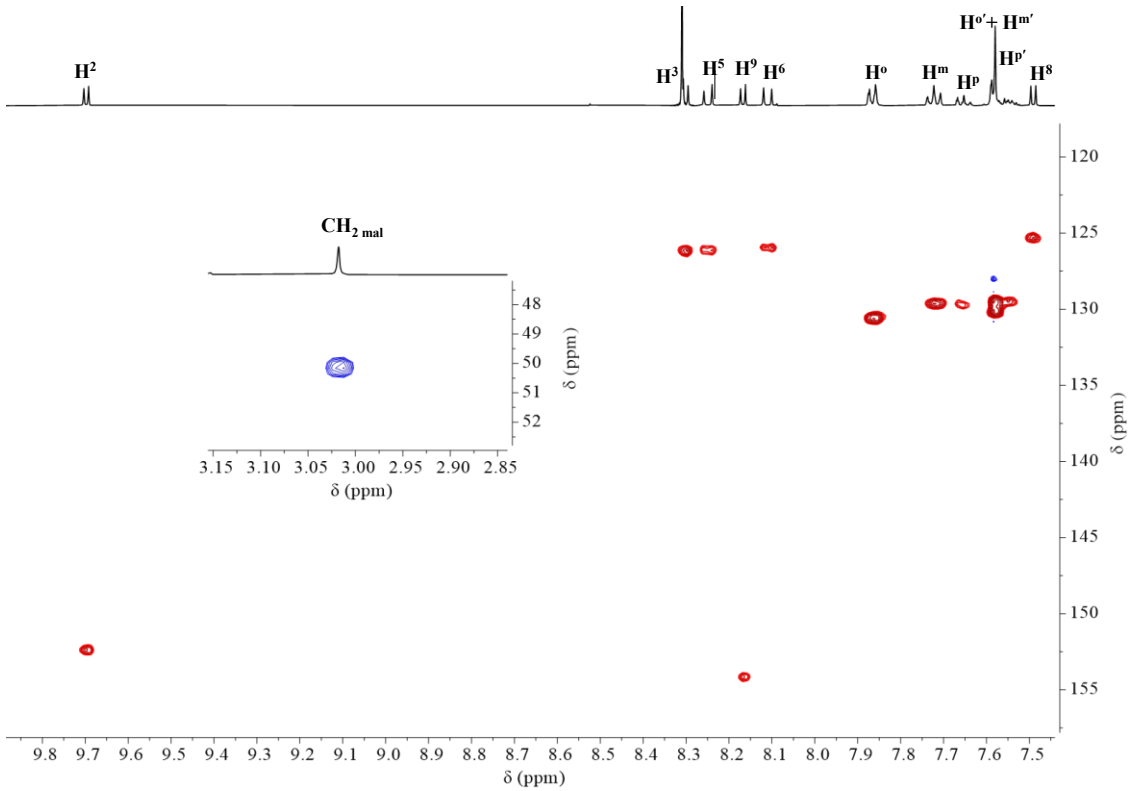

Figure A6.26. Downfield region of the HSQC spectrum (DMSO-d_6) of [Ru(dpphen)$_2$(η^2-mal)] (**49**) see Figure A6.24 for labeling scheme.

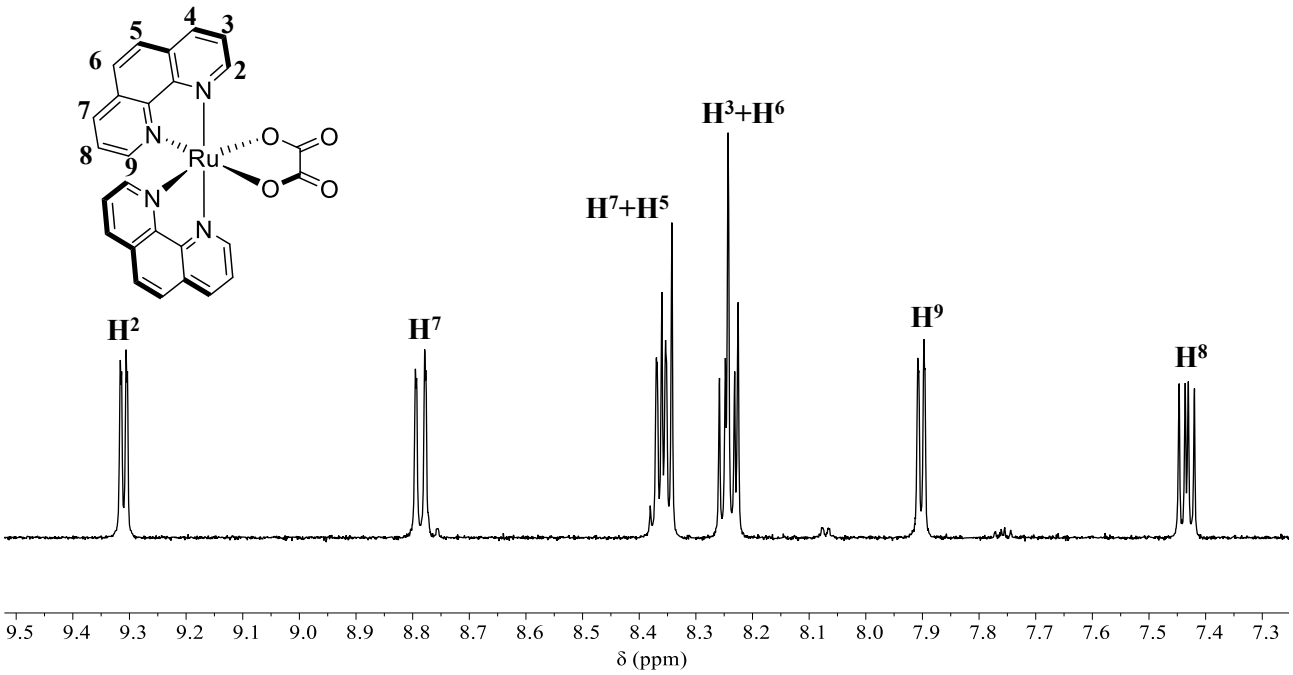

Figure A6.27. ^{1}H NMR spectrum (DMSO-d_6) of [Ru(phen)$_2$(η^2-ox)] (**50**) with labeling scheme.

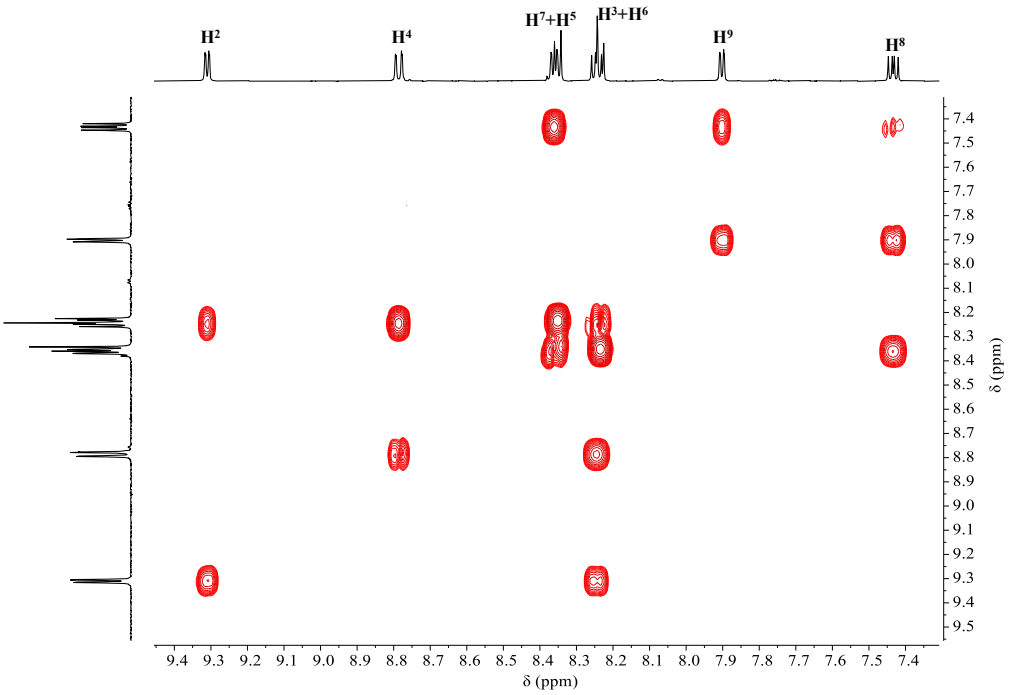

Figure A6.28. H-H COSY spectrum (DMSO-d_6) of [Ru(phen)$_2$(η^2-ox)] (**50**); see Figure A6.27 for labeling scheme.

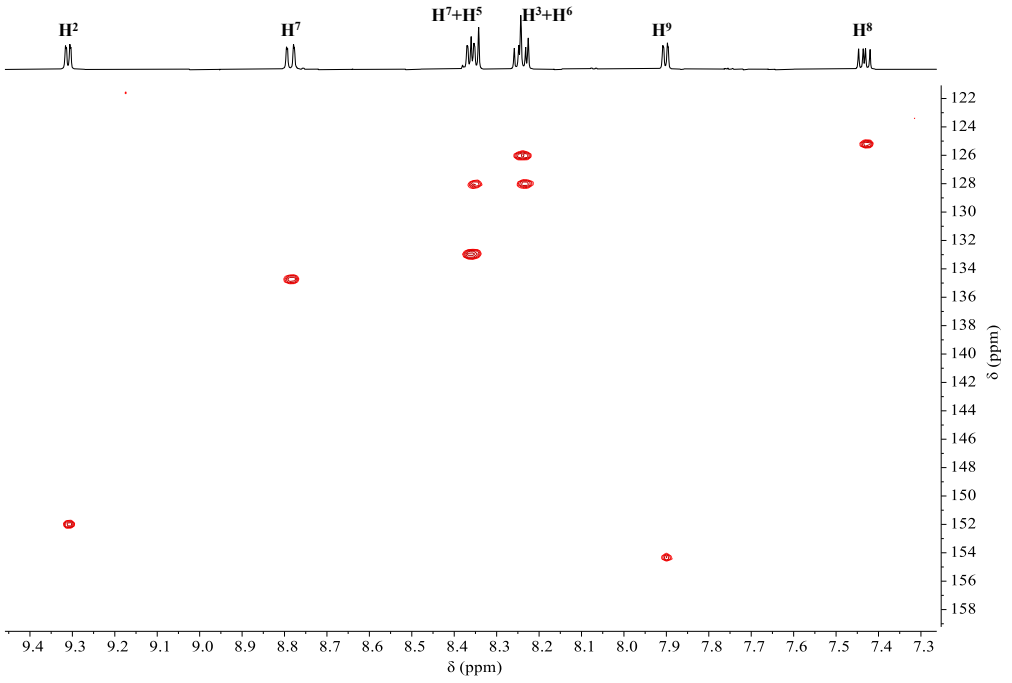

Figure A6.29. HSQC spectrum (DMSO-d_6) of [Ru(phen)$_2$(η^2-ox)] (**50**); see Figure A6.27 for labeling scheme.

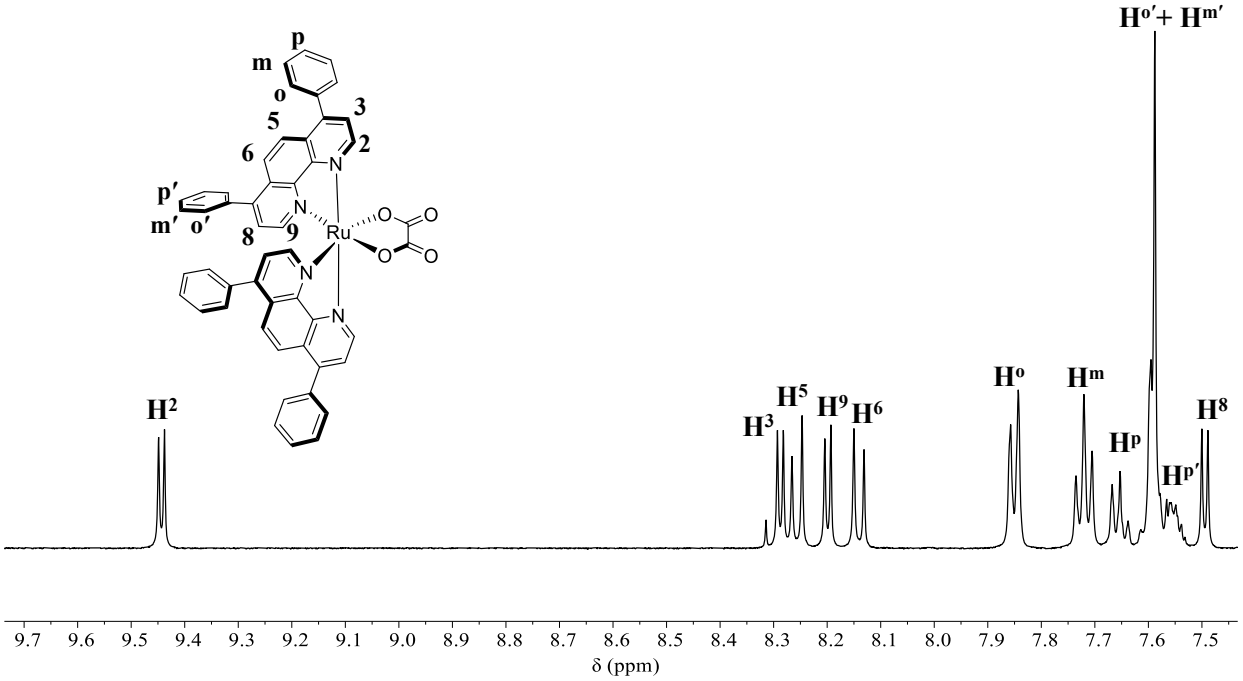

Figure A6.30. ^{1}H NMR spectrum (DMSO-d_6) of [Ru(dpphen)$_2$(η^2-ox)] (51) with labeling scheme.

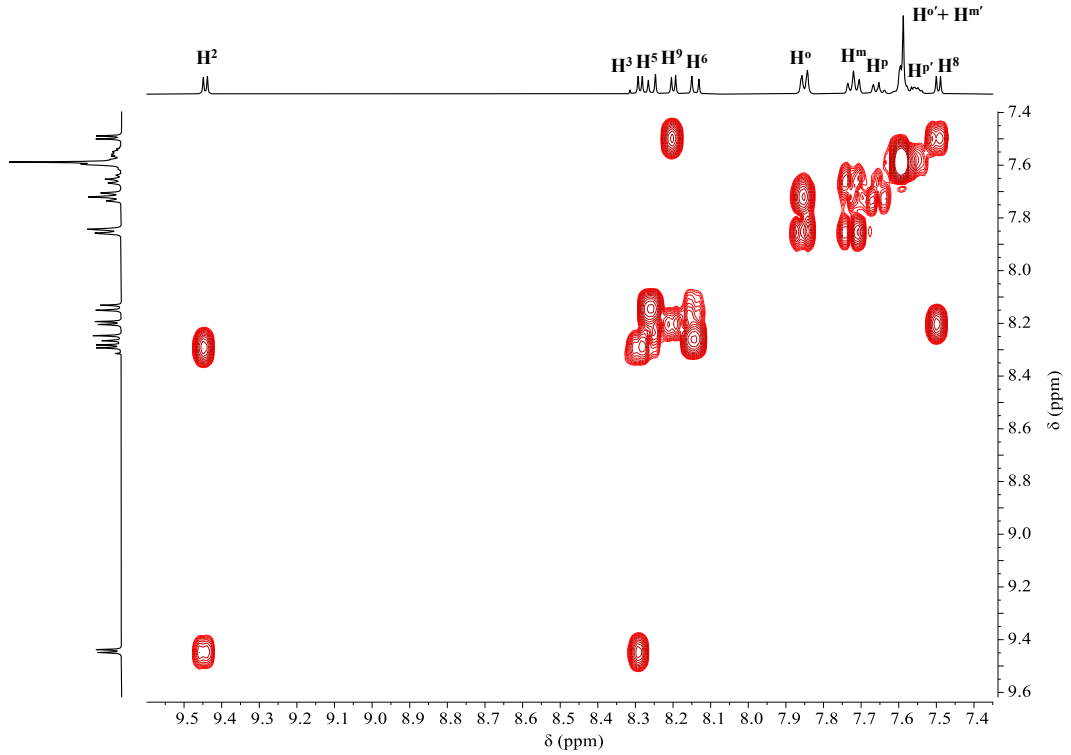

Figure A6.31. H-H COSY spectrum (DMSO-d_6) of [Ru(dpphen)$_2$(η^2-ox)] (**51**) see Figure A6.30 for labeling scheme.

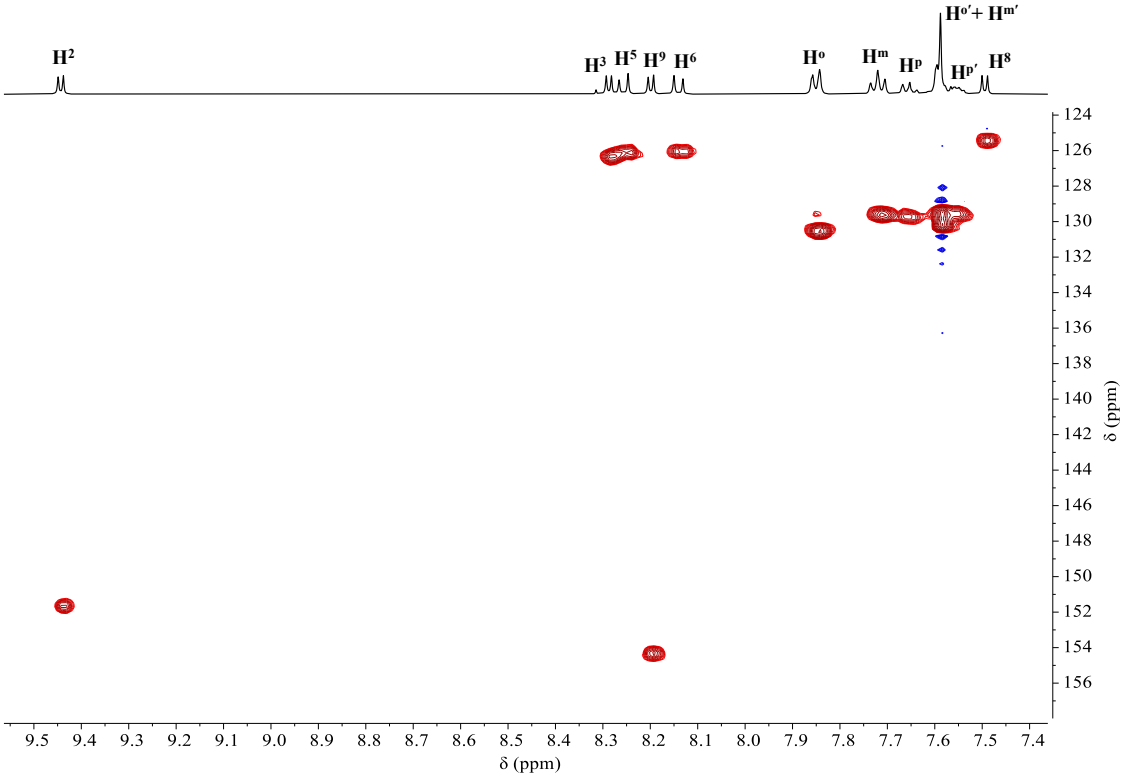

Figure A6.32. HSQC spectrum (DMSO-d_6) of [Ru(dpphen)$_2$(η^2-ox)] (**51**) see Figure A6.30 for labeling scheme.

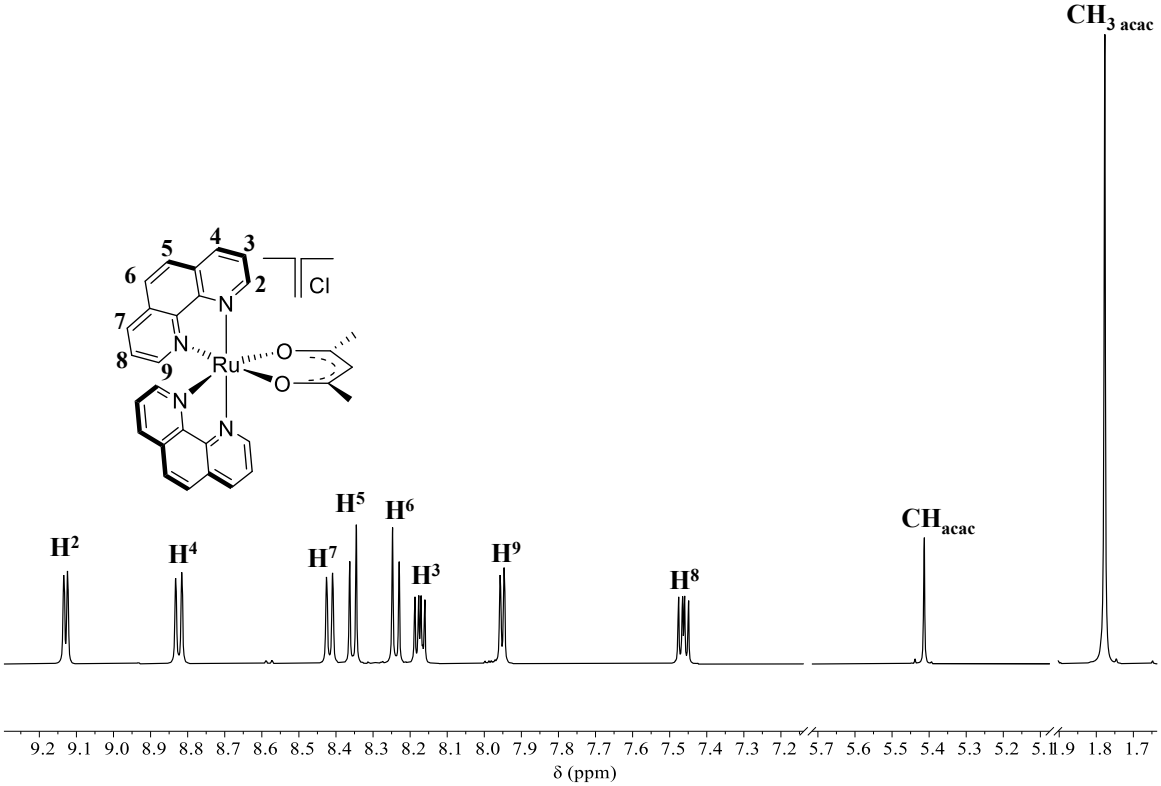

Figure A6.33. ^{1}H NMR spectrum (DMSO-d_6) of [Ru(phen)$_2$(η^2-acac)]Cl (**52**) with labeling scheme.

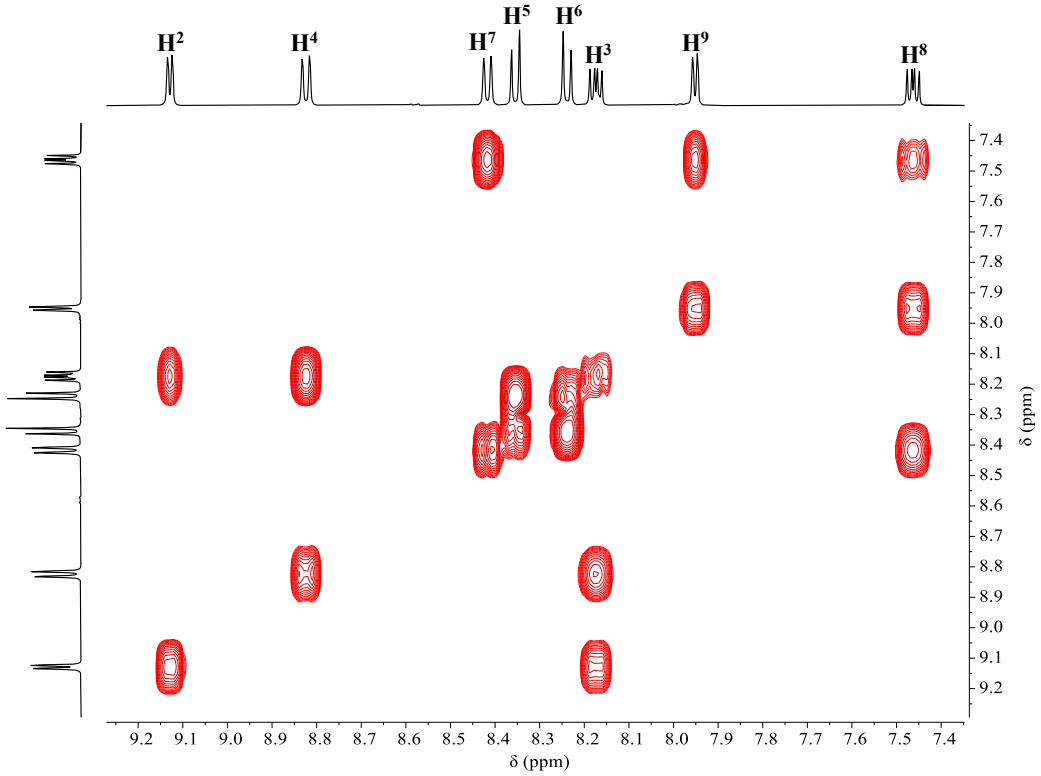

Figure A6.34. H-H COSY spectrum (DMSO-d_6) of [Ru(phen)$_2$(η^2-acac)]Cl (**53**); see Figure A6.33 for labeling scheme.

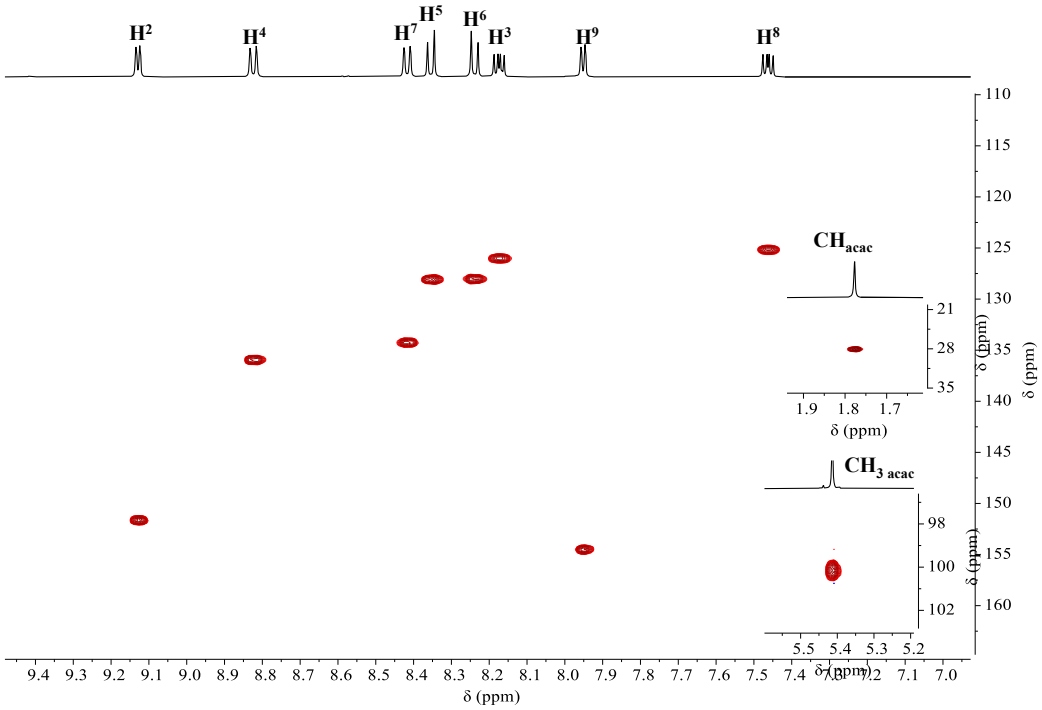

Figure A6.35. HSQC spectrum (DMSO-d_6) of [Ru(phen)$_2$(η^2-acac)]Cl (**53**); see Figure A6.33 for labeling scheme.

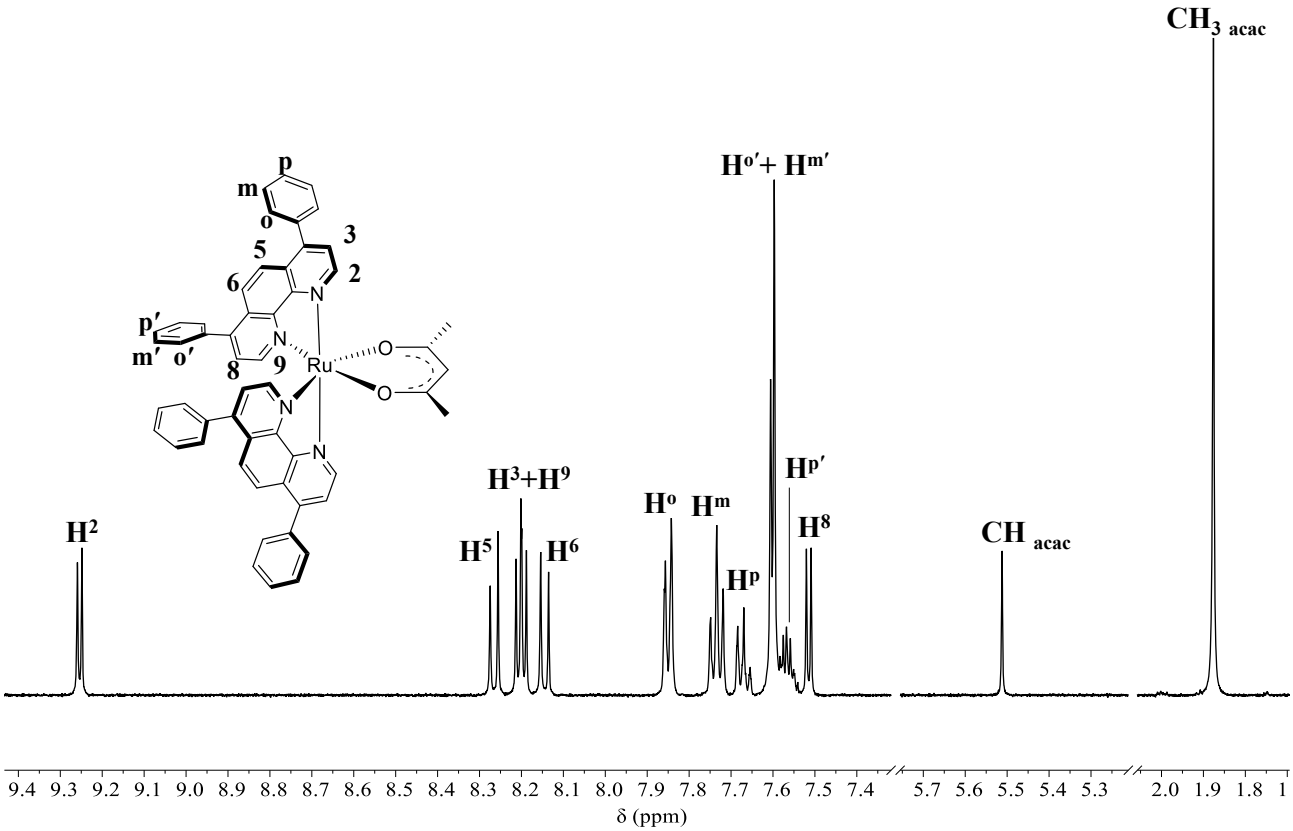

Figure A6.36. ^{1}H NMR spectrum (DMSO-d_6) of [Ru(dpphen)$_2$(η^2-acac)]Cl (**53**) with labeling scheme.

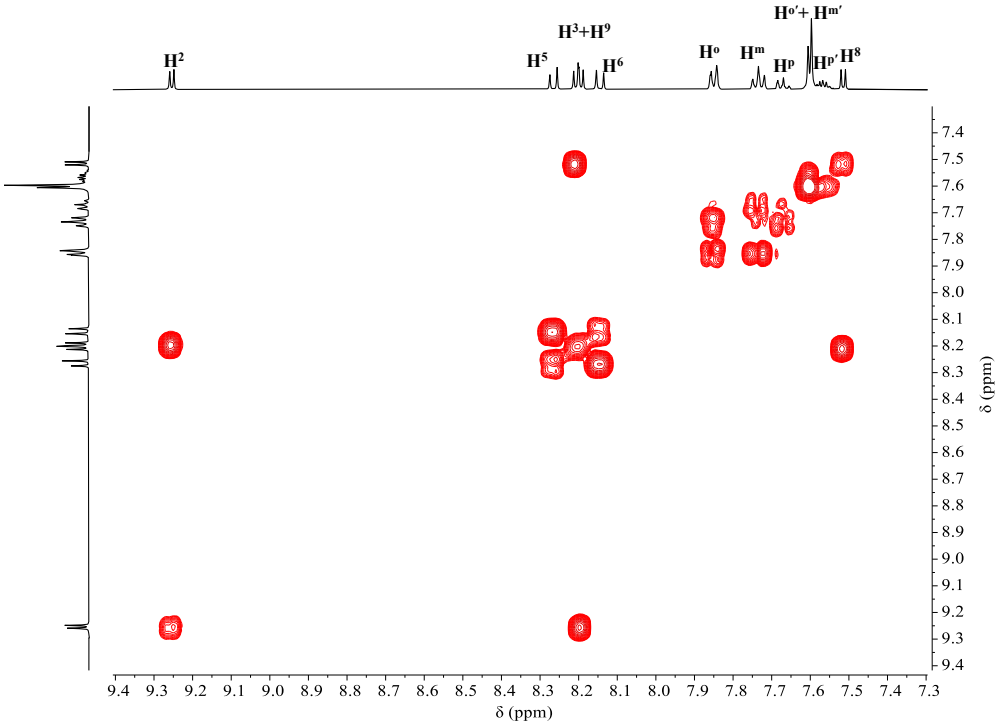

Figure A6.37. H-H COSY spectrum (DMSO-d_6) of [Ru(dpphen)$_2$(η^2-acac)]Cl (**53**); see Figure A6.36 for labeling scheme.

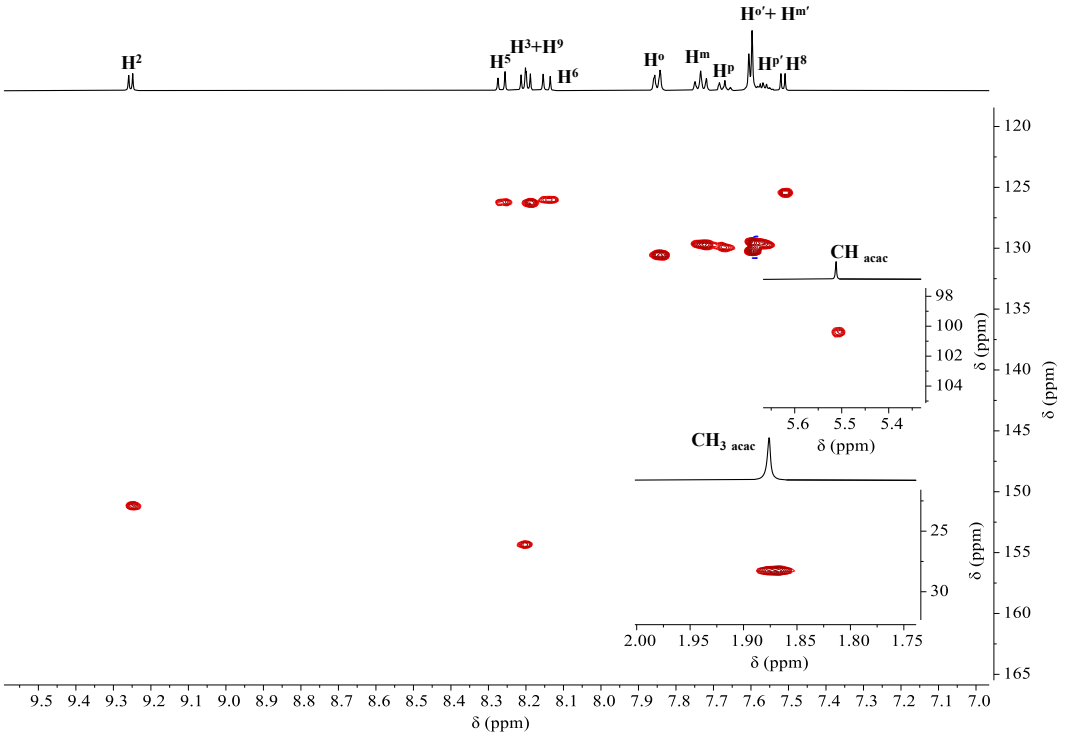

Figure A6.38. HSQC spectrum (DMSO-d_6) of [Ru(dpphen)$_2$(η^2-acac)]Cl (**53**); see Figure A6.38 for labeling scheme.

Spectral characterization of the bis-heteroleptic complexes [Ru(phen)$_2$(bpy)][PF$_6$]$_2$ (54) and [Ru(bpy)$_2$(phen)][PF$_6$]$_2$ (55).

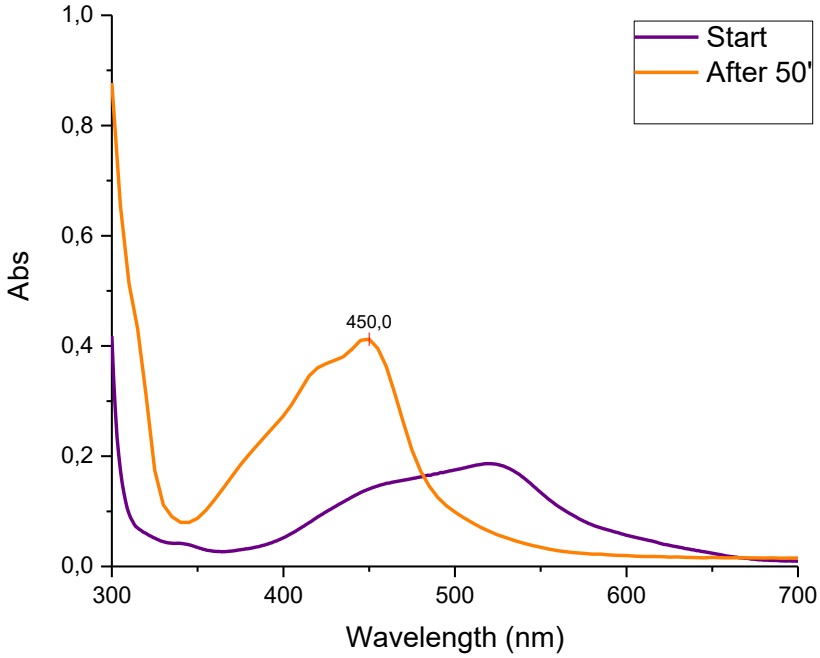

Figure A6.39. Spectral changes in the UV-vis spectrum during the reaction of [Ru(phen)$_2$(η^2-mal)] (**48**) (purple line) with one equiv. of bpy in refluxing EtOH + 10 equiv. of TFA to afford [Ru(phen)$_2$(bpy)]$^{2+}$ quantitatively in ca. 1h (orange line).

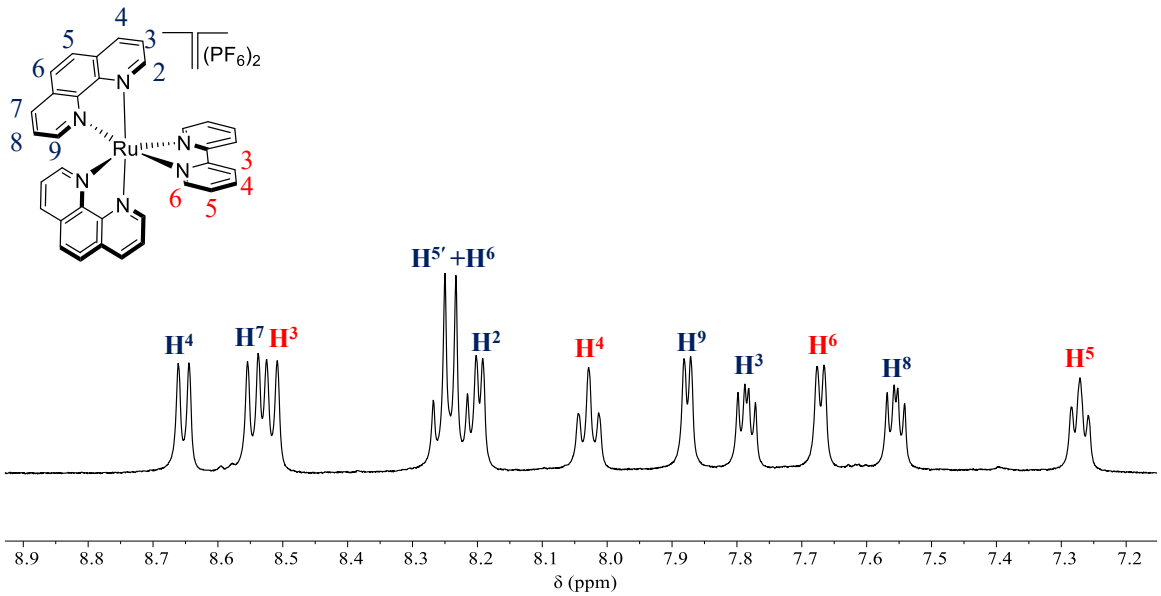

Figure A6.40. ^{1}H NMR spectrum (CD_3CN) of $[Ru(phen)_2(bpy)][PF_6]_2$ (**54**) with labelling scheme (blue for phen, red for bpy).

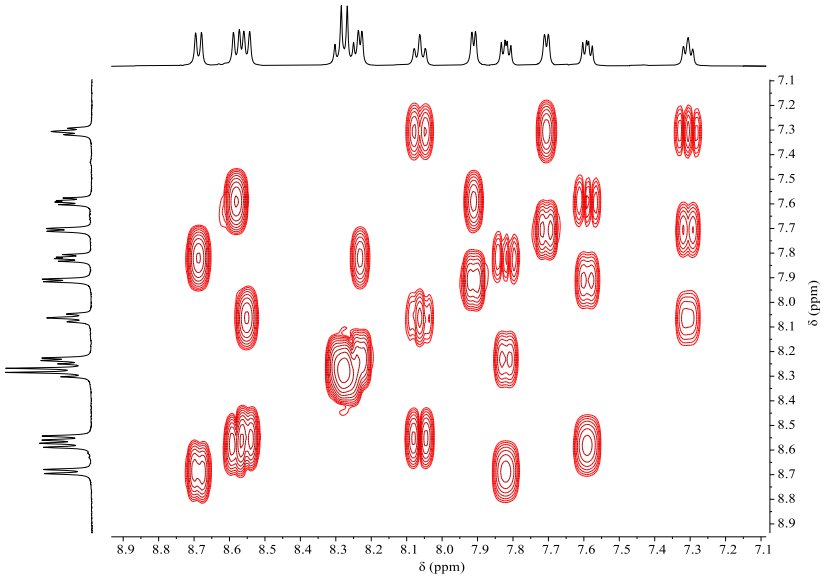

Figure A6.41. H-H COSY spectrum of (CD_3CN) of $[Ru(phen)_2(bpy)][PF_6]_2$ (**54**); see Figure A6.40 for labelling scheme.

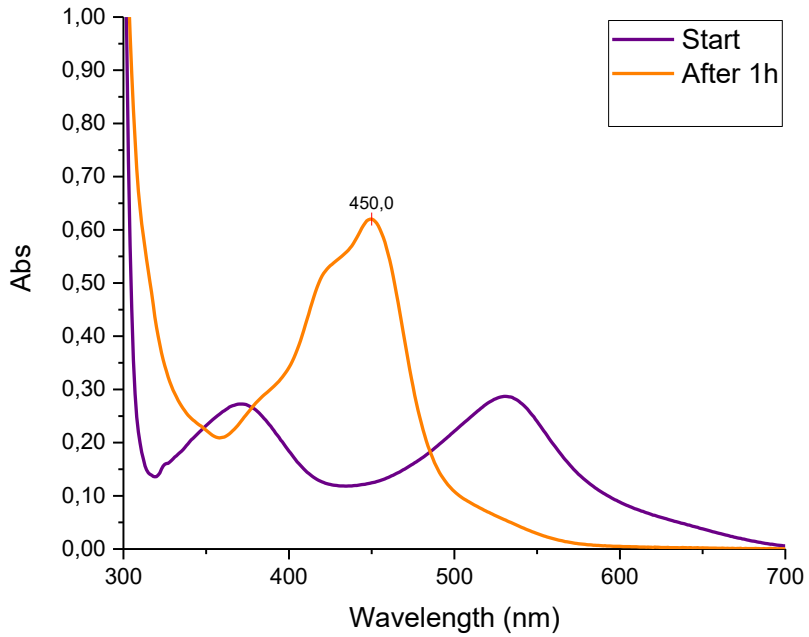

Figure A6.42. Spectral changes in the UV-vis spectrum during the reaction of $[Ru(bpy)_2(\eta^2\text{-mal})]$ (**47**) (purple line) with one equiv. of phen in refluxing EtOH + 10 equiv. of TFA to afford $[Ru(bpy)_2(phen)]^{2+}$ quantitatively in ca. 1h (orange line).

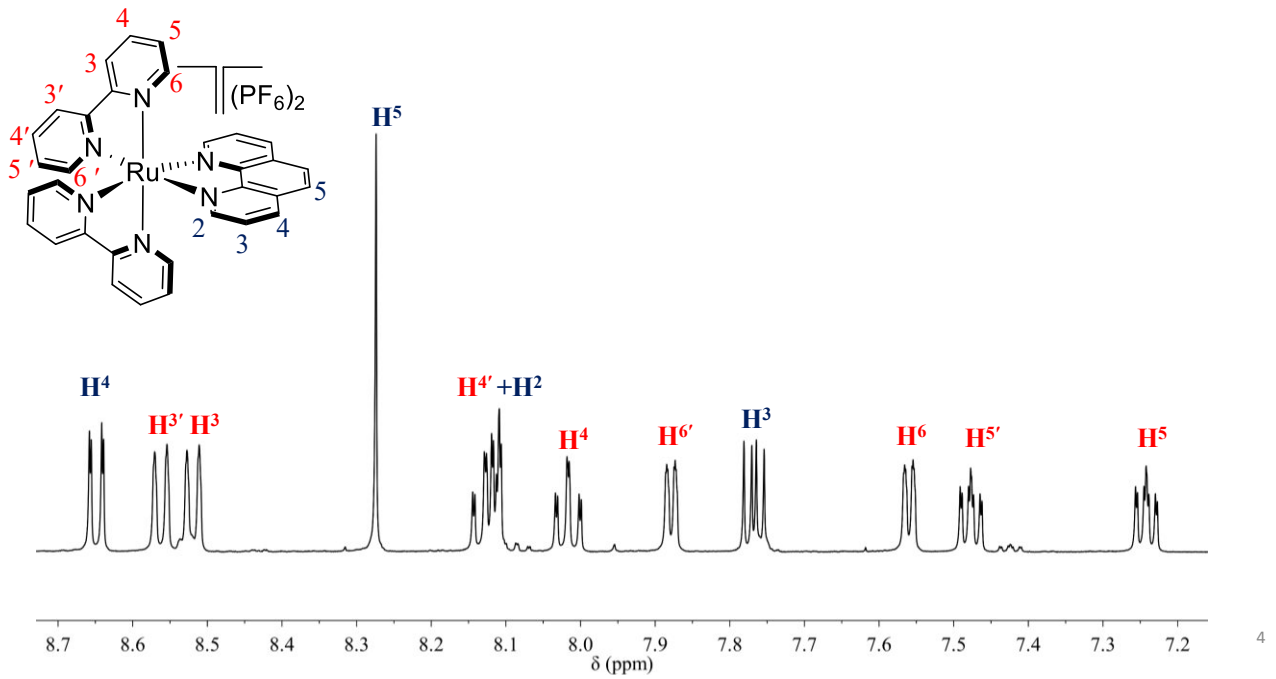

Figure A6.43. ^{1}H NMR spectrum (CD_3CN) of $[Ru(bpy)_2(phen)][PF_6]_2$ (**55**) with labelling scheme (p stands for phen, b for bpy).

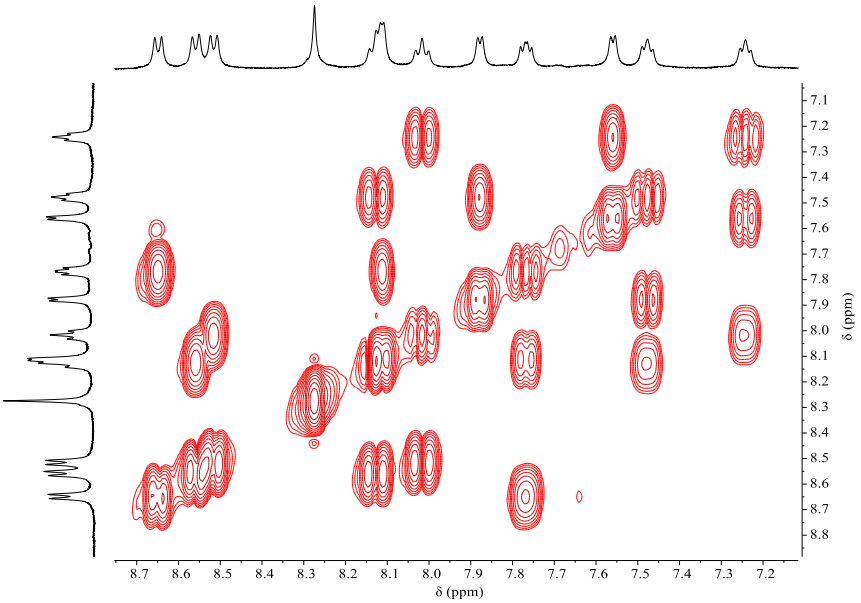

Figure A6.44. H-H COSY spectrum of (CD_3CN) of $[Ru(bpy)_2(phen)][PF_6]_2$ (**55**); see Figure A6.43 for labelling scheme.

Table A6.6. Crystallographic data and refinement details for compounds *fac*-[RuCl(dmso-S)$_3$(η^2-acac)] (**44**), *fac*-[Ru(dmso-O)(dmso-S)$_3$(η^2-acac)][PF_6] (**45**), and *cis,trans*-[$RuCl_2$(dmso-S)$_2$(phen)] (**c**). [Ru(phen)$_2$(η^2-mal)].

	44	**45**	**c**
Empirical Formula	$C_{11}H_{25}ClO_5RuS_3$	$C_{13}H_{31}F_6O_6PRuS_4$	$C_{16}H_{20}Cl_2N_2O_2RuS_2$
Formula weight (Da)	470.01	657.66	508.43
Temperature (K)	100(2)	100(2)	100(2)
Wavelength (Å)	0.700	0.700	0.700
Crystal system	monoclinic	monoclinic	monoclinic
Space Group	P 21/n	P 21/c	P 21/c
a (Å)	8.356(2)	12.435(3)	16.164(7)
b (Å)	14.6850(7)	11.338(1)	19.153(9)
c (Å)	14.9920(6)	17.750(1)	13.189(3)
α (°)	90	90	90
β (°)	95.60(1)	91.79(2)	107.54(2)
γ (°)	90	90	90
V (Å^3)	1830.9(3)	2501.3(8)	3893(3)
Z	4	4	8
ρ (g·cm^{-3})	1.705	1.746	1.735
F(000)	960	1336	2048
μ (mm^{-1})	1.285	1.036	1.237
θ min, max (°)	1.916, 28.227	1.614, 29.998	1.301, 28.227
Resolution (Å)	0.74	0.70	0.74
Total refl. collctd	29469	89392	61622
Independent refl.	4676	7573	9911
Obs. Refl. [Fo>4σ(Fo)]	4673	7517	9898
I/σ(I) (all data)	63.33	45.80	62.71
I/σ(I) (max res)	49.75	34.68	53.01
Completeness (all data)	0.985	0.988	0.982
R_{merge} (all data)	2.0%	4.0%	2.4%
R_{merge} (max res)	2.0%	3.5%	2.7%
Multiplicity (all data)	6.2	11.5	6.1
Multiplicity (max res)	6.1	9.7	5.8
Data/restraint/parameters	4676/0/191	7573/0/291	9911/0/452
GooF	1.136	1.069	1.166
R[I>2.0σ(I)],[a] wR2 [I>2.0σ(I)][a]	0.0230, 0.0561	0.0306, 0.0816	0.0216, 0.0554
R (all data),[a] wR2 (all data)[a]	0.0230, 0.0561	0.0308, 0.0818	0.0217, 0.0554

Table A6.6 contd. Crystallographic data and refinement details for $[Ru(phen)_2(\eta^2\text{-mal})]\cdot 5H_2O$ (**48**$\cdot 5H_2O$)

	10$\cdot 5H_2O$
Empirical Formula	$C_{27}H_{18}N_4O_4Ru\cdot 5H_2O$
Formula weight (Da)	1307.20
Temperature (K)	100(2)
Wavelength (Å)	0.700
Crystal system	triclinic
Space Group	P –1
a (Å)	10.322(3)
b (Å)	10.569(2)
c (Å)	13.064(3)
α (°)	84.832(6)
β (°)	76.176(8)
γ (°)	72.432(5)
V ($Å^3$)	1319.1(5)
Z	1
ρ ($g\cdot cm^{-3}$)	1.646
F(000)	668
μ (mm^{-1})	0.624
θ min, max (°)	1.581, 28.227
Resolution (Å)	0.74
Total refl. collctd	6720
Independent refl.	6720
Obs. Refl. [Fo>4σ(Fo)]	6575
I/σ(I) (all data)	46.09
I/σ(I) (max res)	37.72
Completeness (all data)	0.989
R_{merge} (all data)	3.2%
R_{merge} (max res)	4.1%
Multiplicity (all data)	6.0
Multiplicity (max res)	5.6
Data/restraint/parameters	6720/17/327
GooF	1.072
R[I>2.0σ(I)],[a] wR2 [I>2.0σ(I)][a]	0.0459, 0.1531
R (all data),[a] wR2 (all data)[a]	0.0464, 0.1536